UNIVERSITE DE BOURGOGNE

UFR des Sciences de Santé

THÈSE

Pour obtenir le grade de

Docteur de l'Université de Bourgogne

Discipline :

Sciences de la vie

par

Ange-Line Bruel

21 Septembre 2016

Identification des bases moléculaires et physiopathologiques des syndromes oro-facio-digitaux

Directeur de thèse
Pr Christel Thauvin-Robinet

Co-directeur de thèse
Dr Laurence Jego
Dr Jean-Baptiste Rivière

Jury

Pr Faivre Laurence, Président

Pr Thauvin-Robinet Christel, Directeur de thèse

Dr Saunier Sophie, Rapporteur

Pr Geneviève David, Rapporteur

Pr Attié-Bittach Tania, Examinateur

A ma famille

Remerciements

Je voudrais remercier en premier lieu Laurence Faivre, de m'avoir accueillie au sein du laboratoire Génétique des Anomalies du Développement, pour l'intérêt porté à mes travaux et pour son soutien.

Toute ma reconnaissance va naturellement à Christel Thauvin-Robinet qui a encadrée cette thèse. Merci de m'avoir donnée cette chance de participer à ce beau projet, d'apprendre et d'évoluer au cours de ces trois dernières années. Merci pour ta confiance, ta disponibilité et tes encouragements.

Je remercie également mes deux co-directeurs de thèse : Laurence Jego pour avoir veillée au bon déroulement de ces trois années, et Jean-Baptiste Rivière pour m'avoir fait découvrir le monde du SHD.

Je souhaite remercier les rapporteurs de cette thèse, David Geneviève, Tania Attié-Bitach et Sophie Saunier pour avoir accepté de lire ce manuscrit durant l'été.

Cette thèse est aussi le fruit de nombreuses collaborations nationales et internationales, je tiens donc à remercier tous les collaborateurs qui ont participé à ce travail, ainsi que les patients et leurs familles.

Rien n'aurait été pareil sans la bonne entente qui règne dans l'équipe, je tiens donc à remercier toutes les personnes qui m'ont côtoyée quotidiennement:
Julien Thevenon, pour m'avoir entrainée dans tous ces projets « hors thèse » et toute l'aide qui tu as pu m'apporter,
Yannis Duffourd et Emilie Tisserant, pour votre indispensable savoir en bio-informatique,
L'équipe des techniciens, Charlotte Poë, Judith St-Onge, Thibaut Jouan, Martin Chevarin et Nadège Gigot, pour tous les précieux coups de main dans les manips,
Les post-docs, thésards, étudiants et voisins de bureau, Virginie Carmignac, Mirna Assoum, Romain Da Costa, Arthur Sorlin, Alexia Cossard, Aurélie Boucharny, Mathilde Lefebvre, Paul Kuentz, Sophie Nambot, Antonio Vitobello, pour votre bonne humeur communicative, ainsi que tous les stagiaires qui sont venus gonfler les rangs, le temps de quelques mois.

L’ensemble des cliniciens, internes et personnels administratifs pour leur travail,
Je remercie également Patrick Callier et l’ensemble de l’équipe de biologie moléculaire et cytogénétique du PTB pour leur aide et leur sympathie.

J’adresse aussi une pensée à mes anciens directeurs de stage, Sylvie Mazoyer et Khaled Bouhouch, qui m’ont fait découvrir le monde de la recherche et poussé à poursuivre dans cette voie.

Ces trois années n’auraient pas eu la même saveur sans l’aventure Expérimentarium. Merci à Lionel Maillot, Coralie Biguzzi ainsi que les doctorants dijonnais pour les ateliers Expé, les apéros et les soirées restos que l’on a passé ensemble.

Un grand merci également à ma famille :
A mon petit frère, Benjamin, pour tous nos moments de complicité et de chamaillerie qui, je crois, ne cesseront jamais !
A mes parents, Marie-Claire et Patrick, pour avoir cru en moi, pour votre soutien indéfectible et votre disponibilité au cours de toutes ces années. C’est grâce à vous si j’ai pu en arriver là aujourd’hui, merci infiniment.
A mes grands-parents, Aline et Christian, Annie et René, et mon arrière-grand-mère, Gisèle.
A mes cousins, Renaud, Guillaume, Marline, Anna, Bérengère, Sylvain, Lucie, Elinah, Ayden, Raphael et Louane, pour tous les jeux, rires, … et chutes que l’on a partagé et qui ont marqués les annales familiales à jamais ; sans oublier les nouveaux membres Lucile et Virginie et la nouvelle génération Enoha et Gabriel qui font la joie de tous!
A Chantal, Jean-Marc, Joël, Valérie, Jacques, Philippe, Dominique et Marie-Nöelle, ainsi qu'à toute la famille pour tous ces bons moments partagés. Mention spéciale à Chantal et Jean-Marc pour avoir suivi de très très près mon parcours.

Je souhaite remercier tous mes amis d’Auvergne ou d’ailleurs, la promo M2GP 2013 et les thésards clermontois pour tous les weekends retrouvailles ainsi que les amis globe-trotteurs pour tous les séjours à l’autre bout du monde passés et à venir.

Enfin je remercie tous ceux qui ont suivi de près ou de loin cette thèse.

Résumé

Les syndromes oro-facio-digitaux (OFD) sont caractérisés par la présence d'une atteinte orale, faciale et digitale. Leur classification initiale en 13 sous-types, est basée principalement sur leur mode de transmission et leurs signes cliniques associés (malformations cérébrales, rénales, dysplasie osseuse, atteinte rétinienne). Pendant longtemps seul le gène *OFD1*, responsable du type I et codant pour une protéine centrosomale et du corps basal, était principalement connu, faisant suspecter l'implication du cil primaire dans les syndromes OFD. Des mutations ont été rapportées plus récemment dans les gènes *TMEM216*, *DDX59, SCLT1, TBC1D32* et *TCTN3* chez un ou deux patients. Dans le but d'identifier de nouveaux gènes impliqués dans ces syndromes, nous avons réalisé une stratégie de séquençage haut débit d'exome chez 24 patients. Cette stratégie a permis d'identifier 5 nouveaux gènes (*C2CD3*, *TMEM107*, *INTU*, *KIAA0753, IFT57),* d'étendre aux syndromes OFD le spectre clinique de 3 gènes déjà connus dans d'autres ciliopathies (*C5orf42*, *TMEM138*, *TMEM231*) et de confirmer l'implication de 3 gènes déjà connus comme responsable de syndrome OFD (*OFD1*, *DDX59, WDPCP*). Les analyses fonctionnelles ont montré l'implication de la croissance centriolaire, de la zone de transition et du transport intraflagellaire, avec notamment la caractérisation de 3 complexes protéiques principaux : le complexe ternaire KIAA0753/OFD1/FOPNL, régulant la croissance centriolaire, le complexe MKS (TMEM107, TMEM231, TMEM216) constituant majeur de la zone de transition et le complexe CPLANE (INTU/FUZ/WDPCP), favorisant l'assemblage des protéines périphériques du complexe de transport intraflagellaire IFT-A. En conclusion, cette étude, la plus importante consacrée aux syndromes OFD, démontre la très grande hétérogénéité clinique et génétique de ces syndromes, de même que de nombreux allélismes avec d'autres ciliopathies. Elle étend à 15 le nombre de gènes causaux, rendant la classification clinique initiale de 13 sous-types totalement obsolète et permettant de considérer les syndromes OFD comme un nouveau sous-groupe de ciliopathies à part entière.

Mots-clés : Syndromes oro-facio-digitaux, séquençage haut-débit

Abstract

Oral-facial-digital syndromes (OFDS) are characterized by the association of oral, facial and digital anomalies. The different modes of inheritance and additional features lead to clinically delineate 13 subtypes. For a long time, only the *OFD1* gene, responsible for OFDI subtype and coding for a centrosomal protein, has been known, suggesting the involvement of the primary cilium in OFDS. Mutations have recently been reported in the *TMEM216*, *DDX59*, *SCLT1*, *TBC1D32* and *TCTN3* genes in anecdotic cases. To identify new genes involved in OFDS, we performed whole-exome sequencing in 24 patients. In 14/24 cases, we identified 5 novel genes (*C2CD3*, *TMEM107*, *INTU*, *KIAA0753, IFT57),* enlarged the clinical spectrum of OFDS of 3 known genes responsible for other ciliopathies (*C5orf42*, *TMEM138*, *TMEM231*) and confirmed the involvement of 3 known genes in OFDS (*OFD1*, *DDX59, WDPCP*). Functional studies demonstrated the involvement of the centriolar growth, the transition zone and the intraflagellar transport, through the characterization of 3 major protein complexes: the KIAA0753/OFD1/FOPNL complex controlling the centriole elongation, the MKS module (TMEM107/TMEM231/TMEM216), an essential component of the transition zone, and the CPLANE complex (INTU/FUZ/WDPCP) enabling in the IFT-A assembly.

We demonstrated the large clinical and genetic heterogeneity of OFDS, yielding the initial classification in 13 subtypes obsolete, extending the number of 15 causal genes, and confirming OFDS as a new full subgroup of ciliopathies.

Keywords: Oral-facial-digital syndromes, whole-exome sequencing

Table des matières

Liste des tableaux

Liste des figures

Liste des annexes

Articles faisant l'objet de cette thèse

Wide genetic ciliary heterogeneity in OFD syndrome from centriolar elongation to intraflagellar transport: identification of 5 new causal genes and confirmation of allelism will other ciliopathies. J Med Genet. – Soumis

AL. Bruel, B. Franco, Y. Duffourd, J.Thevenon, L. Jego, E. Lopez, JF. Deleuze, D. Doummar, RH. Giles, CA. Johnson, MA. Huynen, V. Chevrier, L. Burglen, M. Morleo, I. Desguerres, G. Pierquin, B. Doray, B. Gilbert-Dussardier, B. Reversade, E. Steichen-Gersdorf, C. Baumann, I. Panigrahi, A. Fargeot-Espaliat, A. Dieux, A. David, A. Goldenberg, E. Bongers, D. Gaillard, J. Argente, B. Aral, N. Gigot, J. St-Onge, D. Birnbaum, SR. Phadke, V. Cormier-Daire, T. Eguether, GJ. Pazour, V. Herranz-Pérez, JS. Lee, L. Pasquier, P. Loget, S. Saunier, A. Mégarbané, O. Rosnet, MR. Leroux, JB. Wallingford, OE. Blacque, MV. Nachury, T. Attie-Bitach, JB Rivière, L. Faivre, C. Thauvin-Robinet.

Autosomal Recessive *IFT57* hypomorphic mutation cause ciliary transport defect in unclassified oral-facial-digital syndrome with short stature and brachymesophalangia. Clin Genet. 2016 Apr 7. doi: 10.1111/cge.12785

J. Thevenon, L. Duplomb, S. Phadke, T. Eguether, M. Avila, V. Carmignac, **AL. Bruel**, J. St-Onge, Y. Duffourd, GJ. Pazour, B. Franco, T. Attie-Bitach, A. Masurel-Paulet, JB. Rivière, V. Cormier-Daire, L. Faivre and C. Thauvin-Robinet.

OFIP/KIAA0753 forms a complex with OFD1 and FOR20 at pericentriolar satellites and centrosomes and is mutated in Oral-Facial-Digital Syndrome. Hum Mol Genet. 2016 Feb 1;25(3):497-513

AL. Bruel*, V. Chevrier*, B. Franco, JP. Vandam, F. Lembo, S. Audebert, E. Baudelet, Daniel Isnardon, A. Bole, M. Pierres, JP. Borg, J. Thevenon, L. Burglen, L. Faivre, JB. Rivière, M. Huijnen, D. Birnbaum, O. Rosnet, C. Thauvin-Robinet.

TMEM107 recruits ciliopathy proteins to anchored ring-like subdomains of the ciliary transition zone membrane and is mutated in ciliary disease. Nat Cell Biol. 2016 Jan;18(1):122-31

AL. Bruel*, NJ. Lambacher*, TPJ.van Dam, GG. Slaats, K. Szymańska, GJ. McManus, JE. Kennedy, K. Gaff, Robin, R. van der Lee, L. Burglen, D. Doummar, JB. Rivière, L. Faivre, T. Attié-Bitach, S. Saunier, CA. Johnson, RH. Giles, MA. Huynen, C. Thauvin-Robinet#, OE. Blacque#

The oral-facial-digital syndrome gene *C2CD3* encodes a positive regulator of centriole elongation. Nat Genet. 2014 Aug;46(8):905-11

C. Thauvin-Robinet, JS. Lee, E. Lopez, V. Herranz-Pérez, T. Shida, B. Franco, L. Jego,F. Ye, L. Pasquier, P. Loget, N. Gigot, B. Aral, CA. Lopes, J. St-Onge, **AL. Bruel** , J. Thevenon, S. González-Granero, C. Alby, A. Munnich, M. Vekemans, F. Huet, AM. Fry, S. Saunier, JB. Rivière, T. Attié-Bitach, JM. Garcia-Verdugo, L. Faivre, A. Mégarbané, MV. Nachury.

Articles faisant l'objet de cette thèse

Travaux collaboratifs

The ciliopathy-associated CPLANE proteins direct basal body recruitment of intraflagellar transport machinery. Nat Genet. 2016 May 9. doi: 10.1038/ng.3558

M. Toriyama, C. Lee, SP. Taylor, I. Duran, DH. Cohn, **AL. Bruel**, JM. Tabler, K. Drew, MR. Kelley, S. Kim, TJ. Park, D. Braun, G. Pierquin, A. Biver, K. Wagner, A. Malfroot, I. Panigrahi, B. Franco, HA. Al-lami, Y. Yeung, YJ. Choi, University of Washington Center for Mendelian Genomics, Y. Duffourd, L. Faivre, JB. Rivière, J. Chen, KJ. Liu, EM. Marcotte, F. Hildebrandt, C. Thauvin-Robinet, D. Krakow, PK. Jackson and JB. Wallingford.

MKS5 and CEP290 dependent assembly pathway of the ciliary transition zone. PLoS Biol. 2016 Mar 16;14(3):e1002416

C. Li, K. Park, VL. Jensen, J. Kennedy, FR. Garcia-Gonzalo, M. Romani, R. De Mori, **AL. Bruel**, D. Gaillard, B. Doray, E. Lopez, JB. Rivière, L. Faivre, C. Thauvin-Robinet, JF. Reiter, OE. Blacque, EM. Valente, MR. Leroux.

Articles faisant l'objet de travaux annexes*

Autosomal recessive truncating *MAB21L1* mutation associated with a syndromic scrotal agenesis. Clin Genet. 2016 Apr 22. doi: 10.1111/cge.12794.
AL. Bruel, A. Masurel-Paulet, JB. Rivière, Y. Duffourd, D. Lehalle, C. Bensignor, F. Huet, J. Borgnon, F.Roucher, P. Kuentz, JF. Deleuze, C. Thauvin-Robinet, L. Faivre, J. Thevenon.

The value of datasharing of whole exome sequencing results for the clinical delineation of ultra rare disorders: the example of mutations in *GFER*. EJHG, en révision.
S. Nambot, D. Gavrilov, J. Thevenon, **AL. Bruel**, M. Bainbridge, A. Munnich, C. Goizet, D. Lacombe, M. Rio, A. Rötig, D. Lacombe, J. Jaeken, N. Niu, F. Xia, A. Vital, M. Coquet, A. Vital, P. Kuentz, D. Lehalle, Y. Duffourd, JB. Rivière, C. Thauvin-Robinet, AL. Beaudet, L. Faivre.

Dominant mutations in the splicing factor *PUF60* cause a recognizable syndrome with intellectual disability, heart defects and short stature. EJHG, en revision
S. El Chehadeh, WS. Kerstjens-Frederikse, J. Thevenon, P. Kuentz, **AL. Bruel**, C. Thauvin-Robinet, C. Bensignor, H. Dollfus, V. Laugel, JB. Rivière, Y. Duffourd, C. Bonnet, MP. Robert, R. Isaiko, M. Straub, C. Creuzot-Garcher, P. Calvas, N. Chassaing, C. Gilissen, R. Pfundt, JS. Klein Wassink-Ruiter, L. Faivre.

Expanding the Phenotype Associated with NAA10 Related N-terminal Acetylation Deficiency. Hum Mutat. 2016 Apr 20. doi: 10.1002/humu.23001.
C. Saunier, SI. Støve, B.Popp, B. Gérard, M. Blenski, N. AhMew, C. de Bie, P. Goldenberg, B. Isidor, B. Keren, B. Leheup, L. Lampert, C. Mignot, K. Tezcan, GM. Mancini, C. Nava, M. Wasserstein, **AL. Bruel**, J. Thevenon, A. Masurel, Y. Duffourd, P. Kuentz, F. Huet, JB. Rivière, M. van Slegtenhorst, L. Faivre, A. Piton, A. Reis, T. Arnesen, C. Thauvin-Robinet, C. Zweier.

Severe X-linked chondrodysplasia punctata in nine new female fetuses. Prenat Diagn. 2015 Jul;35(7):675-84.
M. Lefebvre, F. Dufernez, **AL. Bruel**, M. Gonzales, B. Aral, J. Saint-Onge, N. Gigot, J. Desir, C. Daelemans, F. Jossic, S. Schmitt, R. Mangione, F. Pelluard, C. Vincent-Delorme, JM. Labaune, N. Bigi, D. D'Olne, AL. Delezoide, A. Toutain, S. Blesson, V. Cormier-Daire, J. Thevenon, S. El Chehadeh, A. Masurel-Paulet, N. Joyé, C. Vibert-Guigue, L. Rigonnot, T. Rousseau, P. Vabres, P. Hervé, A. Lamazière, JB. Rivière, L. Faivre, N. Laurent, C. Thauvin-Robinet.

Oral-Facial-Digital Syndrome Type I. 2002 Jul 24 [Updated 2016 Aug 4]. In: Pagon RA, Adam MP, Ardinger HH, et al., editors. GeneReviews® [Internet]. Seattle (WA): University of Washington, Seattle; 1993-2016.
HV. Toriello, B. Franco, AL. Bruel, and C. Thauvin-Robinet.

*Articles non discutés dans ce manuscrit.

INTRODUCTION

1- Généralités

Une pathologie est dite rare lorsqu'elle affecte moins d'une personne sur 2000. On dénombre actuellement entre 6000 et 8000 maladies rares avec une prévalence combinée d'environ 1 personne sur 20. 80 à 85% sont d'origine génétique et dans la majorité des cas, les bases moléculaires n'ont pas encore été déterminées. Parmi les pathologies rares, environ 2000 sont des anomalies du développement embryonnaire d'origine génétique appelées aussi syndromes dysmorphiques avec ou sans retard mental. Ces syndromes concernent 2 à 4% des naissances soit, en France, 12000 à 24000 nouveau-nés par an. Ils sont liés à un trouble du développement physique et/ou neurologique qui survient au cours la vie embryonnaire ou fœtale suite à des altérations génétiques, des aberrations chromosomiques, ou encore sous l'action de facteurs environnementaux. En effet, au cours du développement embryonnaire, les ébauches des différents organes se mettent en place sous l'action cordonnée de différents gènes et cascades de signalisation qui vont induire les mouvements cellulaires et leur différenciation dans des fenêtres spatio-temporelles bien définies. Une perturbation de ces mécanismes altère dans la plupart des cas la morphogénèse des différents organes alors à l'origine des syndromes dysmorphiques avec des conséquences plus ou moins sévères selon la précocité de l'évènement et du gène en cause.

Il existe une réelle nécessité d'identifier les bases moléculaires afin de permettre une meilleure connaissance de leur histoire naturelle et par conséquent d'optimiser la prise en charge muti-disciplinaire des patients, le conseil génétique, offrir un diagnostic prénatal précoce, et dans certains cas, de développer des thérapeutiques ciblées.

Depuis une vingtaine d'années, les approches de la biologie moléculaire combinées aux avancées de la génétique humaine ont permis d'identifier un grand nombre de gènes responsables de ces syndromes dysmorphiques, d'autant plus avec l'apparition des techniques de séquençage haut débit de nouvelle génération (NGS) qui rend possible désormais l'acquisition rapide de données à l'échelle du génome entier pour chaque individu. Suite à l'identification des mutations causales, les analyses aux niveaux biochimique, cellulaire et des animaux modèles, permettent de mieux comprendre les fonctions protéiques des gènes étudiés, d'améliorer les connaissances sur le développement embryonnaire et surtout de mieux connaitre les rouages physiopathologiques de ces maladies.

Ce projet de thèse s'intéresse aux syndromes oro-facio-digitaux et à l'identification de nouveaux gènes responsables de ces syndromes rares.

2- Les syndromes Oro-Facio-Digitaux

2.1- Classification clinique

Les syndromes oro-facio-digitaux (OFD), caractérisés par l'association d'une atteinte orale, faciale et digitale, constituent un groupe de pathologies développementales rares très hétérogène. L'incidence est estimée entre 1/50000 et 1/250000 naissances. Le premier cas a été décrit en 1941 au sein d'une famille avec plusieurs membres atteints ; depuis, une centaine de cas ont été rapportés dans la littérature (Mohr et al., 1941). Leur description a donné lieu à une classification clinique de 13 sous-types qui repose principalement sur les signes cliniques associés et leur mode de transmission (tableau 1) (Gurrieri et al., 1992).

2.1.1- Le syndrome OFD de type I, syndrome de Papillon-Léage-Psaume

Rapporté pour la première fois par Papillon-Léage en 1954 puis caractérisé en 1962, le syndrome OFD de type I (OFDI, [MIM 311200]) est le sous-type le plus fréquent et le mieux connu (Gorlin and Psaume, 1962). Il se caractérise par un mode de transmission dominant lié à l'X avec une létalité chez les garçons atteints (Toriello, 1993). Il survient le plus souvent de façon sporadique (75% des cas) (Gurrieri et al., 2007).

Les caractéristiques cliniques sont décrites dans le tableau 1, avec principalement la polykystose rénale, très fréquente, évoluant avec l'âge vers une insuffisance rénale, et des atteintes du système nerveux central (SNC) parfois associé à une déficience intellectuelle (Del Giudice et al., 2014; Prattichizzo et al., 2008; Saal et al., 2010). Les anomalies du SNC seraient présentes dans près de 50% des cas et incluent agénésie du corps calleux, kystes arachnoïdiens, porencéphalie, microcéphalie, troubles de la gyration, hétérotopie et malformations cérébelleuses (figure 1).

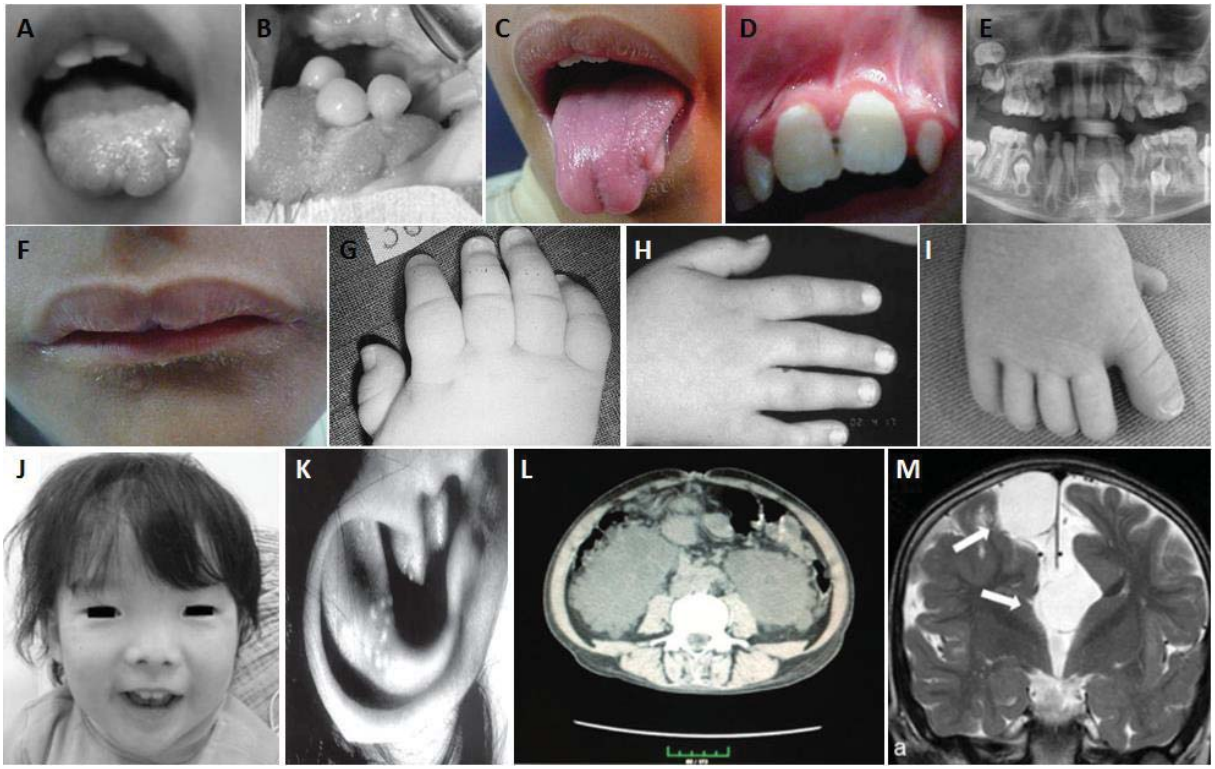

Figure 1 : Principales caractéristiques clinique du syndrome OFD I. *(A-E) Anomalies orales incluant (A) langue lobulée, (B) hamartomes, (C) langue bifide, (D) freins gingivaux anormaux et (E) dents surnuméraires. (G-H) Anomalies des extrémités incluant (G) brachydactylie, (H) clinodactylie et (I) polydactylie pré-axiale. (J) Dysmorphie faciale avec hypertélorisme, épicanthus, arrête nasale large, hypoplasie des ailes du nez et (F) pseudo-fente de la lèvre supérieure. Des anomalies (K) cutanées, (L) kystes rénaux et malformations cérébrales, notamment l'agénésie du corps calleux (M) sont caractéristiques du syndrome OFD I. Photographies de (Dave et al., 2013; Del Giudice et al., 2014; Driva et al., 2004; Mihci et al., 2007; Shimojima et al., 2013; Stoll and Sauvage, 2002; Yavuz et al., 2014).*

2.1.2- Les principaux syndromes OFD autosomiques récessifs

La majorité des sous-types OFD, beaucoup plus rares que le syndrome OFD I, se transmettent selon un mode autosomique récessif. Les principales entités sont représentées par les syndromes OFD II, IV, VI, IX et XI (tableau 1).

Le syndrome de Mohr ou OFD II [MIM 252100] présente de nombreuses similitudes avec le syndrome OFD I mais des différences cliniques subsistent toutefois, notamment l'absence d'anomalies rénales. Plusieurs cas présentent une polydactylie avec un métacarpe central en forme de Y visible en radiographie et un hallux large, suggérant un chevauchement clinique avec le syndrome OFD VI (Ghossaini et al., 2002; Panigrahi et al., 2013). Les malformations cérébrales, principalement porencéphalie et hydrocéphalie, mais aussi des anomalies

cérébelleuses, ont été rapportées (Gurrieri et al., 2007; Rhouma and Horneff, 2014). Les anomalies cardiaques, génitales ou des phanères, et les détresses respiratoires sont plus rarement décrites (Digilio et al., 1996; Dua et al., 2013; Prpić et al., 1995).

Le syndrome OFD IV ou de Baraister-Burn [MIM 258860] se caractérise par la présence d'une atteinte tibiale. Celle-ci peut-être unilatérale ou bilatérale et de présentation variable : d'atteintes épiphysaires et métaphysaires proximales jusqu'à une hypoplasie sévère. Le spectre clinique peut comprendre par ailleurs : petite taille, pectus excavatum, colobomes oculaires, kystes hépatiques et rénaux, atrésie anale, occipitoschisis et malformations cérébrales, cardiaques ou génitales (Gurrieri et al., 2007; Thomas et al., 2012).

Initialement décrit en 1980, le syndrome de Varadi-Papp ou OFD VI [MIM 277170] est caractérisé par la présence d'anomalies cérébrales et/ou du cervelet (hypoplasie du vermis cérébelleux avec signe de la dent molaire à l'IRM cérébrale, malformation de Dandy-Walker, hamartomes hypothalamiques) fréquemment associées une polydactylie. Une déficience intellectuelle modéré à sévère est classiquement observée chez les patients (Darmency-Stamboul et al., 2013). Le syndrome OFD VI est probablement la forme récessive la plus fréquente avec une quarantaine de cas rapportés dans la littérature.

Le syndrome OFD IX ou de Gurrieri [MIM 227170] est définit par la présence de colobome oculaire (rétinien, choroïdien ou du disque optique) et d'une microphtalmie (Gurrieri et al., 2007). La microcéphalie, les anomalies du système nerveux central (agénésie du corps calleux, dilatation ventriculaire) et génitales (micropénis, agénésie du clitoris ou du vagin) sont récurrents. Des épilepsies et une déficience intellectuelle de sévérité variable ont aussi été notées (Adly et al., 2014; Erickson and Bodensteiner, 2007).

2.1.3- Les formes anecdotiques

2.1.3.1- Les formes inclus dans la classification

Pour chacun des types III, V, VII, X, XI, XII, et XIII, seul un ou deux cas sont décrits dans la littérature.

Décrit en 1971, le syndrome OFD III ou syndrome de Sugarman [MIM 258850] associe une atteinte OFD, un retard mental modéré à sévère et des clignements alternés et incessants des yeux, avec une possible hypoplasie vermienne (Roberson et al., 2015; Sugarman et al., 1971).

L' OFD V ou syndrome de Thurston [MIM 174300] est une forme modérée décrite jusqu'à présent uniquement dans la population indienne et caractérisée par l'association d'une fente médiane et d'une polydactylie post-axiale (Naikmasur et al., 2010; Valiathan et al., 2006).

Pour l'OFD X ou syndrome de Figuera [MIM 165590], cette variante de syndrome OFD est uniquement représentée par l'observation d'un nourrisson de sexe féminin de 10 mois, présentant un raccourcissement mésomélique des quatre membres, une polysyndactylie bilatérale du pouce et du premier orteil, et une hypoplasie de tous les doigts et orteils. Sur le plan radiologique, on retrouvait une hypoplasie bilatérale du radius et une aplasie bilatérale de la fibula. Les os du tarse et les troisième et quatrième métatarses étaient fusionnés. Le développement psychomoteur était sans particularité (Figuera et al., 1993).

Le syndrome de Gabrielli ou OFD XI [MIM 612913] est caractérisé par une surdité, un retard mental sévère avec traits autistiques et des stéréotypies, et des atteintes squelettiques spécifiques (hypoplasie de l'odontoïde, fissures de corps vertébraux, fusion des arcs postérieurs des premières vertèbres. A ce jour, trois patients issus de trois familles différentes sont rapportés (Ferrero et al., 2002; Gabrielli et al., 1994; Obregón and Barreiro, 2003).

L'OFD XII ou syndrome de Moran-Barroso est établi d'après l'observation d'un seul nouveau-né de sexe masculin, présentant un myéloméningocèle lombaire, ainsi que des atteintes faciales (hypertélorisme, fentes labiopalatines bilatérales), orales (langue bifide, freins gingivaux, dents surnuméraires) et des extrémités (polydactylie pré et post-axiale). Sur le plan radiologique étaient mis en évidence des tibias courts, et la fusion en Y des métacarpes centraux. L'autopsie a révélé des malformations cérébrales (agénésie du corps calleux, hypoplasie vermienne, sténose de l'aqueduc de Sylvius) et des valves mitrale et tricuspide dysplasiques (Morán-Barroso et al., 1998).

L'OFD XIII ou syndrome de Degner, est caractérisé, outre les signes cardinaux, à partir de l'observation d'une patiente atteinte d'épilepsie et d'un syndrome dépressif, secondaires à une leucoaraïose mise en évidence à l'IRM cérébrale (Degner et al., 1999).

L'unique publication de l'OFD VII ou syndrome de Whelan [MIM 608518] concernait une mère et sa fille. Les atteintes observées correspondaient à une entité proche du type I, mais avec l'association d'une asymétrie faciale et d'une hydronéphrose (Whelan et al., 1975). L'existence de ce syndrome a été remise en cause avec l'apparition secondaire chez ces deux patientes d'une polykystose rénale, et en raison de la localisation en Xp22.2p22.3 du locus impliqué, locus iso-allélique au gène *OFD1*. L'évolution clinique et les résultats de l'étude de liaison ont fait fortement suspecté que les types I et VII correspondent à la même entité, bien qu'aucune mutation du gène *OFD1* n'ait été mise en évidence dans cette famille (Nowaczyk et al., 2003).

Décrit dans une seule famille, l'OFD VIII ou syndrome d'Edwards [MIM 300484] se caractérise par des atteintes proches de celles du syndrome OFD II avec en particulier une polydactylie, et des pouces bifides (Edwards et al., 1988). Le mode de transmission est toutefois différent, avec une transmission verticale et la présence d'atteintes plus marquées dans le sexe masculin: petite taille, atteintes osseuses du tibia, hypoplasie de l'épiglotte et des cartilages arythénoïdes.

Tableau 1 : Caractéristiques phénotypiques des 13 sous-types OFD

ACC (Agénésie du Corps Calleux), DLX (Dominant lié à l'X), RA (Récessif Autosomique), SAS (Sténose Acqueduc de Sylvius), SDM (Signe de la Dent Molaire).

	OFD I	OFD II	OFD III	OFD IV	OFD V	OFD VI	OFD VII	OFD VIII	OFD IX	OFD X	OFD XI	OFD XII	OFD XIII
Anomalies orales	Freins gingivaux Hamartomes linguaux Langue lobulée et/ou fendue Fente palatine	Freins gingivaux Hamartomes linguaux Langue lobulée et/ou fendue Fente palatine	Luette fendue Hamartomes linguaux Langue lobulée Dents hypoplasiques	Freins gingivaux Hamartomes linguaux Langue lobulée Fente palatine	Freins gingivaux (rares)	Freins gingivaux Hamartomes linguaux Langue lobulée Fente palatine	Freins gingivaux Hamartomes linguaux Fente palatine	Freins gingivaux Hamartomes linguaux Langue lobulée	Freins gingivaux Hamartomes linguaux Langue lobulée	Freins gingivaux Fente palatine	Freins gingivaux Fente palatine	Freins gingivaux Langue lobulée	Hamartomes linguaux
Anomalies faciales	Hypertélorisme Fente labiale Pseudofente médiane de la lèvre supérieure	Fente labiale médiane	Hypertélorisme Nez bulbeux Oreilles bas implantées	Epicanthus Micrognathie Oreilles bas implantées	Fente labiale médiane	Hypertélorisme Fente labiale	Hypertélorisme Fente labiale Asymétrie	Fente labiale médiane Télécanthus Nez large	Fente labiale Synophrys Anomalies rétinienne	Télécanthus Racine du nez aplatie Rétrognathie	Hypertélorisme Fente labiale médiane	-	Fente labiale
Anomalies des mains	Brachydatylie Clinodactylie Polydactylie	Brachydatylie Clinodactylie Polydactylie	Polydactylie postaxiale	Brachydatylie Clinodactylie Polydactylie pré/postaxiale	Polydactylie postaxiale	Brachydatylie Clinodactylie Syndactylie Polydactylie médiane	Clinodactylie	Polydactylie pré/postaxiale	Brachydatylie Clinodactylie	Oligodactylie Polydactylie préaxiale	Polydactylie postaxiale	Brachydatylie Clinodactylie Syndactylie	Brachydatylie Clinodactylie Syndactylie
Anomalies des pieds	Polydactylie préaxiale	Hallux large Polydactylie pré/postaxiale	Polydactylie postaxiale	Polydactylie pré/postaxiale	Polydactylie postaxiale	Hallux large Polydactylie préaxiale	-	Polydactylie préaxiale	Orteils bifides	-	Polydactylie postaxiale	Brachydatylie Clinodactylie Syndactylie	Brachydatylie Clinodactylie Syndactylie
Anomalies des phanères	Miliaire Alopécie	Cheveux épais	-	-	-	-	-	-	-	-	-	-	-
Malformations rénales	Polykystose	-	-	-	-	Agénésie Dysplasie	Polykystose	-	-	-	-	-	-
Malformations cardiaques	-	rare	-	-	-	rare	-	-	-	-	-	Septum hypertrophique	Valves mitrale et tricuspide dysplasiques
Malformations cérébrales	ACC Hypoplasie cérébelleuse	Porencéphalie Hydrocéphalie	Myoclonies	Porencéphalie Atrophie cérébrale	-	SDM	-	-	-	-	Dilatation ventriculaire	SAS, ACC Hypoplasie vermienne Myéloménindo-cèle	Leucoaraïose
Anomalies squelettiques	-	-	-	Pectus excavatum Anomalies tibiales	-	-	-	Hypoplasie tibiale et radiale	-	Raccourcissement radial Agénésie fibulaire	Anomalies cranio-vertébrales	-	-
Autres anomalies	-	-	-	Petite taille	-	-	-	Epiglotte hypoplasique	Petite taille	-	-	-	Troubles neuro-psychologiques Epilepsie
Mode de transmission	DLX	RA	RA	RA	RA	RA	RA	DLX	RLX/RA	sporadique	sporadique	sporadique	sporadique

2.1.3.2- Les syndromes OFD inclassables

Différentes observations avec une atteinte OFD sont également rapportées dans la littérature mais leur atteinte clinique ne permet pas de les classer parmi les 13 syndromes OFD individualisés, témoignant de la complexité à délimiter un spectre clinique pour chaque sous-type (Gurrieri et al., 2007).

Un premier groupe concerne des patients avec une atteinte OFD mais également d'autres anomalies considérées comme spécifiques d'au moins un sous-type d'OFD (Chitayat et al., 1992; Gurrieri et al., 1992). Ces observations sont appelées transitionnelles comme par exemple le patient présentant une polydactylie centrale, typique du syndrome OFD VI mais sans anomalie du cervelet, le rendant plutôt suspect d'un syndrome OFD II (Camera et al., 1994). La description de telles observations pose la question de la réalité nosologique de la classification clinique des 13 types d'OFD mais aussi d'un éventuel allélisme des syndromes OFD II et OFD VI (Camera et al., 1994; Gurrieri et al., 2007; Haug et al., 2000; Panigrahi et al., 2013; Shashi et al., 1995). Un chevauchement clinique a aussi été observé entre les syndromes OFD II et IV (Bonioli et al., 1979; Goldstein and Medina, 1974), I et IV (Adès et al., 1994) ainsi qu'entre les types III et VI (Roberson et al., 2015; Smith and Gardner-Medwin, 1993). Seule la mise en évidence des gènes responsables permettra de simplifier cette classification.

Un second groupe concerne des patients présentant de nombreuses autres anomalies non décrites dans les 13 types d'OFD (figure 2): hamartomes hypothalamiques et hypogonadisme, agénésie de la glande pituitaire, surdité, agénésie rénale unilatérale, anomalies cardiaques dont la coarctation de l'aorte, anomalies des clavicules, agénésie du pénis, anomalies laryngées et trachéales (épiglotte rudimentaire), atélectasie et retard mental, nævus comedone (Al-Gazali et al., 1999; Baker and Agim, 2014; Buño et al., 2000; Chung and Chung, 1999; Liu et al., 2012; Muenke et al., 1991; Okten et al., 2005; Saari et al., 2015; Shamseldin et al., 2013; Stenram et al., 2007; Stephan et al., 1994; Yildirim et al., 2002).

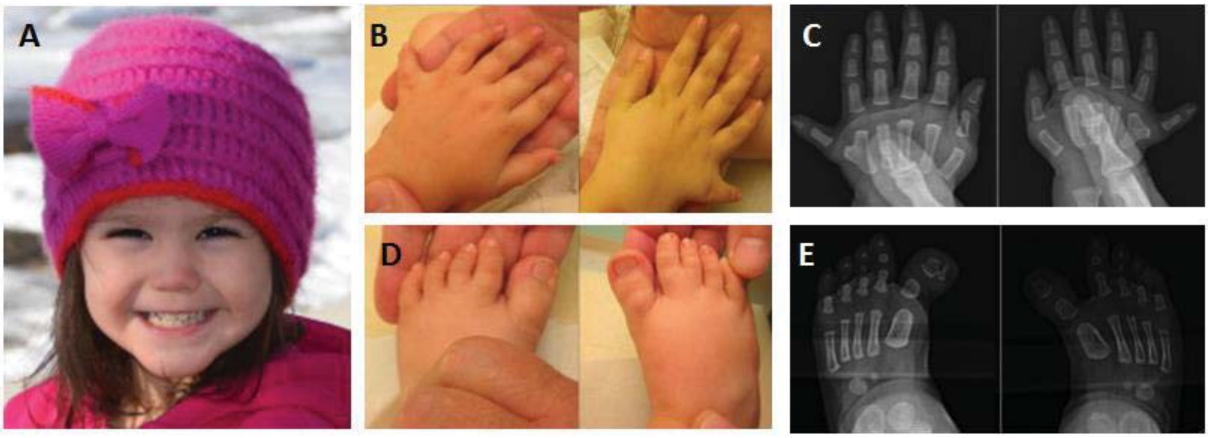

Figure 2: Présentation clinique d'un syndrome OFD non classé rapporté par Saari et al., 2015. *(A) Dysmorphie faciale modérée, (B-C) polydactylie post-axiale, (D-E) syndactylie des 2èmes et 3èmes orteils et hallux larges.*

2.1.4- Diagnostic différentiel

Les diagnostics différentiels incluent principalement les syndromes avec anomalies de la face et des extrémités, notamment avec certaines ciliopathies (annexe 1).

2.1.4.1- OFD I et polykystose rénale

La polykystose rénale étant une complication très fréquente du syndrome OFD I à l'âge adulte, la polykystose rénale autosomique dominante (PKAD) apparait comme son principal diagnostic différentiel. Cependant, les kystes rénaux sont généralement de plus petite taille dans le syndrome OFD I et se développent dans les tubules et le glomérule, tandis que dans la polykystose rénale autosomique dominante, les kystes sont retrouvés principalement dans les tubules. L'échographie ne permettant pas toujours de distinguer ces différences et d'orienter le diagnostic, le diagnostic moléculaire s'avère essentiel en terme de pronostic et de conseil génétique (Toriello and Franco, 1993). En effet, l'atteinte rénale du syndrome OFD I s'avère plus précoce et d'évolution plus sévère avec un mode de transmission dominant lié à l'X alors que la PKAD se transmet sur un mode autosomique dominant (Saal et al., 2010).

2.1.4.2- OFD VI et syndrome de Joubert

Le syndrome OFD VI se caractérise par une hypoplasie cérébelleuse avec un signe de la dent molaire visible à l'IRM cérébrale et qui a été initialement décrit dans le syndrome de Joubert.

Le syndrome de Joubert (JS) est une pathologie rare avec une incidence de 1/100000 naissances et un mode de transmission autosomique récessif ou pour quelques cas anecdotiques récessif lié à l'X (Coene et al., 2009). Il est caractérisé par une dysmorphie faciale (hypertélorisme, front large), une hypotonie néonatale, un retard de développement, un déficit intellectuel plus ou moins sévère et des hyperpnées épisodiques durant la période néonatale. Des mouvements anormaux des yeux, notamment une apraxie oculomotrice ou un nystagmus, sont aussi notés (Bachmann-Gagescu et al., 2015; Parisi et al., 2007). D'autres signes cliniques associés sont décrits (dystrophie rétinienne, anomalies rénales, fibrose hépatique) et ont donné lieu à six sous-types regroupés sous le terme de syndrome de Joubert et maladies associées (SJMA) (Brancati et al., 2010a). Dans cette récente classification des SJMA, le syndrome OFD VI est présenté comme un sous-groupe (JS-OFD), soulignant un continuum clinique entre ces deux pathologies (Brancati et al., 2010b; Darmency-Stamboul et al., 2013; Haug et al., 2000; Poretti et al., 2008).

2.1.4.3- Syndromes OFD et de Meckel-Grüber

Le syndrome de Meckel-Grüber (MKS) est une pathologie rare létale autosomique récessive. La prévalence mondiale est très variable, celle-ci étant plus élevée dans les populations avec un fort taux de consanguinité. En Europe, elle est estimée à 1/38615 naissances (Barisic et al., 2015).

Le syndrome MKS se caractérise par l'association de malformations du système nerveux central (encéphalocèle occipital, hypoplasie cérébelleuse, malformation de Dandy-Walker) de kystes rénaux, d'une fibrose hépatique et d'une polydactylie post-axiale. Les patients décèdent généralement *in utero* ou durant les premiers mois de vie. D'autres anomalies sont rapportées notamment des malformations oro-faciales, une étude européenne estime à 31,8% le pourcentage de cas présentant une fente palatine (Barisic et al., 2015). Un chevauchement clinique et un allélisme a été rapporté avec les syndromes OFD I, III et VI (Chen, 2007; Roberson et al., 2015; Valente et al., 2010).

2.1.4.3- Autres diagnostics différentiels

Le syndrome de Pallister-Hall et l'hydroléthalus ont été décrits dans deux familles distinctes avec des anomalies de la ligne médiane, présentant également des signes cliniques chevauchant avec les syndromes OFD VI et OFD II (Muenke et al., 1991; Shashi et al., 1995).

Malgré une atteinte osseuse radiologique caractéristique, le syndrome d'Ellis Van Creveld (EVC), caractérisé par des anomalies orales, faciales, digitales et un nanisme acromélique a également été discuté devant l'association d'atteintes digitales et de freins oraux (Ghosh et al., 2007; Phadke et al., 1999).
Le syndrome de Treacher-Collins peut aussi associer des anomalies cranio-faciales et digitales, cependant la dysmorphie faciale caractéristique est très différente de celle des syndromes OFD (Emes and Ponting, 2001; Lehalle et al., 2014).

2.2- Variabilité phénotypique inter et intrafamiliale

La classification clinique des syndromes OFD demeure difficile au vu de la variabilité phénotypique observée, impliquant d'une part un élargissement du spectre clinique de certains sous-types, et suggérant d'autre part des allélismes entre sous-types ou encore l'existence d'une multitude d'autres sous-types.

Une des premières difficultés pour établir le diagnostic exact d'un sous-type réside dans la variabilité clinique importante qu'il peut exister au sein d'un même sous-type OFD. A titre d'exemple dans le syndrome OFD I, certains signes cliniques sont fréquemment retrouvés comme la dysmorphie faciale (81% des cas), la présence de dents surnuméraires (87%), les anomalies de la langue (79%), la fente palatine (71%) ou encore l'agénésie du corps calleux (82%). En revanche, certains sont plus rarement décrits tels que les oreilles bas implantées (30%), la luette bifide (8%), la dysplasie tibiale (9%), le retard psychomoteur (19%) ou encore les épilepsies (16%), par ailleurs retrouvé à des fréquences plus élevées dans d'autres sous-types, et pouvant alors conduire à des difficultés pour reconnaitre la pathologie en question (Bisschoff et al., 2013). Un autre exemple, dans le syndrome OFD IV, quelques cas anecdotiques présente une polykystose rénale, classiquement retrouvé dans le syndrome OFD I (Adès et al., 1994).

A ceci, s'ajoute une variabilité intrafamiliale fréquente, notamment dans le syndrome OFD I où un phénotype plus sévère chez les filles que chez les mères est souvent observé (Prpić et al., 1995; Shimojima et al., 2013).

2.3- Bases moléculaires des syndromes OFD

L'identification des bases moléculaires devrait permettre d'éclaircir la classification clinique des syndromes OFD. A ce jour, sept gènes ont été impliqués dans les syndromes OFD (*OFD1*, *TMEM216*, *TCTN3*, *SCLT1*, *TBC1D32*, *C5orf42*, *DDX59*) et l'hétérogénéité clinique fait suspecter l'implication de plusieurs gènes dans ces syndromes.

2.3.1- Le gène *OFD1*

2.3.1.1- Description

Le gène *OFD1* (chrX:g.13752832-13787480) identifié en 2001 et responsable du syndrome OFD I, se compose de 23 exons et code pour une protéine de 1012 acide-aminés (Ferrante et al., 2001). Un transcrit alternatif OFD1b, plus long que le premier décrit (nommé OFD1a ou OFD1), a aussi été rapporté et dérive des exons 1 à 11 (figure 3). Il implique un site accepteur cryptique dans l'intron 9 et conduit à l'apparition d'un codon stop prématuré dans l'exon 11 (Romio et al., 2003).

Ce gène code pour une protéine du centrosome et du cil primaire avec sept régions coiled-coil sont prédites (Budny et al., 2006; Romio et al., 2004). Ces régions, formées de deux ou plus hélices α, sont essentielles pour une bonne localisation d'OFD1 dans le centrosome et confèrent à la protéine, une capacité d'oligomérisation avec d'autres protéines. Par exemple, les régions coiled-coil n°3 à 6 permettent l'interaction entre OFD1 et PCM1 mais aussi CEP290, deux protéines centrosomales. Les deux dernières régions permettent une interaction directe avec SDCCAG8 tandis que les régions n°2 à 4 sont impliquées dans la liaison avec IFT88 (Lopes et al., 2011). Ces régions permettent également une homodimérisation d'OFD1 (Giorgio et al., 2007). En N-terminal se trouve un domaine LisH (Lis1 Homology) qui contribue aux interactions protéine-protéine, à la stabilité et à la localisation. En effet, il semblerait que le domaine LisH soit impliqué dans la régulation de la dynamique des microtubules et du cytosquelette (Lopes et al., 2011).
La protéine résultante du transcrit alternatif OFDb est formée de 367 acide-aminés et contient le motif LisH et 2 régions coiled-coil prédites (Budny et al., 2006).

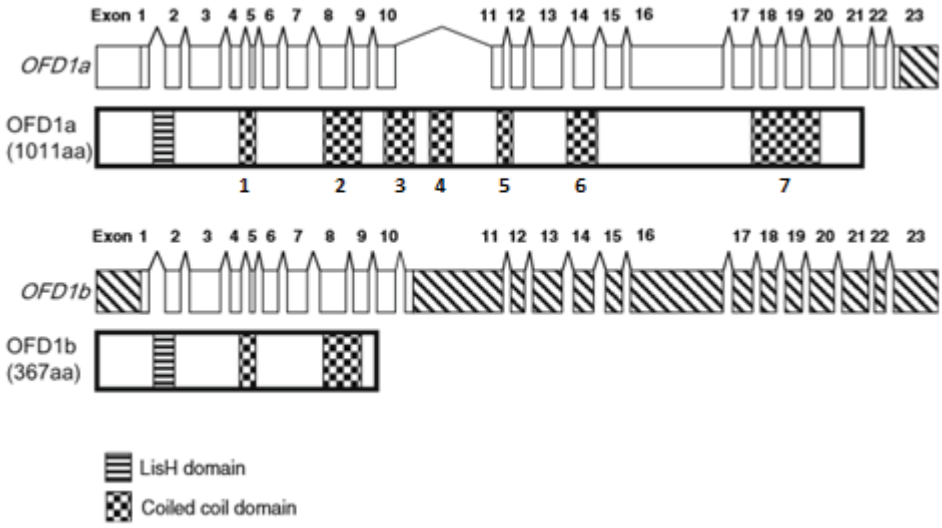

Figure 3: Représentation schématique des transcrits et des protéines OFD1a et OFD1b. *(Budny et al., 2006)*

2.3.1.2- Spectre mutationnel

Plus de 180 mutations différentes chez plus de 200 cas index sont rapportées dans la littérature ou identifiées dans la cohorte recrutée localement (annexe 2). Parmi les mutations identifiées, plus de 50% concernent des délétions ou insertions, 17% des mutations introniques qui affectent l'épissage, 10% des mutations non-sens et 10% des mutations faux-sens (tableau 2). Les exons 3, 9 et 16 sont des séquences fortement mutagènes (plus de 15 variations rapportées) ainsi que les exons 7, 8, 11 et 13 (entre 10 et 15 variations). Aucune mutation n'a été rapportée sur les exons 18, 20, 22, 23 ainsi que sur l'exon 1 (figure 4).

Le séquençage par la méthode de Sanger des exons et des extrémités exon-intron du gène *OFD1* permet d'identifier les mutations chez environ 80% des cas présentant les signes caractéristiques du syndrome OFD I (Prattichizzo et al., 2008; Thauvin-Robinet et al., 2009a).

Tableau 2 : Nombre de mutations rapportées dans le gène OFD1

Faux-sens	Synonyme	Non-sens	Epissage/Intronique	Délétion/Insertion	Réarrangement	TOTAL
Mutations de novo						
10	2	11	12	48	3	86
Mutations héritées						
4	0	5	7	22	0	39
Autres mutations (ségrégation parentale non testée)						
10	0	9	22	51	12	104
						229

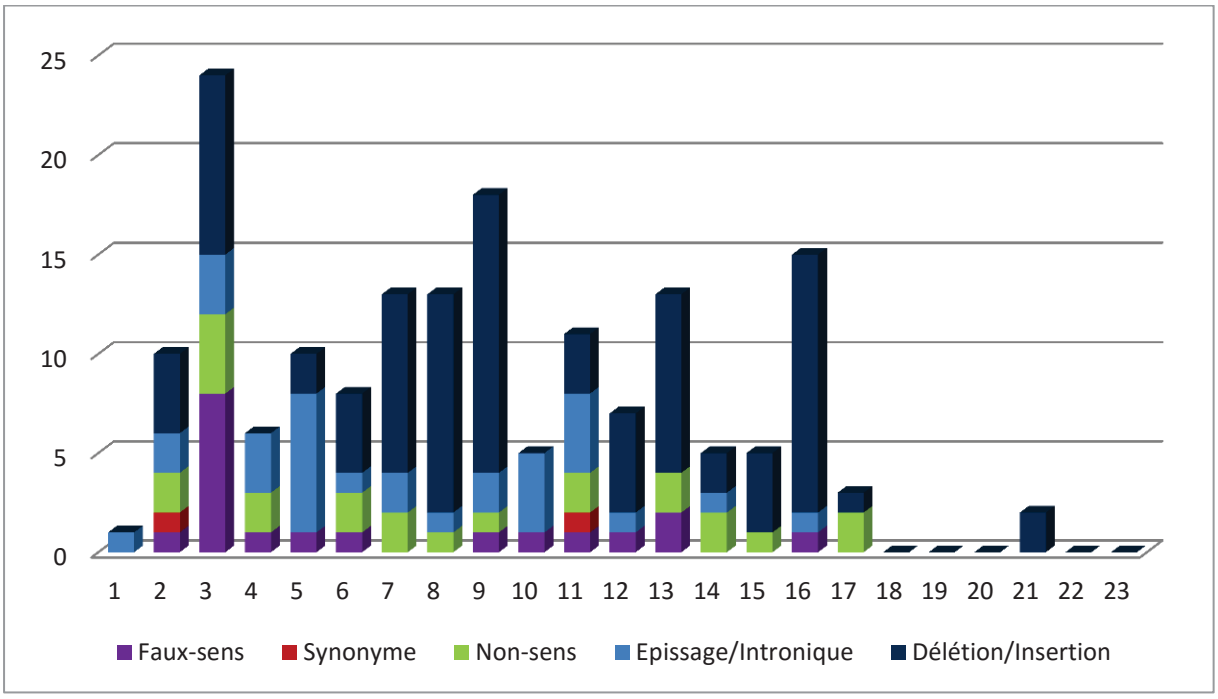

Figure 4: Localisation des mutations rapportées dans le gène OFD1 par exon

Parmi les 20% des cas où le séquençage ciblé du gène *OFD1* n'a pas permis l'identification d'une variation causale, la recherche d'un réarrangement par des techniques de qPCR, QMPSF ou CGH-array à façon peut être réalisée. A ce jour, une quinzaine de micro-réarrangements ont été détectées que cela soit une délétion d'un ou plusieurs exons, voire du gène *OFD1* dans son ensemble (Bisschoff et al., 2013; Del Giudice et al., 2014; Ferrante et al., 2001; Morisawa et al., 2004; Thauvin-Robinet et al., 2009a, 2009b; Toriello and Franco, 1993). Une étude estime à 5%, le pourcentage d'individus avec un réarrangement génomique parmi la totalité des patients diagnostiqués pour un syndrome OFD I, avec un phénotype qui semble plus sévère chez les femmes atteintes (Thauvin-Robinet et al., 2009a).

Cependant pour près de 15% des cas présentant des signes cliniques évocateurs d'un syndrome OFD I, aucune mutation ou réarrangement n'a été mis en évidence. Une des explications est la possibilité de mutations introniques, de mutations en mosaïque ou de phénocopies due à l'hétérogénéité clinique des syndromes OFD.

Cependant, la grande majorité des mutations sont de novo (~70%) (Prattichizzo et al., 2008).

2.3.1.3- Allélisme avec d'autres phénotypes

Bien que la majorité des mutations identifiées soient responsables du syndrome OFD I, quelques mutations ont été associées à d'autres pathologies (annexe 2) dont le syndrome de

Joubert [MIM 300804] avec des variations dans les exons 8, 9 et 21, la rétinite pigmentaire liée à l'X [MIM 300424] avec un seul cas muté dans l'exon 9 et le syndrome de Simpson-Golabi–Behmel [MIM 300209] avec une duplication dans l'exon 16 rapportée chez deux individus non apparentés (Budny et al., 2006; Coene et al., 2009; Field et al., 2012; Kroes et al., 2015; Webb et al., 2012).

2.3.1.4- Fonction

Le gène *OFD1* code pour une protéine du cil primaire, un organite cellulaire sensoriel indispensable à de nombreux processus biologiques (Singla et al., 2010). La protéine OFD1 est localisée au niveau du centrosome, du corps basal et des satellites centriolaires et impliquée activement dans la ciliogenèse (figure 5).

La protéine OFD1 présente plusieurs fonctions essentielles :

- **Régulation de la biogénèse du cil primaire**, contrôlant la longueur des centrioles père et fils (figure 6). OFD1 agit en effet comme un régulateur négatif de la croissance centriolaire, son inactivation conduisant à une hyper-élongation du cil (Singla et al., 2010). Afin de permettre la formation du cil, celle-ci est dégradée par autophagie dans les centrioles (Tang et al., 2013).
- **Formation des appendices distaux**, où elle est recrutée par d'autres protéines de l'appendice distal, BBS4, CEP290 et PCM1 (Lopes et al., 2011; Singla et al., 2010). OFD1 est aussi impliqué dans la stabilisation des microtubules dans le cil primaire (Singla et al., 2010).
- **Transduction des signaux des voies WNT et PCP** (Polarité Cellulaire Planaire) essentiels à la migration des cellules durant l'embryogénèse (Berbari et al., 2009; Hunkapiller et al., 2011). Chez la souris *Bromi*, présentant un knock-out du gène *Ofd1*, la voie SHH est affectée suggérant un rôle d'Ofd1 dans cette voie, mais ceci n'a pas été observé chez le poisson-zèbre (Bimonte et al., 2011; Ferrante et al., 2006, 2009).
- **Remodelage de la chromatine et régulation transcriptionnelle :** la protéine OFD1 a aussi été localisée dans le noyau cellulaire comme une sous-unité du complexe TIP60 impliqué dans l'acétylation histone (Giorgio et al., 2007).

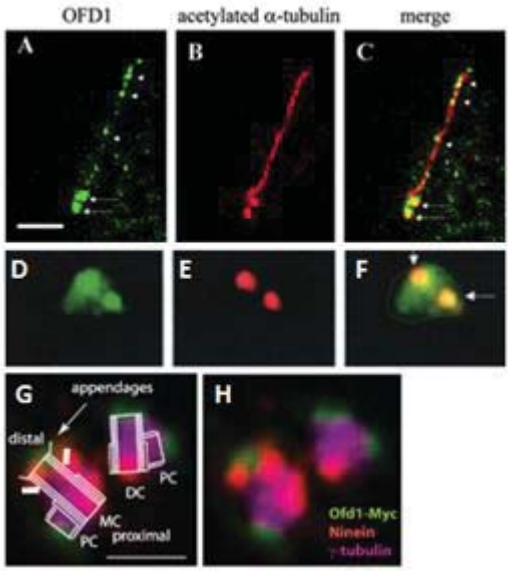

Figure 5: Localisation de la protéine OFD1. *(A-H) Images prises en microscopie à fluorescence. OFD1 en vert (A,D) est localisé au niveau du corps basal du cil primaire (C). OFD1 colocalise aussi (F) avec l'α-tubuline en rouge (B-E) localisée dans le centrosome et plus précisément (G-H) au niveau des centrioles père (MC) et fils (DC) qui deviendra le corps basal. Adapté de (Romio et al., 2004; Singla et al., 2010)*

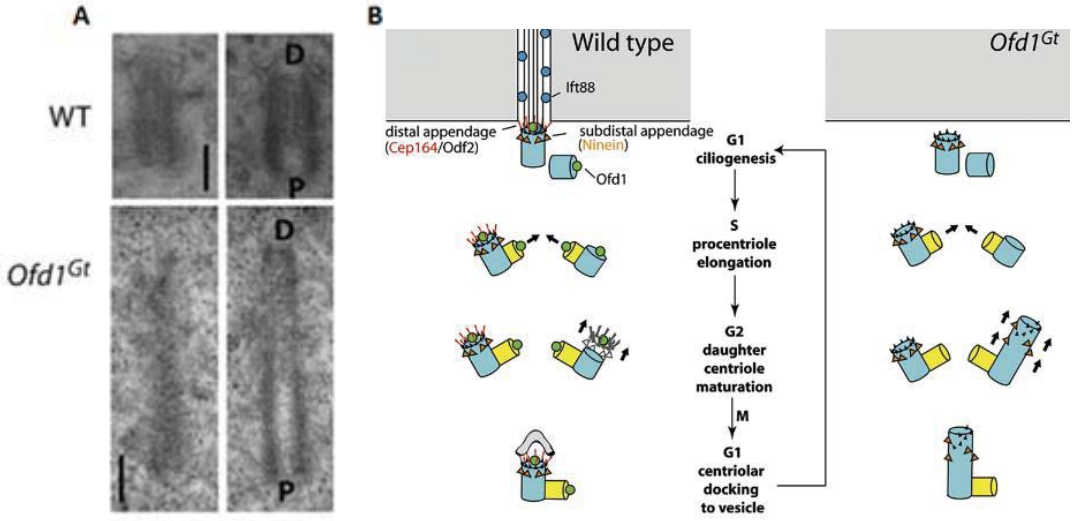

Figure 6: OFD1 est impliqué dans la ciliogenèse. *(A) OFD1 régule négativement la croissance centriolaire, son inactivation induit une hyper-élongation. (B) OFD1 stabilise les centrioles et permet le recrutement des différentes protéines dans le centriole afin d'induire la formation du cil. En absence d'OFD1, les défauts des centrioles ne permettent pas d'initier la ciliogenèse (Singla et al.2009).*

Le knock-out du gène *Ofd1* chez la souris conduit à un phénotype typique des syndromes OFD avec des malformations cranio-faciales, une fente palatine, des membres courts et une poly-syndactylie. Il est aussi noté des anomalies cérébrales, pulmonaires, vésicales ainsi que des kystes rénaux (figure 7). Des anomalies de l'axe droite-gauche sont parfois observées

(Ferrante et al., 2006). Chez le poisson-zèbre, l'inactivation de ce gène conduit à une courbure aberrante du corps, des malformations cardiaques avec un œdème péricardique, des anomalies oculaires, squelettiques et cérébrales (figure 8) (Ferrante et al., 2009).

L'identification du gène *Ofd1* comme gène majeur du cil a fait d'emblée suspecter l'appartenance des syndromes OFD au groupe des ciliopathies.

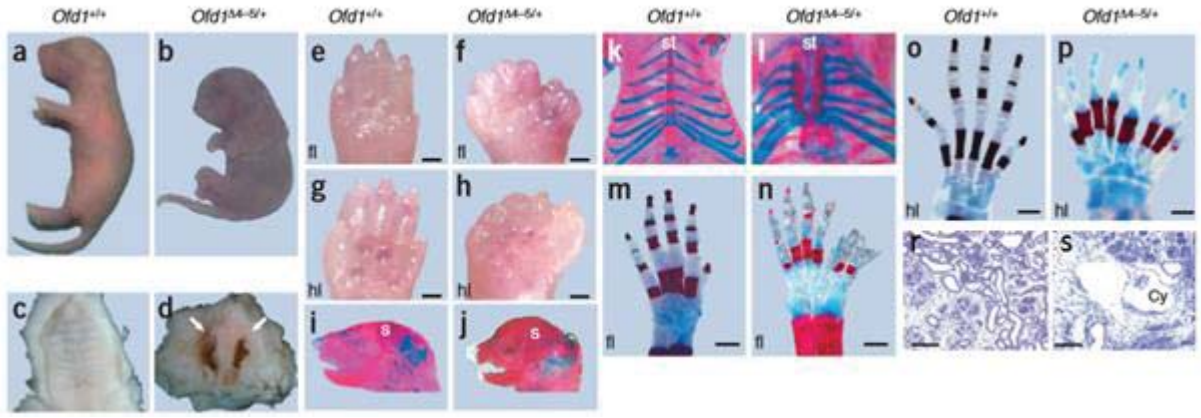

Figure 7 : Phénotype des souris mutées dans le gène Ofd1. *Les souris mutées (b) sont plus petites que les contrôles (a) avec un museau court, une fente palatine (c-d), une polydactylie (e-h), des anomalies squelettiques, au niveau du crane (i-j), du thorax (k-i) avec des côtes surnuméraires et une absence de fusion du sternum, et des extrémités (m-p). Des kystes rénaux sont aussi observé (r-s). Adapté de Ferrante et al., 2006.*

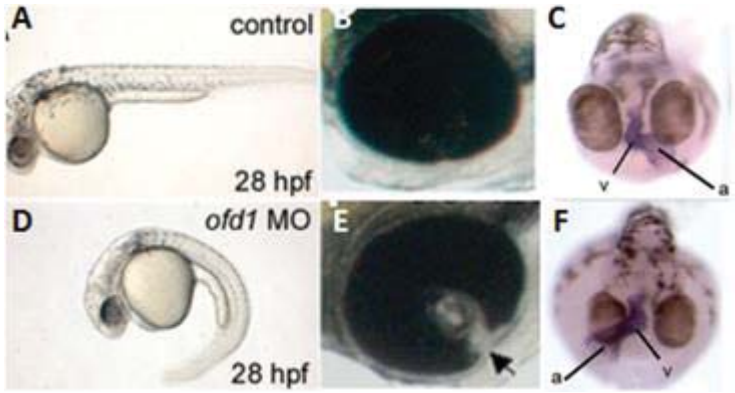

Figure 8 : Phénotype des poisson-zèbres mutées dans le gène Ofd1. *Morpholino Ofd1 par rapport au contrôle (A-C), avec présence d'une courbure de l'axe du corps (D), d'un colobome rétinien (E) et inversion de la position des organes (F). A : atrium, V : ventricule. Adapté de Ferrante et al., 2009.*

2.3.2- Le gène *TMEM216*

2.3.2.1- Spectre mutationnel

En 2010, le séquençage du gène *TMEM216,* responsable des syndromes de Joubert et de Meckel, dans une cohorte de réplication de patients avec des signes cliniques similaires a

permis d'identifier une mutation causale homozygote (NM_001173990.2:p.Arg73Leu) chez deux individus non-apparentés d'origine Juive-Ashkénaze. Ils présentent un tableau clinique chevauchant avec le syndrome de Joubert (apraxie oculomotrice, signe de la dent molaire à l'IRM cérébral) en plus d'hamartomes linguaux, de freins gingivaux multiples et d'une polydactylie, caractéristique d'un syndrome OFD VI (Valente et al., 2010). A ce jour, aucun autre cas n'a été diagnostiqué avec un syndrome OFD et une mutation dans ce gène.

Le gène *TMEM216* se compose de 5 exons codants. Neuf mutations différentes sont actuellement connues (figure 9) avec un effet fondateur pour deux mutations (p.Arg73Leu et p.Gly12Val) dans les populations Juive-Ashkénaze et Turque (Edvardson et al., 2010; Szymanska et al., 2012; Valente et al., 2010).

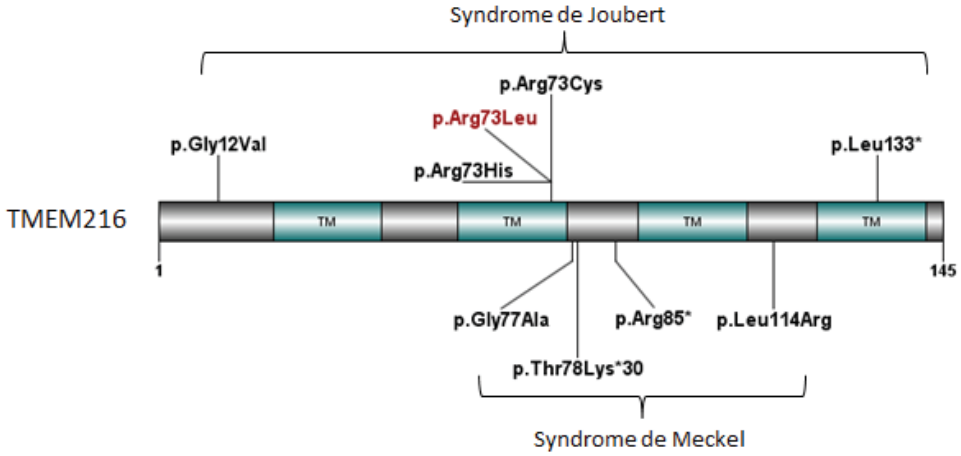

Figure 9 : Spectre mutationnel du gène TMEM216. *Les mutations rapportées dans le syndrome OFD sont notées en rouge, celles rapportées dans d'autres ciliopathies en noir. TM : domaine transmembranaire.*

2.3.2.2- Fonction

Le gène *TMEM216*, s'exprime dans les reins, le cartilage, le système nerveux central mais aussi dans les différents bourgeons embryonnaires (Lee et al., 2012; Valente et al., 2010).

Le gène *TMEM216* code pour une protéine transmembranaire du cil primaire (figure 10). Plus précisément, TMEM216 a été localisée au niveau de la zone de transition et du corps basal du cil (Garcia-Gonzalo et al., 2011a). Une autre étude localise également TMEM216 dans les vésicules post-golgiennes qui acheminent les protéines du cytosol vers le cil (Lee et al., 2012). TMEM216 participe à la ciliogenèse. En effet, l'inactivation de *TMEM216* dans les

cellules épithéliales rénales *in vitro* montre une diminution du nombre de cil primaire avec une défaillance au niveau de l'ancrage du corps basal à la surface apicale des cellules (Logan et al., 2011; Valente et al., 2010). Il interagit avec d'autres protéines de la zone de transition telles que TCTN1 et autres protéines à domaine transmembranaire (TMEM67, TMEM237). Sa localisation requiert, par ailleurs, les protéines ciliaires B9D1, B9D2 et RPGRIP1L chez *c.elegans* (Huang et al., 2011; Logan et al., 2011). Une étude démontre que TMEM216 est une sous-unité d'un complexe majeur de la zone de transition, le module MKS (Garcia-Gonzalo et al., 2011b). Chez la souris et *C.elegans*, une redondance fonctionnelle est suspectée avec TMEM237, un autre composant du module MKS, qui expliquerait le phénotype moins sévère, voir l'absence de défaut du cil primaire (Huang et al., 2011).

L'inactivation de ce gène chez le poisson zèbre conduit à un phénotype incluant des anomalies sévères de l'axe droite-gauche, liées à un défaut de la voie de signalisation de la polarité cellulaire planaire, une queue courbée anormalement, une hydrocéphalie et une effusion péricardique (Lee et al., 2012). La voie WNT semble aussi affectée chez ces morpholinos (Logan et al., 2011).

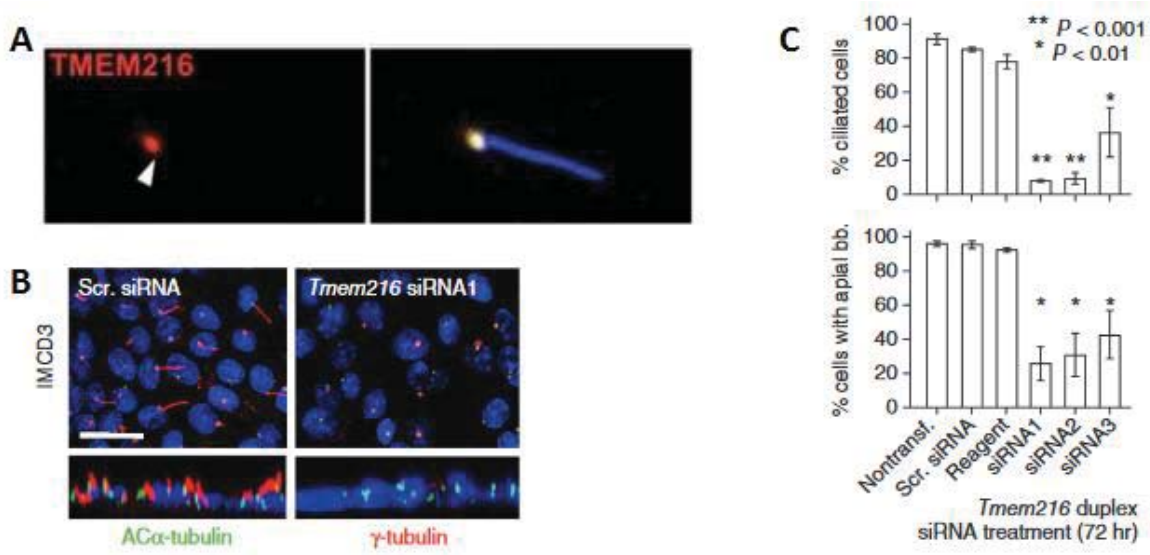

Figure 10 : TMEM216 est localisé dans le cil primaire. *TMEM216 est une protéine avec quatre domaines transmembranaires (A) localisée à la base du cil. (B-C) L'analyse des fibroblastes transfectées par des siRNA dirigés contre TMEM216 montre une diminution du nombre de cellules ciliées (Valente et al., 2010 ; Garcia-Gonzalo et al., 2011).*

2.3.3- Le gène *TCTN3*

2.3.3.1- Identification et caractérisation

Le gène *TCTN3* a été identifié par cartographie par homozygotie et séquençage haut-débit de 1644 gènes ciliaires candidats chez un fœtus, issu de parents consanguins, qui présentait des signes cliniques ayant permis de diagnostiquer un syndrome OFD IV (dysmorphie faciale, langue lobulée, polydactylie, polykystose rénale, encéphalocèle occipital, agénésie du corps calleux, hypoplasie vermienne, courbure des os longs et hypoplasie tibiale). L'étude d'une cohorte de réplication composée d'individus présentant une ciliopathie a mis en évidence sept nouveaux cas mutés (annexe 2) dont cinq présentant un syndrome OFD IV avec une hypoplasie tibiale et deux enfants avec un syndrome de Joubert sans anomalies tibiales (Thomas et al., 2012).
La description de trois nouveaux cas en 2014 et 2015 a confirmé l'allélisme entre les syndromes de Joubert et OFD IV (Bachmann-Gagescu et al., 2015; Ben-Salem et al., 2014; Huppke et al., 2014).

Le gène *TCTN3*, composé de 14 exons, code pour une protéine ciliaire de 607 acide-aminés, de la famille Tectonic impliquée dans la transduction du signal Sonic HedgeHog (SHH). TCTN3 présente un domaine extracellulaire (acide-aminés 23 à 581), un domaine hélical (582-602) et une région intracellulaire (603-607). Toutes les mutations rapportées à ce jour sont localisées dans le domaine extracellulaire (figure 11).

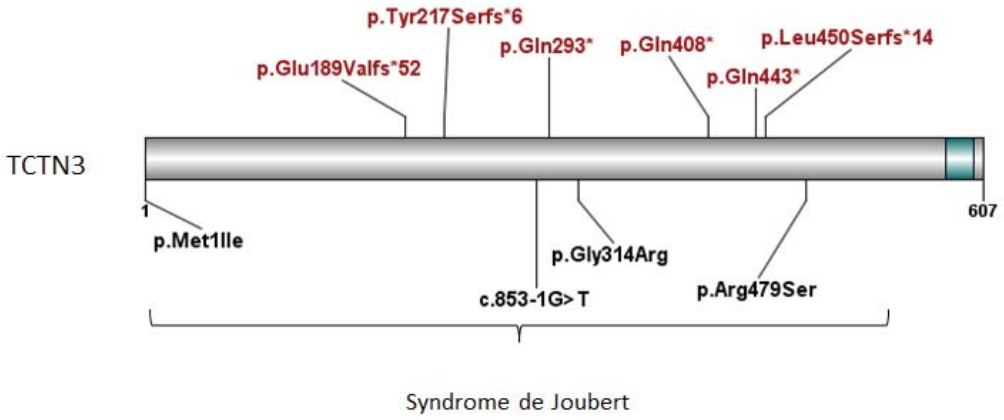

Figure *11:* Spectre mutationnel du gène TCTN3. Les mutations rapportées dans le syndrome OFD sont notées en rouge, celles rapportées dans d'autres ciliopathies en noir. TM : domaine transmembranaire.

2.3.3.2- Fonction

TCTN3 est localisé dans la zone de transition du cil primaire, où il interagit étroitement avec les protéines de la même famille TCTN1 et TCTN2 (figure 12) (Huppke et al., 2014). Sa fonction est peu connue. Les souris mutées dans les gènes *Tctn1* ou *Tctn2*, présentent une polydactylie et des anomalies du tube neural. Il est aussi noté chez ces souris, une dérégulation de la voie Shh (Thomas et al., 2012). L'étude des fibroblastes des patients mutés a montré une inhibition de la voie SHH dans le cil due à une anomalie dans le processus de clivage de GLI3 à l'origine d'une augmentation de la forme clivée et répressive de GLI3 chez les patients (Thomas et al., 2012). Cependant le mécanisme précis selon lequel TCTN3 intervient reste encore inconnu.

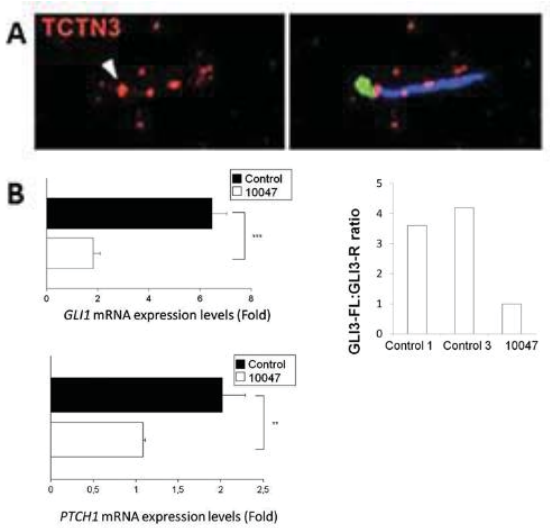

Figure 12 : TCTN3 régule la voie SHH dans le cil primaire*. (A) TCTN3 est localisé dans la zone de transition du cil. (B) Il est noté une diminution de l'expression de GLI1 et PTCH1, effecteurs de la voie SHH dans les cellules d'un patient muté dans le gène TCTN3, et une augmentation de la forme répressive GLI3-R. Adapté de Garcia-Gonzalo et al., 2011a; Thomas et al., 2012.*

2.3.4- Le gène *C5orf42*

Initialement rapporté dans le syndrome de Joubert, des mutations du gène *C5orf42* ont été secondairement identifiées chez des patients présentant un syndrome OFD VI (Lopez et al., 2014; Srour et al., 2012), puis, dans un cas présentant un syndrome de Meckel (Shaheen et al., 2013a).

A ce jour, 38 mutations différentes sont connues, dont 17 sont associées au syndrome OFD VI (figure 13), principalement des mutations faux-sens, réparties entre les exons 5 et 49.

C5orf42 code pour une protéine ciliaire localisée dans le corps basal dont la fonction n'est pas clairement élucidée (Lopez et al., 2014).

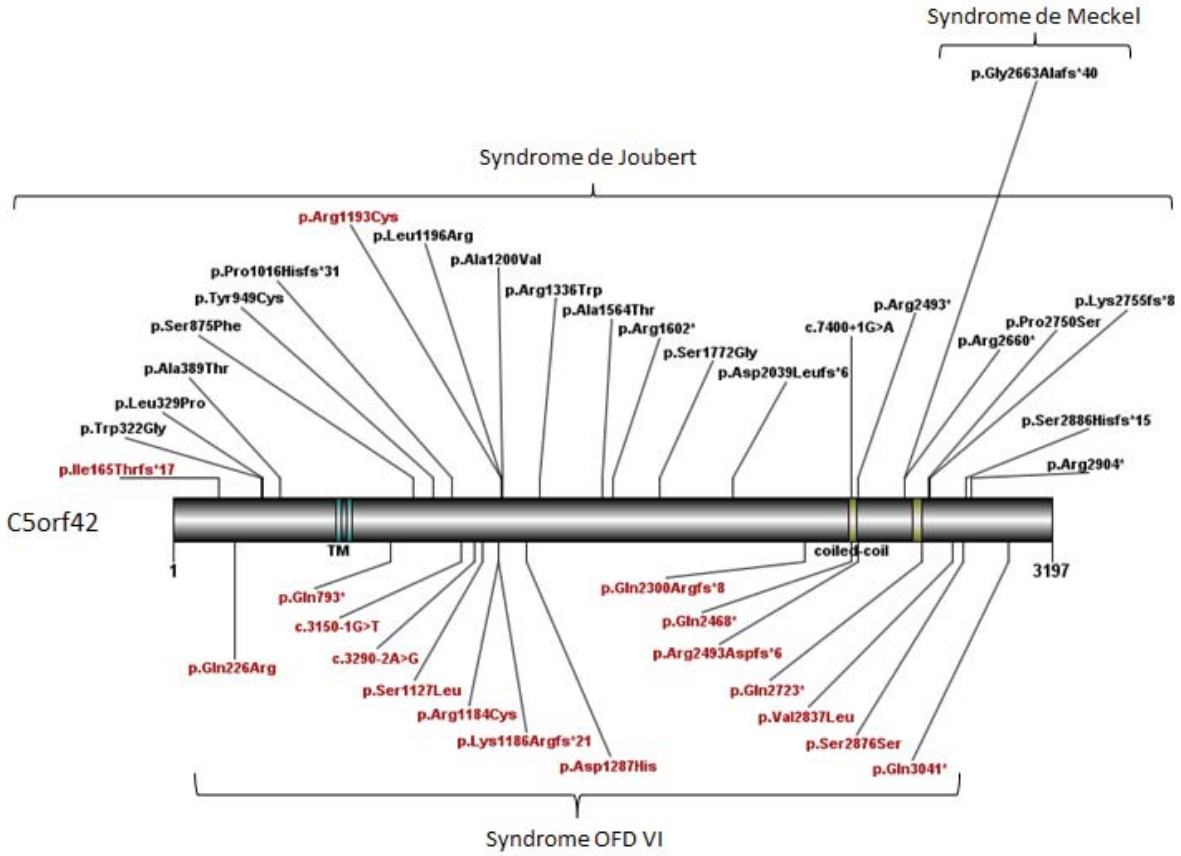

Figure 13 : Spectre mutationnel du gène C5orf42. *Les mutations rapportées dans le syndrome OFD sont notées en rouge, celles rapportées dans d'autres ciliopathies en noir. TM : domaine transmembranaire.*

2.3.5- Le gène *DDX59*

Des mutations homozygotes de ce gène (NM_001031725.4:p.Gly534Arg et p.Val367Gly) ont été décrites chez des patients arabes issus de deux familles consanguines distinctes atteintes d'un syndrome OFD non classé (figure 14). Les cas atteints présentaient des anomalies de la langue (langue lobulé), une fente palatine, des bosses frontales, un hypertélorisme, une polydactylie et un retard mental, plus ou moins associés à des anomalies cérébrales, cardiaques et/ou rénales (Shamseldin et al., 2013)

Figure 14 : Spectre mutationnel du gène DDX59.

Le gène *DDX59* se compose de 8 exons dont 7 sont codants. Il code pour une hélicase ARN de 619 acide-aminés, une famille protéique impliquée généralement dans le métabolisme ARN, l'épissage, l'exportation nucléaire et la biogénèse des ribosomes. La protéine est localisée principalement dans le noyau cellulaire et les granules cytoplasmiques. DDX59 est exprimé dans plusieurs tissus durant l'embryogénèse, notamment au niveau des lèvres, du palais secondaire des yeux et des bourgeons membranaires. Le knock-out de ce gène chez les souris affecte le développement du palais et des membres principalement (Shamseldin et al., 2013).

Sa fonction n'est pas connue, un rôle dans la biogénèse des ARN est suspecté. Contrairement aux autres protéines impliquées dans les syndromes OFD, DDX59 n'a pas été retrouvé dans le cil primaire, cependant les patients mutés montrent un dysfonctionnement de la voie SHH dans le cil, bien que la ciliogenèse ne soit pas affectée (figure 15) (Shamseldin et al., 2013).

Les mutations identifiées sont localisées dans le domaine hélicase de liaison à l'ATP et le domaine hélicase C-terminal suspectant l'importance des domaines hélicases dans la fonction de DDX59 (figure 14).

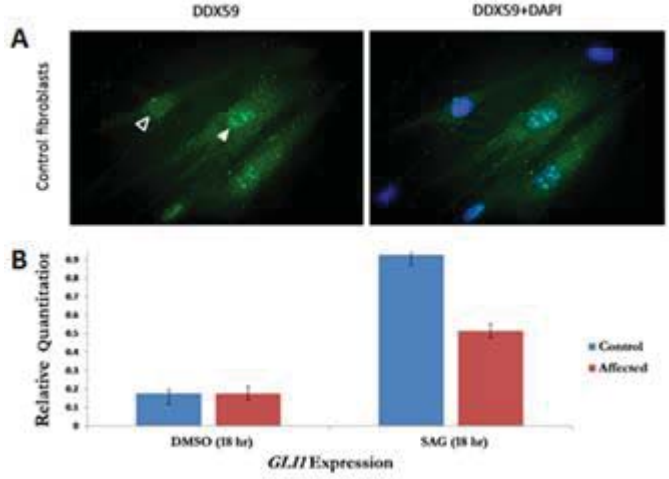

Figure 15 : DDX59 régule la voie SHH. *(A) DDX59 est localisé dans le noyau cellulaire et le cytosol. (B) L'expression de GLI1 est plus faible dans les fibroblastes des patients atteints que dans les contrôles après stimulation de la voie SHH. Adapté de Shamseldin et al., 2013.*

2.3.6- Le gène *SCLT1*

Ce gène n'a été impliqué à ce jour que chez un seul individu atteint d'un syndrome OFD IX et issu d'une famille consanguine (Adly et al., 2014). La mutation est homozygote tronquante (figure 16A).

Le gène *SCLT1* code pour une protéine centrosomale de 688 acide-aminés. SCLT1 est une protéine conservée au cours de l'évolution dans les organismes ciliaires. Elle colocalise avec quatre autres protéines (CEP164, CEP83, CEP89 et FBF1) au niveau de l'appendice distal du centriole et son recrutement est dépendant de CEP83 et C2CD3 (figure 16B,C) (Tanos et al., 2013; Ye et al., 2014). SCLT1 participe à l'assemblage de l'appendice distal et au recrutement des protéines dans le centriole afin de permettre l'extension du cil primaire (Tanos et al., 2013).

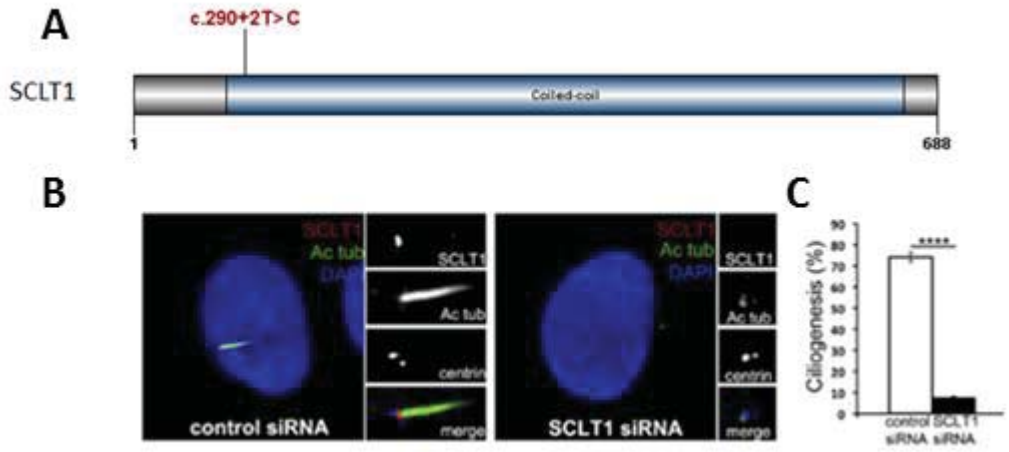

Figure 16 : Spectre mutationnel et caractérisation du gène SCLT1. (A) Unique mutation identifiée dans le gène *SCLT1*. (B) SCLT1 colocalise avec la centrine au niveau de l'appendice distal du centriole. (C) Son knock-down par siARN induit une diminution significative de la ciliogenèse. Adapté de Tanos et al., 2013.

2.3.7- Le gène *TBC1D32/C6orf170*

Comme précédemment, un seul cas muté dans le gène *TBC1D32* est actuellement recensé (Adly et al., 2014).

Le gène *TBC1D32* code pour une GTPase activatrice dont la fonction n'est pas connue. TBC1D32 est une protéine ciliaire qui régule la voie SHH en aval de PTCH1 (Ishikawa et al., 2012; Ko et al., 2010). Le modèle murin mutant présente une microphtalmie sévère, une polydactylie et des anomalies du développement cérébral (Adly et al., 2014). Au niveau du cil, des anomalies de la morphologie et une mauvaise coordination l'élongation de l'axonème et la croissance de la membrane ciliaire sont notées (figure 17). Chez le poisson-zèbre muté, le phénotype ciliaire est similaire à celui retrouvé chez la souris *Bromi* (Ko et al., 2010).

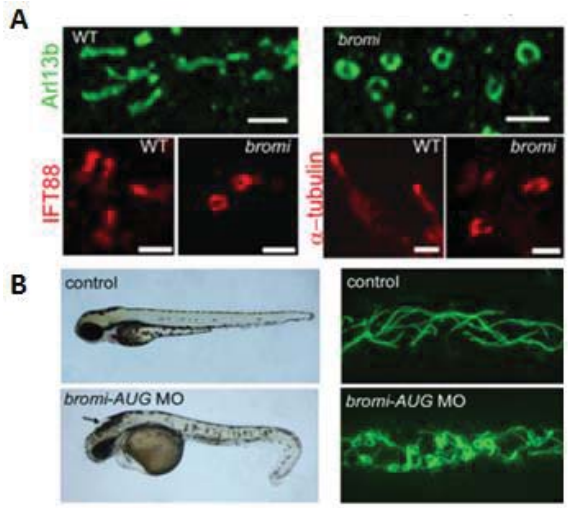

Figure 17 : TBC1D32 est impliqué dans la ciliogenèse. *(A) Chez la souris mutante Bromi, des anomalies de la morphologie des cils sont notées. (B) Le morpholino Bromi présente une courbure anormale de l'axe du corps et des anomalies des cils des cellules rénales. Adapté de Ko et al., 2010.*

2.4- Perspectives thérapeutiques

Les ciliopathies sont un groupe de pathologies rares et hétérogènes. Pour la majorité des patients, les traitements curatifs sont limités voire inexistants, seul un conseil génétique, un suivi médical préventif et des recommandations pour améliorer la qualité de vie sont proposés. Dans certains cas, il peut être proposé une chirurgie réparatrice (fentes labio-palatines, polydactylie), des implants épi-rétiniens (stimulation électrique des cellules rétiniennes), voir une transplantation rénale dans les formes les plus sévères (Bacchetta et al., 2015; Little and Cornwall, 2016; Sahel et al., 2015). Cependant, l'identification des bases moléculaires et physiopathologiques tend à développer de nouvelles stratégies thérapeutiques, notamment contre les symptômes évolutifs tels que la rétinopathie ou la polykystose rénale.

2.4.1- Traitements pharmacologiques

Une meilleure description de la physiopathologie des ciliopathies a montré le rôle clé du cil. Les molécules impliquées dans la formation du cil ou la transduction des signaux sont donc des cibles de choix pour développer de nouveaux traitements. Plusieurs molécules ont fait ou font l'objet d'un essai clinique chez l'Homme.

La formation des kystes rénaux dans plusieurs ciliopathies, implique en partie les voies de la vasopressine et de la somatostatine qui réduisent le taux intracellulaire d'adénosine

monophosphate cyclique (AMPc), la voie mTOR qui est suractivée, ou encore les voies qui contrôlent la prolifération et le cycle cellulaire ; toutes à l'origine de la progression de la pathologie (Riella et al., 2014). Des inhibiteurs de la voie vasopressine (Tolvaptan) et mTOR (everolimus et sirolimus) ou des analogues de la somatostatine (octreotide, pariséotide, lanréotide) ont été développés et testés sur des cohortes de patients présentant une polykystose rénale autosomique dominante (Perico et al., 2010; Serra et al., 2010; Torres et al., 2012; Walz et al., 2010). Dans tous les cas, les patients ont montré une amélioration de la fonction rénale et hépatique mais le traitement engendre des effets secondaires importants.
Les voies de signalisation impliquées dans la prolifération cellulaire sont aussi des cibles thérapeutiques potentielles pour lutter contre les kystes rénaux comme le bosutinib (SKI-606), un inhibiteur de la kinase Src, ou le KD019, un inhibiteur des récepteurs kinases EGFR, Src, HER2, VEGFR et EphB4R, font actuellement l'objet d'essais cliniques (Riella et al., 2014). Par ailleurs, les patients traités à la pravastatine ont montré une diminution significative des kystes rénaux et une bonne tolérance au traitement. Cette molécule n'est actuellement pas approuvée par la FDA (Food and Drug Administration), cependant elle peut être proposée aux patients au vu des résultats obtenus à l'issu de l'essai clinique (Cadnapaphornchai et al., 2014; Riella et al., 2014).

Des traitements pharmacologiques contre la dégénérescence rétinienne, observée pour plusieurs ciliopathies (syndromes de Bardet-Biedl, de Joubert…), sont aussi développés telles que l'acide valproïque qui cible la rhodopsine, une protéine défective dans la dégénérescence rétinienne, le Zepalar, qui retarde l'apoptose des photorécepteurs ou encore l'enrichissement nutritionnel en certaines vitamines (lutéine, vitamines C et A palmitate, acide docosohexanoïque et inhibiteurs des canaux calciques) qui pourrait préserver la fonction des photorécepteurs (Sahel et al., 2015; Shintani et al., 2009).
Les patients atteints de rétinopathie pigmentaire ou d'amaurose congénitale de Leber, mutés dans les gènes *LRAT* ou *RPE65*, montrent une déficience en 11-*cis*-retinal. Un essai clinique en cours est réalisé chez ces patients, et utilise un analogue du 11-*cis*-retinal, le QLT091001 (Sahel et al., 2015).

D'autres molécules développées sont testées à ce jour uniquement sur des modèles murins ou des lignées cellulaires de patients. A titre d'exemple, un inhibiteur de HDAC6 capable de restaurer la structure ciliaire et de limiter le désassemblage, HDAC6 étant un élément clé de la résorption du cil, la combinaison d'inhibiteurs apoptotiques (acide valproïque, guanabenze,

inhibiteur de caspase 12), des facteurs neurotrophiques tels que bFGF (basic Fibroblast Growth Factor) ou CNTF (Ciliary Neurotrophic Factor) ou encore la mefloquine sont aussi développés afin de lutter contre la perte des photorécepteurs de la rétine (Mockel et al., 2012; Shin et al., 2015; Shintani et al., 2009; Yu et al., 2016). De nombreuses molécules sont développées pour cibler d'autres voies de signalisation et testées chez la souris avec polykystose rénale, comme la curcumine et la pyriméthanine dirigées contre la voie STAT3/STAT6, la roscovitine qui cible la voie des cytokines ou encore la metformine, un inhibiteur de la voie mTOR (Riella et al., 2014).

2.4.2- Thérapie cellulaire

L'utilisation des cellules souches et la transplantation des cellules sont des techniques en plein essor. Cette dernière stratégie peut être appliquée pour les cellules rétiniennes. En effet, des études récentes ont démontré la capacité à différencier les cellules souches embryonnaires en photorécepteurs matures et à les transplanter dans la rétine en cours de dégénérescence chez les souris adultes (Sahel et al., 2015). De plus, les cellules souches en culture présentent l'avantage de constituer une source initiale illimitée de matériel pour un traitement thérapeutique potentiel.
Actuellement, un essai clinique basé est réalisé chez des patients avec dégénérescence maculaire (Sahel et al., 2015).

2.4.3- Thérapie génique

La thérapie génique consiste à introduire une copie intacte d'un gène défectueux ou un ARN qui sera transcrit ensuite en protéine, dans des cellules ou organes spécifiquement atteints, à l'aide d'un vecteur, généralement viral, *in vivo* ou *ex vivo*, pour une modification génétique transitoire ou permanente. Les tests réalisés, dans le cadre des ciliopathies, sur les modèles animaux sont plutôt encourageants pour une perspective chez l'Homme. A titre d'exemple, la transfection des gènes *BBS4* et *Dfnb31*, chez un modèle murin des syndromes de Bardet-Biedl et Usher de type 2 respectivement, a permis de prévenir la dégénérescence rétinienne (McIntyre et al., 2013). De même, la restauration de l'expression du gène *Ift88* après sa transfection a permis aux souris ne présentant pas de cil primaire au niveau des neurones olfactifs, de retrouver partiellement l'odorat (McIntyre et al., 2013).

Cette stratégie est actuellement testée chez l'Homme, avec l'introduction des gènes *MERTK* ou *RPE65* à l'aide d'un virus adéno-associé chez les patients présentant une dégénérescence rétinienne (Sahel et al., 2015). Elle peut aussi s'appliquer aux ciliopathies motiles comme la dyskinésie ciliaire primaire (*situs inversus*, infertilité masculine, infections pulmonaires récurrentes). Le gène *DNAI1*, muté chez ces patients, a été délivré sur des cellules de l'épithélium respiratoire, *ex vivo*, à l'aide d'un lentivirus qui a permis une restauration des cils motiles (Chhin et al., 2009).

3- Le cil primaire

3.1-Généralités

Les cils et les flagelles sont des extensions de la membrane cytoplasmique situées à la surface de la majorité des cellules eucaryotes. Cette structure a été décrite pour la première fois en 1675 chez le protozoaire par Anthony van Leeuwenhoek, bien que le terme de « cil » n'ai été attribué qu'en 1786 par Otto Muller (Beales and Jackson, 2012). Seuls quelques types cellulaires exemptés de cils sont rapportées, notamment chez les invertébrés, où la présence de cet organite est restreint aux neurones sensoriels, ou encore dans certaines cellules des lignées lymphoïde et myéloïde chez les mammifères (Bisgrove and Yost, 2006; Pazour and Witman, 2003; Satir et al., 2010).

Zimmerman fut le premier à distinguer le cil motile du cil primaire appelé alors « flagelle central » puis renommé en 1968 « cil primaire ». A cette même période, l'ultrastructure du cil primaire est décrite par Sorokin Sergei (Beales and Jackson, 2012). Le cil motile ou flagelle, permet le mouvement des cellules, comme la propulsion des spermatozoïdes chez les mammifères, ainsi que la mise en mouvement des particules et des fluides à la surface des épithéliums, tels que l'ovocyte dans l'oviducte ou encore le liquide céphalo-rachidien dans les ventricules cérébraux. A l'inverse, le cil primaire ou non-motile, a un rôle sensoriel, impliqué dans la régulation des voies de signalisation et la réception des signaux intracellulaires et extracellulaires, qu'ils soient internes (osmolarité, hormones…) ou externes à l'organisme (perception de la lumière, des odeurs, des sons). Les cellules ne présentent généralement qu'un seul cil primaire visible durant le stade de quiescence cellulaire (G0), à l'exception des cellules du plexus choroïde du cerveau où les cils primaires sont regroupés en cluster à la surface d'une même cellule.

Au cours de ces quinze dernières années, les connaissances fonctionnelles et moléculaires autour du cil primaire se sont considérablement améliorées, celui-ci n'étant plus considéré comme un organite vestigial mais comme un élément clé dans de nombreux processus biologiques. Les mutations identifiées comme responsables des syndromes OFD affectent clairement la formation et/ou la fonction du cil primaire.

3.2- Structure et ultrastructure du cil primaire

Le cil est un organite conservé au cours de l'évolution, présentent une structure cylindrique microtubulaire polarisée entourée d'une membrane ciliaire constituée d'une bicouche lipidique dont la composition en protéines et lipides diffère de la membrane plasmatique (Hildebrandt et al., 2011). Le cil localisé généralement au pôle apical de la cellule, loge au centre d'une invagination membranaire appelé poche ciliaire, qui interagit avec les filaments d'actine, qui participent très probablement au maintien et au positionnement du cil (Benmerah, 2013).

Le cil primaire ou monocil, est classiquement formé d'un axonème avec neuf doublets de microtubules périphériques sans microtubules centraux (axonème 9+0) contrairement au cil motile qui présente une paire de microtubules centraux (axonème 9+2). Cependant, il existe des exceptions à cette classification généraliste (figure 18). En effet, les cils du nœud de Hensen chez l'embryon présentent une structure de type 9+0 mais sont impliqués dans le mouvement des cils essentiel au processus de latérisation, à l'inverse nous trouvons des cils de structure 9+2 au niveau des neurones olfactifs. D'autres formes plus rares ont aussi été décrites (axonème 9+4) chez les vertébrés (Berbari et al., 2009; Fliegauf et al., 2007).

Les centrioles, structures formées de 9 triplets de microtubules, sont à l'origine de la formation du centrosome et du cil. Le centrosome, qui est le centre organisationnel de microtubule (MTOC) est composé de deux centrioles, le plus ancien forme le centriole père et le plus récent un centriole fils, qui sont orientés perpendiculairement l'un par rapport à l'autre (figure 19). Il est entouré d'une matrice dense aux électrons en microscopie électronique appelé matériel péricentriolaire où l'on trouve les satellites centriolaires qui permet l'ancrage des microtubules et contient les protéines indispensables à la maintenance du centrosome et à la ciliogenèse (figure 20) (Bettencourt-Dias et al., 2011; Tollenaere et al., 2015).

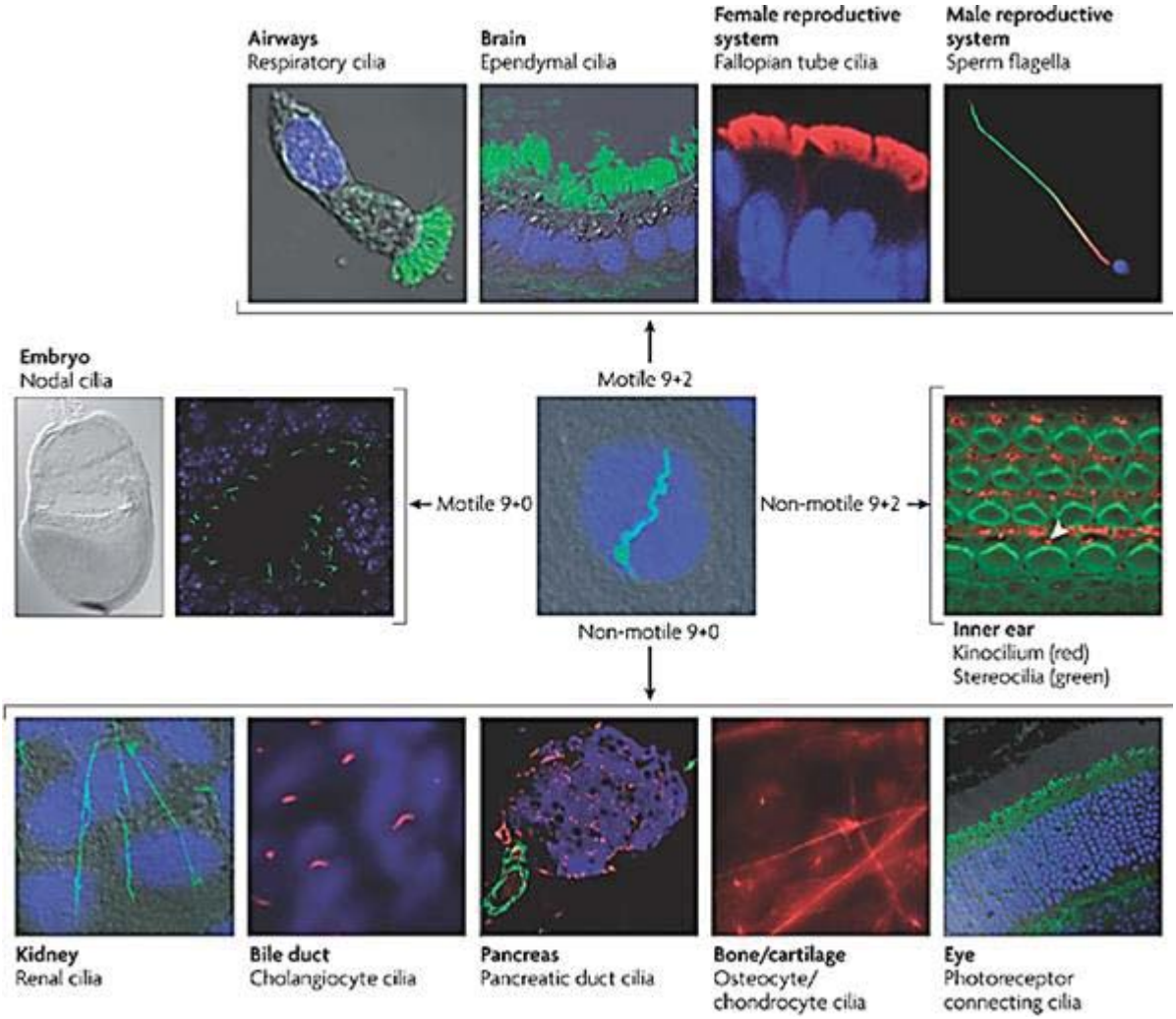

Figure 18 : Les différentes structures ciliaires retrouvées dans les cellules humaines. *Fliegauf et al., 2007.*

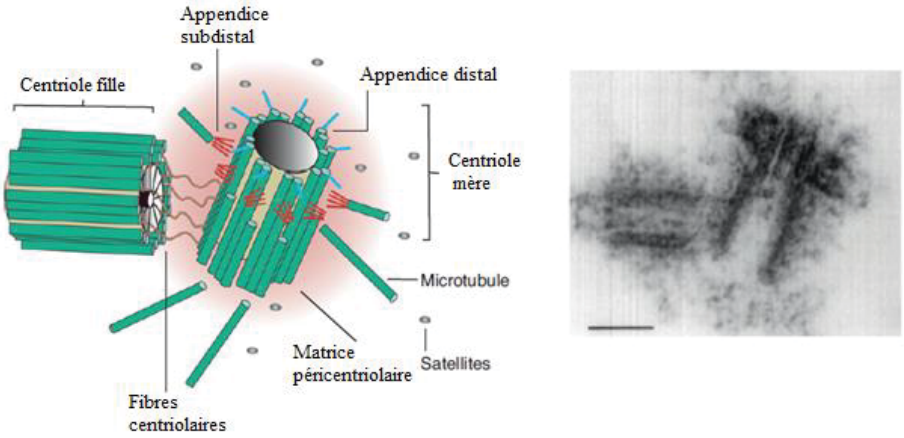

Figure 19 *: Structure du centrosome. Adapté de Bettencourt-Dias et al., 2011*

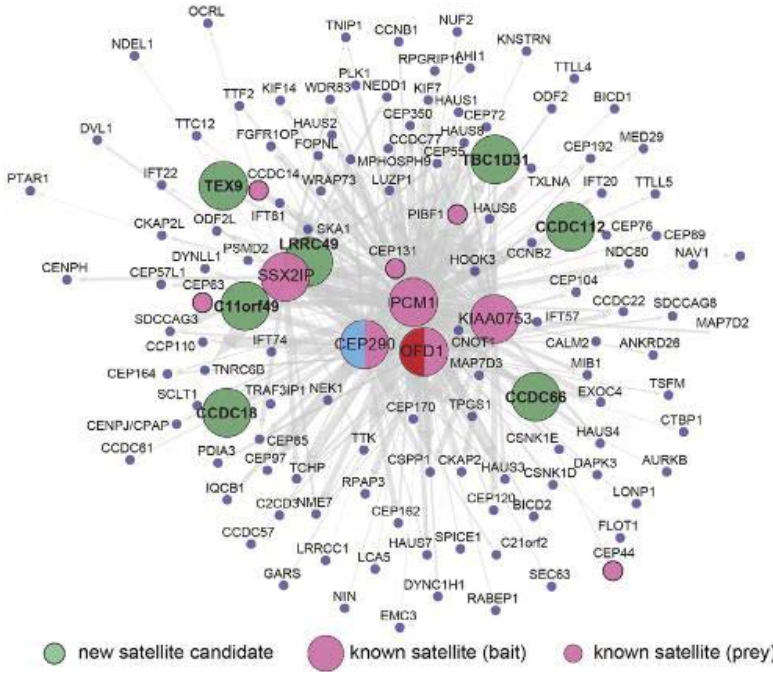

Figure 20 : Interactome des protéines localisées dans les satellites centriolaires. *(Gupta et al., 2015)*

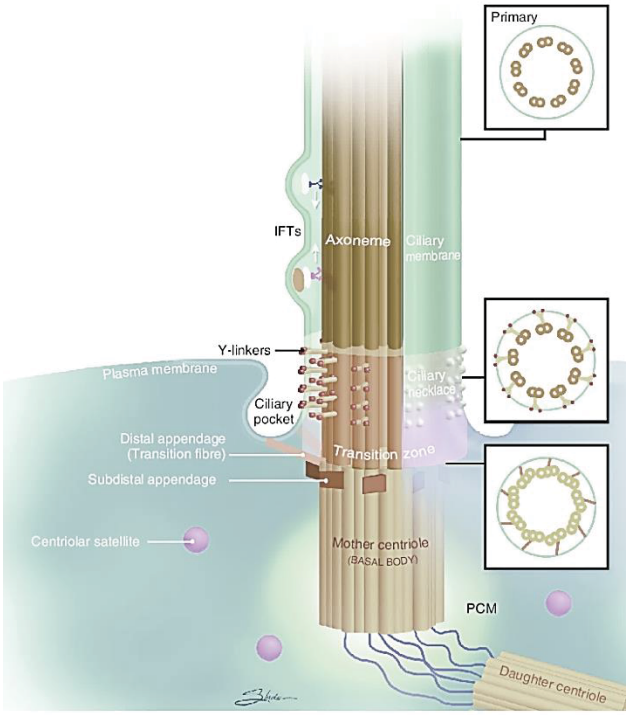

Figure 21: Structure du cil primaire. *Le corps basal ou centriole père mature se compose à son extrémité d'appendice distaux et sub-distaux qui participent à son ancrage à la membrane ciliaire. La zone de transition présente une structure spécifique avec des liens en Y. Au dessus, se trouve l'axonème, prolongation du cil. IFTs : Transport Intraflagellaire (Buchwalter et al., 2016)*

Le cil primaire est organisé en plusieurs compartiments : le corps basal à la base du cil, la zone de transition, et l'axonème avec le compartiment inversine a son extrémité proximale et les récepteurs à l'extrémité distale (figure 21).

Le corps basal, qui dérive du centriole père, va constituer un centre organisateur de microtubules. Il est un lieu privilégié pour les interactions et le stockage des protéines qui seront ensuite dirigées vers le cil. Situé à la base du cil, il est rattaché à la membrane ciliaire par le biais des fibres de transition. A la jonction entre le corps basal et l'axonème, se trouve la zone de transition. Sa structure de base est relativement conservée au cours de l'évolution. En microscopie électronique, des projections denses aux électrons en forme de Y (Y-shapped link) sont observés au niveau de la zone de transition. Ils connectent chaque doublet de microtubules à la membrane ciliaire et sont associés à un collier ciliaire constituée de protéines qui entoure la membrane du cil. Leurs nombres varient selon les espèces et le type cellulaire (Szymanska and Johnson, 2012). Les fibres de transition et la zone de transition forment la « porte ciliaire» (ciliary gate) (Reiter et al., 2012). Cette région est composée d'une barrière de diffusion sur laquelle se trouvent des pores (Ciliary Pore Complex) de structure similaire aux pores nucléaires, qui vont réguler le passage des protéines vers l'axonème (Kee et al., 2012; Musgrave et al., 1986; Ounjai et al., 2013). Ce dernier s'étend du corps basal à l'apex ciliaire où la structure microtubulaire se perd. A l'extrémité distale se concentrent les différents récepteurs nécessaires à la transduction des signaux qui varient selon la fonction de la cellule (Singla and Reiter, 2006). Enfin, une région à l'extrémité proximale de l'axonème a été plus récemment décrite, le compartiment inversine (Sang et al., 2011; Shiba et al., 2009).

3.3- Ciliogenèse

Le cil primaire est présent à la surface des cellules quiescentes (phase G0) et parfois dans les cellules en prolifération durant la phase G1, puis résorbé pendant la phase S ou G2. La ciliogenèse est un processus finement régulé par un certain nombre de protéines et voies de signalisation, dépendant du cycle cellulaire.

3.3.1- Assemblage

La formation du cil primaire débute lorsque le centrosome migre à la surface cellulaire et le centriole père est maturé en corps basal (figure 22). Les radicelles ciliaires sont alors transformées en fibres de transition et les appendices distaux et sub-distaux formeront la base

du cil. A ce stade, une vésicule post-golgienne, la vésicule ciliaire, va encapsuler l'extrémité distale du centriole père et fusionner avec la membrane plasmique pour permettre l'ancrage du corps basal. La formation, le transport et la fusion de la vésicule ciliaire sont permis par le complexe Rab11-Rabin8-Rab8, le BBSome et les protéines golgiennes EHD1 et EHD3 qui seront par la suite essentielles au recrutement des protéines de la zone de transition (CEP290, RPGRIP1L, TMEM67 et B9D2) et IFT20 pour le bon déroulement de l'assemblage du cil primaire. EHD1 favorise par ailleurs la ciliogenèse en inhibant CCP110 (Lu et al., 2015; Tanos et al., 2013; Westlake et al., 2011). L'initiation de la ciliogenèse est régulée principalement par les protéines centrosomales KIAA0586, OFD1, CBY1, ODF2, CEP89, CEP83, SCLT1, FBF1 ou encore AHI1 et CEP164 qui interagissent directement avec Rab8 afin de permettre l'ancrage de la vésicule ciliaire. De plus, la présence de CEP164 dans les centrioles est dépendant du cycle cellulaire, permettant ainsi la formation du cil uniquement pendant les phases G0 ou G1 (Avasthi and Marshall, 2012; Izawa et al., 2015).

Puis, l'axonème est formé à l'extrémité distale du corps basal, par assemblage ordonné des microtubules. Deux possibilités pour générer le cil ont été décrites, d'une part la voie extracellulaire où les microtubules de l'axonème sont assemblés après l'ancrage du centriole père à la membrane, et d'autre part la voie intracellulaire où l'extension de l'axonème débute dans le cytoplasme au moment où se réalise l'association entre le centriole père et la vésicule ciliaire. L'extension de l'axonème est contrôlée par le transport intraflagellaire qui assure le transport bidirectionnel des molécules le long de l'axonème depuis la base jusqu'à l'extrémité distale du cil primaire, et les régulateurs négatifs de la ciliogenèse tel que CCP110, OFD1 et TCHP (figures 23). Les protéines MARK4 et TTBK2, recrutées dans le centriole pendant les phases G0-G1, inhibent le complexe CCP110 en le dissociant et en délocalisant CCP110 du centriole, permettant ainsi, la libération de KIF24 et l'activation de CEP290, des régulateurs positifs de la ciliogénese. De même, la dégradation par autophagie d'OFD1 dans les satellites centriolaires, et de TCHP par une ubiquitine-ligase E3 dans les régions sub-distales et médiales des centrioles permet la formation du cil (Izawa et al., 2015).

Plusieurs protéines engagées dans la biogénèse du cil sont impliquées dans les ciliopathies et notamment dans les syndromes OFD (OFD1, SCLT1).

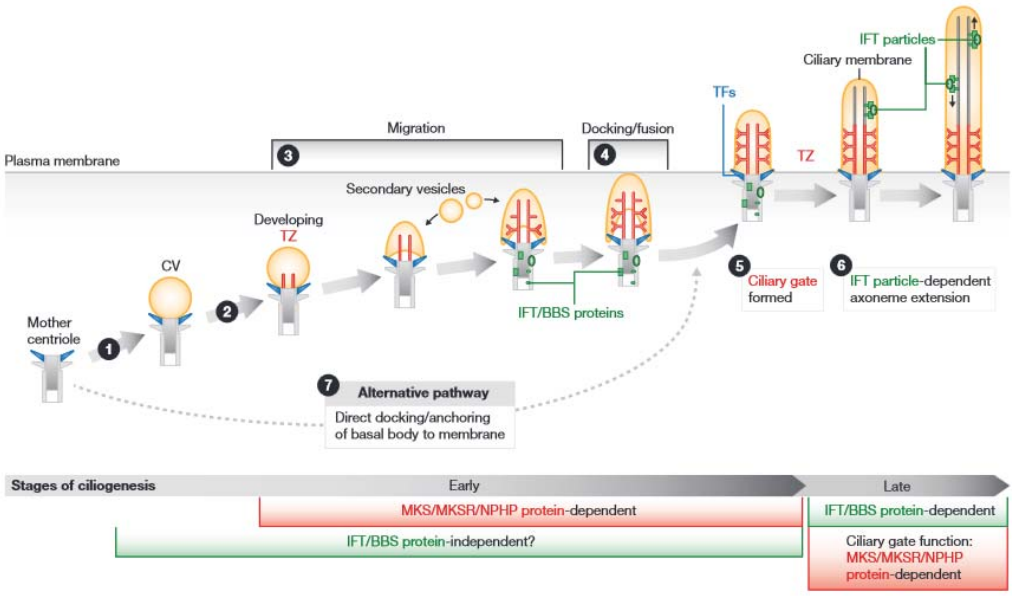

Figure 22 : Les étapes de la formation du cil*. (1) La vésicule ciliaire (CV) se lie à l'appendice distale du centriole père, (2) le centriole mature en corps basal et la zone de transition immature se forme. (3) Des vésicules secondaires viennent fusionner avec la vésicule ciliaire. Après migration jusqu'au pôle apical, la vésicule fusionne avec la membrane plasmatique, (5) la zone de transition maturé permet la formation de la « porte ciliaire » puis (6) l'élongation de l'axonème se met en place. (7) Une autre voie pour la formation du cil où le corps basal est ancré directement à la membrane, est suspectée (Reiter et al., 2012).*

3.3.2- Contrôle de la longueur du cil

La régulation et la maintenance de la longueur du cil impliquent les voies de signalisation (WNT, SHH/Sonic HedgeHog, MAPK, TOR/TSC-target of rapamicin, PCP/Polarité Cellulaire Planaire et Notch) et les protéines impliquées à la fois dans la régulation de la ciliogenèse et du cycle cellulaire telles que NDE1, APC-CDC20 ou les kinases NIMA (Never In Mitosis) NRK ou NEK (figure 23). Un mécanisme d'ubiquitination et dé-ubiquitination permettant une dégradation contrôlée des facteurs clés de la ciliogenèse par le protéasome a par ailleurs été mis en évidence (Avasthi and Marshall, 2012; Broekhuis et al., 2013; Izawa et al., 2015).

A l'extrémité distale de l'axonème les protéines de transport intraflagellaire régulent l'assemblage et le désassemblage continuel des tubulines selon une balance précise afin de maintenir la longueur du cil primaire (Avasthi and Marshall, 2012; Keeling et al., 2016).

3.3.3- Désassemblage ciliaire

Le désassemblage du cil au cours du cycle cellulaire varie selon le type cellulaire et se fait indépendamment de la longueur du cil (Plotnikova et al., 2009). Il est contrôlé par la coordination de plusieurs évènements, qui s'effectuent en deux phases. Dans un premier temps, un désassemblage partiel (« déciliation ») est réalisé durant la phase G1 du cycle cellulaire. Cette phase est principalement régulée par deux voies, Aurora A-HDAC6, activée suite à l'accumulation de la protéine Pitchfork (Pifo) au niveau du corps basal, et Plk1-HDAC6, qui aboutissent à la déacétylation des microtubules de l'axonème. En parallèle, de nombreuses autres modifications post-traductionnelles des tubulines vont aussi induire une instabilité des microtubules (détyronisation) ou estomper l'assemblage (polyglutamylation, polyglycylation). Les protéines ciliaires impliquées dans la croissance ou la maintenance du cil sont méthylées ou ubiquitinylées en vue de leur inactivation et/ou dégradation (Avasthi and Marshall, 2012; Broekhuis et al., 2013). Par ailleurs, la dépolarisation des filaments d'actine participe aussi au désassemblage du cil (Liang et al., 2016). D'autres protéines, telles que Tctex1 sont recrutées pendant la phase G1 afin de faciliter le désassemblage de l'axonème. Cette première étape est indispensable pour permettre le passage de la cellule à la phase S.

Dans un deuxième temps, pendant la phase G2, le cil est totalement résorbé. Cette étape est contrôlée par les protéines kinases NEK2 et KIF24 qui vont induire une dépolarisation des microtubules (figure 23) (Izawa et al., 2015; Kim and Dynlacht, 2013).

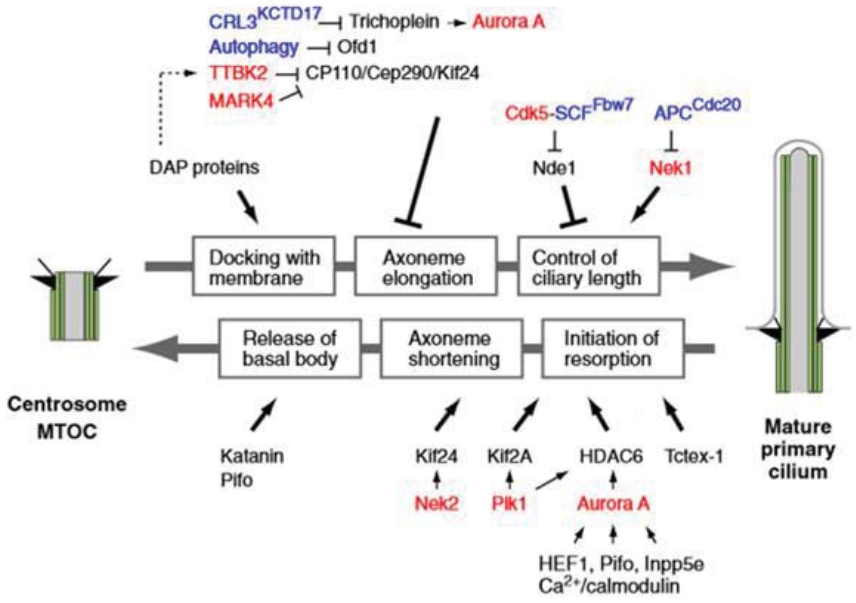

Figure 23: Régulation de l'assemblage et de la résorption du cil. *DAP : Appendice distal centriolaire (Izawa et al., 2015).*

3.4- Protéines et complexes ciliaires

Plus de 1000 protéines ciliaires et centrosomales sont décrites à ce jour dans les bases de données consacrées au ciliome (Alves-Cruzeiro et al., 2014; Arnaiz et al., 2014; van Dam et al., 2013; Gherman et al., 2006). En combinant les données des études transcriptomiques, protéomiques et les prédictions bioinformatiques présents dans la littérature, plus de 3500 protéines putatives (annexe 3) seraient localisées au sein du cil ou du centrosome (Amato et al., 2014; Ishikawa et al., 2012; Ivliev et al., 2012). Bien que pour la majorité de ces protéines, leur localisation précise au sein du cil et/ou leur fonction ne sont pas connues, des complexes ciliaires sont déjà bien décrits. Huit complexes protéiques différents se répartissent dans les 5 compartiments ciliaires (figure 24). La plupart des protéines impliquées dans les syndromes OFD joue un rôle dans ces différents complexes protéiques ciliaires (annexe 4).

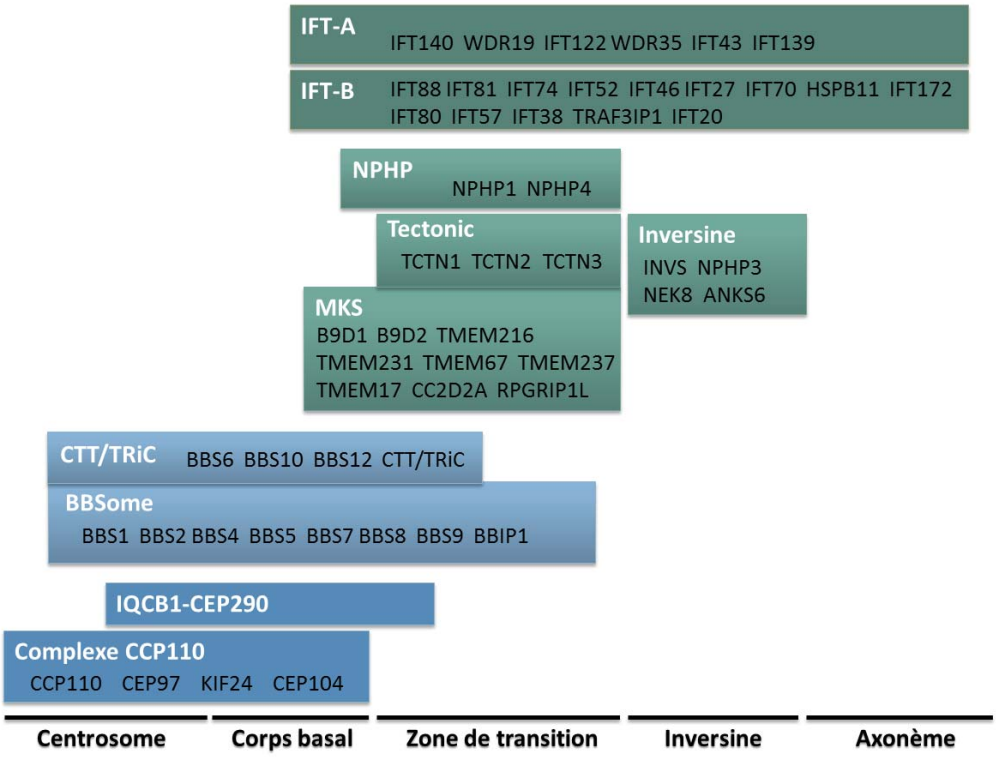

Figure 24 : Les principaux complexes protéiques ciliaires.

3.4.1- Complexe CCP110

La protéine CCP110 impliqué dans la ciliogenèse est principalement localisée au niveau du centrosome et du corps basal. Sa concentration et sa localisation sont dépendantes du cycle cellulaire. Dans le centrosome, la concentration de CCP110 diminue lors des phases G2/M et G0/G1, et est absente dans le corps basal durant la phase de quiescence cellulaire G0 (Tsang and Dynlacht, 2013). CCP110 est un régulateur négatif de l'assemblage du cil primaire, capable de contrôler la longueur des centrioles. Son knock-out entraine la formation prématurée d'un cil pendant la phase de prolifération cellulaire, à l'inverse, une surexpression de CCP110 inhibe la ciliogenèse dans les cellules quiescentes. Jiang et al., précisent la localisation de CCP110 au niveau de l'extrémité distale des centrioles où il interagit et forme un complexe avec les protéines CEP97, KIF24 et CEP104 (Jiang et al., 2012; Kobayashi et al., 2011). CEP97 se comporte comme une chaperonne pour CCP110 tandis que KIF24 permet le recrutement de CCP110 au sein du centrosome et le stabilise. KIF24 agit comme un suppresseur de la ciliogenèse au même titre que CCP110 et CEP97, en permettant la dépolymérisation des microtubules centriolaires. A l'inverse des autres composants du complexe, CEP104 permet d'augmenter la croissance axonémale et est impliqué dans le syndrome de Joubert (Srour et al., 2015).

Le complexe CCP110 limite la ciliogenèse et agit comme un antagoniste à CEP290, un régulateur positif de l'assemblage du cil. A la différence du complexe CCP110, CEP290 est présent dans le centrosome à toutes les étapes du cycle cellulaire. Le complexe CCP110 aurait donc comme rôle de restreindre la fonction de CEP290 durant la prolifération cellulaire (Tsang and Dynlacht, 2013).

3.4.2- Complexe IQCB1-CEP290

L'interaction génétique entre les protéines IQCB1/NPHP5 et CEP290/NPHP6 a été mis en évidence par (Schäfer et al., 2008). Plus récemment, le module IQCB1-CEP290 a été localisé dans le centrosome mais aussi au niveau de la zone de transition (Barbelanne et al., 2013, 2015; Sang et al., 2011). Ce module joue un rôle de « gatekeeper » au sein du cil. En effet, IQCB1 interagit étroitement avec le BBSome et permet de contrôler son entrée dans le cil et de vérifier son intégrité. En absence du module, le transport ciliaire et l'adressage des protéines par le BBsome se retrouvent partiellement affectées (Barbelanne et al., 2015).
Ce complexe est impliqué dans le syndrome de Joubert et maladies associées avec anomalies oculaires et rénales (anciennement syndrome de Senior-Løken) et l'amaurose congénitale de Leber. Le gène *CEP290* est aussi muté dans d'autres ciliopathies : les syndromes de Meckel, de Bardet-Biedl, la néphronophtise (Coppieters et al., 2010; Stone et al., 2011).

3.4.3- BBSome et complexe CTT/TRiC

Le complexe BBSome est composé de huit membres (BBS1/2/4/5/7/8/9 et BBIP1) localisés au niveau de la base du cil, dans le centrosome, le corps basal et la zone de transition (Barbelanne et al., 2015; Zhang et al., 2012). Les protéines BBS2, BBS7 et BBS9 constituent le cœur du complexe tandis que BBS1 et BBS4 sont à la périphérie. Trois protéines chaperonnes-like, BBS6/MKKS, BBS10 et BBS12, forment le complexe avec CTT/TRiC nécessaire à la stabilisation de BBS7, et se dissocient du BBSome une fois celui-ci assemblé (Seo et al., 2010). ARL6 et CEP290 participent au recrutement des membres du complexe dans le cil primaire. Le BBSome permet principalement le transport des protéines vers le cil. Il est régulé par IFT27/BBS19 qui interagit avec IFT25 du complexe IFT-B impliqué dans le transport intraflagellaire. Chez *C. elegans*, le BBSome contrôle même l'assemblage des complexes IFT-A et IFT-B (Wei et al., 2012). Le BBSome joue aussi un rôle dans la

régulation de l'architecture du cytosquelette, dans la biogénèse de la membrane ciliaire et la régulation de la voie de signalisation SHH (Jenkins and Hernandez-Hernandez, 2015; Jin et al., 2010; Zhang et al., 2012).
Les protéines du BBSome sont majoritairement impliquées dans le syndrome de Bardet-Biedl et les rétinopathies pigmentaires (Khan et al., 2016).

3.4.4- Module B9/MKS

Au niveau de la zone de transition, plusieurs modules fonctionnels ont été décrits parmi lesquels le complexe B9 récemment renommé complexe MKS. Une première étude en 2011 a mis en évidence un complexe composé des protéines TCTN1, TCTN2, CEP290, MKS1, B9D1, TMEM216, TMEM67 et CC2D2A (Garcia-Gonzalo et al., 2011b). Ces protéines régulent la ciliogenèse chez les mammifères et sont mutés dans un certain nombre de ciliopathies (syndromes de Meckel, Joubert, COACH). En parallèle, Chih et al se sont intéressés à la protéine ciliaire B9D1 et identifié par spectrométrie de masse neuf protéines localisée dans la zone de transition qui interagissent avec B9D1 (B9D2, TCTN1, TCTN2, MKS1, AHI1, CC2D2A, TMEM231, KCTD10 et TMEM17) (Chih et al., 2012). Depuis, plusieurs études ont été réalisées autour de ce complexe MKS, désormais composé de 9 sous-unités, trois protéines à domaine B9 (MKS1, B9D1/MKSR1, et B9D2/MKSR2), cinq protéines à domaine transmembranaire (TMEM216/MKS2, TMEM231, TMEM67/MKS3, TMEM237/JBTS-14 et TMEM17), une protéine à domaines C2 et coiled-coil (CC2D2A/MKS6) et de la protéine RPGRIP1L/MKS5 (Barker et al., 2014; Czarnecki and Shah, 2012; Huang et al., 2011; Roberson et al., 2015; Williams et al., 2011). Les protéines du complexe MKS sont pour la majorité retrouvées chez la plupart des espèces ciliées et sont hautement conservées au cours de l'évolution, soulignant ainsi l'importance de leur rôle dans la formation et la fonction du cil primaire (Barker et al., 2014).

Le complexe MKS participe au bon fonctionnement du cil notamment en interagissant avec les autres complexes ciliaires NPHP, Tectonic, IFT ou encore avec le BBsome (Cevik et al., 2013; Huang et al., 2011; Williams et al., 2011; Yee et al., 2015). Il est impliqué dans la formation des différents éléments structuraux de la zone de transition et de la « porte ciliaire » (Y-linker, fibres de transition), mais il est aussi essentiel à la formation de la barrière de diffusion (Chih et al., 2012; Garcia-Gonzalo et al., 2011b). En effet le knockdown des protéines du complexe affecte la localisation des récepteurs au niveau de l'axonème. Le

complexe MKS participe activement aux premières étapes de la ciliogenèse en permettant entre autres la fusion des vésicules de transport avec la membrane plasmatique ou encore l'ancrage du corps basal à la membrane plasmatique notamment via les protéines TMEM237, TMEM216 et TMEM67 (Huang et al., 2011; Reiter et al., 2012). Le complexe MKS participe aussi à la régulation des voies de signalisation SHH (Sonic HedgeHog), WNT non-canonicale et PCP (Chih et al., 2012; Huang et al., 2011; Sang et al., 2011; Szymanska and Johnson, 2012).

Les sous-unités du complexe MKS sont toutes impliquées dans le syndrome de Meckel, à l'exception de TMEM237 et TMEM17, et le syndrome de Joubert pour la grande majorité d'entre elles. Des mutations dans les gènes TMEM216 et TMEM67 ont aussi été rapportées dans les syndromes OFD et NPHP respectivement.

3.4.5- Complexe Tectonic

Rapporté comme associé au module fonctionnel MKS ou comme un complexe à part entière, le complexe Tectonic a récemment été localisé dans la zone de transition (Chih et al., 2012; Garcia-Gonzalo et al., 2011b; Romani et al., 2015). Il est composé de deux protéines à domaine transmembranaires TCTN2 et TCTN3, et d'une glycoprotéine extracytosolique TCTN1. Ce complexe interagit étroitement avec les protéines du complexe MKS, principalement avec les protéines MKS1 et TMEM67. TCTN1 permet en effet la localisation de ces deux protéines au niveau de la zone de transition, et en coopération avec TCTN2, CC2D2A et TMEM67 régule la ciliogenèse (Garcia-Gonzalo et al., 2011b). Les protéines Tectonic jouent un rôle important dans la régulation de la voie SHH. Elles permettent notamment le recrutement à la membrane des protéines Smoothened et Pkd2, essentielles à la transduction du signal (Czarnecki and Shah, 2012; Reiter and Skarnes, 2006).

Les trois composants du complexe sont impliqués dans le syndrome de Joubert, TCTN2 est aussi impliquée dans le syndrome de Meckel et TCTN3 dans le syndrome OFD IV.

3.4.6- Module NPHP

Localisé dans la zone de transition, le complexe NPHP est formé de deux sous-unités : NPHP1 et NPHP4, impliquées dans les syndrome de Joubert, Senior-Løken, et la néphronophtise. Chez *C. elegans*, une redondance de fonction est noté entre les modules NPHP et MKS (Williams et al., 2008). Les interactions entre ces deux modules sont

nombreuses, à titre d'exemple RPGRIP1L/MKS5/NPHP8 permet le recrutement de NPHP4 dans la zone de transition des cils sensoriels des cellules neuronales, lui-même nécessaire à la localisation de NPHP1. RPGRIP1L est d'ailleurs parfois présenté comme un troisième membre du module NPHP (Szymanska and Johnson, 2012; Williams et al., 2008, 2011). Le complexe participe à la formation (Y-linker), au recrutement des protéines, à la stabilité de la zone de transition et à la transduction des signaux (Huang et al., 2011; Jauregui and Barr, 2005; Jauregui et al., 2008).

3.4.7- Compartiment inversine

Au niveau du compartiment inversine, les protéines INVS/NPHP2, NPHP3, NEK8 et ANKS6 forment un complexe dont la fonction n'est pas encore bien définie (Malicki and Avidor-Reiss, 2014). La protéine ANKS6 constitue le cœur du complexe, qui permet le recrutement des trois autres membres du complexe tandis que la protéine INVS permet l'ancrage de NPHP3 et NEK8 dans le compartiment inversine. En effet, l'absence de INVS entraine la délocalisation de NPHP3 et NEK8 (Hoff et al., 2013; Shiba et al., 2010). Les mutations dans ces gènes causent la néphronophtise et le syndrome de Senior-Løken.

3.4.8- IFT-A et IFT-B

Identifiées initialement chez *Chlamydomonas reinhardtii* après observation du flagelle en microscopie à contraste interférentiel, les protéines IFT assurent le transport bidirectionnel des molécules le long de l'axonème depuis la base jusqu'à l'extrémité distale du cil primaire (Kozminski et al., 1993).

Deux complexes protéiques ont été mis en évidence, IFT-A et IFT-B, composés respectivement de 6 et 14 sous-unités, différenciées par leur poids moléculaires après purification et migration SDS-PAGE. Le cœur du complexe IFT-A est formé des protéines WDR19/IFT144, IFT140 et IFT122, tandis que WDR35/IFT121, IFT43 et IFT139 sont situées à la périphérie du complexe. Les sous-unités IFT88, IFT81, IFT74, IFT52, IFT46, IFT27, IFT70 et HSPB11/IFT25 composent le cœur du complexe IFT-B (IFT-B1) et cinq sous-unités sont en périphérie (IFT172, IFT80, IFT57, TRAF3IP1/IFT54, IFT38 et IFT20) pour former le sous-groupe stable IFT-B2 (Taschner et al., 2016). Ces complexes sont associés à des protéines motrices, la kinésine II qui permet l'acheminement des différentes protéines vers l'extrémité distale du cil (mouvement antérograde) et la dynéine 1b

cytoplasmique qui assure le mouvement rétrograde, de l'apex vers la base cil. IFT-A et IFT-B sont tous deux impliqués dans le transport intraflagellaire rétrograde, IFT-A étant aussi mis en évidence dans le transport antérograde (Liem et al., 2012; Pedersen and Rosenbaum, 2008).

Les protéines IFT contiennent de nombreux domaines ou motifs tels que les répétitions WD40, tetratricopeptides ou encore des domaines coiled-coils, permettant des interactions protéiques multiples, nécessaires à l'assemblage du complexe mais aussi au transport des protéines ciliaires qui s'associent en cargo (Taschner et al., 2012). Ces deux complexes délivrent de manière efficace les protéines dans les différents compartiments ciliaires nécessaires à l'assemblage et à la maintenance des complexes protéiques et du cil. Outre son rôle dans le transport intraflagellaire, IFT-A et IFT-B sont impliqués dans la régulation de la voie de signalisation SHH et la stabilisation des microtubules (Bizet et al., 2015; Liem et al., 2012).

Les protéines de ces deux complexes sont impliquées dans de nombreuses ciliopathies telles que les syndromes côtes courtes-polydactylie, de Joubert, de Bardet-Biedl, la néphronophtise, la rétinopathie pigmentaire ou encore la dysplasie cranio-ectodermique (annexe 4).

3.5- Trafic protéique

Les protéines du cil primaire ne sont pas directement produites par l'organite. Un système de transport efficace entre le cil et la cellule, et dans le cil, est donc crucial afin de fournir le matériel nécessaire à la formation et au bon fonctionnement du cil.

3.5.1- Structure de la base du cil

La séparation entre le cytoplasme et le cil primaire est marquée par la présence à la base du cil d'une barrière de diffusion qui contrôle le passage des protéines entre les deux compartiments. Cette barrière est régulée principalement par les protéines de la zone de transition (complexes MKS et NPHP), qui ont des rôles différents au sein de cette structure. Par exemple, CC2D2A facilite le passage des vésicules à travers la barrière tandis que CEP290 détourne les protéines non-ciliaires (Hsiao et al., 2012).

Au même niveau, des pores ciliaires (Ciliary Pore Complex) permettant le passage sélectif des protéines, ont été décrits. Ces pores présentent une structure similaire aux pores nucléaires mais son organisation protéique et son ancrage sont différents. Il est formé de nucléoporines (NUP35, NUP37, NUP62, NUP93, NUP133 et NUP214) ancrées à la base du cil par les protéines de la zone de transition et plus probablement par les protéines du complexe NPHP. En effet, le pulldown de NPHP4 et NPHP5 a révélé après spectrophotométrie de masse, la présence de nucléoporines (Malicki and Avidor-Reiss, 2014; Sang et al., 2011). Deux modèles organisationnels ont été proposés, d'une part un unique pore à la base du cil avec au centre l'axonème, d'autre part la présence de 9 pores localisées entre chaque connexion microtubule-membrane ciliaire en forme de en forme de Y (figure 25). Ce dernier modèle a été observé par tomographie cryo-électronique 9 pores d'environ 50nm de diamètre à la base du cil chez *Tetrahymena* (Kee et al., 2012; Ounjai et al., 2013).

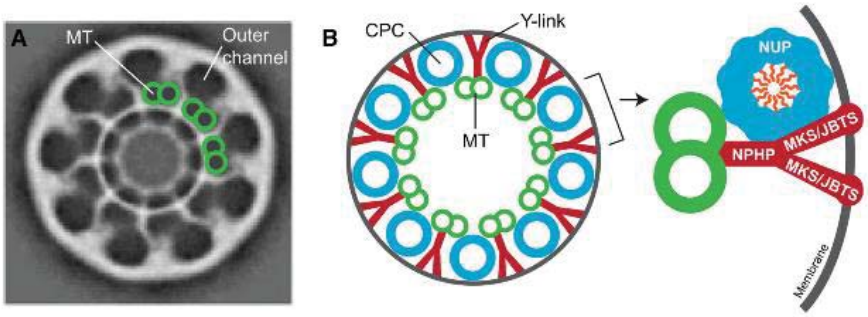

Figure 25: Structures des pores ciliaires. *(A) Image prise en tomographie cryo-électronique des pores ciliaires chez Tetrahymena. (B) Représentation schématique du modèle à 9 pores (en bleu) localisées entre la membrane ciliaire, les microtubules (en vert) et les connections microtubules-membrane (en rouge). (Takao and Verhey, 2015)*

A la base du cil, se trouve aussi une barrière « septines », éléments du cytosquelette qui évite la diffusion latérale des protéines, participe au maintien de la membrane ciliaire et régule le passage des protéines membranaires (Takao and Verhey, 2015).

3.5.2- Protéines hydrophiles

Le passage des protéines solubles à travers les pores ciliaires et la barrière de diffusion est régulé à différentes échelles. Tout d'abord, une sélection selon la taille (40-70kDa) et la conformation des molécules est notée, avec toutefois, une entrée facilité pour certaines protéines ou complexes protéiques de grande taille (Takao and Verhey, 2015).

Des séquences d'adressage au cil ont été décrites pour plusieurs protéines cytosoliques (Dishinger et al., 2010; Hurd et al., 2011). Tout comme cela a été rapportées pour d'autres protéines, ces séquences vont être reconnues et vont permettre d'orienter la protéine vers l'organite approprié. Plusieurs motifs, généralement riches en lysine et arginine, ont été décrits (VxPx, KVxP, KVHPSST, AxEGG, Ax(S/A)xQ…) localisés en N-terminal, C-terminal ou encore dans les boucles intracellulaires pour certaines protéines transmembranaires telles que MCHR1 (Hsiao et al., 2012). Cependant, tous les motifs ne sont pas actifs ou reconnus, le mécanisme précis n'est pas encore élucidé. Le cas le mieux décrit est celui de la protéine KIF17, essentielle à la formation du complexe IFT-B, qui contient deux signaux d'adressage ciliaire, dont un seul est reconnu par l'importine β2 qui va permettre sa localisation.

En parallèle, un gradient RanGDP/RanGTP va orienter le transport. Le cytoplasme, riche en RanGDP, va favoriser l'association entre l'importine β2 et la protéine cible, tandis que le compartiment ciliaire est concentré en RanGTP induit une dissociation du complexe. Le principe est similaire à celui observé pour le transport vers le noyau de la cellule des protéines cytosoliques avec une séquence de localisation nucléaire reconnue par l'importine β2 et favorisé par le gradient RanGDP/RanGTP. L'inactivation de l'importine β2 ou la modification du gradient sont à l'origine de défaut de ciliogenèse (Takao and Verhey, 2015).

3.5.3- Transport vésiculaire

Trois familles des petites protéines GTPases sont impliquées dans le transport des molécules vers la base du cil : RAN, ARF/ARL et RAB. Ces protéines sont dites actives lorsqu'elles sont liées au GTP, et inactives lorsqu'elles sont associées au GDP. L'activation des petites protéines GTPases est réalisée par un facteur d'échange de nucléotide guanine (GEF : guanine exchange factor), l'hydrolyse du GTP par une protéine GTPase activatrice (GAP : GTPase activating protein). Les protéines ARF/ARL et RAB régulent plus particulièrement le transport vésiculaire qui permet l'acheminement des protéines membranaires à la base du cil primaire.

Le complexe ARF4-ASAP1-RAB11-FIP3 joue un rôle important dans la formation, le transport et la fusion des vésicules post-golgiennes (figure 26). ARF4, localisé dans l'appareil de golgi et activé par GBF1 (GEF) permet la construction d'une vésicule dans le trans-golgi

qui intègre les protéines dont la séquence de localisation ciliaire est reconnue par DYNLT1. ARF4 va interagir avec ASAP1 (GAP), Rab11 qui conforte l'activité d'ASAP1 et FIP3, un effecteur de Rab11, pour entrainer une dissociation d'ARF4 du trans-golgi. Le bourgeonnement et le transport de la vésicule vers le cil est permis par les protéines AP-1, RAB8 et la clathrine. D'autres petites protéines GTPases participe au transport (RAB10, RAB17, RAB23…). La protéine Rabin8/ RAB3IP, recrutée et activée par RAB11 et le complexe TRAPII au niveau du centrosome, va activer RAB8 pour initier la fusion de la vésicule avec la membrane ciliaire.

Les protéines RAB8 et RAB11 interagissent avec Sec15, et RAB10 avec Sec8, suggérant une régulation étroite entre le transport des vésicules post-golgiennes et l'exocytose. Le complexe de l'exocyste est composé de huit sous-unités (Sec3, Sec5, Sec6, Sec8, Sec10, Sec15, Exo70 et Exo84) associé à la membrane plasmique et retrouvé au niveau du cil primaire (Rogers et al., 2004). Les sous-unités sont divisées entre la membrane et la surface de la vésicule permettant ainsi un recrutement spécifique et favorisant la fusion et la libération des protéines contenues dans la vésicule (Hsiao et al., 2012). Ce processus, décrit initialement pour le transport de la rhodopsine, est dynamique et permet notamment de délivrer en grand nombre les protéines essentielles au développement et à la fonction du cil, à titre d'exemple, environ 2000 molécules de rhodopsine par minute sont délivrées dans la rétine humaine. Plus récemment, ce mode de transport a été décrit pour d'autres protéines ciliaires telles que PC1 ou PKHD1 (Deretic et al., 1995; Follit et al., 2010; Khanna and Rao, 2015; Ward et al., 2011). Certaines protéines comme PC2 sont reconnues par ARF4 directement dans le cis-golgi (Li et al., 2012).

Indépendamment, après encapsulation par le complexe ARF4-ASAP1-RAB11-FIP3, certaines protéines telles que PCM1, PCNT, NIN, CETN1 ou encore les γ-tubulines sont localisées au niveau du centriole via le transport dynéine-dynactine et microtubule-dépendant, par le biais d'adaptateurs (BBS4, Hook2) qui interagissent à la fois avec les protéines cibles et la dynéine ou dynactine (figure 26) (Madhivanan and Aguilar, 2014).

Une deuxième voie pour le transport vésiculaire est régulée par le BBSome (figure 26). Ce dernier, via BBS1, est recruté par ARL6/BBS3, sous sa forme active, à la base du cil. ARL6/BBS3 permet par la suite la fusion de la vésicule avec la membrane ciliaire et la libération du cargo (Li et al., 2012; Mourão et al., 2014). Le BBSome permet, entre autres, le transport de SSTR3 dont il reconnait la séquence de localisation ciliaire. En absence du

BBSome, SSTR3 s'accumule dans la membrane plasmatique (Nachury et al., 2010). Le BBSome est aussi impliqué dans le transport des molécules du cil vers le cytosol.

D'autres voies indirectes d'endocytose pour fournir les protéines nécessaires au cil primaire sont suspectées, notamment durant les premières étapes de la ciliogenèse. En effet, la poche ciliaire riche en clathrine suggère une forte activité local d'endocytose (Benmerah, 2013; Madhivanan and Aguilar, 2014). Une voie permettant de délivrer les protéines à la membrane plasmatique au pôle apical de la cellule, qui seront ensuite intégrées à la membrane ciliaire par un mouvement latéral membranaire est aussi décrite (figure 26) (Sung and Leroux, 2013).

3.5.4- Transport intraflagellaire

Certaines protéines hydrophobes, regroupées en cargo subissent des modifications lipidiques et bénéficient d'un transport spécifique à travers la barrière de diffusion pour le long de l'axonème (figure 26). Cela est le cas de NPHP3, qui est maintenu sous forme soluble et transporté par UNC119 après N-myristoylation. UNC119 interagit ensuite avec ARL3 et RP2 pour assurer le transport au sein du cil. D'autres modifications lipidiques sont décrits (SUMOylation, palmitoylation) mais le mécanisme de transport restent encore peu connus, bien que la présence d'une séquence de localisation ciliaire indispensable à la bonne localisation ait été démontrée (Hsiao et al., 2012; Malicki and Avidor-Reiss, 2014; McIntyre et al., 2015).

Le transport intraflagellaire implique aussi deux complexes majeurs IFT-A et IFT-B assurant le transport antérograde et rétrograde des molécules. La protéine tubby-like TULP3 se lie au complexe IFT-A et participe au transport de certains récepteurs tels que GPCR (Mukhopadhyay et al., 2010).
IFT27, composant du complexe IFT-B, facilite par ailleurs la sortie des récepteurs par le BBSome. Il active ARL6 afin de permettre l'assemblage du BBSome qui pourra quitter le cil (Liew et al., 2014).

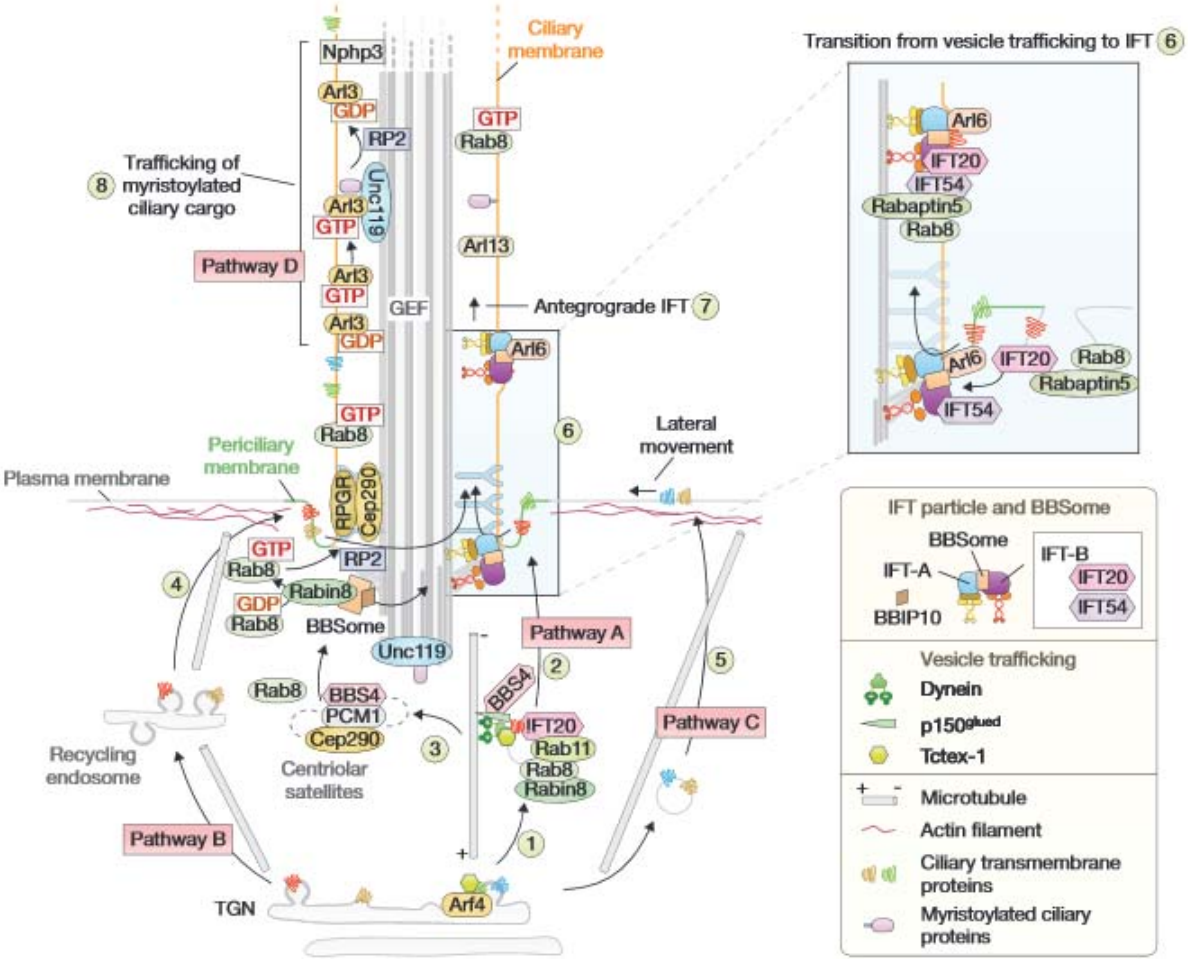

Figure 26: Les différentes voies de transport vers le cil. *Une première voie (pathway A) implique le complexe ARF4-ASAP1-RAB11-FIP3 (1). Une vésicule contenant les protéines ciliaires quitte le trans-golgi (TGN), puis soit IFT20 se greffe au cargo et le dirige vers le centrosome (2) soit la vésicule interagit avec la dynéine et BBS4 pour libérer les protéines au niveau des centrioles (3). Les endosomes de recyclage (pathway B) constituent une voie majeure pour permettre la migration du corps basal et les premières étapes de la ciliogenèse (4). Le contenu des vésicules peuvent être délivrées à la membrane plasmatique apicale (pathway C), qui intègreront la membrane ciliaire par un mouvement latéral (5). Le transport intraflagellaire est assuré principalement par le complexe IFT-A et IFT-B (6, 7), excepté pour les cargos myristoylés impliquant les protéines UNC119, ARL3 et RP2 (pathway D, 8) (Sung and Leroux, 2013).*

3.6- Voies de signalisation ciliaires

3.6.1- La voie HedgeHog

La voie HedgeHog constitue l'une des voies de signalisation majeures du cil primaire (figure 27). Trois ligands sont connus, SHH (Sonic HedgeHog), IHH (Indian HedgeHog) et DHH

(Desert HedgeHog). Ils sont capables de se lier au récepteur transmembranaire PTCH1 (Patched1), qui à son tour va phosphoryler la protéine transmembranaire Smo (Smoothened) qui activera les facteurs de transcription issus de la famille protéique GLI. Ces dernières vont pouvoir quitter le cil primaire et intégrer le noyau pour activer la transcription des gènes cibles. Les deux régulateurs majeurs de cette voie retrouvés au niveau du cil, sont SUFU, un inhibiteur, et KIF7, activateur ou inhibiteur selon les cas (Nozawa et al., 2013).

L'acheminement dans le cil et la localisation des différents composants requièrent de nombreuses protéines du corps basal (OFD1, MKS1, RPGRIP1L, KIAA0586) et de la zone de transition (complexes MKS et NPHP). En effet, les mutations dans les gènes codants pour ces protéines induisent une dérégulation de la voie SHH. De même, les protéines EVC et EVC2 sont indispensables à la localisation de Smo dans la membrane ciliaire (Sasai and Briscoe, 2012). Il a aussi été démontré le rôle du transport intraflagellaire dans la transduction du signal. L'inactivation des gènes codant pour les protéines impliquées dans le transport rétrograde implique une rétention des protéines Smo, PTCH1 et GLI2 dans le cil. Par ailleurs, le BBSome est essentiel à la sortie du cil de PTCH1 et Smo (Nachury, 2014; Nozawa et al., 2013).

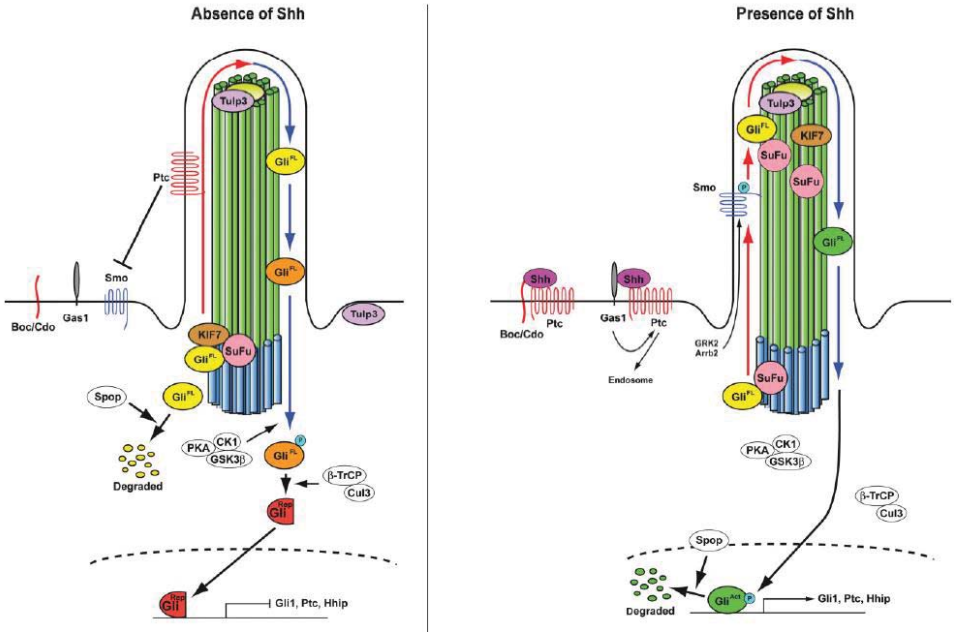

Figure 27: La voie SHH. *(Sasai and Briscoe, 2012)*

3.6.2- La voie PDGF

La voie PDGF (Platelet-Derived Growth Factor) est essentielle à la migration cellulaire. Lorsque le ligand PDGF-AA se lie au récepteur PDGFR localisé au niveau du cil, cela

déclenche une cascade de phosphorilation par les kinases AKT et MEK-ERK. Cette voie n'est pas requise lors des premières étapes de l'embryogénèse, cependant elle est indispensable plus tard, au développement de certaines cellules qui donneront les structures cranio-faciales ou les oligodendrocytes (Goetz and Anderson, 2010; Oh and Katsanis, 2013).

3.6.3- La voie WNT

La protéine WNT est capable d'activer une multitude de cascades de signalisation intra-cellulaire, impliquant les effecteurs Dvl (Dishevelled) et INVS/NPHP2, dont la voie WNT canonicale, dépendante de la β-caténine, et la voie non-canonicale, indépendante de la β-caténine (figure 28). Cette dernière peut se diviser en deux voies : la voie de la polarité planaire cellulaire (PCP) et la voie WNT/Ca^{2+} (Goetz and Anderson, 2010; Sasai and Briscoe, 2012).

La voie de signalisation PCP est notamment impliquée dans la polarisation et la migration cellulaire mais aussi dans l'orientation des fuseaux mitotiques. La voie PCP joue aussi un rôle important dans la ciliogenèse et l'orientation du cil primaire. Chez le *Xenope ou* la souris, un certain nombre de protéines du corps basal semblent être impliquées dans cette voie, notamment OFD1 et les protéines des complexes MKS, BBSome et IFT-B (Kim et al., 2010; Oh and Katsanis, 2013).

Le lien entre le cil primaire et la voie canonicale WNT n'est pas réellement élucidé. Dans les lignées cellulaires et certains embryons avec des anomalies du cil, une sur-activation de la voie WNT est observée, suggérant que la voie WNT est réprimée dans le cil. En revanche, chez le poisson-zèbre, la voie WNT n'est pas affectée chez les mutants. Une hypothèse émet que les effets sur la voie WNT pourrait être dépendant du type cellulaire (Sasai and Briscoe, 2012).

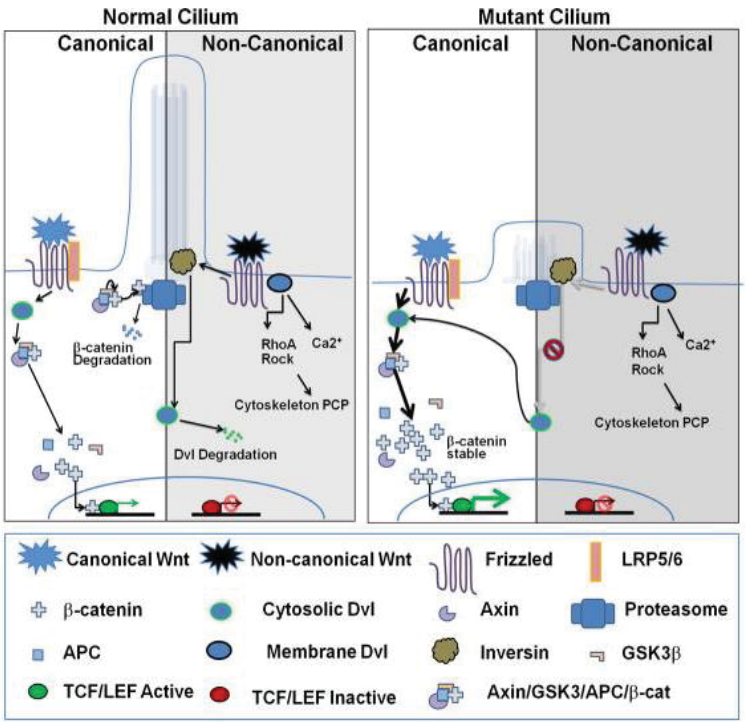

Figure 28 : La voie WNT*.Transduction des signaux dans la voie WNT canonicale ou non-canonicale dans le cil (Berbari et al., 2009)*

3.6.4- Les autres voies de signalisation

Les mutations de la voie FGF chez les mutants murins ou le poisson-zèbre affectent la ciliogenèse et induit la formation de cils courts et des anomalies de la latéralité. De même, la voie inositol semble altérer la longueur des cils ainsi la fréquence de battements chez le poisson-zèbre (Goetz and Anderson, 2010).

La voie *Hippo* implique des sérine/thréonine kinases aboutissant à l'activation des facteurs de transcription YAP et TAZ. Plusieurs régulateurs de cette voie sont localisés dans le cil primaire (NPHP4, NPHP3, NEK8, Crumb3) et leur absence induit une dérégulation de la voie *Hippo*. Cette voie est majoritairement impliquée dans le contrôle de la prolifération cellulaire (Basten and Giles, 2013; Hansen et al., 2015).

La différenciation des cellules endothéliales est régulée par la voie TGFβ via le cil primaire, tandis que la différenciation des cellules de l'épiderme requiert la voie Notch dont les effecteurs NOTCH3 et PSEN2 sont localisés au niveau du corps basal (Basten and Giles, 2013; Sasai and Briscoe, 2012).

3.6.5- Les voies de signalisation ciliaire et le développement embryonnaire

Les voies SHH et WNT sont cruciales pour le développement du tube neural et des structures cranio-faciales. Selon les régions embryonnaires, l'activation ou l'inhibition de ces voies va conduire à la prolifération, à la différenciation ou à l'apoptose des cellules qui conduiront à la formation des différents bourgeons de la face. Par ailleurs, la voie PDGF est impliquée dans le développement des os et cartilages de la face tandis que la voie de signalisation FGF participe au développement des structures fronto-nasales et mandibulaires, et plus tardivement à la formation des sutures entre les os du crâne (Sasai and Briscoe, 2012; Zaghloul and Brugmann, 2011).

Le développement du système nerveux central est dépendant du cil (figure 29). La notochorde donnera lieu à la moelle épinière ventrale comprenant cinq types de neurones : le motoneurone (MN) et les interneurones V0 à V3. La différenciation de ces cellules est organisée par SHH et WNT qui sont exprimés dans la notochorde. Le développement cérébral est lui aussi contrôlé par SHH qui va différencier les différentes régions. Des études suspectent aussi un rôle de WNT et FGF (Lee and Gleeson, 2011; Veland et al., 2009).

SHH est aussi impliqué dans l'activation de petites cellules mésodermiques des bourgeons membranaires appelées zone de polarité, à l'origine de la mise en place de l'axe antéro-postérieur des membres qui contrôle aussi l'identité et le nombre de doigts (Veland et al., 2009). Un dysfonctionnement de cette voie peut expliquer la présence de polydactylie, souvent retrouvée dans les ciliopathies.

La voie PCP impliquée majoritairement dans les processus de migration, de polarité cellulaire et de latéralisation mais aussi dans la fermeture du tube neural et la formation de la cochlée. La deuxième voie WNT non-canonicale (WNT/Ca^{2+}) régule quant à elle, la motilité et l'adhésion des cellules.
La morphogénèse de nombreux autres organes (cœurs, gonades, intestin, vessie et reins) nécessite une activation de la voie SHH (Veland et al., 2009).

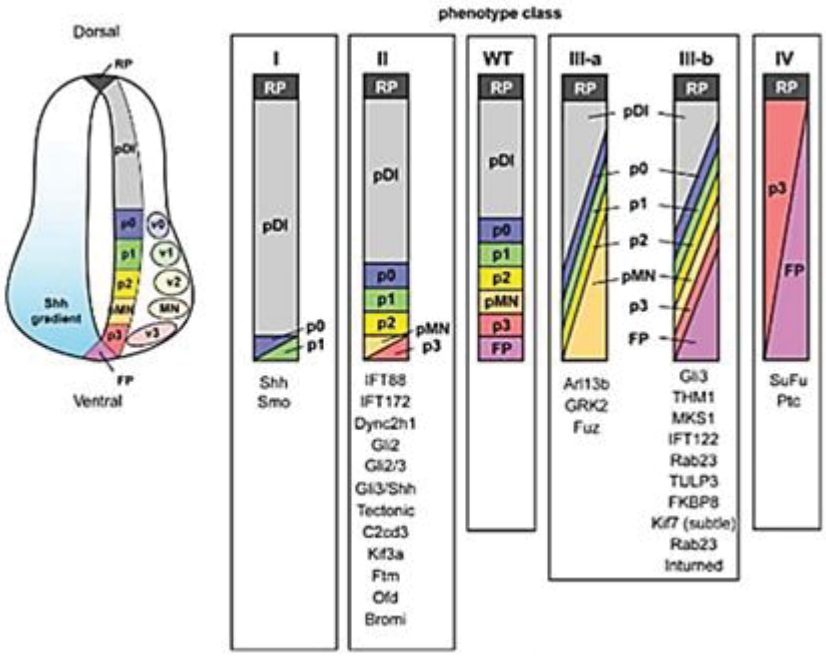

Figure 29 : Classification des anomalies du tube neural liées à des facteurs ciliaires. *Les cinq types de neurones (MN, V0, V1, V2, V3) dérivent des cellules localisées dans des régions précisent (p0, p1, p2, p3 ; pMN). Les mutations sur des gènes ciliaires vont affecter différemment le pattern SHH et induire des phénotypes différents classés 5 catégories. pDI : progéniteurs des interneurones dorsaux, RP : région du toit, FP : plaque du plancher (Sasai and Briscoe, 2012).*

Les mutations sur des gènes codant pour des protéines ciliaires entrainent un spectre phénotypique relativement large, incluant polydactylie, anomalies cranio-faciales, cérébrales, surdité et autres malformations, qui s'explique par l'omniprésence du cil dans les différents processus développementaux.

3.7- Le cil, un organite sensoriel

L'étude des cellules épithéliales du rein issus de divers animaux modèles présentant une polykystose rénale a permis de mettre en évidence pour la première fois cette capacité de mécano et chémo-réception. En effet, les cils sont capables de libérer en quantité du calcium intracellulaire en réponse au mouvement détecté des fluides, afin de réguler en fonction la prolifération, la migration ou l'apoptose cellulaire. Depuis des mécanismes similaires ont été rapportés dans d'autres tissus tels que l'endothélium, les voies biliaires ou encore chez l'embryon au moment de la mise en place de l'axe droite-gauche.

De la même manière, chez certains invertébrés, le cil peut détecter d'autres signaux mécaniques comme les vibrations, la pression ou encore le toucher, et induire en réponse un signal chimique ou électrique (Berbari et al., 2009).

Le cil est donc un organite sensoriel, impliqué entre autre dans la perception des signaux extracellulaires et environnementaux, notamment les vibrations sonores par les cils cochléaires, la lumière par les photorécepteurs de la rétine ou encore l'odorat par les neurones olfactifs (figure 30) (Falk et al., 2015).

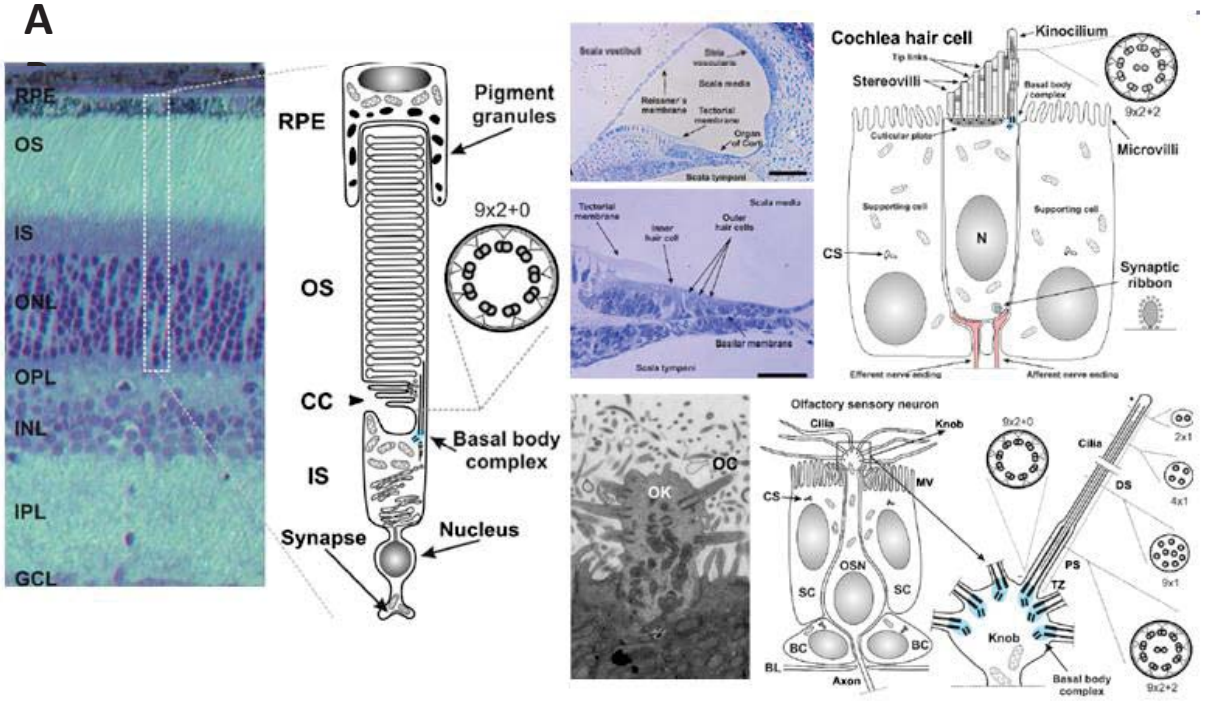

Figure 30: Structure de cellules ciliées impliquées dans la perception des signaux environnementaux chez la souris*. (A) Section verticale de la rétine et schématisation d'un photorécepteur. La rétine se compose de 5 classes de neurones, dont les photorécepteurs, et est divisée en 5 niveaux: la couche nucléaire externe (ONL), la couche nucléaire interne (INL), la couche de cellules ganglionnaires (GCL), les couches plexiformes externe (OPL) et interne (IPL). Le photorécepteur est formé d'un segment externe, sensible à la lumière (OS) recouvert d'un épithélium pigmentaire (RPE) connectés par un pont ciliaire (CC) qui correspond à la zone de transition, au segment interne (IS) et au corps basal (BBC). (B) Sections de la cochlée et représentation schématique d'une cellule cochléaire. (C) Section longitudinale d'un bulbe olfactif (OK) et du cil olfactif (OC), ainsi que le schéma correspondant. Le neurone olfactif (OSN) est entouré par des cellules de soutien (SC) et des cellules basales (BC). Le cil est une extension du bulbe et comprend une zone de transition (TZ) un segment proximal (PS) et distal (DS). Adapté de Falk et al., 2015.*

PREMIERE PARTIE

IDENTIFICATION DES BASES MOLECULAIRES DES SYNDROMES OFD

1- Identifier de nouveaux gènes

Identifier les bases moléculaires des ciliopathies reste un enjeu majeur pour la prise en charge des patients. Les nouvelles technologies de séquençage haut-débit permettent d'avoir accès aux données génétiques du patient. Le recrutement de grandes cohortes finement phénotypées et/ou le partage des données de séquençage peut aider à l'identification des gènes causaux. Cependant l'hétérogénéité génétique et clinique ainsi que la rareté des cas peuvent rendre difficile leur interprétation.

Plusieurs stratégies sont développées afin de faciliter cette interprétation, comme le développement des bases de données consacrées au ciliome ou encore les collections de modèles animaux (Alves-Cruzeiro et al., 2014; Arnaiz et al., 2014; van Dam et al., 2013; Gherman et al., 2006; Vincensini et al., 2011). La possibilité qu'un certain nombre de ciliopathies soit associé à des gènes codants pour des protéines non ciliaires n'est cependant pas à exclure. En effet, des protéines intervenant dans les étapes dites « post-cil », peuvent être impliquées dans le transport ou la transduction des signaux dans le cytosol entre la base du cil et le noyau cellulaire par exemple. Un dysfonctionnement lors de ces étapes pourrait alors avoir un impact direct ou indirect sur la fonction du cil (Tobin and Beales, 2009).

Les syndromes OFD sont un groupe de maladies rares très hétérogène tant sur le plan clinique que génétique. La classification en 13 sous-types est actuellement basée sur les données cliniques mais ne permet pas d'inclure tous les cas. Les récentes avancées en biologie moléculaire et séquençage haut-débit, ont permis d'identifier 7 gènes responsables des syndromes OFD faisant suspecter qu'il s'agisse d'un sous-groupe des ciliopathies. Cette hypothèse est d'ailleurs renforcée par la présence d'allélisme avec les syndromes de Joubert ou de Meckel. Cependant, les bases moléculaires des syndromes OFD restent encore peu connues.

L'objectif de la première partie de cette thèse est d'identifier de nouveaux gènes responsables de syndromes OFD, en utilisant une stratégie de séquençage haut débit d'exome.

2- Patients et méthodes

2.1- Cohorte OFD

Une cohorte internationale de 115 cas index a été recrutée. Les patients présentant un tableau clinique suggérant un syndrome OFD I, bénéficient directement d'un séquençage ciblé du gène *OFD1* et d'une CGH-array enrichie par des oligos localisés dans chaque exons du gène *OFD1*. Parmi les patients négatifs et ceux présentant des signes cliniques atypiques, 24 cas index ont été inclus à ce travail, 17 cas sporadiques et 7 cas issus d'une union consanguine (tableau 3). Tous les patients répondent aux critères cliniques des syndromes OFD, ils présentent des anomalies orales (hamartomes linguaux, langue lobulée, freins gingivaux anormaux), une dysmorphie faciale et des malformations des extrémités, principalement une polydactylie (figure 31). Ces signes cliniques sont associés à des malformations cérébrales (12/24 cas), des rétinopathies (3/24 cas), des malformations rénales (4/24 cas) ou cardiaques (9/24 cas). Le tableau clinique a permis de diagnostiquer un syndrome OFD VI chez 6 individus présentant notamment un signe de la dent molaire à l'IRM cérébrale, un syndrome OFD II chez deux individus, et un syndrome OFD V chez un individu. L'ADN parental est disponible pour 21/24 cas.

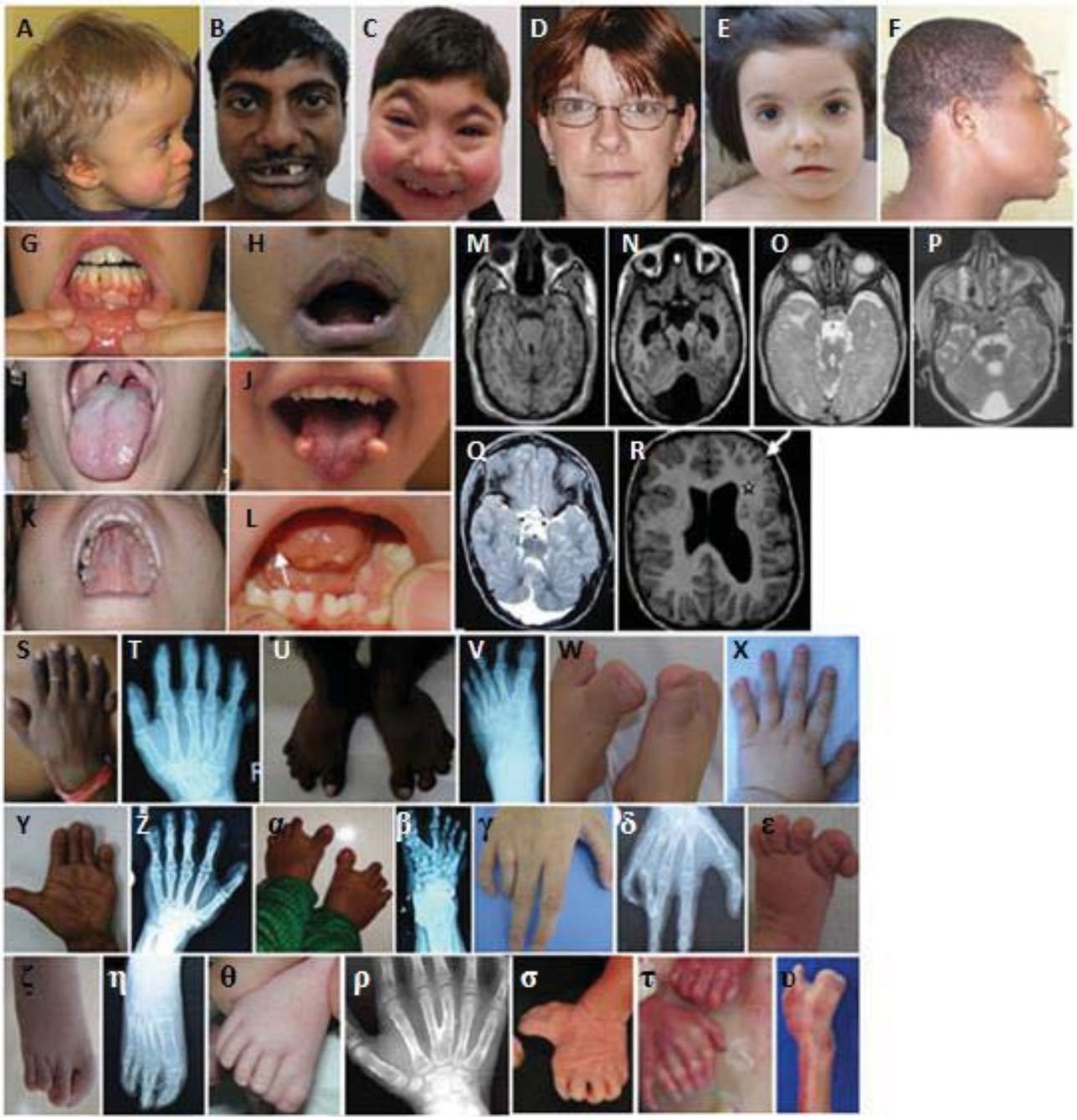

Figure 31 : Photographies cliniques, clichés radiologiques et IRM cérébrales des patients de la cohorte OFD et de réplication. *Cas 3a (M), cas 3b (N), cas 4 (C, P, W), cas 5 (ρ), cas 6a (B, S, T, U, V), cas 6b (H, Y, Z, α, β), cas 7 (G), cas 8 (E, L, Q, γ, δ, ξ, η), cas 10 (J, X), cas 11 (O), cas 17 (D, I, K), cas 19 (G), cas 22 (A, ε), cas 25 (τ,υ), cas 26 (F, R) avec dysmorphie faciale (A-E) incluant des oreilles bas-implantés (A), pseudo-fente médiane de la lèvre supérieure (H) ; des anomalies orales incluant absence d'incisives (B) microcéphalie sévère (C), freins anormaux (G), fente palatine (K), hamartomes linguaux ou langue lobulée (I, J, L), polydactylie pré and post-axiale des extrémités (Y, Z, ε, ρ-υ), hallux dupliqué et/ou dévié (U, V, W, ε, ξ, η, σ, υ), métacarpe central en forme de Y (ρ), et signe de la dent molaire visible à l'IRM cérébrale (M-R).*

Patients											
	1	2	3a	3b	4	5	6a	6b	6c	7	8
Sexe	M	F	F	F	M	M	M	F	M	F	F
Age	29 jours	6 ans	9 ans	9 ans	4 ans	12 ans	25 ans	22 ans	17 ans	17 ans	10 ans
Origine ethnique	Inde	France	Turquie	Turquie	NA	Inde	Inde	Inde	Inde	Japon	France
Consanguinité	+	+	+	+	+	+	+	+	+	-	-
Fente/Pseudofente labiale	+	+	-	-	-	+	+	+	NR	-	
Fente palatine	-	+	-	-	+	-	-	-	NR	-	+
Anomalies des freins	+	-	+	+	+	-	+	+	NR	+	+
Anomalies linguales	Lobulée	Bifide	Hamartome	Hamartome	Hamartome Lobulée Fente linguale	Hamartome	-	-	NR	-	Hamartome, Lobulée
Anomalies oculaires	-	Hyper-métropie	Rétinopathie	Rétinopathie	Rétinopathie	-	-	Enophtalmie	NR	NR	NR
Dysmorphie faciale	OBI	FP, MR	FP, OBI, HT	FP, OBI, HT	+	OBI, BF, MR	PF	PF	NR	NR	NR
Mains	PPo, PPr, S	C, B, S	PPo	PPo	PPo	PPr, Y	B, PPr	B, PPo	NR	-	PPo
Pieds	PPo, PPr, S	S	PPo	PPo	Hallux large	P	PPo	PPo, PPr	NR	PPr	PPr, S
Malformations cérébrales	NR	ACC, Agenesie vermienne	SDM, Hétéro-tropie Hypoplasie cérébelleuse	SDM, Poly-microgyrie, Hétéro-tropie, Hypoplasie cérébelleuse	SDM, ACC, Kystes sub-arachnoïdiens Défauts de myélinisation	NR	NR	NR	NR	Porencephalie, Kystes arachnoïdiens, Hétérotropie nodulaire, Polymicrogyrie SDM, HH	Kystes ara-chnoïdiens, SDM
Anomalies cardiaques	-	+	-	IVC	-	ToF	-	-	NR	-	-
Anomalies rénales	NR	-	NR	NR	-	-	-	-	NR	-	-
Anomalies squelettiques	-	-	-	-	-	-	Méso-phalanges courtes	Déformation thoracique	NR	11 paires de côtes	-
Anomalies cutanées	NR	Milium, Angiome	-	-	-	-	-	-	NR	-	-
Anomalies neurologiques	NR	RPM	AO, RPM, DI, Ataxie	AO, RPM, DI, Ataxie	DI	DI	-	-	NR	NR	NR
Autres			Hyperpnée	Hyperpnée	Epiglotte absente	Micropénis	Petite taille	Petite taille	Infection pulmonaire	Difficultés respiratoires	NR
Classification	OFDV	OFDVI	OFDVI	OFDVI	OFDXIV	-	-	-	-	OFDVI	OFDVI

	Patients											
	9	10	11	12	13	14	15	16a	16b	17	18	19
Sexe	M	M	F	F	F	F	F	F	F	F	M	F
Age	Fœtus	4 ans	NA	Fœtus	1 an	19 ans	4 mois	NA	NA	28 ans	NA	28 ans
Origine ethnique	France	Luxembourg	Italie	France	France	Australie	France	Turquie	Turquie	France	Espagne	Pays-Bas
Consanguinité	-	-	-	-	-	-	-	-	-	-	-	-
Fente/Pseudofente labiale	+	-	+	-	+	+	-	+	+	-	-	+
Fente palatine	+	-	+	-	-	-	-	-	+	-	-	-
Anomalies des freins	-	-	-	+	+	-	+	+	-	+	+	+
Anomalies linguales	-	Hamartome	Lobulée	Hamartome Bifide	Lobulée	Lobulatée	-	Hamartome	Hamartome	Hamartome	Hamartome	Lobulée
Anomalies oculaires	-	-	NR	NR	-	Strabisme	-	NR	NR	-	-	-
Dysmorphie faciale	MR, HT	MR, BF, HT	NR	FP, HT	MR, FB	NA	OBI, HT	+	+	HT	+	BF,HN, HT
Mains	PPo	PPo	PPo	S	-	PPr, S	PPo	PPo, B	PPo, B	S	PPo, S, C	C
Pieds	PPo	S	Hallux bifide	-	PPr, S	PPo, Hallux bifide	PPr	Hallux large	Hallux large	-	PPr	S
Malformations cérébrales	Hypoplasie vermienne, DW	NR	SDM	ACC, Anomalies du vermis	ACC, SDM	-	-	NR	NR	-	NR	-
Anomalies cardiaques	-	NR	NR	-	-	DSP	DSAV	NR	NR	NR	+	NR
Anomalies rénales	-	NR	Hydro-néphrose	+	-	NR	+	NR	NR	-	NR	-
Anomalies squelettiques	Hypoplasie de la 12ème paire de côte	NR	NA	11 paires de côtes	-	-	Hypoplasie radiale	NR	NR	-	-	NR
Anomalies cutanées	-	NR	NR	-	-	NR	NR	NR	NR	-	NR	NR
Anomalies neurologiques	NR	DI	NR	NR	RPM, DI	-	NR	RPM	RPM	-	RPM	-
Autres	NR	-	Difficultés respiratoires	Défaut de lobulation pulmonaire	Hypotonie	Surdité, RPM, Hypolasie de la glotte et du larynx, Sténose de la trachée	Thorax étroit	NR	NR	NR	Micropénis	-
Classification	-	-	OFDVI	OFDI	OFDI	-	-	OFDII	OFDII	-	-	-

Patients							
	20	21	22	23	24	25	26
Sexe	F	M	M	F	F	M	M
Age	7 ans	8 ans	1 ans	36 ans	22 SA	22 SA	22 ans
Origine ethnique	France	Inde	France	Mali	Maroc	France	Caraïbes
Consanguinité	-	-	-	+	-	-	-
Fente/Pseudofente labiale	-	+	-	-	+	-	-
Fente palatine	+	-	-	-	+	-	-
Anomalies des freins	-	+	+	NR	+	+	-
Anomalies linguales	Hamartome Lobulée	Hamartome	Lobulée	NR	-	-	-
Anomalies oculaires	Hypermétropie	-	-	NR	-	-	Rétinopathie
Dysmorphie faciale	+	BF, OBI, MR, HT	FP, BF, MR, OBI, HT	NR	Petites oreilles, HT	+	-
Mains	C, B	P	PPo, C, B	B, C, S	PPo, S, B, Y	PPo	-
Pieds	-	P	C, P	S	PPr	Hallux large	-
Malformations cérébrales	NR	DW	-	-	ACC, Hypoplasie cérébelleuse	ACC, Hypoplasie vermienne, Kystes sub-arachnoïdiens	SDM, Hypoplasie cérébelleuse
Anomalies cardiaques	CIV	ToF	-	-	CIV, Hypoplasie ventriculaire	NR	-
Anomalies rénales	-	-	-	NR	Dysplasique	Hypoplasie	-
Anomalies squelettiques	-	-	-	Scoliose	Femurs courts	NR	-
Anomalies cutanées	Milium	+	NR	-	-	NR	-
Anomalies neurologiques	NR	Epilepsie	NR	-	NR	NR	Ataxie, AO, RPM, DI
Autres	Luette bifide	Turri-céphalie	Post-hypophyse ectopique	Asthme Nodules thyroïdiens,	Anus non perforé	Micro-céphalie, Micropénis	Anomalies du foie
Classification	OFD I	-	-	-	-	OFDXIV	JBS

Tableau 3: Données cliniques des patients OFD analyses en exome (1-24) et de la cohorte de réplication (25-26). *Seuls les patients de la cohorte de réplication présentant une cause moléculaire identifiée sont présentés. ACC : Agénésie du Corps Calleux, AO : Apraxie oculomotrice, B : brachydactylie, BF : Bosses frontales, C : Clinodactylie, CIV : Communication Intra-Ventriculaire, DI : déficience intellectuelle, DSAV : Défaut Septal Atrio-Ventriculaire, DSP : Défaut du Septum Primaire, DW : Malformation de Dandy-Walker, F : Femme, FP : Fissures palpébrales en bas et en dehors, H : Homme, HH : Hamartomes Hypothalamiques, HN : Hypoplasie des ailes du Nez, HT :Hypertélorisme, MR : Micro-Rétrognathie, NR : Non Renseigné, OBI : Oreilles Bas-Implantés, P : Polydactylie, PM : Polydactylie Méso-axiale, PPo : Polydactylie Post-axiale, PPr : Polydactylie Pré-axiale, RPM : Retard Psycho-Moteur, S : Syndactylie, SDM : Signe de la Dent Molaire, ToF : Tératologie de Fallot, Y : Métacarpe en forme de Y.*

2.1- Séquençage et analyse de l'exome

Au vu de la grande hétérogénéité clinique de la cohorte réunie, nous avons opté pour un séquençage haut débit d'exome (SHD-E) en solo à partir des échantillons ADN est réalisé chez 23 cas index, en plus d'un trio (parents et cas index n°12, voir tableau 3). La capture est effectuée par le kit 51 Mb SureSelect Human All exon v5 (Agilent). Le séquençage est réalisé sur un HiSeq 2000 (Illumina) avec une lecture en paired-end et des reads de 100pb, par le centre national de génotypage (CNG, Evry) ou la société Integragen (Evry). Les données générées sont ensuite alignées sur un génome de référence (GRCh37/hg19) à l'aide de l'outil Burrows-Wheeler Aligner (BWA, v0.7.12). Les duplicats sont éliminés par le logiciel picardtools v2.0.1. Le réalignement des indels puis la recalibration des scores de qualité de base est réalisée par le logiciel Genome Analysis Toolkit v3.5. Les variations ayant passé le filtre (un score de qualité >30 et une qualité d'alignement >20) sont annotés avec SeattleSeq SNP annotation v9.09 (http://snp.gs.washington.edu/SeattleSeqAnnotation138/).
Les variations retenus sont ceux qui affectent la séquence codante et les sites d'épissage et qui sont qualifiés de rare, c'est à dire qui ont une fréquence inférieure à 1% dans les bases de données dbSNP138 v2.1.15 (http://www.ncbi.nlm.nih.gov/projects/SNP/), NHLBI Exome Sequencing Project Exome Variant Server v0.0.30 (http://evs.gs.washington.edu/EVS/) et ExAC Browser v0.3 (http://exac.broadinstitute.org/) et sont absents dans les 100 exomes contrôles locaux. Un filtre pour sélectionner les gènes connus dans Online Mendeliean Inheritance in Man (OMIM) est aussi utilisé (http://www.omim.org/). Les variations rares récessives sont priorisés dans notre analyse car les syndromes OFD sont majoritairement transmis selon un mode d'hérédité autosomique récessif. Le score PolyPhen v2.2.2 (http://genetics.bwh.harvard.edu/pph2/) permet de prédire l'impact d'une mutation sur la structure et la fonction de la protéine. Les scores PhastCons et GERP renseignent sur la conservation des bases nucléotidiques au cours de l'évolution. Ces deux scores vont permettre de prioriser les gènes candidats. Les différentes variations sélectionnées sont visualisés sur Integrative Genomics Viewer v2.3.67 (https://www.broadinstitute.org/igv/home).

En parallèle, la liste des variations annotées est croisée avec une liste de gènes ciliaires connus. Cette dernière a été établie à partir des données répertoriées sur deux bases de données Ciliome Database (http://www.sfu.ca/~leroux/ciliome_home.htm), Cildb v2.1 (http://cildb.cgm.cnrs-gif.fr/v2/page/index) et Syscilia v1 (http://www.syscilia.org/goldstandard.shtml). Ces bases de données s'appuient sur de

nombreuses études de protéomique, d'expression transcriptionnelle, de génomique comparative ainsi que des études sur les promoteurs. A cette liste, s'ajoute les résultats de différentes analyses récentes du transciptome ou protéome ainsi que les études bioinformatiques menées sur les cellules ciliées (annexe 3) (Amato et al., 2014; Ishikawa et al., 2012; Ivliev et al., 2012 ; Toriyama et al., non publié).

Dans un premier temps, nous recherchons les variations homozygotes dans les familles consanguines dans les gènes ciliaires puis dans tous les gènes candidats issus de l'exome. Les régions d'homozygotie sont déterminées à l'aide du logiciel HomozygosityMapper (http://www.homozygositymapper.org/). Les variations potentiellement hétérozygotes composites sont ensuite analysés i) dans les gènes connus en pathologie humaine (filtre OMIM), ii) dans les gènes ciliaires puis iii) parmi les gènes non ciliaires et inconnus dans la base de données OMIM. En absence de gènes candidats à cette étape, une analyse des variations rares hétérozygotes connus en pathologie humaine sera réalisée puis parmi les gènes ciliaires (figure 32). Nous recherchons par ailleurs si les variations retenues ont précédemment été rapportées dans les bases de données ClinVar (http://www.ncbi.nlm.nih.gov/clinvar/) et Human Gene Mutation Database (HGMD, http://www.hgmd.org/).

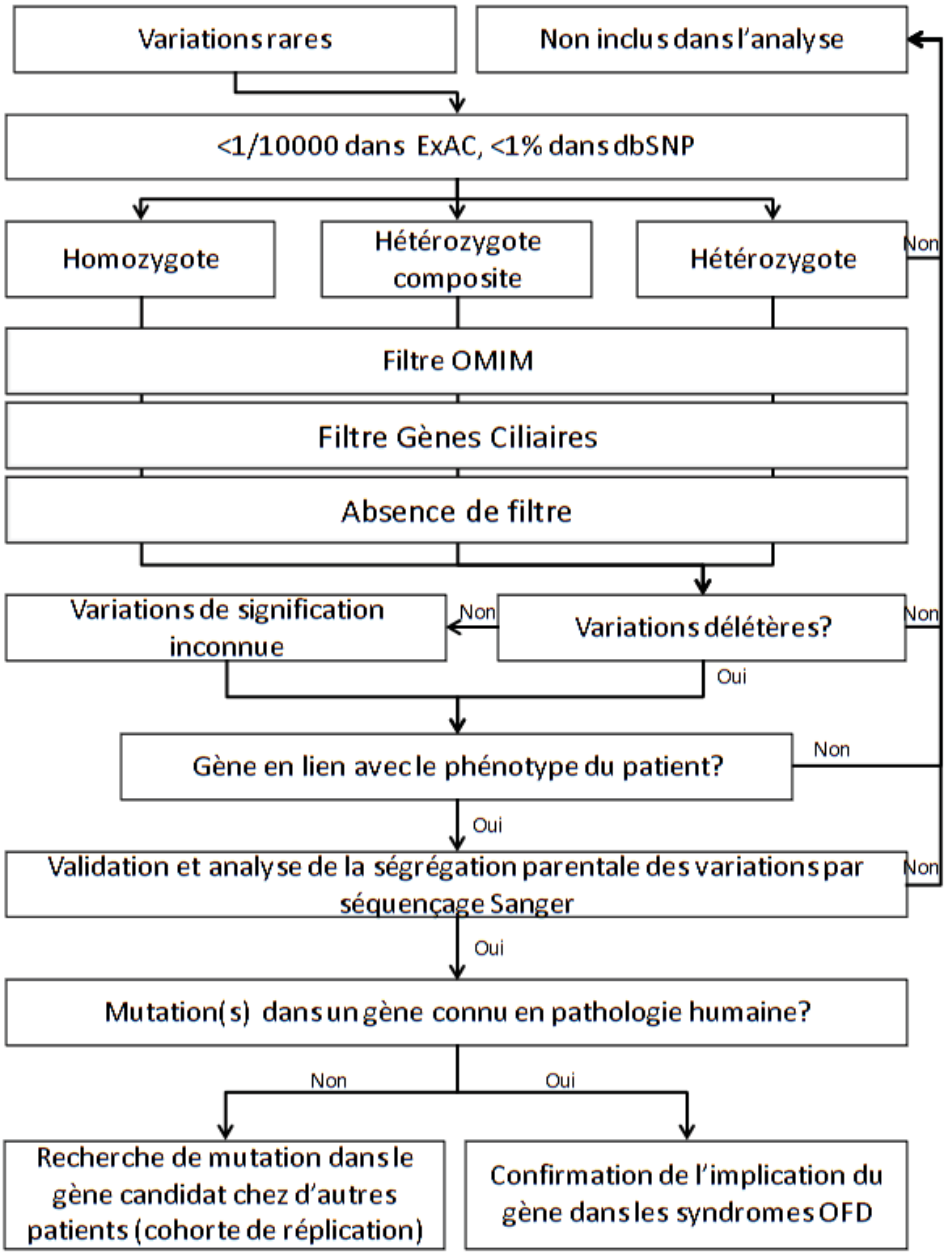

Figure 32 : Stratégie d'analyse du SHD-E pour ce projet.

2.3- Séquençage Sanger

Les mutations sélectionnées sont confirmés par séquençage Sanger. La ségrégation parentale et familiale est aussi vérifiée lorsque cela est possible. Les amorces utilisées sont disponibles dans l'annexe 5. L'ADN génomique est amplifié par PCR (Polymérase Chain Reaction) en utilisant le kit HotStarTaq PCR (Qiagen) selon les recommandations du fournisseur. Les amplicons sont purifiés par la méthode Agencourt CleanSEQ system (Beckman Coulter Genomics) et séquencés à l'aide du kit BigDye Terminator Cycle Sequencing v3.1 (Applied

Biosystems) sur un séquenceur ABI 3730 (Applied Biosystems). Les données de séquençage sont analysées sur le logiciel Mutation Surveyor v4.0.9 (Softgenomics).

2.4- Analyse de l'ADNc

S'il est nécessaire de tester les conséquences de certaines variations sur l'épissage, une étude de l'ADNc est alors réalisée. L'ARN total est ainsi isolé par le TRIzol (Life Technologie) à partir de fibroblastes ou de lignées lymphoblastoïdes des patients. La réverse transcription à partir d'un microgramme d'ARN est réalisée à l'aide du kit QuantiTect Reverse Transcription (Qiagen). Le cDNA obtenu est ensuite amplifié par PCR et séquencé par Sanger. Les amorces utilisées sont disponibles en annexe 5.

2.5- Cohortes de réplications

Dans le but de conforter les résultats obtenus par SHD-E en mettant en évidence au moins un second patient muté dans les nouveaux gènes identifiés au cours de cette étude, des cohortes de réplication ont été séquencés au séquenceur MiSeq (Nextera XT, Illumina). Ces cohortes sont constituées à partir de patients atteints d'un syndrome OFD négatifs au séquençage du gène OFD1 et qui n'ont pas bénéficié d'un SHD-E, 12 autres issus de la cohorte OFD du Pr B. Franco), 16 patients diagnostiqués avec un syndrome de Joubert issus de la cohorte du Dr L.Burglen, et 12 patients présentant un syndrome d'Ellis-Van Creveld, répartis selon les informations cliniques.

3- Résultats

3.1- Mutations génomiques

L'analyse du SHD-E des 24 cas index de la cohorte a permis d'identifier des mutations causales chez 14/24 d'entre eux (58%) ainsi que des gènes candidats probablement pathogènes chez deux autres cas (8,3%) (tableau 4).

L'analyse de variations rares homozygotes chez les patients issus d'une union consanguine a mis en évidence une délétion tronquante dans le gène *INTU* [MIM 610621] à l'origine de l'apparition d'un codon stop prématuré, une mutation non-sens dans le gène *C2CD3* [MIM 615944], une mutation synonyme affectant un site d'épissage du gène *IFT57* [MIM 606621]

ainsi qu'une mutation faux-sens dans les gènes *DDX59* [MIM 615464], *TMEM107* [MIM 616183] et *TMEM138* [MIM 614459] (Bruel et al., 2015a; Li et al., 2016; Thauvin-Robinet et al., 2014; Thevenon et al., 2016; Toriyama et al., 2016).

Nous avons également identifié des mutations hétérozygotes composites dans 5 gènes ciliaires : *TMEM231* [MIM 614949], *WDPCP* [MIM 613580], *KIAA0753* et *C5orf42* [MIM 614571] (Bruel et al., 2015b; Li et al., 2016; Lopez et al., 2014; Toriyama et al., 2016).

En l'absence de gènes candidats porteurs de variations homozygotes ou hétérozygotes composites, des mutations hétérozygotes en lien avec le phénotype du patient sont recherchées dans l'hypothèse d'une transmission dominante autosomique ou liée à l'X. L'analyse des gènes connus dans OMIM a permis d'identifier une mutation tronquante, une mutation faux-sens et une mutation intronique prédite pour affecter l'épissage dans le gène *OFD1* responsable du syndrome OFD I de transmission dominante liée à l'X chez les patients n°12, 13 et 20.

Le séquençage ciblé des gènes *KIAA0753*, *IFT57*, *INTU*, *TMEM107* et *C2CD3* dans une cohorte de réplication a permis d'identifier deux nouveaux cas, présentant un syndrome OFD pour l'un et un syndrome de Joubert pour l'autre, hétérozygotes composites pour les gènes *C2CD3* et *TMEM107* respectivement.

En parallèle, le séquençage ciblé, dans la cohorte de réplication, des gènes *FOPNL*, *FUZ* et *RSG1*, trois gènes codant pour des protéines qui interagissent avec *KIAA0753* et donc constituant de bons candidats, a été réalisée sans donner de résultats.

Des mutations ont, par ailleurs, été identifiées dans deux autres gènes candidats *NEDD1* et *CLIP3,* mais des investigations supplémentaires sont nécessaires afin de confirmer leur pathogénicité. Une mutation homozygote et intronique de *CLIP3* a été identifié chez une patiente issue d'une union consanguine et présentant un syndrome OFD atypique avec anomalies squelettiques. Concernant le gène *NEDD1*, deux variations hétérozygotes ont été identifiées chez un patient indien présentant un syndrome OFD non classé avec une scoliose et des nodules thyroïdiens, cependant en absence d'ADN parental, la ségrégation familiale n'a pu être réalisée.

3.2 Etudes de l'ADNc

Plusieurs mutations identifiées sont localisées à proximité des sites d'épissage et sont prédites pour affecter ces derniers. Le séquençage de l'ADNc a confirmé ces défauts d'épissage.
La mutation intronique c.3911-2A>T identifiée dans le gène *C2CD3* (patient n°25) entraine l'apparition d'un site cryptique à la fin de l'exon 22 à l'origine du décalage du cadre de lecture de 4 nucléotides (figure 33A). La mutation c.1546-3C>A dans le gène *KIAA0753* (patient n°11) conduit à l'excision de l'exon 8 et à l'apparition d'un codon stop prématuré (figure 33C). Enfin la mutation silencieuse homozygote mise en évidence dans le gène *IFT57* chez le patient n°6a, est localisée sur la dernière base de l'exon 6, ce qui induit une excision de l'exon 6 avec l'apparition d'un codon stop prématuré (figure 33B).

Dans le cas du patient n°11, deux mutations hétérozygotes ont été identifiées dans le gène *KIAA0753*, l'une est héritée de la mère, l'autre est *de novo*. Afin de vérifier que les deux mutations ne sont pas localisées sur le même allèle, nous avons réalisé un séquençage moyen-débit (Miseq) de l'ADNc du cas index, amplifiée par PCR à l'aide d'une première amorce localisée en amont de la mutation non-sens et une seconde amorce localisée dans l'exon 8, excisé sur l'allèle portant la mutation c.1546-3C>A. Une amplification de l'allèle portant uniquement la mutation non-sens a été majoritairement séquencée, confirmant que ces deux mutations hétérozygotes sont localisées sur des allèles différents.

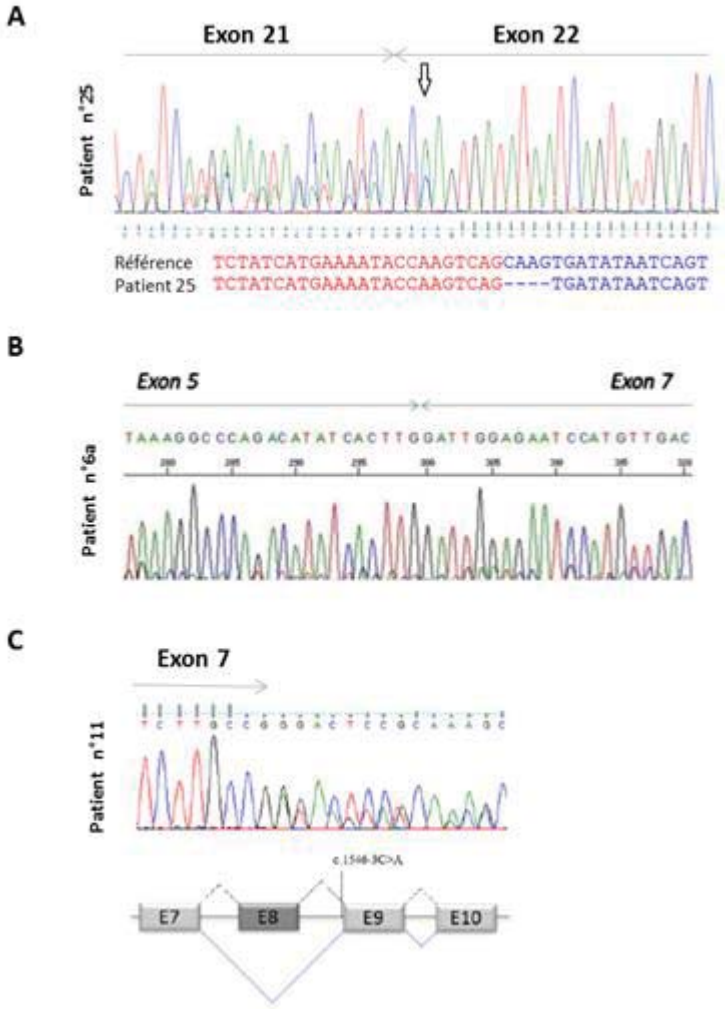

Figure 33 : Chromatogrammes obtenus après séquençage Sanger de l'ADNc. *(A) La mutation intronique c.3911-2A>T identifiée dans le gène C2CD3 entrainne une délétion de 4 nucléotides. (B) La mutation synonyme homozygote p.Lys259Lyslocalisée dans le gène IFT57 induit un saut de l'exon 6. (C) La mutation hétérozygote c.1546-3C>A dans le gène KIAA0753 induit un saut de l'exon 8.*

	Cas	Gène	Gène ciliaire	OMIM	Mutation		Hérédité	EVS	ExAC	Tests ADNc
					c. position	p. position				
Cohorte initiale	1	*DDX59*	-	Oral-facial-digital syndrome V [174300]	c.754G>A c.754G>A	p.Gly252Arg p.Gly252Arg	Maternel Paternel	-	-	-
	2	*TMEM138*	+	Joubert syndrome 16 [614465]	c.352A>T c.352A>T	p.Met118Leu p.Met118Leu	- -	-	-	-
	3a/b	*TMEM107*	+	-	c.134A>G c.134A>G	p.Glu45Gly p.Glu45Gly	Maternel Paternel	-	-	-
	4	*C2CD3*	+	-	c.184C>T c.184C>T	p.Arg62* p.Arg62*	Maternel Paternel	-	-	-
	5	*INTU*	+	-	c.396delT c.396delT	p.Asn132Lysfs*11 p.Asn132Lysfs*11	- -	-	-	-
	6a	*IFT57*	+	-	c.777G>A c.777G>A	p.Lys259Lys p.Lys259Lys	- -	-	-	Défaut d'épissage
	7	*C5orf42*	+	Joubert syndrome 17 [614615]	3557delA c.3577C>T	Lys1186Argfs*22 p.Arg1193Cys	- -	- -	- -	-
	8	*C5orf42*	+	Joubert syndrome 17 [614615]	c.3290-2A>G c.493delA	- p.Ile165Tyrfs*17	Maternel Paternel	- 1/6155	- -	-
	9	*TMEM231*	+	Joubert syndrome 20 [614970] Meckel syndrome 11 [615397]	c.656C>T c.532C>G	p.Pro219Leu p.Pro178Ala	Maternel Paternel	- -	- -	-
	10	*WDPCP*	+	Bardet-Biedl syndrome 15 [209900]	c.160G>A c.526_527delTT	p.Asp54Asn Leu176Ilefs*21	Paternel Maternel	1/11827 -	7/119586 -	-
	11	*KIAA0753*	+	-	c.1546-3C>A c.1891A>T	- p.Lys631*	de novo Maternel	- -	- -	Défaut d'épissage -
	12	*OFD1*	+	Orofaciodigital syndrome I [3111200] Joubert syndrome 10 [300804] Simpson-Golabi-Behmel syndrome 2 [300209] Retinitis pigmentosa 23 [300424]	c.260A>G	p.Tyr87Cys	de novo	-	-	-
	13	*OFD1*	+		c.1840delG	p.Ala614Hisfs*15	de novo	-	-	-
	20	*OFD1*	+		c.655-8A>G	-	de novo	-	-	Non réalisé
	23	*NEDD1*	+	-	c.232-7T>A c.1450A>G	- p.Lys484Glu	- -	- -	- -	Non réalisé -
	15	*CLIP3*	+	-	c.563-8A>G c.563-8A>G	- -	- -	- -	- -	Non réalisé
Cohorte de réplication	25	*C2CD3*	+	-	c.3085T>C c.3911-2A>T	p.Cys1029Gly -	-	- 6/ 12978	- 31/ 120818	- Défaut d'épissage
	26	*TMEM107*	+	Joubert syndrome 17 [614615]	c.316_318delTTC c.402delA	p.Phe106del p.Leu134Phefs*8	Paternel Maternel	- -	- -	-

Tableau 4 : Mutations identifiées par SHD-E dans la cohorte initiale OFD et secondairement dans la cohorte de réplication.

DEUXIEME PARTIE

Etudes fonctionnelles des gènes impliqués dans les syndromes OFD.

1- Introduction

L'identification de plusieurs gènes différents impliqués dans un même sous-type de syndromes OFD, basé sur les données clinique, suggère que certains gènes causaux coderaient pour des protéines assemblées dans un même complexe fonctionnel ou impliquées dans une même voie de signalisation ciliaire.
Pour chacun des gènes précédemment identifiées, des études fonctionnelles réalisées dans le laboratoire ou en collaboration avec des équipes internationales ont permis de révéler la présence de complexes et d'interactions entre protéines ciliaires impliquées dans les ciliopathies, ainsi que d'améliorer les connaissances sur la biogénèse, la fonction et la structure du cil primaire. Seuls les principaux résultats seront présentés, les matériels et méthodes utilisés sont décrits en annexe 6.

2- Résultats

2.1- Les complexes protéiques du centrosome

2.1.1- Caractérisation de *C2CD3*

C2CD3 code pour une protéine centriolaire, constituée d'un domaine C2CDN en N-terminal, et de six domaines C2. En collaboration avec l'équipe du Pr M. Nachury (Stanford, Etats-Unis), la localisation précise et la fonction de C2CD3 ont pu être caractérisées.

C2CD3 est principalement localisée au niveau des satellites centriolaires et colocalise avec OFD1. Une série d'expérience a permis de déterminer qu'OFD1 et C2CD3 formaient un complexe à l'extrémité distale des centrioles pour réguler la croissance centriolaire (figure 34A-C). Plus spécifiquement, C2CD3 recrute OFD1 dans les centrioles (figure 34F).

Deux modèles murins mutés dans le gène *C2cd3* sont connus et sont utilisés pour caractériser la fonction de la protéine: *C2cd3*$^{Hty/Hty}$ dont la mutation est hypomorphe et *C2cd3*$^{Gt/Gt}$ avec absence de la protéine C2cd3.
La colocalisation et interaction entre Ofd1 et C2cd3 suggère une fonction similaire au sein des centrioles. L'observation des centrioles en microscopie à fluorescence des cellules murines mutantes, a montré une diminution de la longueur des centrioles, et une absence de la centrine, marquée par immunofluorescence, localisée dans les centrioles des cellules contrôles. Contrairement à Ofd1, l'absence de C2cd3 n'entraine pas une hyper-élongation des

centrioles. De plus, une perte des satellites centriolaires, marqués par Odf2 et Cep164 (ninéine), est notée dans les cellules mutantes homozygotes (figure 34D, E).
A l'inverse, la surexpression de C2cd3, par transfection de la construction GFP-C2cd3 dans les cellules U2OS, induit une hyper-élongation des centrioles est observée (figure 34G).

Ces études ont montré que C2CD3 favorise la croissance centriolaire, en contraste avec OFD1 qui la réprime. Ainsi, les mutations de C2CD3 entrainent des anomalies de la longueur des centrioles, ce qui a des répercussions directes sur la ciliogenèse.

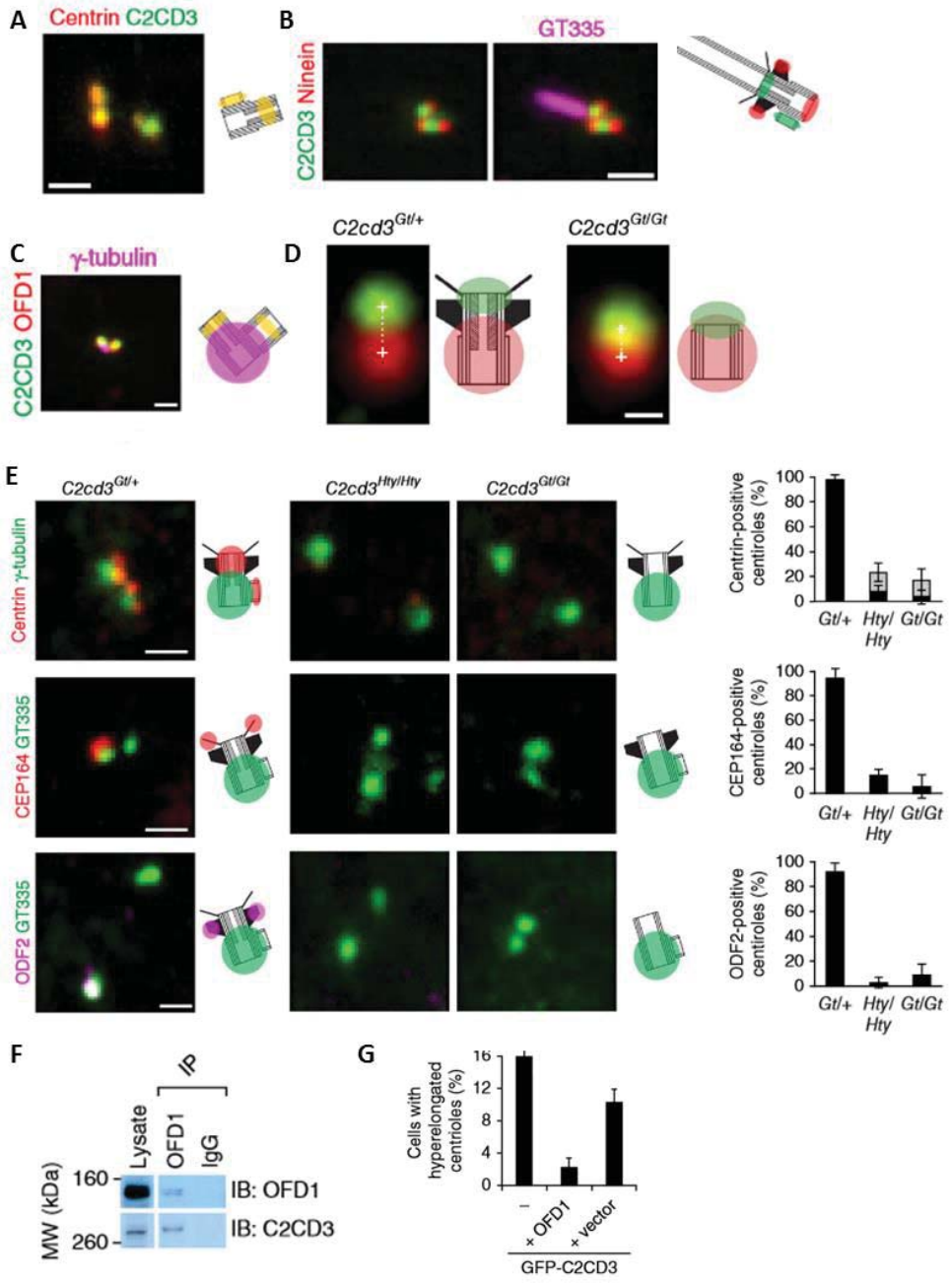

Figure 34: C2cd3 colocalise avec Ofd1 et régule la longueur des centrioles*. (A-C) Localisation de C2cd3 dans les satellites centriolaires, images prises en microscopie à fluorescence après marquage des différentes protéines par immunofluorescence et transfection de la construction GFP-C2cd3 dans les cellules IMCD3. (A) C2cd3 (en vert) colocalise avec la centrine (en rouge) à l'extrémité distale des centrioles, (B) la ninéine/Cep164 (en rouge) est localisée au niveau des appendices subdistaux et à l'extrémité distale des centrioles, la tubuline polyglutaminée (GT335, en rose) marque l'axonème ciliaire, (C) C2cd3 et Ofd1 colocalisent à l'extrémité distale des centrioles, la γ-tubuline (en rose) marque le matériel péricentriolaire autour de la partie proximale du centriole.(D-E) Raccourcissement de la longueur du centriole et perte des satellites centriolaires dans les cellules murines mutantes homozygotes (C2cd3$^{Gt/Gt}$ et C2cd3$^{Hty/Hty}$)par rapport aux souris mutantes hétérozygotes (C2cd3$^{Gt/+}$), échelle 0,2 µm.(C) Marquage par immunofluorescence de Cp110 (en rouge) localisé dans le centriole et de GT335 (en vert) localisé dans l'axonème, (E) Absence de la centrine (en rouge), Cep164 (en rouge) et Odf2 (en rose) dans les centrioles et les satellites chez les*

souris mutantes homozygotes, échelle 1µm. Le nombre de centrioles marqués par la centrine, Cep164 ou Odf2, rapporté sur le graphique, diminue significativement dans les cellules homozygotes par rapport aux cellules hétérozygotes.(F) Immunoprécipitation de Ofd1 à partir des extraits protéiques les cellules RPE1, suivi d'un marquage de C2cd3, démontrant une interaction entre ces deux protéines, IP :ImmunoPrécipitation, MW :Poids Moléculaire, IB :Anticorps dirigé contre Ofd1 ou C2cd3. (G)Pourcentage de cellules U2OS transfectées avec le vecteur exprimant GFP-C2cd3seul (-), GFP-C2cd3 et Myc-Ofd1 ou GFP-C2cd3 et un vecteur Myc vide, les cellules sont marquées pour Cep164 et Myc. Une hyper-élongation des centrioles est notée dans les cellules marquées par la GFP et Myc. Quatre expériences indépendantes avec un comptage d'environ 70 cellules ont été ralisées pour obtenir ce graphique.

2.1.2- Caractérisation de *KIAA0753*

KIAA0753 code pour une protéine de 969 acides aminés localisée dans le centrosome et les satellites péricentriolaires. Les études fonctionnelles de KIAA0753 et l'identification d'un nouveau complexe centriolaire ont pu être réalisées en collaboration avec l'équipe du Pr O. Rosnet (Marseille, France).

La recherche de nouveaux partenaires protéiques de FOPNL/FOR20, une protéine localisée dans les satellites et le corps basal du cil, récemment caractérisée, a permis d'identifier KIAA0753 et OFD1 comme partenaires. KIAA0753 colocalise avec FOPNL dans les centrosomes et les satellites dans les cellules inter-phasiques et mitotiques (figure 35). Afin de mieux caractériser cette interaction, des études de co-immunoprécipitation ont été réalisés en exprimant dans des cellules Cos1 des protéines KIAA0753 complètes, tronquées ou mutées. Cette expérience a démontré que la région C-terminale de KIAA0753 (acide-aminés 885 à 967) permettait l'interaction avec FOPNL et OFD1. Par ailleurs, ces constructions ont permis de mettre en évidence que la région centrale de la protéine KIAA0753 (acide-aminés 300-666) permettait de stabiliser les microtubules.
De même, d'autres constructions ont montré que les domaines TOF et LisH de FOPNL étaient indispensables à l'hétérodimérisation. En revanche, l'intégralité du motif PLL n'est pas requis à cette interaction, seuls quelques acide-aminés autour de ce motif sont impliqués dans l'interaction.
Concernant les cellules lymphoblastoïdes du patient, KIAA0753 est significativement diminué dans le centrosome ainsi que les protéines FOPNL et OFD1 dans les satellites et le centrosome, confirmant que ces trois protéines sont étroitement liées.

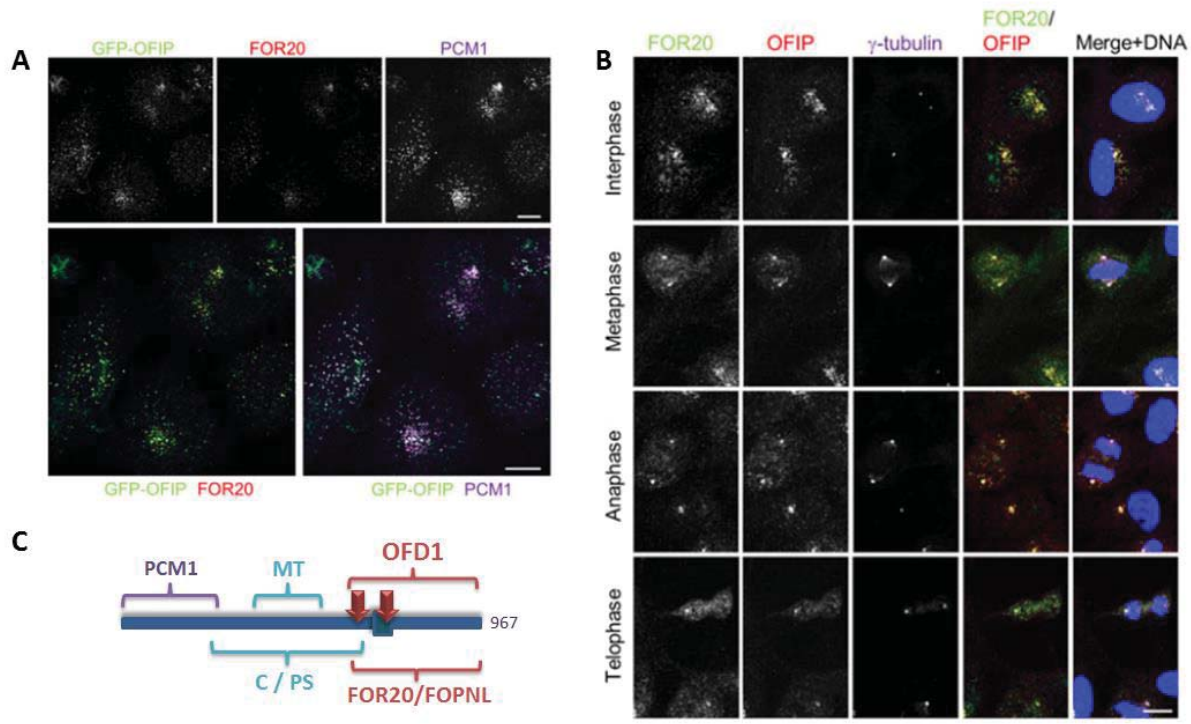

Figure 35 : Localisation dans le centrosome et représentation schématique de KIAA0753*. (A) Cellules HeLA fixées au méthanol qui expriment KIAA0753/OFIP-GFP (vert) et marquées avec un anticorps anti-FOPNL/FOR20 (rouge) ou anti-PCM1 (magenta). KIAA0753 et FOR20 colocalisent avec PCM1 dans les satellites centriolaires. Echelle 10µm. (B) Cellules RPE1 fixées au méthanol et marquées avec un anticorps anti-FOPNL/FOR20 (vert), anti-KIAA0753/OFIP (rouge) et anti-γ-tubuline (magenta) à différents stades du cycle cellulaire. KIAA0753 est localisé dans le centrosome et les satellites, et colocalise avec FOPNL dans les cellules interphasiques et mitotique,s échelle 10µm. (C) KIAA0753 interagit avec la protéine PCM1 en N-terminal, et avec les protéines OFD1 et FOPNL en C-terminal. Elle peut aussi interagir avec les microtubules (MT), les satellites péricentriolaire (PS) et le centrosome (C) via sa région centrale.*

2.1.3- Le complexe ternaire KIAA0753-OFD1-FOPNL

Par une approche protéomique, une troisième protéine, OFD1, interagit avec FOPNL et KIAA0753, formant ainsi un complexe ternaire dans les satellites. La région N-terminale de la protéine OFD1 permet l'interaction avec la région C-terminale de KIAA0753. La combinaison d'analyse par immunoprécipitation et western-blot a montré que FOPNL ne s'associait pas avec OFD1 en absence d'OFIP (données non montrées).

L'inactivation du complexe par siRNA dirigé contre les protéines OFD1, KIAA0753/OFIP et FOPNL dans les cellules RPE1, montre une diminution de la longueur du cil mais ne diminue pas significativement le nombre de cellules ciliées (figure 36).

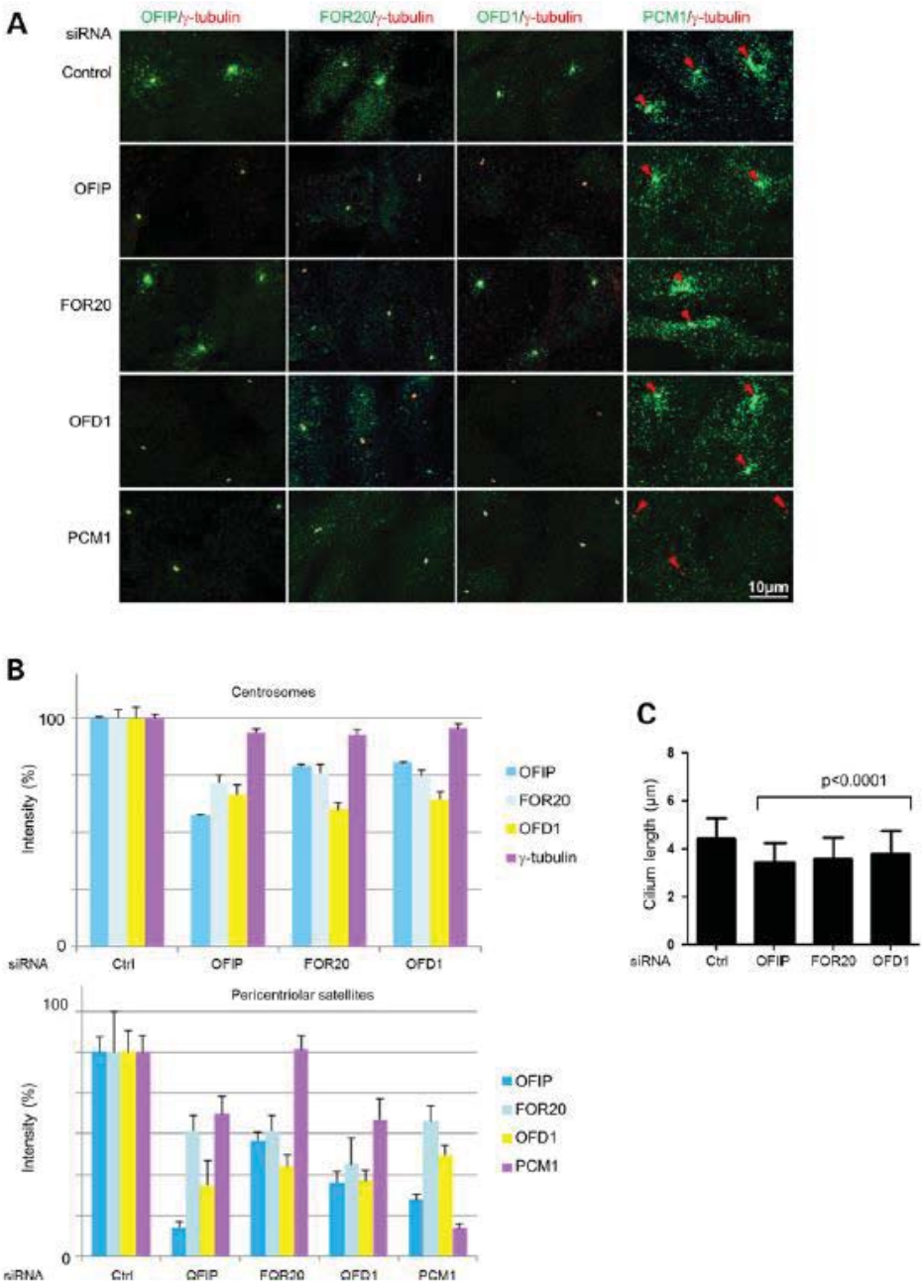

Figure 36: Inactivation par siRNA des différentes sous-unités du complexe dans les cellules RPE1*. (A) Cellules traitées avec siRNA contrôle ou dirigé contre OFD1, KIAA0753/OFIP, FOPNL/FOR20 ou PCM1, pendant 48h, puis fixée au méthanol. Un immunomarquage permet de visualiser en microscopie à fluorescence les différentes protéines et la γ-tubuline, les centrosomes sont indiqués par les flèches rouges. (B) Représentation graphique de l'intensité de fluorescence dans les centrosomes ou les satellites. L'inactivation des différentes sous-unités du complexe (OFD1, FOPNL, KIAA0753) conduit à une diminution des autres sous-unités au niveau des centrosomes et satellites. (C) Mesure de la longueur des cils dans les cellules RPE1 traitées avec un siRNA dirigé contre les protéines OFD1, KIAA0753 ou FOPNL. L'inactivation du complexe ternaire induit une diminution significative de la longueur du cil.*

2.2- Le complexe CPLANE

En collaboration avec l'équipe du Dr J. Wallingford, le complexe CPLANE a pu être caractérisé. Les études par spectrophotométrie de masse ont permis d'identifier un interactome autour de ce complexe, constitué de protéines impliquées dans la ciliogenèse. Il inclut des composants du complexe IFT-A, impliqués dans le transport intraflagellaire, des protéines des complexes dynéine, NPHP et MKS, des protéines impliquées dans le transport vésiculaire ou l'assemblage ciliaire (figure 37).
Ce complexe interagit étroitement avec d'autres protéines ciliaires moins caractérisées dont C5orf42 impliqué dans le syndrome OFD VI ou encore RSG1. Un marquage protéique a permis de localiser les protéines FUZ, INTU, WDPCP, RSG1 et C5orf42 dans le corps basal, WDPCP est aussi localisé dans l'axonème chez le xénope.

C5orf42 est indispensable au recrutement des protéines du complexe CPLANE mais son inactivation par siRNA dans les cellules multi-ciliées de l'épiderme de xénope n'affecte pas le recrutement des protéines de l'appendice distal (OFD1 et CEP164) ou de la zone de transition (MKS1). En revanche, l'inactivation de RSG1 n'affecte pas le recrutement du complexe. (figure 38D).

L'inactivation de C5orf42, et donc l'absence du complexe CPLANE au niveau du corps basal, conduit chez le xénope à des anomalies typiquement retrouvées dans les ciliopathies, notamment des défauts de fermeture du tube neural, des anomalies de la latéralité et de la voie de signalisation SHH (figure 38A-C).
Dans cette étude, des modèles murins ont été produits, mutés dans les gènes Fuz ou Wdpcp, pour lesquels, nous retrouvons un phénotype typique des ciliopathies, rappelant tout particulièrement les syndromes OFD : polydactylie, palais étroit et langue lobulée (figure 38E).

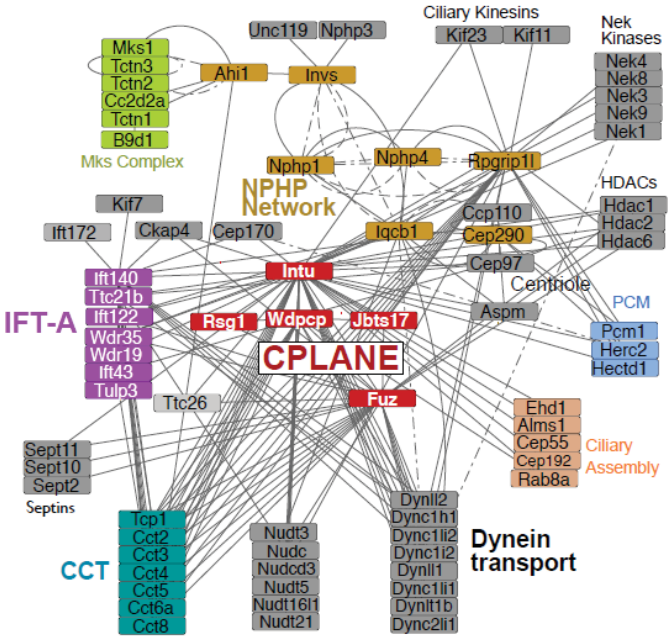

Figure 37 : Interactome du complexe CPLANE

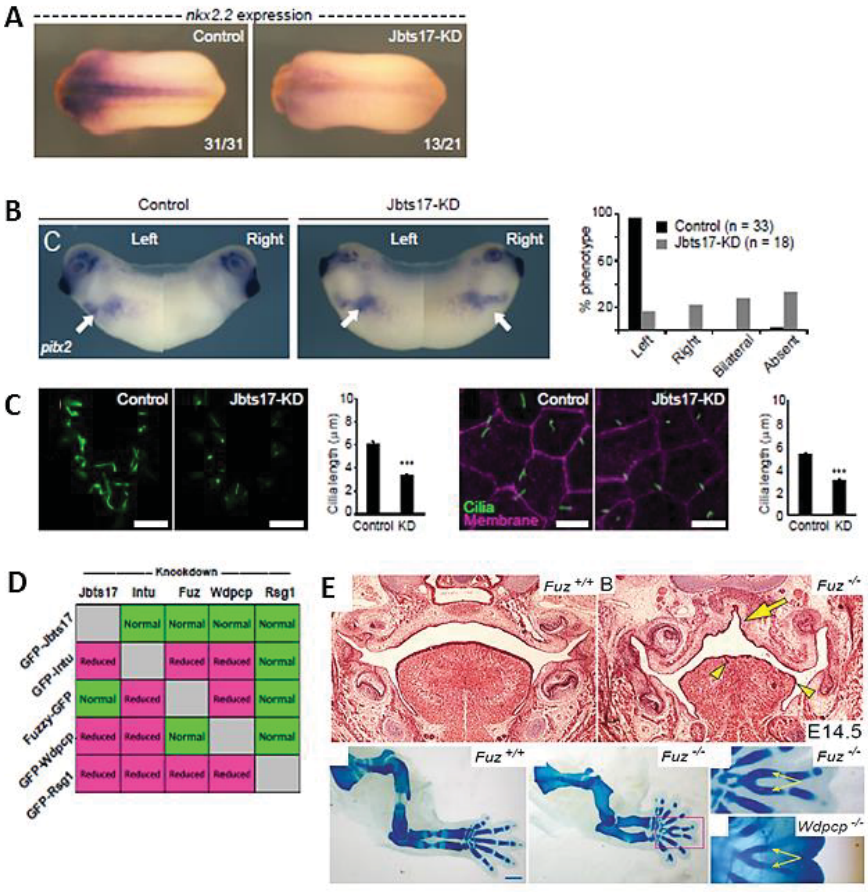

Figure 38: Caractérisation de C5orf42/Jbts17, Fuz et Wdpcp*. (A) Hybridation in situ de nkx2.2, gène cible de la voie SHH chez le xénope muté dans le gène C5orf42. (B) Anomalies de l'axe droite/gauche, défaut d'expression du gène pitx2 dans un embryon xénope. (C) Anomalies de la longueur des cils chez le xénopus mutant. (D) Tableau résumant les observations et le recrutement des différentes sous-unités du complexe CPLANE selon la sous-unité inactivé par siRNA dans les cellules multi-ciliées de*

l'épiderme du xénope. (E) Phénotypes des souris mutantes Fuz-/- et Wdpcp-/-, palais étroit et langue lobulée, polydactylie avec fusion des métacarpes centraux en Y.

La forte interaction entre le complexe CPLANE et le complexe IFT-A suggère un rôle spécifique du premier complexe dans la régulation du transport intraflagellaire. En absence du complexe CPLANE, par inactivation de C5orf42, il montre un défaut de recrutement des sous-unités périphériques du complexe IFT-A (IFT139, IFT121, IFT43) dans le corps basal (figure 39). En revanche, il ne semble pas affecter le recrutement des protéines constituant le cœur du complexe IFT-A (IFT104, IFT144, IFT122) ni du complexe IFT-B.

Le complexe protéique CPLANE intervient dans l'assemblage du complexe IFT-A et intervient indirectement dans la régulation du transport intraflagellaire. En effet, en absence de CPLANE, les protéines du complexe IFT-B s'accumulent et stationnent le long de l'axonème.

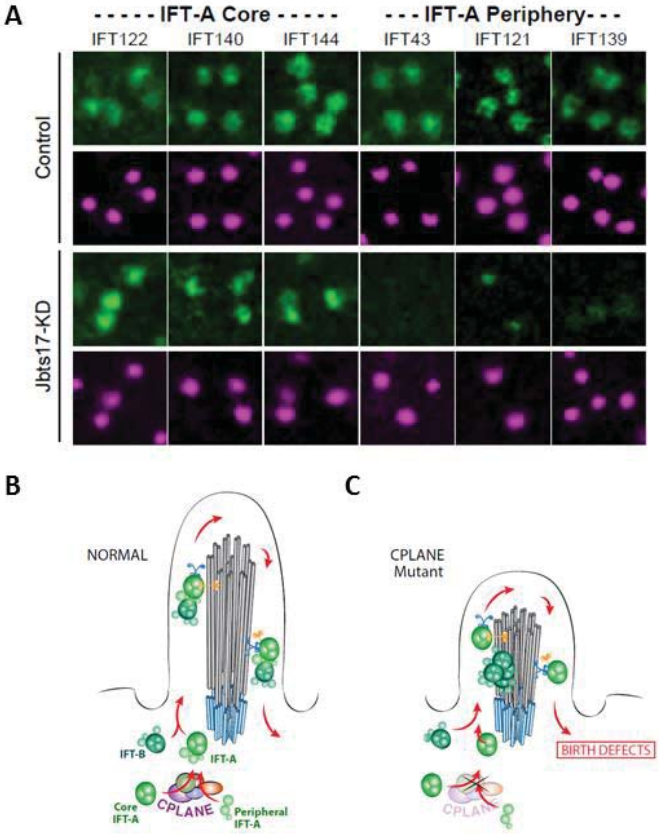

Figure 39: CPLANE permet le recrutement des sous-unités périphériques du complexe IFT-A et régule le transport intra-flagellaire*. (A)Immunodétection desdifférentes sous-unités du complexe IFT-A dans les cellules multi-ciliées de xénope contrôles ou transfectées avec un siRNA dirigé contre C5orf42/Jbts17. Dans les cellules traitées, nous observons une diminution de la fluorescence, soit un défaut de recrutement des protéines périphériques du complexe IFT-A (B-C) Le complexe CPLANE*

est impliqué dans le recrutement et l'assemblage des complexes IFT-A et B (B), en son absence, l'assemblage des complexes ne s'effectue pas et affecte le transport intraflagellaire (C).

2.3- Le complexe MKS

2.3.1- Caractérisation du gène *TMEM107* et des protéines à domaine transmembranaires

Ces travaux de caractérisation ont été réalisés en collaboration avec l'équipe du Pr O. Blacque (Dublin, Irlande). Ce travail est le résultat de deux approches différentes. La première fut notre stratégie classique de SHD-E chez les patients patients atteints d'OFD. La seconde, plus originale, fut de réaliser un criblage des données d'expression de plus de 1600 gènes murins et humains qui co-expriment avec 20 gènes connus codant pour des protéines de la zone de transition (annexe 7). Le top 100 des gènes murins et humains co-exprimés a ensuite été comparé. Cela a permis d'identifier 18 gènes chez les deux espèces, dont 5 codaient pour des protéines dont la localisation subcellulaire n'est pas connue. Ces 5 gènes candidats ont été recherchés dans le génome de quatre espèces ciliées dépourvus de zone de transition (*Physcomitrella patens*, *Selaginella moellendorffii*, *Plasmodium falciparum* et *Giardia intestinalis*) et *TMEM107* se trouvait être absent chez ces espèces.
Un marquage protéique de TMEM107 a confirmé sa localisation dans la zone de transition chez *C.elegans* et chez l'Homme où elle co-localise avec TMEM67 et RPGRIP1L, deux protéines de la zone de transition.

Le gène TMEM107 est impliqué dans la ciliogenèse, l'inactivation par siRNA induit une diminution de la fréquence de ciliation dans les cellules IMCD3 aussi observé dans les fibroblastes du patient présentant un syndrome de Joubert associé à une augmentation de la longueur du cil.

Une série d'analyse chez *C. elegans* permet de mettre en évidence que tmem107 est un composant du complexe MKS, l'un des deux complexes majeurs de la zone de transition. Ce complexe est constitué de nombreuses sous-unités qui sont recrutées selon un ordre précis. TMEM107 occupe une nouvelle place dans son assemblage, nécessitant la présence des protéines rpgrip1l, b9d2, b9d1 et tmem216 pour sa localisation et lui-même requis pour recruter les autres protéines du complexe chez *C.elegans* (figure 40). Chez les mammifères,

TMEM107 est aussi impliqué dans le recrutement et la localisation d'un certain nombre de protéines de la zone de transition telles que TMEM231 ou TMEM237.
Afin de s'affranchir de la redondance fonctionnelle qui existe entre les deux complexes de la zone de transition MKS et NPHP chez *C.elegans*, les études fonctionnelles de *Tmem107* sont réalisées chez un double-mutant tmem107-nphp4.
Chez les mutants n'exprimant pas tmem107, il est observé des anomalies de la morphologie du cil dont une diminution de la longueur du cil, pertes de microtubules, dégénérescence partielle ou totale des connections en forme de Y qui relient les microtubules à la membrane ciliaire, dissociation de la zone de transition de la membrane ciliaire (figure 41A, B)
La zone de transition a une fonction de barrière de diffusion et le marquage de deux protéines TRAM1 et RPI2, habituellement exclues du cil primaire, a démontré chez le mutant tmem107 un dysfonctionnement de la barrière de diffusion. En effet, chez le mutant, TRAM1 est localisé au niveau du cil, en revanche RPI2 reste exclu du cil , ce qui suggère que tmem107 est impliqué dans un contrôle sélectif du passage des protéines, il ne permet pas le passage de certaines protéines dans le cil (figure 41C).

La protéine TMEM107 possède un domaine transmembranaire comme plusieurs sous-unités du complexe MKS (TMEM216/MKS2, CC2D2A/MKS6) qui ont donc une capacité à lier à la membrane avec une région intracellulaire et une région extracellulaire. Ceci fait suspecter une immobilité de ces protéines ainsi que de l'ensemble du complexe MKS dans la zone de transition. Cette hypothèse a été validé, et chez le mutant Tmem216 $^{-/-}$, les protéines du complexe MKS sont mobiles. De plus, l'étude au microscope à fluorescence déplétion par émission stimulée (STED) des protéines à domaine transmembranaire a permis d'obtenir des images en super-résolution révélant l'ancrage de ces protéines à la membrane ciliaire par le biais d'une structure en anneau ou en spirale (figure 42A).

L'ensemble de ces données ont permis de construire un modèle de la zone de transition où les protéines transmembranaires du complexe MKS sont localisées à l'extrémité des connections en Y entre les microtubules et la membrane ciliaire (figure 42B).

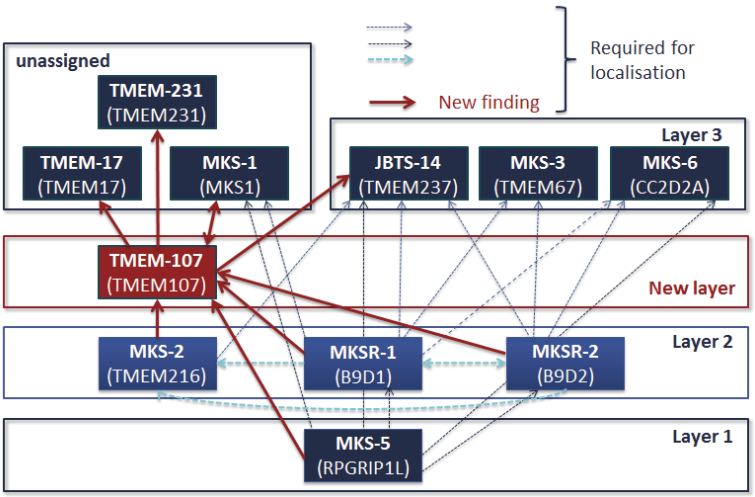

Figure 40: Assemblage du complexe MKS. *Quatre niveaux de recrutement sont désormais connus, MKS5/RPGRIP1L, indispensable au recrutement des protéines du deuxième niveau MKS2/TMEM216, MKSR1/B9D1 et MKSR2/B9D2, elles-mêmes nécessaires au recrutement de TMEM107. Ce dernier permet alors de recruter les protéines périphériques du troisième niveau TMEM237, TMEM67 et CC2D2A, ainsi que les protéines TMEM231, TMEM17 et MKS1.*

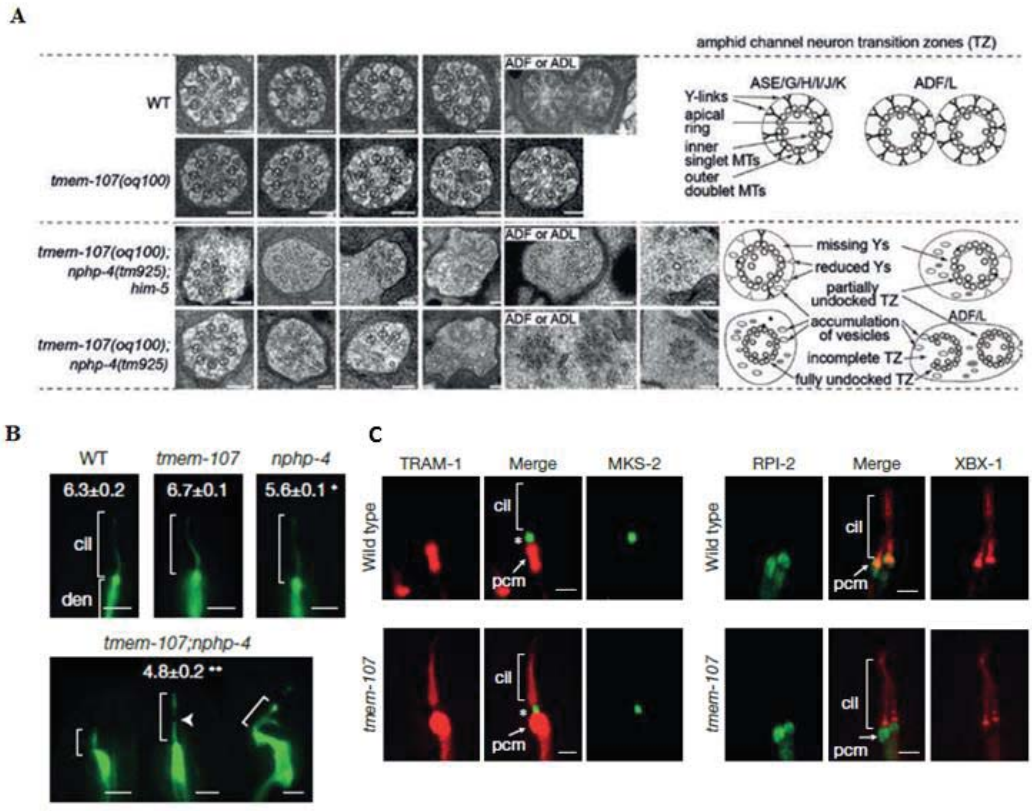

Figure 41: Anomalies de la structure du cil chez C. elegans, double-mutant tmem107-nphp4 ou simple mutant tmem107(oq100) ou nphp4. *(A) Images de coupes transversales et schéma de l'ultrastructure de la zone de transition. Dans les cellules contrôles (WT) ou tmem107(oq100), la zone de transition est composée de 9 doublets de microtubules reliés à la membrane ciliaire par des connections en forme de Y. Chez les double-mutants, est observée une perte partielle ou totale des connections en forme de Y, ce qui conduit à une désorganisation de la zone de transition. (B) Mesure*

de la longueur du cil dans les cellules neuronales de c.elegans qui expriment la GFP. Une diminution significative du cil est notée chez le double-mutant. (C) tmem107 joue un rôle sélectif au sein de la barrière de diffusion. Les cellules neuronales expriment TRAM1-tomato (en rouge)et MKS2-GFP pour marquer la zone de transition, ou RPI1-GFP (en vert)et XBX1-tomato qui marque le cil.TRAM1 et RPI1 sont exclus du cil chez le contrôle (wild type). Chez le mutant, TRAM1 est localisé dans le cil, mais RPI1 reste exclu.

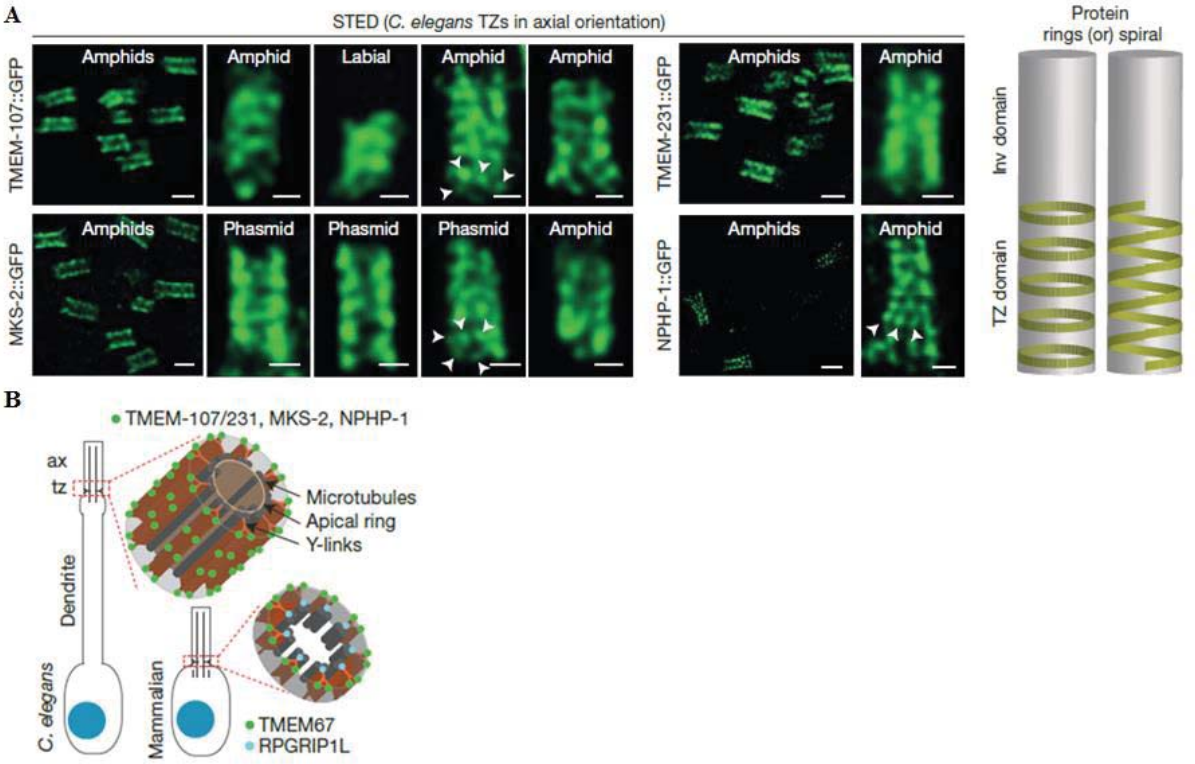

***Figure 42: Structure et localisation des protéines à domaine transmembranaires**. (A) Images prises au microscope à fluorescence déplétion par émission stimulée des cellules ciliées de c.elegans, les protéines des complexes MKS et NPHP sont marquées par la GFP (en vert) La représentation schématique des observations montre une structure en hélice ou en spirale des domaines transmembranaires de protéines de la zone de transition. (B) Proposition de modèle de la structure de la zone de transition et localisation des différentes protéines à domaine transmembranaire chez c.elegans et les mammifères.*

2.3.2- Organisation de la zone de transition

La zone de transition comporte donc deux complexes majeurs : MKS et NPHP. L'inactivation d'un gène d'un des deux modules modifie l'assemblage d'un ou des deux complexes et par conséquent entraine des anomalies de la structure de la zone de transition et affecte la ciliogenèse.

L'assemblage global de la zone de transition est mal connu. De plus, de nouvelles protéines localisées dans cette région ciliaire ont été récemment identifiée associées au complexe MKS (TMEM107, TMEM218, TMEM80) ou parfois à aucun des deux modules fonctionnels (TMEM138, CDKL1). Tous les gènes impliqués dans les syndromes OFD codent pour des sous-unités du complexe MKS (*TMEM107, TMEM231, TMEM216*), excepté *TMEM138*, nouvellement identifié au sein de notre cohorte.

En collaboration avec l'équipe du Dr M. Leroux (Burnaby, Canada), l'organisation et les différentes voies d'assemblage ont été identifiés (figure 43). L'ensemble de ces travaux est principalement centré sur l'identification et la caractérisation d'une nouvelle protéine du complexe MKS, TMEM218, qui ne sera pas détaillé dans ce manuscrit.

De précédentes études ont montré que Rpgrip1l/MKS5 permettait le recrutement des différentes protéines du complexe MKS chez *C. elegans*. En réalisant de multiples expériences, combinant l'utilisation de mutants Rpgrip1l/MKS5 chez *c.elegans* et la visualisation en microscopie à fluorescence des différentes protéines de la zone de transition couplées à la GFP introduites dans les cellules ciliées, il a pu être confirmé que Rpgrip1l/MKS5 était un élément clé dans le recrutement de l'ensemble des protéines à la zone de transition. L'assemblage des deux complexes majeur NPHP et MKS est donc dépendant de Rpgri1l.

Par ailleurs, CEP290 est impliqué dans de nombreuses ciliopathies et code pour une protéine suspectée localisée dans la zone de transition chez *Chlamydomonas*. L'identification de la protéine homologue Y47G6A.17 chez *c.elegans,* renommée Cep290 par la suite et une série d'expériences a permis confirmer sa localisation dans la zone de transition, son rôle dans la régulation du flux protéique et le maintien de la barrière de diffusion. Comme pour les autres protéines de la zone de transition, les mutants Cep290 montrent des anomalies de la structure du cil chez *c.elegans*, notamment un raccourcissement des cils, une perte des connections en forme de Y qui relient les microtubules à la membrane ciliaire ainsi que du microtubule interne ce qui conduit à une désorganisation des doublets de microtubules.
De la même manière que pour Rpgrip1l/MKS5 précédemment, l'étude de modèles *c.elegans* successivement mutés dans les différents gènes codant les protéines de la zone de transition a permis de démontrer que Cep290 était nécessaire au recrutement des différentes sous-unités du complexe MKS mais n'intervient pas dans l'assemblage du complexe NPHP. Cep290

permet également de recruter d'autres protéines de la zone de transition (TMEM138 et CDKL5) qui n'appartiennent à aucun des deux complexes NPHP ou MKS.

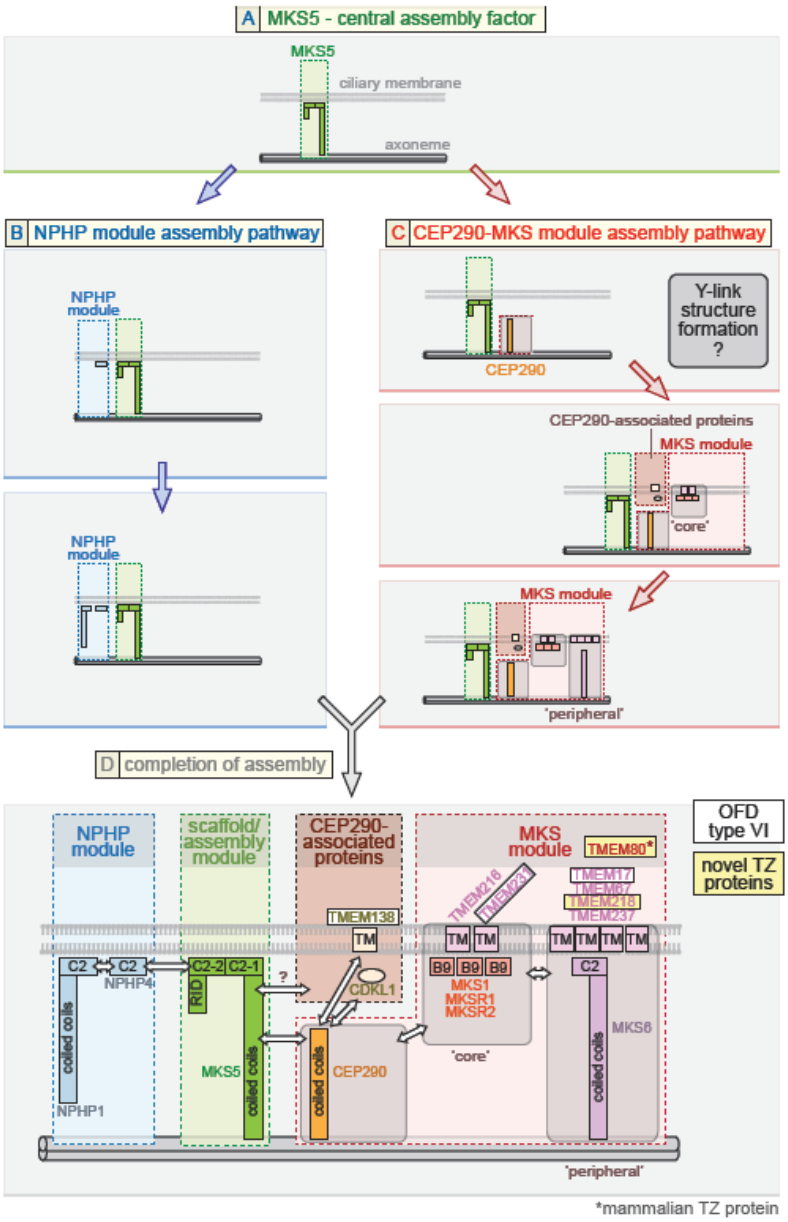

Figure 43: Organisation de la zone de transition. *Deux voies d'assemblage se distinguent après recrutement de MKS: une voie qui permet la constitution du module NPHP et une voie CEP290-dépendante. Cette dernière nécessite le recrutement premier de CEP290 dans la zone de transition, qui a son tour permettra le recrutement des protéines associées à CEP290 (TMEM138, CDKL1), et des protéines constituants le cœur du complexe MKS (TMEM216, TMEM231, MKS1, B9D1, B9D2). Enfin les protéines périphériques du complexe MKS seront assemblées (TMEM17, TMEM67, TMEM218, TMEM237).*

2.4- IFT57, sous-unité du complexe IFT-B

Le gène *IFT57* code pour une protéine du complexe IFT-B2 (protéines périphériques). A ce jour seulement 6/14 sous-unités du complexe IFT-B sont impliqués dans les ciliopathies : IFT27 et IFT172 responsable du syndrome de Bardet-Biedl, IFT80 impliqué dans le syndrome CCP, IFT52 et IFT81 impliqués respectivement dans des ciliopathies squelettiques et dans une forme associant un syndrome NPHP et une polydactylie. Le complexe IFT-B est relativement bien conservé au cours de l'évolution suggérant une fonction essentielle dans le cil primaire.

Afin d'étudier l'impact de cette mutation sur la structure et la fonction du cil primaire, nous avons, au sein de notre laboratoire, induit la ciliogenèse dans les fibroblastes du patient de notre cohorte. Après marquage de la tubuline acétylée à l'aide d'un anticorps pour visualiser les cils, nous n'avons constaté aucune différence du nombre ou de la longueur des cils. En revanche, nous avons démontré une accumulation d'IFT57 au niveau du corps basal alors que cette protéine est localisée dans l'ensemble du cil de façon homogène chez les contrôles (figure 44A).

IFT57 étant impliqué dans le transport intraflagellaire, un rôle dans la régulation de la vois SHH est suspecté. La stimulation de la voie SHH par un agoniste de Smoothened (SAG) a montré, dans les fibroblastes des patients, une faible réponse de Gli1, comparé aux contrôles (figure 44B, C). De même, l'inactivation d'IFT57 par siRNA dans les fibroblastes contrôles, montre une absence de réponse alors qu'une augmentation de 3,7x de l'expression de Gli1 est observée dans les fibroblastes contôles non transfectés après 30h en présence de SAG.

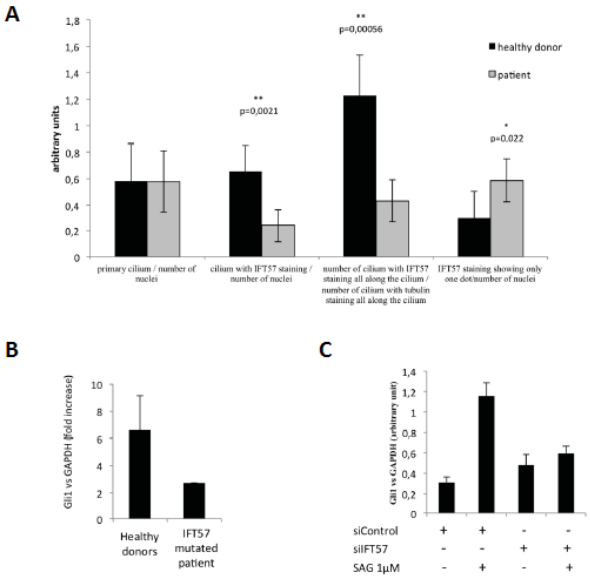

Figure 44: Impact des mutations du gène IFT57 sur le transport ciliaire. *(A) Comparaison entre les fibroblastes du patient muté et contrôles marqués pour IFT57 et la tubuline acétylée. Le nombre et la longueur des cils sont similaires, mais une diminution significative de la protéine IFT57 à l'extrémité apicale du cil est notée dans les fibroblastes du patient. (B-C) Diminution de l'expression de Gli1 dans les fibroblastes mutés ou en présence de siRNA IFT57 après stimulation par SAG.*

Discussion

Ce travail représente la plus grande étude moléculaire et fonctionnelle consacrée aux syndromes OFD, en dehors du syndrome OFDI.

1- Large hétérogénéité clinique et moléculaire des syndromes OFD

L'hétérogénéité clinique et les différents modes de transmission existant dans les syndromes OFD suggèrant une grande hétérogénéité génétique, nous avons choisi d'utiliser le SHD-E, puisque cette technique avait déjà démontré sa redoutable efficacité pour identifier les bases moléculaires des maladies rares très hétérogènes (Nguyen and Charlebois, 2014). Ce choix est apparu judicieux puisque nous avons identifié un gène causal chez 58.5% des cas (Bruel et al., soumis). Les syndromes OFD étant principalement transmis selon un mode d'hérédité autosomique récessif, nous nous sommes tout d'abord intéressés aux variations rares homozygotes ou potentiellement hétérozygotes composites, priorisant celles localisées dans des gènes ciliaires et/ou tronquantes absentes de la base de données OMIM. Parmi les cas où une consanguinité parentale est suspectée, la variation causale est probablement localisée dans une grande région d'homozygotie, rendant ainsi plus facile l'identification de nouveaux gènes.

Des variations causales ont été identifiées dans cinq nouveaux gènes, à l'état homozygote (*C2CD3, INTU, IFT57, TMEM107*) ou hétérozygote composite (*KIAA0753*) (Bruel et al., 2015a; Bruel et al., 2015b; Thauvin-Robinet et al., 2014; Thevenon et al., 2016; Toriyama et al., 2016). Récemment, des mutations additionnelles identifiées dans les gènes *C2CD3*, *TMEM107* et *TMEM231* ont été rapportées et confirment l'implication de ces gènes dans les syndromes OFD (Iglesias et al., 2014; Roberson et al., 2015; Shylo et al., 2015). Des variations causales ont aussi été identifiées dans six gènes précédemment rapportés comme impliqués dans les syndromes OFD (*DDX59*, *OFD1*) ou d'autres ciliopathies (*TMEM138*, *C5orf42*, *TMEM231*, *WDPCP*) (figure 45). Chez l'ensemble des patients de cette cohorte, le phénotype est très hétérogène avec plusieurs sous-types identifiés, OFD I (OFD1), OFD V (DDX59), OFD VI (*TMEM138*, *TMEM107*, *KIAA0753*, *C5orf42*) ou non-classifiés (*TMEM231*, *IFT57*, *INTU*, *WDPCP*) avec hypoplasie cérébelleuse, microcéphalie sévère, chondrodysplasie ou encore cardiopathies. Deux gènes candidats particulièrement intéressants (*CLIP3* et *NEDD1*) et jamais rapportés en pathologie ont aussi été identifiés dans cette cohorte. Ces deux derniers gènes ont été soumis sur GeneMatcher (https://genematcher.org/) afin d'identifier d'éventuels patients additionels, porteurs de mutations récessives et avec un

spectre clinique chevauchant, dans le but de démontrer l'implication de ces gènes dans les syndromes OFD.

Ces résultats démontrent la grande hétérogénéité clinique et génétique des syndromes OFD, avec à ce jour, 15 gènes différents impliqués dans ces maladies. Cependant, les mutations dans la plupart de ces gènes restent rares, du fait de la rareté des phénotypes OFD, de l'hétérogénéité génétique et la possibilité que certaines mutations soient spécifiques d'un groupe ethnique.

2- Allélisme génétique fréquent entre les syndromes OFD et les autres ciliopathies

L'identification progressive des bases moléculaires souligne l'implication du cil primaire dans les syndromes OFD et confirme le chevauchement clinique et génétique entre les syndromes OFD et les autres ciliopathies (Novarino et al., 2011). En effet, *OFD1*, impliqué dans l'OFD I, est aussi rapporté dans le syndrome de Joubert et dans un cas de rétinite pigmentaire sévère (Coene et al., 2009; Field et al., 2012; Kroes et al., 2015; Webb et al., 2012). *TMEM216*, initialement impliqué dans les syndromes de Joubert et Meckel, est aussi rapporté dans le syndrome OFD VI (Valente et al., 2010). Dans cette étude, nous avons identifié des mutations dans un nouveau gène (*TMEM107*) qui cause aussi le syndrome Joubert (Bruel et al., 2015a), tout comme quatre autres gènes initialement rapportés dans d'autres ciliopathies (*TMEM138*, *C5orf42*, *TMEM231*, *WDPCP*). A ce jour, un allélisme avec d'autres ciliopathies est connu pour 9 des 15 gènes impliqués dans les syndromes OFD. L'allélisme le plus fréquent concerne les syndromes OFD VI et de Joubert (*TMEM216, TMEM138, TMEM231, TMEM107, OFD1,* et *C5orf42*) (Bisschoff et al., 2013; Bruel et al., 2015a; Li et al., 2016; Lopez et al., 2014; Toriyama et al., 2016; Valente et al., 2010). Comme les mutations dans les gènes *TMEM231*, *TMEM107* et *C5orf42* causent aussi le syndrome de Meckel, nous pouvons clairement confirmer l'allélisme entre les syndromes OFD VI, Joubert et Meckel avec une expression phénotypique variable (Bruel et al., 2015a; Shaheen et al., 2013a, 2013b). Des variations dans le gène *WDPCP* a aussi été identifiés chez un cas présentant un syndrome de Bardet-Biedl (BBS), cependant l'allélisme entre ces syndromes reste incertain du fait de l'absence de données cliniques (Kim et al., 2010). Récemment, un allélisme avec les syndromes côtes courtes-polydactylie a été rapporté pour le gène *C2CD3* chez deux fœtus et pour le gène *INTU* (Cortés et al., 2016).

3- Caractérisation de trois complexes protéiques ciliaires et des anomalies ciliaires dans les syndromes OFD

La description clinique des différents sous-types suggère que les protéines causales pourraient être rassemblées au sein de différents complexes fonctionnels. Les 15 gènes codent pour des protéines localisées dans différents compartiments du cil primaire, de nouvelles fonctions ciliaires impliquées dans les syndromes OFD ont été suspectées. Les études fonctionnelles ont révélé deux nouveaux complexes ciliaires, CPLANE et OFIP/OFD1/FOPNL, et ont permis une meilleure caractérisation du module MKS localisé dans la zone de transition.

Au niveau du centrosome, la protéine C2CD3 a été identifiée comme un antagoniste d'OFD1, un régulateur positif de la croissance centriolaire (Singla et al., 2010; Thauvin-Robinet et al., 2014). KIAA0753 ou OFIP (OFD1 and FOR20 Interacting Protein) forme un complexe ternaire avec OFD1 et FOPNL/FOR20 pour initier la ciliogenèse et contrôler la longueur du centriole (Bruel et al., 2015b). OFIP est nécessaire au recrutement de FOPNL et OFD1 dans le centriole et les satellites centriolaires, et stabilise les microtubules du centrosome. Par ailleurs, C2CD3 est suspecté de s'associer avec le complexe OFIP/OFD1/FOPNL, probablement via la protéine OFD1. L'inactivation d'OFD1, C2CD3 ou OFIP induit une hyper-élongation (OFD1, OFIP) ou un raccourcissement des centrioles avec une perte des satellites (C2CD3). Ces défauts du centriole affectent l'ancrage à la membrane du corps basal ce qui conduit à une absence totale du cil ou un raccourcissement significatif de la longueur du cil. Toutes ces protéines sont impliquées dans la régulation de l'élongation du centriole, avec des fonctions antagonistes dans la ciliogenèse.

Deux autres gènes candidats, *CLIP3* et *NEDD1*, ont été identifiés au cours de cette étude. CLIP3 est issu de la superfamille des protéines CLIP et contient une région associée au radeau lipidique avec un domaine riche en glycine (CAP-Gly), motif par ailleurs retrouvé dans la structure d'autres protéines centrosomale telles que FOP ou CAP350, qui interagissent fortement avec les protéines golgiennes (Hoppeler-Lebel et al., 2007; Yan et al., 2006) et un domaine LisH également retrouvé dans la structure de plusieurs protéines centrosomales (OFD1, FOPNL). CLIP3 est associé au trans-golgi et joue un rôle dans la stabilisation des microtubules (Lallemand-Breitenbach et al., 2004). Bien qu'en l'état des connaissances actuelles, CLIP3 ne semble pas directement impliqué dans le cil, il constitue néanmoins un candidat non négligeable. La protéine NEDD1 est localisée dans le centrosome ainsi que dans

les satellites centriolaires. NEDD1 joue un rôle dans le recrutement de la γ-tubuline et la maturation des microtubules dans le centrosome. NEDD1 est aussi impliqué dans la cascade de phosphorylation Aurora A-Plk1-HDAC6 qui permet la déacétylation des microtubules de l'axonème et par conséquent le désassemblage du cil, NEDD1 étant phosphorylé par CDK1 et Plk1 (Haren et al., 2006; Wang et al., 2013). De plus, le phénotype d'un modèle poisson-zèbre muté dans ce gène montre des anomalies importante du système nerveux, une fermeture incomplète du tube neural, une courbure de l'axe du corps anormale, une queue courte et des anomalies oculaires inconstantes (Manning et al., 2010). Dans le cas où la pathogénicité de ces deux gènes est confirmée, la variabilité des fonctions ciliaires défectueuses dans les syndromes OFD, inclurait aussi la stabilité des microtubules.

Au niveau du corps basal, un nouveau complexe protéique CPLANE (Ciliogenesis and Planar polarity Effectors) composé de FUZ, RSG1 et de trois protéines impliquées dans les syndromes OFD, INTU, WDPCP et C5orf42, est caractérisé (Toriyama et al., sous-presse). C5orf42 recrute les différentes sous-unités du complexe selon une hiérarchie définie. Le complexe CPLANE interagit fortement avec le complexe IFT-A impliqué dans le transport intraflagellaire rétrograde, il est notamment nécessaire au recrutement des protéines périphériques du complexe IFT-A (IFT144, IFT43, IFT121 and IFT139) et à son pré-assemblage dans le cytosol. L'inactivation de CPLANE affecte le transport intraflagellaire et induit la formation d'un cil court.

Au niveau de la zone de transition, deux modules fonctionnels, MKS et NPHP, interagissent pour réguler la ciliogenèse, mettre en place les connections en forme de Y pour organiser et relier les microtubules à la membrane ciliaire, former la barrière de diffusion et contrôler l'entrée des protéines dans le cil (Bruel et al., 2015a; Li et al., 2016; Williams et al., 2011). Le complexe NPHP est composé de deux sous-unités (NPHP1 et NPHP4), tandis que le complexe MKS est composé de douze sous-unités (RPGRIP1L, TMEM216, B9D1, B9D2, MKS1, TMEM17, TMEM218, TMEM231, TMEM237, TMEM67 et CC2D2A), dont deux sont impliqués dans les syndromes OFD (TMEM231et TMEM216). Chez *c.elegans*, TMEM107 occupe un nouveau niveau intermédiaire dans l'assemblage hiérarchique de MKS, et est nécessaire au recrutement des protéines MKS1, TMEM17, TMEM237 et TMEM231, nouvellement identifiée comme impliquée dans les syndromes OFD (Bruel et al., 2015a). Par ailleurs, Cep290 est requis pour la localisation des sous-unités de MKS mais aussi d'autres

protéines de la zone de transition telles que TMEM138, responsable de syndromes OFD (Li et al., 2016).

Le gène *IFT57* code une sous-unité périphérique du complexe IFT-B, constitué d'un total de 14 sous-unités. Ce complexe est conservé au cours de l'évolution et sa fonction, essentielle à la formation et la maintenance du cil primaire. Seules six sous-unités sont, à ce jour, impliquées dans des ciliopathies (IFT27, IFT80, IFT81, IFT54, IFT172, IFT52) (Perrault et al., 2015). Les mutations du gène *IFT57* affectent la voie de signalisation SHH, ce qui confirme l'implication d'IFT57 dans le transport et la transduction des signaux ciliaires (Thevenon et al., 2016).

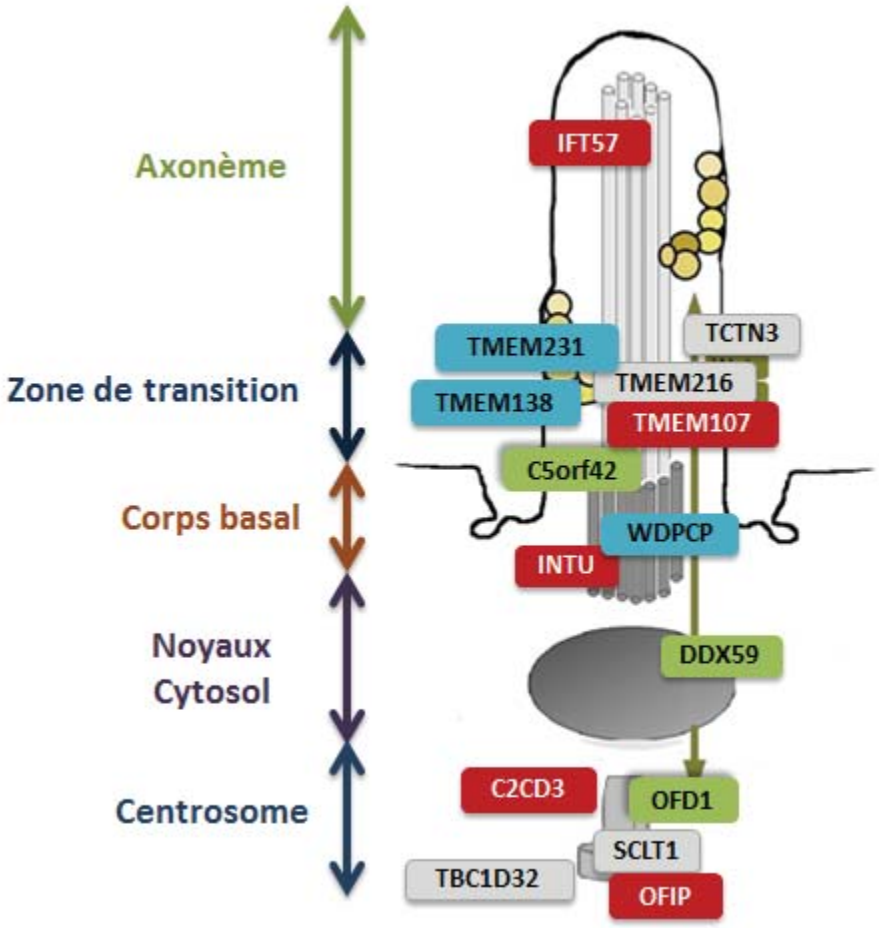

Figure 45 : Localisation des 15 protéines impliquées dans les syndromes OFD*. Dans notre cohorte, nous avons identifié 5 nouveaux gènes (en rouge), 3 gènes déjà connus dans d'autres ciliopathies (en bleu), 3 gènes connus responsables de syndromes OFD (en vert). Les gènes impliqués dans les syndromes OFD non identifié dans notre cohorte sont en gris.*

Les analyses fonctionnelles (*in vitro*, modèles murins, xénope, *C. elegans*) ont donc montré l'implication de la croissance centriolaire, de la zone de transition et du transport intraflagellaire.

5- Conclusion

En conclusion, cette étude, la plus importante consacrée aux syndromes OFD, démontre la très grande hétérogénéité clinique et génétique de ces syndromes, de même que de nombreux allélismes avec d'autres ciliopathies. Elle étend à 15 le nombre de gènes causaux, rendant la classification clinique initiale de 13 sous-types totalement obsolète et permettant de considérer les syndromes OFD comme un nouveau sous-groupe de ciliopathies à part entière.
Parmis les 8 exomes de cette étude sans candidats identifiés à ce jour, 7 ont été analysés en solo et 1 a été analysé en trio, présentant pas ailleurs un phénotype très atypique avec anomalies de la ligne médiane et une sœur avec une holoprosencéphalie faisant suspecter un gène codant pour une protéine impliquée dans la régulation de la voie SHH. Pour aider à la mise en évidence de nouveaux gènes causaux chez ces patients, un séquençage du génome entier pour ces cas index et leurs parents est envisagé afin d'identifier d'éventuelles variations dans des gènes avec une mauvaise courverture à l'exome et connus comme impliqué dans les ciliopathies, mais des variations non-exoniques dans des régions régulatrices de ces gènes. L'analyse en trio permettra aussi de filtrer les variations *de novo* ou hétérozygotes composites.
A l'issus de cette étude, une classification plus simplifiée, décrivant 3 sous-types principaux les plus fréquents (OFDI, OFDIV et OFDVI) et un dernier sous-type regroupant les syndromes OFD non-classés et/ou ultra-rares, est proposée dans l'annexe 8 et prend en compte les nouvelles données moléculaires désormais connues.

Articles

Article 1

Wide genetic ciliary heterogeneity in OFD syndrome from centriolar elongation to intraflagellar transport: identification of 5 new causal genes and confirmation of allelism will other ciliopathies.

J. Med Genet – Soumis

AL. Bruel, B. Franco, Y. Duffourd, J.Thevenon, L. Jego, E. Lopez, JF. Deleuze, D. Doummar, RH. Giles, CA. Johnson, MA. Huynen, V. Chevrier, L. Burglen, M. Morleo, I. Desguerres, G. Pierquin, B. Doray, B. Gilbert-Dussardier, B. Reversade, E. Steichen-Gersdorf, C. Baumann, I. Panigrahi, A. Fargeot-Espaliat, A. Dieux, A. David, A. Goldenberg, E. Bongers, D. Gaillard, J. Argente, B. Aral, N. Gigot, J. St-Onge, D. Birnbaum, SR. Phadke, V. Cormier-Daire, T. Eguether, GJ. Pazour, V. Herranz-Pérez, JS. Lee, L. Pasquier, P. Loget, S. Saunier, A. Mégarbané, O. Rosnet, MR. Leroux, JB. Wallingford, OE. Blacque, MV. Nachury, T. Attie-Bitach, JB Rivière, L. Faivre, C. Thauvin-Robinet.

Résumé :

Les syndromes OFD sont caractérisés par des anomalies orales, faciales et digitales associées à d'autres signes cliniques qui a permis une classification en 13 sous-types. La large hétérogénéité clinique des syndromes OFD suggère l'implication d'autres gènes ciliaire. Ce manuscrit décrit l'ensemble du travail consacré aux syndromes OFD au cours de ces trois dernières années. En effet, nous avons réalisé un séquençage haut-débit d'exome chez 24 cas index présentant un syndrome OFD et identifié des variations causales dans cinq nouveaux gènes (*C2CD3, TMEM107, INTU, OFIP, IFT57*). Nous avons élargi le spectre clinique de quatre gènes impliqués dans d'autres ciliopathies aux syndromes OFD (*C5orf42, TMEM138, TMEM231, WDPCP*). Des mutations ont aussi été identifiées dans des gènes précédemment connus dans les syndromes OFD (*OFD1*, *DDX59*). Les analyses fonctionnelles ont montré l'implication de la croissance centriolaire, de la zone de transition et du transport intraflagellaire, avec notamment la caractérisation de 3 complexes protéiques principaux : le complexe ternaire KIAA0753/OFD1/FOPNL, régulant la croissance centriolaire, le complexe MKS (TMEM107, TMEM231, TMEM216) constituant majeur de la zone de transition et le complexe CPLANE (INTU/FUZ/WDPCP), favorisant l'assemblage des protéines périphériques du complexe de transport intraflagellaire IFT-A. En conclusion, cette étude rend la classification clinique initiale totalement obsolète et confirme désormais les syndromes OFD comme un nouveau sous-groupe de ciliopathies à part entière.

Journal of
Medical Genetics

Wide genetic ciliary heterogeneity in oral-facial-digital syndromes and frequent allelism with other ciliopathies: from centriolar elongation to intraflagellar transport

Journal:	*Journal of Medical Genetics*
Manuscript ID	jmedgenet-2016-104062
Article Type:	Review
Date Submitted by the Author:	01-Jun-2016

Complete List of Authors:	Bruel, Ange-Line; Genetique des anomalies du développement Franco, Brunella; Telethon Institute of Genetic and Medicine, ; Federico II University of Naples, Pediatrics Duffourd, Yannis; Université de Bourgogne, Thevenon, Julien; Equipe émergente GAD « Génétique des Anomalies du développement », IFR Santé STIC, Université de Bourgogne, Dijon, France, Duplomb, Laurence; Université de Bourgogne, Lopez, Estelle; Equipe Génétique et Anomalies du Développement, Université de Bourgogne, Faculté de Médecine Deleuze, Jean-François; Centre National de Genotypage Doummar, Diane; AP-HP, Hôpital Armand Trousseau, service de neuropédiatrie, Giles, Rachel; University Medical Center Utrecht, Nephrology and Hypertension Johnson, Colin; University of Leeds, Ophthalmology and Neuroscience Huijnen, Martjin A.; Radboud Institute for Molecular Life Sciences, Radboud university medical center, Centre for Molecular and Biomolecular Informatics Chevrier, Véronique; Centre de Recherche en Cancerologie de Marseille; Aix-Marseille Universite Burglen, Lydie; APHP-Hôpital TROUSSEAU, Centre de référence des malformations et maladies congénitales du cervelet et Service de Génétique Médicale; INSERM U1141, Morleo, Manuela; Telethon Institute of Genetics and Medicine; Universita degli Studi di Napoli Federico II Desguerre, Isabelle; Hopital Necker Enfants Malades, Department of Paediatric Neurology Pierquin, Genevieve; Centre hospitalier universitaire de Liege, Service de Génétique Doray, Berenice; Hopital de Hautepierre Gilbert, Brigitte; CHU Poitiers, Reversade, Bruno; Institute of Medical Biology Singapore, Laboratory of Human Embryology and Genetics Steichen, Elisabeth; Medical University Innsbruck, Universitätsklinik für Kinder- und Jugendheilkunde Baumann, Clarisse; Hopital Robert Debré, Service de Génétique Clinique

	Panigrahi, Inusha; Advanced Pediatric Centre Pigmer, Genetic-Metabolic Unit, Department of Pediatrics Fargeot-Espaliat, Anne; Centre Hospitalier de Brive, Pédiatrie Neonatalogie Coeslier-Dieux, Anne; Hôpital jeanne de Flandre, Genetics David, Albert; CHU-Nantes, Génétique Médicale Goldenberg, Alice; Hopital charles Nicolle, Service de Génétique Bongers, Ernie; Radboud Universiteit Nijmegen, Department of Human Genetics Gaillard, Dominique; Centre Hospitalier Universitaire de Dijon Argente, Jesus; Hospital Infantil Universitario Nino Jesus Aral, Bernard; CHU de Dijon, Laboratoire de Génétique Moléculaire Gigot, Nadège; CHU de Dijon, Laboratoire de Génétique Moléculaire St-Onge, Judith; Université de Bourgogne, Birnbaum, Daniel Phadke, Shubha; SGPGIMS, Medical Genetics Cormier-Daire, Val&#65533;rie; Hopital Necker, Genetics Eguether, Thibaut; UMass medical school, Molecular medicine Pazour, Greg Herranz-Perez, Vicente; Universitat de Valencia Lee, Jacyln; Stanford University School of Medicine Pasquier, Laurent; CHU Rennes, Service de Génétique Clinique, CLAD Ouest Loget, Philippe; Centre Hospitalier Universitaire de Rennes Saunier, Sophie; INSERM UMR 1163, Molecular bases of hereditary kidney diseases Mégarbané, André; Arabian Gulf University Rosnet, Olivier; Centre de Recherche en Cancerologie de Marseille; Aix-Marseille Universite Leroux, Michel R.; Simon Fraser University Wallingford, John; University of Texas at Austin Blacque, Oliver E.; University College Dublin Nachury, Maxence; Stanford University School of Medicine, Department of Molecular and Cellular Physiology Attie-Bittach, Tania; Hopital universitaire Necker-Enfants malades Rivière, Jean-Baptiste; Equipe Génétique et Anomalies du Développement, Université de Bourgogne, Faculté de Médecine Faivre, Laurence; Hôpital d'Enfants, Centre de Génétique Thauvin-Robinet, Christel; Hôpital d'Enfants, CHU Dijon, , Centre de Génétique
Keywords:	Whole exome sequencing, Oral-Facial-Digital syndromes, Ciliopathies, Genetics

Title

Wide genetic ciliary heterogeneity in oral-facial-digital syndromes and frequent allelism with other ciliopathies: from centriolar elongation to intraflagellar transport

Authors

Ange-Line Bruel[1,2], Brunella Franco[3,4], Yannis Duffourd[1,2], Julien Thevenon[1,2,5], Laurence Jego[1,2], Estelle Lopez[2], Jean-François Deleuze[6], Diane Doummar[7], Rachel H. Giles[8], Colin A. Johnson[9], Martijn A. Huynen[10], Véronique Chevrier[11,12,13,14], Lydie Burglen[7], Manuela Morleo[2,3], Isabelle Desguerres[15], Geneviève Pierquin[16], Bérénice Doray[17], Brigitte Gilbert-Dussardier[18], Bruno Reversade[19], Elisabeth Steichen-Gersdorf [20], Clarisse Baumann[21], Inusha Panigrahi[22], Anne Fargeot-Espaliat[23], Anne Dieux[24], Albert David[25], Alice Goldenberg[26], Ernie Bongers[27], Dominique Gaillard[28], Jesús Argente[29], Bernard Aral[30], Nadège Gigot[1,2,30], Judith St-Onge[1,2], Daniel Birnbaum[11,12,13,14], Shubha R. Phadke[31], Valérie Cormier-Daire[3,32,33], Thibaut Eguether[34], Gregory J. Pazour[34], Vicente Herranz-Pérez[35,36], Jaclyn S. Lee[37], Laurent Pasquier[38], Philippe Loget[39], Sophie Saunier[40,41], André Mégarbané[42,46], Olivier Rosnet[11,12,13,14], Michel R. Leroux[43], John B. Wallingford[44], Oliver E. Blacque[45], Maxence V. Nachury[37], Tania Attie-Bitach[32,33,41], Jean-Baptiste Rivière[1,2,30], Laurence Faivre[1,2,5], Christel Thauvin-Robinet[1,2,5]

Affiliations

1. FHU-TRANSLAD, Université de Bourgogne/CHU Dijon, France
2. Équipe EA42271 GAD, Université de Bourgogne, Dijon, France
3. Department of Translational Medicine, Medical Genetics Ferderico II University of Naples, Italy
4. Telethon Institute of Genetics and Medicine-TIGEM, Naples, Italy
5. Centre de Référence maladies rares « Anomalies du Développement et syndrome malformatifs » de l'Est et Centre de Génétique, Hôpital d'Enfants, CHU, Dijon, France
6. Centre National de Génotypage, Evry, France
7. APHP, hôpital TROUSSEAU, Centre de référence des malformations et maladies congénitales du cervelet et département de génétique, Paris, France
8. Department of Nephrology and Hypertension, University Medical Center Utrecht, Utrecht, The Netherlands
9. Section of Ophthalmology and Neurosciences, Leeds Institute of Molecular Medicine, University of Leeds, Leeds, LS9 7TF, UK
10. Centre for Molecular and Biomolecular Informatics, Radboud Institute for Molecular Life Sciences, Radboud university medical center, Geert Grooteplein 26-28, 6525 GA Nijmegen, Netherlands
11. Centre de Recherche en Cancérologie de Marseille, INSERM UMR1068, F-13009 Marseille, France
12. Institut Paoli-Calmettes, F-13009 Marseille, France
13. CNRS U7258, F-13009 Marseille, France
14. Aix-Marseille Université, F-13007 Marseille, France
15. Service de neurométabolisme, Hôpital Necker-Enfants Malades, CHU, Paris, France

16. Service de Génétique, CHU, Liège, Belgium
17. Service de Génétique Médicale, Hôpital de Hautepierre, CHU, Strasbourg, France
18. Centre de Référence Maladies Rares « Anomalies du Développement et Syndromes malformatifs » de l'Ouest, Service de Génétique Médicale, CHU de Poitiers, EA 3808, Université de Poitiers, France
19. Laboratory of Human Embryology and Genetics, Institute of Medical Biology, Singapore
20. Department of Pediatrics I, Innsbruck Medical University, Innsbruck, Austria
21. Département de Génétique, Unité Fonctionelle de Génétique Clinique, Hôpital Robert Debré, CHU, Paris, France
22. Genetic-Metabolic Unit, Department of Pediatrics, Advanced Pediatric Centre, Pigmer, Chandigarh, India
23. Pédiatrie Neonatalogie, Centre Hospitalier Général, Brive-la-Gaillarde, France
24. Centre de Référence CLAD NdF, Service de Génétique Clinique, Hôpital Jeanne de Flandre, CHRU, Lille, France
25. Service de Génétique Médicale, Unité de Génétique Clinique, Hôpital Mère-Enfant, CHU, Nantes, France
26. Service de Génétique, CHU de Rouen, Centre Normand de Génomique Médicale et Médecine Personnalisée, Rouen, France
27. Department of Human Genetics, Radboud University, Nijmegen, The Netherlands
28. Service de Génétique, Hôpital Maison Blanche, CHRU, Reims, France
29. Department of Pediatrics & Pediatric Endocrinology, Hospital Infantil Universitario Niño Jesús. Departement of Pediatrics, Universidad Autónoma de Madrid. CIBEROBN de fisiopatología de la obesidad y nutrición. Instituto de Salud Carlos III. Madrid, Spain.
30. Laboratoire de Génétique Moléculaire, PTB, CHU, Dijon, France
31. Department of Medical Genetics, Sanjay Gandhi Post Graduate Institute of Medical Sciences, Lucknow, Uttar Pradesh, India
32. INSERM UMR1163, Université de Paris-Descartes-Sorbonne Paris Cité, Institut IMAGINE, Hôpital Necker-Enfants Malades, Paris, France
33. Service de génétique médicale, Hôpital Universitaire Necker-Enfants Malades, AP-HP, Institut Imagine, Paris, France
34. Program in Molecular Medicine, University of Massachusetts Medical School, Worcester, Massachusetts, USA
35. Laboratorio de Neurobiología Comparada, Instituto Cavanilles, Universitat de València, CIBERNED, Spain
36. Unidad mixta de Esclerosis múltiple y neurorregeneración, IIS Hospital La Fe-UVEG, Valencia, Spain
37. Department of Molecular and Cellular Physiology, Stanford University School of Medicine, Stanford, CA, USA
38. Centre de Référence Maladies Rares « Anomalies du Développement et Syndromes malformatifs » de l'Ouest, Unité Fonctionnelle de Génétique Médicale, CHU Rennes, France

39. Laboratoire d'Anatomie-Pathologie, CHU Rennes, France
40. INSERM U983, Institut IMAGINE, Hôpital Necker-Enfants Malades, Paris, France
41. Département de Génétique, Hôpital Necker-Enfants Malades, AP-HP, Paris, France
42. Al Jawhara Center, Arabian Gulf University, Manama, Bahrain
43. Department of Molecular Biology and Biochemistry and Centre for Cell Biology, Development and Disease, Simon Fraser University, Burnaby, British Columbia V5A 1S6, Canada
44. Department of Molecular Biosciences, Center for Systems and Synthetic Biology, and Institute for Cellular and Molecular Biology, University of Texas at Austin
45. School of Biomolecular and Biomedical Science, University College Dublin, Belfield, Dublin 4, Ireland
46. Institut Jérôme Lejeune, Paris, France

There is no conflict of interest

Keywords: oral-facial-digital syndromes

Corresponding author:
Pr Christel Thauvin-Robinet, MD-PhD
Centre de Génétique, Hôpital d'Enfants
10 Bd du Maréchal de Lattre de Tassigny
21034 Dijon cedex
France
tel: 33 3 80 29 53 13
fax: 33 3 80 29 32 66
e-mail: christel.thauvin@chu-dijon.fr

Abstract

Oral-facial-digital (OFD) syndromes encompass rare genetic disorders characterized by facial, oral and digital abnormalities, which associate with a wide range of additional features to delineate 13 OFD subtypes. The most frequent, OFD I, is caused by a heterozygous mutation in the *OFD1* encoding a centrosomal protein. The wide clinical heterogeneity suggests the involvement of other genes implicated in ciliary formation and/or function. For 15 years, we have aimed to identify the molecular bases of OFD syndromes, recently purred by the development of whole exome sequencing (WES). Here, we review all our published and unpublished results secondary to the WES, identifying 24 cases presenting with OFD syndrome causal mutations in five new genes (*C2CD3, TMEM107, INTU, OFIP, IFT57*). We associated the clinical spectrum of four genes in other ciliopathies (*C5orf42*, *TMEM138* and *TMEM231, WDPCP*) to OFD syndromes. Causal variants were also detected in two known genes, previously implicated in OFD syndromes (*OFD1*, *DDX59*). Functional studies unveiled the involvement of centriole elongation, the transition zone and intraflagellar transport defects in OFD syndromes, highlighting the importance of three ciliary protein modules: the ternary complex OFIP-FOR20-OFD1, a regulator of centriole elongation; the MKS module (TMEM107, TMEM231), a major component of the transition zone; and the CPLANE complex (INTU, WDPCP) necessary for IFT-A assembly. Based on our results, which represent the largest OFD cohort examined by WES, we conclude that OFD syndromes represent a distinct subgroup of ciliopathies with wide heterogeneity, which makes the initial, distinctive clinical classification of facial, oral and digital anomalies obsolete.

INTRODUCTION

Oral-facial-digital (OFD) syndromes are a group of inherited disorders initially characterized by the association of abnormalities of the face (hypertelorism, low-set ears), oral cavity (lingual hamartoma, abnormal frenulae, lobulated tongue) and extremities (brachydactyly, polydactyly). OFD syndromes also comprise a broad range of additional features that led to the clinical delineation of 13 OFD subtypes, the most common being OFDI (polycystic kidney disease, corpus callosum agenesis), OFDIV (tibial dysplasia), OFDVI (mesoaxial polydactyly, vermis hypoplasia, molar tooth sign) and OFDIX (retinopathy) [1]. However, such precise phenotypic description revealed new unclassified OFD subtypes, in particular one associated with severe microcephaly [2–5]. Classically, the inheritance pattern is autosomal recessive except for OFDI, which has dominant X-linked inheritance and is lethal in males. Until recently, the molecular bases of OFD syndromes were poorly understood. The first molecular insight was the discovery of the *OFD1* gene [MIM 300170] described as causing the OFDI subtype [6]. *OFD1* encodes a protein located in the centrosome and basal body of primary cilia, suggesting that OFD syndromes are ciliopathies [7,8].

Ciliopathies are human diseases defined by ciliary structural and/or functional defects. Cilia, microtubule-based organelles projecting from the cytoplasmic membrane of the cell body, are divided into motile and non-motile (primary) cilia. Primary cilia are essential for several biological processes especially during development [9] and enable a broad range of specific sensory processes by concentrating receptors and ion channels that sense light, chemical and mechanical stimuli required for the transduction of signalling pathways. Three main structural compartments have been described. The first is the basal body, which represents a modified mother centriole derived from a centrosome, and is accompanied by pericentriolar material [10]. The basal body migrates to and becomes attached to the cell surface via distal appendage (transition fibers), and give rise to the ciliary axoneme. The second is the transition zone, which forms the first segment of the axoneme and is characterized by Y-links connecting microtubules to the ciliary membrane and associated ciliary necklace. This ciliary domain, just distal to the basal body, is now believed to form a ciliary gate or diffusion barrier that regulates the specific composition of the ciliary compartment [11,12]. The remainder of the microtubule-based axoneme extends distally from the basal body, and is unsheathed in a ciliary membrane that is distinct from the plasma membrane and contains receptors and signalling proteins required for sensory transduction. Ciliary proteins must be transported along the axoneme to permit the growth, maintenance and function of the ciliary compartment. This essential function is carried out by the intraflagellar transport (IFT) machinery, which is powered by kinesin anterograde and dynein retrograde motors, as well as three biochemically separable

functional modules: IFT subcomplex A (IFT-A), whose role appears essential for retrograde transport, IFT subcomplex B (IFT-B), important for anterograde transport, and a Bardet-Biedl syndrome (BBS) protein complex termed BBSome, which dynamically mobilize ciliary proteins into as well out the cilia [13,14].

Ciliopathies present a broad range of features (retinopathy, cerebral malformations, bone defects, deafness or renal disease …); they are thus highly genetically heterogeneous diseases, and include nephronophthisis (NPHP), Joubert (JBTS), Meckel-Gruber (MKS), Bardet-Biedl (BBS) syndromes and different chondrodysplasiaes. Multiple cases of allelism have been described, suggesting that human ciliopathies are genetically complex [15]. More recently, mutations in five additional genes that encode ciliary proteins have been identified in one or two patients with OFD syndromes: centrosomal proteins implicated in centriole elongation (*SCLT1* [MIM 611399] and *TBC1D32/C6orf170* [MIM 615867]), proteins located in the transition zone (*TMEM216* [MIM 613277] and *TCTN3* [MIM 613847]) and a protein that regulates ciliary signalling (*DDX59* [MIM 615464]). Each known gene appeared to be implicated in a particular OFD subtype (16): *OFD1* in OFDI [MIM 311200] with polycystic kidney disease and corpus callosum agenesis, *TCTN3* in OFDIV [MIM 258860] with tibial defect, *DDX59* in OFDV [MIM 174300], *TMEM216* in OFDVI [MIM 277170] characterized by cerebellar hypoplasia with the molar sign tooth, *SCTL1* and *TBC1D32/C6orf170* in OFDIX [MIM 258865] with coloboma [6,17–24]. Using a strategy of whole exome sequencing, we identified five new causal genes in OFD syndromes and showed an association between OFD and four additional genes previously reported in other ciliopathies, as well as their different ciliary functions.

PATIENTS AND METHODS

Patient cohort

We ascertained an international cohort of 115 index cases affected with different OFD syndromes. In all cases with a typical OFD I phenotype, we looked for *OFD1* SNV or CNV, by Sanger sequencing of targeted array-CGH respectively [25,26]. Causal *OFD1* SNV or CNV was identified in 59/115 cases. Among 24 other index cases with atypical clinical features or negative for *OFD1* sequencing (Figure 1 and Table S1), we performed whole exome sequencing (WES), including 17 sporadic cases and 7 cases from consanguineous parents. All of the patients presented with oral abnormalities (lingual hamartoma, abnormal frenulae or lobulated tongue), facial dysmorphism and extremity abnormalities (mainly polydactyly), associated with cerebral malformations (12/14 cases), retinopathy (3/16 cases), renal abnormalities (4/14 cases) and/or cardiac malformations (9/17 cases). Six individuals were diagnosed with OFDVI because of the molar tooth sign (MTS) on brain MRI and

positive diagnostic criteria, two with OFDII and one with OFDV [27]. Parental DNA samples were available in 17/24 cases.

Exome Analysis

After written consent had been obtained, blood samples were collected and DNA was extracted. Three micrograms of genomic DNA per index individual was subjected to whole-exome capture and sequencing using the SureSelect Human All Exon V5 kit (Agilent). The resulting libraries were sequenced on a HiSeq 2000 (Illumina) as paired-end 76 bp reads. BAM files were aligned to a human genome reference sequence (GRCh37/hg19) using BWA (Burrows-Wheeler Aligner; v0.6.2). All aligned read data were subject to the following steps: (i) duplicate paired-end reads were removed by Picard 1.77, (ii) indel realignment and (iii) base quality score recalibration were done on the Genome Analysis Toolkit (GATK; v2.1-10). Variants with a quality score >30 and an alignment quality score >20 were annotated with SeattleSeq SNP Annotation (see Web resources). Rare variants present at a frequency above 1% in dbSNP 138, ExAC Browser and the NHLBI GO Exome Sequencing Project or present in 312 exomes of unaffected individuals were excluded (see Web resources). To improve our exome analysis, data were crossed with a list of known cilia-related genes from the Ciliome Database, Cildb v2.1, Syscilia (see Web resources) and transcriptomic, proteomic and bioinformatics studies of cilia to identify putative ciliary genes [28–31]. The analyses focused on genes with homozygous variants in consanguineous families and with two heterozygous variants in other cases and prioritized (i) genes associated with human disease in ClinVar or HGMD databases (see Web resources), (ii) cilia-related genes and (iii) other genes (Figure 2).

Sanger sequencing

Candidate variants and parental segregation were confirmed by Sanger sequencing. The different primers are available on request. Genomic DNA was amplified by Polymerase Chain Reaction (PCR) using HotStarTaq PCR kit (Qiagen, Valencia, CA) according to the manufacturer's protocol. PCR products were purified by the Agencourt CleanSEQ system (Beckman Coulter, Brea, CA) and sequenced with the BigDye Terminator Cycle Sequencing kit, v3.1 (Applied Biosystems) in ABI 3730 sequencer (Applied Biosystems, Foster City, CA). Sequence data were analysed using Mutation Surveyor v4.0.9 (Softgenomics, Oakwood Avenue, PA).

RESULTS

WES identified causal mutations in 13/24 cases. The filtering strategy extracted six homozygous variants in consanguineous families (Table 1): a frameshift in the *INTU* gene [MIM 610621], a

nonsense mutation in the *C2CD3* gene [MIM 615944], a missense mutation in the *DDX59* [MIM 615464], *TMEM138* [MIM 614459] and *TMEM107* genes, and a synonymous variant affecting a splice site in the *IFT57* gene [MIM 606621] [5,32–35]. For all these genes, Sanger sequencing and parental segregation confirmed the homozygous status in the affected cases and the heterozygous status in each parent.

We also identified compound heterozygous variants in four ciliary genes (Table 1): *TMEM231* [MIM 614949], *WDPCP* [MIM 613580], *C5orf42* genes [MIM 614571] and *KIAA0753* [33,36,37]. Sanger sequencing and parental segregation confirmed the compound heterozygous status in the affected cases and the heterozygous status in each parent for all genes, except for the *KIAA0753* gene. For this gene, Sanger sequencing confirmed that the nonsense variant (NM_014804.2:p.Lys631*) was maternally inherited and the intronic substitution (NM_014804.2:c.1546-3C>A) occurred *de novo* and affected a splice-site causing a truncated protein [36].

In the absence of homozygous or compound heterozygous candidate mutations, we focused on rare heterozygous variants in OMIM or ciliary genes. This search identified causal mutations (p.Tyr87Cys and p.Ala614Hisfs*15) in the *OFD1* gene [MIM 311200] in two unrelated cases.

Sequencing of these genes in different replication cohorts identified *C2CD3* and *C5orf42* mutations in additional OFD patients, as well as *TMEM107* and *INTU* mutations in JBTS patients, respectively (Table 1) [5,35,37].

We therefore identified causal mutations in five new genes, four of which were previously implicated in other ciliopathies and two of which were previously known to be responsible for OFD syndromes (Figure 3).

DISCUSSION

This study presents the largest OFD cohort investigated by WES. It led to the identification of causal mutations in 54% of affected cases, thus confirming the power of WES in identifying the genetic cause in well-phenotyped cases and in also highly heterogeneous disorders.

Wide clinical and genetic heterogeneity of OFD syndromes

The wide clinical heterogeneity and variable modes of inheritance in OFD syndromes suggest extreme genetic heterogeneity. Exome sequencing thus appeared the obvious choice, and because OFD syndromes were suspected to be mainly recessive, we initially focused on homozygous or potential compound heterozygous mutations, and prioritized ciliary genes and truncating rare variants in the absence of OMIM genes. In cases of suspected consanguinity, the probable causal

variant was expected to be located within a large stretch of a homozygous region, thereby making it easier to identify new genes. Causal variants were thus identified in five new genes, in homozygous (*C2CD3*, *INTU*, *IFT57, TMEM107*) or compound heterozygous states (*KIAA0753)* [5,34,35]. Recently, additional *C2CD3, TMEM107* and *TMEM231* mutations confirmed the implication of these genes in OFD syndromes (Table 1) (38,39). Causal variants were also identified in six other genes previously implicated in OFD syndromes (*DDX59*, *OFD1*) or in other ciliopathies (*TMEM138*, *C5orf42*, *TMEM231*, *WDPCP*). In all these patients, the OFD phenotype was clinically heterogeneous with OFDI (*OFD1*), OFDV (*DDX59*), OFDVI (*TMEM138, TMEM107, KIAA0753, OFD1, C5orf42*) or OFDIX (*C2CD3),* as well as unclassified OFD (*TMEM231*, *IFT57*, *INTU, WDPCP*), with clinically ailments also including cerebellar hypoplasia, severe microcephaly, chondrodysplasia or cardiopathy. These results demonstrate the wide clinical and genetic heterogeneity of OFD syndromes, which includes, to date, of 15 different genes. However, mutations in most of these genes remain rare because of the sparsity of affected individuals, the wide genetic heterogeneity, and the lack of suspicion of mutations in specific ethnic groups.

Frequent clinical and genetic allelism between OFD and other ciliopathies

The progressive identification of the molecular bases of OFD syndromes has highlighted the involvement of the primary cilia and confirmed the clinical and genetic overlap between OFD and other ciliopathies [40]. Indeed, *OFD1,* responsible for OFDI syndrome, was also reported in JBTS and severe retinitis pigmentosa [41–45]. *TMEM216*, initially implicated in JBTS and MKS, also caused OFDVI [46]. Moreover, we recently uncovered OFD mutations in two new genes (*TMEM107, INTU*), which are also known to cause JBTS and short-rib polydactyly [32,35], as well as in four other genes previously implicated in other ciliopathies (*TMEM138, C5orf42, TMEM231, WDPCP*) (Table 1). To date, allelism with other ciliopathies affects nine of the 15 OFD genes. The most frequent allelism concerns OFDVI and JBTS (*TMEM216*, *TMEM138*, *TMEM231*, *TMEM107, OFD1*, and *C5orf42)* [32,33,35,37,46,47]. Because *TMEM231*, *TMEM107* and *C5orf42* genes also cause MKS [32,48,49], this confirms the clear allelism between OFDVI, MKS and JBTS syndromes with variable phenotypic expression. *WDPCP* mutations are also reported in BBS, respectively, but the allelism remains uncertain because of the absence of clinical data in the reported cases [35,50]. *C2CD3* and *INTU* mutations have also recently been reported in two foetuses with skeletal dysplasia suggesting a short ribs-polydactyly (SRP) syndrome [35,51].

Characterization of three ciliopathy protein complexes and cilia disturbance in OFD syndromes

The clinical description of different subtypes suggested that the causal proteins could be assembled in different functional modules. Because the 15 genes encode proteins located in different compartments of primary cilia, new ciliary functions were suspected of being implicated in OFD

syndromes (Table 2). Different functional studies have revealed two new ciliary complexes, CPLANE and OFIP-OFD1-FOR20, and better characterized the transition zone and MKS module.

At the centrosomal level, the positive regulator C2CD3 was found antagonize OFD1, a negative regulator of centriole elongation [5]. KIAA0753 or OFIP (OFD1 and FOR20 Interacting Protein) formed a ternary complex with OFD1 and FOR20 (also known as FOPNL) to initiate ciliogenesis [36]. Because C2CD3 and the KIAA0753-FOR20 binary complex are both associated with OFD1, a large multisubunit complex may exist to regulate centriole distal end growth and integrity. Knockdown of OFD1 and OFIP induces hyperelongated centrioles, whereas disruption of C2CD3 cause shortened centrioles with the absence of subdistal appendages. FOR20 down regulation also affects centriole distal ends structure. These defects affected basal body membrane anchoring with a concomitant absence of cilia or greatly decreased cilium length. All these proteins control centriole elongation as do other centrosomal complexes, consisting of subunits with antagonist functions in ciliogenesis.

At the basal body level, a new protein complex, CPLANE (Ciliogenesis and Planar polarity Effectors) formed by FUZ, RSG1 and the three OFD proteins INTU, WDPCP and C5orf42, was characterized [35]. C5orf42 initially recruits CPLANE components in the hierarchical assembly of this complex. CPLANE complex binds extensively with the IFT-A complex involved in retrograde intraflagellar transport, which is crucial for the recruitment of peripheral IFT-A proteins (IFT144, IFT43, IFT121 and IFT139) and their cytosolic pre-assembly. CPLANE defects affect intraflagellar transport and induce shortened cilia. Thus *RSG1* and *FUZ* genes are good candidates for OFD syndrome, although Sanger sequencing of a local cohort negative for known OFD genes has not yet revealed mutations in these genes.

At the transition zone (TZ), two functional modules, MKS and NPHP, interact to regulate ciliogenesis, the assembly of membrane-microtubule Y-link connectors, and the formation of a diffusion barrier [32,33,52]. The NPHP module consists of two subunits (NPHP1, NPHP4) and the MKS module of twelve or more subunits (RPGRIP1L, TMEM107, TMEM216, B9D1, B9D2, MKS1, TMEM17, TMEM231, TMEM218, TMEM237, TMEM67 and CC2D2A), some of which are now known to be involved in OFD syndromes (TMEM231, TMEM216). It has been reported that TMEM107 occupies a new intermediate layer in the hierarchical assembly of the MKS module and is necessary to recruit TZ-proteins MKS1, TMEM17, TMEM237 and the novel OFD protein TMEM231 [32]. In *C. elegans*, orthologs of RPGRIP1L and CEP290 are required for the TZ localization of the MKS protein module and of other TZ-proteins, such as TMEM138, involved in OFD syndrome [33].

The new *IFT57* gene encodes a peripheral subunit of the IFT-B complex, which consists minimally of 14 members. The IFT-B complex is highly conserved in evolution and has an essential function in formation and maintenance of primary cilia. Only six subunits are involved in ciliopathies (IFT27, IFT80, IFT81, IFT88, IFT172, IFT54) [53,54]. Immunolocalization studies reveal that *IFT57* mutations restrict IFT57 protein localization to the basal body in OFD patients' fibroblasts, whereas IFT57 was

observed in the whole cilia in controls. Likewise, the *IFT57* mutation affected the Sonic HedgeHog pathway, thus confirming the involvement of IFT57 in ciliary transport and signal transduction [34].

OFD syndromes: a distinct subgroup of ciliopathies

In summary, we identified five new genes responsible for OFD (*C2CD3, KIAA0753/OFIP, IFT57, INTU*, *TMEM107*), confirmed that OFD, BBS, JBTS,MKS and SRP are allelic disorders and extended the clinical spectrum of *TMEM138*, *TMEM231*, *C5orf42, C2CD3* and *WDPCP* genes, thus increasing to 15 the number of genes known to be responsible for OFD (Figure 3). All of the encoded proteins are located at different parts of the centrosome and/or primary cilia and have various ciliary functions, thus illustrating that OFD results from a wide genetic and functional heterogeneity, spanning from centriolar elongation to intraflagellar transport. We note that mutations in TZ-genes and in CPLANE-genes mainly cause OFD VI and unclassified OFD with cardiac malformations, respectively, while mutations in centrosomal genes appear less specific, causing various sub-types (OFD I, IX, XIV and unclassified).

The initial classification of OFD syndromes in 13 subtypes based on clinical data now appears to be obsolete given the wide clinical and molecular heterogeneity, with different overlapping ciliopathies such as JBTS, MKS, BBS and SRP. These findings also confirm that OFD syndromes are a distinct subgroup of ciliopathies.

Acknowledgements

We thank the patients and their families for their participation. We thank the Integragen society, CNG and IBGMC for exome analysis and the Ferdinand Cabanne Biological Ressource Center (CRBFC) for access to the biobank. This work was supported by grants from the GIS-Institut des Maladies Rares (HTS), the French Foundation for Rare Diseases, the French Ministry of Health (PHRC national 2010-A01014-35 and 2013), the Regional Council of Burgundy, Science Foundation Ireland (SFI; grant 11/PI/1037 to OEB), the Canadian Institutes of Health Research (CIHR: grant MOP142243 to MRL), Fondos de Investigación Sanitaria and fondos FEDER (Grants PI100747 and PI1302195), Centro de Investigación Biomédica en Rad Fisiopatología de Obesidad y Nutrición (CIBEROBN), Instituto de Salud Carlos III, Spain. The authors also acknowledge funding from EU-FP7 Programme 241955 SYSCILIA, the Dutch Kidney Foundation KOUNCIL CP11.18, and ICMR. We also thank the NHLBI GO Exome Sequencing Project (see URLs) and its ongoing studies which produced and provided exome variant calls for comparison: the Lung GO Sequencing Project (HL-102923), the WHI Sequencing Project (HL-102924), the Broad GO Sequencing Project (HL-102925), the Seattle GO Sequencing Project (HL-102926) and the Heart GO Sequencing Project (HL-103010).

References

1. Gurrieri F, Franco B, Toriello H, Neri G. Oral-facial-digital syndromes: review and diagnostic guidelines. Am J Med Genet A. 2007 Dec 15;143A(24):3314–23.

2. Al-Gazali LI, Sztriha L, Punnose J, Shather W, Nork M. Absent pituitary gland and hypoplasia of the cerebellar vermis associated with partial ophthalmoplegia and postaxial polydactyly: a variant of orofaciodigital syndrome VI or a new syndrome? J Med Genet. 1999 Feb;36(2):161–6.

3. Chung WY, Chung LP. A case of oral-facial-digital syndrome with overlapping manifestations of type V and type VI: a possible new OFD syndrome. Pediatr Radiol. 1999 Apr;29(4):268–71.

4. Erickson RP, Bodensteiner JB. Oro-facial-digital syndrome IX with severe microcephaly: a new variant in a genetically isolated population. Am J Med Genet A. 2007 Dec 15;143A(24):3309–13.

5. Thauvin-Robinet C, Lee JS, Lopez E, Herranz-Pérez V, Shida T, Franco B, Jego L, Ye F, Pasquier L, Loget P, Gigot N, Aral B, Lopes CA, St-Onge J, Bruel AL, Thevenon J, González-Granero S, Alby C, Munnich A, Vekemans M, Huet F, Fry AM, Saunier S, Rivière JB, Attié-Bitach T, Garcia-Verdugo JM, Faivre L, Mégarbané A, Nachury MV. The oral-facial-digital syndrome gene C2CD3 encodes a positive regulator of centriole elongation. Nat Genet. 2014 Aug;46(8):905–11.

6. Ferrante MI, Giorgio G, Feather SA, Bulfone A, Wright V, Ghiani M, Selicorni A, Gammaro L, Scolari F, Woolf AS, Sylvie O, Bernard L, Malcolm S, Winter R, Ballabio A, Franco B. Identification of the gene for oral-facial-digital type I syndrome. Am J Hum Genet. 2001 Mar;68(3):569–76.

7. Keller LC, Romijn EP, Zamora I, Yates JR, Marshall WF. Proteomic analysis of isolated chlamydomonas centrioles reveals orthologs of ciliary-disease genes. Curr Biol. 2005 Jun 21;15(12):1090–8.

8. Romio L, Wright V, Price K, Winyard PJD, Donnai D, Porteous ME, Franco B, Giorgio G, Malcolm S, Woolf AS, Feather SA. OFD1, the gene mutated in oral-facial-digital syndrome type 1, is expressed in the metanephros and in human embryonic renal mesenchymal cells. J Am Soc Nephrol. 2003 Mar;14(3):680–9.

9. Goetz SC, Anderson KV. The Primary Cilium: A Signaling Center During Vertebrate Development. Nat Rev Genet. 2010 May;11(5):331–44.

10. Kobayashi T, Dynlacht BD. Regulating the transition from centriole to basal body. J Cell Biol. 2011 May 2;193(3):435–44.

11. Reiter JF, Blacque OE, Leroux MR. The base of the cilium: roles for transition fibres and the transition zone in ciliary formation, maintenance and compartmentalization. EMBO Rep. 2012 Jul;13(7):608–18.

12. Szymanska K, Johnson CA. The transition zone: an essential functional compartment of cilia. Cilia. 2012;1(1):10.

13. Sung C-H, Leroux MR. The roles of evolutionarily conserved functional modules in cilia-related trafficking. Nat Cell Biol. 2013 Dec;15(12):1387–97.

14. Taschner M, Bhogaraju S, Lorentzen E. Architecture and function of IFT complex proteins in ciliogenesis. Differentiation. 2012 Feb;83(2):S12-22.

15. Hildebrandt F, Benzing T, Katsanis N. Ciliopathies. N Engl J Med. 2011 Apr 21;364(16):1533–43.

16. Franco B, Thauvin-Robinet C. Update on oral-facial-digital syndromes (OFDS). Cilia. 2016;5:12.

17. Adly N, Alhashem A, Ammari A, Alkuraya FS. Ciliary genes TBC1D32/C6orf170 and SCLT1 are mutated in patients with OFD type IX. Hum Mutat. 2014 Jan;35(1):36–40.

18. Edvardson S, Shaag A, Zenvirt S, Erlich Y, Hannon GJ, Shanske AL, Hannon GJ, Shanske AL, Gomori JM, Ekstein J, Elpeleg O. Joubert syndrome 2 (JBTS2) in Ashkenazi Jews is associated with a TMEM216 mutation. Am J Hum Genet. 2010 Jan;86(1):93–7.

19. Giorgio G, Alfieri M, Prattichizzo C, Zullo A, Cairo S, Franco B. Functional characterization of the OFD1 protein reveals a nuclear localization and physical interaction with subunits of a chromatin remodeling complex. Mol Biol Cell. 2007 Nov;18(11):4397–404.

20. Roberson EC, Dowdle WE, Ozanturk A, Garcia-Gonzalo FR, Li C, Halbritter J, Elkhartoufi N, Porath JD, Cope H, Ashley-Koch A, Gregory S, Thomas S, Sayer JA, Saunier S, Otto EA, Katsanis N, Davis EE, Attié-Bitach T, Hildebrandt F, Leroux MR, Reiter JF.. TMEM231, mutated in orofaciodigital and Meckel syndromes, organizes the ciliary transition zone. J Cell Biol. 2015 Apr 13;209(1):129–42.

21. Romio L, Fry AM, Winyard PJD, Malcolm S, Woolf AS, Feather SA. OFD1 is a centrosomal/basal body protein expressed during mesenchymal-epithelial transition in human nephrogenesis. J Am Soc Nephrol. 2004 Oct;15(10):2556–68.

22. Saari J, Lovell MA, Yu H-C, Bellus GA. Compound heterozygosity for a frame shift mutation and a likely pathogenic sequence variant in the planar cell polarity-ciliogenesis gene WDPCP in a girl with polysyndactyly, coarctation of the aorta, and tongue hamartomas. Am J Med Genet A. 2015 Feb;167(2):421–7.

23. Shamseldin HE, Rajab A, Alhashem A, Shaheen R, Al-Shidi T, Alamro R, Al Harassi S, Alkuraya FS. Mutations in DDX59 implicate RNA helicase in the pathogenesis of orofaciodigital syndrome. Am J Hum Genet. 2013 Sep 5;93(3):555–60.

24. Thomas S, Legendre M, Saunier S, Bessières B, Alby C, Bonnière M, Toutain A, Loeuillet L, Szymanska K, Jossic F, Gaillard D, Yacoubi MT, Mougou-Zerelli S, David A, Barthez MA, Ville Y, Bole-Feysot C, Nitschke P, Lyonnet S, Munnich A, Johnson CA, Encha-Razavi F, Cormier-Daire V, Thauvin-Robinet C, Vekemans M, Attié-Bitach T. TCTN3 mutations cause Mohr-Majewski syndrome. Am J Hum Genet. 2012 Aug 10;91(2):372–8.

25. Thauvin-Robinet C, Cossée M, Cormier-Daire V, Van Maldergem L, Toutain A, Alembik Y, Bieth E, Layet V, Parent P, David A, Goldenberg A, Mortier G, Héron D, Sagot P, Bouvier AM, Huet F, Cusin V, Donzel A, Devys D, Teyssier JR, Faivre L. Clinical, molecular, and genotype-phenotype correlation studies from 25 cases of oral-facial-digital syndrome type 1: a French and Belgian collaborative study. J Med Genet. 2006 Jan;43(1):54–61.

26. Thauvin-Robinet C, Callier P, Franco B, Zuffardi O, Payet M, Aral B, Gigot N, Donzel A, Mosca-Boidron AL, Masurel-Paulet A, Huet F, Teyssier JR, Mugneret F, Faivre L. Search for genomic imbalances in a cohort of 20 patients with oral-facial-digital syndromes negative for mutations and large rearrangements in the OFD1 gene. Am J Med Genet A. 2009 Aug;149A(8):1846–9.

27. Poretti A, Brehmer U, Scheer I, Bernet V, Boltshauser E. Prenatal and neonatal MR imaging findings in oral-facial-digital syndrome type VI. AJNR Am J Neuroradiol. 2008 Jun;29(6):1090–1.

28. Amato R, Morleo M, Giaquinto L, di Bernardo D, Franco B. A network-based approach to dissect the cilia/centrosome complex interactome. BMC Genomics. 2014;15:658.

29. Ishikawa H, Thompson J, Yates JR, Marshall WF. Proteomic analysis of mammalian primary cilia. Curr Biol. 2012 Mar 6;22(5):414–9.

30. Ivliev AE, 't Hoen PAC, van Roon-Mom WMC, Peters DJM, Sergeeva MG. Exploring the transcriptome of ciliated cells using in silico dissection of human tissues. PLoS ONE. 2012;7(4):e35618.

31. Wheway G, Schmidts M, Mans DA, Szymanska K, Nguyen T-MT, Racher H, Phelps IG, Toedt G, Kennedy J, Wunderlich KA, Sorusch N, Abdelhamed ZA, Natarajan S, Herridge W, van Reeuwijk J, Horn N, Boldt K, Parry DA, Letteboer SJ, Roosing S, Adams M, Bell SM, Bond J, Higgins J, Morrison EE, Tomlinson DC, Slaats GG, van Dam TJ, Huang L, Kessler K, Giessl A, Logan CV, Boyle EA, Shendure J, Anazi S, Aldahmesh M, Al Hazzaa S, Hegele RA, Ober C, Frosk P, Mhanni AA, Chodirker BN, Chudley AE, Lamont R, Bernier FP, Beaulieu CL, Gordon P, Pon RT, Donahue C, Barkovich AJ, Wolf L, Toomes C, Thiel CT, Boycott KM, McKibbin M, Inglehearn CF; UK10K Consortium; University of Washington Center for Mendelian Genomics, Stewart F, Omran H, Huynen MA, Sergouniotis PI, Alkuraya FS, Parboosingh JS, Innes AM, Willoughby CE, Giles RH, Webster AR, Ueffing M, Blacque O, Gleeson JG, Wolfrum U, Beales PL, Gibson T, Doherty D, Mitchison HM, Roepman R, Johnson CA. An siRNA-based functional genomics screen for the identification of regulators of ciliogenesis and ciliopathy genes. Nat Cell Biol. 2015 Jul 13;

32. Lambacher NJ, Bruel A-L, van Dam TJP, Szymańska K, Slaats GG, Kuhns S, McManus GJ, Kennedy JE, Gaff K, Wu KM, van der Lee R, Burglen L, Doummar D, Rivière JB, Faivre L, Attié-Bitach T, Saunier S, Curd A, Peckham M, Giles RH, Johnson CA, Huynen MA, Thauvin-Robinet C, Blacque OE. TMEM107 recruits ciliopathy proteins to subdomains of the ciliary transition zone and causes Joubert syndrome. Nat Cell Biol. 2015 Nov 23;

33. Li C, Jensen VL, Park K, Kennedy J, Garcia-Gonzalo FR, Romani M, De Mori R, Bruel AL, Gaillard D, Doray B, Lopez E, Rivière JB, Faivre L, Thauvin-Robinet C, Reiter JF, Blacque OE, Valente EM, Leroux MR. MKS5 and CEP290 Dependent Assembly Pathway of the Ciliary Transition Zone. PLoS Biol. 2016 Mar;14(3):e1002416.

34. Thevenon J, Duplomb L, Phadke S, Eguether T, Saunier A, Avila M, Carmignac V, Bruel AL, St-Onge J, Duffourd Y, Pazour GJ, Franco B, Attie-Bitach T, Masurel-Paulet A, Rivière JB, Cormier-Daire V, Philippe C, Faivre L, Thauvin-Robinet C. Autosomal Recessive IFT57 hypomorphic mutation cause ciliary transport defect in unclassified oral-facial-digital syndrome with short stature and brachymesophalangia. Clin Genet. 2016 Apr 7;

35. Toriyama M, Lee C, Taylor SP, Duran I, Cohn DH, Bruel A-L, Tabler JM, Drew K, Kelly MR, Kim S, Park TJ, Braun DA, Pierquin G, Biver A, Wagner K, Malfroot A, Panigrahi I, Franco B, Al-Lami HA, Yeung Y, Choi YJ, University of Washington Center for Mendelian Genomics, Duffourd Y, Faivre L, Rivière JB, Chen J, Liu KJ, Marcotte EM, Hildebrandt F, Thauvin-Robinet C, Krakow D, Jackson PK, Wallingford JB. The ciliopathy-associated CPLANE proteins direct basal body recruitment of intraflagellar transport machinery. Nat Genet. 2016 May 9;

36. Chevrier V, Bruel A-L, Dam TJP van, Franco B, Scalzo ML, Lembo F, Audebert S, Baudelet E, Isnardon D, Bole A, Borg JP, Kuentz P, Thevenon J, Burglen L, Faivre L, Rivière JB, Huynen MA, Birnbaum D, Rosnet O, Thauvin-Robinet C. OFIP/KIAA0753 forms a complex with OFD1 and FOR20 at pericentriolar satellites and centrosomes and is mutated in one individual with Oral-Facial-Digital Syndrome. Hum Mol Genet. 2015 Dec 7;ddv488.

37. Lopez E, Thauvin-Robinet C, Reversade B, Khartoufi NE, Devisme L, Holder M, Ansart-Franquet H, Avila M, Lacombe D, Kleinfinger P, Kaori I, Takanashi J, Le Merrer M, Martinovic J, Noël C, Shboul M, Ho L, Güven Y, Razavi F, Burglen L, Gigot N, Darmency-Stamboul V, Thevenon J, Aral B, Kayserili H, Huet F, Lyonnet S, Le Caignec C, Franco B, Rivière JB, Faivre L, Attié-Bitach T. C5orf42 is the major gene responsible for OFD syndrome type VI. Hum Genet. 2014 Mar;133(3):367–77.

38. Iglesias A, Anyane-Yeboa K, Wynn J, Wilson A, Truitt Cho M, Guzman E, Sisson R, Egan C, Chung WK. The usefulness of whole-exome sequencing in routine clinical practice. Genet Med. 2014 Dec;16(12):922–31.

39. Shylo NA, Christopher KJ, Iglesias A, Daluiski A, Weatherbee SD. TMEM107 is a Critical Regulator of Ciliary Protein Composition and is Mutated in Orofaciodigital Syndrome. Human Mutation. 2015 Oct 1;n/a-n/a.

40. Novarino G, Akizu N, Gleeson JG. Modeling Human Disease in Humans: the Ciliopathies. Cell. 2011 Sep 30;147(1):70–9.

41. Coene KLM, Roepman R, Doherty D, Afroze B, Kroes HY, Letteboer SJF, Ngu LH, Budny B, van Wijk E, Gorden NT, Azhimi M, Thauvin-Robinet C, Veltman JA, Boink M, Kleefstra T, Cremers FP, van Bokhoven H, de Brouwer AP. OFD1 is mutated in X-linked Joubert syndrome and interacts with LCA5-encoded lebercilin. Am J Hum Genet. 2009 Oct;85(4):465–81.

42. Del Giudice E, Macca M, Imperati F, D'Amico A, Parent P, Pasquier L, Layet V, Lyonnet S, Stamboul-Darmency V, Thauvin-Robinet C, Franco B; Oral-Facial-Digital Type I (OFD1) Collaborative Group. CNS involvement in OFD1 syndrome: a clinical, molecular, and neuroimaging study. Orphanet J Rare Dis. 2014;9:74.

43. Field M, Scheffer IE, Gill D, Wilson M, Christie L, Shaw M, Gardner A, Glubb G, Hobson L, Corbett M, Friend K, Willis-Owen S, Gecz J. Expanding the molecular basis and phenotypic spectrum of X-linked Joubert syndrome associated with OFD1 mutations. Eur J Hum Genet. 2012 Jul;20(7):806–9.

44. Kroes HY, Monroe GR, van der Zwaag B, Duran KJ, de Kovel CG, van Roosmalen MJ, Harakalova M, Nijman IJ, Kloosterman WP, Giles RH, Knoers NV, van Haaften G. Joubert syndrome: genotyping a Northern European patient cohort. Eur J Hum Genet. 2015 Apr 29;

45. Webb TR, Parfitt DA, Gardner JC, Martinez A, Bevilacqua D, Davidson AE, ito I, Thiselton DL, Ressa JH, Apergi M, Schwarz N, Kanuga N, Michaelides M, Cheetham ME, Gorin MB, Hardcastle AJ. Deep intronic mutation in OFD1, identified by targeted genomic next-generation sequencing, causes a severe form of X-linked retinitis pigmentosa (RP23). Hum Mol Genet. 2012 Aug 15;21(16):3647–54.

46. Valente EM, Logan CV, Mougou-Zerelli S, Lee JH, Silhavy JL, Brancati F, Iannicelli M, Travaglini L, Romani S, Illi B, Adams M, Szymanska K, Mazzotta A, Lee JE, Tolentino JC, Swistun D, Salpietro CD, Fede C, Gabriel S, Russ C, Cibulskis K, Sougnez C, Hildebrandt F, Otto EA, Held S, Diplas BH, Davis EE, Mikula M, Strom CM, Ben-Zeev B, Lev D, Sagie TL, Michelson M, Yaron Y, Krause A, Boltshauser E, Elkhartoufi N, Roume J, Shalev S, Munnich A, Saunier S, Inglehearn C, Saad A, Alkindy A, Thomas S, Vekemans M, Dallapiccola B, Katsanis N, Johnson CA, Attié-Bitach T, Gleeson JG. Mutations in TMEM216 perturb ciliogenesis and cause Joubert, Meckel and related syndromes. Nat Genet. 2010 Jul;42(7):619–25.

47. Bisschoff IJ, Zeschnigk C, Horn D, Wellek B, Rieß A, Wessels M, Willems P, Jensen P, Busche A, Bekkebraten J, Chopra M, Hove HD, Evers C, Heimdal K, Kaiser AS, Kunstmann E, Robinson KL, Linné M, Martin P, McGrath J, Pradel W, Prescott KE, Roesler B, Rudolf G, Siebers-Renelt U, Tyshchenko N, Wieczorek D, Wolff G, Dobyns WB, Morris-Rosendahl DJ. Novel mutations including deletions of the entire OFD1 gene in 30 families with type 1 orofaciodigital syndrome: a study of the extensive clinical variability. Hum Mutat. 2013 Jan;34(1):237–47.

48. Shaheen R, Faqeih E, Alshammari MJ, Swaid A, Al-Gazali L, Mardawi E, Khalil MM, Seidahmed MZ, Alnemer M, Alsahan N, Sogaty S, Alhashem A, Singh A, Goyal M, Kapoor S, Alomar R, Ibrahim N, Alkuraya FS. Genomic analysis of Meckel-Gruber syndrome in Arabs reveals marked genetic heterogeneity and novel candidate genes. Eur J Hum Genet. 2013 Jul;21(7):762–8.

49. Shaheen R, Ansari S, Mardawi EA, Alshammari MJ, Alkuraya FS. Mutations in TMEM231 cause Meckel-Gruber syndrome. J Med Genet. 2013 Mar;50(3):160–2.

50. Kim SK, Shindo A, Park TJ, Oh EC, Ghosh S, Gray RS, Lewis RA, Johnson CA, Attie-Bittach T, Katsanis N, Wallingford JB. Planar cell polarity acts through septins to control collective cell movement and ciliogenesis. Science. 2010 Sep 10;329(5997):1337–40.

51. Cortés CR, McInerney-Leo AM, Vogel I, Rondón Galeano MC, Leo PJ, Harris JE, Anderson LK, Keith PA, Brown MA, Ramsing M, Duncan EL, Zankl A, Wicking C. Mutations in human C2CD3 cause skeletal dysplasia and provide new insights into phenotypic and cellular consequences of altered C2CD3 function. Sci Rep. 2016;6:24083.

52. Williams CL, Li C, Kida K, Inglis PN, Mohan S, Semenec L, Bialas NJ, Stupay RM, Chen N, Blacque OE, Yoder BK, Leroux MR. MKS and NPHP modules cooperate to establish basal body/transition zone membrane associations and ciliary gate function during ciliogenesis. J Cell Biol. 2011 Mar 21;192(6):1023–41.

53. Bizet AA, Becker-Heck A, Ryan R, Weber K, Filhol E, Krug P, Halbritter J, Delous M, Lasbennes MC, Linghu B, Oakeley EJ, Zarhrate M, Nitschké P, Garfa-Traore M, Serluca F, Yang F, Bouwmeester T, Pinson L, Cassuto E, Dubot P, Elshakhs NA, Sahel JA, Salomon R, Drummond IA, Gubler MC, Antignac C, Chibout S, Szustakowski JD, Hildebrandt F, Lorentzen E, Sailer AW, Benmerah A, Saint-Mezard P, Saunier S. Mutations in TRAF3IP1/IFT54 reveal a new role for IFT proteins in microtubule stabilization. Nat Commun. 2015;6:8666.

54. Perrault I, Halbritter J, Porath JD, Gérard X, Braun DA, Gee HY, Fathy HM, Saunier S, Cormier-Daire V, Thomas S, Attié-Bitach T, Boddaert N, Taschner M, Schueler M, Lorentzen E, Lifton RP, Lawson JA, Garfa-Traore M, Otto EA, Bastin P, Caillaud C, Kaplan J, Rozet JM, Hildebrandt F. IFT81, encoding an IFT-B core protein, as a very rare cause of a ciliopathy phenotype. J Med Genet. 2015 Aug 14;jmedgenet-2014-102838.

Legends

Figure 1: Clinical pictures, X-rays and brain MRI of OFD cases. Case 3a (M), case 3b (N), case 4 (C, P, X), case 5 (μ), case 6a (B, T, U, V, W), case 6b (H, α, β, γ, δ), case 7 (G), case 8 (E, L, Q, ε, ζ, ι, κ), case 10 (J, Y), case 11 (O), case 17 (D, I, K), case 19 (G), case 22 (A, η), case 25 (ν, ξ), case 26b (F, Z, θ), case 27 (R, ο, ρ, ς) case 28b (S, σ, τ), case 29 (υ,φ) with facial dysmorphism (A-F) including low-set ears (A), median pseudo-cleft of upper lip (H), missing incisors (B) or severe microcephaly (C), abnormal frenulae (G), cleft palate (K), lobulated tongue or hamartoma (I, J, L), pre and postaxial polydactyly of hands and feet (T, U, X, Y, η, θ, λ, μ-φ), broad duplicated and/or deviated hallux (V, W, X, η, θ, ι, κ, ξ, ο, π, φ), Y-sharped metacarpal abnormality (μ, ς), hypothalamic hamartoma (R), cerebellar hypoplasia (S), brain MRI with MTS (M-Q).

Figure 2: Strategy for exome analysis

Figure 3: Localization of proteins encoded by the 15 OFD genes in primary cilia. 5 new OFD genes (in red), 4 genes previously implicated in other ciliopathies (in green), 6 genes previously reported in OFD (2 with presented mutations (blue) and 4 others (white).

Table 1: OFD genes identified by whole-exome sequencing or targeted gene sequencing

Table 2: Summary of OFD phenotype as well as localization and function of OFD proteins

Table S1: Clinical data of all OFD cases with exome analysis (patients 1-24) and the only OFD patients from the replication cohort (patients 25-29) with causal mutations. NA: Not Available, AO: oculomotor apraxia, AVSD: atrio-ventricular septal defects, B: brachydactyly, C: clinodactyly, CCA: Corpus callosum agenesis, DWM: Dandy-Walker malformation, F: female, FB: frontal bossing, UFP: upslanting palpebral fissures, HH: Hypothalamic hamartoma, HM: hypermetropia, HN: hypoplasia of the alae of nose, ID: Intellectual disability, IVC: Intra-ventricular communication, LSE: low-set ears, M: male, MP: mesoaxial polydactyly, MR: micro/retrognathia, MTS: Molar Tooth Sign, NL: The Netherlands, P: polydactyly, PMD: psychomotor delay, PPo: Polydactyly post-axial, PPr: Pre-axial polydactyly, PSD: primary septal defect, S: syndactyly, ToF: teratology of Fallot, Y: Y-shaped metacarpal.

Case	Gene	Ciliary gene	OMIM	Mutation		Inheritance	EVS	ExAC	cDNA tests
				c. position	p. position				
Cohort analyzed by exome									
1	*DDX59*	NA	Oral-facial-digital syndrome V [174300]	c.754G>A c.754G>A	p.Gly252Arg p.Gly252Arg	Maternal Paternal	-	-	-
2	*TMEM138*	+	Joubert syndrome 16 [614465]	c.352A>T c.352A>T	p.Met118Leu p.Met118Leu	NA NA	-	-	-
3a/b	*TMEM107*	+	-	c.134A>G c.134A>G	p.Glu45Gly p.Glu45Gly	Maternal Paternal	-	-	-
4	*C2CD3*	+	-	c.184C>T c.184C>T	p.Arg62* p.Arg62*	Maternal Paternal	-	-	-
5	*INTU*	+	-	c.396delT c.396delT	p.Asn132Lysfs*11 p.Asn132Lysfs*11	NA NA	-	-	-
6a	*IFT57*	+	-	c.777G>A c.777G>A	p.Lys259Lys p.Lys259Lys	NA NA	-	-	Splice defect
7	*C5orf42*	+	Joubert syndrome 17 [614615]	3557delA c.3577C>T	Lys1186Argfs*22 p.Arg1193Cys	NA NA	- -	- -	-
8	*C5orf42*	+	Joubert syndrome 17 [614615]	c.3290-2A>G c.493delA	- p.Ile165Tyrfs*17	Maternal Paternal	- 1/6155	- -	-
9	*TMEM231*	+	Joubert syndrome 20 [614970] Meckel syndrome 11 [615397]	c.656C>T c.532C>G	p.Pro219Leu p.Pro178Ala	Maternal Paternal	- -	- -	-
10	*WDPCP*	+	Bardet-Biedl syndrome 15 [209900]	c.160G>A c.526_527delTT	p.Asp54Asn Leu176Ilefs*21	Paternal Maternal	1/11827 -	7/119586 -	-
11	*KIAA0753*	+	-	c.1546-3C>A c.1891A>T	- p.Lys631*	de novo Maternal	- -	- -	Splice defect -
12	*OFD1*	+	Oral-facial-digital syndrome I [3111200] Joubert syndrome 10 [300804] Simpson-Golabi-Behmel syndrome 2 [300209] Retinitis pigmentosa 23 [300424]	c.260A>G	p.Tyr87Cys	de novo	-	-	-
13	*OFD1*	+		c.1840delG	p.Ala614Hisfs*15	de novo	-	-	-
Replication cohort									
25	*C5orf42*	+	Joubert syndrome 17 [614615]	c.3550C>T c.9121C>T	p.Arg1184Cys p.Gln3041*	Paternal Maternal	- -	- -	-
26a/b	*C5orf42*	+	Joubert syndrome 17 [614615]	c.3150-1G>T c.3150-1G>T	- -	Maternal Paternal	- -	- -	Splice defect Splice defect
27	*C5orf42*	+	Joubert syndrome 17 [614615]	c.2377C>T c.8509G>T	p.Gln793* p.Val2837Leu	Paternal Maternal	- -	2/ 22038 -	-
28b	*C5orf42*	+	Joubert syndrome 17 [614615]	c.493delA c.3380C>T	p.Ile165Tyrfs*17 p.Ser1127Leu	Paternal Maternal	- -	- -	-
29	*C2CD3*	+	-	c.3085T>C c.3911-2A>T	p.Cys1029Gly -	NA	- 6/ 12978	- 31/ 120818	- Splice defect

NA: Not Available

Table 1: OFD genes identified by whole-exome sequencing or single gene sequencing

Gene	Protein localization	Functional protein complex	Protein function	OFD subtype	Pre-axial polydactyly	Post-axial polydactyly	Retinopathy	Renal anomaly	Cerebral malformation	MTS	Tibial dysplasia	Reference
OFD1	Centrosome/BB	OFD1-OFIP-FOPNL	Negative regulator of centriole elongation	OFDI	x			x	x			Ferrante et al., 2001
C2CD3	Centrosome/TF	-	Positive regulator of centriole elongation	OFDXIV		x	x		x			Thauvin-Robinet et al., 2014
OFIP	Centrosome	OFD1-OFIP-FOPNL	Recruitment of OFD1 at centriole	-		x			x	x		Chevrier et al., 2015
SCTL1	Centrosome/TF	-	Unknown, ciliogenesis	OFDIX					x			Adly et al.,2013
TBC1D32	Centrosome	-	Unknown	OFDIX		x			x			Adly et al.,2013
DDX59	Cytosol/?	-	Regulation of ciliary signalling	OFDV		x						Present study
INTU	BB	CPLANE	IFT-A pre-assembly	OFDII?		x		x				Toriyama et al., 2016
WDPCP	BB	CPLANE	IFT-A pre-assembly	-		x						Toriyama et al., 2016
C5orf42	BB/TZ	CPLANE	IFT-A pre-assembly	OFDVI	x	x			x	x		Lopes et al., 2014
TCTN3	TZ	-	Regulation of ciliary signalling	OFDIV	x	x		x	x		x	Thomas et al., 2012
TMEM216	TZ	MKS	Ciliary gate formation	OFDVI	x	x			x			Valente et al., 2012
TMEM231	TZ	MKS	Ciliary gate formation	OFDVI?		x			x			Li et al., 2016
TMEM107	TZ	MKS	Ciliary gate formation	OFDVI		x	x		x	x		Lambacher et al., 2015
TMEM138	TZ	-	Vesicular transport	OFDVI					x	x		Li et al., 2016
IFT57	BB/Axoneme	IFT-B	Intraflagellar transport	-		x						Thevenon et al., 2016

Table 2: Summary of OFD phenotype as well as localization and function of OFD proteins

BB: Basal Body, OFD: Oral-Facial-Digital, TF: Transition fibers

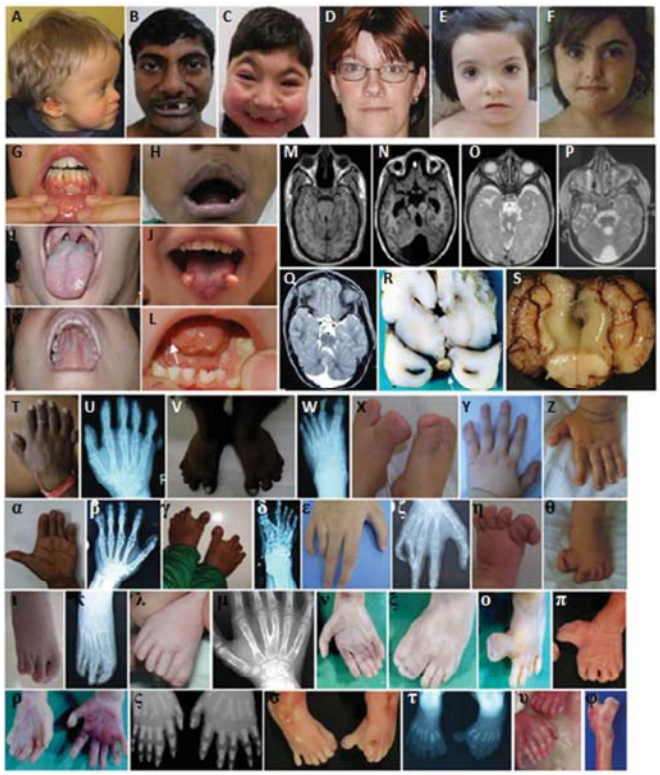

Figure 1: Clinical pictures, X-rays and brain MRI of OFD cases. Case 3a (M), case 3b (N), case 4 (C, P, X), case 5 (μ), case 6a (B, T, U, V, W), case 6b (H, α, β, γ, δ), case 7 (G), case 8 (E, L, Q, ε, ζ, ι, κ), case 10 (J, Y), case 11 (O), case 17 (D, I, K), case 19 (G), case 22 (A, η), case 25 (ν, ξ), case 26b (F, Z, θ), case 27 (R, ο, ρ, ς) case 28b (S, σ, τ), case 29 (υ,φ) with facial dysmorphism (A-F) including low-set ears (A), median pseudo-cleft of upper lip (H), missing incisors (B) or severe microcephaly (C), abnormal frenulae (G), cleft palate (K), lobulated tongue or hamartoma (I, J, L), pre and postaxial polydactyly of hands and feet (T, U, X, Y, η, θ, λ, μ-φ), broad duplicated and/or deviated hallux (V, W, X, η, θ, ι, κ, ξ, ο, π, φ), Y-sharped metacarpal abnormality (μ, ς), hypothalamic hamartoma (R), cerebellar hypoplasia (S), brain MRI with MTS (M-Q).

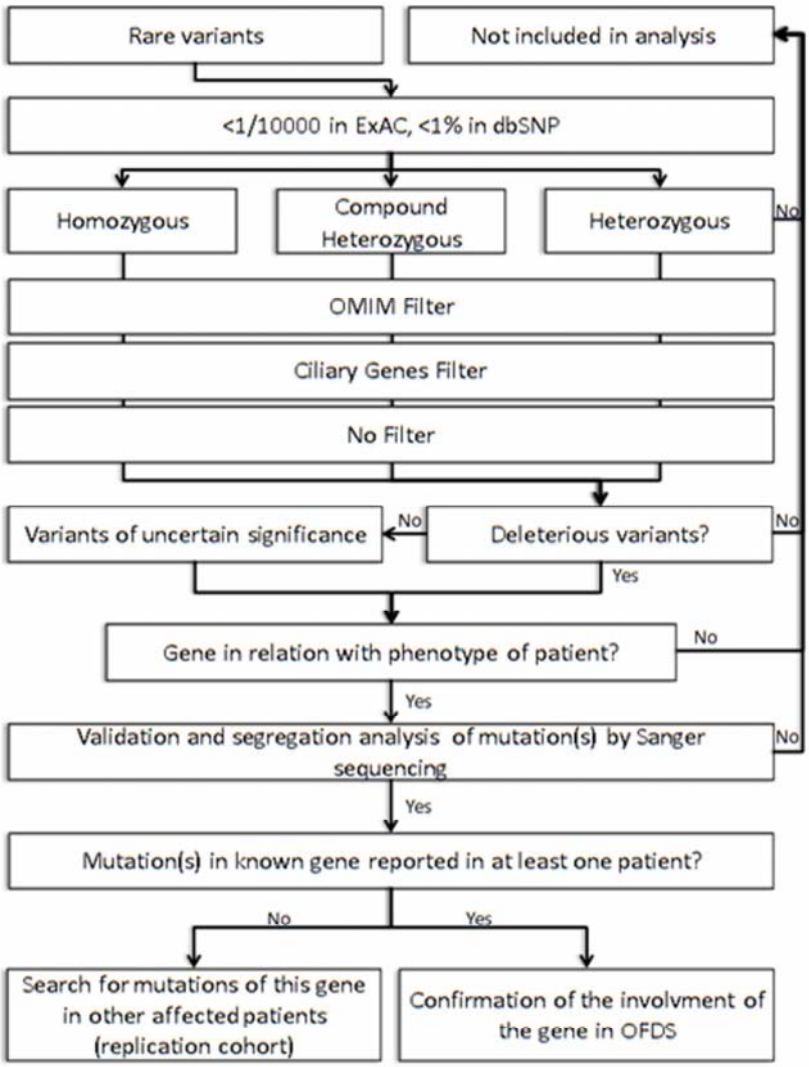

Figure 2: Strategy for exome analysis

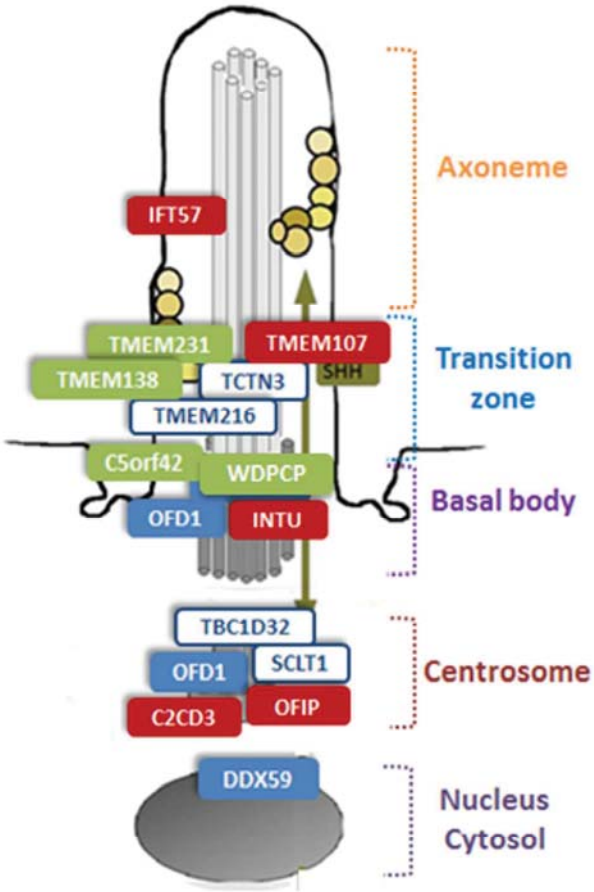

Figure 3: Localization of proteins encoded by the 15 OFD genes in primary cilia. 5 new OFD genes (red), 4 genes previously implicated in other ciliopathies (green), 6 genes previously reported in OFD (2 with presented mutations (blue) and 4 others (white)).

	Patients										
	1	**2**	**3a**	**3b**	**4**	**5**	**6a**	**6b**	**6c**	**7**	**8**
Sex	M	F	F	F	M	M	M	F	M	F	F
Age	29d	6y	9y	9y	4y	12y	25y	22y	17y	17y	10y
Ethnic origin	India	France	Turkey	Turkey	NA	India	India	India	India	Japan	France
Consanguinity	+	+	+	+	+	+	+	+	+	-	-
Cleft/pseudocleft lip	+	+	-	-	-	+	+	+	NA	-	
Cleft palate	-	+	-	-	+	-	-	-	NA	-	+
Abnormal frenulae	+	-	+	+	+	-	+	+	NA	+	+
Tongue abnormalities	Lobulated	Bifid	Hamartoma	Hamartoma	Hamartoma Lobulated Cleft tongue	Hamartoma	-	-	NA	-	Hamartoma, Lobulated
Hypertelorism	-	-	+	+	-	-	-	-	NA	NA	NA
Eye abnormalities	-	Hyper-metropia	Retinopathy	Retinopathy	Retinopathy	-	-	En-ophtalmia	NA	NA	NA
Facial dysmorphism	LSE	PF, MR	PF, LSE	PF, LSE	+	LSE, FB, MR	PF	PF	NA	NA	NA
Hand	PoP, PrP, S	C, B, S	PoP	PoP	PoP	PrP, Y	B, PrP	B, PoP	NA	-	PoP
Foot	PoP, PrP, S	S	PoP	PoP	Broad hallux	P	PoP	PoP, PrP	NA	PrP	PrP, S
Brain malformations	NA	CCA, Vermian agenesis	MTS, Heterotropia Cerebellar hypoplasia	MTS, Poly-microgyria, Heterotropia Cerebellar hypoplasia	MTS, CCA, Subarachnoid cysts, Myelinisation defects	NA	NA	NA	NA	Porencephaly, Arachnoid cysts, Nodular heterotropia, Polymicrogyria MTS, HH	Arachnoid cysts, MTS
Cardiac anomalies	-	+	-	IVC	-	ToF	-	-	NA	-	-
Renal features	NA	-	NA	NA	-	-	-	-	NA	-	-
Skeletal anomalies	-	-	-	-	-	-	Short meso-phalangea	Thoracic deformity	NA	11 pairs of ribs	-
Cutaneous anomalies	NA	Milia, Angioma	-	-	-	-	-	-	NA	-	-
Neurological features	NA	PMD	AO, PMD, ID, Ataxia	AO, PMD, ID, Ataxia	ID	ID	-	-	NA	NA	NA
Others			Hyperpnoea	Hyperpnoea	Absent epiglottis	Micropenis	Short stature	Short stature	Pulmonary infection	Breathing anomaly	NA
OFD subtype	OFDV	OFDVI	OFDVI	OFDVI	OFDXIV	Unclassified	Unclassified	Unclassified	Unclassified	OFDVI	OFDVI

	Patients											
	9	**10**	**11**	**12**	**13**	**14**	**15**	**16a**	**16b**	**17**	**18**	**19**
Sex	M	M	F	F	F	F	F	F	F	F	M	F
Age	Foetus	4y	NA	Foetus	1y	19y	4m	NA	NA	28y	NA	28y
Ethnic origin	France	Luxemburg	Italy	France	France	Austria	France	Turkey	Turkey	France	Spain	NL
Consanguinity	-	-	-	-	-	-	-	-	-	-	-	-
Cleft/pseudocleft lip	+	-	+	-	+	+	-	+	+	-	-	+
Cleft palate	+	-	+	-	-	-	-	-	+	-	-	-
Abnormal frenulae	-	-	-	+	+	-	+	+	-	+	+	+
Tongue abnormalities	-	Hamartoma	Lobulated	Hamartoma Bifid	Lobulated	Lobulated	-	Hamartoma	Hamartoma	Hamartoma	Hamartoma	Lobulated
Hypertelorism	+	+	NA	+	-	-	+	NA	NA	+	-	+
Eye abnormalities	-	-	NA	NA	-	Strabismus	-	NA	NA	-	-	-
Facial dysmorphism	MR	MR, FB	NA	PF	MR, FB	NA	LSE	+	+	+	+	FB,HN
Hand	PoP	PoP	PoP	S	-	PrP, S	PoP	PoP, B	PoP, B	S	PoP, S, C	C
Foot	PoP	S	Bifid hallux	-	PrP, S	PoP, Bifid hallux	PrP	Broad hallux	Broad hallux	-	PrP	S
Brain malformations	Vermian hypoplasia, DWM	NA	MTS	CCA, Vermian anomalies	CCA, MTS	-	-	NA	NA	-	NA	-
Cardiac anomalies	-	NA	NA	-	-	PSD	AVSD	NA	NA	NA	+	NA
Renal features	-	NA	Hydro-nephrosis	+	-	NA	+	NA	NA	-	NA	-
Skeletal anomalies	Hypoplasia 12th pair of rib	NA	NA	11 pairs of ribs	-	-	Radial hypoplasia	NA	NA	-	-	NA
Cutaneous anomalies	-	NA	NA	-	-	NA	NA	NA	NA	-	NA	NA
Neurological features	NA	ID	NA	NA	PMD, ID	-	NA	PMD	PMD	-	PMD	-
Others	NA	-	Breathing anomaly	Pulmonary lobulation defects	Hypotonia	Deafness, PMD, Glottis and larynx hypoplasia, Trachea stenosis	Narrow thorax	NA	NA	NA	Micropenis	-
OFD subtype	Unclassified	Unclassified	OFDVI	OFDI	OFDI	Unclassified	Unclassified	OFDII	OFDII	Unclassified	Unclassified	Unclassified

	Patients											
	20	**21**	**22**	**23**	**24**	**25**	**26a**	**26b**	**27**	**28a**	**28b**	**29**
Sex	F	M	M	F	F	F	F	F	M	F	M	M
Age	7y	8y	1y	36y	22wg	29wg	13y	4y	27wg	12wg	26wg	22wg
Ethnic origin	France	India	France	Mali	Morocco	France	Iraq	Iraq	France	France	France	France
Consanguinity	-	-	-	+	-	-	+	+	-	-	-	-
Cleft/pseudocleft lip	-	+	-	-	+	-	+	+	-	-	-	-
Cleft palate	+	-	-	-	+	-	-	-	-	-	-	-
Abnormal frenulae	-	+	+	NA	+	-	+	+	+	-	-	+
Tongue abnormalities	Hamartoma Lobulated	Hamartoma	Lobulated	NA	-	-	Lobulated Hamartoma	Lobulated Hamartoma Cleft tongue	-	-	-	-
Hypertelorism	-	+	+	NA	+	-	-	-	-	NA	NA	-
Eye abnormalities	Hypermetropia	-	-	NA	-	-	-	-	-	NA	NA	-
Facial dysmorphism	+	FB, LSE, MR	PF, FB, MR, LSE	NA	Little ears	-	+	+	-	NA	NA	+
Hand	C, B	P	PoP, C, B	B, C, S	PoP, S, B, Y	MP	B	B	S	MP	MP	PoP
Foot	-	P	C, P	S	PrP	S	S	S	S	S	S	Broad hallux
Brain malformations	NA	DWM	-	-	CCA, cerebellar hypoplasia	MTS, Hypo-thalamic hamartoma	MTS, Hypo-thalamic hamartoma; CCA, Mega cysterna magna	MTS	MTS, Hypo-thalamic hamartoma	MTS	MTS	CCA, Vermian hypoplasia, Subarachnoïd cysts
Cardiac anomalies	IVC	ToF	-	-	IVC, Ventricular hypoplasia	-	-	-	-	Left ventricular hypoplasia	NA	NA
Renal features	-	-	-	NA	Dysplasic	-	-	-	-	-	NA	Hypoplasia
Skeletal anomalies	-	-	-	Scoliosis	Short femurs	11 pairs of ribs	Cubitus valgus	-	-	-	NA	NA
Cutaneous anomalies	Milia	+	NA	-	-	-	-	-	-	-	NA	NA
Neurological features	NA	Seizures	NA	-	NA	NA	NA	Epilepsy	NA	NA	NA	NA
Others	bifid uvula	Turri-cephalic skull deformity	Ectopic posterior pituitary	Pulmonary malformation Asthma Thyroid nodules Tooth anomalies	Imperforate anus	-	Short stature, Limited supination	Short stature, Microcephaly	-	NA	NA	Microcephaly Micropenis
OFD subtype	Unclassified	Unclassified	Unclassified	Unclassified	Unclassified	OFDVI	OFDVI	OFDVI	OFDVI	OFDVI	OFDVI	OFDXIV

Table S1: Clinical data of all OFD cases with exome analysis (patients 1-24) and the only OFD patients from the replication cohort (patients 25-29) with causal mutations.

NA: Not Available, AO: oculomotor apraxia, AVSD: atrio-ventricular septal defects, B: brachydactyly, C: clinodactyly, CCA: Corpus callosum agenesis, DWM: Dandy-Walker malformation, F: female, FB: frontal bossing, UFP: upslanting palpebral fissures, HH: Hypothalamic hamartoma, HM: hypermetropia, HN: hypoplasia of the alae of nose, ID: Intellectual disability, IVC: Intra-ventricular communication, LSE: low-set ears, M: male, MP: mesoaxial polydactyly, MR: micro/retrognathia, MTS: Molar Tooth Sign, NL: The Netherlands, P: polydactyly, PMD: psychomotor delay, PPo: Polydactyly post-axial, PPr: Pre-axial polydactyly, PSD: primary septal defect, S: syndactyly, ToF: teratology of Fallot, Y: Y-shaped metacarpal.

Article 2

The ciliopathy-associated CPLANE proteins direct basal body recruitment of intraflagellar transport machinery.

Nat Genet. 2016 May 9. doi: 10.1038/ng.3558

M. Toriyama, C. Lee, SP. Taylor, I. Duran, DH. Cohn, AL. Bruel, JM. Tabler, K. Drew, MR. Kelley, S. Kim, TJ. Park, D. Braun, G. Pierquin, A. Biver, K. Wagner, A. Malfroot, I. Panigrahi, B. Franco, HA. Al-lami, Y. Yeung, YJ. Choi, University of Washington Center for Mendelian Genomics, Y. Duffourd, L. Faivre, JB. Rivière, J. Chen, KJ. Liu, EM. Marcotte, F. Hildebrandt, C. Thauvin-Robinet, D. Krakow, PK. Jackson and JB. Wallingford.

Résumé :

Le cil est un organite qui utilise le transport intraflagellaire pour permettre la transduction des signaux. Les ciliopathies résultent d'anomalies des différents complexes protéiques qui affectent la structure ou la fonction du cil. Les mécanismes qui régulent l'assemblage de ces complexes restent peu connus. Dans cette étude, nous avons identifié des mutations dans les gènes *INTU*, *C5orf42* et *WDPCP* chez quatre patients atteints d'un syndrome OFD. En combinant des analyses protéomiques, génétiques et d'imagerie *in vivo* des protéines qui interagissent avec les protéines de la voie de la polarité planaire cellulaire (Inturned, Fuzzy et WDPCP), nous avons identifié et caractérisé le complexe CPLANE. Nous avons montré que CPLANE interagit étroitement avec le complexe IFT-A et est essentiel à son pré-assemblage dans le cytosol à la base du cil. En absence de CPLANE, le transport intraflagellaire est défectueux. De plus, les mutations dans les gènes codants les sous-unités de CPLANE causent des phénotypes typiques de ciliopathies chez les modèles murins et sont associés à des ciliopathies chez l'Homme (détails page 92).

nature genetics

The ciliopathy-associated CPLANE proteins direct basal body recruitment of intraflagellar transport machinery

Michinori Toriyama[1], Chanjae Lee[1], S Paige Taylor[2–4], Ivan Duran[2–4], Daniel H Cohn[5], Ange-Line Bruel[6], Jacqueline M Tabler[1], Kevin Drew[1], Marcus R Kelly[7], Sukyoung Kim[1], Tae Joo Park[1,26], Daniela A Braun[8,9], Ghislaine Pierquin[10], Armand Biver[11], Kerstin Wagner[12], Anne Malfroot[13–15], Inusha Panigrahi[16], Brunella Franco[17,18], Hadeel Adel Al-lami[19], Yvonne Yeung[19], Yeon Ja Choi[20,21], University of Washington Center for Mendelian Genomics[22], Yannis Duffourd[6], Laurence Faivre[6,23,24], Jean-Baptiste Rivière[6,25], Jiang Chen[20,21], Karen J Liu[19], Edward M Marcotte[1], Friedhelm Hildebrandt[8,9], Christel Thauvin-Robinet[6,25], Deborah Krakow[5], Peter K Jackson[7] & John B Wallingford[1]

Cilia use microtubule-based intraflagellar transport (IFT) to organize intercellular signaling. Ciliopathies are a spectrum of human diseases resulting from defects in cilia structure or function. The mechanisms regulating the assembly of ciliary multiprotein complexes and the transport of these complexes to the base of cilia remain largely unknown. Combining proteomics, *in vivo* imaging and genetic analysis of proteins linked to planar cell polarity (Inturned, Fuzzy and Wdpcp), we identified and characterized a new genetic module, which we term CPLANE (ciliogenesis and planar polarity effector), and an extensive associated protein network. CPLANE proteins physically and functionally interact with the poorly understood ciliopathy-associated protein Jbts17 at basal bodies, where they act to recruit a specific subset of IFT-A proteins. In the absence of CPLANE, defective IFT-A particles enter the axoneme and IFT-B trafficking is severely perturbed. Accordingly, mutation of CPLANE genes elicits specific ciliopathy phenotypes in mouse models and is associated with ciliopathies in human patients.

Ciliopathies are a broad class of human diseases that share an etiology of defective cilia structure or function. These diseases span skeletal anomalies, craniofacial defects, cystic kidneys, blindness, obesity and other presentations, highlighting the wide array of physiological functions that require components of the cilium[1,2].

Like all organelles, cilia are assembled and maintained by multiprotein machines. For example, the BBSome is a large complex involved in the trafficking of ciliary membrane proteins[3], the Nphp and Mks–B9 complexes assemble the ciliary transition zone, which controls access to the cilium[4,5], and dynein arms drive motile ciliary beating[6]. Likewise, the IFT system, which links cargos to microtubule motors for transport into and out of cilia, comprises two multiprotein complexes, IFT-A and IFT-B[7–11]. IFT-A and IFT-B are frequently described as controlling retrograde and anterograde traffic, respectively. However, both anterograde kinesin motors and retrograde dynein motors can physically associate with IFT-A[7,12–14], and recent studies highlight the role of IFT-A in ciliary entry and anterograde traffic[15,16]. IFT-A and IFT-B are each composed of a multiprotein 'core' in addition to more loosely bound 'peripheral' components[15,17–19].

Although recent reports have begun to define the interactions between IFT complexes and their cargoes[20,21], substantial questions remain concerning the mechanisms by which IFT proteins are

[1]Department of Molecular Biosciences, University of Texas at Austin, Austin, Texas, USA. [2]Department of Orthopaedic Surgery, David Geffen School of Medicine, University of California, Los Angeles, Los Angeles, California, USA. [3]Department of Human Genetics, David Geffen School of Medicine, University of California, Los Angeles, Los Angeles, California, USA. [4]Department of Obstetrics and Gynecology, David Geffen School of Medicine, University of California, Los Angeles, Los Angeles, California, USA. [5]Department of Molecular, Cell and Developmental Biology, University of California, Los Angeles, Los Angeles, California, USA. [6]EA4271GAD Genetics of Developmental Anomalies, FHU-TRANSLAD, Medecine Faculty, Burgundy University, Dijon, France. [7]Baxter Laboratory, Department of Microbiology and Immunology, Stanford University School of Medicine, Stanford, California, USA. [8]Howard Hughes Medical Institute, Boston Children's Hospital, Harvard Medical School, Boston, Massachusetts, USA. [9]Department of Medicine, Boston Children's Hospital, Harvard Medical School, Boston, Massachusetts, USA. [10]Clinical Genetics Centre, University Hospital Center, Liège, Belgium. [11]Pediatric Unit, Hospital Center, Luxemburg, Luxembourg. [12]Cardiological Pediatric Unit, Hospital Center, Luxemburg, Luxembourg. [13]Clinic of Pediatric Respiratory Diseases, Universitair Ziekenhuis Brussel, Brussels, Belgium. [14]Infectious Diseases, Travel Clinic, Universitair Ziekenhuis Brussel, Brussels, Belgium. [15]Cystic Fibrosis Clinic, Universitair Ziekenhuis Brussel, Brussels, Belgium. [16]Department of Pediatrics Advanced, Pediatric Centre Pigmer, Chandigarh, India. [17]Division of Pediatrics, Department of Medical Translational Sciences, Federico II University of Naples, Naples, Italy. [18]Telethon Institute of Genetics and Medicine (TIGEM), Naples, Italy. [19]Department of Craniofacial and Stem Cell Biology, Dental Institute, King's College London, London, UK. [20]Department of Pathology, Stony Brook University, Stony Brook, New York, USA. [21]Department of Dermatology, Stony Brook University, Stony Brook, New York, USA. [22]A full list of members is available at http://uwcmg.org/#/. [23]Clinical Genetics Centre, FHU-TRANSLAD, Children Hospital, CHU Dijon, Dijon, France. [24]Eastern Referral Centre for Developmental Anomalies and Malformative Syndromes, FHU-TRANSLAD, Children Hospital, CHU Dijon, Dijon, France. [25]Laboratory of Molecular Genetics, FHU-TRANSLAD, PTB, CHU Dijon, Dijon, France. [26]Present address: UNIST, Ulsan, Korea. Correspondence should be addressed to J.B.W. (wallingford@austin.utexas.edu).

Received 9 November 2015; accepted 1 April 2016; published online 9 May 2016; corrected after print 30 May 2016; doi:10.1038/ng.3558

recruited to the base of cilia and assembled into IFT trains. Indeed, ciliopathies can result from defects in cytosolic factors that facilitate dynein arm or BBSome transport and assembly[22–28], yet little is known about similar factors that may act on IFT. For example, basal bodies in *Ttbk2*-mutant mice fail to recruit certain subunits of the IFT-A and IFT-B complexes, but they also fail to remove CP110, a key initial step for ciliogenesis[29]. Likewise, Ofd1, Cep83 (Ccdc41) and C2cd3 are implicated in recruiting certain IFT-B subunits to the basal body, but the specificity of these proteins for IFT recruitment is hard to discern, as only a small subset of IFT proteins have been examined in mutants and these proteins have pleiotropic roles in ciliogenesis[30–32].

Here we combine proteomics, *in vivo* cell biology, mouse models and human genetics to characterize a new mechanism governing basal body recruitment and assembly of IFT-A. This new regulatory module is formed by specific protein–protein interactions among Inturned (Intu), Fuzzy (Fuz) and Wdpcp, well-conserved proteins that control planar cell polarity (PCP) in *Drosophila melanogaster* and govern ciliogenesis in vertebrates[33–37] (**Fig. 1a**). We term this new module CPLANE, for ciliogenesis and planar polarity effectors. We show that this module also includes the poorly understood ciliopathy-associated protein Jbts17, which we show recruits CPLANE to basal bodies where it acts specifically by recruiting the IFT-A peripheral proteins. In the absence of CPLANE function, the IFT-A core denuded of peripheral components still undergoes normal bidirectional transport, but the movement of IFT-B is severely impaired. Finally, examination of mutant mice and ciliopathy-associated alleles from human patients reinforces the connection between CPLANE proteins, Jbts17 and the IFT-A machinery, demonstrating that CPLANE has a broad and essential role in ciliogenesis and human ciliopathies.

RESULTS

The CPLANE interactome

Intu, Fuz and Wdpcp are deeply conserved and are essential for vertebrate ciliogenesis (**Fig. 1a**)[36,37]. To gain unbiased insights into the molecular functions of these proteins, LAP-tagged versions of each mouse protein were stably expressed in ciliated mouse kidney IMCD3 cells, lysates were prepared and interacting proteins were affinity purified (**Supplementary Fig. 1a**,**b**). In addition, similar experiments were performed using diverse IFT-A and ciliopathy-related proteins as baits. Mass spectroscopy showed enrichment of the bait protein in each pulldown (**Supplementary Fig. 1c**,**d** and **Supplementary Data 1**), and none of the baits were copurified with over 30 unrelated control proteins, although all baits did pull down common contaminants (**Supplementary Fig. 1e**). From this experiment, we identified a set of roughly 250 proteins that were individually pulled down by each of the three CPLANE proteins (**Supplementary Fig. 2a**).

We identified an extensive interaction network for the CPLANE proteins that involved a wide array of protein machines, including dynein subunits, clathrin adaptors and chaperonins, among others (**Fig. 1b**, **Supplementary Fig. 2b–d** and **Supplementary Data 2**). Given that CPLANE proteins are essential for vertebrate ciliogenesis[36,37], we were surprised to find only selective links to known ciliogenesis proteins. No links were found within the combined CPLANE interactome to many major ciliary machines, including the IFT-B complex, the BBSome, the inversin compartment and the transition zone B9 complex. An exception was the IFT-A complex, as, between them, pulldowns for Intu, Fuz and Wdpcp identified all six subunits of this complex (**Fig. 1b** and **Supplementary Figs. 1c** and **2c**), although no IFT-B proteins were found. Moreover, although pulldown of the IFT-A proteins themselves also efficiently returned other IFT-A proteins, pulldowns with six other ciliogenesis-related baits did not (**Supplementary Fig. 1d**). These data suggest that CPLANE may regulate IFT-A function, which we address below.

Most strongly enriched in all CPLANE pulldowns were the CPLANE proteins themselves, with Intu, Fuz and Wdpcp reciprocally copurified in all combinations (**Supplementary Figs. 1c** and **2d**, and **Supplementary Data 1**). By contrast, these three proteins were entirely absent from pulldowns of six additional ciliopathy-related proteins (**Supplementary Fig. 1c**). Interaction among some CPLANE proteins has also been observed in high-throughput screens of human proteins[38,39]. Moreover, the interactions are conserved in *Drosophila*[40], although these proteins have no apparent role in ciliogenesis in that animal. In addition, the Rsg1 GTPase, which we had previously observed as a Fuz interacting protein[38,39,41], was also strongly associated with Intu and Wdpcp (**Supplementary Fig. 1c**).

Finally, among the most strongly enriched proteins in the CPLANE interactomes was the largely uncharacterized ciliopathy-associated protein Jbts17 (also called C5orf42) (**Fig. 1b** and **Supplementary Figs. 1c** and **2c**). This protein is associated with Joubert, Oral–Facial–Digital (OFD) and Meckel–Gruber syndromes[42–45], and one recent paper identifies it as a component of the transition zone[46]. We confirmed interaction between Jbts17 and all three CPLANE

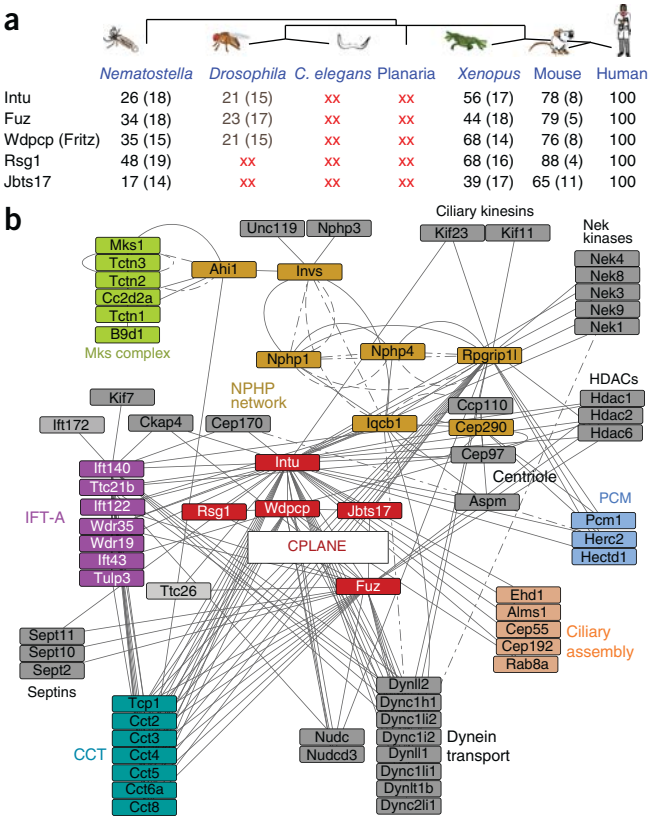

Figure 1 The CPLANE interactome. (**a**) CPLANE proteins are deeply conserved in evolution; numbers indicate percent identity (+ additional percent similarity) to the human protein. "XX" indicates that reciprocal BLAST identified no clear ortholog. (**b**) The extended CPLANE protein network. The results from tandem affinity purification of Intu, Fuz, Wdpcp, IFT-A15 and the published NPHP network[4] were assembled and thresholded for most likely network members; over 2,200 nodes were arranged in Cytoscape (**Supplementary Data 2**), with 78 nodes presented here. Mass spectrometry data will be deposited in ProteomeXchange.

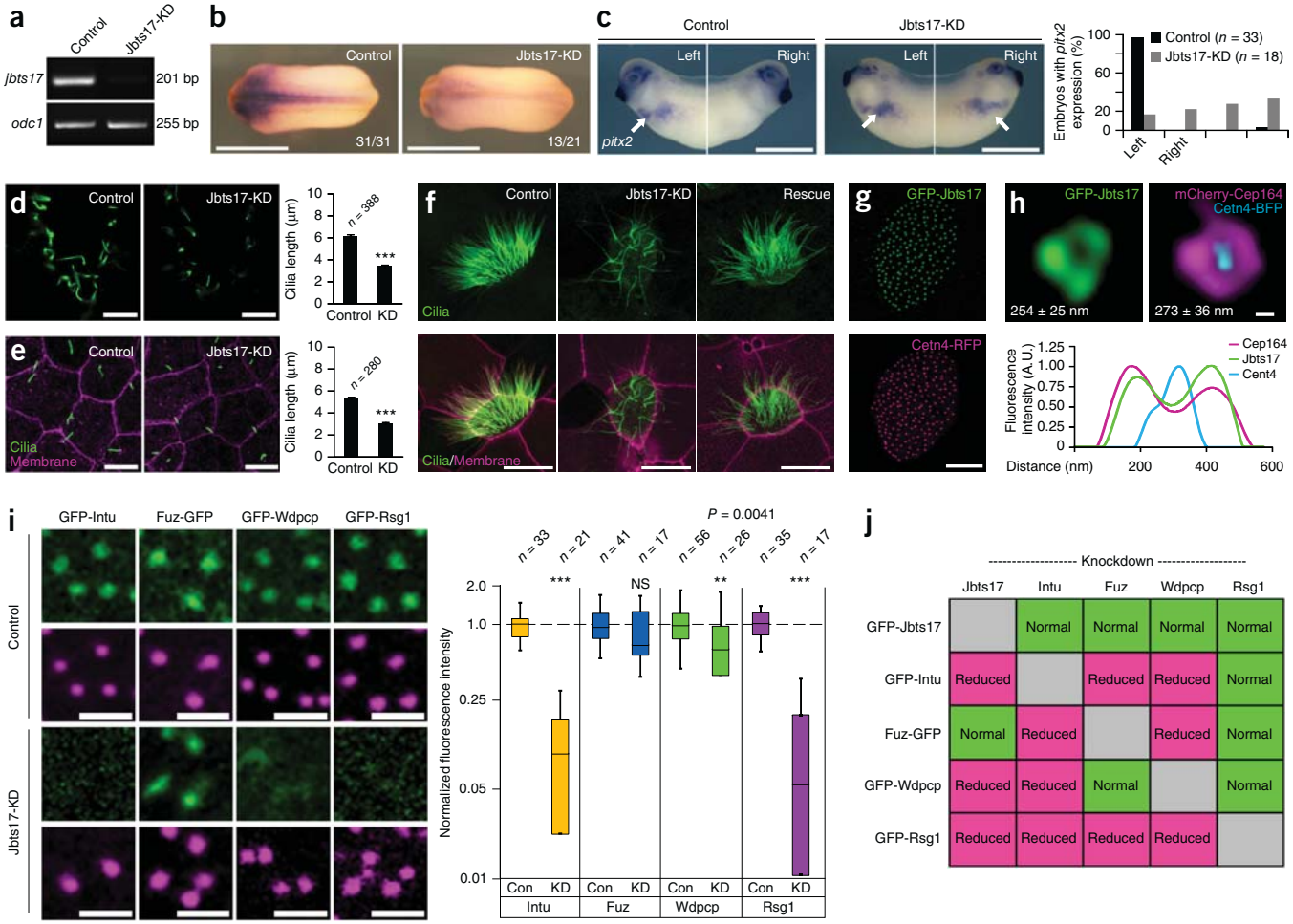

Figure 2 Jbts17 localizes to the base of cilia and is required for ciliogenesis and cilia-mediated patterning. (**a**) RT–PCR demonstrates disrupted *jbts17* splicing after MO injection (Jbts17-KD). *odc1* is the loading control. (**b**) *In situ* hybridization of the Sonic Hedgehog (SHH) direct target *nkx2.2* in control embryos and ones with Jbts17 knockdown (stage 22). Scale bars, 2 mm. Fractions represent the fraction of embryos displaying the phenotype. (**c**) Expression of *pitx2*, which labels the left lateral plate, at stage 26. Arrows indicate signal in left lateral plate mesoderm (LPM); the graph represents *pitx2* expression patterns in embryos. Scale bars, 1 mm. (**d**) Immunostaining for acetylated α-tubulin, which labels cilia, shows ciliogenesis defects after Jbts17 knockdown in the ventral neural tube (stage 22). Scale bars, 10 μm. (**e**) Immunostaining for acetylated α-tubulin shows that Jbts17 knockdown reduces cilia length; cilia numbers are unchanged. Scale bars, 10 μm; membrane-RFP labels membranes. The graphs in **d** and **e** each show pooled data from two independent experiments for cilia length (shown as means ± s.e.m.; $***P < 0.001$). (**f**) MCCs from control embryos, embryos with Jbts17 knockdown showing disrupted cilia, and Jbts17-knockdown embryos rescued with untargeted *jbts17* mRNA labeled by GFP-Cfap20 (green); membrane-RFP labels membranes. Scale bars, 10 μm. (**g**) GFP-tagged Jbts17 localizes near basal bodies (visualized with coexpressed Cetn4-RFP) in an MCC. Scale bar, 10 μm. (**h**) Super-resolution image of GFP-Jbts17 and mCherry-Cep164 at a single basal body; both form rings of ~260 nm in diameter around the basal body, visualized by Cetn4-BFP. Diameters are shown as means ± s.d. in each panel. The graph shows fluorescence intensities (in arbitrary units) for GFP-Jbts17, mCherry-Cep164 and Cetn4-BFP. Scale bar, 100 nm. (**i**) GFP-tagged CPLANE proteins (green) and basal bodies visualized by Cetn4-RFP (magenta) in control and Jbts17-knockdown MCCs. Scale bars, 1 μm. In box plots of CPLANE fluorescence intensities at basal bodies, boxes extend from the 25th to the 75th percentile, with a line at the median; whiskers indicate maximum and minimum values. $**P = 0.0041$, $***P < 0.001$; NS, not significant. Con, control. (**j**) Table summarizing the localization of CPLANE proteins at basal bodies for each knockdown (**Supplementary Fig. 2c–f**).

proteins by coimmunoprecipitation of *in vitro*–translated proteins (**Supplementary Fig. 2e**). Because so little is known about Jbts17, we explored its link to the CPLANE proteins in more detail.

CPLANE protein localization at the base of cilia

Jbts17 is evolutionarily conserved (**Fig. 1a**) and is implicated in varying ciliopathies, but its function remains largely undefined. In *Xenopus laevis*, *jbts17* was expressed in ciliated tissues (data not shown), and knockdown using antisense morpholino oligonucleotides (MOs) to disrupt splicing resulted in ciliopathy-related developmental defects, including failure of neural tube closure, defective Hedgehog signaling and defective left–right patterning (**Fig. 2a–c** and **Supplementary Fig. 3a,b**). Accordingly, ciliogenesis was disrupted in the developing neural tube, in the node and in multiciliated cells (MCCs) (**Fig. 2d–f**). CRISPR-based disruption of *jbts17* also disrupted ciliogenesis, and coinjection with mRNA encoding GFP-Jbts17 rescued both the neural tube and ciliogenesis defects resulting from MO-based knockdown (**Fig. 2f** and **Supplementary Fig. 3a,h**).

Given the physical association of Fuz, Intu and Wdpcp with Jbts17 and Rsg1 (**Supplementary Fig. 1c**), we explored the interrelationships among these proteins in *Xenopus* MCCs, which provide an effective platform for *in vivo* ciliary cell biology. Intu, Fuz, Rsg1 and Jbts17

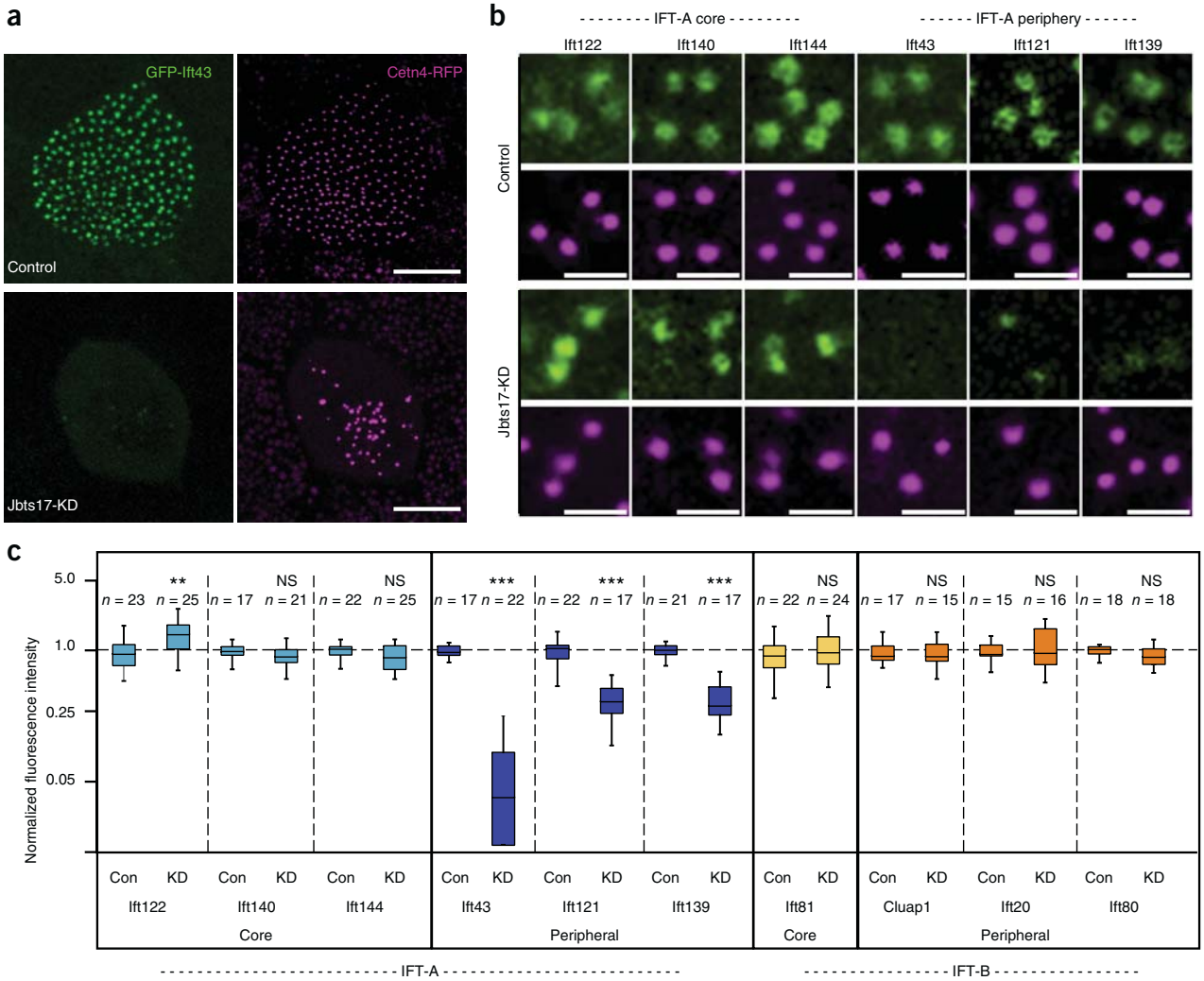

Figure 3 Jbts17 is necessary for recruitment of peripheral IFT-A proteins to basal bodies. (**a**) Ift43 localization at basal bodies in *Xenopus* MCCs, as marked by Cetn4-RFP, is lost in MCCs after Jbts17 knockdown. Scale bars, 10 µm. (**b**) Peripheral IFT-A components are not recruited to Cetn4-RFP-labeled basal bodies after Jbts17 knockdown. IFT-A components are fused to GFP. Scale bars, 1 µm. (**c**) Quantification of IFT protein localization to basal bodies from two independent experiments. Box plots show fluorescence intensities of GFP fusions to indicated IFT proteins normalized against the intensity of Cetn4-RFP (Online Methods). Peripheral IFT-A proteins are specifically lost after Jbts17 knockdown. $^{**}P = 0.0013$, $^{***}P < 0.001$; NS, not significant.

localized robustly around basal bodies but were difficult to detect in axonemes (**Fig. 2g**). Super-resolution imaging showed that GFP-Jbts17 was present in a ring surrounding the basal body, as marked by Centrin 4 (Cetn4)-BFP; this ring was similar to that formed by the distal appendage marker Cep164 (**Fig. 2h**). However, Jbts17 knockdown did not significantly affect recruitment of the distal appendage proteins Cep164 and Ofd1, the transition zone marker Mks1 or the basal body docking protein Hook2 (**Supplementary Fig. 3g**).

To assess the functional relationships of these proteins, we knocked down each CPLANE protein using MOs previously validated by mouse knockout (Online Methods) and then examined basal body localization of the remaining CPLANE components. Our data place Rsg1 at the bottom of the hierarchy: its localization was lost from basal bodies after knockdown of any CPLANE protein, yet its own knockdown did not affect basal body recruitment of any other component (**Fig. 2i,j** and **Supplementary Fig. 3c–f**). Wdpcp and Intu held clear positions upstream of Fuz and Rsg1 but were downstream of Jbts17. Interestingly, Wdpcp and Intu were also each required for the other's basal body localization. The role of Fuz was more complicated: unlike the other CPLANE proteins, Fuz did not require Jbts17 for localization to basal bodies and, although loss of Fuz did disrupt basal body localization of Intu and Rsg1, it did not affect Wdpcp (**Fig. 2i,j**). These data provide an initial framework for the hierarchy of CPLANE protein functions.

A Jbts17 disease variant disrupts Intu localization

JBTS17 (also called *C5orf42*) is mutated in ciliopathies, so we asked whether a disease-causing variant of Jbts17 would disrupt CPLANE function by examining the *Xenopus* cognate of a human Joubert syndrome–associated truncation of Jbts17. The Arg1569* mutant (truncated at the residue equivalent to Arg1602 in humans[45]; **Supplementary Fig. 4a**) failed to localize to basal bodies, whereas another disease-associated truncation mutant (Arg2406*) localized normally, allowing us to map the basal body localization domain of Jbts17 to amino acids 1770–2318 (**Supplementary Fig. 4b**). The pathogenicity of the Arg1569* truncation mutant was apparent: whereas expression of full-length Jbts17 efficiently rescued neural tube defects (NTDs) resulting from Jbts17 knockdown, expression

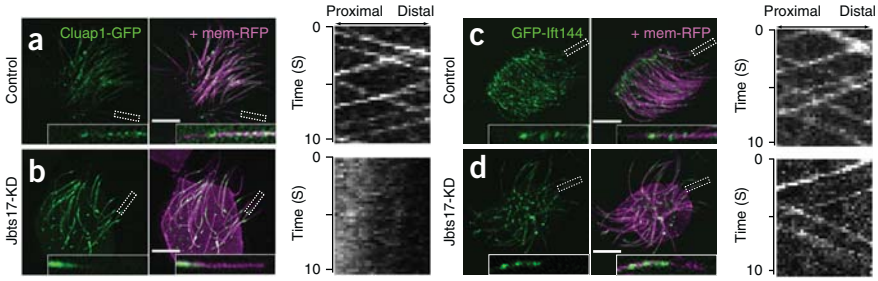

Figure 4 Jbts17 is required for bidirectional axonemal transport of IFT-B particles but not the IFT-A core. (**a**–**d**) Still images from high-speed time-lapse movies of IFT using GFP fusion to IFT proteins (green) and membrane-RFP (magenta). Images are shown for Cluap1-GFP in control (**a**) and Jbts17-morphant (**b**) embryos and for GFP-Ift144 in control (**c**) and Jbts17-morphant (**d**) embryos. Insets show high-magnification views of the localization of IFT particles in a single axoneme in the boxed regions. Scale bars, 10 µm. Associated kymographs representing the movements of IFT particles are shown to the right.

of Jbts17 Arg1569* did not (**Supplementary Fig. 3a**). Linking this embryological defect to cell biological function, Jbts17 Arg1569* also failed to localize to basal bodies (**Supplementary Fig. 4b**), and, unlike wild-type protein, Jbts17 Arg1569* expression could not rescue basal body recruitment of Intu after Jbts17 knockdown (**Supplementary Fig. 4c**). Thus, this Jbts17 disease-associated variant fails to support CPLANE localization and function.

CPLANE recruits peripheral IFT-A proteins to basal bodies

To understand the mechanisms by which CPLANE proteins affect ciliogenesis, we returned to our proteomic data set. We were intrigued by associations between CPLANE proteins and the IFT machinery (**Fig. 1b**) because, although we previously implicated Fuz and Rsg1 in IFT[47,48], their mechanism of action remained ill defined. CPLANE proteins did not interact with IFT-B components but rather specifically interacted with both the IFT-A core and peripheral IFT-A subunits (**Fig. 1b** and **Supplementary Fig. 1c**). Nothing is known about the regulation of peripheral subunit interaction with the IFT-A core, but we reasoned that, by interacting with both, CPLANE could facilitate IFT-A function. Because CPLANE localizes to basal bodies, we tested this notion by assessing basal body recruitment of all six IFT-A proteins after CPLANE disruption.

Strikingly, Jbts17 knockdown specifically disrupted recruitment of the peripheral IFT-A subunits to the basal body. The levels of Ift139, Ift121 and Ift43 at basal bodies were dramatically reduced after Jbts17 knockdown, although recruitment of the three IFT-A core proteins Ift140, Ift144 and Ift122 was not disrupted (**Fig. 3** and **Supplementary Fig. 5a**). In fact, recruitment of Ift122 was consistently increased (**Fig. 3b**,**c**). Although IFT-B is also composed of core and peripheral components, Jbts17 knockdown did not disrupt recruitment of either the peripheral IFT-B proteins Ift20, Ift80 and Cluap1 or the core IFT-B protein Ift81 (**Fig. 3c** and **Supplementary Fig. 5b**). Finally, the link between Jbts17 and IFT-A is likely relevant to disease pathology because, whereas expression of full-length Jbts17 rescued the loss of IFT-A basal body recruitment after Jbts17 knockdown, expression of the Joubert syndrome–associated Jbts17 Arg1569* truncation mutant did not (**Supplementary Fig. 4d**).

Defective IFT-B trafficking in the absence of CPLANE

IFT particles exchange rapidly between axonemes and a cytoplasmic pool around the basal body, so we were curious to know what effect failure to recruit peripheral IFT-A proteins to basal bodies after CPLANE loss would have on IFT trafficking in the axoneme. We used high-speed confocal imaging to assess IFT in MCCs and found that disruption of either Jbts17 or Wdpcp disrupted IFT-B movement, as we previously found with disruption of Fuz[47]. Kymography showed that both peripheral and core components of IFT-B formed stationary accumulations (**Fig. 4a**,**b** and **Supplementary Fig. 5f**), and quantitative microscopy confirmed a significant enrichment of total IFT-B levels in the axoneme ($P = 0.0003$; **Supplementary Fig. 5h**).

These accumulations are reminiscent of the effect of genetic disruption of IFT-A[9,10]. However, the mechanisms by which peripheral IFT-A proteins affect the movement of the IFT-A core have not been examined in detail, and, overall, very little is known yet about the dynamics of IFT-A in vertebrates. We therefore also examined the effect of CPLANE loss on the dynamics of IFT-A peripheral and core proteins in the axoneme. We found that peripheral IFT-A proteins that were not recruited to basal bodies were likewise absent from axonemes after Jbts17 knockdown, consistent with a role for CPLANE in assembly of peripheral subunits onto the IFT-A core (**Supplementary Fig. 5e**).

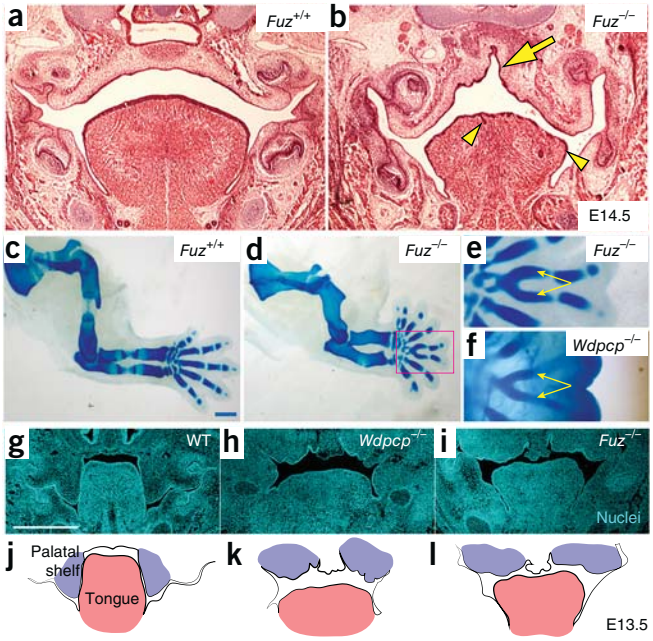

Figure 5 CPLANE-mutant mice display diagnostic features of human OFD6. (**a**,**b**) Frontal sections from wild-type (**a**) and *Fuz*-null (**b**) mice at embryonic day (E) 14.5 show that *Fuz*-mutant mice have high arched palate (arrow) and lobulation of the tongue (arrowheads). Sections were stained with hematoxylin and eosin. (**c**–**e**) Alcian blue staining of E14.5 limbs. *Fuz*-null mice develop polydactyly (the red box in **d** indicates the view shown in **e**). Yellow arrows indicates Y-shaped metacarpals. (**f**) *Wdpcp*-mutant mice develop polydactyly with Y-shaped metacarpals. (**g**–**i**) Frontal sections of E13.5 wild-type (WT) mice (**g**) and *Wdpcp*-mutant (**h**) and *Fuz*-mutant (**i**) embryos. DAPI labels nuclei (cyan). (**j**–**l**) Illustrations highlighting the corresponding palatal condensations (purple) and tongue (pink) in **g**–**i**. Mutant palatal condensations form more medially than do controls and fail to extend into the mouth (see also ref. 50).

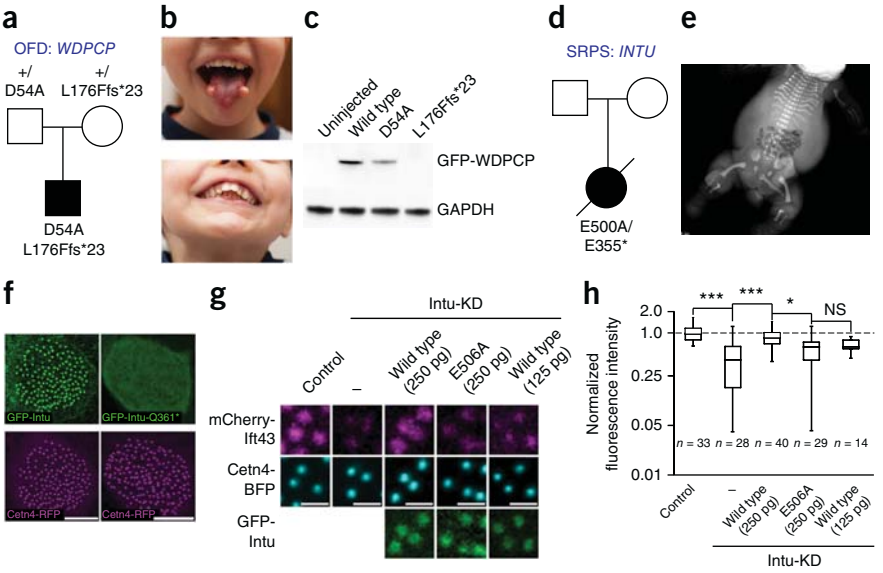

Figure 6 CPLANE gene mutations in human ciliopathies. (**a**) Pedigree showing *WDPCP* mutations in a patient with OFD. (**b**) The patient displays tongue hamartomas and dental anomalies. (**c**) When expressed in *Xenopus* embryos, the allele of human *WDPCP* encoding Asp54Ala produces less protein than the wild-type allele; the allele encoding Leu176Phefs*23 produces no protein. (**d**) Pedigree showing *INTU* mutations in an individual with SRPS. (**e**) X-ray of the affected individual. (**f**) Wild-type *Xenopus* Intu localizes to basal bodies, but the Xenopus cognate of human INTU Glu355* (Gln361*) fails to localize to basal bodies. Scale bars, 10 µm. (**g**,**h**) Expression of *Xenopus* Intu rescues Ift43 localization to basal bodies after Intu knockdown, but the *Xenopus* cognate of human INTU Glu550Ala (*Xenopus* Intu Glu506Ala; see **Supplementary Fig. 6f**) does not. Scale bars, 1 µm. Data shown in **h** are pooled from three independent experiments. $*P < 0.05$, $***P < 0.001$; NS, not significant.

By contrast, IFT-A core proteins were not only present in axonemes at normal levels after Jbts17 knockdown (**Supplementary Fig. 5d**,**h**), but they also underwent bidirectional transport (**Fig. 4c**,**d** and **Supplementary Fig. 5g**), suggesting that the core was intact and could associate with both anterograde and retrograde motors. Similar effects on IFT-A and IFT-B were observed after Wdpcp knockdown (**Supplementary Fig. 5f**,**g**). These data suggest that CPLANE acts by recruiting peripheral IFT-A proteins to the basal body for assembly onto the IFT-A core.

OFD syndrome phenotypes in mouse CPLANE mutants

Together with our proteomic data from mammalian cultured cells, the *in vivo* imaging data from *Xenopus* suggest that Intu, Fuz and Wdpcp are intimately associated with Jbts17, which is encoded by the major gene mutated in human OFD syndrome type 6 (OFD6)[43]. Key diagnostic features of OFD6 include high arched palate, tongue hamartoma and polydactyly characterized by Y-shaped metacarpals[49]. Examining these same features in *Fuz*-null mice, we consistently observed high arched palates, lobulated tongues and Y-shaped metacarpals (**Fig. 5a–e**,**g**,**i**,**j**,**l**) (see also ref. 50). We also observed Y-shaped metacarpals and defects in tongue and palate morphology in *Wdpcp* mutants (**Fig. 5f**,**h**,**k**). These genetic data linking CPLANE components to developmental defects characteristic of OFD are consistent with our proteomic link between CPLANE and Jbts17.

Human CPLANE genes are mutated in diverse ciliopathies

Our data argue for a functional and physical association of CPLANE proteins with Jbts17, on the one hand, and with retrograde IFT machinery, on the other hand. We therefore examined CPLANE gene sequences in the exomes of human patients with ciliopathies, focusing on OFD for its connection to Jbts17 (ref. 43) and on short-rib polydactyly syndrome (SRPS) for its association with IFT-A[51,52].

OFD VI, for which *JBTS17* is the major gene[43], has substantial phenotypic overlap with OFD II, including high arched palate, tongue hamartomas and Y-shaped metacarpals[53,54]. Consistent with our data above, exome sequencing of patients with OFD demonstrating these characteristics identified disease-associated mutations in both *WDPCP* and *INTU*. In one patient, a 5-year-old male presenting with facial dysmorphism, tongue hamartoma, high arched palate, tooth abnormalities and postaxial polydactyly, we found transheterozygous mutations in *WDPCP*. One mutation was a frameshift (c.526_527delTT; p.Leu176Ilefs*21), and the other was a missense mutation (c.160G>A; p.Asp54Asn) predicted to alter splicing by Human Splice Finder and ASSP (**Fig. 6a**,**b** and **Supplementary Table 1**). Sanger sequencing confirmed the variants and compound heterozygosity for *WDPCP* by parental segregation (**Fig. 6a**). The altered aspartic acid residue (Asp54) of WDPCP is highly conserved (**Supplementary Fig. 6a**) and has been associated with atypical OFD in one previous patient[55], but no disease-associated alleles of *WDPCP* have yet been tested functionally. We therefore expressed these proteins in *Xenopus* MCCs and found that the frameshift allele resulted in total loss of protein, whereas the point mutation led to a consistent but more modest defect in protein stability (**Fig. 6c**).

We also examined a 10-year-old male presenting with facial dysmorphisms, tongue nodular tags, high arched palate and bilateral central Y-shaped metacarpals (**Supplementary Fig. 6b** and **Supplementary Table 1**). Exome sequencing identified a homozygous frameshift mutation (c.396delT; p.Asn132Lysfs*11) in the *INTU* gene, and Sanger sequencing confirmed that the homozygous *INTU* variant segregated with the phenotype (**Supplementary Fig. 6c**). Brain magnetic resonance imaging (MRI) for both patients with OFD showed no cerebellar abnormality, but cardiac ultrasound showed aortic coarctation and tetralogy of Fallot in the patients with OFD harboring CPLANE gene mutations (**Supplementary Table 1**), consistent with recent data implicating CPLANE genes in cardiac malformation[56].

In addition, we identified a homozygous missense mutation (encoding p.Ala452Thr) in *INTU* in a child with nephronophthisis and growth retardation. The boy, who presented with end-stage renal failure at 10 years of age, was the only affected child of three in a consanguineous family (**Supplementary Table 1**). The identified allele segregated with affected status, and homozygosity mapping showed that the genomic locus of *INTU* was located within a stretch of homozygosity on chromosome 4 (**Supplementary Fig. 6d** and data not shown). This change affects a relatively poorly conserved residue (**Supplementary Fig. 6e**), suggesting that it may be a hypomorphic allele. We also identified a heterozygous mutation (encoding p.Glu365Gly) in *WDPCP* in a boy with cerebellar vermis hypoplasia, ataxia and retinal dystrophy (**Supplementary Table 1**), which may be a modifying allele contributing to this ciliopathy.

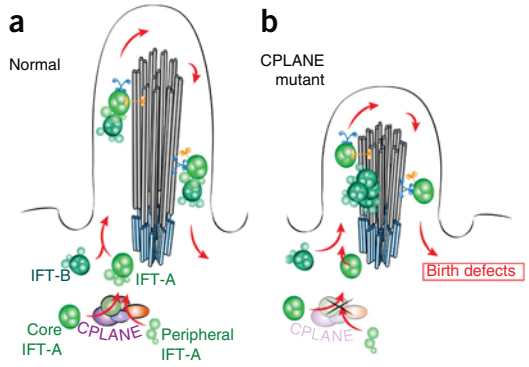

Figure 7 Models for CPLANE function and structure. (**a**) Schematic of normal IFT. Peripheral proteins are assembled onto the IFT-A core in the cytoplasm, and the resulting particles are injected together with IFT-B for bidirectional transport in axonemes. (**b**) In the absence of CPLANE, IFT-A core particles lacking peripheral proteins are injected into axonemes and traffic normally; IFT-B enters axonemes but fails to move in the retrograde direction and accumulates.

Finally, we examined the exomes of individuals with SRPS and identified an affected individual with compound heterozygosity for two *INTU* mutations confirmed by Sanger sequencing (c.1063G>T; p.Glu355* and c.1499A>C; p.Glu500Ala) (**Fig. 6d**,**e** and **Supplementary Fig. 6f**). The affected individual was born preterm at 30 weeks with multiple congenital anomalies, including wide-open fontanel, microphthalmia, tongue hamartomas and tetralogy of Fallot (**Supplementary Table 2**). Radiographic analyses showed multiple skeletal anomalies, including short horizontal ribs, shortened long bones with smooth edges, and pre- and postaxial polydactyly (**Fig. 6e** and **Supplementary Table 2**). To confirm that the identified alleles caused the patient's disease, we examined the function of the INTU mutants. The Glu355* variant failed to localize to basal bodies when expressed in *Xenopus* MCCs (**Fig. 6f**), and, although the p.Glu500Ala alteration did not affect basal body localization, it did significantly impair the ability of the protein to recruit Ift43 (**Fig. 6g**,**h**).

Another case presented with strikingly similar SRPS features (**Supplementary Fig. 6g**,**h** and **Supplementary Table 2**), and a single truncating mutation in *INTU* was confirmed by Sanger sequencing (c.826C>T; p.Gln276*). This change was inherited from the unaffected mother (**Supplementary Fig. 6i**), but, despite extensive analysis, no other changes were found in *INTU*. We examined over 500 changes in the patient's genome that segregated with the disease phenotype, finding only a single change in a gene previously associated with SRPS, a heterozygous change in *WDR35* (encoding IFT121). This change (c.932G>T; p.Trp311Leu) was confirmed by Sanger sequencing and was inherited from the unaffected father (**Supplementary Fig. 6i**); the affected residue is invariant in vertebrates (**Supplementary Fig. 6j**). The clinical presentation of this patient was remarkably similar to that of the individual with compound heterozygosity for *INTU* mutations (**Supplementary Table 2**). The most striking similarity was the distinct polydactyly: whereas most patients with SRPS have 6 or 7 fingers and toes, these two patients both had 9 or 10. Thus, although we cannot rule out a role for mutations in unknown ciliopathy-related genes, the known role for *WDR35* in SRPS, our finding of a role for *INTU* in SRPS, and our finding of physical and functional interactions between IFT-A and CPLANE lead us to suggest that SRPS in this patient results from digenic inheritance of mutations in *WDR35* and *INTU*.

DISCUSSION

Here we characterize an essential but poorly understood protein module, which we term CPLANE (ciliogenesis and planar polarity effector). The CPLANE proteins Intu, Fuz and Wdpcp (Fritz) are deeply conserved in animal evolution (**Fig. 1a**) and were first identified as PCP proteins in *Drosophila*[33–37,40]. In vertebrates, mutation of these genes causes ciliogenesis defects, and, although their role in PCP remains murky, recent reports do suggest that Wdpcp and Intu may govern the localization of core PCP proteins[57–59]. Here we combined proteomics in mammalian cell culture, *in vivo* cell biology in *Xenopus*, and genetic analysis in both mice and humans to demonstrate that CPLANE is an important physical and functional unit governing a specific facet of ciliogenesis, namely the recruitment of IFT-A proteins to the base of cilia and the insertion of complete IFT-A particles into the axoneme (**Fig. 7a**,**b**).

Guided by our proteomic screen, imaging experiments here showed that, in the absence of CPLANE, peripheral IFT-A proteins fail to localize to basal bodies and do not assemble onto the IFT-A core. This connection between CPLANE and IFT-A is strengthened by genetic data linking CPLANE proteins to SRPS, which is generally associated with defects in IFT-A[51,52]. CPLANE does not traffic along axonemes, arguing that it is not a component of the IFT particle itself, a result supported by the fact that CPLANE proteins associate relatively strongly with one another in our proteomic data but comparatively weakly with IFT proteins (**Supplementary Fig. 1c**). Together, these data argue that CPLANE facilitates IFT-A recruitment and assembly at basal bodies, although the precise mechanisms by which it acts remain to be determined.

One possibility is that CPLANE may direct cytoplasmic transport of IFT-A proteins to the base of cilia. This idea is supported by the many links to cytoplasmic dynein machinery in our proteomics data (**Fig. 1** and **Supplementary Fig. 2**). A second line of evidence comes from computational modeling of protein structures (Online Methods), which suggests that CPLANE proteins contain structural domains common in vesicle trafficking machinery (**Supplementary Fig. 7**). Fuz contains a longin domain, and Intu is predicted to fold into a Sec23/Sec24 domain. Likewise, Wdpcp is predicted to form an α solenoid attached to a β propeller, a configuration present in coat proteins, as well as IFT and BBSome subunits[60]. Finally, Jbts17 is an enormous protein (3,167 amino acids) and can be threaded onto multiple protein models, including a Sec23/Sec24 fold, a β-propeller fold and an importin domain.

Another possibility is that the CPLANE proteins may instead influence IFT-A at the level of protein stability and assembly. This possibility is supported by our proteomic data linking Intu, Fuz and Wdpcp individually to all eight subunits of the CCT chaperone complex (**Fig. 1b** and **Supplementary Data 1**). This latter mechanism would be particularly intriguing because similar mechanisms have been proposed linking protein folding to assembly of dynein arms[22,23] and the BBSome[27,28]. Notably, as is true for the CPLANE proteins, disruption of cytosolic assembly factors for dynein arms and the BBSome also cause ciliopathies. This latter possibility is especially exciting because, despite this long history of study, cytosolic factors facilitating basal body recruitment and assembly of IFT particles have not been described.

We also found that peripheral IFT-A proteins were not present in axonemes after CPLANE knockdown, although IFT-A core proteins entered axonemes and trafficked bidirectionally. Because we also observed accumulations of IFT-B in axonemes similar to those found following direct disruption of IFT-A[9–11], our data argue that the peripheral components of IFT-A are essential for association of

IFT-B with IFT-A, at least during retrograde transport (**Fig. 7a**,**b**). This role for the peripheral IFT-A proteins raises interesting questions concerning the mechanism of IFT-B anterograde transport because biochemical data suggest that heterotrimeric kinesin also associates with IFT particles via the IFT-A complex[7,13]. Given that IFT-B moves into axonemes and accumulates there after CPLANE knockdown (**Supplementary Fig. 5c**), it may be that the role for IFT-A peripheral proteins in linking IFT-A to IFT-B is specific to retrograde transport, consistent with the known remodeling of IFT particles upon turnaround[11,12]. Alternatively, homodimeric kinesin 2 associates directly with IFT-B in *Caenorhabditis elegans*, and, although the situation in vertebrates is less clear[61,62], IFT-B could move into cilia after CPLANE knockdown via direct association with the homodimeric Kif17. Finally, the role for diffusion in axonemal transport is only now coming into focus[20,63], so it is at least possible that IFT-B in this case moves in the axoneme in such a manner.

Finally, our data implicate CPLANE in diverse ciliopathies. Because SRPS is generally associated with disruption of IFT-A[51,52], our identification of *INTU* mutations in patients with SRPS provides a genetic complement to our proteomic and cell biological linkage of CPLANE to IFT-A. Our identification of CPLANE gene mutations in patients with OFD similarly parallels the physical and functional association of CPLANE with Jbts17. Additional insights into the mechanism of CPLANE gene mutation in human disease will certainly emerge as we venture deeper into the CPLANE protein interaction network. For example, *WDPCP* mutations have been found in at least one patient with Bardet–Biedl syndrome[36]; thus, the links between CPLANE proteins and CCT are interesting because BBS6, BBS10 and BBS12 also interact with CCT[27,28]. Our data may also shed light on the still murky role of *FUZ* in human neural tube defects[64]. Finally, our data suggest that CPLANE may be relevant not only to congenital defects but also to infectious disease, as recent data link FUZ and the endocytic machinery to alphavirus entry[65], and we observed extensive interactions between CPLANE and the vesicle trafficking machinery (**Fig. 1b** and **Supplementary Fig. 2b**). In sum, our data establish CPLANE as a new ciliogenic protein module with important roles in development and human disease.

URLs. ProteomeXchange, http://www.proteomexchange.org/; Cytoscape, http://www.cytoscape.org/.

METHODS

Methods and any associated references are available in the online version of the paper.

Note: Any Supplementary Information and Source Data files are available in the online version of the paper.

ACKNOWLEDGMENTS

We thank the patients and their families, the IntegraGen society for exome analysis and the NHLBI GO Exome Sequencing Project, which produced and provided exome variant calls for comparison: Lung GO Sequencing Project (HL-102923), WHI Sequencing Project (HL-102924), Broad GO Sequencing Project (HL-102925), Seattle GO Sequencing Project (HL-102926) and Heart GO Sequencing Project (HL-103010). We thank the Biological Resources Center–Ferdinand Cabanne (Dijon, France) for fibroblast centralization and storage. Sequencing was provided by the University of Washington Center for Mendelian Genomics (UW CMG) and was funded by the NHGRI and NHLBI (grant 1U54 HG006493) to D. Nickerson, J. Shendure and M. Bamshad. This work was supported by grants from the following: Uehara Memorial Foundation Fellowship to M.T.; an NIDCR NRSA to J.M.T.; the French Rare Diseases Foundation, the French Ministry of Health (PHRC national 2010-A01014-35 to C.T.-R.) and the Regional Council of Burgundy to C.T.-R.; NIDDK (DK1068306) to F.H., who is a Howard Hughes Medical Institute investigator, a Doris Duke Distinguished Clinical Scientist and the Warren E. Grupe Professor; NIAMS (AR061485) to J.C.; BBSRC (BB/K010492/1) and MRC (MR/L017237/1) to K.J.L.; NIH, NSF, CPRIT and the Welch Foundation (F-1515) to E.M.M.; R01 AR066124, March of Dimes and the Joseph Drown Foundation, NIH/NCATS UCLA CTSI grant UL1TR000124 to D.K.; R01 AR062651 to D.H.C.; NIGMS (GM114276), Baxter Laboratory, the Stanford Department of Research and NIGMS (GM114276) to P.K.J.; and NIGMS (GM104853) and NHLBI (HL117164) to J.B.W., who was a Howard Hughes Medical Institute Early Career Scientist.

AUTHOR CONTRIBUTIONS

M.T. contributed to the design, execution and interpretation of the overall research plan, with special emphasis on all *Xenopus* embryo experiments and *in vitro* binding assays. M.T. also contributed to writing the manuscript. C.L. designed, performed and interpreted live imaging of IFT particles in axonemes and contributed to other imaging experiments in *Xenopus*. K.D. and E.M.M. provided protein structural models. J.M.T., J.C. and K.J.L. contributed to the design, execution and interpretation of mouse genetic data. M.R.K. contributed to the execution and analysis of the proteomic data. S.K. contributed targeted coimmunoprecipitation data that confirmed CPLANE interactions. T.J.P. contributed to *Xenopus* studies. S.P.T., I.D., D.H.C., A.-L.B., D.A.B., G.P., A.B., K.W., A.M., I.P., B.F., H.A.A., Y.Y., Y.J.C., the University of Washington Center for Mendelian Genomics, Y.D., L.F. and J.-B.R. contributed to the collection of human patient and sequencing data. F.H., C.T.-R. and D.K. contributed to the design, execution and interpretation of human genetic data. P.K.J. contributed to coordinating the overall research effort with a focus on the design and interpretation of the proteomic screen and contributed to writing the manuscript. J.B.W. coordinated the overall research effort, oversaw experimental design and interpretation, and wrote the manuscript.

COMPETING FINANCIAL INTERESTS

The authors declare no competing financial interests.

1. Hildebrandt, F., Benzing, T. & Katsanis, N. Ciliopathies. *N. Engl. J. Med.* **364**, 1533–1543 (2011).
2. Oh, E.C. & Katsanis, N. Cilia in vertebrate development and disease. *Development* **139**, 443–448 (2012).
3. Nachury, M.V. *et al.* A core complex of BBS proteins cooperates with the GTPase Rab8 to promote ciliary membrane biogenesis. *Cell* **129**, 1201–1213 (2007).
4. Sang, L. *et al.* Mapping the NPHP–JBTS–MKS protein network reveals ciliopathy disease genes and pathways. *Cell* **145**, 513–528 (2011).
5. Garcia-Gonzalo, F.R. *et al.* A transition zone complex regulates mammalian ciliogenesis and ciliary membrane composition. *Nat. Genet.* **43**, 776–784 (2011).
6. Kobayashi, D. & Takeda, H. Ciliary motility: the components and cytoplasmic preassembly mechanisms of the axonemal dyneins. *Differentiation* **83**, S23–S29 (2012).
7. Cole, D.G. *et al. Chlamydomonas* kinesin-II-dependent intraflagellar transport (IFT): IFT particles contain proteins required for ciliary assembly in *Caenorhabditis elegans* sensory neurons. *J. Cell Biol.* **141**, 993–1008 (1998).
8. Kozminski, K.G., Johnson, K.A., Forscher, P. & Rosenbaum, J.L. A motility in the eukaryotic flagellum unrelated to flagellar beating. *Proc. Natl. Acad. Sci. USA* **90**, 5519–5523 (1993).
9. Pazour, G.J., Wilkerson, C.G. & Witman, G.B. A dynein light chain is essential for the retrograde particle movement of intraflagellar transport (IFT). *J. Cell Biol.* **141**, 979–992 (1998).
10. Piperno, G. *et al.* Distinct mutants of retrograde intraflagellar transport (IFT) share similar morphological and molecular defects. *J. Cell Biol.* **143**, 1591–1601 (1998).
11. Iomini, C., Babaev-Khaimov, V., Sassaroli, M. & Piperno, G. Protein particles in *Chlamydomonas* flagella undergo a transport cycle consisting of four phases. *J. Cell Biol.* **153**, 13–24 (2001).
12. Pedersen, L.B., Geimer, S. & Rosenbaum, J.L. Dissecting the molecular mechanisms of intraflagellar transport in *chlamydomonas*. *Curr. Biol.* **16**, 450–459 (2006).
13. Rompolas, P., Pedersen, L.B., Patel-King, R.S. & King, S.M. *Chlamydomonas* FAP133 is a dynein intermediate chain associated with the retrograde intraflagellar transport motor. *J. Cell Sci.* **120**, 3653–3665 (2007).
14. Ou, G., Blacque, O.E., Snow, J.J., Leroux, M.R. & Scholey, J.M. Functional coordination of intraflagellar transport motors. *Nature* **436**, 583–587 (2005).
15. Mukhopadhyay, S. *et al.* TULP3 bridges the IFT-A complex and membrane phosphoinositides to promote trafficking of G protein–coupled receptors into primary cilia. *Genes Dev.* **24**, 2180–2193 (2010).
16. Liem, K.F. Jr. *et al.* The IFT-A complex regulates Shh signaling through cilia structure and membrane protein trafficking. *J. Cell Biol.* **197**, 789–800 (2012).
17. Behal, R.H. *et al.* Subunit interactions and organization of the *Chlamydomonas reinhardtii* intraflagellar transport complex A proteins. *J. Biol. Chem.* **287**, 11689–11703 (2012).

18. Lucker, B.F. *et al.* Characterization of the intraflagellar transport complex B core: direct interaction of the IFT81 and IFT74/72 subunits. *J. Biol. Chem.* **280**, 27688–27696 (2005).
19. Taschner, M., Bhogaraju, S. & Lorentzen, E. Architecture and function of IFT complex proteins in ciliogenesis. *Differentiation* **83**, S12–S22 (2012).
20. Craft, J.M., Harris, J.A., Hyman, S., Kner, P. & Lechtreck, K.F. Tubulin transport by IFT is upregulated during ciliary growth by a cilium-autonomous mechanism. *J. Cell Biol.* **208**, 223–237 (2015).
21. Bhogaraju, S. *et al.* Molecular basis of tubulin transport within the cilium by IFT74 and IFT81. *Science* **341**, 1009–1012 (2013).
22. Tarkar, A. *et al.* DYX1C1 is required for axonemal dynein assembly and ciliary motility. *Nat. Genet.* **45**, 995–1003 (2013).
23. Omran, H. *et al.* Ktu/PF13 is required for cytoplasmic pre-assembly of axonemal dyneins. *Nature* **456**, 611–616 (2008).
24. Mitchison, H.M. *et al.* Mutations in axonemal dynein assembly factor *DNAAF3* cause primary ciliary dyskinesia. *Nat. Genet.* **44**, 381–389, S1–S2 (2012).
25. Horani, A. *et al.* Whole-exome capture and sequencing identifies *HEATR2* mutation as a cause of primary ciliary dyskinesia. *Am. J. Hum. Genet.* **91**, 685–693 (2012).
26. Diggle, C.P. *et al.* HEATR2 plays a conserved role in assembly of the ciliary motile apparatus. *PLoS Genet.* **10**, e1004577 (2014).
27. Seo, S. *et al.* BBS6, BBS10, and BBS12 form a complex with CCT/TRiC family chaperonins and mediate BBSome assembly. *Proc. Natl. Acad. Sci. USA* **107**, 1488–1493 (2010).
28. Zhang, Q., Yu, D., Seo, S., Stone, E.M. & Sheffield, V.C. Intrinsic protein–protein interaction-mediated and chaperonin-assisted sequential assembly of stable Bardet–Biedl syndrome protein complex, the BBSome. *J. Biol. Chem.* **287**, 20625–20635 (2012).
29. Goetz, S.C., Liem, K.F. Jr. & Anderson, K.V. The spinocerebellar ataxia-associated gene Tau tubulin kinase 2 controls the initiation of ciliogenesis. *Cell* **151**, 847–858 (2012).
30. Ye, X., Zeng, H., Ning, G., Reiter, J.F. & Liu, A. C2cd3 is critical for centriolar distal appendage assembly and ciliary vesicle docking in mammals. *Proc. Natl. Acad. Sci. USA* **111**, 2164–2169 (2014).
31. Singla, V., Romaguera-Ros, M., Garcia-Verdugo, J.M. & Reiter, J.F. *Ofd1*, a human disease gene, regulates the length and distal structure of centrioles. *Dev. Cell* **18**, 410–424 (2010).
32. Joo, K. *et al.* CCDC41 is required for ciliary vesicle docking to the mother centriole. *Proc. Natl. Acad. Sci. USA* **110**, 5987–5992 (2013).
33. Adler, P.N., Charlton, J. & Park, W.J. The *Drosophila* tissue polarity gene *inturned* functions prior to wing hair morphogenesis in the regulation of hair polarity and number. *Genetics* **137**, 829–836 (1994).
34. Collier, S. & Gubb, D. *Drosophila* tissue polarity requires the cell-autonomous activity of the *fuzzy* gene, which encodes a novel transmembrane protein. *Development* **124**, 4029–4037 (1997).
35. Collier, S., Lee, H., Burgess, R. & Adler, P. The WD40 repeat protein fritz links cytoskeletal planar polarity to frizzled subcellular localization in the *Drosophila* epidermis. *Genetics* **169**, 2035–2045 (2005).
36. Kim, S.K. *et al.* Planar cell polarity acts through septins to control collective cell movement and ciliogenesis. *Science* **329**, 1337–1340 (2010).
37. Park, T.J., Haigo, S.L. & Wallingford, J.B. Ciliogenesis defects in embryos lacking inturned or fuzzy function are associated with failure of planar cell polarity and Hedgehog signaling. *Nat. Genet.* **38**, 303–311 (2006).
38. Huttlin, E.L. *et al.* The BioPlex network: a systematic exploration of the human interactome. *Cell* **162**, 425–440 (2015).
39. Rual, J.F. *et al.* Towards a proteome-scale map of the human protein–protein interaction network. *Nature* **437**, 1173–1178 (2005).
40. Wang, Y., Yan, J., Lee, H., Lu, Q. & Adler, P.N. The proteins encoded by the *Drosophila* planar polarity effector genes *inturned*, *fuzzy* and *fritz* interact physically and can re-pattern the accumulation of "upstream" planar cell polarity proteins. *Dev. Biol.* **394**, 156–169 (2014).
41. Gray, R.S. *et al.* The planar cell polarity effector Fuz is essential for targeted membrane trafficking, ciliogenesis and mouse embryonic development. *Nat. Cell Biol.* **11**, 1225–1232 (2009).
42. Alazami, A.M. *et al.* Molecular characterization of Joubert syndrome in Saudi Arabia. *Hum. Mutat.* **33**, 1423–1428 (2012).
43. Lopez, E. *et al. C5orf42* is the major gene responsible for OFD syndrome type VI. *Hum. Genet.* **133**, 367–377 (2014).
44. Shaheen, R. *et al.* Genomic analysis of Meckel–Gruber syndrome in Arabs reveals marked genetic heterogeneity and novel candidate genes. *Eur. J. Hum. Genet.* **21**, 762–768 (2013).
45. Srour, M. *et al.* Mutations in *C5orf42* cause Joubert syndrome in the French Canadian population. *Am. J. Hum. Genet.* **90**, 693–700 (2012).
46. Damerla, R.R. *et al.* Novel *Jbts17* mutant mouse model of Joubert syndrome with cilia transition zone defects and cerebellar and other ciliopathy related anomalies. *Hum. Mol. Genet.* **24**, 3994–4005 (2015).
47. Brooks, E.R. & Wallingford, J.B. Control of vertebrate intraflagellar transport by the planar cell polarity effector Fuz. *J. Cell Biol.* **198**, 37–45 (2012).
48. Brooks, E.R. & Wallingford, J.B. The small GTPase Rsg1 is important for the cytoplasmic localization and axonemal dynamics of intraflagellar transport proteins. *Cilia* **2**, 13 (2013).
49. Gurrieri, F., Franco, B., Toriello, H. & Neri, G. Oral-facial-digital syndromes: review and diagnostic guidelines. *Am. J. Med. Genet. A.* **143A**, 3314–3323 (2007).
50. Tabler, J.M. *et al. Fuz* mutant mice reveal shared mechanisms between ciliopathies and FGF-related syndromes. *Dev. Cell* **25**, 623–635 (2013).
51. Merrill, A.E. *et al.* Ciliary abnormalities due to defects in the retrograde transport protein DYNC2H1 in short-rib polydactyly syndrome. *Am. J. Hum. Genet.* **84**, 542–549 (2009).
52. Mill, P. *et al.* Human and mouse mutations in *WDR35* cause short-rib polydactyly syndromes due to abnormal ciliogenesis. *Am. J. Hum. Genet.* **88**, 508–515 (2011).
53. Hsieh, Y.C. & Hou, J.W. Oral-facial-digital syndrome with Y-shaped fourth metacarpals and endocardial cushion defect. *Am. J. Med. Genet.* **86**, 278–281 (1999).
54. Panigrahi, I., Das, R.R., Kulkarni, K.P. & Marwaha, R.K. Overlapping phenotypes in OFD type II and OFD type VI: report of two cases. *Clin. Dysmorphol.* **22**, 109–114 (2013).
55. Saari, J., Lovell, M.A., Yu, H.C. & Bellus, G.A. Compound heterozygosity for a frame shift mutation and a likely pathogenic sequence variant in the planar cell polarity–ciliogenesis gene *WDPCP* in a girl with polysyndactyly, coarctation of the aorta, and tongue hamartomas. *Am. J. Med. Genet. A.* **167A**, 421–427 (2015).
56. Li, Y. *et al.* Global genetic analysis in mice unveils central role for cilia in congenital heart disease. *Nature* **521**, 520–524 (2015).
57. Cui, C. *et al.* Wdpcp, a PCP protein required for ciliogenesis, regulates directional cell migration and cell polarity by direct modulation of the actin cytoskeleton. *PLoS Biol.* **11**, e1001720 (2013).
58. Butler, M.T. & Wallingford, J.B. Control of vertebrate core planar cell polarity protein localization and dynamics by Prickle 2. *Development* **142**, 3429–3439 (2015).
59. Zilber, Y. *et al.* The PCP effector Fuzzy controls cilial assembly and signaling by recruiting Rab8 and Dishevelled to the primary cilium. *Mol. Biol. Cell* **24**, 555–565 (2013).
60. van Dam, T.J. *et al.* Evolution of modular intraflagellar transport from a coatomer-like progenitor. *Proc. Natl. Acad. Sci. USA* **110**, 6943–6948 (2013).
61. Pan, X. *et al.* Mechanism of transport of IFT particles in *C. elegans* cilia by the concerted action of kinesin-II and OSM-3 motors. *J. Cell Biol.* **174**, 1035–1045 (2006).
62. Snow, J.J. *et al.* Two anterograde intraflagellar transport motors cooperate to build sensory cilia on *C. elegans* neurons. *Nat. Cell Biol.* **6**, 1109–1113 (2004).
63. Harris, J.A., Liu, Y., Yang, P., Kner, P. & Lechtreck, K.F. Single particle imaging reveals IFT-independent transport and accumulation of EB1 in *Chlamydomonas* flagella. *Mol. Biol. Cell* **27**, 295–307 (2016).
64. Seo, J.H. *et al.* Mutations in the planar cell polarity gene, Fuzzy, are associated with neural tube defects in humans. *Hum. Mol. Genet.* **20**, 4324–4333 (2011).
65. Ooi, Y.S., Stiles, K.M., Liu, C.Y., Taylor, G.M. & Kielian, M. Genome-wide RNAi screen identifies novel host proteins required for alphavirus entry. *PLoS Pathog.* **9**, e1003835 (2013).

ONLINE METHODS

Study overview. The methods used in this study were essentially those described previously. Immunoprecipitation of LAP-tagged CPLANE proteins was performed as described[4]. General methods for experiments with *Xenopus* were performed as described[36,37]. Imaging of IFT proteins at basal bodies and time-lapse imaging of IFT were performed as described[47]. Exome sequencing was performed essentially as described[4,43].

Tandem affinity purification and mass spectrometry. To best optimize the LAP purification procedure and minimize the possibility of carryover, we standardized the growth of cells, the preparation of extracts and the method of tandem affinity purification. Briefly, cell lines with stable expression of LAP-tagged proteins were collected using detergent. The mouse IMCD3 renal cell line was obtained from the American Type Culture Collection (CRL-2123). The cell line was authenticated by examining the expression of renal markers (AQP2), polarization, establishment of tight junctions and ciliation, as outlined in ref. 66. Cells tested negative for mycoplasma contaminaiton. Lysates were clarified by centrifugation at 280,000*g* and subjected to immunoprecipitation with an affinity-purified rabbit antibody to GFP produced in house. Bound proteins were eluted from antibody-conjugated beads using TEV protease, recaptured on S-protein agarose (Novagen) and eluted in 4× NuPAGE sample buffer (Invitrogen). Following purification, great care was taken to ensure a lack of contamination from both environmental sources and other purified proteins. Each purified set of interacting proteins was separated on an individual 10% Bis-Tris polyacrylamide gel and stained with Coomassie Brilliant Blue. IMCD3 samples were run on gels for 20–40 mm and divided into 20- to 40-mm × 1-mm slices. Each excised lane was reduced, carboxyamidomethylated and digested with trypsin. Peptide identification of each digestion mixture was performed by microcapillary reverse-phase HPLC nanoelectrospray tandem mass spectrometry (mLC-MS/MS) on an LTQ-Orbitrap Velos or XL mass spectrometer (Thermo Fisher Scientific). The Orbitrap repetitively surveyed a mass/charge (m/z) range from 395 to 1,600, while data-dependent MS/MS spectra on the 20 (Velos) or 10 (XL) most abundant ions in each survey scan were acquired in the linear ion trap. MS/MS spectra were acquired with a relative collision energy of 30%, an isolation width of 2.5 Da and dynamic exclusion of recurring ions for 60 s. Preliminary sequencing of peptides was facilitated with the SEQUEST algorithm with a mass tolerance of 30 ppm against a species-specific (mouse or human) subset of the UniProt Knowledgebase. With a custom version of the Harvard Proteomics Browser Suite (Thermo Fisher Scientific), peptide spectrum matches (PSMs) were accepted with mass error <2.5 ppm and score thresholds to attain an estimated false discovery rate (FDR) of <1% using a reverse-decoy database strategy. For IMCD3 LAP-GFP control samples, peptide identification was performed using NanoAcquity UPLC (Waters Corp.). Samples were analyzed on-line via nanospray ionization into a hybrid LTQ-Orbitrap mass spectrometer (Thermo Scientific). Data were collected in data-dependent mode with the parent ion analyzed in the FTMS and the top eight most abundant ions selected for fragmentation and analysis in the LTQ. Tandem mass spectrometry data were analyzed using the Mascot search algorithm (Matrix Sciences) against the mouse UniProt database (including reverse hits and contaminants) and filtered to a 5% FDR.

Tandem affinity purification and network generation with mass spectrometry data. For individual genes identified in each affinity purification/MS sample, we calculated the normalized spectral abundance factor (NSAF)

$$\mathrm{NSAF} = \frac{P_g / L_g}{\sum_i P_i / L_i}$$

where P_g represents the number of spectral counts mapped to gene g and L_g is the mean length, in residues, of reference protein isoforms derived from that gene. The P/L quotient is normalized to the sum of the P/L quotients for all genes in the data set, excluding those derived from the bait protein and those derived from known exogenous proteins. We excluded, for example, proteins commonly found in skin and enzymes added during sample preparation. Using an unpublished set of eight negative-control data sets, we systematically searched for genes whose score in an experimental data set was highly unlikely. These filtered genes are provided as a Cytoscape network file (**Supplementary Data 2**); a manually curated, simplified subset of these is shown in **Figure 1b**.

***Xenopus* embryo manipulations and microinjections.** Female adult *Xenopus* were induced to ovulation by injection with human chorionic gonadotropin, and eggs were fertilized *in vitro*, dejellied in 3% cysteine (pH 7.9) at the two-cell stage and subsequently reared in 0.3× Marc's modified Ringer's (MMR) solution. For microinjections, embryos were placed in a solution of 2% Ficoll in 0.3× MMR and handled using forceps and an Oxford universal micromanipulator. After injections, embryos were reared for 3 h in 2% Ficoll in 0.3× MMR and then washed and reared in 0.3× MMR until the appropriate stages were reached. All experiments were repeated in multiple embryos from multiple clutches, as is standard in the field. No explicit randomization or blinding strategy was employed. Sex cannot be practically determined for the tadpoles used in these studies. This work was carried out with the approval of the University of Texas Animal Care and Use Committee.

Morpholinos, mRNA and genomic RNA injections. Capped mRNA was synthesized using an mMESSAGE mMACHINE kit (Ambion). mRNA and antisense MOs were injected into two ventral blastomeres or two dorsal blastomeres at the four-cell stage to target the epidermis and neural tissues, respectively[67]. MO sequences and working concentrations are provided in **Supplementary Table 3**.

We note that the *intu*, *fuz* and *wdpcp* MOs used here elicit phenotypes validated by genetic disruption of the corresponding genes in mice[36,37,57,68]. The *rsg1* MO has been validated by disruption of the Rsg1 GTPase by expression of a dominant-negative mutant[41].

Plasmid constructs. Three cDNA fragments encoding *Xenopus* Jbts17 were amplified by PCR from a stage 25 *Xenopus* cDNA library with the primers listed in **Supplementary Table 3**. These three PCR products were then fused to generate full-length cDNA by PCR with SmaI and NotI restriction enzyme sites at 5′ and 3′ ends, respectively. Truncated mutants were generated by PCR. The cDNAs were then subcloned into various pCS107 vectors that established fusion with an EGFP, mRFP or Myc tag at the N terminus of the encoded protein.

Full-length *ofd1*, *cep164*, *hook2*, *mks1*, *ift122*, *ift140*, *ift144*, *ift43*, *ift121*, *ift139*, *ift81*, *ift80* and *cluap1* cDNAs were identified in Xenbase[69], amplified by PCR and subcloned into pCS107 vectors to encode proteins fused with GFP, RFP or mCherry at their N termini. Rsg1, Ift20, Ift43, Cetn4 and Intu constructs were previously described[47,48,70]. GFP-tagged CFAP20 was kindly gifted by B. Mitchell (Northwestern University).

***In vitro* protein translation and pulldown assays.** GFP-tagged Intu, Fuz and Wdpcp and FLAG-tagged Jbts17 (amino acids 907–1569) were synthesized using a TNT SP6 Coupled Wheat Germ Extract System (Promega). After centrifugation at 17,000*g* at 4 °C for 10 min, the synthesized soluble proteins were mixed and incubated in binding buffer (20 mM Tris-HCl, pH 8.0, 1 mM EDTA, 1 mM DTT and 150 mM NaCl) for 2 h at 4 °C. FLAG-tagged Jbts17 protein was precipitated with anti-FLAG M2 magnetic beads (Sigma-Aldrich). The beads were washed with binding buffer containing 0.1% Triton X-100 four times and eluted with 200 ng/ml FLAG peptide in 1× TBS. The eluted proteins were analyzed by immunoblotting with antibody to GFP (Abcam) and anti-FLAG M2 antibody (Sigma-Aldrich) (1:2,000 dilution).

sgRNA synthesis, CRISPR/Cas9-induced genomic editing and genotyping. CRISPR/Cas9-mediated genome editing in *Xenopus* was performed as previously described[71]. Briefly, the amplicon was purified by PCR purification kit (Qiagen) and used as a template for single guide RNA (sgRNA) synthesis. sgRNA was generated using the T7 MEGAscript kit (Ambion) and purified by MEGAclear Transcription Cleanup kit (Ambion). 1.25 ng of Cas9 protein (PNABIO) and 250 pg of sgRNA were injected into the animal pole at the one-cell stage. Genomic DNA was extracted from stage 25 embryos using the DNeasy Blood and Tissue kit (Qiagen) following the manufacturer's protocol, and the 46-bp genomic region that contained the sgRNA target sequence was amplified by PCR. The efficiency of CRISPR/Cas9-mediated genome editing

was examined by T7 endonuclease I (T7EI) assay and NcoI digestion, with fragments analyzed by 2% agarose gel.

Basal body imaging and quantification. Fluorescence images of GFP, RFP or BFP fusion proteins at basal bodies in stage 25–28 MCCs were captured with an LSM700 inverted confocal microscope (Carl Zeiss) with a Plan-APOCHROMAT 63×/1.4 NA oil-immersion objective. The fluorescence intensities of GFP, RFP or BFP fusion proteins at basal bodies in 2-mm slices of apical surface were measured by the three-dimensional object counter plugin of Fiji software as described previously[47,48]. The object size was set to 20, and the threshold was determined empirically to maximize detection of apparent foci. At least 14 basal bodies per cell from at least 12 cells in four independent embryos were analyzed. Statistical analysis was subsequently performed, making use of Student's *t* test.

Live imaging of IFT particles and analysis. For high-speed *in vivo* imaging, *Xenopus* embryos injected with mRNAs encoding GFP-tagged IFT proteins and membrane-RFP were anaesthetized with 0.005% benzocaine at stages 25–28. Images were acquired on a Nikon Eclipse Ti confocal microscope with a 63×/1.4 NA oil-immersion objective. Time-lapse series were captured at 266.5 ms/frame. Kymographs were generated and IFT velocities were measured in Fiji with the kymograph plugin.

Super-resolution microscopy. GFP-Jbts17, mCherry-Cep164 and Cetn4-BFP were coexpressed by mRNA injection of epidermis in stage 27 *Xenopus* embryos. Fluorescence signals were captured on an LSM710/Elyra S.1 microscope (Carl Zeiss) via a 63×/1.3 NA oil-immersion objective. Raw fluorescence images were processed by structured illumination algorithm using Zen software (Carl Zeiss). The arbitrary units of fluorescence intensity for the ring-shaped structures of GFP-Jbts17 and mCherry-Cep164 at basal bodies were measured using the Plot Profile plugin in Fiji software.

Immunostaining. Immunostaining was performed as described[72]. Embryos were fixed in MEMFA for 2 h at room temperature after removing the vitelline envelop and washing with PBST (1× PBS containing 0.05% Triton X-100). Transverse sections of neural tube were generated from stage 22 embryos using a Vibratome series 1000, and the gastrocoel roof plate (GRP) region was manually dissected form stage 17 embryos using forceps. Sections were completely dehydrated in methanol at −20 °C overnight. After rehydration, sections were blocked with 10% FBS in PBST for 60 min and incubated with antibody to acetylated α-tubulin (1:2,000 dilution; clone 6-11B-1, Sigma) diluted in blocking solution. Primary antibody was detected with Alexa Fluor 488–conjugated goat anti-mouse IgG (Invitrogen). Fluorescence images were obtained using a Zeiss LSM700 confocal microscope. Cilia length in the neural tube and GRP was measured in Fiji software.

***In situ* hybridization.** Whole-mount *in situ* hybridization of *Xenopus* embryos was performed as described previously[73] using digoxigenin-labeled RNA probes against *nkx2.2*, *vax1* and *pitx2c*. Bright-field images were captured on a Zeiss Axiozoom V16 stereomicroscope.

RT–PCR. *jbts17* MO was injected into all cells at the four-cell stage, and total RNA was isolated using TRIzol reagent (Invitrogen) from four stage 25 *Xenopus* embryos. The stage 25 cDNA library was synthesized using M-MLV reverse transcriptase (Invitrogen) with random hexamers. *jbts17* and an ornithine decarboxylase 1 (*odc1*) internal control were amplified using Phusion High-Fidelity DNA polymerase (New England BioLabs) with the primers listed in **Supplementary Table 3**. The abundance of the resulting amplicon was analyzed on a 2% agarose gel stained with ethidium bromide under a UV transilluminator.

Protein structure modeling. For fold recognition studies of Fuz, Intu, Wdpcp, Jbts17 and Rsg1, we used HHpred[74] and pGenThreader[75] with default parameters searched against the latest set of Protein Data Bank (PDB) structures. We used the respective Modeller pipelines on the HHpred and pGenThreader servers to build homology models based on high-confidence fold recognition results. The validity of the homology models was checked using automated scores provided by HHpred. Additionally, DaliLite[76] was used to align the homology models with the original template for visual inspection of the fold.

Human subjects. The committees approving work with human subjects included GAD collection DC2011-1332 (C.T.-R.), the institutional review boards of the University of Michigan and Boston Children's Hospital (F.H.), and the Human Subjects Institutional Review Board of the University of California, Los Angeles (D.K.). Informed consent was obtained from all study participants, and consent was obtained for use of all images of human subjects.

66. Giles, R.H., Ajzenberg, H. & Jackson, P.K. 3D spheroid model of mIMCD3 cells for studying ciliopathies and renal epithelial disorders. *Nat. Protoc.* **9**, 2725–2731 (2014).
67. Moody, S.A. & Kline, M.J. Segregation of fate during cleavage of frog (*Xenopus laevis*) blastomeres. *Anat. Embryol. (Berl.)* **182**, 347–362 (1990).
68. Zeng, H., Hoover, A.N. & Liu, A. PCP effector gene *Inturned* is an important regulator of cilia formation and embryonic development in mammals. *Dev. Biol.* **339**, 418–428 (2010).
69. Karpinka, J.B. *et al.* Xenbase, the *Xenopus* model organism database; new virtualized system, data types and genomes. *Nucleic Acids Res.* **43**, D756–D763 (2015).
70. Park, T.J., Mitchell, B.J., Abitua, P.B., Kintner, C. & Wallingford, J.B. Dishevelled controls apical docking and planar polarization of basal bodies in ciliated epithelial cells. *Nat. Genet.* **40**, 871–879 (2008).
71. Nakayama, T. *et al.* Cas9-based genome editing in *Xenopus tropicalis*. *Methods Enzymol.* **546**, 355–375 (2014).
72. Lee, C., Kieserman, E., Gray, R.S., Park, T.J. & Wallingford, J. Whole-mount fluorescence immunocytochemistry on *Xenopus* embryos. *CSH Protoc.* **2008**, pdb.prot4957 (2008).
73. Sive, H.L., Grainger, R.M. & Harland, R.M. *Early Development of Xenopus* laevis: *A Laboratory Manual* (Cold Spring Harbor Press, 2000).
74. Söding, J. Protein homology detection by HMM-HMM comparison. *Bioinformatics* **21**, 951–960 (2005).
75. Lobley, A., Sadowski, M.I. & Jones, D.T. pGenTHREADER and pDomTHREADER: new methods for improved protein fold recognition and superfamily discrimination. *Bioinformatics* **25**, 1761–1767 (2009).
76. Hasegawa, H. & Holm, L. Advances and pitfalls of protein structural alignment. *Curr. Opin. Struct. Biol.* **19**, 341–348 (2009).

Corrigendum: The ciliopathy-associated CPLANE proteins direct basal body recruitment of intraflagellar transport machinery

Michinori Toriyama, Chanjae Lee, S Paige Taylor, Ivan Duran, Daniel H Cohn, Ange-Line Bruel, Jacqueline M Tabler, Kevin Drew, Marcus R Kelly, Sukyoung Kim, Tae Joo Park, Daniela A Braun, Ghislaine Pierquin, Armand Biver, Kerstin Wagner, Anne Malfroot, Inusha Panigrahi, Brunella Franco, Hadeel Adel Al-lami, Yvonne Yeung, Yeon Ja Choi, University of Washington Center for Mendelian Genomics, Yannis Duffourd, Laurence Faivre, Jean-Baptiste Rivière, Jiang Chen, Karen J Liu, Edward M Marcotte, Friedhelm Hildebrandt, Christel Thauvin-Robinet, Deborah Krakow, Peter K Jackson & John B Wallingford
***Nat. Genet.* 48, 648–656 (2016); published online 9 May 2016; corrected after print 30 May 2016**

In the version of this article initially published, the name of author Daniela A. Braun was misspelled. The error has been corrected in the HTML and PDF versions of the article.

Article 3

Autosomal Recessive *IFT57* hypomorphic mutation cause ciliary transport defect in unclassified oral-facial-digital syndrome with short stature and brachymesophalangia. Clin Genet. 2016 Apr 7. doi: 10.1111/cge.12785

J. Thevenon, L. Duplomb, S. Phadke, T. Eguether, M. Avila, V. Carmignac, AL. Bruel, J. St-Onge, Y. Duffourd, GJ. Pazour, B. Franco, T. Attie-Bitach, A. Masurel-Paulet, JB. Rivière, V. Cormier-Daire, L. Faivre and C. Thauvin-Robinet.

Résumé :

Les 13 sous-types de syndromes oro-facio-digitaux (OFD) forment un groupe de ciliopathies très hétérogènes. Les gènes causaux codent pour des protéines centrosomales, de la zone de transition ou impliquées dans les voies de signalisation ciliaires. Une unique famille consanguine présentant un syndrome OFD non classé avec une dysplasie squelettique et une brachymésophalangie, a bénéficié d'un séquençage haut-débit d'exome qui a conduit à l'identification d'une mutation homozygote sur le gène *IFT57*. IFT57 code pour une protéine impliquée dans le transport ciliaire. La mutation entraine un défaut d'épissage à l'origine d'une diminution de l'expression du gène. Le transport intraflagellaire antérograde et la voie de signalisation Sonic HedgeHog sont significativement diminués dans les fibroblastes des patients comparés aux contrôles. Le séquençage Sanger d'IFT57 dans une cohorte de réplication constituée de 13 cas avec OFD et 12 cas avec un syndrome d'Ellis-Van Creveld est négatif. Cette étude rapporte l'implication d'IFT57 en pathologie et la première description d'un défaut du transport ciliaire dans les syndromes OFD. Les résultats sont présentés page 101.

CLINICAL GENETICS An International Journal of Genetics, Molecular and Personalized Medicine

Clin Genet 2016
Printed in Singapore. All rights reserved

CLINICAL GENETICS
doi: 10.1111/cge.12785

Original Article

Autosomal recessive IFT57 hypomorphic mutation cause ciliary transport defect in unclassified oral–facial–digital syndrome with short stature and brachymesophalangia

Thevenon J., Duplomb L., Phadke S., Eguether T., Saunier A., Avila M., Carmignac V., Bruel A.-L., St-Onge J., Duffourd Y., Pazour G.J., Franco B., Attie-Bitach T., Masurel-Paulet A., Rivière J.-B., Cormier-Daire V., Philippe C., Faivre L., Thauvin-Robinet C. Autosomal recessive IFT57 hypomorphic mutation cause ciliary transport defect in unclassified oral–facial–digital syndrome with short stature and brachymesophalangia.
Clin Genet 2016. © John Wiley & Sons A/S. Published by John Wiley & Sons Ltd, 2016

The 13 subtypes of oral–facial–digital syndrome (OFDS) belong to the heterogeneous group of ciliopathies. Disease-causing genes encode for centrosomal proteins, components of the transition zone or proteins implicated in ciliary signaling. A unique consanguineous family presenting with an unclassified OFDS with skeletal dysplasia and brachymesophalangia was explored. Homozygosity mapping and exome sequencing led to the identification of a homozygous mutation in IFT57, which encodes a protein implicated in ciliary transport. The mutation caused splicing anomalies with reduced expression of the wild-type transcript and protein. Both anterograde ciliary transport and sonic hedgehog signaling were significantly decreased in subjects' fibroblasts compared with controls. Sanger sequencing of IFT57 in 13 OFDS subjects and 12 subjects with Ellis–Van Creveld syndrome was negative. This report identifies the implication of IFT57 in human pathology and highlights the first description of a ciliary transport defect in OFDS, extending the genetic heterogeneity of this subgroup of ciliopathies.

Conflict of interest

The authors declare no conflict of interest.

J. Thevenon[a,b,c*], L. Duplomb[a,b*], S. Phadke[d], T. Eguether[e], A. Saunier[f], M. Avila[a,b], V. Carmignac[a,b], A.-L. Bruel[a,b], J. St-Onge[a,b,g], Y. Duffourd[a,b], G.J. Pazour[e], B. Franco[h,i,j], T. Attie-Bitach[k], A. Masurel-Paulet[a,c], J.-B. Rivière[a,b,g], V. Cormier-Daire[k], C. Philippe[f], L. Faivre[a,b,c] and C. Thauvin-Robinet[a,b,c]

[a]FHU-TRANSLAD, Université de Bourgogne/CHU Dijon, Dijon, France, [b]Equipe EA4271 GAD, Université de Bourgogne, Dijon, France, [c]Centre de Référence maladies rares "Anomalies du Développement et syndrome malformatifs" de l'Est et Centre de Génétique, Hôpital d'Enfants, CHU, Dijon, France, [d]Department of Medical Genetics, Sanjay Gandhi Post Graduate Institute of Medical Sciences, Lucknow, India, [e]Program in Molecular Medicine, University of Massachusetts Medical School, Worcester, MA, USA, [f]Laboratoire de Génétique Médicale, CHU – Hopitaux de Brabois, Vandoeuvre les Nancy cedex, France, [g]Laboratoire de Génétique Moléculaire, PTB, CHU Dijon, Dijon, France, [h]Telethon Institute of Genetics and Medicine, Naples, Italy, [i]Medical Genetics, Department of Medical Translational Sciences, University of Napoli Federico II, Naples, Italy, [j]Department of Medical Translational Sciences, Division of Pediatrics, Federico II University of Naples, Naples, Italy, and [k]Service de Génétique, Hôpital Necker-Enfants Malades, APHP, Institut Imagine, INSERM UMR1163, University Sorbonne-Paris-Cité, Paris, France

*These authors contributed equally to the manuscript.

Key words: ciliopathy – exome sequencing – IFT57 – oral–facial–digital syndrome

Corresponding author: Julien Thevenon, MD, PhD, Centre de Génétique, Hôpital d'Enfants, 10Bd du Maréchal de Lattre de Tassigny, 21034 Dijon cedex, France.
Tel.: +33 3 80 29 53 13;
fax: +33 3 80 29 32 66;
e-mail: julien.thevenon@chu-dijon.fr

Received 4 January 2016, revised and accepted for publication 1 April 2016

Oral–facial–digital syndromes (OFDS) are characterized by malformations of the face, oral cavity and extremities (1). Clinically, OFDS may be diagnosed by the presence of: (i) oral anomalies such as tongue hamartomas, oral frenulae, cleft palate, abnormal teething; (ii) facial dysmorphism such as hypertelorism, lateral or medial cleft lip and (iii) digital anomalies such as pre-, meso- or post-axial polydactyly, abnormal Y-shaped metacarpes, or syndactylies. Besides these common features, each sub-type of OFDS bears clinical hallmarks, namely polycystic kidney disease (OFDI), hallux valgus and normal intelligence (OFDII), tibia anomalies (OFDIV), cerebellar hypoplasia with the molar tooth sign (OFDVI) and coloboma (OFDIX) (2). Among the 13 clinical subtypes, inheritance is autosomal recessive in most subtypes except OFDI. While most OFDS are ciliopathies caused by mutated centrosomal proteins (OFD1, SCLT1 and TBC1D32/C6orf170) or components of the transition zone (TMEM216 and TCNT3) (3–6). Mutations in some OFD genes have also been reported in overlapping ciliopathies such as Joubert Syndrome and Related Disorders (JSRD)/Meckel syndrome (OFD1, C5orf42, TMEM216 and TCNT3) (6–8).

Clinical entities secondary to mutations in genes encoding for proteins implicated in ciliary transport are represented by the short-rib polydactyly syndromes (SRPS), which includes at least six distinct entities (9). Among these, Ellis–Van Creveld syndrome (EVCS) is distinct from the others by the presence of post-axial polydactyly, congenital cardiac defects, mesomelic limb shortening, short ribs, dysplastic nails and teeth, and labio-gingival adhesion (9). In 1999, Phadke et al. reported a unique consanguineous family with three affected siblings presenting with clinical features overlapping between OFDS and EVCS (10). This family was re-assessed and the causal gene mutation of this untyped OFD syndrome was identified by homozygosity mapping and exome analysis.

Methods

Homozygosity mapping and exome sequencing

Two affected siblings (Subject II-1 and II-2, Fig. 1a) were genotyped with an Affymetrix 250 K NspI array (Affymetrix, Santa Clara, CA). Array experiments and analysis were conducted according to protocols from the manufacturer and with Homozygosity Mapper, respectively (www.homozygositymapper.org). Homozygous stretches of more than 1 megabase with quality over 250 were selected (arbitrary unit from homozygosity mapper software). Exome sequencing was performed on Subject II-1 (Fig. 1a) according to standard procedures using the Nimblegen SeqCap EZ Exome v2.0 kit, from 8 µg of DNA sample from affected individuals and both parents. The resulting exome-capture libraries underwent 2×100-bp paired-end sequencing on an Illumina HiSeq 2000. Reads were aligned to the human reference genome (GRCh37/hg19) with the Burrows–Wheeler Aligner (BWA, v0.5.6) (11) and potential duplicate paired-end reads were removed using the picardtools v1.22 (www.picard.sourceforge.net). The Genome Analysis Toolkit (GATK) 1.0.57 was used for base quality score recalibration and indel realignment (12), as well as for single-nucleotide variant and indel discovery and genotyping using standard hard filtering parameters. Variants with quality scores of <30, sequencing depth of <4, quality/depth ratio of <5.0, length of homopolymer run of >5.0 and strand bias of ≥0.10 were flagged and excluded from subsequent analyses. Coverage was assessed with the GATK Depth of Coverage tool by ignoring reads with mapping quality of <20 and bases with base quality of <30. All variants identified in the affected individuals were annotated with SeattleSeq SNP annotation (University of Burgundy Centre de Calcul, https://haydn2005.u-bourgogne.fr/dsi-ccub/Seattle; Seq Annotation tool: snp.gs.washington.edu/SeattleSeq Annotation137/). Candidate variants were selected by fulfilling the following criteria: (i) variants included in the previously identified homozygous intervals (defined with allele balance from 75 to 100% of the

Fig. 1. Clinical features of the subjects with unclassified oral–facial–digital syndrome (OFDS). (**a**) Family tree with the three affected cases. (**b**, **c**) Pictures and X-ray (respectively of subjects II-1 and II-2) showing the clinical hallmarks overlapping OFD (median pseudo cleft of upper lip, oral frenulae, pre- and post-polysyndactyly) and Ellis–Van Creveld syndrome (EVCS) (missing incisors, short stature with mesomelic limb shortening). Skeleton features included additional brachymesophalangia, stocky femoral necks, and vertebral notches. Brain magnetic resonance imaging (MRI) was normal.

reads supporting the variant); (ii) variants affecting in the coding sequence; (iii) rare variants, absent from 50 local exomes of unaffected individuals and present at a frequency below 1% in dbSNP (http://www.ncbi.nlm.nih.gov/projects/SNP/) 138 and the NHLBI GO Exome Sequencing Project (http://evs.gs.washington.edu/EVS/).

Sanger sequencing in the replicative cohort

IFT57 primers were designed on the RefSeq NM_018010 (Table S1, Supporting Information). Polymerase chain reaction (PCR) fragments were purified with the multiscreen Vacuum Manifold system (Millipore, Billerica, Ma, USA). Sequencing was performed with the ABI BigDye Terminator Cycle Sequencing kit (v.3.1) (Applied Biosystems, Foster City, CA, USA) in ABI 3130 sequencer 7 (Applied Biosystems) according to the manufacturer's instructions. Sequence data were analyzed with SeqScape v.2.7 (Applied Biosystems).

Cell culture

Fibroblasts from healthy controls and the IFT57 mutated subject (Subject II-1, Fig. 1a) were obtained after written consent for skin biopsy. Cells were cultured in Dulbecco's Modified Eagle Medium (DMEM) supplemented with 10% fetal calf serum (FCS) and 1% penicillin/streptomycin (P/S) and were grown at 37 °C in a 5% CO_2 atmosphere. For cilium induction, cells were FCS-starved for 48 h before subsequent analysis. For studies of the sonic hedgehog (SHH) pathway, cells were FCS-starved overnight, then stimulated with 1 µM Smoothened Agonist (SAG) (Merck Millipore, Darmstadt, Germany) for 30 h (6).

ARN extraction and real-time RT-quantitative polymeras chain reaction (qPCR)

Total RNA was extracted using TRI reagent® (Sigma, Saint Quentin Fallavier, France), according to the manufacturer's protocol. First strand cDNA was synthesized from 0.5 µg total RNA using Maxima First Strand cDNA Synthesis Kit for RT-qPCR from Fermentas (Thermo Scientific). The real-time PCR contained, in a final volume of 20 µl, 2 ng reverse transcribed total RNA, SYBR green buffer (Bio-Rad, Marnes-la-Coquette, France), 300 nM of the forward and reverse primers: and (Bio-Rad). PCRs were performed in triplicate in 96-well plates, using the CFX96 Real-Time PCR detection system (Bio-Rad, Hercules, CA, USA). Human glyceraldehyde 3-phosphate dehydrogenase (GAPDH) was used as an invariant control (Table S1).

Analysis of the IFT57 transcripts by RT-PCR and Sanger sequencing

Total RNAs from cultured fibroblast with the Kit QIAmp RNA Blood Mini kit (Qiagen, Hilden, Germany). RNA quality (RNA Integrity Number >9) was assessed with the Agilent 2100 Bioanalyzer. For inhibition of the nonsense mediated mRNA decay (NMD) pathway, fibroblast cells were grown for 12 h in DMEM GlutaMAX media (Gibco, ThermoFisher scientific, Waltham, Ma, USA) supplemented with 10% calf serum, in the presence of 200 µg/ml puromycin (SIGMA-Aldrich) and then harvested in lysis buffer prior to RNA extraction. Prior to RT-PCR, RNAs were treated with DNase I (Sigma-Aldrich) at room temperature for 15 min, DNase I was inactivated at 70 °C for 10 min. RT-PCR was performed on total RNAs from fibroblasts with primers located in exon 2 (Forward 5′ TGATGACCCTAATGCAACAATATCT 3′) and exon 11 (Reverse 5′ GCCAATTCTAATGTCCATCTCTACA

3′) (NM_018010.3) with the QIAGEN OneStep kit. RT-PCR products were separated on 2% agarose gel and bidirectionally sequenced.

Ciliary transport

α-Acetylated tubulin antibody was purchased from (Invitrogen, Thermo Scientific, France), IFT57 antibodies were generated in rabbit (13). Cells were washed in PBS and fixed in 4% PFA for 20 min, incubated in NH_4Cl 50 mM for 10 min, permeabilized in PBS/0.3% Triton for 7 min and blocked in PBS/0.1% Tween 20/3% BSA for 15 min. Incubations with primary antibodies were performed in PBS/0.1% Tween 20/3% BSA for 3 h at room temperature. After three washes in PBS, incubations with appropriate secondary (Alexa-Fluor-488- and Alexa-Fluor-588-conjugated goat anti-mouse and goat anti-rabbit) were performed for 1 h at room temperature. After three washes, cells were mounted with Fluorshield™ with 4′,6′-diamidino-2-phénylindole (DAPI) (Sigma).

RNA interference

Small interference RNAs (siRNA) against IFT57 and negative control siRNA (both siGENOME SMARTpool, sequences available on request) were purchased from ABgene Ltd. (Thermo Scientific). Transfection of siRNA was obtained using Lipofectamine™ RNAiMAX reagent (Invitrogen, Carlsbad, CA, USA) according to the manufacturer's protocol. Briefly, 0.1×106 fibroblasts from healthy controls were seeded in 2 ml of DMEM containing 1% P/S and 10% FCS. After 24 h, cells were FCS-starved and siRNA (100 pmol)/lipofectamine™ RNAiMAX (5 µl) complexes (in 500 µl Opti-MEM® Medium) were added to the cells. The next day, SAG (1 µM) was added for 30 h. The efficiency of siRNA delivery against IFT57 was confirmed by RT-qPCR. IFT57 mRNA expression was decreased by 95% ($n = 3$, data not shown).

Subjects and results

Subjects

Index family

The reported subjects born to healthy consanguineous parents (Fig. 1a) were first published during childhood (10) and followed up for 15 years. Subject II-3 died at 17 years of age because of a complicated pulmonary infection.

Subject II-1 was interviewed at 25 years of age. Intelligence was normal. He had short stature with a final height of 155 cm (−3 SD), weight 45 kg (≤3 SD) and occipito-frontal circumference (OFC) 50 cm (mean). The clinical examination showed a square face with short forehead, upslanting palpebral fissures, high nasal bridge with pyriform nose above a short philtrum and a medial clefting of upper lip (Fig. 1b). Oral anomalies included supernumerary frenulae and missing incisors. Digital anomalies included pronounced brachydactyly, upper-limb post-axial polydactyly. Lower limb extremities showed spacing between the first and second rays. There was no thoracic deformity. X-rays of the hands and feet showed severe mesophalangeal shortening. Pre-axial polydactyly was diagnosed, because of first metatarsal duplication. Bone studies showed bilateral short femoral necks with varus femurs, symmetric genu valgus and no vertebral anomalies. Heart, renal and abdominal ultrasound examinations were normal.

Subject II-2 was interviewed at 22 years of age. Intelligence was normal; she was married with no children. She had short stature with a final height of 122 cm (−5 SD), weight 37 kg (−2 SD) and a conserved OFC at 51 cm (mean). Clinical examination showed a square face with narrow forehead, enophtalmia with up-slanting palpebral fissures, broad nasal bridge. Facial features included bilateral hypopigmented pseudo-clefts associated with medial labial clefting and oral anomalies such as missing incisors and supernumerary frenulae (Fig. 1c). Digital anomalies included marked brachydactyly, four-limb post-axial polydactyly, surgically removed during infancy. There was neither thoracic deformity nor dolichostenomelia. Puberty was not delayed. Hand X-rays revealed mesophalangeal shortening and residual right hand post-axial polydactyly with fused proximal phalanges and bifid telephalanges. Foot X-rays revealed duplication of the first-ray metatarsus and absent intermediary phalanges, suggesting lower limb pre-axial polydactyly. Abnormal vertebral bodies with medial notches but no platyspondyly, bilateral cervical ribs without narrow thorax were also present. Long bones were gracile with shortened femoral neck. Brain magnetic resonance imgaging (MRI), abdominal and heart ultrasounds were normal.

Replication cohort

A replication cohort was collected: (i) 13 subjects with OFDS selected from a franco-italian cohort. Inclusion criteria were the association of polydactyly and cleft lip/palate; (ii) 12 subjects with EVCS negative for EVC1 and EVC2 screening; (iii) next-generation sequencing data of the exome or ciliome from more than 172 subjects with various ciliopathy phenotypes were consulted (6).

Genetic analysis and mutation characterization

Considering the parental consanguinity, homozygosity regions were screened using homozygosity mapping in subjects 1 and 2. This approach identified 11-megabase of shared runs of homozygosity spreading from chr3:104822019–111671862 and chr10:1372501–6029726 (Hg19) (Fig. 2a). These homozygous intervals did not overlap with genes previously associated with a recessive ciliopathy.

Exome sequencing was performed on subject 2. Over 4.7 gigabases of mappable sequences were generated by exome sequencing, resulting in a depth of coverage of at least 10 reads for 95% of RefSeq coding exons (Table S2). First, causative variants affecting genes

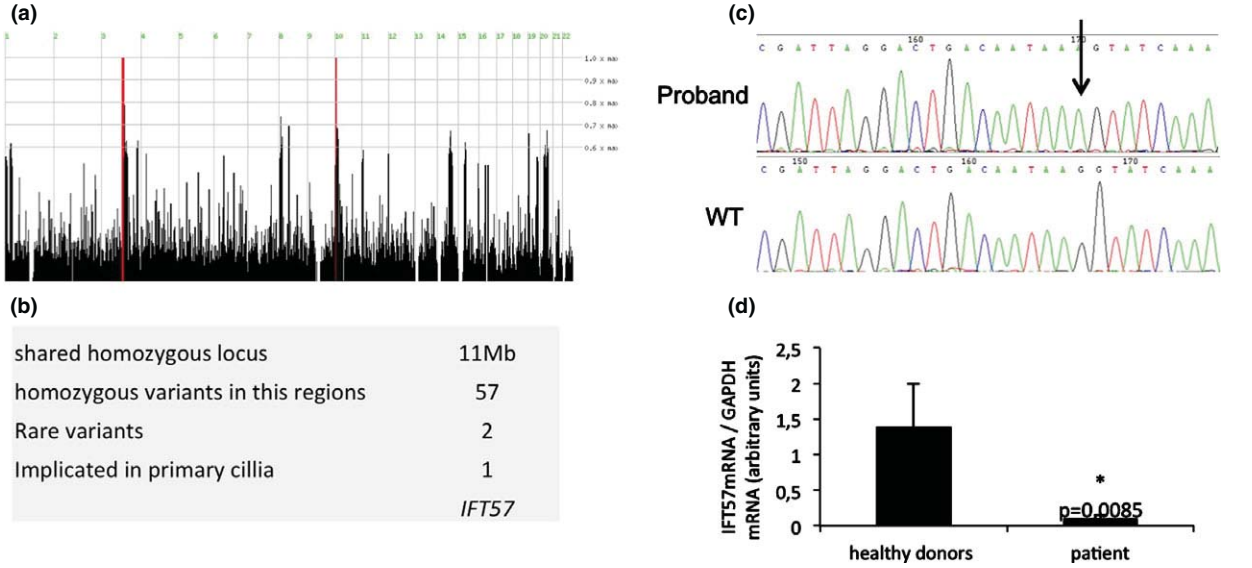

Fig. 2. Evidence of the pathogenicity of the IFT57 homozygous p.Lys259Lys mutation. (**a**) Homozygosity mapping in subjects 2 and 3 identifying two shared homozygous runs on chromosome 3 and 10, totaling 11 megabases. (**b**) Whole-exome sequencing for Subject 1, interpretation and variant prioritization focused on variants included in the homozygous regions. (**c**) Sanger sequencing confirmed the familial segregation of the IFT57 variant in the three affected sibs. (**d**) IFT57 cDNA was quantified in cultured fibroblasts, demonstrating a lower quantity of mRNA in the case than in multiple controls.

previously implicated in OFDS and EVCS syndromes were searched. Then, exome data analysis focused on the two homozygosity regions identified by homozygosity mapping in subjects 1 and 2. This strategy allowed the identification of 32 homozygous variants, and among these, 5 variants that affected the coding sequence (Table S2). Extended familial segregation with Sanger sequencing in subject 3 excluded one of the two homozygous interval [i.e. a AKR1C3 missense variation (chr10: 5147835 C/A, p.Leu298Ileu) was found heterozygous in Subject 3]. In the remaining interval, only 1 homozygous variation was represented at a frequency lower than 1 of 100 in ESP, namely an IFT57 synonymous variation (chr3:g.107910368C > T, c.777G > A, p.Lys259Lys, RefSeq accession number NM_018010.3). This variant was absent from the ExAC database [Exome Aggregation Consortium (ExAC), Cambridge, MA (URL: http://exac.broadinstitute.org) (February 2016 accessed)]. Sanger sequencing confirmed the variation at a homozygous status in the three affected subjects. Considering the underrepresentation of Indian subjects in public databases of genomic variants, absence of the rare variants was verified in 50 healthy subjects from northern India. At least, IFT57 was considered for further analysis in this family (Fig. 2c). The c.777G>A substitution affecting the last base of exon 6 induces a complex splicing pattern including the normal transcript (A) but also three pathological mRNAs resulting from exon(s) skipping (B, C, and D). The pathological transcripts are only detected after inhibition of the NMD pathway. As expecting with sequence variation affecting consensus splice sites, the c.777G>A mutation leads to exon 6 skipping. More unusually, this variation in exon 6 has a bearing on retention of exons 5 and 4 of IFT57 in fibroblasts. Skipping of exon 6 in IFT57 pre-mRNA might induces modifications of the RNA secondary structure with a cis-acting effect on inclusion of adjacent exons 4 and 5.

Sanger sequencing for the 11 coding exon and intron boundaries of IFT57 was performed on 25 OFDS and EVCS subjects. No causative mutation was identified. Exome or ciliome data from 172 subjects with various ciliopathy phenotypes did not identify any biallelic causative mutations.

Ciliary transport

Because the variant in IFT57 was predicted to alter splicing, we performed cDNA quantification. RNA isolated from the subject's fibroblasts had significantly less IFT57 mRNA than did that of controls (Fig. 2d). This suggests that the mutation causes a partial splicing defect resulting in the degradation of the altered cDNA so that only a residual amount of the normal mRNA remains. We then determined whether the remaining wild-type IFT57 was sufficient for proper ciliary assembly. Fibroblasts from the subject and controls were stained for IFT57 and for cilia using an antibody against acetylated tubulin. Primary cilia number and length in fibroblasts from the subject with the IFT57 mutation were similar to those in controls (Fig. 3a, b). However, significant differences were observed between the subject and controls for intraflagellar transport. In control fibroblasts, IFT57 staining was observed in the whole primary cilium, merging with the staining of α-acetylated tubulin (Fig. 3a, b). In the subject's fibroblasts, staining of the ciliary tip with IFT57 was significantly decreased (90 *vs* 35%; $p < 0.001$) while staining of the basal body of the primary cilium was significantly increased ($p < 0.01$).

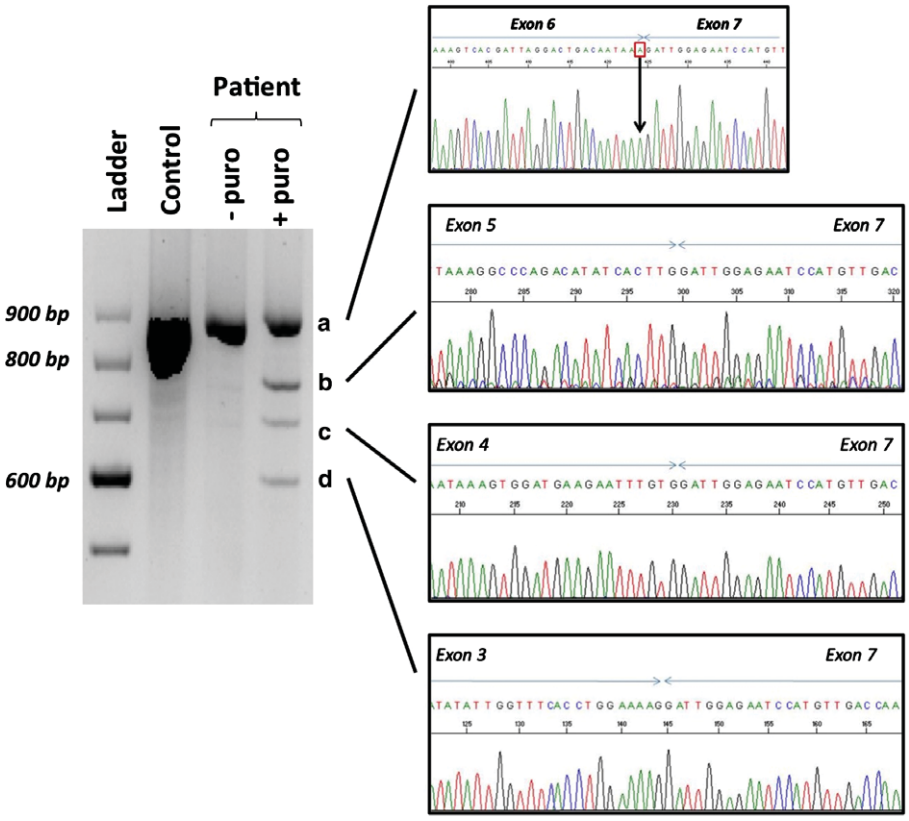

Fig. 3. The synonymous c.777G>A substitution in exon 6 affects IFT57 pre-mRNA splicing. (**a**) Exon 6 is present in the normal transcripts. The G>A substitution identified at the genomic level is detected in all IFT57 normal mRNAs. (**b**) In frame exon 6 skipping. (**c**) In frame skipping of exons 5 and 6. (**d**) Out of frame skipping of exons 4, 5 and 6. Legend: − puro: no puromycin treatment, + puro: puromycine treatment.

SHH pathway activation

Because ciliary assembly was not affected by the IFT57 mutation, we wondered whether ciliary transport defect altered SHH signaling. Stimulation of the SHH pathway by SAG showed poor induction of Gli1 mRNA expression in fibroblasts from the IFT57-mutated subject compared with control fibroblasts (Fig. 3c). This indicates that although ciliary assembly is normal in these cells the reduction in IFT57 causes dysfunctional SHH signaling. To confirm this result, IFT57 mRNA expression was knocked down in control fibroblasts using siRNA technology, with an efficiency of 95% (data not shown). A 3.7-fold increase in GLI1 transcript expression was observed in siRNA control-transfected cells after 30 h in the presence of SAG (Fig. 3c) whereas no induction of Gli1 mRNA expression was observed in siRNA IFT57-transfected cells.

Discussion

Here, we report on a unique consanguineous family with an unclassified type of OFDS with short stature and brachymesophalangia overlapping with EVCS, and caused by a homozygous hypomorphic mutation of IFT57, affecting splicing and altering protein function.

The family was first published as a new overlapping OFDS-EVCS phenotype based on the association of median clefting, oral frenulae, missing incisors, short stature with mesomelic shortening, and pre and post-axial polysyndactyly (10). When reviewed, the clinical evaluation was in favor of an unclassified OFDS type associated with skeletal dysplasia rather than EVCS (Fig. 1b, c). Indeed, the reported subjects did not present rib shortening or thorax narrowness/deformity, but displayed a short stature, brachymesophalangia and stocky femoral necks, which suggests a new OFDS subtype with skeletal dysplasia. OFDII could first be suspected because of hallux valgus and normal intelligence, but short stature was atypical. Thus, an unclassified type of OFDS was evoked, once more underlying the clinical and genetic heterogeneity of OFDS (Fig. 4).

IFT57 was first reported as HIPPI (Huntingtin-Interacting-protein Hip1), a gene coding for a caspase activator in adult neurons, implicated in neuronal death in Huntington disease (14). However, further analysis indicated that IFT57 is a subunit of intraflagellar transport complex B (15). IFT complex B is composed of 16 proteins (16), and in mice, null mutations in components of this complex typically alter ciliary assembly, provoke ciliary transport defect, inappropriate Sonic Hedgehog (SHH) signaling and cause lethality at mid gestation (17). Consistently, null mutations in mouse Ift57 blocked ciliary assembly in the node. The affected embryos died during embryogenesis and showed ciliopathy features such as upper and lower limb polydactyly,

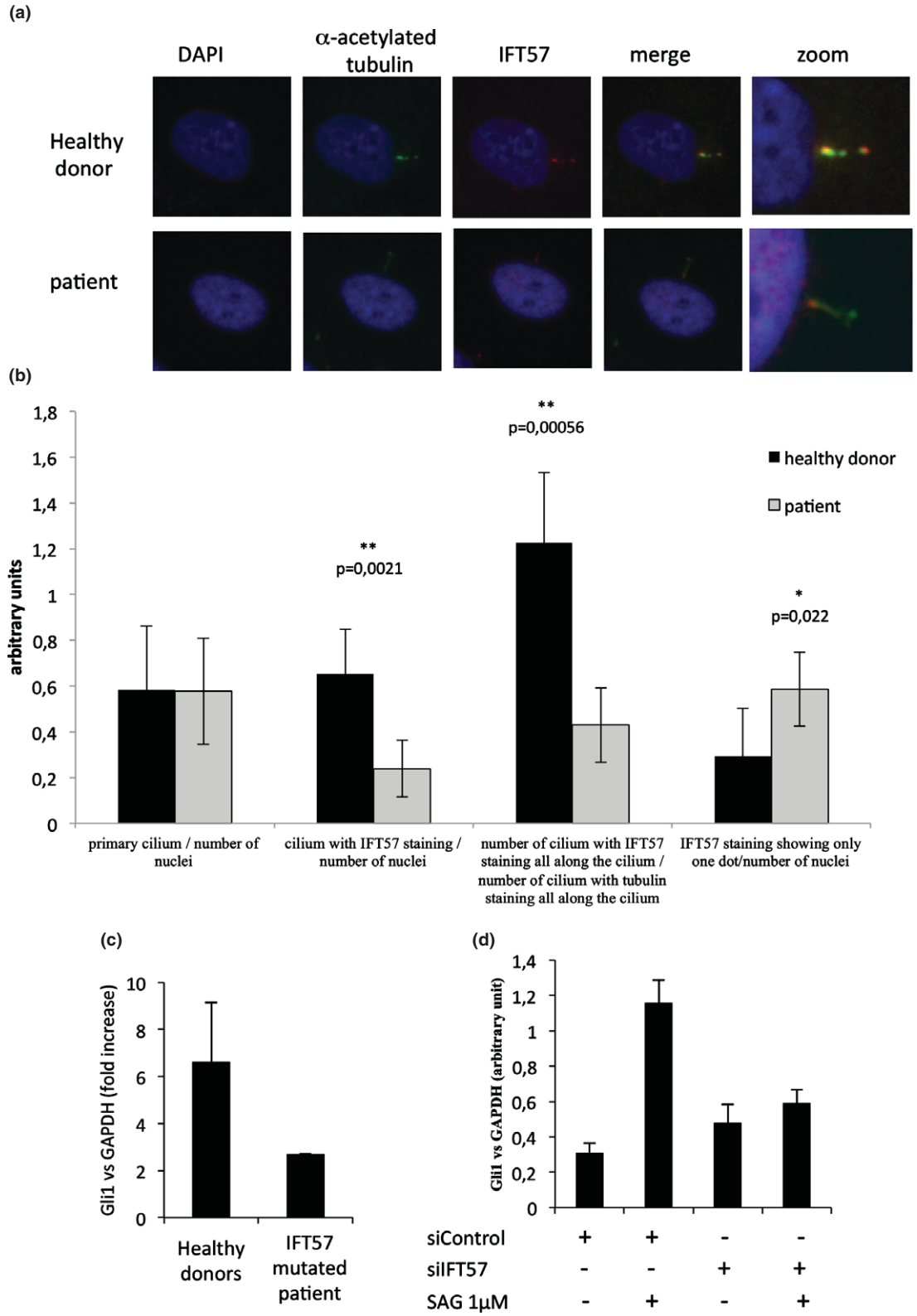

Fig. 4. Functional impact of the mutation on ciliary transport. (**a**) Immunofluorescence showing decreased anterograde ciliary transport in the subject's fibroblasts. IFT57 staining was low and restricted in most cells to the ciliary bases compared with control cells, which showed base and tip staining. (**b**) Count of ciliary transport showing comparable ciliary number but decreased ciliary tip staining, black bar: healthy control; grey bar: subject. (**c**) Decreased GLI1 transcription activation secondary to lowered SHH signaling pathway in the subject's fibroblasts compared with healthy controls (representative experiment of 4) and in control fibroblasts after siRNA IFT57 delivery (representative experiment of 3).

failed fusion and reduced length of the maxillary processes, neural tube defects, exencephaly and left-right axis pattern defects (18). Similarly, zebrafish mutants for IFT57 displayed anomalies typical of ciliopathies (19, 20).

In human pathology, disease-causing mutations in genes implicated in ciliary transport are mainly identified in the SRPS group of ciliopathies (9). Most of the mutated genes are in the motor for retrograde transport and in IFT complex A. Complex B is underrepresented with few cases reported (21–23). Among the 60+ cases reported with mutations in genes coding for ciliary transporters, bi-allelic truncating mutations were never observed (21, 24–29) suggesting that null alleles in IFT genes would cause a severe phenotype not compatible with early development. This observation supports the hypothesis of a mild clinical presentation caused by the splice-site mutation in our subject that reduced but did not completely block the synthesis of IFT57 message. Among the whole-exome sequencing data of 62 000 individuals, no homozygous loss-of-function mutations are reported, suggesting that it may lead to a lethal phenotype. Here, the reduced level of message and protein is still able to support ciliary assembly, but the cilia are defective in hedgehog signaling. It is likely that defective hedgehog signaling underlies many of the phenotypes in our subject, as hedgehog signaling is critical for bone, digit and cranial facial development (30). There is literature evidence for the role of IFT57 in retinal physiology, suggesting that there might be an ophthalmological involvement such as a retinopathy in the patients. However, these three individuals did not have visual complaints and there was no exclusion of ophthalmological involvement such as a retinopathy (31).

In conclusion, we report on a unique consanguineous family with three affected siblings with an unclassified OFDS subtype with short stature and brachymesophalangia, harboring a homozygous *IFT57* hypomorphic splice mutation altering ciliary transport defect and SHH signaling pathway.

Supporting Information

Additional supporting information may be found in the online version of this article at the publisher's web-site.

Acknowledgements

We thank the family for their participation. This work was supported by grants from GIS-Institut des Maladies Rares for high-throughput-sequencing approach, the French Ministry of Health (PHRC national 2010 and 2012), Dijon University Hospital, the Regional Council of Burgundy, the project ANR (2010 FOETOCILPATH N° BLAN 1122 01 to T. A. B.), the Indian Council of Medical Research (63/8/2010 – BMS for S.P.). Finally, the authors would like to thank the NHLBI GO Exome Sequencing Project and its ongoing studies which produced and provided exome variant calls for comparison: the Lung GO Sequencing Project (HL-102923), the WHI Sequencing Project (HL-102924), the Broad GO Sequencing Project (HL-102925), the Seattle GO Sequencing Project (HL-102926) and the Heart GO Sequencing Project (HL-103010).

References

1. Baraitser M. The orofaciodigital (OFD) syndromes. J Med Genet 1986: 23: 116–119.
2. Gurrieri F, Franco B, Toriello H, Neri G. Oral-facial-digital syndromes: review and diagnostic guidelines. Am J Med Genet A 2007: 143A: 3314–3323.
3. Giorgio G, Alfieri M, Prattichizzo C, Zullo A, Cairo S, Franco B. Functional characterization of the OFD1 protein reveals a nuclear localization and physical interaction with subunits of a chromatin remodeling complex. Mol Biol Cell 2007: 18: 4397–4404.
4. Valente EM, Logan CV, Mougou-Zerelli S et al. Mutations in TMEM216 perturb ciliogenesis and cause Joubert, Meckel and related syndromes. Nat Genet 2010: 42: 619–625.
5. Adly N, Alhashem A, Ammari A, Alkuraya FS. Ciliary genes TBC1D32/C6orf170 and SCLT1 are mutated in patients with OFD type IX. Hum Mutat 2014: 35: 36–40.
6. Thomas S, Legendre M, Saunier S et al. TCTN3 mutations cause Mohr-Majewski syndrome. Am J Hum Genet 2012: 91: 372–378.
7. Huang L, Szymanska K, Jensen VL et al. TMEM237 is mutated in individuals with a Joubert syndrome related disorder and expands the role of the TMEM family at the ciliary transition zone. Am J Hum Genet 2011: 89: 713–730.
8. Lopez E, Thauvin-Robinet C, Reversade B et al. C5orf42 is the major gene responsible for OFD syndrome type VI. Hum Genet 2014: 133: 367–377.
9. Huber C, Cormier-Daire V. Ciliary disorder of the skeleton. Am J Med Genet C Semin Med Genet 2012: 160C: 165–174.
10. Phadke SR, Pahi J, Pandey A, Agarwal SS. Oral-facial-digital syndrome with acromelic short stature: a new variant – overlap with Ellis Van Creveld syndrome. Clin Dysmorphol 1999: 8: 185–188.
11. Li H, Durbin R. Fast and accurate short read alignment with Burrows-Wheeler transform. Bioinformatics 2009: 25: 1754–1760.
12. McKenna A, Hanna M, Banks E et al. The Genome Analysis Toolkit: a MapReduce framework for analyzing next-generation DNA sequencing data. Genome Res 2010: 20: 1297–1303.
13. Pazour GJ, Baker SA, Deane JA et al. The intraflagellar transport protein, IFT88, is essential for vertebrate photoreceptor assembly and maintenance. J Cell Biol 2002: 157: 103–113.
14. Gervais FG, Singaraja R, Xanthoudakis S et al. Recruitment and activation of caspase-8 by the Huntingtin-interacting protein Hip-1 and a novel partner Hippi. Nat Cell Biol 2002: 4: 95–105.
15. Cole DG, Diener DR, Himelblau AL, Beech PL, Fuster JC, Rosenbaum JL. Chlamydomonas kinesin-II-dependent intraflagellar transport (IFT): IFT particles contain proteins required for ciliary assembly in *Caenorhabditis elegans* sensory neurons. J Cell Biol 1998: 141: 993–1008.
16. Follit JA, Xu F, Keady BT, Pazour GJ. Characterization of mouse IFT complex B. Cell Motil Cytoskeleton 2009: 66: 457–468.
17. Murcia NS, Richards WG, Yoder BK, Mucenski ML, Dunlap JR, Woychik RP. The Oak Ridge Polycystic Kidney (orpk) disease gene is required for left-right axis determination. Development 2000: 127: 2347–2355.
18. Houde C, Dickinson RJ, Houtzager VM et al. Hippi is essential for node cilia assembly and Sonic hedgehog signaling. Dev Biol 2006: 300: 523–533.
19. Sun Z, Amsterdam A, Pazour GJ, Cole DG, Miller MS, Hopkins N. A genetic screen in zebrafish identifies cilia genes as a principal cause of cystic kidney. Development 2004: 131: 4085–4093.
20. Lunt SC, Haynes T, Perkins BD. Zebrafish ift57, ift88, and ift172 intraflagellar transport mutants disrupt cilia but do not affect hedgehog signaling. Dev Dyn 2009: 238: 1744–1759.
21. Cavalcanti DP, Huber C, Sang K-HLQ et al. Mutation in IFT80 in a fetus with the phenotype of Verma-Naumoff provides molecular evidence for Jeune-Verma-Naumoff dysplasia spectrum. J Med Genet 2011: 48: 88–92.
22. McIntyre JC, Davis EE, Joiner A et al. Gene therapy rescues cilia defects and restores olfactory function in a mammalian ciliopathy model. Nat Med 2012: 18: 1423–1428.
23. Aldahmesh MA, Li Y, Alhashem A et al. IFT27, encoding a small GTPase component of IFT particles, is mutated in a consanguineous family with Bardet-Biedl syndrome. Hum Mol Genet 2014: 23: 3307–3315.
24. Beales PL, Bland E, Tobin JL et al. IFT80, which encodes a conserved intraflagellar transport protein, is mutated in Jeune asphyxiating thoracic dystrophy. Nat Genet 2007: 39: 727–729.

25. Arts HH, Bongers EMHF, Mans DA et al. C14ORF179 encoding IFT43 is mutated in Sensenbrenner syndrome. J Med Genet 2011: 48: 390–395.
26. Perrault I, Saunier S, Hanein S et al. Mainzer-Saldino syndrome is a ciliopathy caused by IFT140 mutations. Am J Hum Genet 2012: 90: 864–870.
27. Baujat G, Huber C, El Hokayem J et al. Asphyxiating thoracic dysplasia: clinical and molecular review of 39 families. J Med Genet 2013: 50: 91–98.
28. Schmidts M, Arts HH, Bongers EMHF et al. Exome sequencing identifies DYNC2H1 mutations as a common cause of asphyxiating thoracic dystrophy (Jeune syndrome) without major polydactyly, renal or retinal involvement. J Med Genet 2013: 50: 309–323.
29. Schmidts M, Frank V, Eisenberger T et al. Combined NGS approaches identify mutations in the intraflagellar transport gene IFT140 in skeletal ciliopathies with early progressive kidney Disease. Hum Mutat 2013: 34: 714–724.
30. Schneider RA, Hu D, Helms JA. From head to toe: conservation of molecular signals regulating limb and craniofacial morphogenesis. Cell Tissue Res 1999: 296: 103–109.
31. Krock BL, Perkins BD. The intraflagellar transport protein IFT57 is required for cilia maintenance and regulates IFT-particle-kinesin-II dissociation in vertebrate photoreceptors. J Cell Sci 2008: 121: 1907–1915.

Article 4

MKS5 and CEP290 dependent assembly pathway of the ciliary transition zone.

PLoS Biol. 2016 Mar 16;14(3):e1002416

C. Li, K. Park, VL. Jensen, J. Kennedy, FR. Garcia-Gonzalo, M. Romani, R. De Mori, AL. Bruel, D. Gaillard, B. Doray, E. Lopez, JB. Rivière, L. Faivre, C. Thauvin-Robinet, JF. Reiter, OE. Blacque, EM. Valente, MR. Leroux.

Résumé:

La zone de transition est une barrière de diffusion qui dirige les protéines vers le compartiment ciliaire adapté. Deux complexes majeurs sont localisés à ce niveau, MKS et NPHP, dont la composition et l'organisation moléculaire, et leur lien avec les ciliopathies, sont encore mal connus. Au cours de cette étude, nous avons identifié Cep290 chez *c.elegans* comme un facteur d'assemblage central, spécifique du complexe MKS et dépendant de MKS5/Rpgrip1l pour sa localisation dans la zone de transition. CEP290 contrôle l'entrée dans le cil des protéines associées à la membrane et Arl13b. Nous avons identifié une nouvelle sous-unité du complexe MKS, Tmem218, qui requiert Cep290 et d'autres protéines du complexe MKS pour sa localisation et son interaction avec le complexe NPHP pour faciliter la ciliogénèse. Nous avons démontré que la localisation de Tmem138 et CDKL-1, qui ne sont associé à un des complexes de la zone de transition, est dépendant de Cep290, mais totalement indépendant des interactions avec les composants des complexes MKS ou NPHP, suggérant qu'ils forment un module distinct. Enfin, nous avons mis en évidence des mutations dans les gènes *TMEM17*, *TMEM231* et *TMEM138* chez des patients présentant un syndrome OFD VI. Cette étude a permis de caractériser les différentes voies d'assemblage de la zone de transition et d'inclure de nouvelles protéines associées au complexe MKS (détails page 98).

PLOS | BIOLOGY

RESEARCH ARTICLE

MKS5 and CEP290 Dependent Assembly Pathway of the Ciliary Transition Zone

Chunmei Li[1], Victor L. Jensen[1☯], Kwangjin Park[1☯], Julie Kennedy[2], Francesc R. Garcia-Gonzalo[3¤a], Marta Romani[4], Roberta De Mori[4], Ange-Line Bruel[5], Dominique Gaillard[6], Bérénice Doray[7], Estelle Lopez[5], Jean-Baptiste Rivière[5,8], Laurence Faivre[5,9], Christel Thauvin-Robinet[5,9], Jeremy F. Reiter[3], Oliver E. Blacque[2], Enza Maria Valente[4,10], Michel R. Leroux[1]*

1 Department of Molecular Biology and Biochemistry and Centre for Cell Biology, Development and Disease, Simon Fraser University, Burnaby, British Columbia, Canada, **2** School of Biomolecular & Biomedical Science, University College Dublin , Belfield, Dublin 4, Ireland, **3** Department of Biochemistry and Biophysics, Cardiovascular Research Institute, University of California, San Francisco, San Francisco, California, United States of America, **4** Neurogenetics Unit, Mendel Laboratory, IRCCS Casa Sollievo della Sofferenza, San Giovanni Rotondo, Italy, **5** EA4271 GAD Génétique des Anomalies du Développement, FHU-TRANSLAD, Université Fédérale Bourgogne Franche-Comté, Dijon, France, **6** Service de Génétique clinique, CHU Reims, Reims, France, **7** Service de Génétique clinique, CHRU Strasbourg, Strasbourg, France, **8** Laboratoire de Génétique moléculaire, Plateau Technique de Biologie, CHU Dijon, Dijon, France, **9** Centre de Génétique, FHU-TRANSLAD, Hôpital d'Enfants, CHU Dijon, Dijon, France, **10** Department of Medicine and Surgery, University of Salerno, Salerno, Italy

☯ These authors contributed equally to this work.
¤a Current address: Departamento de Bioquímica, Facultad de Medicina, and Instituto de Investigaciones Biomédicas "Alberto Sols" UAM-CSIC, Universidad Autónoma de Madrid, Madrid, Spain
* leroux@sfu.ca

Citation: Li C, Jensen VL, Park K, Kennedy J, Garcia-Gonzalo FR, Romani M, et al. (2016) MKS5 and CEP290 Dependent Assembly Pathway of the Ciliary Transition Zone. PLoS Biol 14(3): e1002416. doi:10.1371/journal.pbio.1002416

Academic Editor: Renata Basto, Institut Curie, FRANCE

Received: July 16, 2015

Accepted: February 24, 2016

Published: March 16, 2016

Data Availability Statement: All relevant data are within the paper and its supporting information files.

Funding: MRL acknowledges funding from the Canadian Institutes of Health Research (CIHR; grant MOP 142243) and the March of Dimes, as well as a senior investigator award from the Michael Smith Foundation for Health Research (MSFHR). EMV is funded by grants from the European Research Council (ERC Starting Grant 260888) and Telethon Foundation Italy (grant GGP13146). OEB is funded by grants from Science Foundation Ireland (SFI-11-1037) and the European Community's Seventh Framework Programme FP7/2009 (241955

Abstract

Cilia have a unique diffusion barrier ("gate") within their proximal region, termed transition zone (TZ), that compartmentalises signalling proteins within the organelle. The TZ is known to harbour two functional modules/complexes (Meckel syndrome [MKS] and Nephronophthisis [NPHP]) defined by genetic interaction, interdependent protein localisation (hierarchy), and proteomic studies. However, the composition and molecular organisation of these modules and their links to human ciliary disease are not completely understood. Here, we reveal *Caenorhabditis elegans* CEP-290 (mammalian Cep290/Mks4/Nphp6 orthologue) as a central assembly factor that is specific for established MKS module components and depends on the coiled coil region of MKS-5 (Rpgrip1L/Rpgrip1) for TZ localisation. Consistent with a critical role in ciliary gate function, CEP-290 prevents inappropriate entry of membrane-associated proteins into cilia and keeps ARL-13 (Arl13b) from leaking out of cilia via the TZ. We identify a novel MKS module component, TMEM-218 (Tmem218), that requires CEP-290 and other MKS module components for TZ localisation and functions together with the NPHP module to facilitate ciliogenesis. We show that TZ localisation of TMEM-138 (Tmem138) and CDKL-1 (Cdkl1/Cdkl2/Cdkl3/Cdlk4 related), not previously linked to a specific TZ module, similarly depends on CEP-290; surprisingly, neither TMEM-138 or CDKL-1 exhibit interdependent localisation or genetic interactions with core MKS or NPHP module components, suggesting they are part of a distinct, CEP-290-associated module. Lastly, we show that families presenting with Oral-Facial-Digital syndrome type 6

SYSCILIA). JFR is funded by grants from the NIH (AR054396 and GM095941), Burroughs Wellcome Fund, the Packard Foundation, and the Sandler Family Supporting Foundation. CTR was supported by the GIS-Institut des Maladies Rares, the French Fondation for Rare Disease, the French Ministry of Health (PHRC national 2010-A01014-35 and 2013), and the Regional Council of Burgundy. KP is the recipient of a Vanier Canada Graduate Scholarship. VLJ holds MSFHR and KRESCENT postdoctoral fellowships. The funders had no role in study design, data collection and analysis, decision to publish, or preparation of the manuscript.

Competing Interests: The authors have declared that no competing interests exist.

Abbreviations: BBS, Bardet-Biedl syndrome; CIZE, ciliary zone of exclusion; GFP, green fluorescent protein; IFT, intraflagellar transport; JATD, Jeune asphyxiating thoracic dystrophy; JBTS, Joubert syndrome; LCA, Leber Congenital Amaurosis; MMP, Million Mutation Project; MKS, Meckel syndrome; NGS, next generation sequencing; NMD, nonsense-mediated mRNA decay; NPHP, Nephronophthisis; OFD6, Oral-Facial-Digital syndrome type 6; SLNS, Senior Løken syndrome; TEM, transmission electron microscopy; TMEM, transmembrane; TZ, transition zone.

(OFD6) have likely pathogenic mutations in CEP-290-dependent TZ proteins, namely Tmem17, Tmem138, and Tmem231. Notably, patient fibroblasts harbouring mutated Tmem17, a protein not yet ciliopathy-associated, display ciliogenesis defects. Together, our findings expand the repertoire of MKS module-associated proteins—including the previously uncharacterised mammalian Tmem80—and suggest an MKS-5 and CEP-290-dependent assembly pathway for building a functional TZ.

Author Summary

The primary cilium is a structure found in most animal cell types. Much like an antenna, it is responsible for sensing extracellular signals, including light and small molecules, and conveying this information to the receiving cell and respective tissue or organ. At the base of the cilium is the transition zone (TZ), which acts as a "gate" to regulate the entry and exit of ciliary proteins required for signal transduction. Here, we use the nematode *Caenorhabditis elegans* as a model system to dissect how different proteins within the TZ assemble to form a functional barrier. We find that the TZ protein MKS-5 (Rpgrip1/Rpgrip1L orthologue) forms the foundation for two different assembly pathways involving two distinct modules: Nephronophthisis (NPHP) and Meckel syndrome (MKS). We show that at the base of the MKS module is CEP-290, another TZ protein that assembles MKS module proteins, including a novel TZ protein we identify as TMEM-218. CEP-290 also helps assemble a potentially separate submodule containing TMEM-138 and CDKL-1. Notably, we provide evidence that the MKS module protein TMEM-17 facilitates cilium formation and is disrupted in the human disorder (ciliopathy) Oral-Facial-Digital Syndrome type 6 (OFD6). Together, our findings provide essential insights into the assembly pathway of the ciliary TZ and suggest further connections between the transition zone and human health.

Introduction

The eukaryotic cilium represents a functionally diverse organelle whose microtubule-based axoneme is templated from a modified centriole-termed basal body [1]. Motile cilia (also called flagella) propel cells or generate flow across cell surfaces, and their dysfunction results in primary ciliary dyskinesia [2]. Nonmotile or primary cilia are present in most metazoan cell types and enable sensory processes, including chemosensation/olfaction, mechanosensation, and photosensation [3,4]. In vertebrates, primary cilia are associated with several signalling pathways (Hedgehog, Wnt, PDGF, cyclic nucleotide) [5–8]. Since primary cilia have pervasive roles in signalling, disruption of their function is linked to numerous human disorders (ciliopathies) that affect sensory physiology (vision, smell, hearing), as well as the development and function of most organs, including eyes, kidney, skeleton, and brain [4,9–12].

Several ciliopathies, such as Jeune asphyxiating thoracic dystrophy (JATD) and Bardet-Biedl syndrome (BBS), result from defects in the evolutionarily conserved intraflagellar transport (IFT) machinery [13–16]. IFT is responsible for the formation and maintenance of cilia. It uses kinesin anterograde motor(s) to mobilise cargo (e.g., structural components, receptors) from the basal body transition fibres to the ciliary tip, and a dynein retrograde motor to recycle components back to the base [17–19]. The IFT machinery comprises over 20 core components and a cargo-adaptor protein complex (BBSome) consisting of several BBS proteins [13,18]. Defects in core IFT and BBS proteins cause several multisystemic ailments, including cystic kidney disease, retinal degeneration, obesity, and skeletal malformations [20].

Another large macromolecular complex linked to a growing number of ciliopathies is the transition zone (TZ). The TZ represents the proximal-most domain of the ciliary axoneme, found immediately distal to the basal body [21–24]. Its ultrastructure, as observed by transmission electron microscopy (TEM), reveals doublet microtubules that are connected to the ciliary membrane, typically via Y-shaped structures [25]. These Y-links likely organise the so-called ciliary necklace, a repeating unit of membrane-associated proteinaceous "beads" that form rings or a spiral at the TZ membrane surface [21–23]. As detailed below, the Y-links and, presumably, the associated necklace appear to perform two principal functions: one in cilium formation, and the other as a ciliary "gate" that maintains the correct composition of the ciliary organelle.

TZ-associated ciliopathies include Meckel syndrome (MKS), Nephronophthisis (NPHP), Joubert syndrome (JBTS), Leber Congenital Amaurosis (LCA), and Senior Løken syndrome (SLNS) [10,26]. Collectively, the clinical ailments of these ciliopathies partially overlap with those arising from IFT/BBS dysfunction and include brain malformations, cystic kidneys, retinal dystrophy, liver fibrosis, and polydactyly. Many genes encoding TZ-localised proteins are mutated in one or more ciliopathies; however, for most ciliopathies, not all causative genes have been identified, suggesting that additional TZ proteins remain to be discovered [26,27].

Genetic interaction studies of TZ genes in *Caenorhabditis elegans* have defined two major functional modules, termed "MKS module" and "NPHP module." The MKS module includes MKS-1 (mammalian Mks1 orthologue), MKSR-1 (B9d1/Mksr1), MKSR-2 (B9d2/Mksr2), MKS-2 (Mks2/Tmem216), MKS-3 (Mks3/Tmem67/Meckelin), MKS-6 (Mks6/Cc2d2a), TMEM-231 (Tmem231), JBTS-14 (Jbts14/Tmem237), TMEM-107, and TCTN-1 [25,28–32]. The *C. elegans* NPHP module thus far includes NPHP-1 and NPHP-4 [33]. Genetic (synthetic) interactions between the two modules are apparent. If one or more gene(s) within one module (either MKS or NPHP) are disrupted, ciliogenesis is essentially normal, although a subset of cilia are modestly truncated in *nphp-4* mutants [29,34]; in contrast, deleting individual genes from both modules severely disrupts TZ/ciliary structures [28–30,35,36]. For example, the *mks-6;nphp-4* double mutant has prominent ciliary phenotypes not observed in the individual single mutants [25,35]. These phenotypes include significantly fewer or no observable TZ Y-links, loss of basal body-transition fibre membrane attachments, and axonemal defects (missing or shorter microtubules) [25,28,30]. Hence, MKS and NPHP module proteins play genetically redundant roles in anchoring the basal body-ciliary axoneme and forming an ultrastructurally normal, functional TZ. Another established TZ protein, MKS-5 (RPGRIP1L/MKS5), is thought to act as a "scaffold" or "assembly factor" for most, if not all, MKS and NPHP module proteins [25,28,30,31].

Importantly, the genetically defined MKS and NPHP modules are consistent with physical interaction networks obtained through proteomic (pull-down) studies in mammalian cells, in which complexes containing the same (orthologous) MKS module proteins, or NPHP proteins, are observed [22,37–41]. In both *C. elegans* and mammalian cells, the modules can be further confirmed and defined hierarchically by testing for interdependent protein localisation at the TZ. Interestingly, mammalian Mks5 is found in a complex with Nphp1/Nphp4 proteins [39], a functional association not yet observed in *C. elegans*. Also, in *C. elegans* and mammalian cells, the TZ is thought to form early during ciliogenesis, following the docking of the basal body to either a ciliary vesicle or the plasma membrane, where the incipient ciliary axoneme is subsequently extended in an IFT-dependent manner [13,21,25,42].

Early evidence that the TZ forms a membrane diffusion barrier which concentrates signalling machinery within cilia came from Musgrave and colleagues (1986) [43], who presented cytological evidence suggesting that the unique composition of *Chlamydomonas eugametos* motile cilia is maintained by a membrane diffusion barrier. Spencer and colleagues (1988) [44]

obtained similar evidence, showing that sequestration of rhodopsin to the outer segment of ciliary photoreceptors requires the TZ (connecting cilium). Together, these studies hinted at a "gate" or "barrier," but until recently, the components involved and the mechanistic basis of this TZ functionality remained unknown.

At least 14 evolutionarily conserved TZ-localised proteins are now implicated in the formation of a selective membrane diffusion barrier that precludes nonciliary proteins from entering and helps to compartmentalise ciliary proteins [21,22,45]. In *C. elegans*, two membrane-associated proteins, RPI-2 (orthologue of Retinitis Pigmentosa 2) and TRAM-1 (Translocating Chain-Associating Membrane Protein) are present at the base of cilia and are excluded from the ciliary compartment unless TZ protein(s) are disrupted [25]. In mammals, several signalling proteins (e.g., Adcy3, Arl13b, Inpp5e, Sstr3, Pkd2, and Smo) either fail to enter cilia or are no longer concentrated within the organelle in various individual TZ mutants [31,38,40]. Similarly, the ciliary composition of cilia is altered in the TZ mutants of *Chlamydomonas* (*cep290* and *nphp4*), *Drosophila* (*Cep290*), and ciliary photoreceptor (*Rpgr*) [46–49].

Although many TZ components have been identified and their role in establishing a ciliary gate is generally accepted, many questions regarding the TZ remain unanswered. Are there additional components of the TZ awaiting discovery, and do they fit within the known MKS or NPHP functional modules? Aside from Mks5/Rpgrip1L, are there other essential "core" scaffolding and/or assembly factors of the MKS and/or NPHP modules at the TZ? Finally, how are the different proteins and modules spatiotemporally assembled at the TZ?

In this study, we provide new insights into the composition, organisation, assembly, and function of the *C. elegans* TZ, as well as provide evidence for an expanded role for TZ proteins in ciliopathies. We identify *C. elegans* TMEM-218 (mammalian Tmem218) as a novel TZ protein. Our genetic interaction, hierarchical, and in vivo functional analyses reveal that TMEM-218 is a new MKS module component. We show that, in addition to *C. elegans* MKS-5 (Rpgrip1L/Rpgrip1), another TZ protein, CEP-290 (Cep290/Mks4/Nphp6), functions as an assembly factor for not only TMEM-218 but all MKS module proteins tested. Consistent with a key role for CEP-290 in establishing TZ ultrastructure, the *cep-290* mutant lacks all characteristic features of a TZ, including Y-links. Notably, removal of CEP-290 does not significantly perturb the localisation of NPHP module proteins or MKS-5, whereas removal of MKS-5 results in CEP-290 delocalisation. Our findings suggest an assembly pathway that is initiated by MKS-5 and involves two separate branches. One branch requires CEP-290 for the assembly of MKS module proteins as well as two other TZ proteins (TMEM-138 and Cyclin-Dependent Kinase-Like CDKL-1) that may form a separate module. The other branch of the pathway, which can assemble separately, involves the NPHP module. Finally, we present evidence that three human genes encoding CEP-290-dependent TZ components, *TMEM17*, *TMEM138*, and *TMEM231*, are mutated in Oral-Facial-Digital type 6 (OFD6) syndrome families; furthermore, a novel mammalian TZ protein we uncovered, Tmem80, represents an excellent ciliopathy candidate. Notably, *TMEM17* has not yet been associated with a human disorder, and patient-derived cells with the *TMEM17* mutation display impaired ciliogenesis. Collectively, our work provides essential insights into the formation, organisation, and function of the TZ and expands the number of likely or potential ciliopathy-associated TZ proteins.

Results

C. elegans tmem-218 Encodes a Novel Ciliary Transition Zone Protein and Is Genetically Associated with the MKS Module

Recently, a large-scale mutagenesis screen uncovered a knockout mouse strain with NPHP and retinal degeneration phenotypes reminiscent of SLSN (OMIM 266900), a known ciliopathy

[50]. Although this strain was found to harbour a mutation in Tmem218, the protein was not characterised at the molecular or cellular level. Tmem218 encodes a small protein with three transmembrane domains that is conserved across metazoans, including *C. elegans* and humans (Fig 1A). Tmem218 is detectable in at least some, if not all, ciliated protists, including the green algae *Chlamydomonas reinhardtii*, the Chromalveolate *Guillardia theta*, and Choanoflagellates, the most closely related unicellular metazoan ancestors.

To determine if the unstudied *C. elegans* orthologue of Tmem218 (TMEM-218) plays a cilium-associated role, we generated an expression construct consisting of the endogenous promoter and entire coding region fused in-frame to green fluorescent protein (GFP). Transgenic strains expressing this construct were observed by confocal microscopy to ascertain which cell types the gene is expressed in. We found that *tmem-218* is expressed exclusively in cells that possess cilia, including amphid (head) and phasmid (tail) sensory neurons (Fig 1B). This expression pattern is like that of most *C. elegans* ciliary genes, including those encoding IFT, BBS, and TZ proteins [3,15,25,36,51]. The GFP-tagged TMEM-218 protein is specifically concentrated at the base of cilia, immediately distal to the basal body-associated transition fibres (Fig 1B; an IFT-dynein comarker, XBX-1::tdTomato, marks transition fibres and axoneme). This subcellular localisation for TMEM-218 is identical to known TZ proteins [25,28,31,35].

Next, we investigated whether TMEM-218 could be assigned to one of the two established genetic modules, MKS or NPHP [25]. Since a null mutant allele of *tmem-218* was not available from knockout consortia or the Million Mutation Project (MMP), we used transposon-mediated mutagenesis (imprecise excision) to generate one. Using this approach, we uncovered a deletion allele, *tmem-218(nx114)*, that removes the entire coding region of *tmem-218* without affecting neighbouring genes (Fig 1C). Mutant animals outcrossed to wild-type are viable and appear grossly normal in terms of morphology, movement, and development.

To determine if *tmem-218* displays genetic interactions with other TZ genes, we subjected single and double mutant strains to a dye-filling assay that tests for cilia structure defects [51–53]. Wild-type animals incubated with fluorescent DiI solution display dye-filling in several head (amphid) and tail (phasmid) sensory neurons, indicating normal exposure of cilia to the external environment (see schematic, Fig 1D). As with all previously tested TZ mutants, the *tmem-218* single mutant shows normal dye-filling (Fig 1D). However, a double mutant with *tmem-218* and an NPHP module mutant, *nphp-4*, shows a prominent dye-filling phenotype (Fig 1D). Such a genetic interaction is consistent with TMEM-218 acting together with NPHP-4 to facilitate TZ and cilium ultrastructure formation, a possibility that will need to be confirmed by TEM analysis. We also show that, as expected for an MKS module mutant [25], combining the *tmem-218* mutation with another MKS module mutant, *mks-2* [28], does not cause a dye-filling phenotype (Fig 1D). Altogether, our findings that *tmem-218* encodes a TZ protein and genetically interacts with *nphp-4* but not *mks-2* are consistent with TMEM-218 representing a novel MKS module protein.

TMEM-218 Localisation at the Transition Zone Depends on MKS-5 and MKS Module Proteins

Our previous studies on *C. elegans* TZ proteins revealed that MKS-5 (mammalian Rpgrip1L/Rpgrip1) plays a central role in assembling MKS module components at the TZ [25,28,30,31]. We therefore queried if MKS-5 is also required for the TZ localisation of TMEM-218. To test this, we introduced the TMEM-218::GFP fusion protein into the *mks-5* mutant. While TMEM-218::GFP is concentrated at the TZ in wild-type animals, it is consistently mislocalised (absent from the TZ) in the *mks-5* mutant background (Fig 2A). This finding supports the notion that TMEM-218 is functionally associated with the established network of TZ proteins, and confirms MKS-5 as a critical assembly factor for all known MKS module proteins tested thus far.

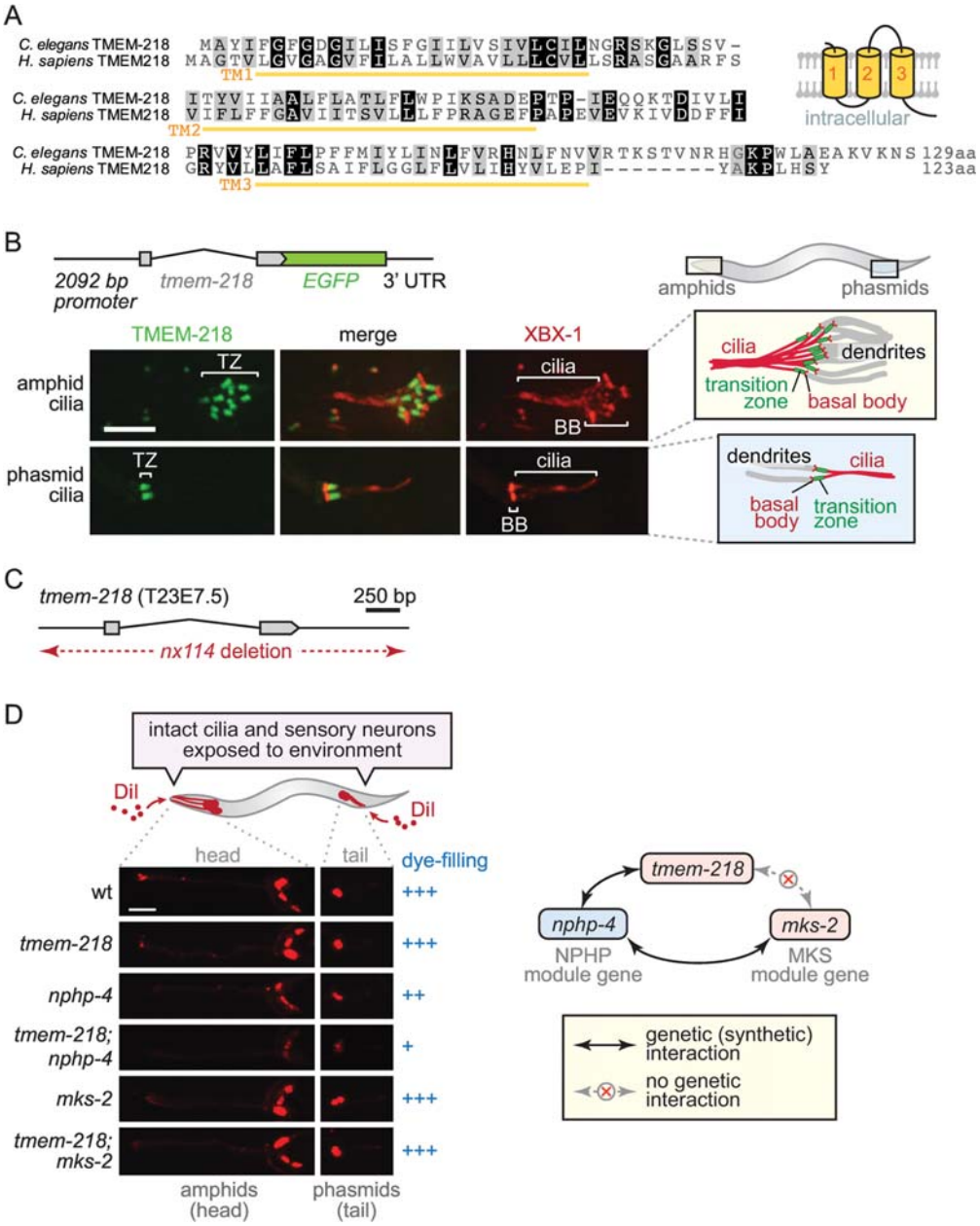

Fig 1. *C. elegans tmem-218* encodes a novel transition zone protein and genetically interacts with *nphp-4* but not *mks-2*, consistent with it being part of the Meckel syndrome (MKS) module. (**A**) Amino acid sequence alignment of *C. elegans* TMEM-218 and its *Homo sapiens* orthologue. Both proteins are predicted to encode proteins with three transmembrane domains (TM1-3), with the predicted topology shown schematically. (**B**) *C. elegans tmem-218* (T23E7.5) is expressed specifically in ciliated sensory neurons and its encoded product (TMEM-218) tagged with green fluorescent protein (GFP; green) localises to the ciliary transition zone (TZ) at amphid (head) and phasmid (tail) cilia found at the distal ends of dendrites. The tdTomato-tagged intraflagellar transport (IFT) protein XBX-1 (red) marks basal bodies (BB) and ciliary axonemes. Scale bar, 4 μm. (**C**) The *tmem-218(nx114)* mutant allele used in this study, generated using transposon-mediated mutagenesis, represents a complete and specific deletion of the *tmem-218* gene. (**D**) Dye-filling assay schematic shows the fluorescent dye DiI (red) penetrating sensory neurons via structurally intact, environmentally exposed ciliated endings. Dye-filling of the *tmem-218* and *nphp-4* strains is normal (+++) or slightly reduced (++), respectively, whereas dye-filling of the *tmem-218;nphp-4* double mutant is mostly disrupted (+). A lack of genetic (synthetic) interaction between *tmem-218* and *mks-2* is also consistent with TMEM-218 belonging to the MKS module (as depicted schematically). Scale bar, 40 μm.

doi:10.1371/journal.pbio.1002416.g001

To provide additional evidence that TMEM-218 is specifically associated with the MKS module, we assessed whether its TZ localisation is perturbed upon disruption of a"core" MKS module protein. Indeed, TMEM-218 is no longer present at the TZ in the *mks-2* MKS module mutant (Fig 2B). In contrast, and as expected for an MKS module protein, TMEM-218 remains correctly localised in the *nphp-4* core NPHP module mutant (Fig 2B). Reciprocal experiments were performed to query if TMEM-218 is itself required for the localisation of other TZ proteins. Our data show that TMEM-218 is not required for the localisation of MKS-5, MKS-2 ("core" MKS module protein), or NPHP-4 ("core" NPHP module protein) (Fig 2C).

Overall, our findings point to a specific association between TMEM-218 and MKS module components, potentially as a more "peripheral" TZ component compared to other "core" MKS module proteins, which include MKS-2, MKSR-1, MKSR-2, and TMEM-231 (Fig 2D) [25,28,30,31]. Consistent with this possibility, these "core" TZ proteins are all necessary for TZ gate function—namely, restricting the inappropriate entry of membrane-associated TRAM-1a into cilia—but TMEM-218, similar to the "peripheral" TZ protein MKS-3 [25], does not appear to influence this aspect of TZ function (Fig 2C).

C. elegans CEP-290 Plays an Essential Role in Transition Zone Function and Assembly

Given our discovery of a novel MKS module protein dependent on MKS-5 for TZ localisation, we wondered if there are additional proteins that participate in anchoring/assembling MKS module proteins at the TZ. We hypothesised that Cep290, which is implicated in several ciliopathies (including MKS and JBTS) [54] and is suggested to be a structural component of the TZ in *Chlamydomonas* [48], might represent such a protein. We sought to analyse the *C. elegans* homologue of Cep290, encoded by the gene Y47G6A.17.

To test our hypothesis, we created a construct encompassing the full-length cDNA of Y47G6A.17 fused in-frame to GFP. As anticipated, the Y47G6A.17::GFP translational fusion protein is specifically enriched at the TZ of all cilia (Fig 3A); importantly, we confirmed that the GFP-tagged protein is functional and, hence, its localisation is physiologically relevant (see below). Based on Y47G6A.17 consisting largely of coiled coils and having sequence homology to mammalian Cep290, its TZ localisation, and our finding that it plays an important role in the assembly and function of the TZ (see below), our data support the notion that it is indeed the functional homologue of Cep290; we therefore named the nematode protein CEP-290. Notably, Schouteden and colleagues also recently confirmed that *C. elegans* CEP-290 localises to the TZ [55].

To provide evidence that *C. elegans* CEP-290 is implicated in ciliary gate function, we first acquired a strain (VC30108) from the MMP [56] that contains a nonsense mutation (Q638*) in the coding region of *cep-290* (Y47G6A.17) (Fig 3B). Quantitative RT-PCR analyses show that the *cep-290* transcript in this mutant is eliminated by nonsense-mediated mRNA decay (NMD) (S1A Fig). The strain, *cep-290(gk415029)*, therefore very likely contains a null allele of *cep-290*, consistent with its ciliary phenotypes being indistinguishable from those described for a different strain harboring a complete loss-of-function allele of *cep-290* [55]; our strain was outcrossed to wild-type to remove unlinked background mutations.

We then tested for the abnormal entry of two membrane-associated proteins into the cilia of *cep-290* mutant animals. Both RPI-2 (mammalian RP2 orthologue) and TRAM-1a (TRAM in mammals) are normally excluded from cilia in wild-type animals (Fig 3C) [25]. In contrast, visualisation of fluorescently-tagged RPI-2 and TRAM-1a in the *cep-290* mutant consistently reveals their abnormal "leaking" or accumulation in cilia (Fig 3C). These findings parallel those found with several previous TZ mutants [25] and provide evidence that CEP-290 is required for the ciliary gating function of the TZ.

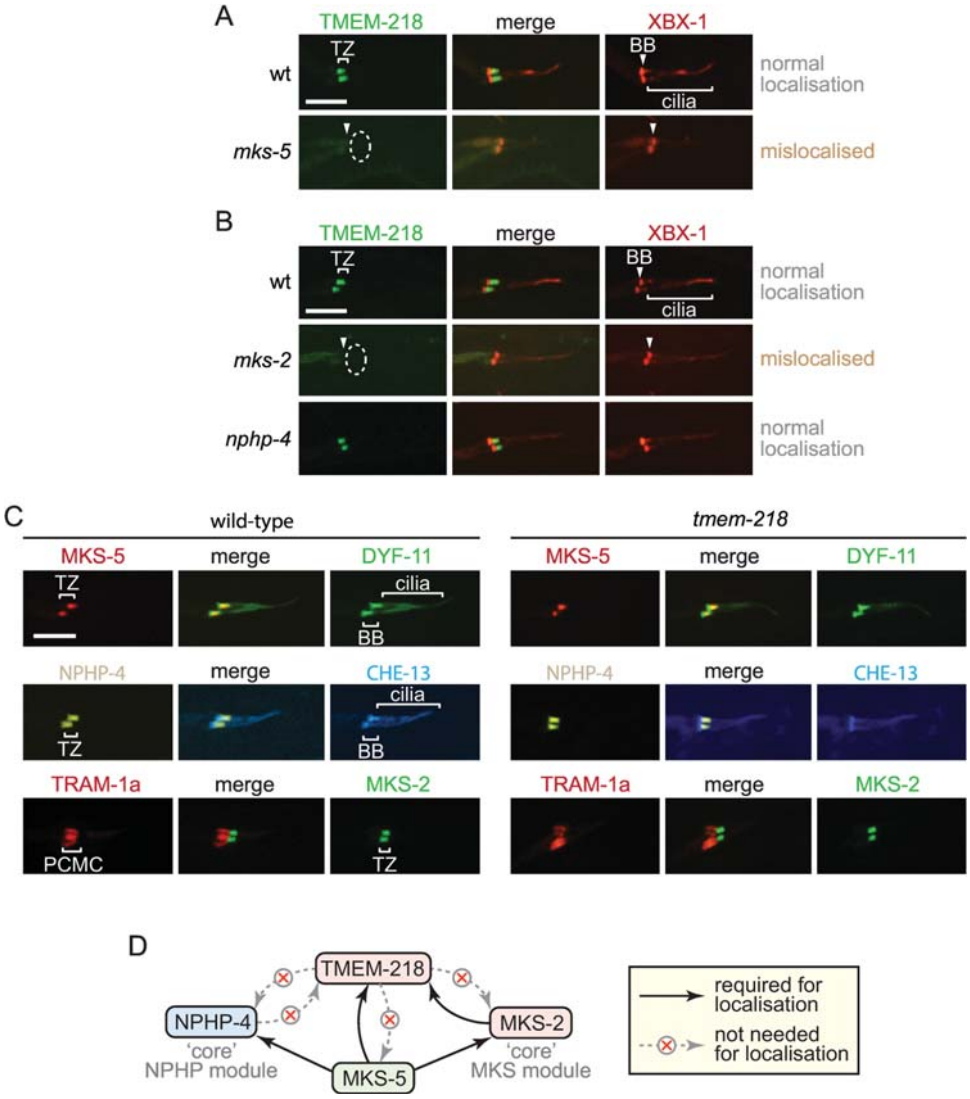

Fig 2. TMEM-218 depends on MKS-5 and a core MKS module component (MKS-2) for transition zone localisation but does not itself influence other TZ proteins. (**A**) GFP-tagged TMEM-218 (green) localises to the transition zone (TZ) normally in a wild-type background and is mislocalised in the *mks-5* mutant (dotted ellipse). The tdTomato-tagged IFT protein XBX-1 (red) marks basal bodies (BB) and ciliary axonemes. Scale bars in panels **A–C** are 4 μm. (**B**) GFP-tagged TMEM-218 displays normal localisation in the core NPHP module mutant *nphp-4* but is mislocalised in the core MKS module mutant *mks-2* (dotted ellipse), consistent with TMEM-218 being part of the MKS module. (**C**) In the *tmem-218* mutant, MKS-5 (tdTomato-tagged; red), the MKS module protein MKS-2::GFP (green), and the NPHP module protein NPHP-4::YFP (yellow) are correctly localised to the TZ. DYF-11::GFP (green), CHE-13::CFP (blue), and XBX-1::tdTomato (red) are IFT proteins that mark the basal body (BB) and ciliary axoneme. TRAM-1a::tdTomato (red) is a periciliary membrane compartment (PCMC) protein that localises correctly in the *tmem-218* mutant, suggesting that TMEM-218 is not necessary for TZ gate function. (**D**) Localisation-dependence studies are consistent with TMEM-218 being a peripherally-associated MKS module protein of the TZ.

doi:10.1371/journal.pbio.1002416.g002

Further support for this possibility stems from our observation of ARL-13 (Arl13b in mammals), which freely diffuses within the ciliary membrane [45,57]. In wild-type animals, palmitoylated ARL-13 (and other membrane-associated proteins) are completely excluded from the TZ, a reflection of the TZ acting as a membrane diffusion barrier [30,45]. In the *cep-290*

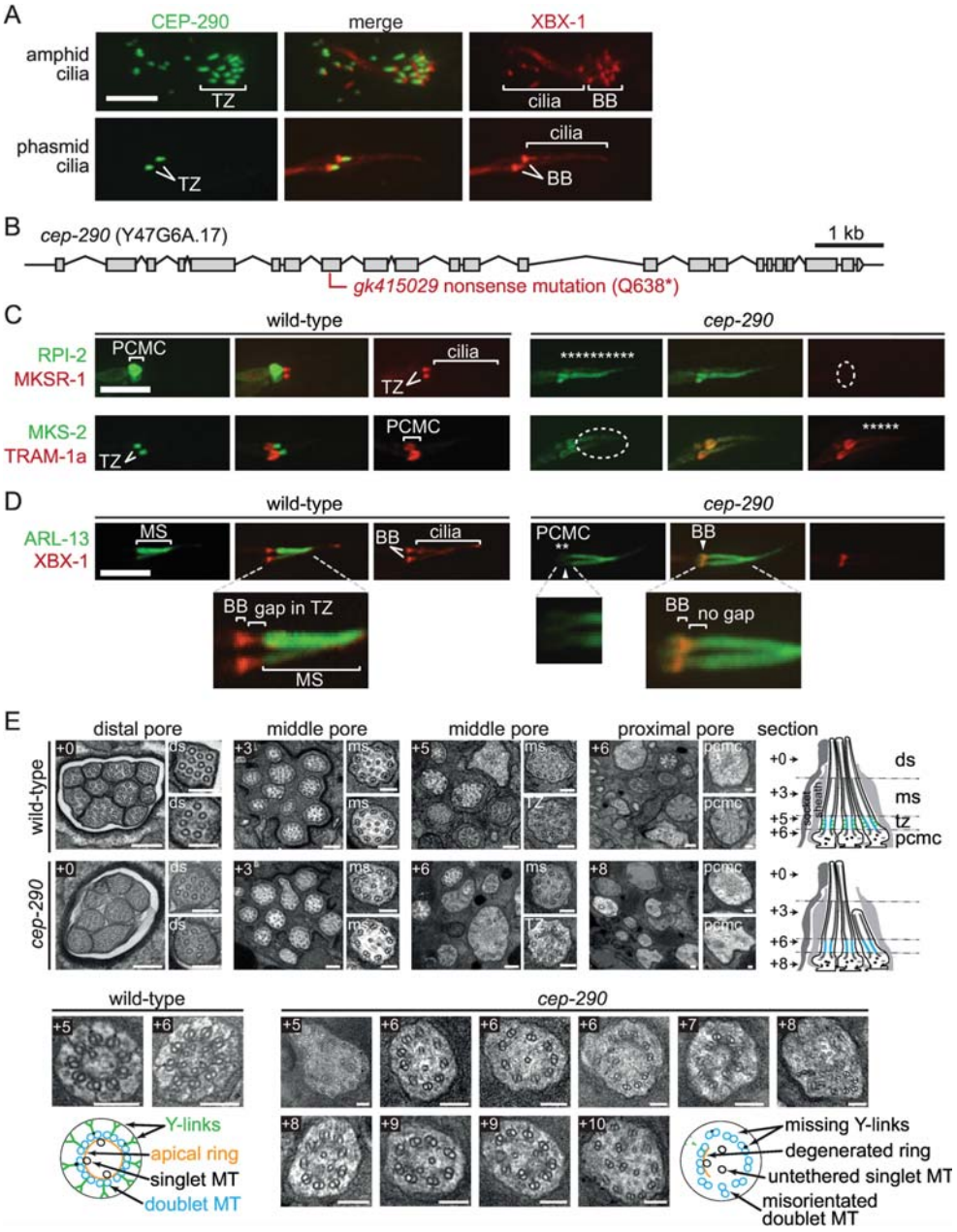

Fig 3. *C. elegans* CEP-290 is a transition zone protein required for ciliary gate (membrane diffusion barrier) function and transition zone assembly. (**A**) *C. elegans* CEP-290 (Y47G6A.17) tagged with GFP (green) is expressed only in ciliated sensory neurons (including amphids and phasmids) and is specifically enriched at the ciliary transition zone (TZ). tdTomato-tagged XBX-1 (red) is an IFT protein that marks the basal body (BB) and axoneme. Scale bars in panels **A, C,** and **D** are 4 μm. (**B**) *cep-290* gene structure and likely null allele (*gk415029* nonsense mutation) isolated from the Million Mutation Project (MMP) mutant strain VC30108. (**C**) CEP-290 is required for maintaining the functional integrity of the TZ. Two membrane-associated proteins (TRAM-1a::tdTomato and RPI-2::GFP) normally present at the base of cilia and not present within cilia show abnormal ciliary entry ("leakage") or accumulation in the *cep-290* mutant (shown as asterisks). MKSR-1::tdTomato and MKS-2::GFP are TZ protein comarkers (in wild-type) that mislocalise in the *cep-290* mutant (dotted ellipse). (**D**) CEP-290 is required to exclude membrane-associated GFP-tagged ARL-13 (green) from the transition zone and compartmentalise it within the ciliary middle segment (MS), consistent with a role for CEP-290 in TZ gate function. In the *cep-290* mutant, ARL-13 is also seen outside of the cilium in the periciliary membrane compartment (PCMC) region (mislocalisation shown with asterisks). (**E**) Transition zone ultrastructure is missing in *cep-290* mutants. Transmission electron microscopy images from serial cross-sections of the amphid channel (pore) in wild-type and *cep-290* mutant worms. Boxed numbers denote positioning of sections relative to anterior-most section (+0); section positions also shown in schematics on right-hand side. Wild-type amphid channels possess ten ciliary axonemes, each with distal segment (ds; outer singlet A-tubules), middle segment (ms; outer doublet A/B tubules), and transition zone (TZ; outer doublet A/B tubules, Y-links, apical ring) compartments. In *cep-290* mutants, one to two cilia are missing from the distal pore, indicating that one to two axonemes are short. TZ ultrastructure is severely disrupted in *cep-290* worms; most or all Y-link structure is missing, as is the apical

ring that draws together outer doublet MTs with varying numbers of inner singlet microtubules. MT doublets are also frequently disorganised near the ciliary base. Schematics denote the observed ultrastructural phenotypes (only three ciliary axonemes shown for simplicity). pcmc; periciliary membrane compartment. Scale bars, 200 nm (large, low-magnification top panel images) and 100 nm (small, high-magnification top panel images and all bottom panel TZ images).

doi:10.1371/journal.pbio.1002416.g003

mutant, the ARL-13 ciliary zone of exclusion (CIZE) at the TZ is substantially disrupted, with ARL-13 visible within the proximal region of the cilium and at the periciliary membrane (Fig 3D); this is similar to that observed for ARL-13 and other membrane-associated proteins in the *mks-5* mutant or TZ double mutants [30,45]. Together, our two complementary TZ functional assays suggest that CEP-290 plays an essential role in maintaining a functional TZ "gate" or membrane diffusion barrier.

To assess the potential role of CEP-290 in assembling TZ ultrastructure, which would help explain its role in TZ gate function, we subjected the *cep-290* mutant to TEM analyses. In wild-type animals, the following structures are observed in TEM cross-sections of the amphid channel ciliary bundle: transition fibres that connect the distal end of the basal body to the base of the ciliary membrane, a TZ with prominent Y-links, a middle segment axoneme with doublet microtubules, and, finally, a distal segment with singlet microtubules (Fig 3E). In the *cep-290* mutant, most cilia are present throughout the pore, although one to two axonemes are missing from the distal regions, indicating that they are short (Fig 3E). Like wild-type worms, *cep-290* mutants also possess clearly distinguishable middle and distal segments. Strikingly, however, *cep-290* mutant cilia reveal no structures characteristic of the TZ, displaying a lack of Y-link axoneme-to-membrane attachments; furthermore, the apical ring structure (of unknown composition) that is present inside the doublet microtubules is also absent (Fig 3E; see also [55]). In addition, microtubule doublets are frequently disorganised near the ciliary base and in the periciliary membrane compartment of some neurons (Fig 3E). Notably, the *cep-290* null mutant TZ phenotype is essentially indistinguishable from that of the *mks-5* null mutant [30]. Together, our findings reveal a critical role for *C. elegans* CEP-290 in the formation of TZ ultrastructure as well as in ciliary gate function.

C. elegans CEP-290 Is Essential for Assembly of TMEM-218 and MKS Module Components at the Transition Zone, Requires MKS-5 Coiled Coil Region for its Localisation, and Behaves Genetically as an MKS Module Component

Having confirmed that CEP-290 is important for the formation of the TZ and function of the ciliary gate, we tested for its potential role in localising MKS module components (including TMEM-218) as well as NPHP module proteins and MKS-5 at the TZ. We first observed that TMEM-218 is consistently absent from the TZ in the *cep-290* mutant (Fig 4A). Moreover, four additional MKSome components, namely, the "core" TZ proteins MKSR-1 (mammalian B9d1), MKS-2 (Tmem216), and TMEM-231 (Tmem231), as well as TMEM-17 (Tmem17), are all mislocalised in the *cep-290* mutant (Figs 3C and 4A). Notably, how the proteins are mislocalised may be different (e.g., MKS-2 "leaks'"into the axoneme, whereas TMEM-17 remains in the dendrite; Figs 3C and 4A); the reason for this is unclear.

In contrast, we find that MKS-5 remains largely within the proximal region of *cep-290* mutant cilia in the area where the TZ would normally form (Fig 4A). This suggests that while both CEP-290 and MKS-5 play critical roles in the assembly of MKS module proteins at the TZ, MKS-5 can localise independently of CEP-290 and, therefore, may function "upstream" of CEP-290 during TZ assembly. We note that the localisation of MKS-5 in the *cep-290* mutant is not entirely wild-type, as it is in some cases more spread out and present within a more distal

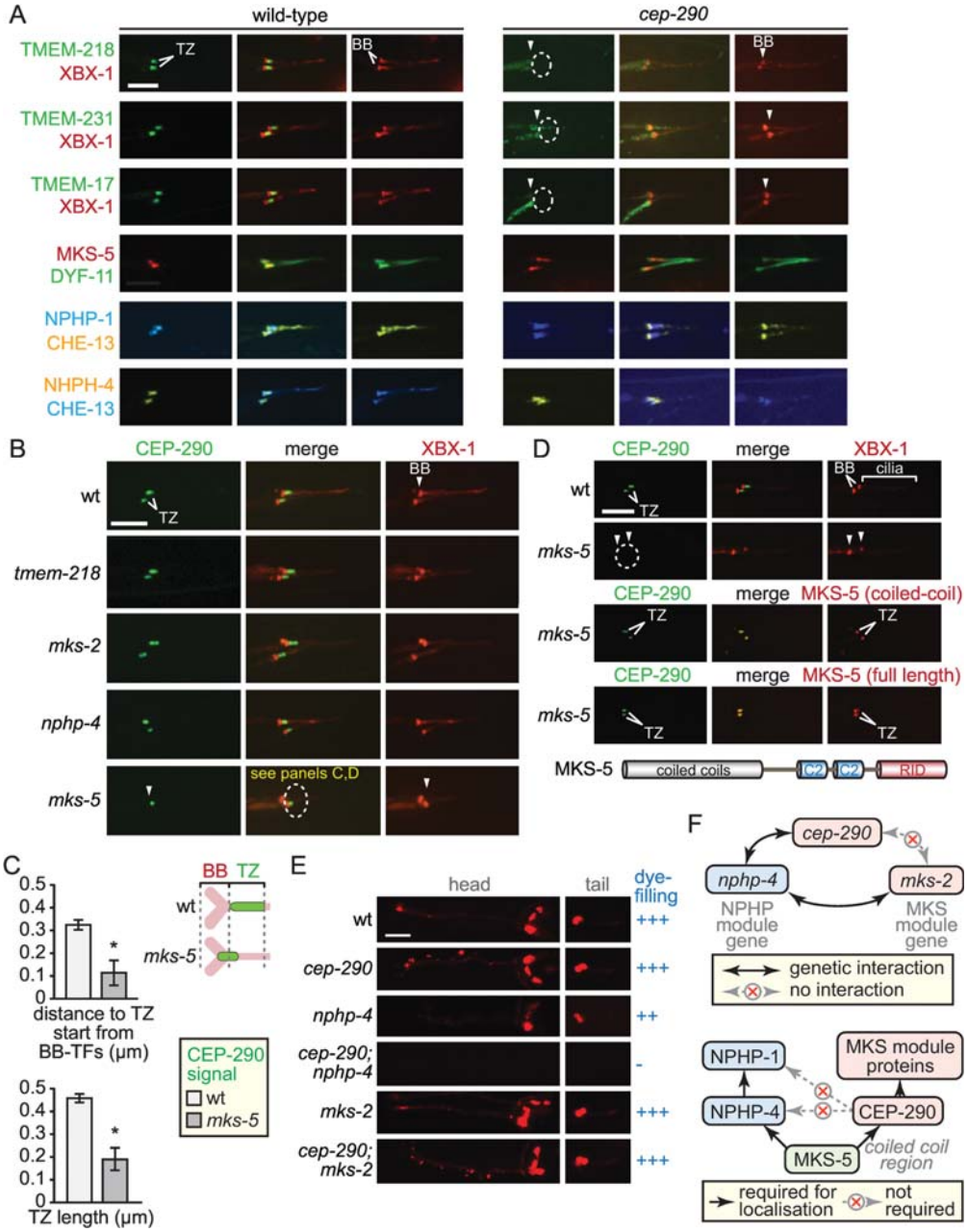

Fig 4. CEP-290 is specifically required for the assembly of the MKS module but not NPHP module components, and depends on MKS-5 for its own TZ localisation. (**A**) TMEM-218::GFP and other MKS module components (TMEM-231::GFP, TMEM-17::GFP) no longer localise to the TZ in the *cep-290* mutant (dotted ellipses). However, MKS-5::tdTomato and NPHP module proteins (NPHP-1::CFP, NPHP-4::YFP) retain their localisation at the base of cilia (in the same region as the TZ) in the *cep-290* mutant. Scale bars (panels **A and B**), 4 μm. (**B**) Transition zone localisation of GFP-tagged CEP-290 (green) requires MKS-5 (dotted ellipse) but is not affected by loss of MKS or NPHP module components. XBX-1::tdTomato (red) marks the basal body-transition fibres and axoneme. CEP-290 levels are reduced in the *mks-5* mutant, and remaining signals are closer to the basal body-transition fibres (see panel **C;** panel D shows complete loss of CEP-290 in the *mks-5* mutant). (**C**) Analysis of CEP-290 localisation in wild-type and *mks-5* mutant. Quantitation of CEP-290::GFP signal in the *mks-5* mutant reveals closer localisation to the basal body-transition fibre region (marked by XBX-1::tdTomato) and reduced signal length compared to that of wild-type animals. *, Fisher's exact test for significance, $p < 0.05$. Schematic depicts differences in wild-type and *mks-5* mutant CEP-290::GFP localisation patterns. BB, basal body; TF, transition fibres. **(D)** Loss of CEP-290 TZ localisation in the *mks-5* mutant (dotted ellipse) is restored through expression of full length MKS-5, as well as the coiled coil domain of MKS-5 alone (refer to schematic for MKS-5 domain structure; RID, RPGR-interacting domain). XBX-1 is used to mark the basal body-transition fibres and axoneme. Scale bar, 4 μm. (**E**) Dye-filling assays, which probe for intact ciliary structures, reveal a genetic (synthetic) interaction between *cep-290* and an NPHP module mutant (*nphp-4*; dye-filling lost, shown as "-") but not an MKS module mutant (*mks-2*; dye-filling normal, "+++"). Scale bar, 40 μm. (**F**) Schematics showing *cep-290* genetic interaction with *nphp-4* but not *mks-2* (top),

and interdependent organisational hierarchy of MKS-5, CEP-290, and MKS and NPHP components (bottom). Together, the data point to CEP-290 functioning downstream of MKS-5 and upstream of MKS module components.

doi:10.1371/journal.pbio.1002416.g004

region of the axoneme (Fig 4A). This suggests that CEP-290 may provide additional stability and/or specificity to MKS-5 localisation at the TZ. In addition, both NPHP module proteins (NPHP-1 and NPHP-4) remain associated with the proximal region of the axoneme in the *cep-290* mutant, in a manner that is very similar to MKS-5 (Fig 4A; note that NPHP-1/NPHP-4 also localises to the basal body-transition fibres, as shown in Jensen et al. [30]). Hence, CEP-290 is required for the localisation of MKS module components but is not essential for the largely normal TZ localisation of the NPHP module or MKS-5. As we elaborate in the discussion, this result is both striking and surprising: in the absence of CEP-290, both MKS-5 and NPHP module proteins are present at the base of the cilium, in a region where the TZ is expected, even though no TZ ultrastructure (Y-links) is present (Fig 3E).

We performed reciprocal localisation experiments to ascertain if CEP-290 itself depends on other TZ proteins for its localisation. We show that CEP-290 is correctly localised in the *tmem-218* mutant and the core MKS module TZ mutant, *mks-2* (Fig 4B). Similarly, CEP-290 localisation is not affected by disruption of the core NPHP module protein, NPHP-4 (Fig 4B). In contrast, CEP-290 localisation to the TZ is lost when the core assembly factor, MKS-5, is ablated (Fig 4B). Specifically, the CEP-290::GFP signal is significantly reduced in the absence of MKS-5 and is often undetectable at the distal end of the dendrite despite the lower but not highly different *cep-290* transcript levels between wild-type and *mks-5* mutant (approximately 50% lower); notably, expression of *cep-290* in the *mks-2* mutant is slightly lower than in the *mks-5* mutant, yet localisation of CEP-290 is unperturbed (Figs 4B, 4D and S1B). This suggests that, in the absence of MKS-5, the CEP-290 protein is not incorporated into to the TZ region, may not be transported to the dendritic tip, and/or may be degraded. Furthermore, of the remaining CEP-290 observable near the ciliary region, the signal is closer to the basal body-transition fibers compared to its TZ localisation in wild-type animals (Fig 4C); it is also significantly lower in intensity and occupies a smaller volume (S1C Fig). Given the limiting resolving power of confocal microscopy, our results suggest that, in the absence of MKS-5, residual CEP-290 can localise to the very distal end of the dendrite but is not incorporated within the proximal region of the cilium.

To ascertain how MKS-5 might enable CEP-290 localisation to the TZ, we queried whether the coiled coil N-terminal domain of MKS-5 alone could confer this activity. Notably, the coiled coil region is both necessary and sufficient for MKS-5 localisation to the TZ, independent of its two C2 and RPGR-interacting domain regions [30]. We expressed the MKS-5 coiled coil region in the *mks-5* mutant, and found that it fully rescues CEP-290 localisation at the TZ, similar to full-length MKS-5 (Fig 4D). Furthermore, the MKS-5 coiled coil region restores the space (volume) normally occupied by CEP-290 at the TZ (S1C Fig).

We then sought to uncover if *cep-290* is genetically associated with the MKS module using genetic interaction and dye-filling studies. The *cep-290* mutant is able to dye-fill normally (Fig 4E), as expected from having largely intact, environmentally-exposed ciliary axonemes (Fig 3E). A synthetic dye-filling phenotype is observed when *cep-290* is combined with the *nphp-4* mutant, but not with the *mks-2* mutant (Fig 4E); this behaviour mimics that of other MKS module genes (e.g., *mksr-1*, *mks-2*, and *mks-6*). Rescue of the *cep-290* mutant with our CEP-290::GFP translational reporter confirms that *cep-290* is responsible for this phenotype and that the GFP-tagged protein is functional—making its TZ localisation biologically relevant (S2 Fig). Genetically, *cep-290* is, therefore, aligned with the MKS module of TZ genes (Fig 4F). Together, our findings are consistent with a hierarchical organisation at the TZ, wherein MKS-

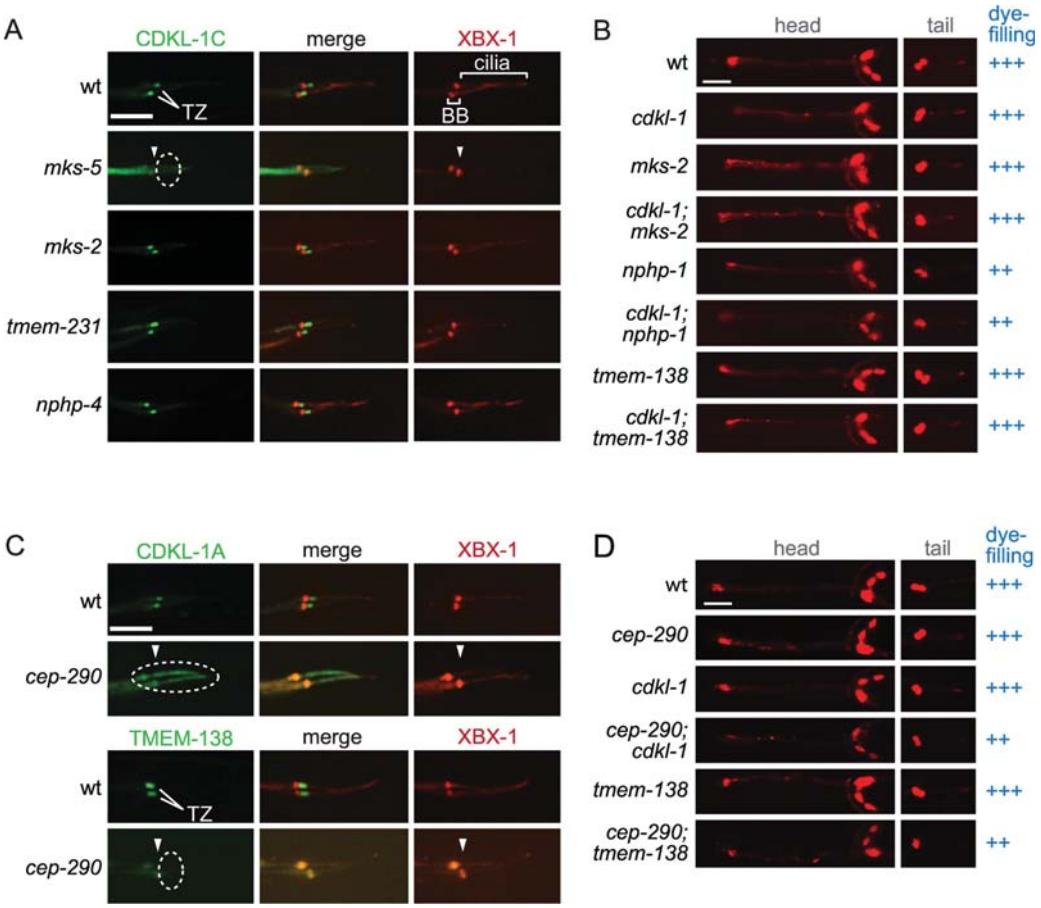

Fig 5. CDKL-1 and TMEM-138 require CEP-290 for their transition zone localisation and are functionally independent of the MKS or NPHP module. (**A**) GFP-tagged CDKL-1 (green) requires MKS-5 (dotted ellipse) but not other "core" MKS (MKS-2, TMEM-231) or NPHP (NPHP-4) module proteins for its TZ localisation. XBX-1 is used to mark the basal body-transition fibres and axonemes. Scale bar, 4 μm. (**B**) Dye-filling assays of head (amphid) and tail (phasmid) sensory neurons reveal that *cdkl-1* does not genetically interact (i.e., shows synthetic dye-filling phenotype) with either MKS (*mks-2*) or NPHP (*nphp-1*) module mutants. *cdkl-1* also does not show a genetic interaction with *tmem-138*. Scale bar, 40 μm. (**C**) Both GFP-tagged CDKL-1 and TMEM-138 depend on CEP-290 for their localisation to the TZ (dotted ellipse). Scale bar, 4 μm. **(D)** Partial (weak) dye-filling phenotype in the *cep-290;tmem-138* and *cep-290;cdkl-1* double mutants (++) compared to wild-type and the individual mutants (normal dye-filling, +++).

doi:10.1371/journal.pbio.1002416.g005

5 is positioned at the very "base," influencing both NPHP and MKS module assembly, and CEP-290 is positioned between MKS-5 and MKS module components (Fig 4F).

CDKL-1 and TMEM-138 Assembly at the TZ Requires CEP-290 but Is Independent of Core MKS Module Proteins

In *C. elegans*, all TZ proteins tested fit genetically within the MKS or NPHP module, the exception being the central organising or assembly factor, MKS-5, which shows interactions with both modules [25,28,30]. Here, we show that two proteins (CDKL-1 and TMEM-138) that require MKS-5 for TZ localisation and do not behave as either MKS or NPHP module proteins depend on CEP-290 for their correct localisation. The *C. elegans* CDKL-1 kinase, homologous to mammalian Cdkl proteins (Cdkl1/Cdkl2/Cdkl3/Cdkl4), localises to the TZ and influences cilium length, similar to the recently described *Chlamydomonas* CDKL5 protein (manuscript in preparation) [58]. We find that CDKL-1 (isoform A or C) is still TZ-localised when core MKS or NPHP module proteins are removed (Fig 5A). Furthermore, combining the *cdkl-1*

mutant with either the *mks-2* mutant or the *nphp-1* mutant does not cause a synthetic dye-filling defect (Fig 5B). Hence, CDKL-1 cannot be assigned to either the MKS or NPHP module. Remarkably, however, CDKL-1 not only requires MKS-5 for its TZ localisation but also depends on CEP-290 (Fig 5C).

To determine if additional TZ proteins exhibit this behaviour, we examined TMEM-138, the *C. elegans* orthologue of mammalian Tmem138 [59]. Similar to CDKL-1, TMEM-138 requires MKS-5 for its localisation but does not depend on either core MKS or NPHP module proteins; furthermore, the *tmem-138* mutant shows no synthetic dye-filling defect with *mksr-1* or *nphp-4*, making an assignment to either module not feasible [30]. Remarkably, TMEM-138 also depends on CEP-290 for its TZ localisation (Fig 5C). Together, our findings suggest hierarchical/functional characteristics for CDKL-1 and TMEM-138 that differ from all other MKS module proteins but that share a dependence on both MKS-5 and CEP-290 for their TZ localisation. For the purpose of discussion below, we refer to CDKL-1 and TMEM-138 as CEP-290-associated proteins. We wondered if the two genes interact genetically, but the *tmem-138; cdkl-1* double mutant does not show a synthetic ciliogenesis (dye-filling) phenotype (Fig 5B). We further queried if there are genetic interaction(s) between *cep-290* and *tmem-138* and/or *cdkl-1*. Only a small difference in dye-filling (weaker uptake) was found between the double mutants (*tmem-138;cep-290* and *cdkl-1;cep-290*) compared to the single mutants, consistent with the positioning of *tmem-138*, *cdkl-1*, and *cep-290* in the same genetic module (Fig 5D).

Evidence for Expanded Role for TZ Proteins in Ciliopathies and Ciliogenesis

The majority of known TZ proteins are associated with one or more ciliopathies, including MKS, JBTS, SLNS, and NPHP [21,22,26]. Our recent discovery that *C. elegans* TMEM-17 is an MKS module protein [30] that depends on CEP-290 for TZ localisation (Fig 4A) suggests that it may also be linked to one or more ciliopathies; however, such a possibility has not been reported. We therefore included *TMEM17* in a panel of 101 ciliary genes (S1 Table) that underwent next-generation sequencing (NGS) in a cohort of 330 patients with a neuroradiologically confirmed diagnosis of JBTS and variable organ involvement (S2 Table). Interestingly, we uncovered a homozygous missense mutation in *TMEM17* (p.N102K) in two siblings whose clinical profile is consistent with OFD6 (Figs 6A and S3A), a subtype of JBTS [60].

The *TMEM17* variation fully segregates with the disease in the family (Figs 6A and S3A) and is not detected in 150 in-house controls or in over 73,000 samples from the public databases EXAC and EVS. Furthermore, the p.N102K variant is predicted to be pathogenic by four distinct bioinformatic predictors (PolyPhen2, SIFT, Mutation Assessor, Mutation Taster) and affects a highly conserved amino acid residue (S3B Fig). Importantly, we show that fibroblast cells isolated from a *TMEM17*-mutated sibling display a much reduced ability to form cilia compared to cells obtained from the healthy heterozygous mother (Fig 6B and 6C). Together, the discovery of a homozygous mutation in a highly conserved residue of Tmem17 that is not present in control genomes and is correlated with a defect in ciliogenesis provides strong evidence that disruption of Tmem17 results in a ciliopathy, OFD6.

Notably, the *C5orf42* gene was previously thought to be the main cause of OFD6 [61], although this is now debated [62]; and a second gene related to *TMEM17—TMEM216* (*MKS2*)—has also been associated with OFD6 [63]. We therefore sought to identify additional genes that encode CEP-290-dependent TZ proteins that may be mutated in OFD6 patients. We identified individual families with missense mutations in two genes, *TMEM138* (homozygous p.M118L) and *TMEM231* (compound heterozygous p.P179A/p.P219L) (Figs 6D, 6E and S4; S2 Table). All mutant alleles are predicted to be pathogenic in that they affect conserved residues,

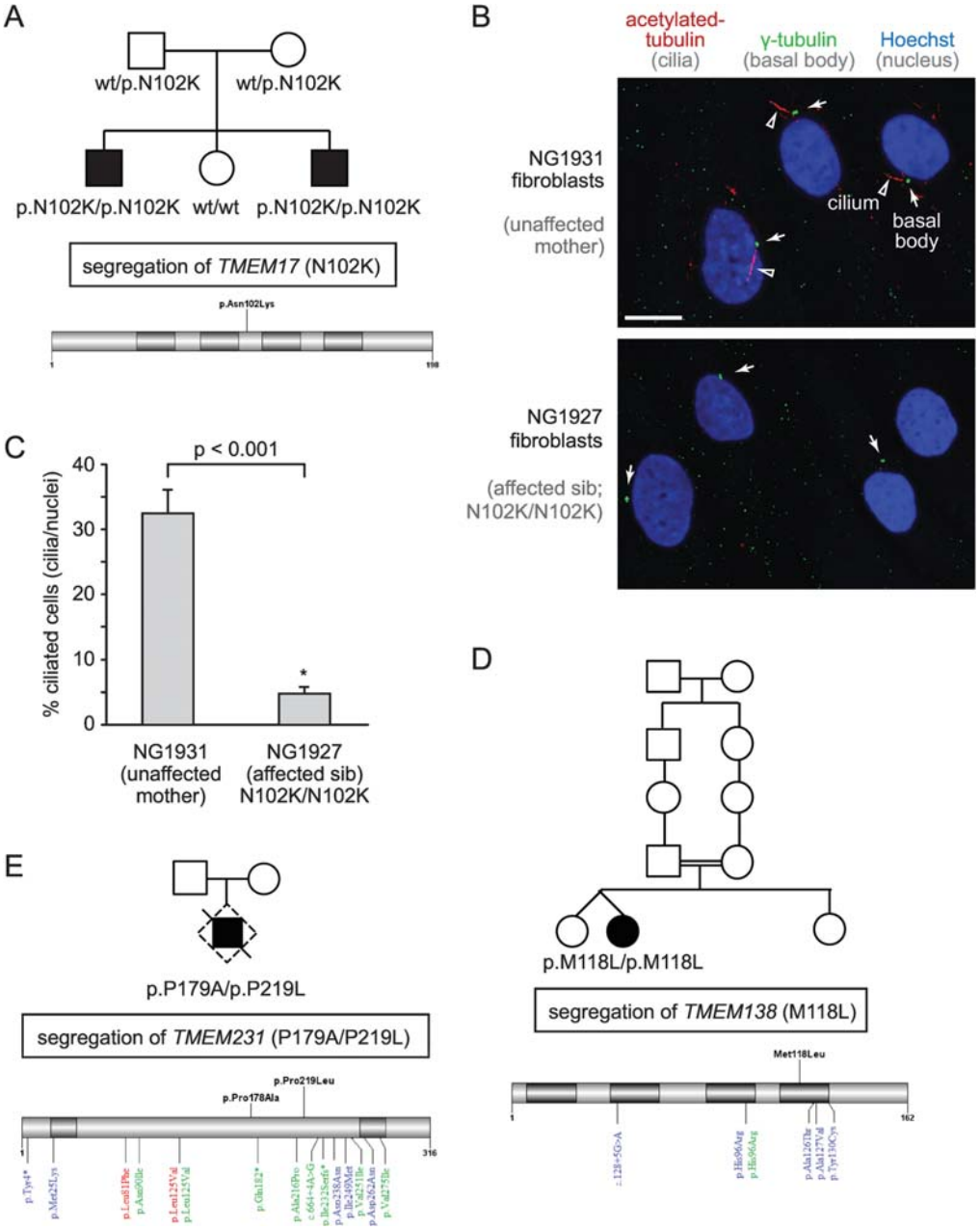

Fig 6. Potential expanded role for TZ proteins in ciliopathies and ciliogenesis: Tmem17, Tmem138, and Tmem231 are mutated in Oral-Facial-Digital type 6 (OFD6) syndrome families, and Tmem17 mutant fibroblast cells display ciliogenesis defects. (**A**) Pedigree of OFD6-affected individuals with a recessive missense mutation in *TMEM17* that affects a conserved amino acid (p.N102K). Schematic displays the position of the mutation within the *TMEM17* gene (NM_198276). (**B**) Fluorescence images of fibroblasts reveals full-length cilia in a healthy control but significantly fewer cilia in the OFD6-affected patient. Cilia and basal bodies are detected with antibodies against acetylated tubulin (arrowheads; red) and γ-tubulin (arrow; green), respectively, and nuclei are stained with Hoechst (blue). Scale bar, 10 μm. (**C**) Quantitation showing a ciliogenesis defect (cilia/nuclei) in Tmem17 (p.N102K/p.N102K)-mutant fibroblast cells compared to the unaffected control. Statistical significance inferred from Student's *t* test. (**D, E**) Family pedigrees of OFD6-affected individual with a recessive homozygous mutation in *TMEM138* (p.M118L) and compound heterozygous composite mutations in *TMEM231* (p.P179A/p.P219L). Schematics of *TMEM138* (NM_016464.4) and *TMEM231* (NM_001077416.2) gene structures, with previously identified mutations implicated in Oral-Facial-Digital type 3 (red), Joubert (blue), and Meckel (green) syndromes (bottom); new mutations are shown on top (black).

doi:10.1371/journal.pbio.1002416.g006

are not found in control cohorts or public databases, and fully segregate with the disease in the respective families (Fig 6D and 6E).

Collectively, our findings provide strong evidence that Tmem17 is a novel OFD6-associated protein that is necessary for ciliogenesis and suggest a potentially expanded spectrum of TZ-associated proteins (Tmem138, Tmem231) linked to this JBTS phenotype. Since not all genes linked to TZ-associated ciliopathies have been uncovered, we speculated that other TZ-associated ciliopathy proteins likely exist. Indeed, the Tmem17/Tmem216-related protein that emerged in tetrapods (S5A Fig), Tmem80, also represented an excellent, uncharacterised candidate. Using immunofluorescence analysis of wild-type and TZ mutant mouse embryonic fibroblasts, we show that mammalian Tmem80 localises to the TZ in a manner dependent on MKS module-associated proteins (Cc2d2a/Mks6, Tctn1, and Tctn2) (S5B Fig). Although we sequenced *TMEM80* (as well as *TMEM218*) in our patient cohort and did not find any pathogenic variants (S1 Table), we propose that both genes represent excellent candidates for being associated with OFD6 or other related ciliopathies, including MKS and JBTS.

Discussion

The TZ represents a major, evolutionarily conserved domain at the base of cilia whose supramolecular organisation and mechanism of function as a selective membrane diffusion barrier remains largely unknown. Our findings uncover *C. elegans* CEP-290 as an essential assembly factor for the genetically and biochemically defined "MKS" functional module. Loss of CEP-290 abrogates the TZ localisation of MKS module components, including that of a novel TZ protein we discovered, TMEM-218. Our genetic, cell biology, and in vivo functional assays reveal a critical role for CEP-290 in formation of the membrane diffusion barrier. Furthermore, the findings reported here—combined with our previous work and consistent with proteomic analyses—allow us to propose a plausible, comprehensive model for the assembly pathway of the TZ. In this model, MKS-5 (Rpgrip1L/Rpgrip1 orthologue) represents the foundation of two distinct assembly pathways for the MKS and NPHP modules, with the MKS pathway having CEP-290 as its core (Fig 7A).

MKS-5-Dependent Pathway for the Assembly of NPHP Transition Zone Module Components

One branch of the MKS-5-dependent pathway involves the assembly of the NPHP module, consisting of NPHP-1 and NPHP-4 (Fig 7B). Our work reveals that its assembly at the TZ can occur independently of CEP-290. Notably, when CEP-290 is disrupted, both NPHP-1 and NPHP-4, as well as MKS-5, colocalise within the proximal region of cilia, where the TZ is normally found (Fig 4A). This represents evidence for a functional association between the NPHP-1/NPHP-4 and MKS-5 proteins, consistent with the discovery by Sang and colleagues that mammalian Nphp1/Nphp4 proteins are observed in a complex with Mks5 (Nphp8/Rpgrip1L) [39]. Our results also suggest the possibility that MKS-5 together with NPHP-1/NPHP-4 represent the first components to establish a region at the base of cilia that give rise to the canonical TZ. Indeed, this MKS-5-NPHP-1-NPHP-4 domain is established in the *cep-290* mutant, which has no discernible TZ ultrastructure, including Y-links (Fig 3E). Given these findings, we speculate that MKS-5 and the NPHP module might help nucleate the assembly of Y-links—whose structural makeup may include CEP-290 and, perhaps, other associated proteins—as well as establish the position and appropriate length of the TZ. Hence, in the *cep-290* mutant, Y-links are absent, but the ciliary axoneme "foundation" for a TZ remains. Such an intriguing possibility will require further confirmation.

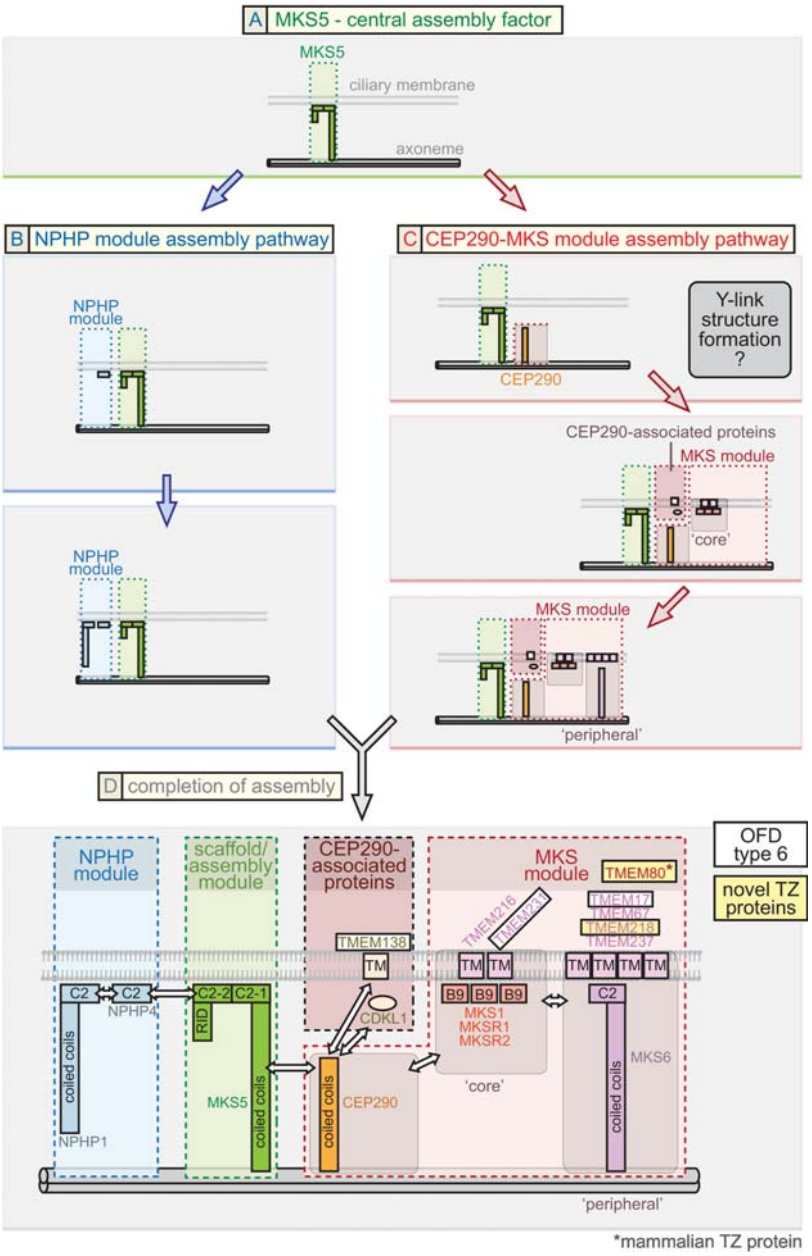

Fig 7. Proposed model for ciliary transition zone assembly. This model for the assembly of proteins at the TZ is based mostly on *C. elegans* data but is largely consistent with findings from other organisms, including mammals, *Chlamydomonas*, and *Drosophila*. (**A**) **MKS5: central assembly factor**. *C. elegans* MKS-5 (mammalian Rprgrip1L/Rpgrip1 orthologue) is essential for the assembly of all known TZ proteins (including CEP-290) and, therefore, may be the first component to establish the TZ. MKS-5 directs two genetically separable (distinct) assembly pathways, involving NPHP module proteins (blue arrows) as well as CEP-290, CEP-290-associated proteins, and MKS module proteins (red arrows). (**B**) **NPHP module assembly pathway**. Results from this study, other *C. elegans* findings, and mammalian work suggest that NPHP module proteins function together with MKS-5. We propose that the NPHP module, which can assemble at the TZ in the absence of CEP-290 (red pathway), assembles either before or in conjunction with the CEP-290-dependent pathway. NPHP-1 requires NPHP-4 for assembly at the TZ and is, therefore, positioned "downstream" in the pathway. (**C**) **CEP290-MKS module assembly pathway**. CEP-290 depends on MKS-5 for its TZ localisation and is, therefore, shown to assemble "downstream" in the pathway. Established MKS module proteins, including "core" components, require CEP-290 for TZ localization and are shown to assemble "downstream." Another subset of TZ proteins (CDKL-1, TMEM-138) depends on CEP-

290, but not MKS module proteins, for TZ localization (termed "CEP290-associated proteins"); their assembly is tentatively shown to occur simultaneously with the "core" MKS module components. TZ ultrastructure (Y-links) can be observed when "core" MKS or NPHP module proteins are disrupted, but not when CEP-290 is removed, and so we tentatively assign the formation of the Y-links at the CEP-290 assembly stage. More "peripheral" MKS module components require "core" MKS module components for TZ localisation and, hence, are proposed to assemble "downstream" of the core components. CEP-290, CEP-290-associated proteins, and MKS module ("core" and "peripheral") proteins are shown being incorporated at distinct steps of an assembly process, but the possibility of pre-assembly exists; for example, "core" MKS module proteins might pre-assemble prior to incorporation into the TZ, and "peripheral" proteins might interact with the "core" proteins prior to the assembly stage shown. (**D**) **Completion of TZ assembly and link to the ciliopathy OFD6**. MKS-5, the NPHP module, and the CEP-290-MKS module all combine to yield the complete TZ. A detailed spatial/topological/hierarchical map of TZ proteins, relative to the axoneme (double cylinders at bottom) and ciliary membrane (bilayer shown), is suggested. Pertinent domains shown in the TZ proteins include membrane-associated C2 and related B9 domains, transmembrane (TMEM) domains, and coiled coils. Major connections (potentially direct or indirect) between different modules or proteins are depicted with double-headed arrows and based on a combination of data from *C. elegans* and other organisms. Novel TZ proteins we uncovered in this study (*C. elegans* TMEM-218 and mammalian Tmem80) and proteins we provide evidence for being associated with OFD6 (Tmem17, Tmem138, Tmem231), are highlighted in yellow and white boxes, respectively.

doi:10.1371/journal.pbio.1002416.g007

MKS-5 and CEP-290-Dependent Pathway for the Assembly of MKS Module Transition Zone Components

The second branch of the MKS-5-dependent pathway first involves the assembly of CEP-290 (Fig 7C, first step) and then MKS module components, including "core" and "peripheral" TZ proteins, which are all predicted to be transmembrane proteins or have membrane associations via C2 or B9 domains (Fig 7C). Notably, *C. elegans* CEP-290 is specifically required for MKS module protein assembly, as it is not needed for NPHP module protein assembly at the TZ (Figs 3C and 4A). This is consistent with the finding that in *Drosophila*, NPHP module proteins are not present and Cep290 is required for the correct localisation of B9-domain MKS module proteins (Mks1, B9d1, and B9d2) [47]. Pull-down studies in mammalian cells are similarly consistent with an association between Cep290 and various MKS module proteins [40,64]. Also consistent with the above, Nphp4 is TZ-localised in the *Chlamydomonas* Cep290 mutant [46]. Finally, we observe a genetic interaction between *cep-290* and an NPHP module gene (*nphp-4*) that is required for ciliogenesis, but no interaction between *cep-290* and an MKS module gene (*mks-2*) (Fig 4E and 4F), precisely as with all known MKS module genes [25,28,31].

Given these findings, we propose that CEP-290 is specifically required for the assembly of the entire MKS module. Since MKS-1/MKSR-1/MKSR-2/MKS-2/TMEM-231 all depend on each other for their TZ localisation [25,28,36], we propose that these are "core" TZ proteins that assemble "downstream" of CEP-290 (Fig 7C, second step). This hierarchical definition implies that TMEM-17, TMEM-67 (MKS-3), TMEM-218, and TMEM-237 are more "peripheral," as they fail to assemble at the TZ when any "core" TZ protein is disrupted and do not themselves influence the localisation of the "core" TZ proteins (this study and refs. [25,28,30]). Assembly of "peripheral" TZ proteins is likely to be "downstream" of "core" TZ proteins (Fig 7C, third step). Together with these localisation studies, a genetic interaction between *cep-290* and a core NPHP module mutant (*nphp-4*), but not a core MKS module mutant (*mks-2*), argues for a clear positioning of CEP-290 as the core component of the MKS module (Fig 7C). Notably, our hierarchy for *C. elegans* CEP-290 differs from that of Schouteden and colleagues [65], who propose that the TZ protein occupies an entirely different (third) module.

CDKL-1 and TMEM-138 Are Assembled at the TZ in a CEP-290-Dependent and MKS Module-Independent Manner

Aside from MKS-5, which is the core assembly factor, all *C. elegans* TZ-localised proteins analysed heretofore can be assigned to an MKS or NPHP module. Here, we show that CDKL-1 (a novel TZ protein homologous to uncharacterised human CDKL family members) and TMEM-138 (whose human orthologue Tmem138 is mutated in JBTS [59]) both require CEP-290 for their TZ localisation (Fig 5C). Given our above-mentioned findings, this might suggest an association between CDKL-1/TMEM-138 and the MKS module. Intriguingly, however, neither protein is delocalised when core MKS module proteins are disrupted (see Fig 5A and Jensen et al. [30]). Moreover, the *tmem-138* and *cdkl-1* genes do not behave like MKS module genes, in that their respective mutants do not show a synthetic ciliogenesis defect with NPHP genes (Fig 5B and [30]). Altogether, these findings suggest that CEP-290 may itself organise two "branches" of an extended MKS module: one that harbours "canonical" MKS module proteins and another that consists of CDKL-1, TMEM-138, and, perhaps, additional TZ proteins (Fig 7D). Interestingly, CDKL-1 does not appear to influence cilium gate function but does influence cilium length (manuscript in preparation), the latter being similar to its CDKL5 homologues in *Chlamydomonas* [58,66]. Thus, CEP-290 may help organise a novel module that may be hierarchically and functionally different from the well-established NPHP and MKS modules. Interestingly, Lee and colleagues [59] provided some insights into possible behavioural differences between Tmem138 and Mks2, including with respect to Cep290. The Cdkl1/Cdkl2/Cdkl3/Cdkl4 family of kinases is largely unstudied, but a zebrafish knockdown study of Cdkl1 suggests ciliary-like phenotypes (including abrogated Hedgehog signalling) [67].

CEP-290 Is Required for Ciliary Gate Function and Assembly of Y-Links

Having ascertained that CEP-290 plays a central role in the assembly of the MKS module, we confirmed that it is also essential for the formation of a functional ciliary gate. Specifically, loss of CEP-290 causes two proteins (TRAM-1a and RPI-2) normally found at the periciliary membrane (just outside of the cilium) to accumulate abnormally within the organelle (Fig 3C). This "leakiness" has been observed with most MKS and NPHP module mutants and is also consistent with changes to ciliary composition in the *Chlamydomonas* Cep290 mutant [48]. Furthermore, we show that ARL-13 enters the TZ and accumulates at the periciliary membrane in the *cep-290* mutant (Fig 3D), which represents additional evidence that CEP-290 helps form a functional TZ membrane diffusion barrier.

Previous TEM analyses of *C. elegans* TZ gene mutants revealed that disruption of one or more MKS module component(s), or NPHP module component(s), does not abrogate the formation of Y-links (with the exception of *nphp-4*, which has modest defects [29]). However, various MKS-NPHP double mutants, such as *mks-2;nphp-4* or *mksr-1;nphp-4*, result in the apparently complete loss of Y-shaped structures [25,28,36]. Here we show that disruption of CEP-290 alone is sufficient to eliminate Y-links (Fig 3E). This *cep-290* phenotype is striking in that it influences to a great extent only the TZ region, wherein Y-links are absent. Yet, as discussed above, in the *cep-290* mutant, the most "central" assembly factor, MKS-5, together with the NPHP module, are present at the base of the cilium, in the same position expected for the TZ. Hence, removal of MKS-5 may cause a loss of Y-link structures [30], potentially because CEP-290 itself cannot assemble at the TZ.

Based on this reasoning, we suggest in our model for the assembly pathway of the TZ that Y-link structures are established at the step at which CEP-290 assembles at the TZ (Fig 7C, first step). This inference is based on the fact that Y-link formation is not impaired when one or more "core" or "peripheral" MKS module proteins are disrupted, which likely results in all

MKS module proteins being mislocalised [25,28,30,36]. Although the MKS module proteins are likely a part of the Y-links, they are all membrane-associated (using transmembrane of C2/B9 domains) and, therefore, may be more closely linked to the formation of the ciliary necklace (intramembraneous "beads" [68]) rather than the central/prominent region of the Y-shaped structure. We speculate that although Y-links are missing in the *C. elegans* TZ of the *cep-290* mutant, similar to that found by Schouteden et al. [65] and in the *Chlamydomonas* Cep290 mutant [48], structural proteins other than CEP-290 might make up these prominent Y-shaped structures.

Tmem218 and Tmem80 Represent Novel TZ Proteins that May Be Ciliopathy-Associated

Virtually all genes encoding TZ proteins are linked to one or more ciliopathies, namely MKS, JBTS, SLNS, Leber Congenital Amaurosis, and NPHP [21,22,26,27]. Recently, disruption of Tmem218 in a mouse mutagenesis screen was found to cause retinal degeneration and NPHP phenotypes that resemble SLNS [50]. While the murine protein was not characterised, we show that the nematode orthologue (TMEM-218) localises to the TZ, as with other ciliopathy-associated TZ proteins (Fig 1B). Furthermore, TMEM-218 can be positioned genetically and hierarchically within the MKS module, likely as a peripheral component, similar to MKS-3 (Tmem67), JBTS-14 (Tmem237), and MKS-6 (Cc2d2a), which are all ciliopathy-associated (Figs 1D, 2D and 7). In addition, we show for the first time that the unchracterised Tmem17/Tmem216-related mammalian protein, Tmem80, localises to the TZ in ciliated mouse embryonic fibroblasts (S5 Fig). Notably, Tmem80 depends on at least three known TZ-localised ciliopathy proteins (Tctn1, Tctn2, and Mks6/Cc2d2a) for its localisation, positioning it within a growing functional network of TZ proteins.

Hence, both Tmem218 and Tmem80 represent prime candidates for being implicated in one or more of the above ciliopathies or OFD6, as discussed below. Although sequencing of *TMEM80* and *TMEM218* in a large cohort of patients with JBTS-related phenotypes did not identify pathogenic mutations, the possibility that such mutations represent a rare cause of OFD6 cannot be excluded at present, especially since the number of OFD6 patients in our cohort is quite low due to the rarity of this condition (17 probands).

CEP290-Dependent Proteins May Be Linked to OFD6

Aside from Tmem218 and Tmem80, one of the few TZ proteins that remains to be linked to one or more ciliopathies is Tmem17. Here, we present evidence that a variation in an evolutionarily conserved residue of Tmem17 causes OFD6 syndrome. The mutation (N102K), not present in control cohorts, is predicted to be deleterious and segregates specifically with affected siblings in the family (Fig 6A). Importantly, we show that patient fibroblast cells with the pN102K mutation display a prominent ciliogenesis defect compared to control cells (Fig 6B and 6C). Notably, many TZ proteins, including B9d1, Tmem67/Mks3, Tmem231, Tmem237, Cc2d2a/Mks6, Cep290, and Tectonics (Tctn1 and Tctn2) are known to influence ciliogenesis in mammalian cells [28,38,40,69], consistent with our findings. Although only present in single families, we also provide evidence that the human orthologues of two additional proteins that require CEP-290 for their TZ localisation in *C. elegans*, Tmem138 and Tmem231, are also mutated in OFD6 (Figs 6D, 6E and S4). Uncovering additional families with mutations in *TMEM17*, *TMEM138*, and *TMEM231* will be important to conclusively assign these genes to OFD6. Finally, what TZ/ciliary defect may result in OFD6 rather than other related ciliopathies, including OFD3, remains unclear. For example, Tmem231 is linked to OFD3 as well as MKS [31].

Conclusions

Understanding what components make up the TZ and how they assemble into different functional modules represent important goals for shedding light on how the TZ forms during ciliogenesis and acts as a membrane diffusion barrier. In addition to uncovering *C. elegans* TMEM-218 and mammalian Tmem80 as novel TZ proteins, our work illuminates the central roles of MKS-5 and CEP-290 in the assembly of NPHP and MKS modules, and of TZ ultrastructure (Fig 7). Aside from CEP-290, which proteins constitute the Y-links remains an open question. How at least two TZ proteins (CDKL-1 and TMEM-138) assemble in a CEP-290-dependent but MKS module-independent manner is unclear, but hints at the existence of a TZ module that is distinct from the MKS and NPHP modules. It will be interesting to confirm and further investigate in mammalian cells our overall model for TZ assembly (Fig 7) as well as obtain evidence for the involvement of the novel TZ proteins we uncovered (Tmem218 and Tmem80) in ciliopathies.

Materials and Methods

Preparation of *C. elegans* Transgenic Constructs

The translational construct for the *cep-290* (Y47G6A.17) gene was generated by fusing the *bbs-8* promoter (941 bp) to the cDNA of *cep-290* and EGFP together with the *unc-54* 3' UTR. The translational construct for *tmem-218* (T23E7.5) was generated by fusing its native promoter (2,092 bp upstream of the start codon) and all exons and introns to EGFP together with the *unc-54* 3' UTR. For *cdkl-1* (Y42A5A.4), we generated two constructs. One was made by fusing the *bbs-8* promoter (941 bp) to the genomic region of *cdkl-1* (isoform C) and EGFP with the *unc-54* 3' UTR. The other was generated by fusing its native promoter (1,869 bp) and all exons and introns (*cdkl-1* isoform A) to EGFP with the *unc-54* 3' UTR. Transgenic lines were generated as reported previously [51].

C. elegans Strain Maintenance, Construction, and Imaging

All *C. elegans* strains used in this study (S3 Table) were maintained and cultured at 20°C. Those carrying mutations in *C. elegans mks-5(tm3100)*, *tmem-231(tm5963)*, *cdkl-1(tm4182)*, *cep-290(gk415029)*, *tmem-138(tm5624)*, *nphp-1(ok500)*, and *nphp-4(tm925)* were obtained from the *C. elegans* Gene Knockout Consortium or National Bioresource Project and outcrossed to wild-type (N2) a minimum of five times. Standard mating procedures were used to introduce GFP-tagged protein constructs into different genetic backgrounds. Genotyping the various mutants was done by single-worm PCR. Confocal microscopy was used to assess the subcellular localisation of the various fluorescent reporters for both the wild-type and each TZ mutant strain, as indicated. A minimum of 50 animals for each strain were analysed for all reported mislocalisation phenotype. We obtained a *cep-290(gk415029)* allele, which has a G→A nonsense mutation at nucleotide 3989 in the *cep-290* gene. The *gk415029* allele is likely to be null, as it contains a stop codon 36.7% into the coding region.

The mutagenesis protocol for generating a *tmem-218* (T23E7.5) allele was modified from Huang et al. (2011) using the ttTi20388 allele [70], which contains a Mos1 insertion in the intron of *tmem-218*. Sequencing of the *tmem-218(nx114)* allele revealed a 2721 bp deletion plus 4 bp insertion that removes the entire *tmem-218* coding region. Before analysis, *tmem-218 (nx114)* worms were outcrossed six times to wild type (N2).

C. elegans Dye-Filling Assay for Assessing Intact Ciliary Structure

C. elegans were exposed to the lipophilic dye, DiI, to assay for uptake of dye through intact, environmentally exposed ciliary structures, as previously described [25]. Stained worms were imaged with fluorescence microscopy, and intensities were analysed with ImageJ.

Transmission Electron Microscopy of *C. elegans* Amphid Cilia

Young adult worms were fixed, sectioned, and imaged as described previously [71], with the exception that worms were fixed overnight at 4°C in 2.5% gluteraldehyde, 1% paraformaldehyde in Sørensen's buffer.

Analysis of CEP-290 Subcellular Localisation

CEP-290::GFP localisation in wild-type or *mks-5* mutant animals was assessed relative to the position of the basal body-transition fibres marked by the XBX-1::tdTomato IFT protein marker. Distance (in μm) from the peak fluorescence value of XBX-1 (middle of the basal body-transition fibres) to the first CEP-290 pixel above 0.5 (relative intensity) is defined here as the start of the TZ. The size of the TZ is the length (in μm) from the first pixel of CEP-290 fluorescence over 0.5 to the last pixel over 0.5.

CEP-290 Localisation Volume Analysis

All images were taken on a spinning-disc confocal of phasmid (PHA and PHB) cilia, as described above, with the same settings for the same exposure time (600 ms). CEP-290::GFP localisation volumes were detected by the Volocity software "find object" program with an automatic threshold offset of 200. *p*-values were calculated by Dunn Kruskal-Wallis multiple comparison (Holm-Sidak method).

Quantification of Transgene Expression Levels in Phasmid Neurons

Anaesthetized L4 stage transgenic worms in 10 mM levamisole were prepared for spinning-disc confocal microscopy. Fluorescence in at least 20 pairs of cell bodies of PHA and PHB neurons from strains expressing TMEM-218::GFP, TMEM-231::GFP, or CDKL-1::GFP (isoforms A and C) was visualized and analyzed using Volocity software (Perkin Elmer). To obtain relative fluorescence intensity for each strain, the background fluorescence signal was subtracted and the absolute fluorescence intensity measurements were divided by the median fluorescence intensity in wild type. The relative fluorescence intensity data were plotted using Box and Dot plots in R. The assessment of normal distribution of each dataset was done using the Shapiro–Wilk test. The *p*-value of the dataset that shows normal distribution was obtained by Tukey multiple comparisons of means of 95% family-wise confidence level. The *p*-value of the dataset that shows non-normal distribution was calculated using the Kruskal-Wallis test; Dunn Kruskal-Wallis multiple comparison (Holm-Sidak method) was used for comparing more than two groups. Results are presented in S1D–S1G Fig.

Quantitative RT-PCR to measure CEP-290::GFP and *cep-290* transcript levels was performed as previously described [68] using iTaq Universal SYBR green supermix (Biorad), an Applied Biosystems StepOne real-time PCR system, SuperScript III reverse transcriptase (Invitrogen), and the following primers: control, *tba-1* forward: tcaacactgccatcgccgcc and reverse: tccaagcgagaccaggcttcag, GFP forward: atggtgttcaatgcttctcg and reverse: tgtagttcccgtcatctttga, and *cep-290* forward: tgctcagcgagttgaatagg and reverse: aagcttcccaatttgctcat.

Screening of Ciliopathy Patients

The patient cohort included about 330 probands with JBTS, selected by the unique neuroimaging criterion of the molar tooth sign (MTS), including 17 probands with the OFD6 phenotype. For each patient, a standardised clinical questionnaire completed by the referring clinician provided detailed information on the phenotypic spectrum and organ involvement. Written

informed consent was obtained from all families, and the study was approved by the local ethics committee.

All patients underwent simultaneous target sequencing of 100 genes (including genes known to cause human ciliopathies and candidate genes derived from functional studies) on a Solid 5500xL platform (Life Technologies). Probes were designed to cover all exons, with splice-site junctions and at least 25 bp of flanking introns. Bioinformatic analyses were conducted to filter data and remove low-quality calls as well as variants with a frequency of >1% in public databases dbSNP ver.141 (http://www.ncbi.nlm.nih.gov/SNP/) and Exome Variant Server (http://evs.gs.washington.edu/EVS/) or found in internal controls. The identified mutation in the *TMEM17* gene (NM_198276) was validated using bidirectional Sanger sequencing using the Big Dye Terminator chemistry (Life Technologies) and was searched against public databases dbSNP and Exome Variant Server. Potential pathogenicity was predicted using prediction software PolyPhen-2 ver.2.2.2 (http://genetics.bwh.harvard.edu/pph2/) and SIFT (http://sift.jcvi.org/). Nomenclature was assigned according to the Human Genome Variant Society (http://www.hgvs.org/mutnomen/). Sanger sequencing was also used to birectionally sequence all coding exons and exon–intron boundaries of *TMEM218* in a subset of 160 Joubert patients who had tested negative at the previous NGS experiment.

Probands from two large families diagnosed with OFD6 directly underwent whole exome sequencing. Three micrograms of genomic DNA per individual were subjected to whole-exome capture and sequencing using the SureSelect Human All Exon V5 kit (Agilent). The resulting libraries were sequenced on a HiSeq 2000 (Illumina) as paired-end 76 bp reads. BAM files were aligned to a human genome reference sequence (GRCh37/hg19) using BWA (Burrows-Wheeler Aligner; v0.6.2). All aligned read data were subject to the following steps: (1) duplicate paired-end reads were removed by Picard 1.77, and (2) indel realignment and (3) base quality score recalibration were done on Genome Analysis Toolkit (GATK; v2.1–10). Variants with a quality score >30 and alignment quality score >20 were annotated with SeattleSeq SNP Annotation (http://snp.gs.washington.edu/SeattleSeqAnnotation138/). Rare variants present at a frequency above 1% in dbSNP 138 (http://www.ncbi.nlm.nih.gov/SNP/) and the NHLBI GO Exome Sequencing Project or present from 312 exomes of unaffected individuals were excluded (http://evs.gs.washington.edu/EVS/). To improve exome analysis, data are crossreferenced with a list of known cilia-related genes from Ciliome Database, Cildb v2.1 (http://cildb-archive.cgm.cnrs-gif.fr/) and transcriptomic study of cilia [72]. The analyses were focused on genes with homozygous variants in consanguineous families and with two heterozygous variants in other cases, prioritising (1) genes associated with human pathology in ClinVar (http://www.ncbi.nlm.nih.gov/clinvar/) or HGMD databases (http://www.hgmd.cf.ac.uk/ac/index.php), (2) cilia-related genes, and (3) other non cilia-related genes. Candidate variants and parental segregation were confirmed by DNA PCR/Sanger sequencing using targeted primers (S5 and S6 Tables) and following usual protocols.

Ciliogenesis Assays for Human Fibroblast Cells

Fibroblasts from one patient homozygous for *TMEM17* mutations and from his healthy mother (heterozygous carrier) were plated on coverslips and cultured in DMEM with 20% FBS until they were 80% confluent after being starved for 24 h in DMEM 0.1% FBS to allow cilia formation. Cells were fixed in cold methanol, and coverslips were rinsed and blocked in PBS with 10% BSA prior to incubation with antibodies. Fixed cells were incubated with the following antibodies: acetylated-α-tubulin (1:1000, SIGMA), γ-tubulin (1:500, SIGMA) overnight followed by incubation with goat anti-mouse Alexa fluor 555 (1:3000), and goat anti-rabbit Alexa fluor 488 (1:3000). Nuclei were stained with Hoechst (Invitrogen). Images were captured with

a confocal microscopy (C2 Confocal Microscopy System), by using the laser lines 488 nm (green) or the 561 nm (red) and a 60X 1.4 NA Plan Apo objective (Nikon Corporation) controlled by NIS Element AR 4.13.04 software. To count cilia, acetylated-α-tubulin and γ-tubulin positive cilia were manually counted within 15 images for each phenotype in at least three independent experiments. Variables were analysed by Student's *t* test, and a value of $p < 0.05$ was deemed statistically significant. Values are expressed as standard error (S.E.).

Immunofluorescence Analyses in Mouse Embryonic Fibroblasts

Tctn1, Tctn2, Cc2d2a, Tmem67, B9d1, and Tmem231 mouse embryonic fibroblasts (MEFs) have already been described [31,40,73]. For Tmem80 immunofluorescence, cells were plated on glass coverslips, grown to confluency in DMEM+10%FBS, and starved for 48 h in Opti-MEM. Cells were then fixed for 90 s at -20°C in freezer-cold methanol, incubated for 30 min at RT in block (PBS+0.1%Triton-X100+2%BSA+1% donkey serum), and incubated overnight at 4°C in block containing these primary antibodies: mouse anti-Tmem80 (Origene, TA501452, dilution 1:200), rabbit anti-detyrosinated tubulin (Millipore, AB3201, dilution 1:500), and goat anti-γ-tubulin (Santa Cruz Biotechnology, sc-7396, dilution 1:200). Coverslips were then rinsed thrice in PBS, incubated 1 h at RT with block containing DAPI and AlexaFluor-conjugated donkey secondary antibodies, rinsed twice more in PBS, mounted on slides using gelvatol, and visualised in a Leica TCS SPE confocal microscope.

Supporting Information

S1 Fig. Expression analyses and rescue of CEP-290 TZ localisation by full-length MKS-5 and coiled coil region of MKS-5. (**A**) Analysis of *cep-290* transcript abundance in wild type and *cep-290(gk415029)*. Consistent with degradation by nonsense-mediated mRNA decay (NMD) [74], we see an approximately 5-fold reduction of *cep-290* transcript level in the mutant. (**B**) Relative levels of CEP-290::GFP transcripts measured by quantitative qPCR are similar between wild-type and different TZ mutants, as indicated. (**C**) CEP-290::GFP localisation volume characteristics (in μm^3) near or at the TZ in wild-type, *mks-5*, or MKS-5 rescue strains (*mks-5* mutant expressing full length MKS-5 or the MKS-5 coiled coil region). Results are shown as box plots, and * denotes statistically different volume. (**D-G**) Fluorescence intensity measurements of different GFP-tagged fusion proteins (TMEM-218::GFP, TMEM-231::GFP, CDKL-1A::GFP and CDKL-1C::GFP) in phasmid cell bodies of wild-type and mutant strains (as indicated) shown as box and dot plots. All transgenes are expressed at similar levels, although a few are statistically different (indicated by asterisk). *, $p < 0.05$ compared to wild-type (TMEM-218::GFP and CDKL-1A::GFP, Kruskal-Wallis test, Dunn's method with Holm-Sidak adjustment; TMEM-231::GFP, Kruskal-Wallis test; CDKL-1C::GFP, Tukey's test).
(EPS)

S2 Fig. Rescue of the dye-filling phenotype of the *cep-290;nphp-4* double mutant strain with the wild-type CEP-290::GFP translational reporter. *cep-290;nphp-4* animals fail to uptake the lipophilic dye DiI, a phenotype rescued by low-level expression of the CEP-290::GFP construct. Shown is a transgenic animal that expresses the reporter (see arrows and inset) and can uptake the dye, while a nontransgenic sibling cannot uptake the dye (dotted circles).
(EPS)

S3 Fig. Genotyping of family members with Tmem17 homozygous mutation in OFD6-affected individuals and evolutionary conservation of the mutated Tmem17 residue. (**A**) DNA Sanger sequencing results showing segregation of the homozygous C-to-A mutation (c.306C>A) causing the amino acid variation p.N102K/p.N102K. (**B**) Partial amino acid

sequence alignment of Tmem17 and related proteins (Tmem80, Tmem216) in humans and divergent species showing the region encompassing the N102K mutated residue.
(EPS)

S4 Fig. *TMEM138* and *TMEM231* patient mutations and *TMEM231* foetus phenotypes. (**A**) Clinical pictures of the foetus with *TMEM231* mutations at 21 wk of gestation, with asymmetric face, hypertelorism, down-slanting palpebral fissures, micrognathia, unilateral left cleft lip (a,e), hand left postaxial polydactyly (b), feet bilateral postaxial polydactyly (c,d) and normal skeletal X-rays excepting for polydactyly (f). (**B**) DNA Sanger chromatograms of the homozygous *TMEM138* c.352A>T (pM118L) mutation and the heterozygous composite *TMEM231* c656C>T / c.532C>G (pP219L / p.P178A) mutations. pest–people environment science technology SCEPTre.
(EPS)

S5 Fig. Mammalian Tmem80 is a novel transition zone protein. (**A**) Phylogenetic distribution of Tmem17 superfamily proteins. While Tmem17 and a Tmem216/Tmem80-related protein are ubiquitously found across ciliated eukaryotes, only tetrapods (e.g., frogs, chickens, mammals) possess Tmem80-related orthologues. Bd, *Batrachochytrium dendrobatidis*; Cr, *Chlamydomonas reinhardtii*; Tb, *Trypanosoma brucei*, Pt, *Paramecium tetraurelia*; Ce, *Caenorhabditis elegans*; Dm, *Drosophila melanogaster*; Sp, *Strongylocentrotus purpuratus*; Od, *Oikopleura diodica*; Dr, *Danio rerio*; Gg, *Gallus gallus*; Mm, *Mus musculus*; Hs, *Homo sapiens*. (**B**) Immunofluorescence localisation of Tmem80 (red) in wild-type, homozygous mutant, or heterozygous mutant mouse embryonic fibroblasts (MEFs) for the indicated genes. Tmem80 transition zone localisation depends on several established ciliopathy-associated TZ proteins (Tctn1, Tctn2, Cc2d2a/Mks6). Antibodies against γ-tubulin (green) and detyrosinated tubulin (blue) mark the basal body and ciliary axoneme, respectively.
(EPS)

S1 Table. Target sequence analysis of 101 known and candidate ciliopathy genes uncovers a homozygous mutation in *TMEM17*[1].
(DOCX)

S2 Table. Genotypes and detailed clinical features of patients with mutations in *TMEM17*, *TMEM138*, and *TMEM231*.
(DOCX)

S3 Table. List of *Caenorhabditis elegans* strains used in this study.
(DOCX)

S4 Table. Target-sequencing statistics and identification of *TMEM17*.
(DOCX)

S5 Table. Whole-exome statistics and identification of *TMEM138* and *TMEM231*.
(DOCX)

S6 Table. Primer sequences for PCR and Sanger sequencing of TMEM17, TMEM138, and TMEM231 regions with mutations.
(DOCX)

Acknowledgments

We thank CGC for the distribution of several *C. elegans* strains. Mos mutant strains were generated by the Ewbank and Segalat labs as part of the NEMAGENETAG project funded by the

European Community. They were distributed by M. Carre-Pierrat at the UMS 3421, supported by the CNRS.

Author Contributions

Conceived and designed the experiments: MRL CL KP VLJ OEB FRGG EMV JFR CTR. Performed the experiments: CL VLJ KP JK FRGG MR RDM ALB DG BD EL JBR LF. Analyzed the data: CL VLJ KP JK OEB MRL EMV JFR CTR FRGG. Contributed reagents/materials/analysis tools: MRL OEB JFR EMV CTR. Wrote the paper: MRL CL KP VLJ OEB JFR EMV CTR.

References

1. Carvalho-Santos Z, Azimzadeh J, Pereira-Leal JB, Bettencourt-Dias M (2011) Evolution: Tracing the origins of centrioles, cilia, and flagella. J Cell Biol 194: 165–175. doi: 10.1083/jcb.201011152 PMID: 21788366
2. Praveen K, Davis EE, Katsanis N (2015) Unique among ciliopathies: primary ciliary dyskinesia, a motile cilia disorder. F1000Prime Rep 7: 36. doi: 10.12703/P7-36 PMID: 25926987
3. Inglis PN, Ou G, Leroux MR, Scholey JM (2007) The sensory cilia of Caenorhabditis elegans. WormBook. doi: 10.1895/wormbook.1.126.2 http://www.wormbook.org/chapters/www_ciliumbiogenesis.2/ciliumbiogenesis.html
4. Oh EC, Katsanis N (2012) Cilia in vertebrate development and disease. Development 139: 443–448. doi: 10.1242/dev.050054 PMID: 22223675
5. Mukhopadhyay S, Rohatgi R (2014) G-protein-coupled receptors, Hedgehog signaling and primary cilia. Semin Cell Dev Biol 33: 63–72. doi: 10.1016/j.semcdb.2014.05.002 PMID: 24845016
6. Nachury MV (2014) How do cilia organize signalling cascades. Philos Trans R Soc Lond B Biol Sci 369: pii: 20130465
7. Johnson JL, Leroux MR (2010) cAMP and cGMP signaling: sensory systems with prokaryotic roots adopted by eukaryotic cilia. Trends Cell Biol 20: 435–444. doi: 10.1016/j.tcb.2010.05.005 PMID: 20541938
8. May-Simera HL, Kelley MW (2012) Cilia, Wnt signaling, and the cytoskeleton. Cilia 1: 7. doi: 10.1186/2046-2530-1-7 PMID: 23351924
9. Valente EM, Rosti RO, Gibbs E, Gleeson JG (2014) Primary cilia in neurodevelopmental disorders. Nat Rev Neurol 10: 27–36. doi: 10.1038/nrneurol.2013.247 PMID: 24296655
10. Hurd TW, Hildebrandt F (2011) Mechanisms of nephronophthisis and related ciliopathies. Nephron Exp Nephrol 118: e9–14. doi: 10.1159/000320888 PMID: 21071979
11. Brown JM, Witman GB (2014) Cilia and Diseases. Bioscience 64: 1126–1137. PMID: 25960570
12. Fry AM, Leaper MJ, Bayliss R (2014) The primary cilium: guardian of organ development and homeostasis. Organogenesis 10: 62–68. doi: 10.4161/org.28910 PMID: 24743231
13. Sung CH, Leroux MR (2013) The roles of evolutionarily conserved functional modules in cilia-related trafficking. Nat Cell Biol 15: 1387–1397. doi: 10.1038/ncb2888 PMID: 24296415
14. Pedersen LB, Christensen ST (2012) Regulating intraflagellar transport. Nat Cell Biol 14: 904–906. doi: 10.1038/ncb2569 PMID: 22945257
15. Blacque OE, Reardon MJ, Li C, McCarthy J, Mahjoub MR et al. (2004) Loss of C. elegans BBS-7 and BBS-8 protein function results in cilia defects and compromised intraflagellar transport. Genes Dev 18: 1630–1642. PMID: 15231740
16. Sedmak T, Wolfrum U (2011) Intraflagellar transport proteins in ciliogenesis of photoreceptor cells. Biol Cell 103: 449–466. doi: 10.1042/BC20110034 PMID: 21732910
17. Williams CL, McIntyre JC, Norris SR, Jenkins PM, Zhang L et al. (2014) Direct evidence for BBSome-associated intraflagellar transport reveals distinct properties of native mammalian cilia. Nat Commun 5: 5813. doi: 10.1038/ncomms6813 PMID: 25504142
18. Taschner M, Bhogaraju S, Lorentzen E (2012) Architecture and function of IFT complex proteins in ciliogenesis. Differentiation 83: S12–22. doi: 10.1016/j.diff.2011.11.001 PMID: 22118932
19. Scholey JM (2008) Intraflagellar transport motors in cilia: moving along the cell's antenna. J Cell Biol 180: 23–29. doi: 10.1083/jcb.200709133 PMID: 18180368
20. Baker K, Beales PL (2009) Making sense of cilia in disease: the human ciliopathies. Am J Med Genet C Semin Med Genet 151C: 281–295. doi: 10.1002/ajmg.c.30231 PMID: 19876933

21. Reiter JF, Blacque OE, Leroux MR (2012) The base of the cilium: roles for transition fibres and the transition zone in ciliary formation, maintenance and compartmentalization. EMBO Rep 13: 608–618. doi: 10.1038/embor.2012.73 PMID: 22653444

22. Garcia-Gonzalo FR, Reiter JF (2012) Scoring a backstage pass: Mechanisms of ciliogenesis and ciliary access. J Cell Biol 197: 697–709. doi: 10.1083/jcb.201111146 PMID: 22689651

23. Fisch C, Dupuis-Williams P (2011) Ultrastructure of cilia and flagella—back to the future! Biol Cell 103: 249–270. doi: 10.1042/BC20100139 PMID: 21728999

24. Szymanska K, Johnson CA (2012) The transition zone: an essential functional compartment of cilia. Cilia 1: 10. doi: 10.1186/2046-2530-1-10 PMID: 23352055

25. Williams CL, Li C, Kida K, Inglis PN, Mohan S et al. (2011) MKS and NPHP modules cooperate to establish basal body/transition zone membrane associations and ciliary gate function during ciliogenesis. J Cell Biol 192: 1023–1041. doi: 10.1083/jcb.201012116 PMID: 21422230

26. Valente EM, Dallapiccola B, Bertini E (2013) Joubert syndrome and related disorders. Handb Clin Neurol 113: 1879–1888. doi: 10.1016/B978-0-444-59565-2.00058-7 PMID: 23622411

27. Szymanska K, Hartill VL, Johnson CA (2014) Unraveling the genetics of Joubert and Meckel-Gruber syndromes. J Pediatr Genet 3: 65–78. PMID: 25729630

28. Huang L, Szymanska K, Jensen VL, Janecke AR, Innes AM et al. (2011) TMEM237 is mutated in individuals with a Joubert syndrome related disorder and expands the role of the TMEM family at the ciliary transition zone. Am J Hum Genet 89: 713–730. doi: 10.1016/j.ajhg.2011.11.005 PMID: 22152675

29. Lambacher NJ, Bruel AL, van Dam TJ, Szymańska K, Slaats GG et al. (2015) TMEM107 recruits ciliopathy proteins to subdomains of the ciliary transition zone and causes Joubert syndrome. Nat Cell Biol - doi: 10.1038/ncb3273 [Epub ahead of print]

30. Jensen VL, Li C, Bowie RV, Clarke L, Mohan S et al. (2015) Formation of the transition zone by Mks5/Rpgrip1L establishes a ciliary zone of exclusion (CIZE) that compartmentalises ciliary signalling proteins and controls PIP2 ciliary abundance. EMBO J 34: 2537–2556. doi: 10.15252/embj.201488044 PMID: 26392567

31. Roberson EC, Dowdle WE, Ozanturk A, Garcia-Gonzalo FR, Li C et al. (2015) TMEM231, mutated in orofaciodigital and Meckel syndromes, organizes the ciliary transition zone. J Cell Biol 209: 129–142. doi: 10.1083/jcb.201411087 PMID: 25869670

32. Yee LE, Garcia-Gonzalo FR, Bowie RV, Li C, Kennedy JK et al. (2015) Conserved Genetic Interactions between Ciliopathy Complexes Cooperatively Support Ciliogenesis and Ciliary Signaling. PLoS Genet 11: e1005627. doi: 10.1371/journal.pgen.1005627 PMID: 26540106

33. Winkelbauer ME, Schafer JC, Haycraft CJ, Swoboda P, Yoder BK (2005) The C. elegans homologs of nephrocystin-1 and nephrocystin-4 are cilia transition zone proteins involved in chemosensory perception. J Cell Sci 118: 5575–5587. PMID: 16291722

34. Jauregui AR, Nguyen KC, Hall DH, Barr MM (2008) The Caenorhabditis elegans nephrocystins act as global modifiers of cilium structure. J Cell Biol 180: 973–988. doi: 10.1083/jcb.200707090 PMID: 18316409

35. Williams CL, Winkelbauer ME, Schafer JC, Michaud EJ, Yoder BK (2008) Functional Redundancy of the B9 Proteins and Nephrocystins in *C. elegans* Ciliogenesis. Mol Biol Cell 19: 2154–2168. doi: 10.1091/mbc.E07-10-1070 PMID: 18337471

36. Bialas NJ, Inglis PN, Li C, Robinson JF, Parker JD et al. (2009) Functional interactions between the ciliopathy-associated Meckel syndrome 1 (MKS1) protein and two novel MKS1-related (MKSR) proteins. J Cell Sci 122: 611–624. doi: 10.1242/jcs.028621 PMID: 19208769

37. Diener DR, Lupetti P, Rosenbaum JL (2015) Proteomic analysis of isolated ciliary transition zones reveals the presence of ESCRT proteins. Curr Biol 25: 379–384. doi: 10.1016/j.cub.2014.11.066 PMID: 25578910

38. Chih B, Liu P, Chinn Y, Chalouni C, Komuves LG et al. (2012) A ciliopathy complex at the transition zone protects the cilia as a privileged membrane domain. Nat Cell Biol 14: 61–72.

39. Sang L, Miller JJ, Corbit KC, Giles RH, Brauer MJ et al. (2011) Mapping the NPHP-JBTS-MKS protein network reveals ciliopathy disease genes and pathways. Cell 145: 513–528. doi: 10.1016/j.cell.2011.04.019 PMID: 21565611

40. Garcia-Gonzalo FR, Corbit KC, Sirerol-Piquer MS, Ramaswami G, Otto EA et al. (2011) A transition zone complex regulates mammalian ciliogenesis and ciliary membrane composition. Nat Genet 43: 776–784. doi: 10.1038/ng.891 PMID: 21725307

41. Roepman R, Wolfrum U (2007) Protein networks and complexes in photoreceptor cilia. Subcell Biochem 43: 209–235. PMID: 17953396

42. Lu Q, Insinna C, Ott C, Stauffer J, Pintado PA et al. (2015) Early steps in primary cilium assembly require EHD1/EHD3-dependent ciliary vesicle formation. Nat Cell Biol 17: 228–240. doi: 10.1038/ncb3109 PMID: 25686250

43. Musgrave A, de Wildt P, van Etten I, Pijst H, Scholma C et al. (1986) Evidence for a functional membrane barrier in the transition zone between the flagellum and cell body of Chlamydomonas eugametos gametes. Planta 167: 544–553. doi: 10.1007/BF00391231 PMID: 24240371

44. Spencer M, Detwiler PB, Bunt-Milam AH (1988) Distribution of membrane proteins in mechanically dissociated retinal rods. Invest Ophthalmol Vis Sci 29: 1012–1020. PMID: 2843476

45. Cevik S, Sanders AA, Van Wijk E, Boldt K, Clarke L et al. (2013) Active transport and diffusion barriers restrict Joubert Syndrome-associated ARL13B/ARL-13 to an Inv-like ciliary membrane subdomain. PLoS Genet 9: e1003977. doi: 10.1371/journal.pgen.1003977 PMID: 24339792

46. Awata J, Takada S, Standley C, Lechtreck KF, Bellvé KD et al. (2014) NPHP4 controls ciliary trafficking of membrane proteins and large soluble proteins at the transition zone. J Cell Sci 127: 4714–4727. doi: 10.1242/jcs.155275 PMID: 25150219

47. Basiri ML, Ha A, Chadha A, Clark NM, Polyanovsky A et al. (2014) A migrating ciliary gate compartmentalizes the site of axoneme assembly in Drosophila spermatids. Curr Biol 24: 2622–2631. doi: 10.1016/j.cub.2014.09.047 PMID: 25447994

48. Craige B, Tsao CC, Diener DR, Hou Y, Lechtreck KF et al. (2010) CEP290 tethers flagellar transition zone microtubules to the membrane and regulates flagellar protein content. J Cell Biol 190: 927–940. doi: 10.1083/jcb.201006105 PMID: 20819941

49. Rao KN, Li L, Anand M, Khanna H (2015) Ablation of retinal ciliopathy protein RPGR results in altered photoreceptor ciliary composition. Sci Rep 5: 11137. doi: 10.1038/srep11137 PMID: 26068394

50. Vogel P, Gelfman CM, Issa T, Payne BJ, Hansen GM et al. (2014) Nephronophthisis and Retinal Degeneration in Tmem218-/- Mice: A Novel Mouse Model for Senior-Loken Syndrome? Vet Pathol 52: 580–595. doi: 10.1177/0300985814547392 PMID: 25161209

51. Inglis PN, Blacque OE, Leroux MR (2009) Functional genomics of intraflagellar transport-associated proteins in C. elegans. Methods Cell Biol 93: 267–304. doi: 10.1016/S0091-679X(08)93014-4 PMID: 20409822

52. Starich TA, Herman RK, Kari CK, Yeh WH, Schackwitz WS et al. (1995) Mutations affecting the chemosensory neurons of Caenorhabditis elegans. Genetics 139: 171–188. PMID: 7705621

53. Tong YG, Burglin TR (2010) Conditions for dye-filling of sensory neurons in Caenorhabditis elegans. J Neurosci Methods 188: 58–61. doi: 10.1016/j.jneumeth.2010.02.003 PMID: 20149821

54. Drivas TG, Bennett J (2014) CEP290 and the primary cilium. Adv Exp Med Biol 801: 519–525. doi: 10.1007/978-1-4614-3209-8_66 PMID: 24664739

55. Schouteden C, Serwas D, Palfy M, Dammermann A (2015) The ciliary transition zone functions in cell adhesion but is dispensable for axoneme assembly in C. elegans. J Cell Biol 210: 35–44. doi: 10.1083/jcb.201501013 PMID: 26124290

56. Thompson O, Edgley M, Strasbourger P, Flibotte S, Ewing B et al. (2013) The Million Mutation Project: A new approach to genetics in Caenorhabditis elegans. Genome Res 23(10):1749–62. doi: 10.1101/gr.157651.113 PMID: 23800452

57. Cevik S, Hori Y, Kaplan OI, Kida K, Toivenon T et al. (2010) Joubert syndrome Arl13b functions at ciliary membranes and stabilizes protein transport in Caenorhabditis elegans. J Cell Biol 188: 953–969. doi: 10.1083/jcb.200908133 PMID: 20231383

58. Tam LW, Ranum PT, Lefebvre PA (2013) CDKL5 regulates flagellar length and localizes to the base of the flagella in Chlamydomonas. Mol Biol Cell 24: 588–600. doi: 10.1091/mbc.E12-10-0718 PMID: 23283985

59. Lee JH, Silhavy JL, Lee JE, Al-Gazali L, Thomas S et al. (2012) Evolutionarily assembled cis-regulatory module at a human ciliopathy locus. Science 335: 966–969. doi: 10.1126/science.1213506 PMID: 22282472

60. Poretti A, Vitiello G, Hennekam RC, Arrigoni F, Bertini E et al. (2012) Delineation and diagnostic criteria of Oral-Facial-Digital Syndrome type VI. Orphanet J Rare Dis 7: 4. doi: 10.1186/1750-1172-7-4 PMID: 22236771

61. Lopez E, Thauvin-Robinet C, Reversade B, Khartoufi NE, Devisme L et al. (2014) C5orf42 is the major gene responsible for OFD syndrome type VI. Hum Genet 133: 367–377. doi: 10.1007/s00439-013-1385-1 PMID: 24178751

62. Romani M, Mancini F, Micalizzi A, Poretti A, Miccinilli E et al. (2015) Oral-facial-digital syndrome type VI: is C5orf42 really the major gene. Hum Genet 134: 123–126. doi: 10.1007/s00439-014-1508-3 PMID: 25407461

63. Valente EM, Logan CV, Mougou-Zerelli S, Lee JH, Silhavy JL et al. (2010) Mutations in TMEM216 perturb ciliogenesis and cause Joubert, Meckel and related syndromes. Nat Genet 42: 619–625. doi: 10.1038/ng.594 PMID: 20512146

64. Gorden NT, Arts HH, Parisi MA, Coene KL, Letteboer SJ et al. (2008) CC2D2A is mutated in Joubert syndrome and interacts with the ciliopathy-associated basal body protein CEP290. Am J Hum Genet 83: 559–571. doi: 10.1016/j.ajhg.2008.10.002 PMID: 18950740

65. Schouteden C, Serwas D, Palfy M, Dammermann A (2015) The ciliary transition zone functions in cell adhesion but is dispensable for axoneme assembly in C. elegans. J Cell Biol 210: 35–44. doi: 10.1083/jcb.201501013 PMID: 26124290

66. Hu Z, Liang Y, He W, Pan J (2015) Cilia disassembly with two distinct phases of regulation. Cell Rep 10: 1803–1810. PMID: 25801021

67. Hsu LS, Liang CJ, Tseng CY, Yeh CW, Tsai JN (2011) Zebrafish Cyclin-Dependent Protein Kinase-Like 1 (zcdkl1): Identification and Functional Characterization. Int J Mol Sci 12: 3606–3617. doi: 10.3390/ijms12063606 PMID: 21747697

68. Gilula NB, Satir P (1972) The ciliary necklace. A ciliary membrane specialization. J Cell Biol 53: 494–509. PMID: 4554367

69. Rachel RA, Yamamoto EA, Dewanjee MK, May-Simera HL, Sergeev YV et al. (2015) CEP290 alleles in mice disrupt tissue-specific cilia biogenesis and recapitulate features of syndromic ciliopathies. Hum Mol Genet 24: 3775–3791. doi: 10.1093/hmg/ddv123 PMID: 25859007

70. Vallin E, Gallagher J, Granger L, Martin E, Belougne J et al. (2012) A genome-wide collection of Mos1 transposon insertion mutants for the C. elegans research community. PLoS ONE 7: e30482. doi: 10.1371/journal.pone.0030482 PMID: 22347378

71. Sanders AA, Kennedy J, Blacque OE (2015) Image analysis of Caenorhabditis elegans ciliary transition zone structure, ultrastructure, molecular composition, and function. Methods Cell Biol 127: 323–347. doi: 10.1016/bs.mcb.2015.01.010 PMID: 25837399

72. Ivliev AE, 't Hoen PA, van Roon-Mom WM, Peters DJ, Sergeeva MG (2012) Exploring the transcriptome of ciliated cells using in silico dissection of human tissues. PLoS ONE 7:e35618. doi: 10.1371/journal.pone.0035618 PMID: 22558177

73. Dowdle WE, Robinson JF, Kneist A, Sirerol-Piquer MS, Frints SG et al. (2011) Disruption of a ciliary b9 protein complex causes meckel syndrome. Am J Hum Genet 89: 94–110. doi: 10.1016/j.ajhg.2011.06.003 PMID: 21763481

74. Chang YF, Imam JS, Wilkinson MF (2007) The nonsense-mediated decay RNA surveillance pathway. Annu Rev Biochem 76: 51–74. PMID: 17352659

Article 5

OFIP/KIAA0753 forms a complex with OFD1 and FOR20 at pericentriolar satellites and centrosomes and is mutated in Oral-Facial-Digital Syndrome.

Hum Mol Genet. 2016 Feb 1;25(3):497-513

AL. Bruel*, V. Chevrier*, B. Franco, JP. Vandam, F. Lembo, S. Audebert, E. Baudelet, Daniel Isnardon, A. Bole, M. Pierres, JP. Borg, J. Thevenon, L. Burglen, L. Faivre, JB. Rivière, M. Huijnen, D. Birnbaum, O. Rosnet, C. Thauvin-Robinet. (*equally contribution)

Résumé :

Les syndromes oro-facio-digitaux sont des maladies rares souvent causées par des mutations dans les gènes codants pour des protéines de la zone de transition ou du centrosome. Ces deux structures sont essentielles à la formation du cil primaire et à la transduction des signaux durant l'embryogénèse. Au cours de cette étude, nous avons identifié des mutations dans le gène *KIAA0753/OFIP* chez une patiente présentant un syndrome OFD VI. Nous avons montré que KIAA0753 est localisé dans le centrosome/centriole et les satellites péri-centriolaires dans les cellules humaines, stabilise les microtubules et forme un complexe avec FOPNL et OFD1. La diminution de l'expression des différents composants du complexe dans les cellules RPE1 conduit à des défauts de recrutement dans les satellites et le centrosome. Dans les cellules mutantes de la patiente, KIAA0753 perd sa capacité à interagir OFD1 et FOPNL. Les protéines centriolaires constituent des candidats particulièrement ciblées dans les ciliopathies du fait de l'importance de cette structure dans la ciliogénèse (détail page 89).

HMG Advance Access published January 2, 2016

Human Molecular Genetics, 2016, 1–17

doi: 10.1093/hmg/ddv488
Advance Access Publication Date: 7 December 2015
Original Article

ORIGINAL ARTICLE

OFIP/KIAA0753 forms a complex with OFD1 and FOR20 at pericentriolar satellites and centrosomes and is mutated in one individual with oral-facial-digital syndrome

Véronique Chevrier[1,2,3,4,†], Ange-Line Bruel[5,6,†], Teunis J. P. Van Dam[9], Brunella Franco[10,11], Melissa Lo Scalzo[12], Frédérique Lembo[1,2,3,4], Stéphane Audebert[1,2,3,4], Emilie Baudelet[1,2,3,4], Daniel Isnardon[1,2,3,4], Angélique Bole[4], Jean-Paul Borg[1,2,3,4], Paul Kuentz[5,6], Julien Thevenon[5,6,7], Lydie Burglen[13,14], Laurence Faivre[5,6,7], Jean-Baptiste Rivière[5,6,8], Martijn A. Huynen[9], Daniel Birnbaum[1,2,3,4], Olivier Rosnet[1,2,3,4,‡,*] and Christel Thauvin-Robinet[5,6,7,*]

[1]Centre de Recherche en Cancérologie de Marseille, INSERM UMR1068, [2]Institut Paoli-Calmettes and [3]CNRS U7258, F-13009 Marseille, France, [4]Aix-Marseille Université, F-13007 Marseille, France, [5]Equipe d'Accueil 4271, Génétique des Anomalies du Développement, Université Fédérale Bourgogne – Franche Comté, F-21079 Dijon, France, [6]Fédération Hospitalo-Universitaire Médecine Translationnelle et Anomalies du Développement (TRANSLAD), [7]Centre de Génétique et Centre de Référence Anomalies du Développement et Syndromes Malformatifs de l'Interrégion Est, [8]Laboratoire de Génétique Moléculaire, Plateau Technique de Biologie, Centre Hospitalier Universitaire Dijon, Dijon F-21079, France, [9]Centre for Molecular and Biomolecular Informatics, Radboud University Medical Centre, Nijmegen, The Netherlands, [10]Telethon Institute of Genetics and Medicine, Naples, Italy, [11]Medical Genetics, Department of Medical Translational Sciences, University of Napoli Federico II, Naples, Italy, [12]All Children Hospital, Saint Petersburg, FL, USA, [13]Centre de Référence des Malformations et Maladies Congénitales du Cervelet and [14]Service de Génétique, Hôpital Armand Trousseau, AP-HP, Paris, France

*To whom correspondence should be addressed. Tel: +33 380295313; Fax: +33 380293266; Email: christel.thauvin@chu-dijon.fr (C.T.-R.)/Tel: +33 491269704; Fax: +33 491269748; Email: olivier.rosnet@inserm.fr (O.R.)

Abstract

Oral-facial-digital (OFD) syndromes are rare heterogeneous disorders characterized by the association of abnormalities of the face, the oral cavity and the extremities, some due to mutations in proteins of the transition zone of the primary cilia or the closely associated distal end of centrioles. These two structures are essential for the formation of functional cilia, and for

[†]The authors wish it to be known that, in their opinion, the first two authors should be regarded as joint First Authors.
[‡]Present address: Institut de Biologie du Développement de Marseille, Aix-Marseille-Université, CNRS, UMR 7288, F-13009 Marseille, France.
Received: October 12, 2015. **Revised and Accepted:** November 20, 2015

signaling events during development. We report here causal compound heterozygous mutations of KIAA0753/OFIP in a patient with an OFD VI syndrome. We show that the KIAA0753/OFIP protein, whose sequence is conserved in ciliated species, associates with centrosome/centriole and pericentriolar satellites in human cells and forms a complex with FOR20 and OFD1. The decreased expression of any component of this ternary complex in RPE1 cells causes a defective recruitment onto centrosomes and satellites. The OFD KIAA0753/OFIP mutant loses its capacity to interact with FOR20 and OFD1, which may be the molecular basis of the defect. We also show that KIAA0753/OFIP has microtubule-stabilizing activity. OFD1 and FOR20 are known to regulate the integrity of the centriole distal end, confirming that this structural element is a target of importance for pathogenic mutations in ciliopathies.

Introduction

Cilia, which include the long-known motile flagella of swimming protists and sperm cells, have gained a great interest in the biology of human development and diseases during the last 15 years, because defects in these organelles are linked to an increasing number of genetic syndromes now called ciliopathies (1,2).

In vertebrates, cilia exist as primary cilia (PC), immotile solitary protrusions at the surface of many cell types, and as multiple motile cilia (MMC) at the surface of specialized epithelia such as the oviduct and the respiratory tract, which produce directional fluid flows of biological importance. A transient and solitary motile cilium is also present at the embryonic node to break left–right symmetry (3). PC are required, to various extent, for the cellular response to several signaling molecules including WNT, Hedgehog and platelet-derived growth factor. An alteration of this function underpins the developmental defects observed in patients with syndromic ciliopathies. Ciliopathies have various but overlapping phenotypes, such as polydactyly, intellectual disability, obesity, renal cystic disease, craniofacial abnormalities and retinitis pigmentosa.

The anchoring unit and seeding platform of a newly formed cilium are the modified centriole known as the basal body. PC are extending from basal bodies derived from the mother centriole, and MMC originate mainly from basal bodies amplified from daughter centriole-associated deuterosomes (4,5). Building a cilium requires the initial recruitment of post-Golgi vesicles at the distal end of centrioles by distal appendages that subsequently fuse together to initiate the formation of a ciliary shaft (6,7).

The construction and maintenance of a functional cilium rely on the activity of several molecular complexes. Remarkably, all of these complexes can be targeted in ciliopathies by gene mutation affecting individual components. The intraflagellar transport (IFT) complex associates with bidirectional molecular motors and carries building blocks, such as tubulin, into the cilium for extension and removes constituents to maintain a steady state (8,9). IFT assembly and turnover are regulated by the BBSome complex, which also regulates the ciliary trafficking of several signaling molecules (10,11). The BBS4 BBSome subunit associates with pericentriolar satellites (PSs) to regulate the recruitment of the BBSome into the cilium (12). PSs also associate with many centriole and basal body (CBB) proteins and may be assembly points for cilia proteins (13). Additional interlinked complexes of ciliopathy proteins were recently identified, localizing at the cilia transition zone and regulating its function as a ciliary gate to allow or prevent the selective entry of some membrane proteins (14).

Among ciliopathies, oral-facial-digital (OFD) syndromes are rare, clinically and genetically heterogeneous disorders characterized by the association of abnormalities of the face, the oral cavity and the extremities (15). OFD syndromes follow an autosomal recessive pattern of inheritance, except for the OFD I type that shows dominant X-linked inheritance and lethality in males. The OFD VI type is distinguished from the other types by the specific occurrence of cerebellar malformation, also described as molar tooth sign (MTS), and by metacarpal abnormalities. Because of these phenotypes, OFD VI is included into the Joubert syndrome-related disorders (JSRDs) (16). To date, causal mutations in nine ciliary genes (OFD1, C2CD3, TBC1D32/C6orf170, SCLT1, DDX59, WDPCP, C5orf42, TCTN3 and TMEM216) have been identified in OFD patients (17–21), and particularly OFD1, C5orf42 and TMEM216 in the OFD VI type. Interestingly, the best-characterized OFD proteins, OFD1 and C2CD3, bind together and colocalize at PSs and at the distal end of the centriole where they cooperate to regulate centriole length, providing an additional pathogenic mechanism in ciliopathies (22–24).

Here, we have identified two causal heterozygous mutations in the *KIAA0753* gene in a newborn female presenting with an OFD VI syndrome. KIAA0753 is a conserved centrosome and PS protein that binds directly to FOR20, a protein required for the structural integrity of CBB distal ends and membrane anchoring (25,26). We show that a ternary complex is formed between FOR20 and OFD1 and KIAA0753 [hence subsequently named OFD1 and FOR20 interacting protein (OFIP)], and may be a prerequisite for recruitment onto PC and centrosomes, and for ciliogenesis.

Results

KIAA0753 is mutated in OFD

Exome sequencing of blood cells DNA of a newborn female born with OFD syndrome type VI identified two heterozygous mutations in the *KIAA0753* gene (RefSeq NM_014804.2) (see whole-exome statistics in Supplementary Material, Table S1). The female was born from non-consanguineous parents at 38 weeks of gestation. Birth measurements appeared normal, but she presented with facial dysmorphism (flat facial profile, straight palpebral fissures, hypertelorism, a wide nasal bridge with upturned nares, posteriorly low-set left ear and normal right ear), lobulated tongue, clefting of the alveolar ridges, left hand postaxial polydactyly, broad right and left hallux duplication and intermittent respiratory difficulties. Brain magnetic resonance imaging (MRI) evidenced vermis hypoplasia with MTS (Fig. 1A and 1B), agenesis of corpus callosum, ventricular dilatation and several other cerebral abnormalities. Abdominal ultrasound revealed bilateral hydronephrosis. OFD syndrome type VI was thus diagnosed due to the association of oral defects, polydactyly and MTS.

Both *KIAA0753* mutations, one nonsense variant (c.1891A>T; p.Lys631*) and one substitution in Intron 8 (c.1546-3C>A), were confirmed by Sanger sequencing, as well as the maternal

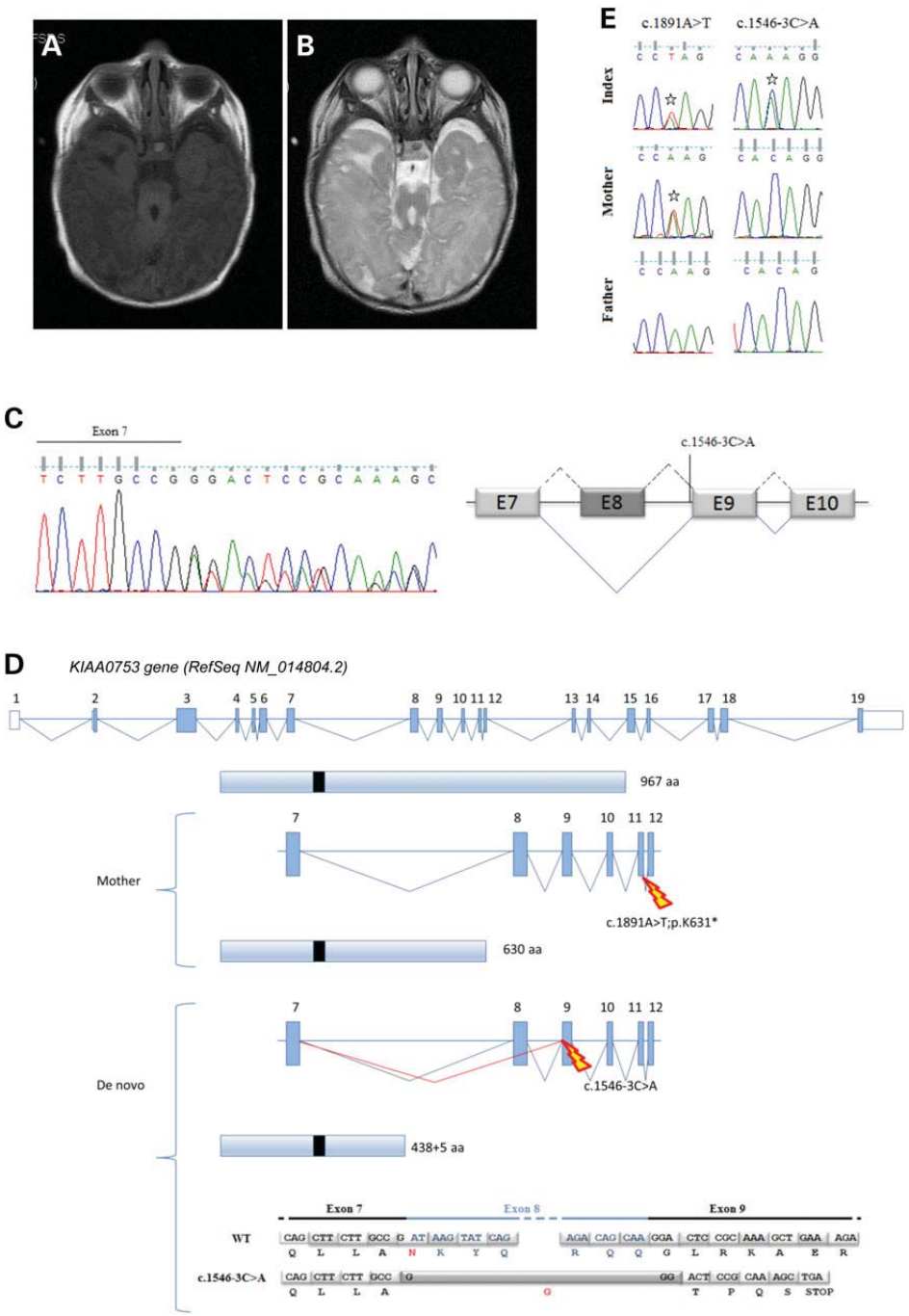

Figure 1. Phenotypical and molecular data of both *KIAA0753* mutations. (**A**) Axial T1 flair and (**B**) axial T2 brain MRI imaging evidence MTS. (**E**) DNA Sanger chromatograms of the heterozygous composite *KIAA0753* variants in the proband from a maternal nonsense mutation (c.1891A>T; p.K631*) and a *de novo* substitution in Intron 8 (c.1546-3C>A). (**C**) cDNA Sanger chromatogram and diagram, confirming the heterozygous skipping of Exon 8, secondary to the c.1546-3C>A substitution. (**D**) *KIAA0753* transcripts and protein diagrams, showing that both mutations lead to premature stop codon.

heterozygous status (Fig. 1C). The sporadic occurrence of the c.1546-3C>A variant was confirmed by samples concordance.

We hypothesized that the intronic substitution (c.1546-3C>A) caused a splicing defect and analyzed the effect of this variant on the splicing products. cDNA Sanger sequencing revealed a heterozygous skipping of Exon 8 that caused a frameshift, changed the amino acids sequence and led to the occurrence of a premature stop codon (Fig. 1C and D).

Because both mutations appeared truncating and probably compound heterozygous, they were considered as potentially causal.

Since the allelic OFD VI and JBSs are due to mutations in several genes, we also sequenced the *KIAA0753* genes in 32 OFD VI or JBS individuals (Supplementary Material, Table S2). The secondary functional results (see below) led us to also sequence the *FOR20* gene in the same cohort (Supplementary Material, Table S2). No additional mutation was identified.

KIAA0753 is a centrosome and PS protein interacting with FOR20

In parallel to clinical studies, our work to identify proteins involved in ciliogenesis had led to the identification of KIAA0753 as a binding partner of FOR20 (FOPNL), a recently characterized PS and basal body protein, using a two-hybrid screening approach (Supplementary Material, Fig. S1). KIAA0753 was subsequently named OFIP (see below). To further characterize OFIP, we produced a panel of monoclonal antibodies resulting from the immunization of rats with the 300 carboxy-terminal residues expressed in bacteria as a GST fusion protein. A mix of two selected antibodies detected OFIP as a ~115 kDa protein in the soluble fraction of Radio-immunoprecipitation assay (RIPA) lysate of RPE1 cells (Fig. 2A). In contrast, OFIP was detected in the Triton-X100-insoluble fraction of RPE1 and lymphoblastoid KE37 cells, as expected for proteins associated with centrosomes and PSs (25). OFIP was indeed detected in a cellular extract enriched in centrosomes (Fig. 2A). IF stainings were done on methanol-fixed RPE1 cells to localize OFIP at different phases of the cell cycle. OFIP was detected at centrosomes and PSs and perfectly colocalized with FOR20 in interphasic and mitotic cells (Fig. 2B). PSs are typically defined by a staining with anti-PCM1 antibodies. We confirmed colocalization of OFIP and FOR20 on PSs by triple-labeling experiments on Hela Kyoto cells expressing Green fluorescent protein (GFP)-tagged OFIP [TransgeneOmics cells (27), see 'Materials and Methods' section] (Fig. 2C). We also co-labeled OFIP and PCM1 in pre-embedding immunoelectron microscopy experiments in RPE1 cells. Analysis of ultrathin sections showed the presence of OFIP and PCM1-specific grains on PSs (Fig. 2D).

We used Hela Kyoto TransgeneOmics cells that express GFP-tagged mouse OFIP or FOR20 at physiological level to confirm the interaction between the two proteins: immunoprecipitations

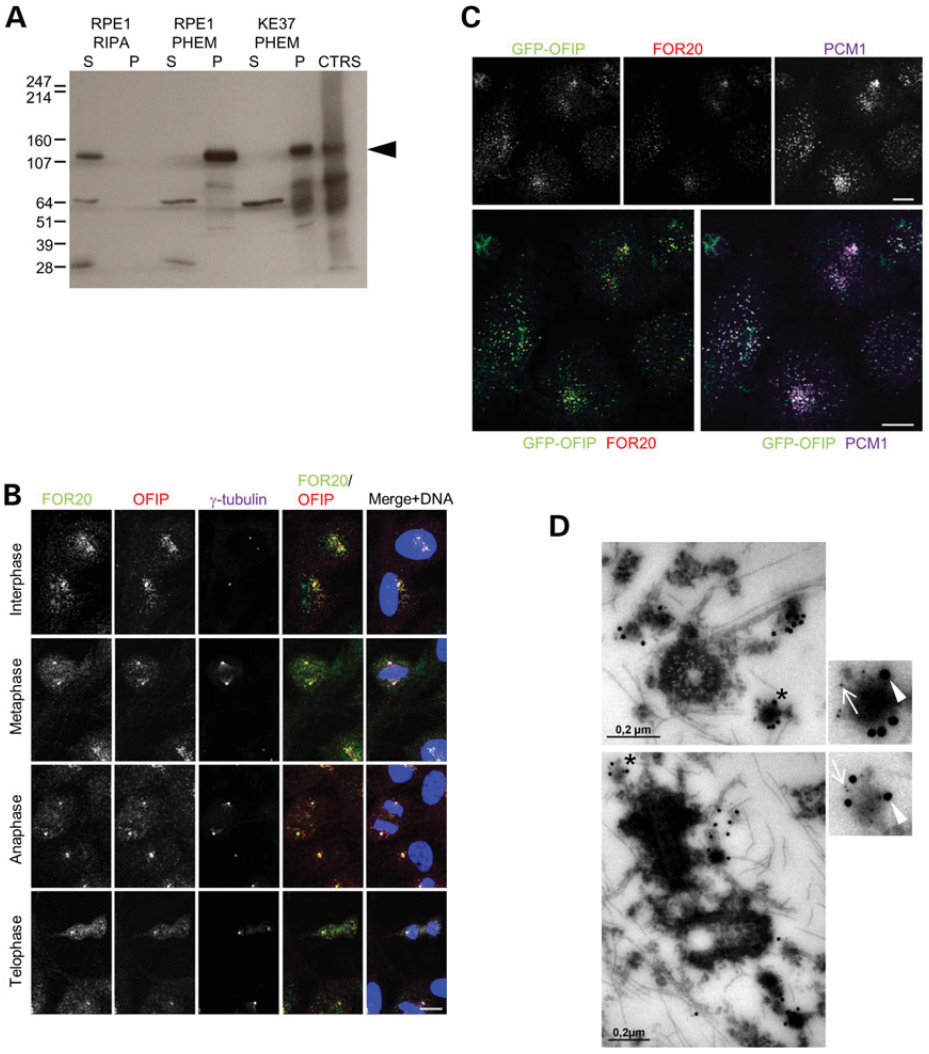

Figure 2. Characterization of OFIP/KIAA0753. (**A**) Fifty micrograms of protein from detergent-soluble (S) and -insoluble (P) and centrosome-enriched (CTRS) fractions were resolved by 4–12% SDS–PAGE. After transfer onto nitrocellulose, the membrane was immunoblotted with rat anti-OFIP monoclonal antibody. (**B**) Asynchronous RPE1 cells were fixed in cold methanol and labeled with rabbit anti-FOR20 (green), rat anti-OFIP (red) and mouse anti γ-tubulin (magenta). Scale bar, 10 µm. (**C**) Hela Kyoto cells (TransgeneOmics cells) expressing GFP-OFIP (green) were fixed in cold methanol and labeled with rat anti-FOR20 (red) and rabbit anti-PCM1 (magenta) antibodies, scale bar, 10 µm. (**D**) Fixed RPE1 cells were labeled with rat anti-OFIP and rabbit anti-PCM1 antibodies and detected with secondary antibodies conjugated to 6 and 18 nm colloidal gold, respectively. On the left are zoomed images of the PS labeled with asterisks in the right micrographs. Of note, 6 and 18 nm grains are indicated by white arrows and arrowheads, respectively. Scale bar, 200 µm.

with anti-GFP antibodies demonstrated the association of endogenous FOR20 with OFIP-GFP and of endogenous OFIP with FOR20-GFP (Fig. 3A).

To determine the portions of each protein involved in the interaction, co-immunoprecipitation (CoIP) experiments were done in Cos1 cells following ectopic expression of full-length and truncated or mutated proteins (see Fig. 5A for OFIP constructs). A first set of experiments demonstrated that the 83 C-terminal residues of OFIP (885–967) were necessary and sufficient to bind FOR20 (Fig. 3B and Supplementary Material, Fig. S2A). In a second set of experiments, various Myc-tagged FOR20 constructs (25) (Fig. 3C) were co-expressed with full-length GFP-tagged OFIP. Anti-Myc immunoprecipitates revealed that the poorly conserved C-terminus of FOR20 was dispensable for the interaction with OFIP (Fig. 3D). In contrast, the conserved FOR20 TOF domain and some residues surrounding the PLL motif were required for the interaction, but the integrity of this motif was not, because a mutation of the first leucine to an arginine in PLL did not preclude the interaction. In addition, mutation in the FOR20 LisH domain known to inhibit homodimerization (25) also affected the CoIP of the two proteins (Fig. 3D).

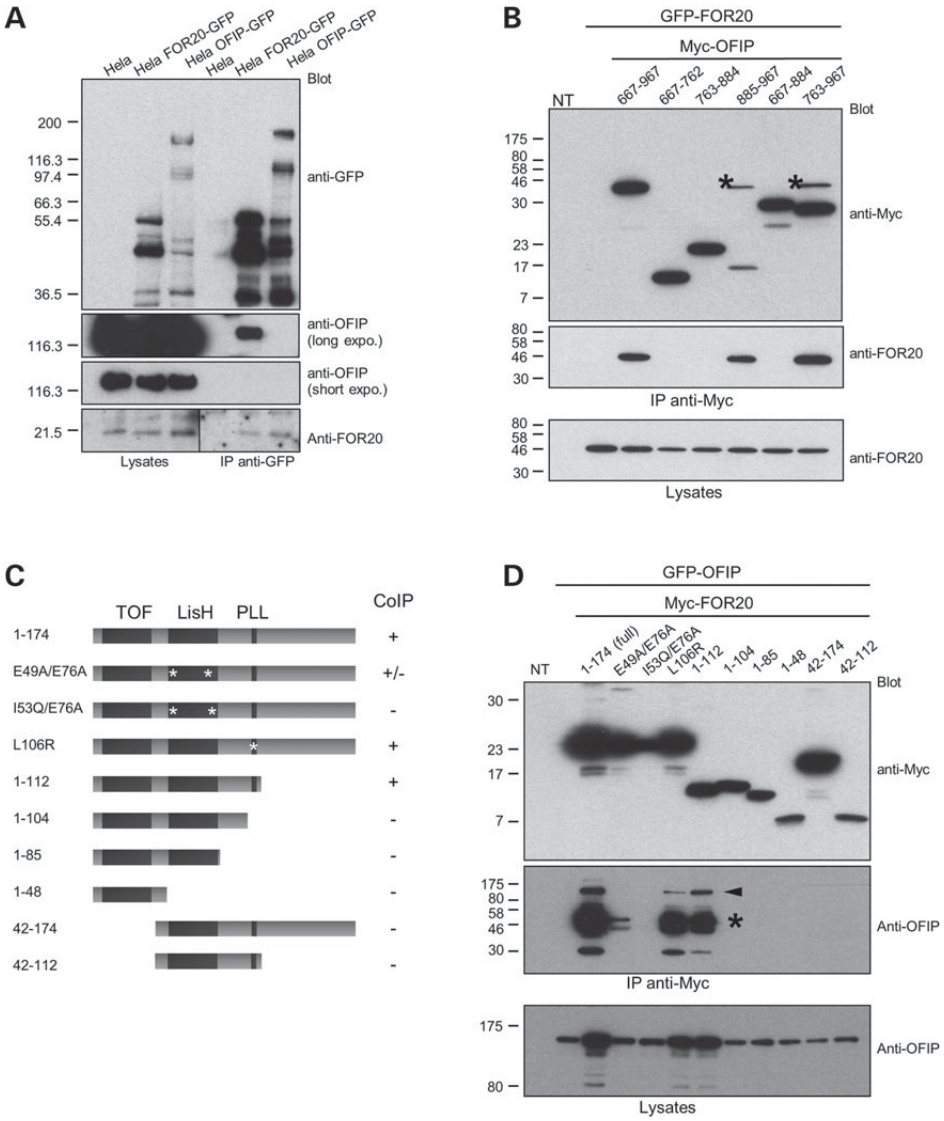

Figure 3. OFIP interacts with FOR20. (**A**) Hela Kyoto TransgeneOmic cells expressing mouse FOR20 or OFIP tagged at their C-termini with GFP were lysed and tagged proteins were precipitated with rabbit anti-GFP-conjugated agarose beads. Immunoprecipitates were separated by 4–20% SDS–PAGE, transferred onto nitrocellulose and immunoblotted with the indicated antibodies. Rabbit anti-FOR20 detection was done with a peroxidase-conjugated donkey anti-rabbit-IgG (H + L) on lysates and with a mouse mAb anti-rabbit γ-chain on IPs. (**B**) Cos1 cells were left untransfected or transfected with FOR20-GFP alone or in combination with Myc-tagged OFIP C-terminus coding constructs. Cells were lysed 24 h post-transfection, and lysates were subjected to immunoprecipitation with anti-Myc agarose beads and immunoprecipitates were resolved by 4–12% SDS–PAGE. After transfer onto nitrocellulose, the membrane was immunoblotted with anti-Myc and anti-FOR20 antibodies, as indicated. Asterisks show bands corresponding to incomplete anti-FOR20 stripping. (**C**) Schematic representation of wild-type and various FOR20 mutants. On the right of the scheme, +, – and ± recapitulate the CoIP with OFIP as shown in Figure 2D. (**D**) Cos1 cells were left untransfected or transfected with GFP-OFIP alone or in combination with Myc-tagged FOR20-coding constructs. Cells were treated as in (**B**), and immunoprecipitates were resolved by 15% (IP anti-Myc) or 10% (lysates) SDS–PAGE. After transfer onto nitrocellulose, the membrane was immunoblotted with anti-Myc and anti-OFIP antibodies, as indicated. Arrowhead indicates full-length GFP-OFIP and asterisk indicates degradation products repeatedly observed in IPs, but not in cell lysates.

The use of human proteins as baits and preys in yeast two-hybrid experiments allows the detection of direct interaction in most cases, especially when the proteins are not conserved in yeast, which was the case in our study. Ponceau-S staining of immunoprecipitated Myc-FOR20 associated with GFP-tagged OFIP C-terminus after sodium dodecyl sulphate–polyacrylamide gel electrophoresis (SDS–PAGE) and transfer onto membrane demonstrated the sole presence of the two overexpressed proteins in the immunoprecipitates, together with Ig chains (Supplementary Material, Fig. S2B). Thus, the interaction is very likely to be direct.

OFIP overexpressed in cells decorates microtubules (MTs) (see below for more details). Therefore, the association of OFIP and FOR20 was also ascertained in Cos1 cells by the capacity of overexpressed GFP–OFIP to recruit FOR20 onto MTs. As expected, this recruitment did not require the C-terminus of FOR20, but was dependent on OFIP C-terminal tail (Supplementary Material, Fig. S3).

OFIP, FOR20 and OFD1 form a complex associated with PSs and centrosomes

We next used a proteomic approach to identify additional proteins interacting with OFIP. Non-transfected cells and cells expressing GFP only were used as controls. In addition, OFIP constructs that could associate with FOR20 (OFIP 300–967 and 667–967) were co-expressed with mCherry-tagged FOR20 to identify proteins binding to OFIP indirectly through FOR20 or to the OFIP-FOR20 binary complex. GFP-tagged and copurifying proteins were isolated from lysates using anti-GFP nanobodies (see 'Materials and Methods' section), digested with trypsin, and analyzed by mass spectrometry (see Supplementary Material, Table S3 for complete results). Interestingly, we could specifically identify PCM1 associated with OFIP N-terminal region (1–299) and OFD1 with the C-terminal region (300–967 and 667–967) only when overexpressed with FOR20 (Table 1).

We used Hela Kyoto TransgeneOmics cells expressing mouse GFP-tagged OFIP or PCM1 to confirm the interaction. We could demonstrate CoIP of endogenous OFD1 and PCM1 with OFIP–GFP and of endogenous OFIP with PCM1–GFP (Fig. 4A).

To better define a putative OFIP-FOR20-OFD1 complex, different combinations of proteins tagged with various recognition sequences were transfected in Cos1 cells, and the associations were probed following immunoprecipitation and immunoblotting. The results are shown in Figure 4B and Supplementary Material, Figure S4. The conclusion of this series of experiments is that a weak interaction between the OFIP C-terminus and OFD1 was strongly increased by the presence of FOR20 in the complex (see Lanes 5 and 6 in Fig. 4B, right panel). Remarkably, OFD1 and FOR20 did not associate in the absence of OFIP (Lane 7 in Fig. 4B, right panel). The conserved N-terminus of OFD1 was necessary and sufficient to strongly interact with OFIP C-terminus in the presence of FOR20.

In support of our biochemical observations, overexpressed full-length OFD1 or its conserved N-terminus colocalized with OFIP on MTs in transfected cells in the absence or presence of FOR20 (Supplementary Material, Fig. S5A). In addition, the three proteins expressed together colocalized perfectly. The lack of interaction of OFD1 and FOR20 in the absence of OFIP was also confirmed by the lack of colocalization of the two proteins when overexpressed in Cos1 cells. The requirement of the most C-terminal 82 residues of OFIP and OFD1 N-terminus for complex formation was also confirmed in colocalization experiments (Supplementary Material, Fig. S5B). Thus, OFD1 can interact with OFIP in a FOR20-independent manner, but FOR20 increases the stability of the interaction.

Finally, we showed that OFIP, OFD1 and FOR20 have similar localization at PSs and centrioles (Fig. 4C).

Taken together these results suggest that OFIP, FOR20 and OFD1 form an independent ternary complex that may associate with PSs through the binding of OFIP N-terminus to PCM1.

The central region of OFIP stabilizes MTs

The subcellular localization of full-length and truncated OFIP constructs (Fig. 5A) was assessed by IF after expression in RPE1 (Supplementary Material, Fig. S6) and NIH3T3 cells (not shown). The N-terminus (residues 1–299) was sufficient for localization to PSs and centrosomes. Strikingly, overexpressed full-length OFIP and its isolated central region (residues 300–666) and truncated proteins retaining this region strongly decorated a population of cytoplasmic MTs (Supplementary Material, Fig. S6). Expression of these latter OFIP constructs induced MT resistance to depolymerization by high concentrations of nocodazole (Fig. 5B). MT-pelleting assays showed a quantitative increase of insoluble MTs from nocodazole-treated cells expressing GFP-OFIP, but not from control cells, in two different experimental settings, confirming that OFIP protects from depolymerization and stabilizes MTs (Fig. 5C). The stabilization effect was also observed in the presence of the central 300–666 OFIP fragment (Fig. 5C, right panel).

Depletion of individual proteins of the complex affects centrosomes, PSs and ciliogenesis

Each protein of the above-identified protein complex was down-regulated by siRNA transfection in RPE1 cells and cells were

Table 1. Identification of OFIP-associated proteins by mass spectrometry

	Non-transfected		GFP		1–299[a]		300–666		667–967		300–967		667–967 +FOR20[b]		300–967 +FOR20	
	Cov.[c]	Pep.[d]	Cov.	Pep.	Cov.	Pep.	Cov.	Pep.	Cov.	Pep.	Cov.	Pep.	Cov.	Pep.	Cov.	Pep.
OFIP	0	0	0	0	16.65	127	26.99	318	21.82	345	46.43	681	20.48	379	41.99	455
FOR20	0	0	0	0	0	0	0	0	0	0	16.09	4	89.08	85	85.06	63
PCM1	0	0	0	0	15.27	40	1.58	3	0	0	1.73	2	0	0	0	0
OFD1	0	0	0	0	0	0	0	0	0	0	0	0	25.2	45	3.56	4

[a]GFP-tagged OFIP fragments expressed in RPE1 cells for pull-down and mass spectrometry analysis.
[b]GFP-tagged OFIP fragment were co-expressed with FOR20-mCherry.
[c]Percentage of coverage.
Total number of peptides.
CBB, centriole and basal body; IFT, intraflagellar transport; JBS, Joubert syndrome; JSRD, Joubert syndrome-related disorders; MMC, multiple motile cilia; MRI, magnetic resonance imaging; MT, microtubule; MTS, molar tooth sign; OFD, oral facial digital; PC, primary cilium; PS, pericentriolar satellite.

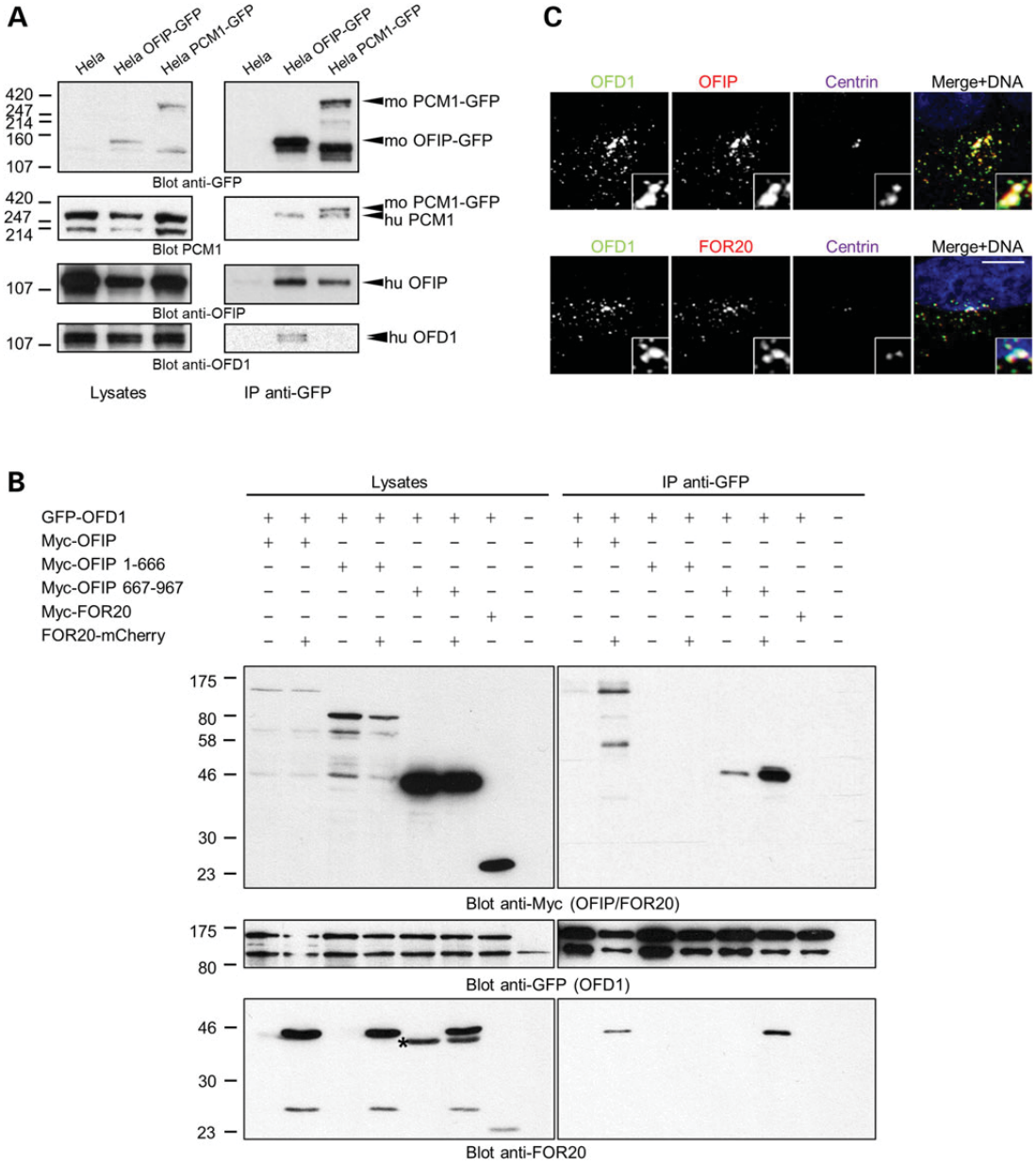

Figure 4. OFIP forms a ternary complex with FOR20 and OFD1. (**A**) Hela Kyoto TransgeneOmic cells expressing mouse OFIP or mouse PCM1 tagged at their C-termini with GFP were lysed and tagged, and proteins were precipitated with GFP-Trap® alpaca anti-GFP conjugated agarose beads. Lysates and immunoprecipitates were separated by 4–12% SDS–PAGE, transferred onto nitrocellulose and immunoblotted with antibodies to GFP, PCM1, OFIP and OFD1, from the top to the bottom panel, respectively. (**B**) Cos1 cells were transfected with several combinations of expression plasmids as indicated. GFP-tagged OFD1 was precipitated with GFP-Trap® alpaca anti-GFP-conjugated agarose beads and immunprecipitates and corresponding lysates were resolved by 10% SDS–PAGE. After transfer onto nitrocellulose, the membrane was immunoblotted with the indicated antibodies. Asterisk show bands corresponding to incomplete anti-Myc stripping. (**C**) RPE1 cells were fixed in cold methanol and labeled with mouse anti-centrin (magenta) and rabbit anti-OFD1 (green) together with rat anti-OFIP (red, upper panel) or and rat anti-FOR20 (red, lower panel). Insets show magnified (2.5×) images of the centriolar region. Scale bar, 5 µm.

analyzed by IF. PCM1-labeled PS were poorly affected by depletion of OFIP, OFD1 and FOR20 (Fig. 6A and B). In contrast, PCM1 depletion suppressed PS localization of all three proteins as expected. Remarkably, however, the localization of all three proteins in cytoplasmic PSs and in close proximity of the centrosome showed strong inter-dependence, mainly at PSs (Fig. 6A and B). This indicates that an intact protein complex is required for localization at the PSs, and possibly at the centrosomes. When PC were studied in serum-starved siRNA-treated cells, a 15–20% decrease in cilium length was observed (Fig. 6C).

The OFIP-OFD1-FOR20 complex is defective in OFD patient cells

The heterozygous compound mutations of *OFIP* in the OFD VI patient predict OFIP products lacking the C-terminus (Fig. 1). In agreement with this prediction, the immunoblot analysis of

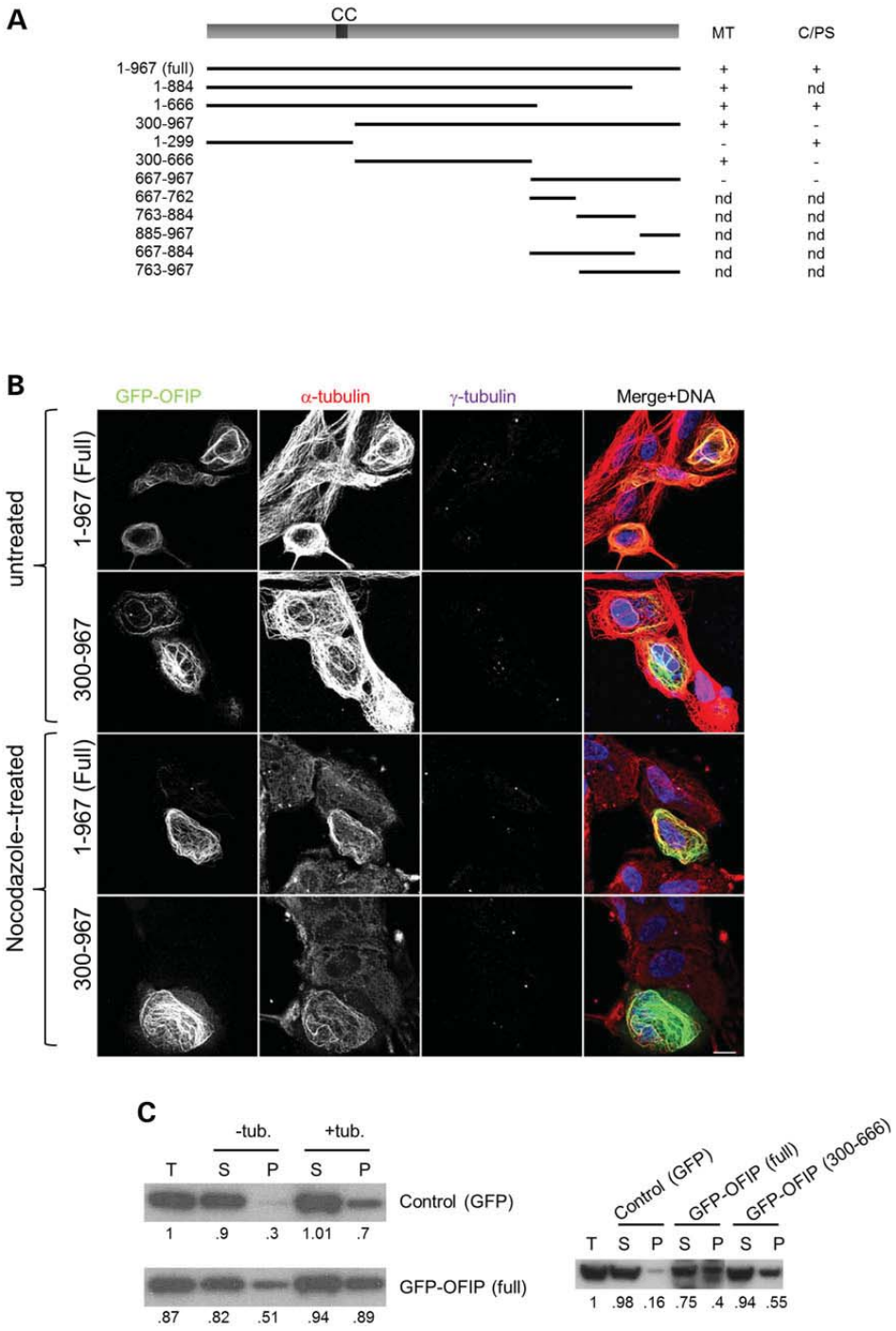

Figure 5. OFIP stabilizes microtubules. (**A**) Schematic representation of wild-type and various OFIP mutants used in our study together with their localization with respect to MT and centrosomes (C)/PSs. (**B**) RPE1 cells were transfected with plasmids encoding GFP-tagged full-length or 300–666 fragment of OFIP. Twenty-four hours post-transfection, cells were treated or not with a high dose (10 μM) of nocodazole for 2 h and subsequently fixed in cold methanol. Cells were labeled with mouse anti-α-tubulin (red) and rabbit anti γ-tubulin (magenta). Nocodazole-treated cells expressing OFIP constructs showed persistence of MT filaments and bundles, in contrast to control cells. Bar, 10 μM. (**C**) Left panel: RPE1 cells were transfected to express GFP-OFIP or GFP. Twenty-four hours after transfection, cells were lysed in hypotonic buffer and tubulin polymerization from soluble extracts was enabled in the presence and/or absence of exogenous tubulin. Insoluble (pellet, P) and soluble (supernatant, S) fractions were separated by SDS–PAGE and transferred onto nitrocellulose. The membrane was immunoblotted with mouse anti-α-tubulin antibody. Band intensities were quantified using the ImageJ software and normalized compared with the signal observed from total cell extracts (T) lane. In the right panel, RPE1 cells were transfected to express GFP, GFP-OFIP as full-length or 300–666 central fragment. Twenty-four hours after transfection cells were treated with10 μg/ml nocodazole for 2 h lysed in hypotonic conditions, as described above. Insoluble (pellet, P) and soluble (supernatant, S) fractions were obtained and analyzed by SDS–PAGE and immunoblotting with anti-α-tubulin antibody.

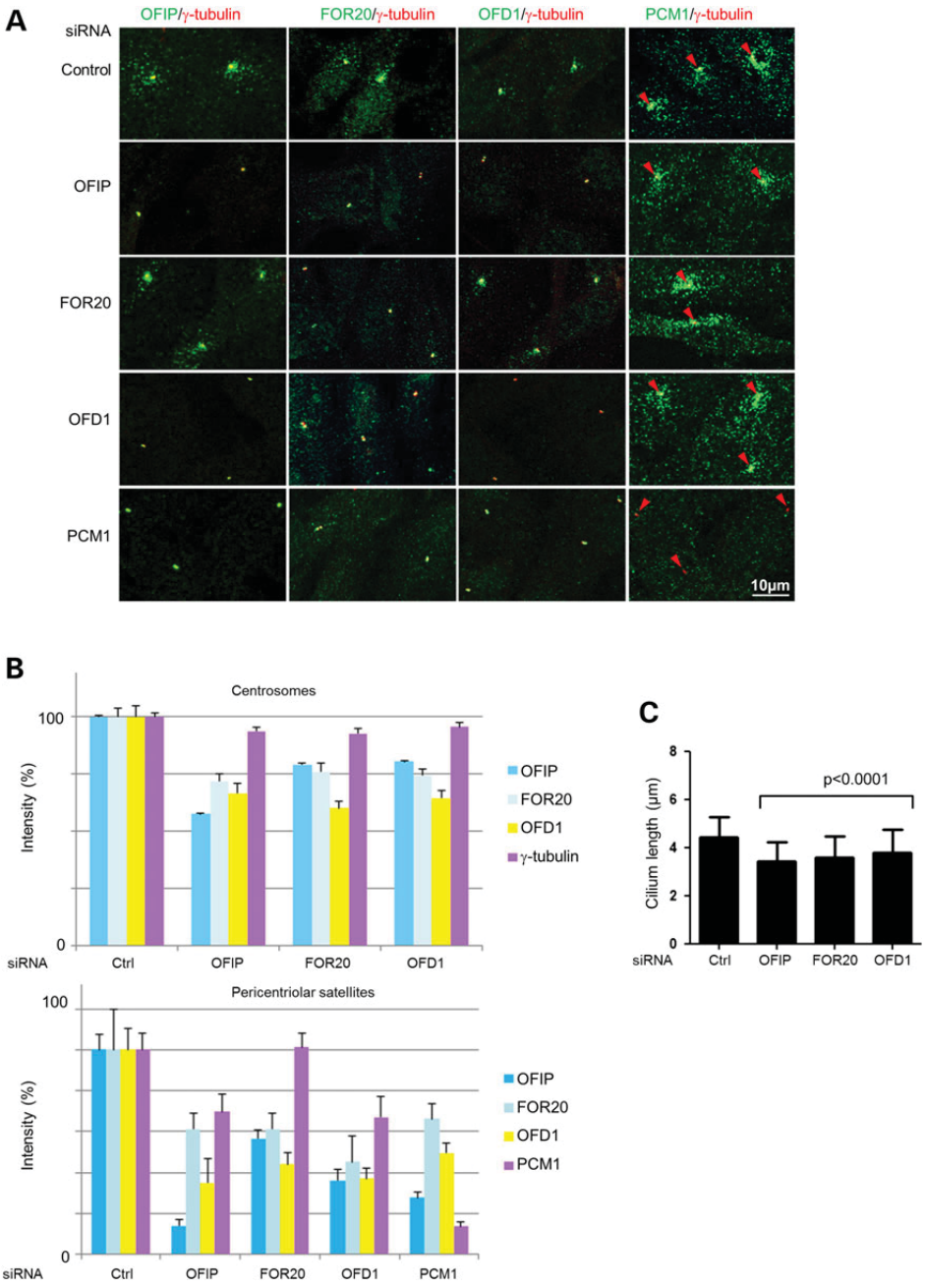

Figure 6. Effects of siRNA-mediated protein depletion in RPE1 cells. (**A**) RPE1 cells were treated for 48 h with control siRNA or siRNA targeting *OFIP/KIAA0753*, *FOR20*, *OFD1* or *PCM1*. Cells were subsequently fixed in cold methanol and stained with various combinations of antibodies to detect the target proteins (green staining) in addition to γ-tubulin (red). The centrosomes are pointed out by red arrowheads. (**B**) Fluorescence intensity of anti-PS protein labeling around centrosomes was quantified in cells treated with the indicated siRNA (see 'Materials and Methods' section for quantification details). (C) RPE1 cells were treated for 48 h with control siRNA or specific siRNA before serum starvation for 24 h. Cells were subsequently fixed in cold methanol and stained with antibodies against acetylated and γ-tubulin to label basal bodies and primary cilia, respectively. The length of cilia was measured on >100 cells in each condition and the mean value is reported along with SD (vertical bars).

control and patient extracts from Epstein–Barr virus (EBV)-immortalized cells with anti-OFIP mAb recognizing the C-terminus barely detected OFIP in patient cells (Fig. 7A). This was confirmed by IF staining of patient cells, which showed faint OFIP at the centrosomes, contrasting with OFIP protein abundance at the centrosomes and PSs in control cells (Fig. 7B). This indicates that the *de novo* splicing site mutation somehow allows minimal normal splicing. Because of the lack of antibodies reacting with the N-terminus of OFIP, it was not possible to control the production of truncated proteins, which could anyway be absent due to nonsense-mediated mRNA decay.

Importantly, in agreement with the experiments in RPE1 cells, the patient cells showed a strong reduction of FOR20 and OFD1 at the centrosome and PSs (Fig. 7B). CEP290, another transition zone and centriolar protein associated with PSs was not affected, excluding a more general effect (Supplementary Material, Fig. S7).

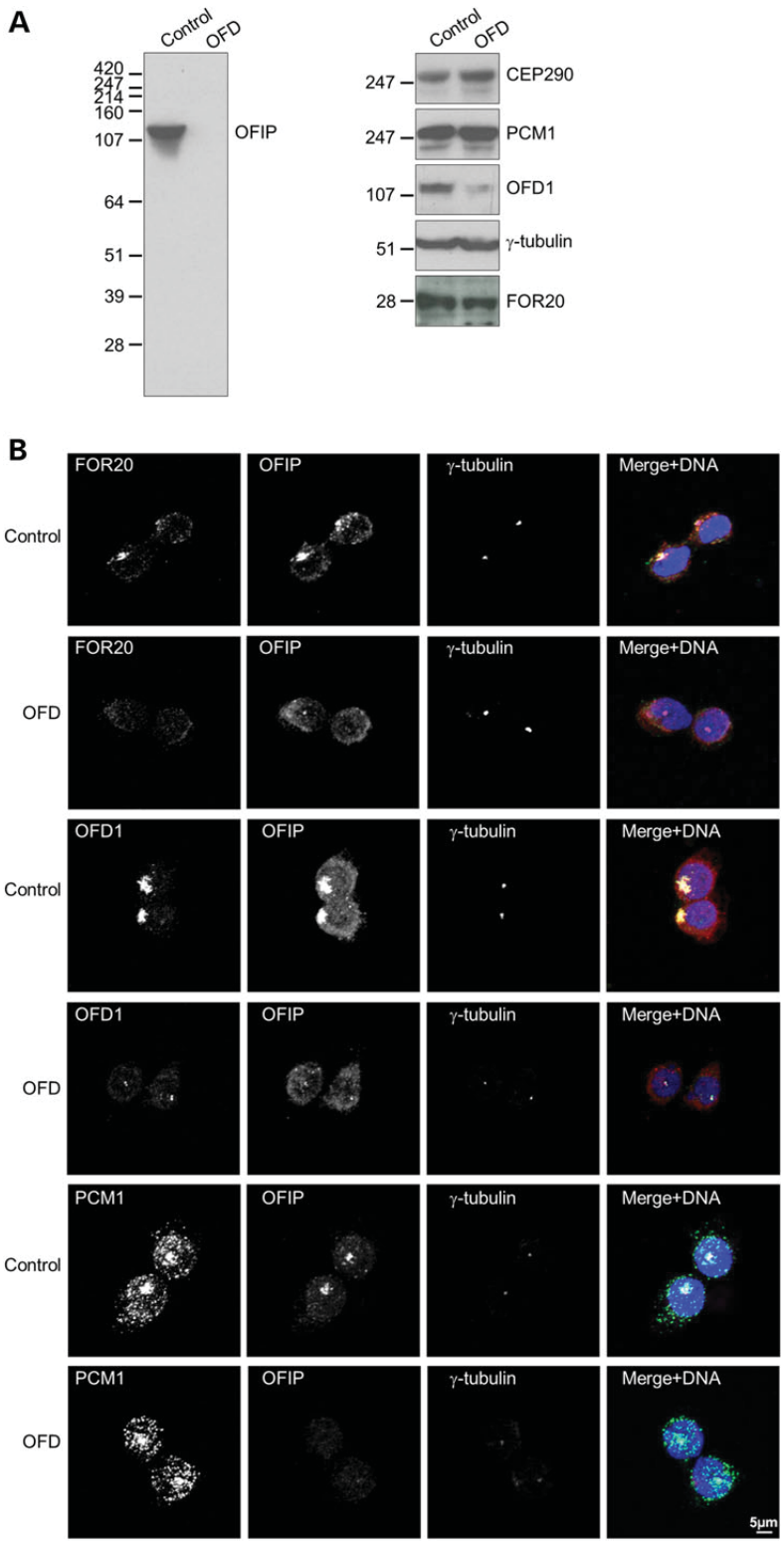

Figure 7. Wild-type OFIP is nearly absent in OFD cells. (**A**) Proteins from EBV-immortalized B lymphocytes of control donor and OFD patient were extracted in modified RIPA buffer and separated by 4–12% gradient SDS–PAGE. After transfer onto nitrocellulose, the membrane was immunoblotted with rat anti-OFIP (left), then stripped and immunoblotted to detect the indicated proteins (right). (**B**) EBV-immortalized B lymphocytes of control donor and OFD patient were seeded on polylysine-coated coverslips and fixed in cold methanol. Cells were labeled with mouse anti-γ-tubulin (magenta) and rat anti-OFIP (red), in combination with rabbit anti-FOR20, OFD1 or PCM1 antibodies, respectively (green). Scale bar, 5 μm.

This reduction is likely the consequence of lower levels cellular pools of OFD1 and FOR20 (Fig. 7A), suggesting that the formation of a ternary complex is required for the stability and subcellular localization of these proteins.

OFIP is an evolutionary-conserved protein in ciliated species

To find further evidence of OFIP association with the cilium, we examined its phylogenetic distribution, i.e. is OFIP present only in species with cilia? Cilia are ancient eukaryotic organelles that, together with their genes, have been lost multiple times in evolution like in most Fungi and in the flowering plants. Comparative genomics has been proved to be powerful in finding new ciliary proteins, including ones associated with ciliopathies (28). We performed sensitive sequence similarity searches to identify OFIP homologs. This resulted in the identification of OFIP homologs in animals, but also in distantly related ciliated species like *Chlamydomonas reinhardtii*, *Paramecium tetrauralia*, *Leishmania major* and one of the few ciliated fungi, the Chytrid *Batrachochytrium dendrobatidis*. No homologs could be detected in species without cilia, like most Fungi and flowering plants, and in some species with minimal cilia like *Plasmodium falciparum* and *Cryptosporidium parvum*. Species that do have a homolog of OFIP have only a single copy indicating that the proteins are likely orthologs. These observations suggest that OFIP is a cilia specific protein.

OFIP does not appear to have any known protein domains. We applied IUpred (29) and observed that OFIP consists of a large extent of disordered non-globular structures. The C-terminus of the protein is one of the few regions that are predicted to be globular. It is the C-terminus of the protein, which is conserved among orthologs (Fig. 8). It contains a peculiar pattern of alternating conserved negatively charged residues and hydrophobic residues that are predicted to form an α-helix by PhD (30). From such alternating charged and hydrophobic residues one might expect an amphipathic helix, but helical wheel projections did not show enrichment of either charged or non-charged residues on one side of the helix (data not shown).

To further study potential interactions between OFIP and other proteins linked to OFD (OFD1, C2CD3, TMEM107, TMEM216, C5orf42, WDPCP, DDX59, TCTN3, SCLT1 and TBC1D32) as well as FOR20, we examined whether their genes have similar phylogenetic distributions. Although almost all genes in this group occur only in ciliated species (with the exception of *DDX59*), their phylogenetic distributions are not very similar to *OFIP*, except for *TMEM107* and *FOR20*, suggesting that either, or both are somehow functionally linked to *OFIP* (Supplementary Material, Fig. S8). Interestingly, OFIP and FOR20 appear to form an evolutionary module with other known transition zone proteins (TMEM107, TCTN3 and TMEM216), which would be consistent with a previously described role of FOR20 in the assembly of the transition zone (26,31), suggesting that OFIP may be part of the same assembly pathway.

Discussion

The present study extends both our knowledge of molecular players of ciliogenesis and their contribution to the pathogenesis of human diseases. Among human syndromic diseases of genetic origin, ciliopathies have recently emerged as a prominent group characterized by developmental abnormalities linked to defects in primary and motile cilia (2,32). They can be categorized according to the combination of phenotypes they display, which are overlapping over different syndromes. Accordingly, some genes are targets for mutations in specific syndromes, but the involvement of one gene in two or more syndromes is becoming common from the results of sequencing of more and more exomes (33). OFD syndromes are characterized by mouth and craniofacial abnormalities and polydactyly, which can be associated with other features such as kidney diseases and central nervous system malformations. To date, 13 types have been classified based on this variability (15). OFD syndrome I is the most common and well-characterized OFD syndrome and is caused only by mutation in the *OFD1* gene, which is also mutated in JBS

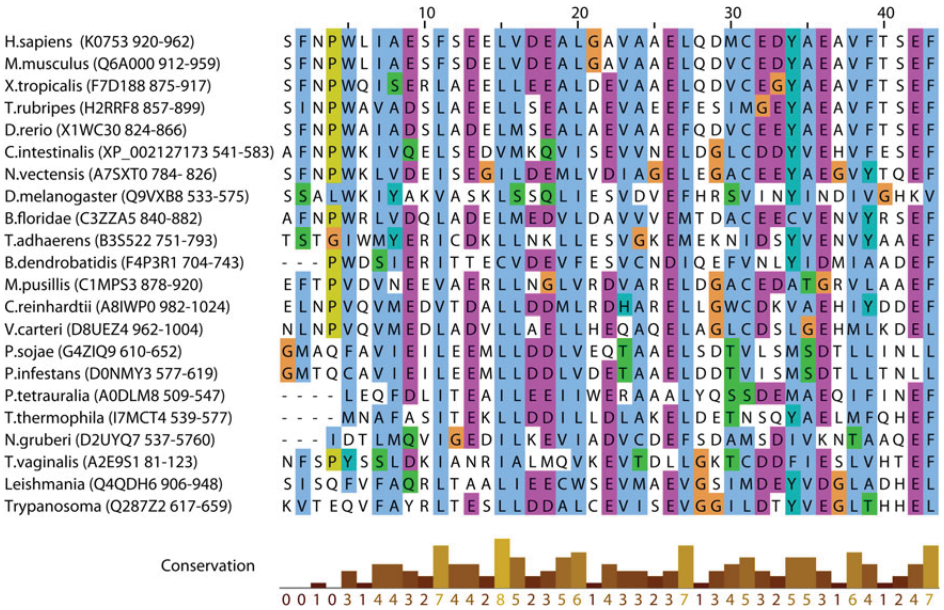

Figure 8. Multiple sequence alignment of the conserved OFIP C-terminus. Orthologs of OFIP in diverse eukaryotic species contain a conserved region of ~43 amino acids at the c-terminus. The region is predicted to form an α-helical structure with a peculiar pattern of conserved alternating negatively charged and hydrophobic residues.

(18,34,35). Genes causal to other OFD types can be found mutated in JBTS, Bardet–Biedl and Meckel syndromes, emphasizing the genetic and phenotypic complexity of ciliopathies. Our work has identified a causal compound heterozygous mutation of the *OFIP/KIAA0753* gene in one case of OFD type VI. Distinctive features of this subtype are cerebellar abnormalities with MTS and central polydactyly. This is the first described mutation in this gene, which codes for a recently identified centrosomal and PS protein (36,37). This rarity of *OFIP* mutations may be due to an embryonic lethal effect. The case studied here may result from a hypomorphic mutation, due to leakage of the correctly spliced OFIP product. We previously reported CBB defects in patients and mutant mice with OFD syndromes caused by mutations in the centrosome and PS proteins OFD1 and C2CD3, resulting in undocked basal bodies and short centrioles, respectively (24,38).

Preliminary functional characterization of OFIP indicated a possible role in centriole duplication (37). We have here extensively characterized OFIP, showing that it is a direct interactor of FOR20, a protein involved in primary ciliogenesis in human cells and required for assembly of the cilium transition zone and basal body anchoring at the cell cortex in *Paramecium* (25,26). We show that OFIP directly interacts with OFD1 in the absence of FOR20, but the interaction between OFIP and OFD1 is much stronger when FOR20 is present in the complex. FOR20 and OFD1 have a similar localization at the distal part of CBB and are necessary for basal body anchoring (22,26,38), in agreement with their inclusion in a unique complex. Cells lacking either FOR20 or OFD1 have abnormalities at the CBB distal ends (22,26). However, these observations have been made in different model systems, i.e. *Paramecium* and human cells, respectively. Remarkably, OFD1 also interacts with C2CD3, and the two proteins are proposed to play antagonistic role in regulating the length of centriole distal ends (24). C2CD3 may thus be associated with the ternary complex we have described, but was not identified in our proteomic analysis of OFIP- and/or FOR20-associated proteins. That OFD1, C2CD3 and OFIP are targets of causal mutations in OFD syndromes confirms the hypothesis that affecting CBB distal end length and/or structure by disrupting this molecular complex is a pathogenic mechanism of some ciliopathies.

The mutations described here disrupt the integrity of the complex as they truncate the C-terminus of OFIP, which interacts with FOR20 and OFD1, and strongly down-regulate OFD1 in patient cells. Remarkably, the C-terminal end is the conserved region among the OFIP orthologs which, together with the similar conservation of FOR20 and OFD1 (Supplementary Material, Fig. S8), stresses out the biological importance of this complex. Overexpressed OFIP decorates and stabilizes a population of MTs, but does not organize in rod-like fashion at the centrosome, like an overexpressed C2CD3 (24). It will be interesting to know if these structures, which correspond to elongated centrioles, require and/or recruit OFIP to stabilize longer MT triplets. The centrosomal protein FOP is evolutionary related to FOR20 and OFD1 and interacts with the CEP350 protein, which stabilizes Golgi-associated and centriolar MTs (39,40). An emerging scheme of mechanism may be that related molecular complexes at CBB associate MT-stabilizing/-binding activity coupled with an unknown structural or functional role of FOR20, OFD1 and FOP. In support of this, the molecular determinant of the OFIP-FOR20 and CEP350-FOP interaction are very similar, involving the last C-terminal residues on one partner and the conserved TOF and LisH-domain containing N-terminus on the other. The activity of the OFIP-associated complex is likely to take place at the centriole distal end to regulate MT triplet length and assembly of the adjacent transition zone. As recently established, several protein complexes involving ciliopathy proteins localized at the transition zone to regulate its assembly and function as a cellular gate to organize cilium structure and signaling pathways (14,41–43). How the distal end of centriole participates in the assembly of the transition zone is unclear. A number of transition zone proteins are already present on undocked centrioles indicating that transition zone is partly organized before cilium formation (44). Recently, the CEP162 centriole distal end protein has been shown to promote assembly of the transition zone by connecting core transition zone component to ciliary MTs (45). It will be of interest to study transition zone assembly in the absence of OFIP and its partners to assign it a role similar to CEP162 in ciliogenesis.

Our study also points out to a role of complex formation in the stability of OFD1 and to a lower extent of FOR20. An effective quality control mechanism exists in the cytoplasm to recognize and eliminate misfolded proteins by the ubiquitin-proteasome-dependent pathway (46). It is possible that correct folding of OFD1 and FOR20 is dependent on their interaction with OFIP, but the possible involvement of chaperone to assist this process, like in BBSome formation, is not excluded (47).

Recently, >20 proteins were characterized as associated with PSs (48,49). Most of them are also centrosome and basal body proteins, raising the possibility that PSs play a role in ciliogenesis. However, the depletion of PCM1 in differentiating mouse trachea cells does not inhibit centriole multiplication and MMC formation (50). In contrast, several studies point to a role of PSs in the formation of PC and an emerging picture is that (i) PCM1 depletion inhibits primary ciliogenesis (12,51,52), (ii) PSs adopt a regulated dynamics during primary ciliogenesis, a process regulated by TALPID3 and CEP290 (53) (iii) PS proteins, such as CEP72, CEP290 and SSX2IP control the accumulation of RAB8 and the BBSome complex, two key effectors of cilia formation (12,54) and (iv) PSs are an assembly point for proteins affected in ciliopathies such as ODF1, CEP290 and BBS4 (13). PSs and PCM1 are only present in metazoa and possibly arose during evolution to regulate ciliogenesis in the context of complex tissues. Strikingly, however, no mutations in PCM1 were detected in ciliopathies. Like for OFIP, PCM1 mutations may be incompatible with the development of an embryo. Both OFIP (this study) and OFD1 are able to interact with PCM1 (13), the major constituent of PS. Because OFIP and OFD1 are conserved in ciliated protists, the two proteins have probably evolved to acquire the capacity of binding PCM1 and PS in metazoa. The ternary complex we have identified is likely a cargo of PSs to be addressed to CBB. PSs are indirectly associated with the dynactin subunit p150glued and move along MTs in a dynein–dynactin-dependant manner (55–57). It has been reported that kinesin 1 has higher affinity for acetylated and detyrosinated (58,59) and that tubulin glutamylation, another feature of stable MTs, regulates axonemal dynein (60). It is thus possible that local stabilization of MTs by PS-associated OFIP is important for the dynamics of PSs.

The recent plethora of information on the phenotypic and genetic complexity of ciliopathy does not fit with a simple genotype–phenotype correlation and raises the central question of the qualitative and quantitative signaling defect caused by a given mutation or combination of mutations. For a subset of ciliopathies, this is underpinned by the hypothesis that mutations in different genes affect the gating capacity of the transition zone to similar extent, thus giving similar phenotypes. KIAA0753 and also FOR20 are thus candidate genes for most non-motile ciliopathies described to date.

In conclusion, we have uncovered a previously unidentified protein complex involved in centriole and cilium regulation, and affected in ciliopathies, particularly in the OFD syndromes.

Materials and Methods

Exome sequencing

Exome sequencing was performed on the patient DNA according to standard procedures using the SureSelect Human All Exon V2 kit (Agilent), using three micrograms of genomic to whole-exome capture. The resulting libraries were sequenced on a HiSeq 2000 (Illumina) as paired-end 75 bp reads in accordance with the manufacturer's recommendations. Raw data were processed as previously described (24). BAM files were aligned to a human genome reference sequence (GRCh37/hg19) using BWA (Burrows–Wheeler Aligner; v0.7.6) and potential duplicate paired-end reads were removed by Picard 1.77. Indel realignment and base quality score recalibration were conducted with Genome Analysis Toolkit (GATK; v2.1-10). Variants with quality scores of <30, allele balance of >0.75, sequencing depth of <4, quality/depth ratio of <5.0, length of homopolymer run of >5.0 and strand bias of >−0.10 were flagged and excluded from subsequent analyses. Variants with a quality score of >30 and alignment quality score >20 were annotated with SeattleSeq SNP Annotation (see URLs). Rare variants present at a frequency >1% in dbSNP 138 and the NHLBI GO Exome Sequencing Project or present from 69 local exomes of unaffected individuals were excluded (see URLs). Variant filtering was as follows: (i) variants affecting the coding sequence, (ii) rare variants, absent from public databases (see URLs), (iii) homozygous or compound heterozygous variants and (iv) ciliary/centrosomal genes.

OFIP/KIAA0753 and *FOR20 mutation validation*

Genomic DNA was amplified by polymerase chain reaction (PCR) using HotStarTaq PCR kit (Qiagen) according to the manufacturer's protocol. OFIP/*KIAA0753* and *FOR20* primers were designed on the RefSeq NM_014804.2 and NM_ 144600.2) (primers available on request). PCR products were purified by the Agencourt CleanSEQ system (Beckman Coulter) and sequenced with the BigDye Terminator Cycle Sequencing kit, v3.1 (Applied Biosystems) in ABI 3730 sequencer (Applied Biosystems). Sequence data were analyzed using Mutation Surveyor v4.0.9 (Softgenomics).

OFIP/KIAA0753 cDNA analysis

Total RNA was isolated with TRIzol Reagent (Life Technologies) from EBV transformed lymphoblastoid cell line of the patient, according to the manufacturer's instructions. One microgram of RNA was transcribed into cDNA with the QuantiTect Reverse Transcription Kit (Qiagen). Using PCR primers positioned in Exons 6, 10 and 11 in KIAA0753 gene (primers available on request), cDNA was amplified using the HotStartTaq Plus DNA Polymerase Kit (Qiagen) following the instructions provided by the manufacturer.

Replication cohort sequencing

All coding region of *OFIP/KIAA0753* and *FOR20/FOPNL* gene was amplified by PCR long-range with PrimeStar GXL kit (Takara) for 32 patients of replication cohort (primers available on request). PCR products were pooled for each case. Nextera XT DNA Preparation kit (Illumina) was used to create a DNA library tagged and fragmented according to the manufacturer's protocol. Samples obtained were pooled and sequenced in Miseq (Illumina). Resulting data were aligned to the gene reference sequence (GRCh37/hg19) using BWA (Burrows–Wheeler Aligner; v0.7.6). The Genome Analysis Toolkit (GATK; v2.1-10) enabled indel realignment and base quality score recalibration. Variants with a quality score of >30 and alignment quality score >20 were annotated with SeattleSeq SNP Annotation.

Yeast two-hybrid

The baits were clones into pDBa (Leu) using the Gateway technology (Invitrogen™). The bait plasmids were transformed in MAV03 yeast strain (MATα; leu2-3,112; trp1-901; his3Δ200; ade2-101; gal4 Δ; gal80 Δ; SPAL10UASGAL1::URA3, GAL1::lacZ, GAL1::His3@LYS2, can1R, cyh2R) in accordance with the previously described transformation protocol (61). The self-activation of the resulting yeast strains was tested with the four phenotypes. Mav203 cells were then transformed with the cDNA library of choice (cloned into pEXP502-AD (Trp), Proquest libraries™, Invitrogen™) as described previously (61). Following transformation with the cDNA library, yeast were plated onto synthetic complete (SC) medium minus leucine (–L), minus tryptophane (–W), minus histidine (–H) +25 mM 3-amino-1,2,4-triazole (3-AT) and incubated at 30°C for 4–5 days. Positive clones where then selected and patched onto SC-WHL +3-AT in 96-well plate format and incubated for 3 days at 30°C. Yeast clones are then transferred in liquid SC-WL for 3 days at 30°C with agitation to normalize the yeast cell concentration used for the phenotypic assay. The cells are then diluted 1/20 in water and spotted onto different selective medium (–WHL + 25 mm 3-AT, –WL + 0.2% 5-5-fluoroorotic acid and –WUL). To perform the β-galactosidase assay, the undiluted yeast cells are spotted onto yeast extract peptone dextrose (YPD) medium plate with a nitrocellulose filter.

Plates are incubated at 30°C for 4–5 days, except the YPD plate which is removed after 1 day, and β-galactosidase activity is evaluated as described.

Plasmids

The *OFIP/KIAA0753* full-length cDNA in pBluescript II was obtained from the Kazusa DNA Research Institute (Chiba, Japan). The OFD1 ORF cDNA was obtained from Genecopoeia™.

The sequence coding for the full-length and truncated proteins were amplified by PCR using Platinum HiFi polymerase (Invitrogen) and Gateway-compatible primers and transferred into pDONR/ZEO using Gateway technology-mediated recombination. The sequences were subsequently transferred by recombination into modified Gateway-compatible pRK5/Myc, pEGFP-C1 and pmCherry-C1 expression vectors.

Cells, antibodies and reagents

Immortalized human retinal pigment epithelial cells htert-RPE1 (thereafter referred as RPE1) were grown in Dulbecco's modified Eagle's medium F12 (DMEM/F12) (Life Technologies) supplemented with 10% heat-inactivated fetal calf serum (FCS). Hela Kyoto and Cos1 cells were grown in DMEM supplemented with 10% heat inactivated FCS. Lymphocytes (patient and control) cells were grown in RPMI supplemented with 10% heat inactivated FCS.

Anti-human OFIP monoclonal antibodies were obtained following immunization of rats with the OFIP carboxy terminus (residues 667–967) fused to GST protein. Immune spleen cells were fused with the non-secreting myeloma X63-Ag8.653 cells and grown in selective medium. Hybridoma supernatants were

first screened by ELISA on GST-OFIP and GST alone. GST-OFIP-only positive populations were screened by immunofluorescence on methanol-fixed RPE1 cells and western blotting of lysates from Cos1 cells overexpressing Myc-tagged OFIP. Selected clones were cloned three times before large-scale antibody production.

A rabbit anti-OFIP/KIAA0753 antibody was from Sigma-Aldrich. Anti-γ-tubulin antibodies were from Sigma-Aldrich (mouse monoclonal GTU-88 and rabbit polyclonal T3559). Rabbit anti-PCM1 was from Bethyl Laboratories. Mouse anti-c-Myc (9E10) was from Santa Cruz Biotechnology. Anti-GFP antibodies were purchased from Abcam (rabbit polyclonal) and Roche (mouse monoclonal).

Cell transfection

For plasmids, cells were transfected with Fugene6 or Fugene HD (Roche Applied Science) according to manufacturer's protocol.

siRNA oligonucleotides were transfected into cells using INTERFERin® (Polyplus Transfection) according to the manufacturer's protocol. The sequences are the following: OFIP (5′-GCUCAAAGCUGAAGAAAUG-3′), FOR20 (5′-GAGAGUAUUUAGAAUUCAA-3′) (25), PCM1 (5′-UCAGCUUCGUGAUUCUCAGTT-3′) (55), OFD1 (5′-GCUCAUAGCUAUUAAUUCA-3′) (13), CEP290 (pool of 4 siRNAs: 5′-GAAGUAGAGUCCCUCAGAA-3′, 5′-GAAAGUUAAUGAGCAAUUG-3′, 5′-GGAAUUGACUUACCUGAUG-3′, 5′-GGAUUCGGAUGAAUGAAA-3′). A non-targeting siRNA was used for controls. All siRNAs were purchased from Dharmacon as ON-TARGETplus siRNAs.

Cell extracts

Cells were washed in phosphate buffered saline (PBS) and lysed in 20 mm Tris–HCl pH 7.5, 2 mM EDTA, 150 mM NaCl, 1% Igepal CA630 (Sigma) or 50 mM Tris–HCl pH 7.5, 150 mM NaCl, 1 mM EDTA, containing 1% NP-40 and 0.25% sodium deoxycholate (modified RIPA) plus a complete protease inhibitor cocktail (Roche Applied Science) buffer on ice. After centrifugation for 20 min at 13 000 rpm at 4°C, cleared lysates were obtained.

Triton-X100 soluble and insoluble fractions were obtained as follows: cells were washed in PBS, lysed in PHEM buffer (45 mM PIPES, 45 mM HEPES, 10 mM ethylene glycol tetra-acetic acid (EGTA), 5 mM $MgCl_2$, pH 6.9) plus 1% Triton X-100 and protease inhibitors and centrifuged at 400 g for 45 min. The supernatant was collected (soluble fraction) and the pellet was washed in PHEM alone and solubilized in 1% SDS containing buffer (insoluble fraction) and sonicated. Cell extracts separated on polyacrylamide gels were transferred onto Hybond™-C membrane (GE Healthcare Life Science) followed by detection with antibodies.

Immunoprecipitation and western blot analysis

For anti-Myc immunoprecipitation, extracts were incubated with agarose beads conjugated to mouse anti-Myc antibodies (Santa Cruz Biotechnology) for 3 h at 4°C. Beads were pelleted and washed five times with lysis buffer. For anti-GFP immunoprecipitations, extracts were incubated with agarose beads conjugated to rabbit anti-GFP antibodies (Abcam) or with GFP-Trap® alpaca anti-GFP-conjugated agarose beads. Samples were separated using in house SDS–PAGE or NuPAGE 4–12% Novex Bis–Tris gels according to manufacturer's instructions (Invitrogen).

Immunofluorescence

Cells were grown on coverslips, fixed in cold methanol (6–8 min at −20°C) and incubated with the appropriate mixture of primary antibodies for 30 min at room temperature. After washing in PBS 0.1% Tween, they were incubated for another 30 min with the adequate secondary antibodies conjugated to cy2, cy3 or cy5 (Jackson laboratories) to which was added 250 ng/ml DAPI for DNA staining, rinsed and mounted in Prolong Gold antifade reagent (Life Technologies). Confocal images were acquired by capturing Z-series with 0.3 µm step size on a Zeiss LSM 510 laser scanning confocal microscope.

Immunoelectron microscopy

Cells grown on Lab-Tek permanox Chamber were permeabilized 6 min in 45 mM PIPES, 10 mM EGTA, 5 mM $MgCl_2$, pH 69 (PEM) 0.25% triton and were prefixed in PEM 0.25% glutaraldehyde 10 min at room temperature. After three washes in PBS containing 0.1% bovine serum albumin (BSA) and 0.1% Tween, the cells were incubated with anti-OFIP (1/20 000) and anti-PCM1 (1/1000) antibodies for 1 h. The cells were washed three times with PBS containing 0.1% BSA and 0.1% Tween-20, and were incubated with goat anti-rat antibody conjugated to 6 nm colloidal gold (1/40; Jackson Laboratories) and goat anti-rabbit antibody conjugated to 18 nm colloidal gold (1/40; Jackson Laboratories) for 1 h. For electron, microscopy cells were fixed with 2.5% glutaraldehyde and processed for dehydration and embedding, as described previously (62).

MT stability assay

Cells were lysed with 2 mµ EGTA, 1 mM $MgCl_2$ (EM) buffer and proteases inhibitor coktail 10 min on ice and homogenized with 10 strokes of potter. Of note, 0.5 M K-Pipes was added for a final concentration of 100 mM. Lysates were centrifuged at 4°C for 1 h at 55 000 rpm. Supernatants were incubated with 1 mM GTP, 1 mM DTT ± 10 µM nocodazole and ±50 µg purified porcine tubulin for 90 min at 37°C and overlaid on PEM buffer (100 mM K-Pipes [pH 6.8], 1 mM EGTA 1 mM $MgCl_2$) containing 10% sucrose. After centrifugation at 25°C for 30 min at 19 000 rpm, supernatants and pellets were analyzed by electrophoresis and western blotting.

Fluorescence quantification

The image analysis was performed on maximum intensity projection images that were generated from confocal stacks. Image processing was done using ImageJ.

To quantify the centrosome fluorescence, regions in these images were defined by γ-tubulin staining for each cell using threshold. Centrosome mask was created, and integrated density of individual centrosomes within the mask was measured.

To quantify satellites fluorescence, the centrosome mask was subtracted to mask cell obtained using threshold. Integrated density was measured. All data were analyzed by Prism.

Phylogenetic analysis

We used BLAST (63) for initial sequence searches for orthologs of OFIP and other OFD-related genes. To identify additional homologs, we employed Jackhammer (64) to perform profile-based homology searches. We compared the OFIP phylogenetic pattern with those of transition zone and centriolar proteins using a predefined set of organisms used previously (Lambacher *et al.*, submitted for publication). UIpred was used to predict disordered regions and globular folds within the protein structure. The protein C-terminal sequences of OFIP orthologs were aligned with clustalx (65) and visualized with JalView (66).

Web Resources

NHLBI Exome Sequencing Project Exome Variant Server, http://evs.gs.washington.edu/EVS/
dbSNP, http://www.ncbi.nlm.nih.gov/projects/SNP/
Picard, www.picard.sourceforge.net
University of Burgundy Centre de Calcul, https://haydn2005.u-bourgogne.fr/dsi-ccub/Seattle
Seq Annotation tool, snp.gs.washington.edu/SeattleSeqAnnotation137/
Human Gene Mutation Database HGMD, http://www.hgmd.org/
ClinVar, http://www.ncbi.nlm.nih.gov/clinvar/
UIpred, http://iupred.enzim.hu/

Supplementary Material

Supplementary Material is available at *HMG* online.

Acknowledgements

We thank the patients and their families for their participation. We thank the Integragen society for exome analysis. We also thank the NHLBI GO Exome Sequencing Project (see URLs) and its ongoing studies which produced and provided exome variant calls for comparison: the Lung GO Sequencing Project (HL-102923), the WHI Sequencing Project (HL-102924), the Broad GO Sequencing Project (HL-102925), the Seattle GO Sequencing Project (HL-102926) and the Heart GO Sequencing Project (HL-103010). We are grateful to Aicha Aouane and Jean-Paul Chauvin (Electron Microscopy service, Institut de Biologie du Développement de Marseille, Marseille, France) for assistance on electron microscopy experiments and to Michel Pierres (Centre d'Immunologie de Marseille-Luminy, Marseille, France) for helping with antibody production. We acknowledge the France-BioImaging/PICsL infrastructure (supported by the French National Research Agency, ANR-10-INSB-04-01, 'Investments for the future'). We thank Andrew Fry (University of Leicester, Leicester, UK) for the gift of OFD1 plasmid and antibody. We are also indebted to Ina Poser and Anthony Hyman (Max Planck Institute of Molecular Cell Biology and Genetics, Dresden, Germany) for the TransgeneOmics cell lines and BAC constructs. J.P.B. is scholar of Institut Universitaire de France.

Conflict of Interest statement. None declared.

Funding

This work was supported by INSERM and Institut Paoli-Calmettes and by grants from the GIS-Institut des Maladies Rares (HTS), the French Ministry of Health (PHRC national 2010-A01014-35 to C.T.-R.), the Italian Telethon Foundation (TGM11CB3 to B.F.), the Regional Council of Burgundy (to C.T.-R.) and the European Community's Seventh Framework Programme FP7/2009 under grant agreement 241955 SYSCILIA. The Marseille proteomic plateform is recognized by IBiSA (Infrastructures en Biologie-Santé et Agronomie) and supported by Institut Paoli-Calmettes, Inserm and Aix-Marseille University.

References

1. Nigg, E.A. and Raff, J.W. (2009) Centrioles, centrosomes, and cilia in health and disease. *Cell*, **139**, 663–678.
2. Badano, J.L., Mitsuma, N., Beales, P.L. and Katsanis, N. (2006) The ciliopathies: an emerging class of human genetic disorders. *Annu. Rev. Genomics Hum. Genet.*, **7**, 125–148.
3. Nonaka, S., Tanaka, Y., Okada, Y., Takeda, S., Harada, A., Kanai, Y., Kido, M. and Hirokawa, N. (1998) Randomization of left-right asymmetry due to loss of nodal cilia generating leftward flow of extraembryonic fluid in mice lacking KIF3B motor protein. *Cell*, **95**, 829–837.
4. Nigg, E.A. and Stearns, T. (2011) The centrosome cycle: centriole biogenesis, duplication and inherent asymmetries. *Nat. Cell Biol.*, **13**, 1154–1160.
5. Jord, A.A., Lemaitre, A.I., Delgehyr, N., Faucourt, M., Spassky, N. and Meunier, A. (2014) Centriole amplification by mother and daughter centrioles differs in multiciliated cells. *Nature*, **516**, 104–107.
6. Rohatgi, R. and Snell, W.J. (2010) The ciliary membrane. *Curr. Opin. Cell Biol.*, **22**, 541–546.
7. Lu, Q., Insinna, C., Ott, C., Stauffer, J., Pintado, P.A., Rahajeng, J., Baxa, U., Walia, V., Cuenca, A., Hwang, Y.S. *et al.*(2015) Early steps in primary cilium assembly require EHD1/EHD3-dependent ciliary vesicle formation. *Nat. Cell Biol.*, **17**, 531.
8. Bhogaraju, S., Cajanek, L., Fort, C., Blisnick, T., Weber, K., Taschner, M., Mizuno, N., Lamla, S., Bastin, P., Nigg, E.A. *et al.* (2013) Molecular basis of tubulin transport within the cilium by IFT74 and IFT81. *Science*, **341**, 1009–1012.
9. Pedersen, L.B. and Rosenbaum, J.L. (2008) Intraflagellar transport (IFT) role in ciliary assembly, resorption and signalling. *Curr. Top. Dev. Biol.*, **85**, 23–61.
10. Wei, Q., Zhang, Y., Li, Y., Zhang, Q., Ling, K. and Hu, J. (2012) The BBSome controls IFT assembly and turnaround in cilia. *Nat. Cell Biol.*, **14**, 950–957.
11. Pedersen, L.B. and Christensen, S.T. (2012) Regulating intraflagellar transport. *Nat. Cell Biol.*, **14**, 904–906.
12. Stowe, T.R., Wilkinson, C.J., Iqbal, A. and Stearns, T. (2012) The centriolar satellite proteins Cep72 and Cep290 interact and are required for recruitment of BBS proteins to the cilium. *Mol. Biol. Cell*, **23**, 3322–3335.
13. Lopes, C.A., Prosser, S.L., Romio, L., Hirst, R.A., O'Callaghan, C., Woolf, A.S. and Fry, A.M. (2011) Centriolar satellites are assembly points for proteins implicated in human ciliopathies, including oral-facial-digital syndrome 1. *J. Cell Sci.*, **124**, 600–612.
14. Chih, B., Liu, P., Chinn, Y., Chalouni, C., Komuves, L.G., Hass, P.E., Sandoval, W. and Peterson, A.S. (2012) A ciliopathy complex at the transition zone protects the cilia as a privileged membrane domain. *Nat. Cell Biol.*, **14**, 61–72.
15. Gurrieri, F., Franco, B., Toriello, H. and Neri, G. (2007) Oral-facial-digital syndromes: review and diagnostic guidelines. *Am. J. Med. Genet A*, **143A**, 3314–3323.
16. Poretti, A., Vitiello, G., Hennekam, R.C., Arrigoni, F., Bertini, E., Borgatti, R., Brancati, F., D'Arrigo, S., Faravelli, F., Giordano, L. *et al.* (2012) Delineation and diagnostic criteria of Oral-Facial-Digital Syndrome type VI. *Orphanet J. Rare Dis.*, **7**, 4.
17. Adly, N., Alhashem, A., Ammari, A. and Alkuraya, F.S. (2014) Ciliary genes TBC1D32/C6orf170 and SCLT1 are mutated in patients with OFD type IX. *Hum. Mutat.*, **35**, 36–40.
18. Ferrante, M.I., Giorgio, G., Feather, S.A., Bulfone, A., Wright, V., Ghiani, M., Selicorni, A., Gammaro, L., Scolari, F., Woolf, A.S. *et al.* (2001) Identification of the gene for oral-facial-digital type I syndrome. *Am. J. Hum. Genet.*, **68**, 569–576.
19. Lopez, E., Thauvin-Robinet, C., Reversade, B., Khartoufi, N.E., Devisme, L., Holder, M., Ansart-Franquet, H., Avila, M., Lacombe, D., Kleinfinger, P. *et al.* (2014) C5orf42 is the major gene responsible for OFD syndrome type VI. *Hum. Genet.*, **133**, 367–377.
20. Saari, J., Lovell, M.A., Yu, H.C. and Bellus, G.A. (2015) Compound heterozygosity for a frame shift mutation and a likely

pathogenic sequence variant in the planar cell polarity-ciliogenesis gene WDPCP in a girl with polysyndactyly, coarctation of the aorta, and tongue hamartomas. *Am. J. Med. Genet A*, **167A**, 421–427.
21. Shamseldin, H.E., Rajab, A., Alhashem, A., Shaheen, R., Al-Shidi, T., Alamro, R., Al Harassi, S. and Alkuraya, F.S. (2013) Mutations in DDX59 implicate RNA helicase in the pathogenesis of orofaciodigital syndrome. *Am. J. Hum. Genet.*, **93**, 555–560.
22. Singla, V., Romaguera-Ros, M., Garcia-Verdugo, J.M. and Reiter, J.F. (2010) Ofd1, a human disease gene, regulates the length and distal structure of centrioles. *Dev. Cell*, **18**, 410–424.
23. Ye, X., Zeng, H., Ning, G., Reiter, J.F. and Liu, A. (2014) C2cd3 is critical for centriolar distal appendage assembly and ciliary vesicle docking in mammals. *Proc. Natl Acad. Sci. USA*, **111**, 2164–2169.
24. Thauvin-Robinet, C., Lee, J.S., Lopez, E., Herranz-Perez, V., Shida, T., Franco, B., Jego, L., Ye, F., Pasquier, L., Loget, P. *et al.* (2014) The oral-facial-digital syndrome gene C2CD3 encodes a positive regulator of centriole elongation. *Nat. Genet.*, **46**, 905–911.
25. Sedjai, F., Acquaviva, C., Chevrier, V., Chauvin, J.P., Coppin, E., Aouane, A., Coulier, F., Tolun, A., Pierres, M., Birnbaum, D. *et al.* (2010) Control of ciliogenesis by FOR20, a novel centrosome and pericentriolar satellite protein. *J. Cell Sci.*, **123**, 2391–2401.
26. Aubusson-Fleury, A., Lemullois, M., de Loubresse, N.G., Laligne, C., Cohen, J., Rosnet, O., Jerka-Dziadosz, M., Beisson, J. and Koll, F. (2012) The conserved centrosomal protein FOR20 is required for assembly of the transition zone and basal body docking at the cell surface. *J. Cell Sci.*, **125**, 4395–4404.
27. Poser, I., Sarov, M., Hutchins, J.R., Heriche, J.K., Toyoda, Y., Pozniakovsky, A., Weigl, D., Nitzsche, A., Hegemann, B., Bird, A.W. *et al.* (2008) BAC TransgeneOmics: a high-throughput method for exploration of protein function in mammals. *Nat. Methods*, **5**, 409–415.
28. Li, J.B., Gerdes, J.M., Haycraft, C.J., Fan, Y., Teslovich, T.M., May-Simera, H., Li, H., Blacque, O.E., Li, L., Leitch, C.C. *et al.* (2004) Comparative genomics identifies a flagellar and basal body proteome that includes the BBS5 human disease gene. *Cell*, **117**, 541–552.
29. Dosztanyi, Z., Csizmok, V., Tompa, P. and Simon, I. (2005) IUPred: web server for the prediction of intrinsically unstructured regions of proteins based on estimated energy content. *Bioinformatics*, **21**, 3433–3434.
30. Rost, B. and Sander, C. (1994) Combining evolutionary information and neural networks to predict protein secondary structure. *Proteins*, **19**, 55–72.
31. Lambacher, N.J., Bruel, A.L., van Dam, T.J.P., Szymańska, K., Slaats, G.G., Kuhns, S., McManus, G.J., Kennedy, J.E., Gaff, K., Wu, K.M. *et al.* (2015) TMEM107 recruits ciliopathy proteins to anchored periodic subdomains of the ciliary transition zone membrane and is mutated in Joubert syndrome. *Nat. Cell Biol.*, doi: 10.1038/ncb3273.
32. Davis, E.E. and Katsanis, N. (2012) The ciliopathies: a transitional model into systems biology of human genetic disease. *Curr. Opin. Genet. Dev.*, **22**, 290–303.
33. Novarino, G., Akizu, N. and Gleeson, J.G. (2011) Modeling human disease in humans: the ciliopathies. *Cell*, **147**, 70–79.
34. Ferrante, M.I., Zullo, A., Barra, A., Bimonte, S., Messaddeq, N., Studer, M., Dolle, P. and Franco, B. (2006) Oral-facial-digital type I protein is required for primary cilia formation and left-right axis specification. *Nat. Genet.*, **38**, 112–117.
35. Coene, K.L., Roepman, R., Doherty, D., Afroze, B., Kroes, H.Y., Letteboer, S.J., Ngu, L.H., Budny, B., van Wijk, E., Gorden, N.T. *et al.* (2009) OFD1 is mutated in X-linked Joubert syndrome and interacts with LCA5-encoded lebercilin. *Am. J. Hum. Genet.*, **85**, 465–481.
36. Jakobsen, L., Vanselow, K., Skogs, M., Toyoda, Y., Lundberg, E., Poser, I., Falkenby, L.G., Bennetzen, M., Westendorf, J., Nigg, E. A. *et al.* (2011) Novel asymmetrically localizing components of human centrosomes identified by complementary proteomics methods. *EMBO J.*, **24**, 664–670.
37. Firat-Karalar, E.N., Rauniyar, N., Yates, J.R. III and Stearns, T. (2014) Proximity interactions among centrosome components identify regulators of centriole duplication. *Curr. Biol.*, **24**, 664–670.
38. Thauvin-Robinet, C., Thomas, S., Sinico, M., Aral, B., Burglen, L., Gigot, N., Dollfus, H., Rossignol, S., Raynaud, M., Philippe, C. *et al.* (2013) OFD1 mutations in males: phenotypic spectrum and ciliary basal body docking impairment. *Clin. Genet.*, **84**, 86–90.
39. Hoppeler-Lebel, A., Celati, C., Bellett, G., Mogensen, M.M., Klein-Hitpass, L., Bornens, M. and Tassin, A.M. (2007) Centrosomal CAP350 protein stabilises microtubules associated with the Golgi complex. *J. Cell Sci.*, **120**, 3299–3308.
40. Yan, X., Habedanck, R. and Nigg, E.A. (2006) A complex of two centrosomal proteins, CAP350 and FOP, cooperates with EB1 in microtubule anchoring. *Mol. Biol. Cell.*, **17**, 634–644.
41. Williams, C.L., Li, C., Kida, K., Inglis, P.N., Mohan, S., Semenec, L., Bialas, N.J., Stupay, R.M., Chen, N., Blacque, O.E. *et al.* (2011) MKS and NPHP modules cooperate to establish basal body/transition zone membrane associations and ciliary gate function during ciliogenesis. *J. Cell Biol.*, **192**, 1023–1041.
42. Sang, L., Miller, J.J., Corbit, K.C., Giles, R.H., Brauer, M.J., Otto, E.A., Baye, L.M., Wen, X., Scales, S.J., Kwong, M. *et al.* (2011) Mapping the NPHP-JBTS-MKS protein network reveals ciliopathy disease genes and pathways. *Cell*, **145**, 513–528.
43. Garcia-Gonzalo, F.R., Corbit, K.C., Sirerol-Piquer, M.S., Ramaswami, G., Otto, E.A., Noriega, T.R., Seol, A.D., Robinson, J.F., Bennett, C.L., Josifova, D.J. *et al.* (2011) A transition zone complex regulates mammalian ciliogenesis and ciliary membrane composition. *Nat. Genet.*, **43**, 776–784.
44. Czarnecki, P.G. and Shah, J.V. (2012) The ciliary transition zone: from morphology and molecules to medicine. *Trends Cell Biol.*, **22**, 201–210.
45. Wang, W.J., Tay, H.G., Soni, R., Perumal, G.S., Goll, M.G., Macaluso, F.P., Asara, J.M., Amack, J.D. and Tsou, M.F. (2013) CEP162 is an axoneme-recognition protein promoting ciliary transition zone assembly at the cilia base. *Nat. Cell Biol.*, **15**, 591–601.
46. Amm, I., Sommer, T. and Wolf, D.H. (2014) Protein quality control and elimination of protein waste: the role of the ubiquitin-proteasome system. *Biochim. Biophys. Acta*, **1843**, 182–196.
47. Zhang, Q., Yu, D., Seo, S., Stone, E.M. and Sheffield, V.C. (2012) Intrinsic protein-protein interaction-mediated and chaperonin-assisted sequential assembly of stable Bardet-Biedl syndrome protein complex, the BBSome. *J. Biol. Chem.*, **287**, 20625–20635.
48. Tollenaere, M.A., Mailand, N. and Bekker-Jensen, S. (2015) Centriolar satellites: key mediators of centrosome functions. *Cell Mol. Life Sci.*, **72**, 11–23.
49. Barenz, F., Mayilo, D. and Gruss, O.J. (2011) Centriolar satellites: busy orbits around the centrosome. *Eur. J. Cell Biol.*, **90**, 983–989.

50. Vladar, E.K. and Stearns, T. (2007) Molecular characterization of centriole assembly in ciliated epithelial cells. *J. Cell Biol.*, **178**, 31–42.
51. Kim, J., Krishnaswami, S.R. and Gleeson, J.G. (2008) CEP290 interacts with the centriolar satellite component PCM-1 and is required for Rab8 localization to the primary cilium. *Hum. Mol. Genet.*, **17**, 3796–3805.
52. Nachury, M.V., Loktev, A.V., Zhang, Q., Westlake, C.J., Peranen, J., Merdes, A., Slusarski, D.C., Scheller, R.H., Bazan, J.F., Sheffield, V.C. *et al.* (2007) A Core Complex of BBS Proteins Cooperates with the GTPase Rab8 to Promote Ciliary Membrane Biogenesis. *Cell*, **129**, 1201–1213.
53. Kobayashi, T., Kim, S., Lin, Y.C., Inoue, T. and Dynlacht, B.D. (2014) The CP110-interacting proteins Talpid3 and Cep290 play overlapping and distinct roles in cilia assembly. *J. Cell Biol.*, **204**, 215–229.
54. Barenz, F., Inoue, D., Yokoyama, H., Tegha-Dunghu, J., Freiss, S., Draeger, S., Mayilo, D., Cado, I., Merker, S., Klinger, M. *et al.* (2013) The centriolar satellite protein SSX2IP promotes centrosome maturation. *J. Cell Biol.*, **202**, 81–95.
55. Dammermann, A. and Merdes, A. (2002) Assembly of centrosomal proteins and microtubule organization depends on PCM-1. *J. Cell Biol.*, **159**, 255–266.
56. Kim, J.C., Badano, J.L., Sibold, S., Esmail, M.A., Hill, J., Hoskins, B.E., Leitch, C.C., Venner, K., Ansley, S.J., Ross, A.J. *et al.* (2004) The Bardet-Biedl protein BBS4 targets cargo to the pericentriolar region and is required for microtubule anchoring and cell cycle progression. *Nat. Genet.*, **36**, 462–470.
57. Kubo, A., Sasaki, H., Yuba-Kubo, A., Tsukita, S. and Shiina, N. (1999) Centriolar satellites: molecular characterization, ATP-dependent movement toward centrioles and possible involvement in ciliogenesis. *J. Cell Biol.*, **147**, 969–980.
58. Dunn, S., Morrison, E.E., Liverpool, T.B., Molina-Paris, C., Cross, R.A., Alonso, M.C. and Peckham, M. (2008) Differential trafficking of Kif5c on tyrosinated and detyrosinated microtubules in live cells. *J. Cell Sci.*, **121**, 1085–1095.
59. Cai, D., McEwen, D.P., Martens, J.R., Meyhofer, E. and Verhey, K.J. (2009) Single molecule imaging reveals differences in microtubule track selection between Kinesin motors. *PLoS Biol.*, **7**, e1000216.
60. Wloga, D. and Gaertig, J. (2010) Post-translational modifications of microtubules. *J. Cell Sci.*, **123**, 3447–3455.
61. Walhout, A.J. and Vidal, M. (2001) High-throughput yeast two-hybrid assays for large-scale protein interaction mapping. *Methods*, **24**, 297–306.
62. Acquaviva, C., Chevrier, V., Chauvin, J.P., Fournier, G., Birnbaum, D. and Rosnet, O. (2009) The centrosomal FOP protein is required for cell cycle progression and survival. *Cell Cycle*, **8**, 1217–1227.
63. Altschul, S.F., Madden, T.L., Schaffer, A.A., Zhang, J., Zhang, Z., Miller, W. and Lipman, D.J. (1997) Gapped BLAST and PSI-BLAST: a new generation of protein database search programs. *Nucleic Acids Res.*, **25**, 3389–3402.
64. Johnson, L.S., Eddy, S.R. and Portugaly, E. (2010) Hidden Markov model speed heuristic and iterative HMM search procedure. *BMC Bioinformatics*, **11**, 431.
65. Thompson, J.D., Higgins, D.G. and Gibson, T.J. (1994) CLUSTAL W: improving the sensitivity of progressive multiple sequence alignment through sequence weighting, position-specific gap penalties and weight matrix choice. *Nucleic Acids Res.*, **22**, 4673–4680.
66. Waterhouse, A.M., Procter, J.B., Martin, D.M., Clamp, M. and Barton, G.J. (2009) Jalview Version 2—a multiple sequence alignment editor and analysis workbench. *Bioinformatics*, **25**, 1189–1191.

Article 6

TMEM107 recruits ciliopathy proteins to anchored ring-like subdomains of the ciliary transition zone membrane and is mutated in ciliary disease.

Nat Cell Biol. 2016 Jan;18(1):122-31

AL. Bruel*****, NJ. Lambacher*, TPJ.van Dam, GG. Slaats, K. Szymańska, GJ. McManus, JE. Kennedy, K. Gaff, Robin, R. van der Lee, L. Burglen, D. Doummar, JB. Rivière, L. Faivre, T. Attié-Bitach, S. Saunier, CA. Johnson, RH. Giles, MA. Huynen, C. Thauvin-Robinet, OE. Blacque (*equally contribution)

Résumé:

La zone de transition contrôle la composition ciliaire et les voies de signalisation en créant une barrière de diffusion localisée à la base du cil. Les anomalies de la zone de transition sont à l'origine de ciliopathies notamment les syndromes de Joubert, de Meckel ou encore la néphronophtise. Cependant, la composition moléculaire, l'organisation et le mécanisme de régulation de la barrière de diffusion sont peu connus. Afin d'identifier de nouveaux gènes codants pour des protéines de la zone de transition, nous avons utilisé des outils bio-informatiques et identifié TMEM107, muté dans les syndromes OFD et Joubert. Les études réalisées chez *c.elegans* ont montré que TMEM107 contrôle la composition ciliaire et régule l'intégrité du cil, l'ancrage de la zone de transition et connecte les microtubules à la membrane. TMEM107 occupe une nouvelle étape intermédiaire dans l'assemblage hiérarchique du complexe MKS. Enfin, les protéines à domaine transmembranaire sont immobiles et les observations en microcopie super-résolution ont révélé une localisation périodique ce ces protéines dans les cellules mammifères et de *c.elegans*. Cette étude a permis de mieux caractériser la fonction et la structure du complexe MKS (détails page 95).

nature cell biology

TMEM107 recruits ciliopathy proteins to subdomains of the ciliary transition zone and causes Joubert syndrome

Nils J. Lambacher[1,15], Ange-Line Bruel[2,15], Teunis J. P. van Dam[3,15], Katarzyna Szymańska[4], Gisela G. Slaats[5], Stefanie Kuhns[1], Gavin J. McManus[6], Julie E. Kennedy[1], Karl Gaff[1], Ka Man Wu[5], Robin van der Lee[3], Lydie Burglen[7,8], Diane Doummar[7], Jean-Baptiste Rivière[2,9], Laurence Faivre[2,9], Tania Attié-Bitach[10,11,12,13], Sophie Saunier[10,11,12], Alistair Curd[14], Michelle Peckham[14], Rachel H. Giles[5], Colin A. Johnson[4], Martijn A. Huynen[3,16], Christel Thauvin-Robinet[2,9,16] and Oliver E. Blacque[1,16]

The transition zone (TZ) ciliary subcompartment is thought to control cilium composition and signalling by facilitating a protein diffusion barrier at the ciliary base. TZ defects cause ciliopathies such as Meckel–Gruber syndrome (MKS), nephronophthisis (NPHP) and Joubert syndrome[1] (JBTS). However, the molecular composition and mechanisms underpinning TZ organization and barrier regulation are poorly understood. To uncover candidate TZ genes, we employed bioinformatics (coexpression and co-evolution) and identified TMEM107 as a TZ protein mutated in oral–facial–digital syndrome and JBTS patients. Mechanistic studies in *Caenorhabditis elegans* showed that TMEM-107 controls ciliary composition and functions redundantly with NPHP-4 to regulate cilium integrity, TZ docking and assembly of membrane to microtubule Y-link connectors. Furthermore, nematode TMEM-107 occupies an intermediate layer of the TZ-localized MKS module by organizing recruitment of the ciliopathy proteins MKS-1, TMEM-231 (JBTS20) and JBTS-14 (TMEM237). Finally, MKS module membrane proteins are immobile and super-resolution microscopy in worms and mammalian cells reveals periodic localizations within the TZ. This work expands the MKS module of ciliopathy-causing TZ proteins associated with diffusion barrier formation and provides insight into TZ subdomain architecture.

Cilia are microtubule-based structures serving motility, sensory and signalling functions, and ciliary defects cause broad-spectrum symptoms including cystic kidneys, blindness and nervous system defects[2]. Cilia possess subcompartments with distinct molecular compositions, enriched for receptors, channels and signalling components[3]. Protein targeting to cilia depends on intraflagellar transport (IFT) and membrane trafficking pathways that sort, deliver and recycle ciliary components[4]. A recently established paradigm implicates 'gated' diffusion barriers at the ciliary base that regulate protein entry in a size-dependent manner and restrict lateral transport between ciliary and non-ciliary membranes[1,5–10].

The ciliary gate is associated with the proximal-most 0.2–0.8 μm of the axoneme, termed TZ, characterized by Y-shaped structures that connect the microtubules and membrane. Y-links are also thought to organize the ciliary necklace, a membrane specialization consisting of intramembranous particles that may contribute to diffusion barrier properties[11,12]. Multiple MKS, JBTS and NPHP proteins are TZ-localized and regulate ciliary composition and signalling[5–7,13]. In *C. elegans* sensory neurons, 13 ciliopathy protein orthologues localize at the TZ, where they functionally associate as MKS (MKS-1, MKS-2, MKS-3, MKS-5, MKS-6, MKSR-1, MKSR-2, JBTS-14, TMEM-17, TMEM-231), NPHP (NPHP-1, NPHP-4) or CEP-290-associated modules to regulate Y-link formation and TZ docking during cilium assembly[10,13–19].

[1]School of Biomolecular and Biomedical Science, UCD Conway Institute, University College Dublin, Belfield, Dublin 4, Ireland. [2]EA4271 GAD, Genetics of Development Abnormalities, Burgundy University, 21078 Dijon, France. [3]Centre for Molecular and Biomolecular Informatics, Radboud Institute for Molecular Life Sciences, Radboud University Medical Center, Geert Grooteplein 26-28, 6525 GA Nijmegen, Netherlands. [4]Section of Ophthalmology and Neurosciences, Leeds Institute of Biomolecular & Clinical Sciences, University of Leeds, Leeds LS9 7TF, UK. [5]Department of Nephrology and Hypertension, University Medical Center Utrecht, 3584 CX Utrecht, The Netherlands. [6]School of Biochemistry and Immunology, Microscopy Facility, Trinity Biomedical Sciences Institute, Trinity College Dublin, 152-160 Pearse Street, Dublin 2, Ireland. [7]Centre de référence des malformations et maladies congénitales du cervelet et Service de Génétique, APHP, Hôpital Trousseau, 75012 Paris, France. [8]INSERM U1141, 75019 Paris, France. [9]FHU TRANSLAD, CHU Dijon, 21079 Dijon, France. [10]INSERM UMR1163, Hôpital Necker-Enfants Malades, 75015 Paris, France. [11]Université Paris Descartes, Sorbonne Paris Cité, 75006 Paris, France. [12]Institut IMAGINE, 75015 Paris, France. [13]Département de Génétique, Hôpital Necker-Enfants Malades, AP-HP, 75015 Paris, France. [14]School of Molecular and Cellular Biology, Faculty of Biological Sciences, University of Leeds, Leeds LS2 9JT, UK. [15]These authors contributed equally to this work.
[16]Correspondence should be addressed to M.A.H., C.T.-R. or O.E.B. (e-mail: martijn.huijnen@radboudumc.nl or christel.thauvin@chu-dijon.fr or oliver.blacque@ucd.ie)

Received 11 August 2015; accepted 20 October 2015; published online 23 November 2015; DOI: 10.1038/ncb3273

To predict new TZ genes, we employed a weighted gene coexpression screening strategy[20], and a training set of 20 known TZ genes (Supplementary Table 1)[1], to interrogate >1,600 mouse and human expression microarray data sets in GEO (Supplementary Table 2; top 500 coexpressed genes shown in Supplementary Table 3). In the integrated data sets, TZ genes exhibit higher coexpression with each other than the genomic background (Mann–Whitney *U* tests: $P = 1.57 \times 10^{-14}$ (human); $P = 1.42 \times 10^{-9}$ (mouse); Fig. 1a and Supplementary Fig. 1a). Ciliary genes[21] are also enriched (Mann–Whitney *U* tests: $P = 7.35 \times 10^{-55}$ (human); $P = 1.43 \times 10^{-44}$ (mouse)), but less than TZ genes (Mann–Whitney *U* tests: $P = 1.36 \times 10^{-10}$ (human); $P = 1.01 \times 10^{-6}$ (mouse); Fig. 1a and Supplementary Fig. 1a). Cross-validation (leave-one-out analysis) shows that our method retrieves TZ genes versus ciliary genes, although this is not pronounced among top scoring genes (Fig. 1b).

We compared the top 100 coexpressed human and mouse genes and identified 18 common genes, of which 13 encode proteins with known cilia associations (Supplementary Table 3). For the remaining 5 genes, we examined the genomes of ciliated species lacking a TZ (*Physcomitrella patens*, *Selaginella moellendorffii*, *Plasmodium falciparum* and *Giardia intestinalis*; ref. 22) and found a TZ phylogenetic distribution for *TMEM107* (Supplementary Fig. 1b). Although this gene was previously shown to regulate mammalian ciliogenesis and Shh signalling[23], the basis of these functions is unknown.

In *C. elegans*, the TMEM107 orthologue (F39B2.9; TMEM-107) is exclusively expressed in ciliated cells and localizes at the TZ (Fig. 1c,d and Supplementary Fig. 2a). Like other TZ genes, worm and human *TMEM107* possess X-box promoter motifs and nematode *tmem-107* expression is exclusively dependent on the RFX transcription factor DAF-19 (Supplementary Fig. 2b,c). TMEM107 possesses four predicted transmembrane helices and short cytosolic amino and carboxy termini (Supplementary Fig. 1c,d). Disruption of the nematode transmembrane domain linkers or cytosolic N or C termini did not affect localization, suggesting that the TZ association of TMEM-107 depends on its transmembrane helices (Supplementary Fig. 2d). Similar to *C. elegans* TMEM-107, human TMEM107::GFP also localizes at the TZ (Fig. 1e).

The TZ localization, combined with reported ciliogenesis and signalling roles[23], makes *TMEM107* a strong ciliopathy gene candidate. Indeed, similarly to observations for other ciliopathy gene disruptions[24] and the *Tmem107 Schlei* mouse[23], *Tmem107*-depleted IMCD3 cells exhibit reduced ciliation and lumen size in three-dimensional spheroids (Fig. 2a,b). To explore disease associations, *TMEM107* exons were screened for mutations in 238 JBTS or oral–facial–digital syndrome (OFD) type VI individuals using Sanger and next-generation sequencing. We identified a homozygous missense variant (NM_183065: g.8079298T>C; p.Glu45Gly) in OFDVI female twins with consanguineous parents, and a compound heterozygous mutation comprising a frameshift deletion (NM_032354.3: g.8077560delT; p.Leu134Phe *fs**8) and an in-frame codon deletion (NM_032354.3: g.8077890_8077893delGAA; p.Phe106del) in a JBTS male (Fig. 2c and Supplementary Fig. 3a,b). All patients possess similar neurological disturbances, retinopathy and the JBTS-associated molar tooth sign (Fig. 2d–g and Supplementary Fig. 3c). The females were diagnosed with OFDVI because they also exhibit hamartoma and frenulae phenotypes (Supplementary Fig. 3c). All three variants segregated in the families, were predicted to be pathogenic by Human Splicing Finder and PolyPhen2(p.Phe106del and p.Glu45Gly), and were absent in the heterozygous and homozygous state in human variation databases (NHLBI Exome Variant Server, ExAC). In further support of pathogenicity, fibroblasts from the JBTS male exhibited reduced ciliation, and those cilia that formed were abnormally long (Fig. 2h–j). The latter contrasts with the short cilia of hypomorphic *Schlei* mouse fibroblasts, carrying a missense mutation (E125G) in Tmem107 (ref. 23); which may be explained by cell type, species or allelic distinctions. We could not use complementation experiments to investigate how the patient mutations affect TMEM107 function because even moderate TMEM107(WT) over-expression was toxic to fibroblast cilium formation. However, TMEM107(E45G) and TMEM107(F106del) retained the ability to localize at the TZ, indicating that these mutations exert their pathogenicity by disrupting TMEM107 functions at the TZ, rather than a gross effect on TMEM107 localizations or stability (Supplementary Fig. 2e).

Next, we investigated the role of TMEM107 in *C. elegans* TZs. As loss-of-function alleles were unavailable, we used CRISPR-Cas9 (ref. 25) to isolate *oq100*, a 27-base-pair (bp) deletion + 14-bp insertion (Fig. 3a). This mutation causes a frameshift and premature stop, which disrupts transmembrane domains 3 and 4, and is likely to be a null allele as *tmem-107(oq100)::GFP* is not expressed (Fig. 3b). *tmem-107(oq100)* mutants seem normal for dye-filling (indirect measure of cilium integrity[26]), cilium length and morphology, and amphid cilium ultrastructure (Fig. 3c,d and Supplementary Fig. 4a). Also, *tmem-107* mutants possess normal cilia-related chemoattraction and foraging sensory behaviours (Fig. 3e). Thus, *tmem-107* loss does not grossly affect cilium structure and function.

We examined whether *tmem-107* functions redundantly with other TZ genes and found a synthetic genetic interaction with *nphp-4*. Like worms with mutations in a *C. elegans* MKS and an NPHP module gene[10,15], *tmem-107;nphp-4* double mutants exhibit defects in dye-filling, cilium length and morphology, as well as sensation (Fig. 3c–e). The synthetic cilium structure defects were confirmed by transmission electron microscopy (TEM), which showed that 3–5 amphid pore cilia are truncated or missing in *nphp-4;tmem-107* mutants, whereas most or all axonemes are present in the corresponding single mutants (Supplementary Fig. 4a). Conversely, *tmem-107* does not synthetically interact with *mksr-1* as assessed by dye-filling (Fig. 3c), suggesting that *tmem-107* is part of the MKS module whose genes synthetically interact with NPHP module genes but not with each other[10,15,27]. Importantly, transgenic expression of *tmem-107(WT)::gfp* in *tmem-107;nphp-4* worms rescued the cilium structure and function phenotypes, confirming phenotypic linkage to *oq100* (Fig. 3c,e). Surprisingly, *tmem-107* constructs mimicking the human TMEM107 patient mutations also rescued the *tmem-107;nphp-4* Dyf phenotype (Supplementary Fig. 4c), and in agreement with these variants retaining functionality, the encoded proteins localized normally (Supplementary Fig. 2d).

TZ ultrastructure was also disrupted in *tmem-107;nphp-4* worms compared with single mutants of *tmem-107* (unaffected) and *nphp-4* (modestly affected; discussed below). In double mutants, Y-links were reduced or missing, and in agreement with loss of these membrane–microtubule connectors, many TZs were undocked from the plasma membrane, frequently extending from ectopic positions within the

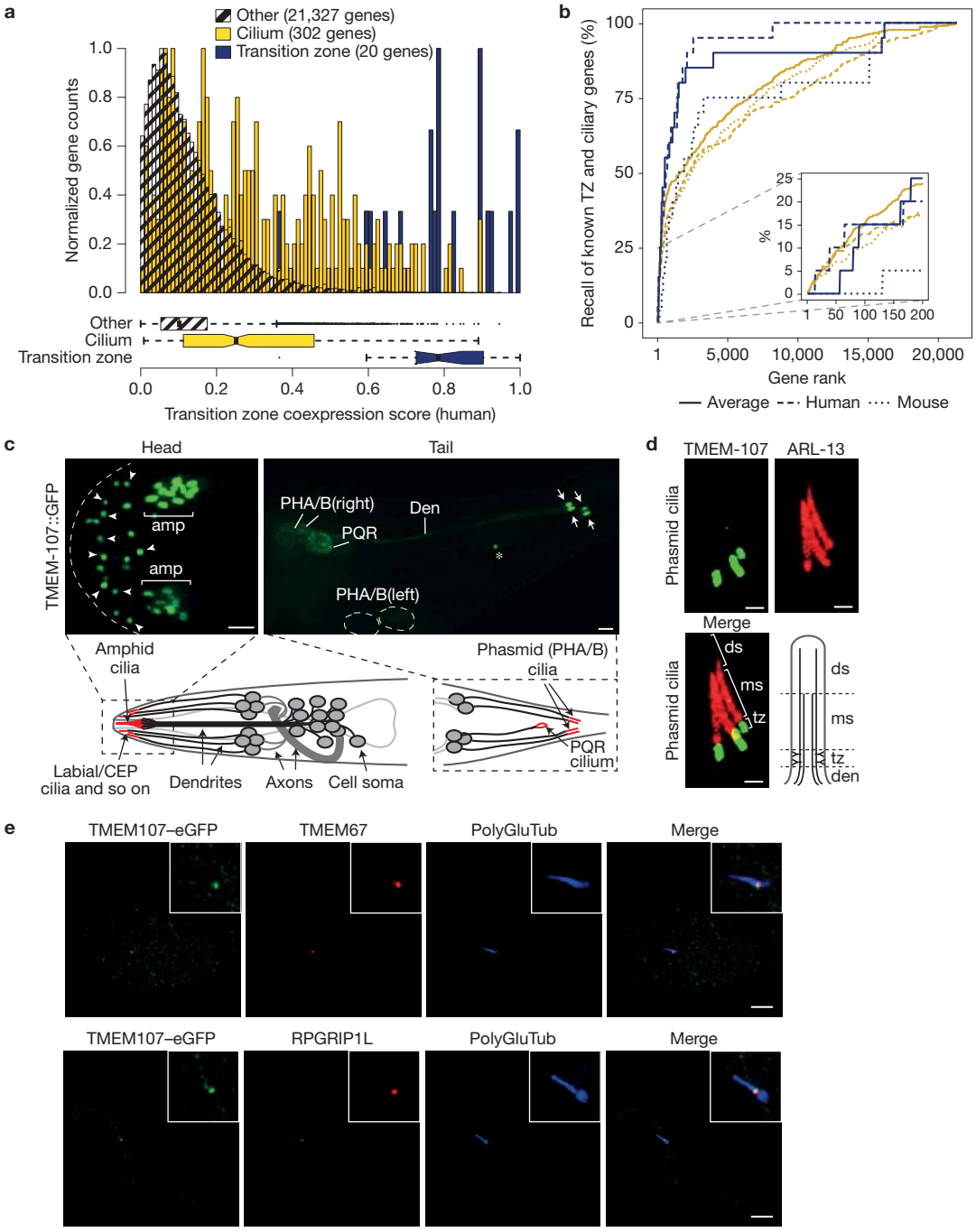

Figure 1 A weighted coexpression approach to discover TZ genes identifies TMEM107 as a TZ protein. (**a**) Frequency histogram of binned human gene coexpression scores, derived from weighted analyses of gene expression data sets using a training set of 20 known TZ genes (Supplementary Table 1). Frequencies normalized to compare different distributions. SYSCILIA gold standard genes[21] in yellow; TZ gene training in blue; all other genes in grey hatched. Box plots show median and quartiles for histogram distributions. Whiskers (hashed lines) denote the minimum and maximum extent of the data set. (**b**) Recall performance (also known as sensitivity) of the coexpression approach retrieves known TZ (blue lines) and ciliary (yellow lines) genes. The graph shows that TZ genes can be preferentially retrieved compared with ciliary genes. Inset: recall performance for top 200 ranked genes. Ciliary genes taken from the SYSCILIA gold standard[21]. (**c**,**d**) *C. elegans* TMEM-107::GFP localizes at the TZ. Shown are fluorescence images from worms expressing TMEM-107::GFP alone (**c**) or together with an ARL-13::tdTomato reporter (**d**). (**c**) Accumulation of TMEM-107::GFP at the ciliary base region of 12 bilateral amphid cilia (amp; brackets), labial and CEP cilia (subset denoted by arrowheads), bilateral phasmid cilia (arrows) and the right-sided PQR cilium (asterisk) in the tail. Note that the head schematic shows only a subset of the hermaphrodite's ciliated head neurons. (**d**) TMEM-107::GFP localizes immediately proximal to middle segment (ms)-restricted ARL-13::tdTomato. Image shows all four phasmid cilia (left and right). Schematic denotes major subcompartments in phasmid cilia with microtubule doublets (only two shown) in the TZ and middle segments, and microtubule singlets in the distal segment (ds). Den, dendrite. Scale bars, 2 μm (left two images), 1 μm (right images). (**e**) Human TMEM107 localizes at the TZ. Shown are images of hTERT-RPE1 cells stably expressing GFP-tagged human TMEM107 (green) at a low level, co-stained with antibodies for ciliary axonemes (polyglutamylated tubulin, PolyGluTub) and the TZ (RPGRIP1L, TMEM67). Scale bars, 5 μm.

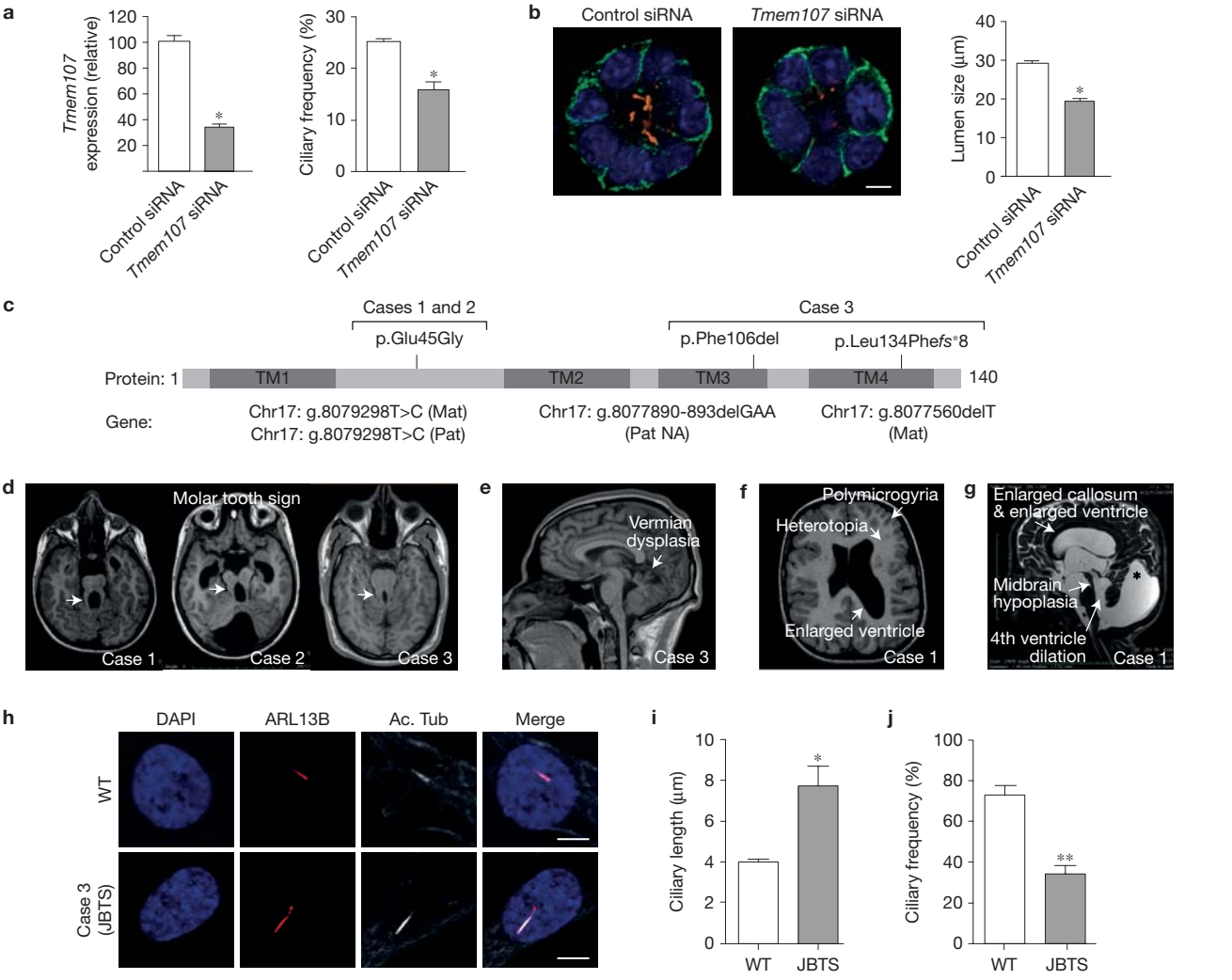

Figure 2 *TMEM107* regulates mammalian ciliogenesis and is mutated in OFDVI and JBTS individuals. (**a**) IMCD3 cells transfected with *Tmem107* siRNA possess reduced *Tmem107* mRNA expression (versus scrambled siRNA control; qPCR data) and reduced mean ciliary frequency. Data represent mean ± s.e.m. ($n=350$ cells, 1 experiment). $^{*}P<0.05$ (unpaired *t*-test; versus control). (**b**) When grown in three-dimensional culture, IMCD3 cells transfected with *Tmem107* siRNA form spheroids with a reduced mean size. Cilia (orange) stained for acetylated α-tubulin; cell junctions (green) stained for beta-catenin. Data represent mean ± s.e.m. ($n=25$ spheroids pooled from 2 independent experiments). $^{*}P<0.05$ (unpaired *t*-test; versus control). Scale bar, 5 μm. (**c**) Schematic of the human TMEM107 protein showing the position of identified patient mutations. Grey rectangles correspond to the transmembrane domains. Mat, maternal; Pat, paternal; NA, not available. (**d**) Brain magnetic resonance imaging (MRI) images (axial views) showing the molar tooth sign, linked to elongated, thick and mal-oriented superior peduncles (white arrows) and hypoplastic vermis. (**e**) Brain MRI showing a dysplastic and highly hypoplastic vermis in sagittal view. A secondary enlargement of the fourth ventricle with displacement of the fastigium is also evident. (**f**) Brain MRI (axial view) showing heterotopias, enlarged lateral ventricles and polymicrogyria. (**g**) Brain MRI (sagittal view) showing enlarged posterior fossa (asterisk) with a cystic dilation of the fourth ventricle, a severe midbrain dysplasia and a thin corpus callosum with enlarged ventricles. (**h**) Fibroblasts derived from skin biopsies of healthy control (wild type, WT) and patient 3 (JBTS) immunostained for cilia using antibodies against ARL13B (red; ciliary membrane) and acetylated tubulin (white; axonemal microtubules). (**i**,**j**) Compared with control cells, JBTS cell cilia possess increased lengths (**i**) and reduced frequencies (**j**). Data represent mean ± s.e.m. ($n=10$ (**i**) and 25 (**j**) cells; data represent 1 of 3 independent experiments). $^{*}P<0.05$, $^{**}P<0.01$ (unpaired *t*-test; versus WT); scale bars, 5 μm.

distal dendrite (Supplementary Fig. 4b). Also, *tmem-107;nphp-4* mutant cilia often exhibited abnormal vesicle accumulations in the TZ and PCMC regions (Supplementary Fig. 4b). Consistent with these structural defects, MKS-2 TZ localization is disrupted in *tmem-107;nphp-4* worms, but not in single mutants (Fig. 3f; *nphp-4* data shown in ref. 15). Furthermore, *tmem-107;nphp-4* neuronal dendrites (phasmids) are frequently short, indicating dendritic tip anchoring defects during dendrite elongation (Fig. 3g)[10,17,27]. Thus, like known MKS module components, TMEM-107 functionally interacts with NPHP-4 to facilitate TZ formation, composition and dendrite formation.

As mentioned above, *nphp-4* single mutants exhibit modest ultrastructural TZ defects, despite previous reports that TZs were normal in these worms[16]. In *nphp-4* worms carrying *tm925* (deletion) or *gk529336* (nonsense) mutations, Y-link densities were frequently reduced and sometimes missing, and undocked TZs were observed in ADF and ADL neurons (Supplementary Fig. 4b). Thus, *C. elegans nphp-4* alone regulates aspects of Y-link assembly or stability, which

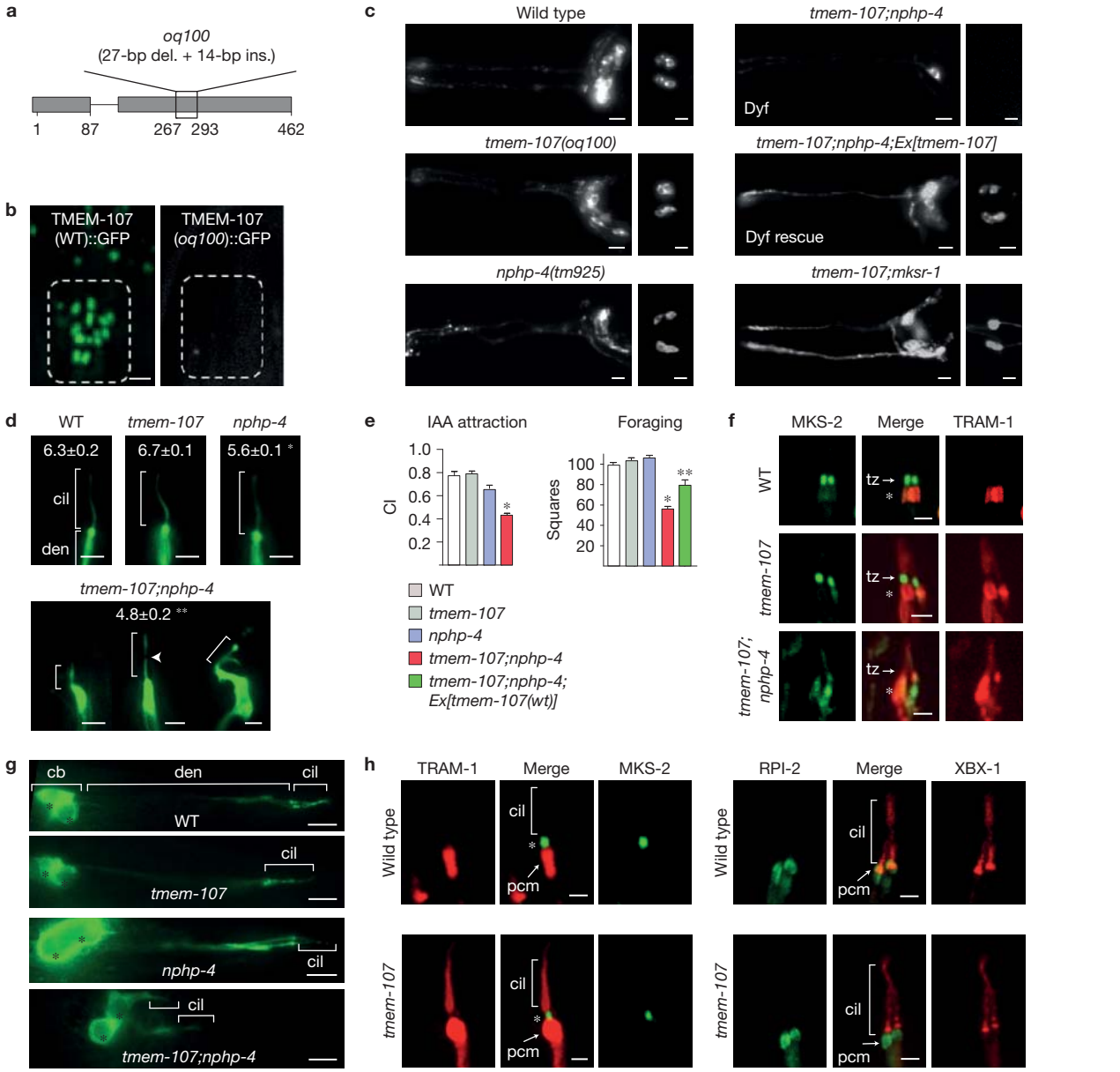

Figure 3 *C. elegans tmem-107* controls diffusion barrier integrity and functions with *nphp-4* to regulate ciliary and TZ structural integrity. (**a**) Schematic of *oq100* indel mutation in the *tmem-107* gene. Exons denoted by grey rectangles (numbers show nucleotide positions). del., deletion; ins., insertion. (**b**) *oq100* mutation disrupts TMEM-107 expression. Shown are amphid cilia TZs in worms expressing GFP-tagged wild-type or mutant (*oq100*) TMEM-107. Scale bar, 2 μm (images identically scaled). (**c**) Dye-filling assay (measure of cilium integrity for 6 amphid (head) and 2 phasmid (tail) ciliated neurons) showing dye-filling defects (Dyf) in *tmem-107(oq100);nphp-4(tm925)* double mutants, but not single mutants, or a *tmem-107(oq100);mkrs-1(tm3083)* double mutant. The Dyf phenotype is rescued by expression of wild-type *tmem-107* (GFP-tagged; see Fig. 1c,d). Scale bars, 10 μm. (**d**) Images of ASER neuronal cilia from worms expressing a *gcy-5p::gfp* that stains the ASER neuron. Numbers refer to cilium length measurements; mean ± s.e.m. ($n = 28$ (N2), 44 (*tmem-107*), 46 (*nphp-4*) and 81 (*tmem-107;nphp-4*) cilia). Brackets denote ciliary axonemes (cil). Arrowhead indicates occasional break in GFP staining observed only in double mutant. den; dendrite. $^{*}P < 0.01$ (unpaired *t*-test; versus WT), $^{**}P = 0.01$ (unpaired *t*-test; versus *nphp-4*); scale bars, 3 μm. (**e**) *tmem-107(oq100);nphp-4(tm925)* double mutants possess defects in cilia-related behaviours. Shown are population assays of isoamyl alcohol (IAA) attraction and single-worm foraging assays. Data represent mean ± s.e.m. For IAA assays, $n = 30$ (N2), 20 (*tmem-107*), 22 (*nphp-4*) and 29 (*tmem-107;nphp-4*); for foraging assays, $n = 44$ (N2), 43 (*tmem-107*), 63 (*nphp-4*), 54 (*tmem-107;nphp-4*) and 37 (*tmem-107;nphp-4;Ex[tmem-107(wt)]*) independent experiments, respectively; $^{*}P < 0.01$ (unpaired *t*-test; versus WT), $^{**}P < 0.01$ (unpaired *t*-test; versus *tmem-107;nphp-4*). CI, chemotaxis index. (**f**) TZ composition is altered in *tmem-107(oq100);nphp-4 (tm925)* double mutants. Shown are phasmid cilia from worms expressing TZ-localized MKS-2::GFP and periciliary membrane-localized, TRAM-1::tdTomato (asterisk). Scale bars, 2 μm. (**g**) *tmem-107(oq100);nphp-4(tm925)* double mutants possess short phasmid (PHA/B) dendrites and misplaced cilia. Neurons stained with OSM-6(IFT52)::GFP. cil, ciliary axonemes; den, dendrite; cb, cell bodies (also denoted by asterisks). Brackets denote PHA/B cilia. Scale bars, 5 μm. (**h**) TZ membrane diffusion barrier is selectively disrupted in *tmem-107(oq100)* mutants. Shown are phasmid cilia from worms expressing TRAM-1::tdTomato (and MKS-2::GFP; marks TZ) (left images) or RPI-2::GFP (and XBX-1::tdTomato; marks cilia) (right images). TRAM-1 (translocon subunit) and RPI-2 (retinitis pigmentosa 2) are excluded from wild-type (WT) cilia, whereas TRAM-1 (but not RPI-2) leaks into *tmem-107(oq100)* cilia. Asterisk, TZ localization of MKS-2; pcm, periciliary membrane; cil, ciliary axoneme. Scale bars, 2 μm.

agrees with the mild cilium structure defects in corresponding mutants[16] (Supplementary Fig. 4a). We conclude that NPHP and MKS modules are not fully redundant in building TZs in at least some amphid channel neurons.

Similar to known MKS module gene mutants[10,15,19], TRAM-1 abnormally leaks into *tmem-107* mutant cilia, suggesting membrane diffusion barrier defects and altered ciliary composition in these worms (Fig. 3h). However, membrane-associated RPI-2 does not leak into *tmem-107(oq100)* cilia indicating that the barrier is selectively disrupted (Fig. 3h), which contrasts with other MKS module gene mutants, where both TRAM-1 and RPI-2 leak into cilia[10].

To further investigate TMEM107 associations with MKS module proteins, and the evolutionary conservation of these interactions, three complementary approaches were taken. First, we employed protein localization dependency assays. In *C. elegans*, the MKS module is proposed to assemble hierarchically[10,13,15,19]. In this model, MKS-5 occupies the root of the hierarchy (Layer 1), required for TZ localization of all MKS module components. In contrast, MKS-3, JBTS-14, MKS-6 and TMEM-17 occupy a peripheral level (Layer 3) not required for localization of other proteins, whereas MKSR-1, MKSR-2, TMEM-231 and MKS-2 form an intermediate level (Layer 2), required for Layer 3 but not Layer 1 protein targeting. To evaluate whether TMEM-107 is part of this model, TMEM-107::GFP localization was assessed in MKS module gene mutants, and MKS module protein localizations were analysed in *tmem-107(oq100)* mutants. We found that TMEM-107 is not required for Layer 1 and most Layer 2 protein localizations, but is required for the organization of Layer 3 proteins (JBTS-14, TMEM-17), as well as MKS-1 (unassigned layer) and TMEM-231 (layer 2) (Fig. 4a). In reverse experiments, TMEM-107 localization depends on Layer 1, 2 and MKS-1 proteins, but not Layer 3 proteins (Fig. 4a). Furthermore, TMEM-107 and NPHP module proteins are not localization interdependent (Fig. 4a). These data show that TMEM-107 recruits an MKS submodule of proteins (TMEM-17, TMEM-231, JBTS-14, MKS-1) and suggest that TMEM-107 occupies an intermediate layer, connecting Layer 2 to a Layer 3 subset (Fig. 4b). Interestingly, TZ recruitment of TMEM-17 and TMEM-231 by TMEM-107 is independent of its short cytosolic N and C termini, suggesting that this function is orchestrated by the transmembrane helices or interhelical linkers (Fig. 4c). In agreement with our nematode data, depletion of mammalian *Tmem107* also alters the localization of some MKS module proteins (Tmem231 and Tmem237) but not others (Rpgrip1l; Fig. 4d).

In the second approach, co-immunoprecipitation (coIP) assays were performed to determine whether mammalian TMEM107 biochemically associates with MKS module proteins. GFP-tagged TMEM107 was exogenously coexpressed with FLAG-tagged TMEM216, TMEM231, TMEM17 or TMEM237, or with myc-tagged MKS1, and assessed for associations in IMCD3 cells using binding conditions optimized for membrane proteins[28]. We found that TMEM107 immunoprecipitates full-length TMEM216, TMEM231, TMEM237 and MKS1, but not TMEM17 (Fig. 4e). For TMEM237, TMEM107 did not detectably interact with an N-terminal cytoplasmic domain of this protein (TMEM237Nt), indicating that the TMEM237 association depends on its transmembrane helices or C-terminal cytoplasmic domain (Fig. 4e).

In the third approach, we used differential Dollo parsimony[29] to obtain co-evolutionary relationships for MKS module proteins. In agreement with the nematode hierarchy[10,15], Layer 2 orthologues TMEM216, B9D1 and B9D2 form a co-evolving MKS core (Fig. 4f). This 'core' co-evolves with Layer 3 orthologues TMEM67 and CC2D2A, consistent with localization dependencies in mammalian systems[5], although not in worms (Fig. 4f). We also identified a co-evolving TMEM107, TMEM17 and TMEM231 submodule, again agreeing with nematode localization dependencies (Fig. 4f). Unexpectedly, this submodule does not include TMEM237 because orthologues are missing in stramenopiles, alveolates and excavates (Supplementary Fig. 1b), indicating late incorporation into the MKS module. Also surprising was that RPGRIP1L only marginally co-evolves with the MKS module, despite its central role in module organization[10,19] (Fig. 4f). This may be explained by low RPGRIP1L sequence conservation and difficulties in assigning orthologues. Finally, the interdependent MKS1 and TMEM107 localizations are not reflected in the co-evolution data. Thus, our evolutionary findings support conserved roles for *C. elegans* TMEM-107 in organizing an MKS submodule with TMEM-231 and TMEM-17, but differences in the modular arrangements of TMEM-107 with other MKS proteins might exist between species.

The specific TZ localization of MKS module proteins, together with their requirement for Y-link assembly with NPHP proteins, could suggest that this module interacts with Y-links or associated structures. If true, MKS module proteins should be immobile. Using fluorescence recovery after photobleaching (FRAP) assays in *C. elegans*, photobleaching one half of the TZ signal for TMEM-107::GFP, MKS-2::GFP and MKS-6::GFP resulted in no signal recovery (30 min), indicating that the non-bleached TZ pool is immobile (Fig. 5a). Also, no recovery was observed when entire TZ signals were photobleached (MKS-2::GFP), demonstrating that MKS module proteins possess slow TZ entry kinetics (Supplementary Fig. 5a). This immobility depends on other MKS module proteins because MKS-2 is highly mobile in *mksr-1* (B9D1) mutants (Fig. 5b). Therefore, we conclude that transmembrane (TMEM-107, MKS-2) and membrane-associated (MKS-6) proteins are anchored at the TZ membrane. Furthermore, at least for MKS-2, anchoring requires an intact MKS module.

Next, we used stimulated emission depletion (STED) super-resolution microscopy to further investigate *C. elegans* MKS (TMEM-107, MKS-2 and TMEM-231) and NPHP (NPHP-1) module protein distributions within TZs. Side-view TZ images (axial orientation) revealed that these proteins are periodically distributed along the axial plane, frequently appearing as multiple independent rings (partial or complete), or possibly spiral structures (Fig. 5c and Supplementary Fig. 5b). However, in some images with slightly better resolution, individual dots of signal were evident within ring-like domains (Fig. 5c; arrowheads), suggesting that these domains consist of multiple discrete protein clusters. Punctate signals were also observed for NPHP-1, suggesting that MKS and NPHP module proteins possess similar axial TZ distributions (Fig. 5c). We were unable to determine protein distributions from true tranverse (radial) views of the TZ because of the orientation of worms (and cilia) on the imaging slide.

We also performed STED imaging on endogenous RPGRIP1L and TMEM67 in human cells (RPTEC-TERT1). Imaging of TZs in the radial orientation revealed that these proteins can form discrete clusters arranged as a complete or near-complete single shallow ring (Fig. 5d and Supplementary Fig. 5c). Although the number of resolved

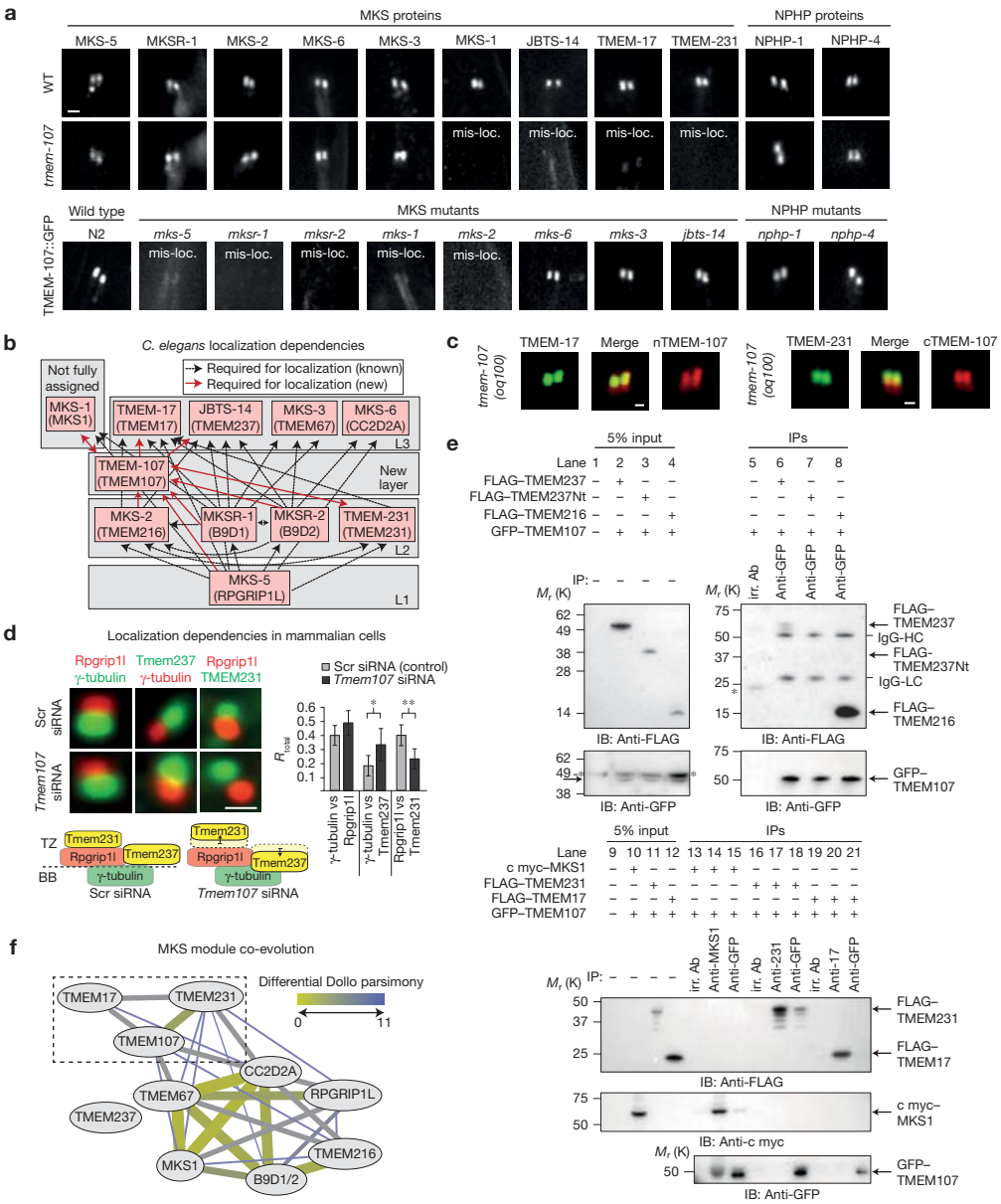

Figure 4 Evolutionarily conserved association of TMEM107 with the TZ-localized MKS module. (**a**) Phasmid TZ localizations of GFP-tagged MKS and NPHP module proteins in WT and *tmem-107(oq100)* mutant worms, and TMEM-107::GFP in MKS and NPHP mutants. Scale bar, 1 μm (all images similarly scaled). mis-loc., mislocalized. (**b**) Schematic summarizing TZ localization dependencies in **a**. TMEM-107 positioned at an intermediate level within a hierarchical three-layer (L1-3) MKS module assembly model (drawn on the basis of refs 10,13,15,19; MKS-1 'unassigned' because hierarchical analysis has not yet been conducted using an *mks-1* null allele). Human orthologues denoted in brackets. (**c**) Expression of TMEM-107::RFP with disrupted cytosolic N or C termini (nTMEM-107, cTMEM-107; see Methods) rescues mislocalized TMEM-17::GFP and TMEM-231::GFP in *tmem-107(oq100)* mutants. Shown are phasmid cilia TZs. Scale bars, 0.5 μm. (**d**) *Tmem107* depletion (siRNA) in IMCD3 cells disrupts relative localizations of endogenous MKS module proteins. Cells double-stained as indicated and co-localization determined as an R_{total} Pearson correlation value (FIJI 'Co-localization Threshold' plug-in). In *Tmem107*-depleted cells, Rpgrip1l localization is unaffected (relative to basal body (BB) γ-tubulin), whereas Tmem231 and Tmem237 proteins shift (black arrows) relative to γ-tubulin or Rpgrip1l. Data in graph represent mean ± s.e.m. ($n = 150$ cells pooled from 3 independent experiments). Scr siRNA, siRNA scrambled control. $^{**}P < 0.01$, $^{*}P < 0.05$ (unpaired *t*-test; versus Scr siRNA control). Scale bar, 1 μm. (**e**) Co-immunoprecipitation (coIP) assays in IMCD3 cells. Upper panels, lanes 1–4: input material from whole cell extracts (WCEs) transfected with the indicated constructs and immunoblotted (IB) with anti-GFP or anti-FLAG. Lanes 5–8: proteins immunoprecipitated (IP) by an irrelevant antibody (irr. Ab; anti-MICU3) or anti-GFP, and then immunoblotted for FLAG or GFP. IgG heavy chain (HC) and light chain (LC) in co-immunoprecipitates are indicated. Asterisks (*) mark nonspecific proteins. Lower panels, lanes 9–12: input WCE showing expression of FLAG–TMEM231, FLAG–TMEM17 and c myc–MKS1. Lanes 13–21: IPs with antibodies against MKS1 (lane 14), TMEM231 (231; lane 17) and TMEM17 (17; lane 20) and then immunoblotted as indicated. Note that although TMEM107 co-immunoprecipitates TMEM231, TMEM231 does not co-immunoprecipitate detectable levels of TMEM107. Unprocessed original scans of blots are shown in Supplementary Fig. 6. (**f**) Co-evolution relationships between MKS components using differential Dollo parsimony that counts along a phylogenetic tree how often two genes are lost independently from each other. Thickness and colour gradient indicate strong co-evolution. Edges with differential Dollo parsimony scores >11 are not shown. Dashed rectangle: co-evolving MKS submodule.

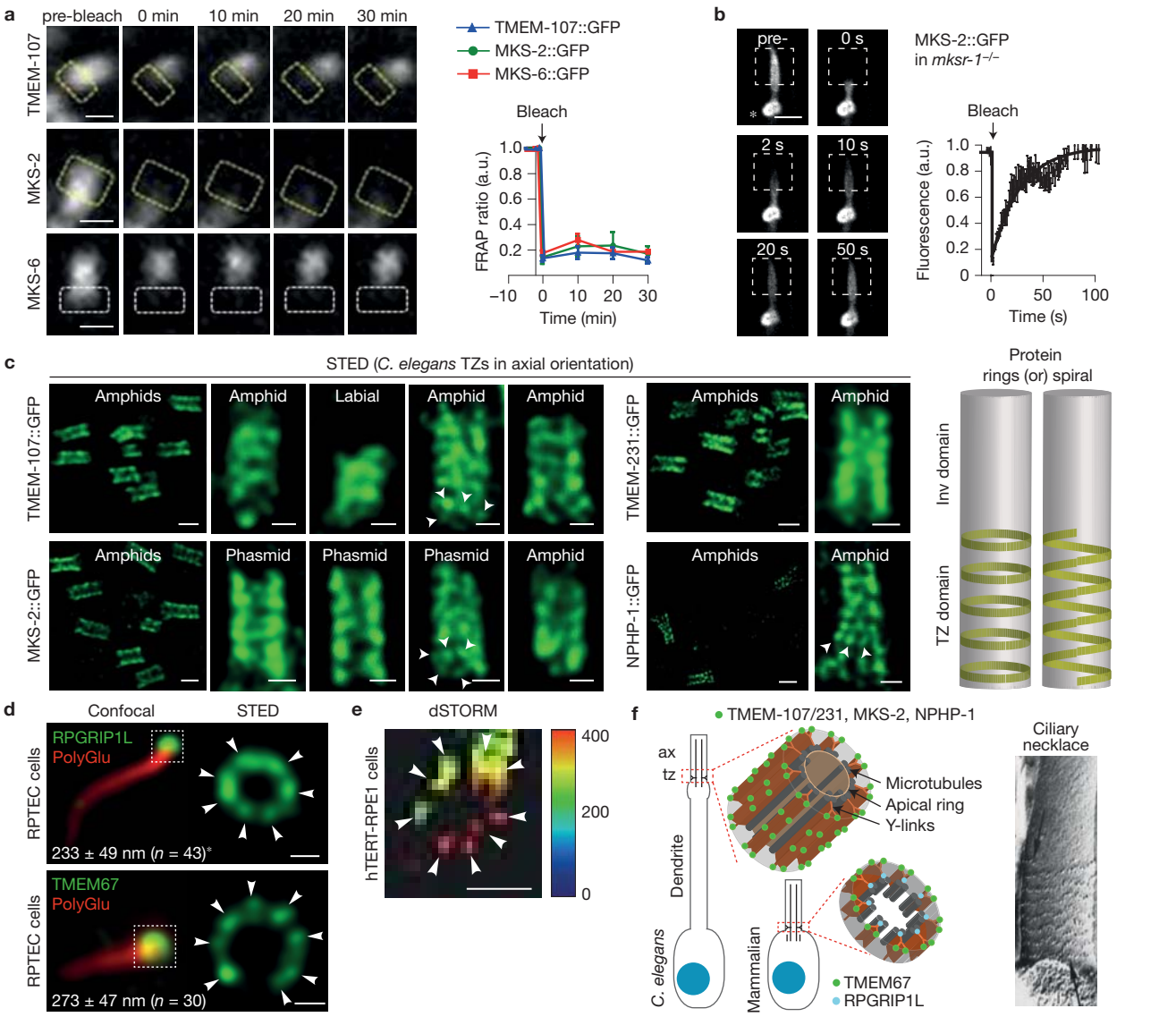

Figure 5 Anchoring and periodic distributions of MKS module proteins within the TZ. (**a**) GFP-tagged TMEM-107, MKS-2 and MKS-6 are immobile within the *C. elegans* TZ. Shown are FRAP curves and representative time-lapse images after photobleaching one half of a TZ signal (outlined region). Data points represented as mean ± s.e.m. ($n = 3$ (MKS-6) or 4 (TMEM-107, MKS-2) independent experiments). Scale bars, 500 nm. (**b**) *C. elegans* MKS-2 immobility depends on MKS module proteins. Shown is a FRAP curve and representative time-lapse images (phasmid cilia) after photobleaching MKS-2::GFP signals (boxed region) in an *mksr-1* mutant. Asterisk, periciliary membrane. Data points represented as mean ± s.e.m. ($n = 4$ independent experiments). a.u., arbitrary units; scale bar, 2 μm. (**c**) STED super-resolution microscopy images of *C. elegans* MKS and NPHP module protein (all GFP-tagged) distributions in transition zones. Shown are single focal plane images of TZs in axial orientation (from the side) taken from head (amphid, labial) and tail (phasmid) ciliated neurons. Note the smaller size of the labial cilium TZ. Schematics indicate ring-like or spiral-like domains formed by the *C. elegans* MKS/NPHP module proteins. Arrowheads show independent signal clusters within a ring-like domain. Scale bars, 200 nm (high-magnification images), 500 nm (low-magnification images). (**d**) STED images of endogenous human RPGRIP1L and TMEM67 in renal RPTEC cells showing clusters (arrowheads) of protein in a single ring of differing diameters (mean ± s.d.) at the TZ. Corresponding confocal images co-stained for cilia with polyglutamylated tubulin antibody. $^*P = 0.001$ (unpaired *t*-test; versus TMEM67). Scale bars, 100 nm. (**e**) dSTORM of human RPGRIP1L (visualized with Alexa Fluor 647) with 10 nm binning, image smoothing and contrast enhancement in FIJI (raw images shown in Supplementary Fig. 5d), showing periodic localization (arrowheads) in a loose ring at the TZ. Image depth-coded by colour. *Z*-axis scale bar (nm) on right. Scale bar, 100 nm. (**f**) Models. MKS module proteins (and *C. elegans* NPHP-1) occupy periodic radial and axial TZ subdomains. Mammalian RPGRIP1L and TMEM67 localize as independent clusters, forming a single ring domain at the TZ core (RPGRIP1L) or membrane (TMEM67). *C. elegans* MKS and NPHP proteins also localize as discrete independent clusters, forming multiple ring domains (or possible spiral domains) along the TZ length. The nematode axial distribution may correspond to the ciliary necklace (TEM example from ref. 12). Periodicity and immobility of MKS module proteins suggests association with Y-links, which form extended sheets in *C. elegans* (Supplementary Video 1) and are implicated in necklace formation.

clusters was variable, rings with 7–8, or possibly 9 clusters were observed. In addition, RPGRIP1L ring diameters were significantly narrower than TMEM67 ring diameters (Fig. 5d). As an alternative approach, we imaged endogenous RPGRIP1L using direct stochastic optical reconstruction microscopy (dSTORM). Similar to our STED findings, dSTORM imaging of RPGRIP1L revealed a single shallow

ring of TZ signal, comprised of at least 7–8 independent puncta (Fig. 5e and Supplementary Fig. 5d). Thus, both mammalian RPGRIP1L and TMEM67 seem to be organized as discrete clusters within ring-like domains of differing diameters, indicating distinct radial positioning at the TZ membrane (TMEM67) and core (RPGRIP1L). The periodicity of these clusters approaches the nine-fold symmetry of Y-links, suggesting possible association with these structures.

Our super-resolution imaging indicates that MKS module proteins occupy periodic radial and axial subdomains of the TZ core and membrane (Fig. 5f). The nematode axial pattern is reminiscent of the ciliary necklace, a conserved TZ membrane specialization comprised of 1–7 rows of intramembrane leaflet particles identified over 40 years ago[11,12] (Fig. 5f). In further support of a necklace association, *C. elegans* MKS module proteins are anchored at the TZ membrane, and the periodic radial distribution of mammalian TMEM67 at the TZ membrane approaches the periodicity of Y-links implicated in necklace formation[11]. In one model, Y-links would anchor MKS module proteins at the necklace (Fig. 5f). However, a tomographic (TEM) reconstruction of a portion of the *C. elegans* TZ indicates that Y-links are continuous structures running the TZ length (Supplementary Video 1 and Fig. 5f; see also ref. 18); thus, any association of MKS proteins with Y-links would occur at various axial positions along continuous Y-link sheets (Fig. 5f). Unfortunately, we could not identify a necklace pattern for mammalian MKS module proteins because of spatial constraints and resolution limits conferred by the short TZ (<200 nm). Future super-resolution imaging on mammalian cells with longer TZs should clarify the nematode observations.

In summary, we have identified TMEM107 as a ciliopathy TZ protein and conserved MKS module component. Causality of the mutations identified here to JBTS and OFDVI is supported by very recent reports of additional *TMEM107* mutations linked to MKS and OFD (refs 30,31). Furthermore, we show that ciliopathy proteins are anchored at the TZ membrane, and exhibit periodic radial and axial distributions at the TZ core and membrane. In addition, our finding that MKS-2 is mobile in *mksr-1* (B9D1) mutant cilia indicates that protein anchoring at the TZ is important for barrier functions. Strikingly, membrane diffusion barriers of the axon initial segment (AIS) that limit free exchange of phospholipids also depend on anchored membrane proteins[32], and sodium channels within the AIS membrane are coordinately localized with evenly spaced (180–190 nm) actin–spectrin cytoskeletal rings[33]. Thus, the TZ and AIS cellular compartments may share comparable molecular organization underpinning common mechanisms of barrier function. Finally, our bioinformatics analysis to discover genes of the TZ compartment goes beyond most comparative genomics studies that focus on the entire cilium. Indeed, distinct phylogenetic signatures exist for other ciliary modules such as IFT-A, IFT-B and BBSome assemblies[34]. Thus, exploitation of genomics data can help to disentangle ciliary modules, ultimately leading to a greater understanding of ciliary transport, signalling and disease. □

METHODS

Methods and any associated references are available in the online version of the paper.

Note: Supplementary Information is available in the online version of the paper

ACKNOWLEDGEMENTS

This work was financially supported via the European Community's Seventh Framework Programme FP7/2009 (SYSCILIA grant agreement 241955 to O.E.B., M.A.H., R.H.G. and C.A.J., and Gencodys to M.A.H.), Science Foundation Ireland (11/PI/1037 to O.E.B.), the Dutch Kidney Foundation CP11.18 'KOUNCIL' (to R.H.G.), the GIS-Institut des Maladies Rares (HTS to C.T.-R.), the French Fondation for Rare Disease (to C.T.-R.), the Virgo consortium (FES0908 to M.A.H.), the Netherlands Genomics Initiative (050-060-452, RvdL to M.A.H.), the French Ministry of Health (PHRC national 2010-A01014-35 and 2013 to C.T.-R.), the Fondation pour la Recherche Médicale (DEQ20130326532 to S.S.), the Regional Council of Burgundy (to C.T.-R.), a Sir Jules Thorn Award for Biomedical Research (JTA/09 to C.A.J.), and the UK Medical Research Council (MR/K011154/1 to C.A.J., and MR/K015613/1 to M.P.). We thank the patients and their families for their participation. We also thank the NHLBI GO Exome Sequencing Project and its ongoing studies that produced and provided exome variant calls for comparison: the Lung GO Sequencing Project (HL-102923), the WHI Sequencing Project (HL-102924), the Broad GO Sequencing Project (HL-102925), the Seattle GO Sequencing Project (HL-102926) and the Heart GO Sequencing Project (HL-103010). We thank M. Leroux (Simon Fraser University, Canada), B. Yoder (University of Alabama, USA), the *Caenorhabditis elegans* Genetics Center (Minnesota, USA), the National Bioresource project (Tokyo, Japan), the International *C. elegans* gene knockout consortium, and the *C. elegans* Million Mutation Project for nematode reagents. We are grateful to C. Eggeling and C. Lagerholm (Weatherall Institute of Molecular Medicine and the Wolfson Imaging Center, Oxford, UK) for assistance with STED microscopy, D. Scholz and T. Toivonen (UCD Conway Institute imaging facility, Dublin, IRL) for imaging support, and R. Dijkstra (Scientific Volume Imaging bv, Hilversum, NL) for assistance with STED image deconvolution. We also thank A. Cleasby (Faculty of Biological Sciences, University of Leeds, Leeds, UK) for help with developing the dSTORM technique, B. Chih (Genentech, South San Francisco, CA, USA) for the kind gift of polyclonal anti-TMEM17 and TMEM231 antibodies, and T. McMorrow (University College Dublin, Dublin, Ireland) for the generous gift of the RPTEC/TERT1 cells. We thank D. Rodriguez (Trousseau hospital, Paris) for assistance with analysis of brain MRIs. The dSTORM microscope was generously funded by alumnus M. Beverly, in support of the University of Leeds 'making a world of difference campaign'.

AUTHOR CONTRIBUTIONS

N.J.L., J.E.K., K.G. and O.E.B. performed and interpreted experiments with *C. elegans*. T.J.P.v.D., R.v.d.L. and M.A.H. performed all bioinformatics analyses. A.-L.B., L.B., D.D., T.A.-B., S.S. and C.T.-R. collected and purified patient samples, performed exome sequencing and analysed sequencing data. N.J.L., S.K. and G.J.M. performed the STED imaging. A.C., M.P. and C.A.J. conducted the dSTORM imaging and processing. K.S., S.K., G.G.S., K.M.W. and R.H.G. conducted transfection and immunofluorescence microscopy in mammalian cells. K.S. and C.A.J. contributed the co-immunoprecipitation experiments. J.-B.R., L.F. and C.T.-R. diagnosed and referred patients. The co-corresponding authors shared supervision of the work. M.A.H. uncovered TMEM107 as a candidate ciliary gene, and directed the bioinformatics work. C.T.-R. collated JBTS and OFD patient samples, performed clinical characterization and directed the sequencing. O.E.B. directed research, analysed and collated data for the manuscript. O.E.B., M.A.H., R.H.G. and C.A.J. conceived and executed the study, and O.E.B., N.J.L., T.J.v.D. and M.A.H. wrote the manuscript.

COMPETING FINANCIAL INTERESTS

The authors declare no competing financial interests.

Published online at http://dx.doi.org/10.1038/ncb3273
Reprints and permissions information is available online at www.nature.com/reprints

1. Reiter, J., Blacque, O. & Leroux, M. The base of the cilium: roles for transition fibres and the transition zone in ciliary formation, maintenance and compartmentalization. *EMBO Rep.* **13,** 608–618 (2012).
2. Goetz, S. C. & Anderson, K. V. The primary cilium: a signalling centre during vertebrate development. *Nat. Rev. Genet.* **11,** 331–344 (2010).
3. Blacque, O. E. & Sanders, A. A. Compartments within a compartment: what *C. elegans* can tell us about ciliary subdomain composition, biogenesis, function, and disease. *Organogenesis* **10,** 126–137 (2014).
4. Hsiao, Y. C., Tuz, K. & Ferland, R. J. Trafficking in and to the primary cilium. *Cilia* **1,** 4 (2012).
5. Chih, B. *et al.* A ciliopathy complex at the transition zone protects the cilia as a privileged membrane domain. *Nat. Cell Biol.* **14,** 61–72 (2011).
6. Craige, B. *et al.* CEP290 tethers flagellar transition zone microtubules to the membrane and regulates flagellar protein content. *J. Cell Biol.* **190,** 927–940 (2010).
7. Garcia-Gonzalo, F. R. *et al.* A transition zone complex regulates mammalian ciliogenesis and ciliary membrane composition. *Nat. Genet.* **43,** 776–784 (2011).

8. Hu, Q. *et al.* A septin diffusion barrier at the base of the primary cilium maintains ciliary membrane protein distribution. *Science* **329,** 436–439 (2010).
9. Kee, H. L. *et al.* A size-exclusion permeability barrier and nucleoporins characterize a ciliary pore complex that regulates transport into cilia. *Nat. Cell Biol.* **14,** 431–437 (2012).
10. Williams, C. L. *et al.* MKS and NPHP modules cooperate to establish basal body/transition zone membrane associations and ciliary gate function during ciliogenesis. *J. Cell Biol.* **192,** 1023–1041 (2011).
11. Gilula, N. B. & Satir, P. The ciliary necklace. A ciliary membrane specialization. *J. Cell Biol.* **53,** 494–509 (1972).
12. Heller, R. F. & Gordon, R. E. Chronic effects of nitrogen dioxide on cilia in hamster bronchioles. *Exp. Lung Res.* **10,** 137–152 (1986).
13. Roberson, E. C. *et al.* TMEM231, mutated in orofaciodigital and Meckel syndromes, organizes the ciliary transition zone. *J. Cell Biol.* **209,** 129–142 (2015).
14. Cevik, S. *et al.* Active transport and diffusion barriers restrict Joubert syndrome-associated ARL13B/ARL-13 to an Inv-like ciliary membrane subdomain. *PLoS Genet.* **9,** e1003977 (2013).
15. Huang, L. *et al.* TMEM237 is mutated in individuals with a Joubert syndrome related disorder and expands the role of the TMEM family at the ciliary transition zone. *Am. J. Hum. Genet.* **89,** 713–730 (2011).
16. Jauregui, A. R., Nguyen, K. C., Hall, D. H. & Barr, M. M. The *Caenorhabditis elegans* nephrocystins act as global modifiers of cilium structure. *J. Cell Biol.* **180,** 973–988 (2008).
17. Williams, C. L., Winkelbauer, M. E., Schafer, J. C., Michaud, E. J. & Yoder, B. K. Functional redundancy of the B9 proteins and nephrocystins in *Caenorhabditis elegans* ciliogenesis. *Mol. Biol. Cell* **19,** 2154–2168 (2008).
18. Schouteden, C., Serwas, D., Palfy, M. & Dammermann, A. The ciliary transition zone functions in cell adhesion but is dispensable for axoneme assembly in *C. elegans*. *J. Cell Biol.* **210,** 35–44 (2015).
19. Jensen, V. L. *et al.* Formation of the transition zone by Mks5/Rpgrip1L establishes a ciliary zone of exclusion (CIZE) that compartmentalises ciliary signalling proteins and controls PIP2 ciliary abundance. *EMBO J.* **34,** 2537–2556 (2015).
20. Baughman, J. M. *et al.* A computational screen for regulators of oxidative phosphorylation implicates SLIRP in mitochondrial RNA homeostasis. *PLoS Genet.* **5,** e1000590 (2009).
21. van Dam, T. J., Wheway, G., Slaats, G. G., Huynen, M. A. & Giles, R. H. The SYSCILIA gold standard (SCGSv1) of known ciliary components and its applications within a systems biology consortium. *Cilia* **2,** 7 (2013).
22. Barker, A. R., Renzaglia, K. S., Fry, K. & Dawe, H. R. Bioinformatic analysis of ciliary transition zone proteins reveals insights into the evolution of ciliopathy networks. *BMC Genomics* **15,** 531 (2014).
23. Christopher, K. J., Wang, B., Kong, Y. & Weatherbee, S. D. Forward genetics uncovers Transmembrane protein 107 as a novel factor required for ciliogenesis and Sonic hedgehog signaling. *Dev. Biol.* **368,** 382–392 (2012).
24. Giles, R. H., Ajzenberg, H. & Jackson, P. K. 3D spheroid model of mIMCD3 cells for studying ciliopathies and renal epithelial disorders. *Nat. Protoc.* **9,** 2725–2731 (2014).
25. Friedland, A. E. *et al.* Heritable genome editing in *C. elegans* via a CRISPR-Cas9 system. *Nat. Methods* **10,** 741–743 (2013).
26. Starich, T. A. *et al.* Mutations affecting the chemosensory neurons of *Caenorhabditis elegans*. *Genetics* **139,** 171–188 (1995).
27. Williams, C. L., Masyukova, S. V. & Yoder, B. K. Normal ciliogenesis requires synergy between the cystic kidney disease genes MKS-3 and NPHP-4. *J. Am. Soc. Nephrol.* **21,** 782–793 (2010).
28. Valente, E. M. *et al.* Mutations in TMEM216 perturb ciliogenesis and cause Joubert, Meckel and related syndromes. *Nat. Genet.* **42,** 619–625 (2010).
29. Kensche, P. R., van Noort, V., Dutilh, B. E. & Huynen, M. A. Practical and theoretical advances in predicting the function of a protein by its phylogenetic distribution. *J. R. Soc.* **5,** 151–170 (2008).
30. Iglesias, A. *et al.* The usefulness of whole-exome sequencing in routine clinical practice. *Genet. Med.* **16,** 922–931 (2014).
31. Shaheen, R. *et al.* Identification of a novel MKS locus defined by TMEM107 mutation. *Hum. Mol. Genet.* **24,** 5211–5218 (2015).
32. Nakada, C. *et al.* Accumulation of anchored proteins forms membrane diffusion barriers during neuronal polarization. *Nat. Cell Biol.* **5,** 626–632 (2003).
33. Xu, K., Zhong, G. & Zhuang, X. Actin, spectrin, and associated proteins form a periodic cytoskeletal structure in axons. *Science* **339,** 452–456 (2013).
34. van Dam, T. J. *et al.* Evolution of modular intraflagellar transport from a coatomer-like progenitor. *Proc. Natl Acad. Sci. USA* **110,** 6943–6948 (2013).

DOI: 10.1038/ncb3273

METHODS

Coexpression analyses. We collected a set of 20 genes known to localize at the TZ (ref. 1). Nucleoporins were excluded because they have an additional role in nuclear transport and are therefore likely to have substantially different expression profiles compared with other TZ proteins. The SYSCILIA gold standard (SCGSv1; http://www.syscilia.org/goldstandard.shtml)[21] was used to evaluate the approach for retrieving cilia-related genes. A large collection of publicly available microarray data sets was obtained from the NCBI gene expression omnibus (GEO) database: 809 data sets for mouse (~13,000 individual experiments) and 868 data sets for human (~22,000 individual experiments); the full list of the human and mouse GEO (microarray) data sets (GDS) employed is shown in Supplementary Table 2. Each expression data set was assessed for its potential to find new TZ-related genes by determining the expression coherence of the 20 genes known to localize to the TZ. Experiments where known TZ genes show coherent expression obtain a high weighting, and contribute more to the coexpression calculation than experiments with less coherent expression. These weightings are used to calculate an integrated probability for each gene, according to how much its expression profile correlates with that of TZ genes across the expression data sets. We calculated TZ coexpression separately for mouse and human, obtaining scores for ~15,000 mouse genes and ~21,000 human genes.

Sequence analysis and evolutionary analysis. Worm and human MKS and NPHP module protein sequences were extracted from NCBI. Orthologous sequences were detected by BLAST and PSI-BLAST and extracted from an in-house protein sequence and orthology database[34]. Retrieved sequences were manually verified by reverse BLAST searches. Hidden Markov Models (HMMs) were created for each protein family by first aligning the sequence using MAFFT (version v6.884b, options *–localpair –maxiterate 1000*). Highly fragmented sequences were removed from the alignment. Custom HMMs were created using HMMer 3.0 and searched against our in-house protein sequence database again for sequences missed by PSI-BLAST. Finally we searched the genomic and EST sequences using TBLASTN to find orthologues not found by gene prediction algorithms. For MKS-5 (RPGRIP1L), we also employed sequential sequence searches using NCBI PSI-BLAST using stepwise more diverse orthologous sequences as the seed (for example, we used the *Phytophthora infestans* sequence to find the *Chlamydomonas reinhardtii* sequence and used that sequence to find the *Volvox carteri* orthologue). Discovered sequences were confirmed by reverse PSI-BLAST searches and sequence alignments. All presences and absences were noted for each species considered (Supplementary Fig. 1). The TMEM107 alignment was made using MAFFT (options *–globalpair –maxiterate 1000*) and edited to fix minor alignment errors. For the differential Dollo parsimony (diff Dollop)[29] analysis, which counts the number of independent losses of proteins along a phylogenetic tree, we used a script provided by P. Kensche[29]. The network was constructed and visualized in Cytoscape.

Targeted next-generation and exome sequencing analysis. Next-generation sequencing analyses were performed on 5 µg of DNA sample from each of 198 JBTS and OFD individuals. In 192 JBTS individuals, simultaneous target sequencing was performed using a panel of 25 candidate or causal JBTS genes on an Illumina MiSeq in accordance with the manufacturer's recommendations. In 6 OFD individuals, exome capture was achieved using the SureSelect Human All Exon 50Mb kit (Agilent). The resulting libraries underwent 2 × 100-bp paired-end sequencing on an Illumina HiSeq 2000 in accordance with the manufacturer's recommendations. Reads were aligned to the human reference genome (GRCh37/hg19) with the Burrows–Wheeler Aligner (BWA.0.5.6) and potential duplicate paired-end reads were removed using picardtools.1.22 (http://picard.sourceforge.net). The Genome Analysis Toolkit (GATK) 1.0.57 was used for base quality score recalibration and indel realignment, as well as for single-nucleotide variant and indel discovery and genotyping using standard hard filtering parameters. Homozygous variants with quality scores of >30, sequencing depth of >4, quality/depth ratio of >5.0 and strand bias of <−0.10 were retained for subsequent analyses. Coverage was assessed with the GATK Depth of Coverage tool by ignoring reads with mapping quality of <20 and bases with base quality of <30. Candidate events were inspected using Integrative Genomics Viewer (IGV). Variants were excluded when the frequency was >1/1,000 in the Exome Variant Server, NHLBI (http://evs.gs.washington.edu/EVS). The sequencing data have been deposited in the European Nucleotide Archive (http://www.ebi.ac.uk/ena); accession number PRJEB11176.

Sanger sequencing. *TMEM107* (NM_183065) mutation screening was performed by direct sequencing of PCR products (coding exons and adjacent intronic junctions) in 40 additional JBTS individuals, 54 MKS patients (mutation-negative for known genes), and 32 other patients with a clinical diagnosis consistent with a ciliopathy. PCR primers (sequences available on request) were designed with Primer3 (http://bioinfo.ut.ee/primer3-0.4.0/primer3). PCR products were purified using the Exo-SAP cleanup kit (USB). Sequencing was performed using the ABI BigDye Terminator Cycle Sequencing kit (v3.1; Applied Biosystems) following the manufacturer's instructions in an ABI 3130 sequencer 7 (Applied Biosystems). Sequence data were analysed with SeqScape v2.7 (Applied Biosystems). The impact of the missense mutation was assessed using PolyPhen-2 (http://genetics.bwh.harvard.edu/pph2). Written consent was obtained from patients for generation and use of their molecular data.

***C. elegans* strains, maintenance and crossing.** *C. elegans* were maintained and cultured at 20 °C using standard techniques. All strains employed are shown in Supplementary Table 4. Standard genetic crossing techniques were used to make double mutants and to introduce transgenes into genetic backgrounds. Genotyping was performed using PCR (primer sequences available on request). The *daf-19(m86)* mutation was followed using the dye-filling assay[35].

Generation of the *oq100* mutation by CRISPR. sgRNA template and Cas9 plasmids were obtained from Addgene (46168, 46169). The *tmem-107*-sgRNA was generated following ref. 25, targeting the sequence 5′-ATAGAGATCGAG ACGGCGAC-3′. sgRNA and Cas9 constructs were each injected at 125 ng µl^{-1}, together with the pCeh361 (*dpy-5*(+)) construct at 50 ng µl^{-1}, into *dpy-5*(*e907*) hermaphrodites. A total of 204 *dpy-5* rescued F1 worms were screened for a *tmem-107*-associated Hpy99I (NEB R0615) restriction fragment length polymorphism (RFLP). Three independent lines with an RFLP were subjected to Sanger sequencing to identify the *tmem-107* mutations. Two worms had the same in-frame 6-bp deletion (P74S75del), predicted to cause no serious effects and were not investigated further. The third worm possessed a 27-bp deletion in exon 2 (genomic breakpoints: I:14758954/14758955—14758981/14758982) replaced with a 14-bp insertion (5′-G TGACAACGTGGAA-3′). This allele designated *oq100* features a frameshift leading to a predicted truncated protein of 72 native amino acids followed by an ectopic 17 amino acids and a premature stop.

***C. elegans* reporters.** All constructs were generated by fusion PCR as previously described[36]. For the transcriptional (promoter) *tmem-107p*::GFP reporter, GFP amplified from pPD95.67 was fused with 559 bp of *tmem-107* 5′UTR sequence along with the first 15 bp of exon 1 (with the adenine of the start codon mutated to cytosine). For the translational (protein) *tmem-107::gfp* reporter, the entire exonic and intronic sequence of each gene, together with upstream promoter sequence (see above), was fused in-frame with GFP amplified from pPD95.77. For substituting extramembranous TMEM-107 sequences Polyphobius software (http://phobius.sbc.su.se/poly.html) was employed to determine TMEM-107 residue topology twice: based on *C. elegans* only; and based on sequence conservation in *C. elegans* close relatives. Subsequently, a consensus prediction was compiled, establishing that amino acids 1–9 (N terminus), 30–47 (linker 1), 73–78 (linker 2) and 100–103 (linker 3) are very likely extramembranous. Next, we searched the literature for tetraspan transmembrane proteins not associated with ciliary TZs and identified with the software Phobius (http://phobius.sbc.su.se) similar sized linker sequences, suitable for replacing TMEM107 linkers; amino acids 131–148 of SNG-1 to substitute linker 1, amino acids 74–79 of SPE-38 to replace linker 2, and amino acids 49–52 to substitute linker 3. In addition, we generated three constructs replacing the TMEM-107 linkers (1–3) with sequences containing scrambled versions of the same residues. The TMEM-107 C-terminal truncation construct TMEM-107(aa1–129)::GFP—called cTMEM107 in Fig. 4c—was similarly amplified except that the C-terminal 7 amino acid encoding sequence was not included. The TMEM-107 N-terminal substituted construct (SPH-1(aa1–11)::TMEM-107 (10–136)::GFP)—called nTMEM-107 in Fig. 4c—was amplified to contain the N-terminal 11 amino acids of SPH-1 fused to TMEM-107 lacking its N terminus. The SPH-1 N terminus was chosen as the replacement because SPH-1 and TMEM-107 are topologically similar; both are predicted tetraspan transmembrane proteins with cytosolic N-terminal tails (albeit of different sequence). Note that full-length SPH-1::GFP, SNG-1::GFP and SPE-38::GFP translational reporters (under the control of an *arl-13* promoter active in most ciliated cells) do not localize to ciliary TZs (data not shown). For mimicking the TMEM-107 patient variants, PCR was used to engineer E46G (equivalent to human HsE45G) and F96del (equivalent to HsF106del) mutations into nematode TMEM-107. For simulating the HsL134F*fs**8 mutation, TMEM-107 was truncated at L120, and nucleotides corresponding to the human ectopic residues (FSSPSLG) were added. Transgenic worms expressing the above constructs were generated using gonadal transformation through microinjection. The transcriptional construct was injected into *dpy-5(e907)* worms at 50 ng µl^{-1}, together with the *dpy-5*(+)-containing rescuing construct (at 50 ng µl^{-1}), pCeh361. Translational constructs were injected into N2 worms typically at 5 ng µl^{-1}, together with a coelomycete cell-expressed (*unc-122p::gfp* or *unc-122p::dsRed*) co-injection marker at 100 ng µl^{-1}.

***C. elegans* immobilization for microscopy.** Live worms were immobilized on 10% agarose pads using microbeads (Polysciences no. 00876-15) or with 40 mM tetramisole (Sigma no. L9756).

***C. elegans* fluorescence imaging and FRAP assay.** Imaging was performed on an epifluorescence-fitted upright Leica DM5000B compound microscope or an inverted Nikon Eclipse Ti microscope with a Yokogawa spinning-disc unit (Andor Revolution). Image analysis and formatting was conducted using ImageJ software (NIH). Fluorescence recovery after photobleaching (FRAP) assays were performed using the above confocal system, with an attached FRAPPA unit. Samples were imaged pre-bleach, and then bleached using a single pulse of the 488 nm laser at 100% with a dwell time of 100 µs. Images were recorded immediately post-bleach (that is, 0 minute time point) and at varying time points post-bleach until recovery plateaued. All images were taken using the same camera settings (exposure time, gain) and images were subsequently stacked to ensure identical background intensities. Using ImageJ, photobleached and non-photobleached regions were selected and the intensity (grey value) was measured at each time point. After background subtraction, ratios of bleached/non-bleached regions were calculated, and ratios were normalized to a pre-bleach ratio of 1.0.

Dye-filling, chemosensory and roaming (foraging) assays. Assays for dye-filling (DiI), roaming and chemoattraction to a volatile odorant (isoamyl alcohol) were performed as previously described[35]. A chemotaxis index was calculated at 30 min and 60 min. For the roaming assay, single worms were placed for 16 h onto seeded plates and track coverage was assessed using a grid reference.

Transmission electron microscopy. Young adult worms were fixed, sectioned and imaged using previously reported methodology[35]. For the TEM electron tomography, 200-nm-thick sections were collected onto Formvar carbon-coated slot grids and a tilt series acquired from −60 to +60 in 1° increments using FEI software. The tilt series was converted to a *z* stack using serial EM and then visualized using Amira software (FEI).

Cloning of mammalian constructs. Full-length *TMEM107* was cloned into the pcDNA3.0 vector (Invitrogen), and then shuttled into mCherry-, EGFP-, and FLAG- containing vectors. Mutations were introduced into TMEM107-pEGFP-N3 by QuickChange mutagenesis (Stratagene).

Immortalized mammalian cell lines and antibodies. Mouse inner medullary collecting duct (IMCD3), human retinal pigmented epithelial (hTERT-RPE1) and human embryonic kidney (HEK293) cells were derived from the American Type Culture Collection (ATCC). The genomic status was assessed by array CGH and karyotyping (May 2013) and tested every three months for mycoplasma. Cells were maintained in DMEM/Ham's F12 medium supplemented with 10% fetal calf serum (FCS), under standard conditions (37 °C, 5% CO_2) at low passages (<25). Human renal proximal epithelial cells (RPTEC-TERT1) were provided by T. McMorrow (University College Dublin). Three-dimensional spheroids (IMCD3 cells) were grown and scored as previously described[24]. Primary antibodies: mouse monoclonal anti-denatured GFP (Sigma-Aldrich cat. no. G6539, clone GFP-20), rabbit polyclonal anti-native GFP (A.V. peptide, 'Living Colors', Clontech cat. no. 632377), mouse anti-γ-tubulin, mouse anti-acetylated-tubulin (Sigma-Aldrich cat. no. T7451, clone 6-11B-1), rabbit anti-γ-tubulin and mouse anti-β actin (Abcam cat. no. ab6276, clone AC-15). Guinea pig anti-RPGRIP1L (ref. 37), rabbit anti-TMEM237 (ref. 15), and rabbit anti-TMEM231 (ref. 5) have been previously described. Secondary antibodies: polyclonal Alexa Fluor 488-, Alexa Fluor 594- and Alexa Fluor 568-conjugated goat anti-mouse IgG, and goat anti-rabbit IgG (Molecular Probes; cat. no. A-11001/A-11005/A-11031/A-110034).

Ciliogenesis assays with human primary fibroblast cells. Patient fibroblasts were stored in the CRB Ferdinand Cabanne Biobank (Dijon). Fibroblasts were grown from skin biopsies in DMEM supplemented with 10% FCS and 1% P/S. Cells were incubated at 37 °C in 5% CO_2 to approximately 90% confluence. Fibroblasts were serum starved for 24 h before fixation with 4% PFA for 5 min at room temperature followed by ice-cold methanol for 3 min and blocked in PBS (containing 1% BSA and 0.1% Triton X-100) for 30 min. Fixed cells were incubated in primary antibodies diluted in block solution (mouse anti-acetylated tubulin; Sigma T6793; 1:10,000, rabbit anti-ARL13b; ProteinTech 17711-1-AP; 1:400) for 90 min at room temperature and Alexa Fluor-conjugated secondary antibodies from Life Technologies (donkey anti-rabbit 568; 1:400, donkey anti-mouse 647; 1:400) and Hoechst333 for 60 min at room temperature. Coverslips were mounted using Fluoromount G. Confocal imaging was performed using a Zeiss LSM700. Approximately 70 events per condition were scored. GraphPad Prism 5.0 was used to perform two-tailed Student's *t*-tests.

Immunofluorescence assays with *Tmem107*-depleted IMCD3 cells. For co-localization assays (Fig. 4d), murine IMCD3 cells were seeded at 2.5 × 10 (ref. 5) cells per well on sterile glass coverslips in six-well plates. Lipofectamine RNAiMAX (LifeTechnologies) was used to transfect cells with the siRNA SMARTpool targeting *Tmem107* (Dharmacon) according to the manufacturer's protocol. After 72 h, cells were fixed in ice-cold methanol, blocked in 1% non-fat milk and processed for immunofluorescence microscopy via standard methods[38] using Alexa Fluor 488- or Alexa Fluor 568-conjugated secondary antibodies (1:500, LifeTechnologies). Confocal images were obtained using a Nikon A1R confocal microscope with a ×100 oil objective lens controlled by NIS-Elements AR 4.20.01 (Nikon) software. Optical sections were generated through structured processing using AxioVision 4.3 (Zeiss) or NIS-Elements AR 4.20.01 (Nikon) software. Co-localization analyses were performed using the FIJI software plug-in 'Co-localization Threshold'. For knockdown experiments in Fig. 2a,b, murine IMCD3 cells were transfected with a siRNA SMARTpool targeting *Tmem107* (Dharmacon), and spheroids were grown and scored as previously described[24].

Co-immunoprecipitation assays. For transfection with plasmids, cells at 90% confluency were transfected using Lipofectamine 2000 (Invitrogen) according to the manufacturer's instructions. Cells were incubated for 24 to 72 h before lysis or immunostaining. Co-immunoprecipitation was performed as described previously, except that 10 mM CHAPS was used as zwitterionic detergent in the lysis buffer[28]. Whole-cell extracts (WCEs) were prepared from confluent IMCD3 cells transiently transfected with 1.0 µg plasmid constructs in 90 mm tissue culture dishes, or scaled down as appropriate. WCE supernatants were processed for immunoprecipitation experiments by using 5 µg affinity-purified mouse anti-GFP ('Living Colors', Clontech), or 5 µg monoclonal antibodies, or 5–10 µg purified IgG fractions from rabbit polyclonal antisera, coupled to protein G- and/or protein A-Sepharose beads (GE Healthcare). The affinity-purified rabbit polyclonal anti-TMEM17 and TMEM231 have been described previously[5]. Immunoprecipitations were performed in reduced-salt incubation buffer (20 mM Tris, pH 7.5, 25 mM NaCl, 2 mM EDTA, 0.5 mM EGTA, 0.02% (w/v) NaN_3, 10% (v/v) glycerol, 10% (v/v) ethanol, 0.1% (v/v) protease inhibitor cocktail) containing 1 mM CHAPS. Proteins were analysed by SDS–PAGE (using 4–12% polyacrylamide gradient gels) and western immunoblotting according to standard protocols using either rabbit polyclonal antisera (final dilutions of 1:200-1000) or monoclonal antibodies (1:1,000–5,000). Appropriate HRP-conjugated secondary antibodies (Dako) were used (final dilutions of 1:10,000–25,000) for detection by the enhanced chemiluminescence 'Femto West' western blotting detection system (Pierce).

Stimulated emission depletion (STED) microscopy. STED imaging was performed on a Leica DMI6000 SP8X CW gated STED system with a 592 nm depletion laser and an HCX PL APO ×100 NA1.40 oil objective. Samples were excited at 488 nm and emission was detected between 510 and 540 nm. Pixel size was <20 nm (typically ~15 nm). Images were deconvolved using Huygens Professional software (Scientific Volume Imaging B.V), which is part of the standard configuration of the Leica STED system. For deconvolution a signal to noise ratio of 7 was employed and the 'classic' algorithm selected. All other parameters used were default values (contained in the meta data for each image file), as defined by the Huygen's 'deconvolution wizard.'

Mammalian cell preparation for STED microscopy. RPTEC-TERT1 cells were seeded on glass coverslips and cultured for at least 7 days on reaching confluence to induce primary cilia formation. Cells were fixed with 3% PFA for 5 min at room temperature followed by ice-cold methanol for 5 min. After blocking with 3% BSA in 0.2% Triton X-100/PBS for 30 min, cells were stained for TZ proteins (guinea pig anti-RPGRIP1L, 1:500, or rabbit anti-TMEM67, 1:200) and the ciliary axoneme (mouse anti-polyglutamylated tubulin, 1:1,000; Adipogen; cat. no. AG-20B-0020-C100; clone GT335) at room temperature for 2 h. Primary antibodies were detected with polyclonal Alexa Fluor-conjugated secondary antibodies (1:100 dilution; 1 h at room temperature): goat anti-guinea pig 488 (Molecular Probes; cat. no. A11073), goat anti-rabbit 488 (Molecular Probes; cat. no. A11008) or goat anti-mouse 568. All antibodies were diluted in blocking solution. Coverslips were mounted on glass slides in ProLong Diamond (Life Technologies).

Direct stochastic optical reconstruction microscopy (STORM) system. The dSTORM system was based on the 3D PALM system in ref. 39. We used an inverted microscope (Olympus, IX81 with additional side-port ILL100-TIRZD) fitted with an automated *x*–*y* stage with additional piezoelectric adjustment in *z* (Applied Scientific Instrumentation, PZ-2000). The objective lens was a ×60, 1.2 NA, water immersion lens (Olympus, UPLSAPO60XW). The system included a focus locking device that reduced *z*-drift during calibration and data acquisition (Mad City Labs, C-focus) and a cylindrical lens (Thorlabs, $f = 100$ mm, LJ1567RM-A). Images were captured by a back-thinned, electron-multiplying CCD (charge-coupled device) camera, cooled to −80 °C (Andor Technology, iXON Ultra, model DU-897U-CSO-#BV), using published scripts called from the camera interface (Andor Technology, SOLIS). This also converted SIF images generated by the camera to DAT format for processing.

DOI: 10.1038/ncb3273

Preparation of secondary antibody and samples for dSTORM. Affinity-purified guinea pig anti-RPGRIP1L has been described previously[37], and was used at 1:200 dilution. Polyclonal donkey anti-guinea pig IgG (H+L) secondary antibody (100 µg) was labelled ('AffiniPure', Jackson ImmunoResearch Europe cat. no. 706-005-148) in PBS containing 120 mM $NaHCO_3$ with 2 µg carboxylic acid succinimidyl ester of the photoswitchable dye Alexa Fluor 647 (A37573, Life Technologies). Labelling was performed for 30 min at room temperature, and unincorporated dye was removed by gel filtration through NAP-5 columns (17-0853-02, GE Healthcare) according to the manufacturer's protocol. Antibody/dye labelling ratios of approximately 1:1 were confirmed by measured absorbances in a spectrophotometer, with a final concentration of 0.3 µg µl^{-1}. Secondary antibodies were used at titres of 1:100.

Human hTERT-RPE1 cells were seeded on cleaned coverslips (no. 1.5, 25-mm diameter CS-25R15; Warner Instruments) at 2.5 × 10 (ref. 5) cells per well on the coverslips in six-well plates and serum starved in normal media with 0.2% FCS for 48 h to induce ciliogenesis. Coverslips were processed for immunofluorescence staining using standard methods, and post-fixed with 3% paraformaldehyde/0.1% glutaraldehyde in PBS. Coverslips were then incubated with 0.01% poly-L-lysine (Sigma-Aldrich, P4707) for 10 min followed by a suspension of 100 nm gold nanoparticles (1:10, Sigma-Aldrich 724031, in PBS) for use as fiducials. Calibration series for depth information (see below) were taken at this point, using the relevant excitation laser(s). Data were acquired in the presence of fluorescence quenching buffer consisting of 10 mM Tris-HCl (pH 8.0), 50 mM NaCl, 5 mg ml^{-1} glucose, 114 mM β-mercaptoethanol, 0.5 mg ml^{-1} glucose oxidase and 40 µg ml^{-1} catalase.

dSTORM image acquisition, processing and analysis. Imaging software employed was described previously[39] (see https://github.com/AndrewGYork/palm3d for further details). Calibration images were taken to calculate the point spread function (PSF) in steps of 50 nm over a 4 µm range, using fluorescence of selected fiducials. Labels were then excited until emission was quenched and then stochastically re-activated using a 405 nm laser initially at low power (0.4 mW), followed by data collection. Fluorescence emission events were localized in x–y and z using the PSFs captured in the calibration series[39]. Drift was recorded and corrected using images of the fiducials. Emission events were binned into a histogram for display and to correct for distortion by the cylindrical lens. Binning was at either 20 nm or 10 nm, with x–y–z localization precisions of 20 × 30 × 50 nm for fiducial markers[39]. The software applied smoothing to reflect the limits of localization precision, and z-stacks were displayed in FIJI.

Statement of image representation and reproducibility. Representative images are shown for all worm and mammalian cell imaging. The following states how many samples were imaged in each figure panel where a representative image is shown: Fig. 1c,d (>30 worms), Fig. 1e (30 cells), Fig. 2b (50 spheroids), Fig. 2h (75 cells), Fig. 3b (>20 worms for each strain), Fig. 3c (>50 worms for each strain), Fig. 3d (>20 worms for each strain), Fig. 3f (>30 worms for each strain), Fig. 3g (>50 worms for each strain), Fig. 3h (>30 worms for each strain), Fig. 4a (>40 worms for each strain), Fig. 4c (>20 worms for each strain), Fig. 4d (50 cells for each experiment), Fig. 5a (>20 worms for each strain), Fig. 5b (10 worms), Fig. 5c (>100 worms imaged per strain), 5d (>30 cells per experiment), Fig. 5e (>20 TZs for each marker), Supplementary Fig. 2a (>20 worms), Supplementary Fig. 2b (>40 worms), Supplementary Fig. 2d (>20 worms), Supplementary Fig. 2e (>30 cells), Supplementary Fig. 4a (2–4 amphid pores), Supplementary Fig. 4b (>20 transition zones), Supplementary Fig. 4c (>30 worms per strain), Supplementary Fig. 5a (>10 sets of amphid transition zones).

35. Sanders, A. A., Kennedy, J. & Blacque, O. E. Image analysis of *Caenorhabditis elegans* ciliary transition zone structure, ultrastructure, molecular composition, and function. *Methods Cell Biol.* **127,** 323–347 (2015).
36. Hobert, O. PCR fusion-based approach to create reporter gene constructs for expression analysis in transgenic *C. elegans*. *BioTechniques* **32,** 728–730 (2002).
37. Arts, H. H. *et al.* Mutations in the gene encoding the basal body protein RPGRIP1L, a nephrocystin-4 interactor, cause Joubert syndrome. *Nat. Genet.* **39,** 882–888 (2007).
38. Dawe, H. R. *et al.* Nesprin-2 interacts with meckelin and mediates ciliogenesis via remodelling of the actin cytoskeleton. *J. Cell Sci.* **122,** 2716–2726 (2009).
39. York, A. G., Ghitani, A., Vaziri, A., Davidson, M. W. & Shroff, H. Confined activation and subdiffractive localization enables whole-cell PALM with genetically expressed probes. *Nat. Methods* **8,** 327–333 (2011).

Article 7

The oral-facial-digital syndrome gene *C2CD3* encodes a positive regulator of centriole elongation.

Nat Genet. 2014 Aug;46(8):905-11

C. Thauvin-Robinet, JS. Lee, E. Lopez, V. Herranz-Pérez, T. Shida, B. Franco, L. Jego,F. Ye, L. Pasquier, P. Loget, N. Gigot, B. Aral, CA. Lopes, J. St-Onge, AL. Bruel , J. Thevenon, S. González-Granero, C. Alby, A. Munnich, M. Vekemans, F. Huet, AM. Fry, S. Saunier, JB. Rivière, T. Attié-Bitach, JM. Garcia-Verdugo, L. Faivre, A. Mégarbané, MV. Nachury.

Résumé :

Les centrioles sont des structures microtubulaire qui initie l'assemblage des centrosomes et des cils. La protéine OFD1 réprime l'élongation des centrioles, cependant les mécanismes précis de régulation de la croissance centriolaire restent encore peu connus. Dans cette étude, nous décrivons un nouveau sous-type des syndromes oro-facio-digitaux caractérisé par une microcéphalie sévère et des malformations cérébrales. Des mutations dans le gène C2CD3 ont été identifiées dans deux familles non-apparentées, atteintes d'un nouveau sous-type de syndrome OFD caractérisé par une microcéphalie très sévère et un signe de la dent molaire à l'IRM cérébrale. C2CD3 colocalise et interagit avec OFD1 à l'extrémité distale des centrioles. Cette étude a permis de démontrer que C2CD3 est un antagoniste d'OFD1 et de préciser le mécanisme de régulation de la longueur des centrioles. Les résultats sont présentés page 87.

nature genetics

The oral-facial-digital syndrome gene *C2CD3* encodes a positive regulator of centriole elongation

Christel Thauvin-Robinet[1,2,17], Jaclyn S Lee[3,17], Estelle Lopez[1], Vicente Herranz-Pérez[4,5], Toshinobu Shida[3], Brunella Franco[6,7], Laurence Jego[1], Fan Ye[3], Laurent Pasquier[8], Philippe Loget[9], Nadège Gigot[1,10], Bernard Aral[1,10], Carla A M Lopes[11], Judith St-Onge[1,10], Ange-Line Bruel[1], Julien Thevenon[1,2], Susana González-Granero[4,5], Caroline Alby[12,13], Arnold Munnich[12–14], Michel Vekemans[12–14], Frédéric Huet[1,2], Andrew M Fry[11], Sophie Saunier[13,15], Jean-Baptiste Rivière[1,10], Tania Attié-Bitach[12–14], Jose Manuel Garcia-Verdugo[4,5], Laurence Faivre[1,2], André Mégarbané[16] & Maxence V Nachury[3]

Centrioles are microtubule-based, barrel-shaped structures that initiate the assembly of centrosomes and cilia[1,2]. How centriole length is precisely set remains elusive. The microcephaly protein CPAP (also known as MCPH6) promotes procentriole growth[3–5], whereas the oral-facial-digital (OFD) syndrome protein OFD1 represses centriole elongation[6,7]. Here we uncover a new subtype of OFD with severe microcephaly and cerebral malformations and identify distinct mutations in two affected families in the evolutionarily conserved *C2CD3* gene. Concordant with the clinical overlap, C2CD3 colocalizes with OFD1 at the distal end of centrioles, and C2CD3 physically associates with OFD1. However, whereas OFD1 deletion leads to centriole hyperelongation, loss of C2CD3 results in short centrioles without subdistal and distal appendages. Because C2CD3 overexpression triggers centriole hyperelongation and OFD1 antagonizes this activity, we propose that C2CD3 directly promotes centriole elongation and that OFD1 acts as a negative regulator of C2CD3. Our results identify regulation of centriole length as an emerging pathogenic mechanism in ciliopathies.

OFD syndromes are ciliopathies characterized by malformations of the face, oral cavity and digits[8]. A 4-year-old male born from consanguineous parents presented with canonical OFD syndrome as well as severe microcephaly, micropenis and severe intellectual disability (**Fig. 1a**,**b** and **Supplementary Table 1**), indicative of an unclassified OFD syndrome. Brain magnetic resonance imaging (MRI) showed the presence of molar tooth sign (MTS; a cerebellar anomaly characteristic of Joubert syndrome and related disorders[9]) and several other cerebral malformations (**Fig. 1c–e** and **Supplementary Table 1**). The proband's younger sister presented with similar anomalies and cardiac malformation, leading to neonatal death. Homozygosity mapping identified a candidate region of 4 Mb at 11q13.4-q14.1 (**Supplementary Fig. 1a**), and coupled exome sequencing identified a homozygous nonsense mutation in the *C2CD3* gene (NM_015531.5: c.184C>T in exon 2; p.Arg62*), which was confirmed by Sanger sequencing and was found to be heterozygous in his parents (**Supplementary Fig. 1b**).

We next screened the coding exons of *C2CD3* for mutations in 34 individuals with OFD who were negative for mutations in known OFD-associated genes. We identified a male fetus with compound heterozygous *C2CD3* mutations consisting of one missense variant (NM_015531.5: c.3085T>G; p.Cys1029Gly) and a substitution in the splice acceptor consensus sequence of exon 22 (NM_015531.5: c.3911–2A>T). Transcript analysis for the affected fetus showed that the c.3911–2A>T substitution caused splicing of the 5′ end of exon 22 to a downstream cryptic splice site, leading to a 4-nt frameshift deletion (NM_015531.5: c.3911_3914delCAAG; p.Ala1304Valfs*3) (**Supplementary Fig. 1c–e**). In close similarity to the index case, the second individual with OFD exhibited severe microcephaly combined with canonical OFD symptoms (**Fig. 1f–j** and **Supplementary Table 1**). Both mutations were absent from the Exome Variant Server (see

[1]Equipe d'Accueil 4271 Génétique des Anomalies du Développement, Fédération Hospitalo–Universitaire, Université de Bourgogne, Dijon, France. [2]Centre de Référence Maladies Rares "Anomalies du Développement et Syndromes Malformatifs" de l'Est, Centre de Génétique et Pédiatrie 1, Hôpital d'Enfants, Centre Hospitalier Universitaire Dijon, Dijon, France. [3]Department of Molecular and Cellular Physiology, Stanford University School of Medicine, Stanford, California, USA. [4]Laboratorio de Neurobiología Comparada, Instituto Cavanilles, Universitat de València, Centro Investigación Biomédica en Red Enfermedades Neurodegenerativas, Valencia, Spain. [5]Unidad Mixta de Esclerosis Múltiple y Neurorregeneración, Instituto de Investigación Sanitaria Hospital La Fe, Universitat de València, Valencia, Spain. [6]Telethon Institute of Genetics and Medicine (TIGEM), Naples, Italy. [7]Department of Medical Translational Sciences, Division of Pediatrics, Federico II University of Naples, Naples, Italy. [8]Centre de Référence Maladies Rares "Anomalies du Développement et Syndromes Malformatifs" de l'Ouest, Unité Fonctionnelle de Génétique Médicale, Centre Hospitalier Universitaire Rennes, Rennes, France. [9]Laboratoire d'Anatomie-Pathologie, Centre Hospitalier Universitaire Rennes, Rennes, France. [10]Laboratoire de Génétique Moléculaire, Plateau Technique de Biologie, Centre Hospitalier Universitaire Dijon, Dijon, France. [11]Department of Biochemistry, University of Leicester, Leicester, UK. [12]INSERM U781, Institut IMAGINE, Hôpital Necker–Enfants Malades, Paris, France. [13]Paris Descartes–Sorbonne Paris Cité University, Institut IMAGINE, Paris, France. [14]Département de Génétique, Hôpital Necker–Enfants Malades, Paris, France. [15]INSERM, UMRS 1163, Laboratory of Inherited Kidney Diseases, Paris, France. [16]Unité de Génétique Médicale, Faculté de Médecine, Université Saint-Joseph, Beirut, Lebanon. [17]These authors contributed equally to this work. Correspondence should be addressed to M.V.N. (nachury@stanford.edu) or C.T.-R. (christel.thauvin@chu-dijon.fr).

Received 23 December 2013; accepted 17 June 2014; published online 6 July 2014; doi:10.1038/ng.3031

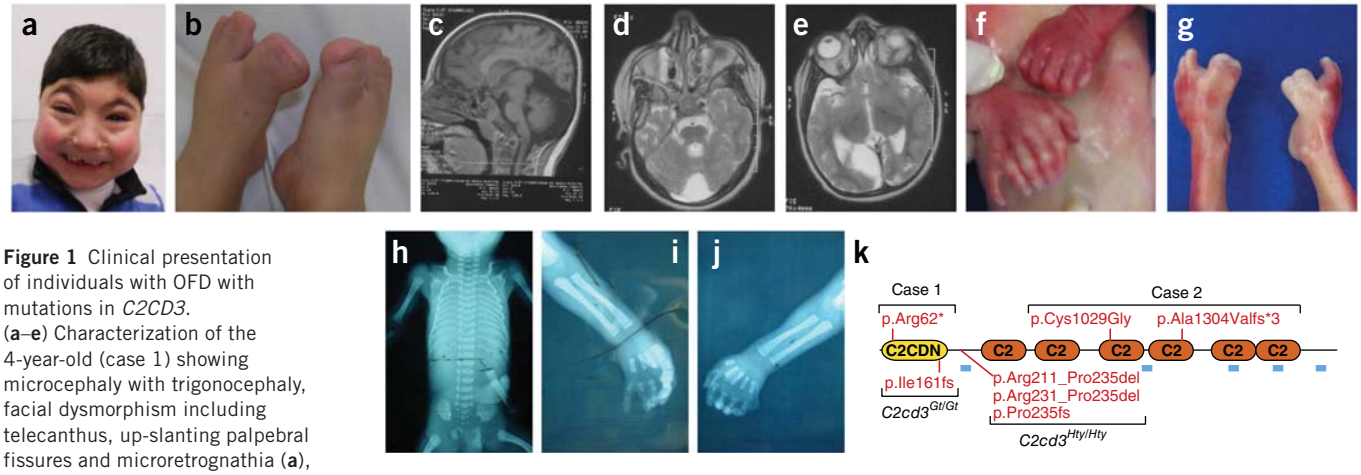

Figure 1 Clinical presentation of individuals with OFD with mutations in *C2CD3*. (**a**–**e**) Characterization of the 4-year-old (case 1) showing microcephaly with trigonocephaly, facial dysmorphism including telecanthus, up-slanting palpebral fissures and microretrognathia (**a**), bilateral broad duplicated and deviated hallux (**b**) and brain MRI with corpus callosum hypoplasia (**c**), MTS (**d**), subarachnoid cysts in the right occipital lobe (**d**) and the posterior fossa (**e**), and incomplete myelinization of the white matter (**c**–**e**). Informed consent to publish these images was obtained from this individual's family. (**f**–**j**) Pictures of the fetus at 22 weeks of gestation (case 2) showing bilateral hand postaxial polydactyly (**f**) and broad duplicated hallux (**g**) and X-rays showing normal thorax (**h**) and postaxial polydactyly of the left (**i**) and right (**j**) hands. (**k**) Domain organization of C2CD3 (C2 calcium-dependent domain containing 3). The six orange ovals correspond to canonical C2 domains, and the yellow oval represents the signature C2CD3N C2 domain[10]. Alterations identified in cases are indicated in red on top of the diagram, mouse mutants are shown under the diagram, and peptides identified in LAP-BBS4 preparations are mapped onto the diagram by blue bars. The splice-site mutation c.3911–2A>T leads to a 4-nt frameshift deletion (c.3911_3914delCAAG) predicted to result in a premature stop codon at position 1307.

URLs) and were predicted to be damaging by Human Splicing Finder or PolyPhen-2 (see URLs).

C2CD3 encodes a protein with seven C2 domains that is universally conserved in organisms that assemble centrioles or cilia[10] (**Fig. 1k**). A *C2cd3* mutant named Hearty (Hty) was isolated in a screen for Hedgehog signaling components in mice, and ciliogenesis is severely compromised in $C2cd3^{Hty/Hty}$ (hypomorph) or $C2cd3^{Gt/Gt}$ (null) mice[11] (**Fig. 1k**). In a remarkable resemblance to OFD syndromes, $C2cd3^{Hty/Hty}$ and $C2cd3^{Gt/Gt}$ mice exhibit embryonic lethality, exencephaly in the midbrain and posterior forebrain with a characteristic tight mesencephalic flexure, a twisted body axis, pericardial edema, a rightward-turned heart and severe polydactyly in all four limbs[11,12]. Thus, together with our finding of *C2CD3* mutations in two unrelated individuals with OFD, these results demonstrate that *C2CD3* mutations cause OFD. On the basis of the unique features of microcephaly and cerebral malformations observed for the two individuals with OFD with *C2CD3* mutations reported here, we propose the alias *OFD14* for the *C2CD3* gene. Together with the mutations in *TMEM216* reported in Joubert syndrome (JBTS2; MIM 608091), Meckel-Gruber syndrome (MKS2; MIM 603194) and OFD VI (ref. 13), the mutations

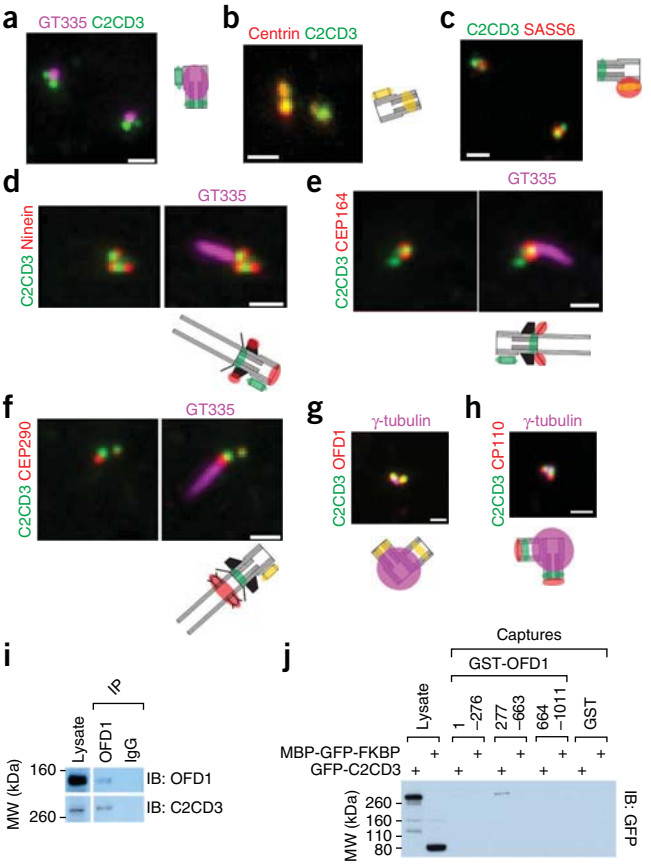

Figure 2 C2CD3 colocalizes with OFD1 at the distal end of centrioles and procentrioles and physically interacts with OFD1. (**a**–**h**) IMCD3 cells expressing GFP-fused mouse C2CD3 were stained for the centriolar marker branched glutamylated tubulin (GT335; pink) (**a**), the distal centriole and procentriole marker centrin (red) (**b**), the procentriole marker SASS6 (red) (**c**), ninein (red; marks the subdistal appendages and the proximal end of the centrioles and procentrioles) and glutamylated tubulin (GT335; pink; marks the ciliary axoneme) (**d**), CEP164 (red; marks the distal appendages) and glutamylated tubulin (GT335; pink) (**e**), CEP290 (red; marks the transition zone) and glutamylated tubulin (GT335; pink) (**f**), OFD1 (red) and γ-tubulin (pink; marks the pericentriolar material near the proximal part of the centriole) (**g**), and the distal cap marker CP110 (red) and γ-tubulin (pink) (**h**). All cells were treated with nocodazole before processing for immunofluorescence. All scale bars indicate 1 μm. (**i**) Immunoprecipitation of OFD1 from RPE cell extract recovers C2CD3. For the C2CD3 immunoblot, 160 equivalents of the eluates and 1 equivalent of lysate were run on the gel. For the OFD1 immunoblot, 4 equivalents of the eluates and 1 equivalent of lysate were run on the gel. The eluate and lysate panels are cropped from the same film exposure. MW, molecular weight; IP, immunoprecipitation; IB, immunoblot. (**j**) GST capture assays. GFP-C2CD3 and MBP-GFP-FKBP (negative control) expressed in HEK293FT cells were captured by bacterially expressed GST fusions with OFD1 fragments. Captured proteins were detected by immunoblotting for GFP; 80 equivalents of the eluates and 1 equivalent of lysate were run on the gel.

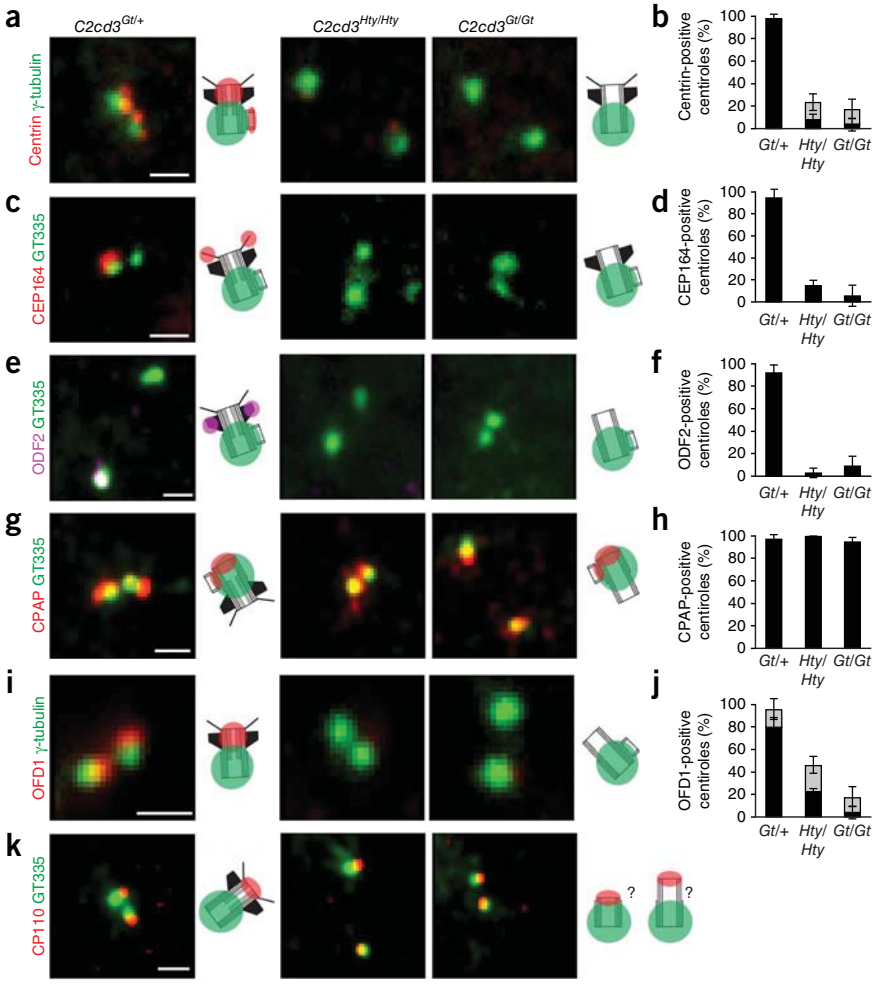

Figure 3 Loss of C2CD3 results in the disappearance of distal centriole structures. (**a**) MEFs derived from heterozygous (*C2cd3*$^{Gt/+}$) and homozygous *C2cd3*-mutant mice (*C2cd3*$^{Hty/Hty}$ and *C2cd3*$^{Gt/Gt}$) were stained for γ-tubulin (green) and centrin (red). (**b**) Counting of centrin-positive centrioles. Black bars correspond to centrioles strongly positive for centrin (as in the left panel of **a**), and gray bars correspond to centrioles weakly positive for centrin (as with the centriole in the lower right corner of the middle panel in **a**). Error bars denote s.d. between microscopy fields. Centrioles were identified by γ-tubulin staining. At least 50 cells of each genotype were counted. (**c**) MEFs were stained for polyglutamylated tubulin (GT335; green) and CEP164 (red). (**d**) Counting of CEP164-positive mother centrioles. Error bars denote s.d. between microscopy fields. Cells with at least one focus of CEP164 colocalizing with GT335 were counted as having CEP164-positive mother centrioles. At least 50 cells of each genotype were counted. (**e**) MEFs were stained for polyglutamylated tubulin (GT335; green) and ODF2 (pink). (**f**) Counting of ODF2-positive mother centrioles. Error bars denote s.d. between microscopy fields. Cells with at least one focus of ODF2 colocalizing with GT335 were counted as having ODF2-positive mother centrioles. At least 50 cells of each genotype were counted. (**g**) MEFs were stained for γ-tubulin (green) and CPAP (red). CPAP localization to the proximal end of centrioles and procentrioles leads to an overlap in signals at these two locations, and only one diffraction-limited focus of CPAP was detected. (**h**) Counting of CPAP-positive centrioles. Error bars denote s.d. between microscopy fields. Centrioles were identified by GT335 staining. At least 50 cells of each genotype were counted. (**i**) MEFs were stained for γ-tubulin (green) and OFD1 (red). (**j**) Counting of OFD1-positive centrioles. Black bars correspond to centrioles strongly positive for OFD1, and gray bars correspond to centrioles weakly positive for OFD1. Error bars denote s.d. between microscopy fields. Centrioles were identified by GT335 staining. At least 50 cells of each genotype were counted. (**k**) MEFs were stained for polyglutamylated tubulin (GT335; green) and CP110 (red). All scale bars indicate 1 μm.

in *C5orf42* in Joubert syndrome (JBTS17; MIM 614615) and OFD VI (refs. 14,15), and the mutations in *TCTN3* identified in OFD IV (OFD4; MIM 258860), Meckel-Gruber syndrome and Joubert syndrome[16], our identification of a new OFD subtype with severe cerebral malformations including MTS further reinforces the clinical continuum of the ciliopathy spectrum and the inclusion of OFD in the ciliopathies.

Besides its requirement for cilium assembly[11], the function of C2CD3 remains largely elusive. A first clue was provided by the mass spectrometry–based identification of C2CD3 as a BBSome-interacting protein (**Fig. 1k** and **Supplementary Fig. 2a**). The BBSome is a complex of proteins that is altered in the ciliopathy Bardet-Biedl syndrome (BBS; MIM 209900) and is present in cilia and cytoplasmic granules termed centriolar satellites[17–20]. To determine the localization of C2CD3, we expressed GFP-fused mouse C2CD3 at low levels in a stable clone of mouse IMCD3 Flp-In kidney cells. Whereas C2CD3 was never detected inside cilia, we found robust colocalization of C2CD3 with the core centriolar satellite component PCM-1 (**Supplementary Fig. 2b**). However, knockdown of *C2CD3* in human retinal pigmented epithelial RPE1-hTERT cells and *C2cd3* mutations in immortalized mouse embryonic fibroblasts (MEFs) did not perturb centriolar satellite function (**Supplementary Fig. 2c**).

In addition to finding C2CD3 localized at centriolar satellites, we consistently found C2CD3 at two to four bright juxtanuclear foci that did not overlap with PCM-1 foci (**Supplementary Fig. 2b**, insets). Costaining with a monoclonal antibody against glutamylated tubulin (GT335)—a modified tubulin found at centrioles and ciliary axonemes—showed that these PCM-1–negative foci of C2CD3 were centrioles (**Supplementary Fig. 3a**). Although centriolar satellites deliver proteins such as pericentrin to the centrosome[17,21], inhibiting the movement of centriolar satellites using the microtubule poison nocodazole did not affect C2CD3 abundance at centrioles (**Supplementary Fig. 3b**).

We then mapped the precise location of C2CD3 within centrioles. We frequently observed two juxtaposed foci of C2CD3 associated with a single focus of glutamylated tubulin (**Fig. 2a**). Because the two juxtaposed foci of C2CD3 were each positive for centrin, which marks the distal lumen of mature centrioles and procentrioles (**Fig. 2b** and **Supplementary Fig. 4a**), and because procentriole microtubules are not polyglutamylated[22], the C2CD3 focus negative for glutamylated tubulin likely represents the procentriole. Staining cells for SASS6, a marker of procentrioles but not mature centrioles[23], confirmed that C2CD3 is present at procentrioles (**Fig. 2c**). In mature centrioles, we found C2CD3 slightly distal to the subdistal appendages marked by ninein[24]

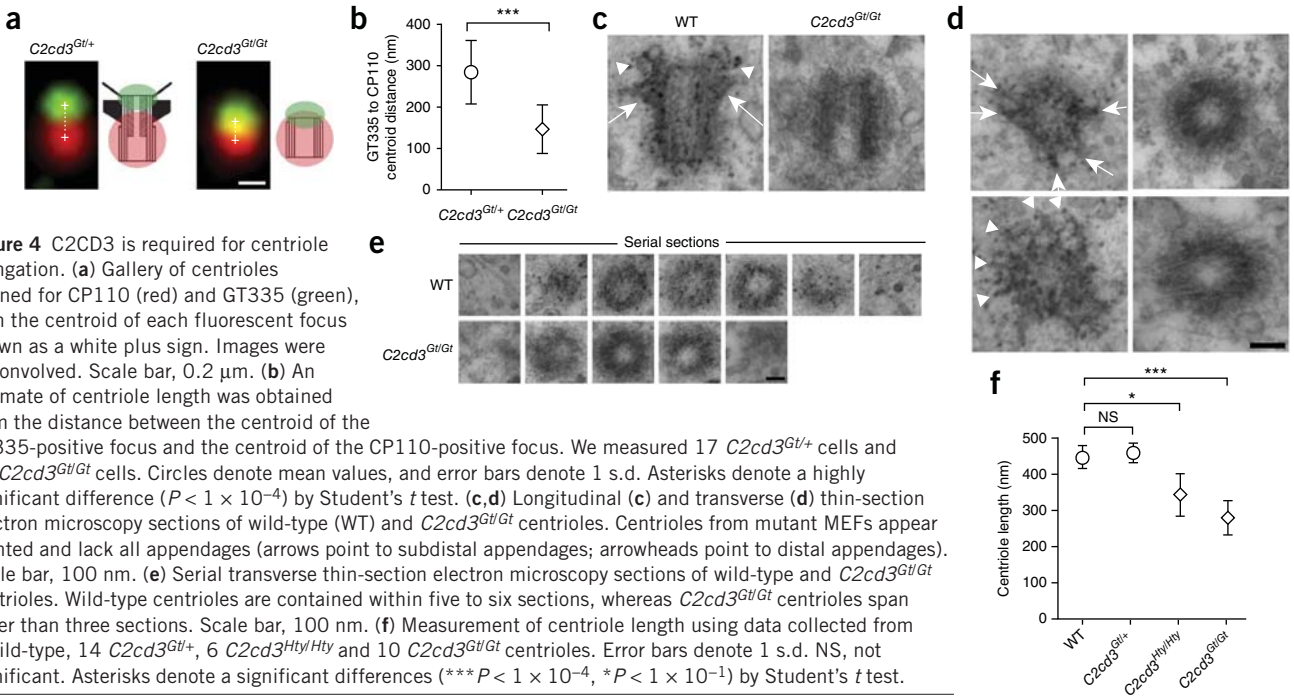

Figure 4 C2CD3 is required for centriole elongation. (**a**) Gallery of centrioles stained for CP110 (red) and GT335 (green), with the centroid of each fluorescent focus shown as a white plus sign. Images were deconvolved. Scale bar, 0.2 µm. (**b**) An estimate of centriole length was obtained from the distance between the centroid of the GT335-positive focus and the centroid of the CP110-positive focus. We measured 17 *C2cd3*$^{Gt/+}$ cells and 27 *C2cd3*$^{Gt/Gt}$ cells. Circles denote mean values, and error bars denote 1 s.d. Asterisks denote a highly significant difference ($P < 1 \times 10^{-4}$) by Student's *t* test. (**c**,**d**) Longitudinal (**c**) and transverse (**d**) thin-section electron microscopy sections of wild-type (WT) and *C2cd3*$^{Gt/Gt}$ centrioles. Centrioles from mutant MEFs appear stunted and lack all appendages (arrows point to subdistal appendages; arrowheads point to distal appendages). Scale bar, 100 nm. (**e**) Serial transverse thin-section electron microscopy sections of wild-type and *C2cd3*$^{Gt/Gt}$ centrioles. Wild-type centrioles are contained within five to six sections, whereas *C2cd3*$^{Gt/Gt}$ centrioles span fewer than three sections. Scale bar, 100 nm. (**f**) Measurement of centriole length using data collected from 4 wild-type, 14 *C2cd3*$^{Gt/+}$, 6 *C2cd3*$^{Hty/Hty}$ and 10 *C2cd3*$^{Gt/Gt}$ centrioles. Error bars denote 1 s.d. NS, not significant. Asterisks denote a significant differences (***$P < 1 \times 10^{-4}$, *$P < 1 \times 10^{-1}$) by Student's *t* test.

or ODF2 (**Fig. 2d** and **Supplementary Fig. 4b**). C2CD3 was precisely located between the CEP164-marked distal appendages (**Fig. 2e**). Finally, the transition zone[25] marker CEP290 was clearly distal to C2CD3 (**Fig. 2f**), leading us to conclude that C2CD3 is localized near the distal tip of centrioles. CP110 and OFD1 have also been found to localize near the distal end of centrioles, with CP110 marking a slightly more distal location than OFD1 (ref. 7), namely, the centriole cap whose removal allows for elongation of the ciliary axoneme[26]. C2CD3 perfectly colocalized with OFD1 (**Fig. 2g**) and was slightly proximal to CP110 (**Fig. 2h**).

Because C2CD3 colocalizes with OFD1 and both of these proteins are altered in OFD syndromes, we tested whether these proteins physically interact. Using antibodies raised against the endogenous proteins, C2CD3 and OFD1 were found to coimmunoprecipitate out of human RPE cells (**Fig. 2i**). To further confirm this interaction, glutathione S-transferase (GST) fusions of human OFD1 fragments were expressed in bacteria, immobilized on beads and used to capture GFP-fused mouse C2CD3 expressed in HEK293FT cells. Remarkably, the central fragment of OFD1, which is also responsible for homodimerization[27], specifically interacted with GFP-C2CD3 (**Fig. 2j** and **Supplementary Fig. 4c**). We conclude that C2CD3 forms a complex with OFD1 at the distal end of centrioles, where it colocalizes with other known regulators of centriole elongation, such as centrin[28] or POC5 (ref. 29).

Because OFD1 and C2CD3 associate physically and cytologically and because the genes encoding them are mutated in the same syndrome, we hypothesized that C2CD3 deletion would mimic loss of OFD1 and result in centrin-positive hyperelongation of centrioles[7]. Surprisingly, centrin was undetectable in the vast majority of *C2cd3*$^{Hty/Hty}$ and *C2cd3*$^{Gt/Gt}$ centrioles (**Fig. 3a**,**b**) even though total centrin levels stayed constant (**Supplementary Fig. 5a**), in agreement with a recent study[30]. Similarly, staining for glutamylated tubulin did not show centriole hyperelongation in *C2cd3*-mutant MEFs (**Fig. 3c**). Thus, unlike loss of OFD1, loss of C2CD3 does not result in elongation of the distal centriole compartment.

Remarkably, distal appendages (stained by CEP164; **Fig. 3c**,**d**) as well as subdistal appendages (stained by ODF2; **Fig. 3e**,**f**) were absent from *C2cd3*-mutant centrioles. Ninein staining confirmed the absence of subdistal appendages and the intactness of the proximal end of centrioles (**Supplementary Fig. 5b**). Similarly, CPAP, a marker of the proximal segment of centrioles, was retained in *C2cd3* mutants (**Fig. 3g**,**h**). OFD1 levels were greatly reduced at *C2cd3*-mutant centrioles (**Fig. 3i**,**j**), suggesting that C2CD3 recruits OFD1 to centrioles through the physical interaction of these proteins. Whereas *C2cd3*-mutant centrioles lost most markers of the distal centrioles, the centriole cap protein CP110 was still present at the distal end of centrioles (**Fig. 3k**), concordant with the inability of *C2cd3*-mutant cells to assemble a primary cilium[11].

An appealing explanation for the loss of distal centriole structures in *C2cd3*-mutant cells is incomplete centriole elongation. Alternatively, it is conceivable that maturation of the distal centriole is affected independently of alterations in centriole length. In support of the former hypothesis, the distance between the centriole cap and centriole center—measured by fluorescence microscopy—was significantly ($P < 1 \times 10^{-4}$) reduced in *C2cd3*$^{Gt/Gt}$ cells compared to control cells (**Fig. 4a**,**b**). To precisely assess the structural defects in *C2cd3*-mutant centrioles, we performed thin-section electron microscopy on *C2cd3*-mutant MEFs. Confirming our immunofluorescence findings, distal and subdistal appendages were absent from *C2cd3*-mutant centrioles (**Fig. 4c**–**e** and **Supplementary Fig. 6a**,**b**). Total centriole length was precisely assessed by thin-section electron microscopy, and we found *C2cd3*-mutant centrioles to be shorter than controls by ~150 nm (**Fig. 4f**). We conclude that C2CD3 is required for the extension of procentrioles into full-length centrioles.

To gain insight into the mechanisms by which C2CD3 controls centriole length, we examined the effects of overexpressing GFP-fused mouse C2CD3 (**Fig. 5**). Strikingly, in RPE cells, we observed one or two juxtanuclear straight rods of >2 µm in length marked by GFP-C2CD3 and acetylated microtubules along their length (**Fig. 5a**, insets) and resistant to nocodazole treatment (**Supplementary Fig. 7a**). By synchronizing cells in S phase and releasing them in G2 phase[31], we found that 15–25% of U2OS human osteosarcoma cells transfected with plasmid encoding GFP-C2CD3 possessed GFP-positive rods, in line with previously described centriole-lengthening activities[31,32]. The morphological resemblance of centrioles from

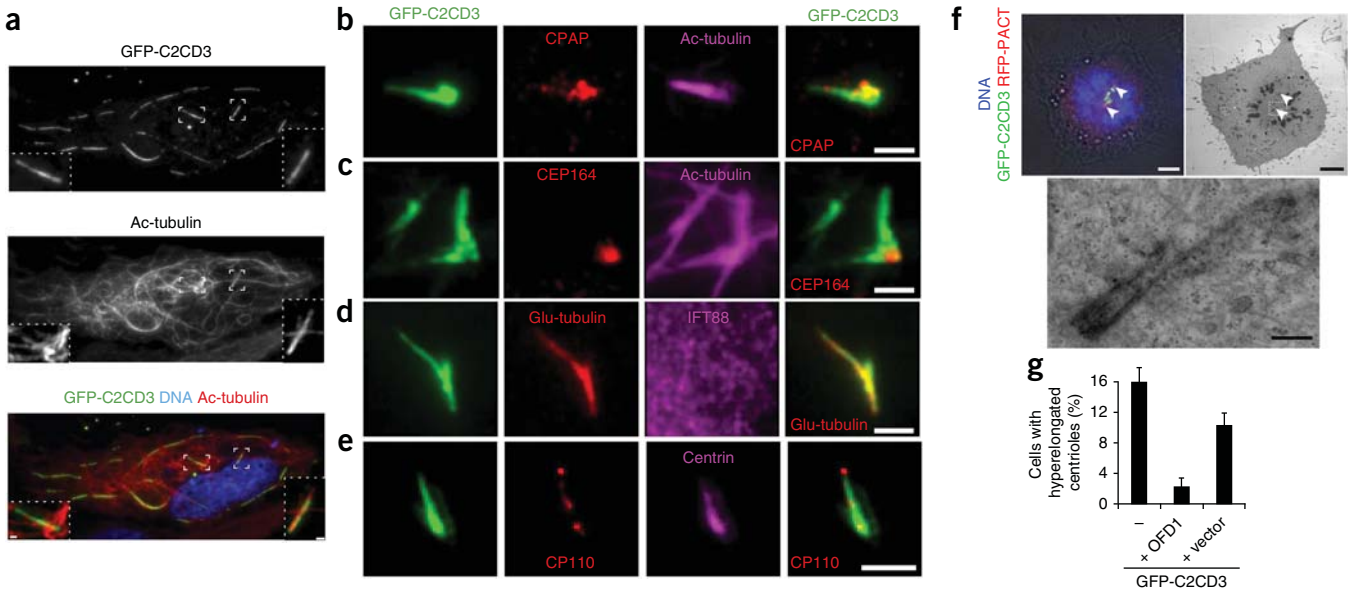

Figure 5 OFD1 antagonizes the centriole-elongating activity of C2CD3. (**a**) RPE cells transfected with vector expressing GFP-C2CD3 were stained for acetylated tubulin (ac-tubulin; red) and DNA (blue). GFP-C2CD3 colocalizes extensively with acetylated microtubules, in particular, at two straight juxtanuclear rods (insets). Scale bar, 5 µm. (**b**–**e**) U2OS osteosarcoma cells transfected with vector expressing GFP-C2CD3, subjected to a block in S phase and release into G2 phase were stained for CPAP (red) and acetylated tubulin (magenta) (**b**), CEP164 (red) and acetylated tubulin (magenta) (**c**), glutamylated tubulin (glu-tubulin; GT335; red) and IFT88 (magenta) (**d**), and CP110 (red) and centrin (magenta) (**e**). The contrast in the IFT88 channel was maximized to show background levels of staining. Scale bars, 2 µm. (**f**) CLEM of an elongated GFP-C2CD3–positive filament connected to the centriole. The centrosomes (arrowheads) were located using a fusion of the red fluorescent protein (RFP) with the pericentrin/AKAP450 centrosome-targeting domain (PACT). The cell of interest was first imaged by fluorescence (left) and located in thin sections imaged by electron microscopy (right). Serial sections were aligned and projected to show centriole hyperelongation (bottom). Individual sections are shown in **Supplementary Figure 7b** and **Supplementary Video 1**. Scale bars: 5 µm (top), 200 nm (bottom). (**g**) U2OS cells were transfected with vector expressing GFP-C2CD3 alone (–), GFP-C2CD3 and Myc-OFD1, or GFP-C2CD3 and an empty Myc vector. Cells were stained for CEP164 and Myc, and hyperelongated centrioles were scored in cells positive for GFP and Myc. At least 70 cells were counted for each condition. Error bars represent the s.d. for four independent experiments.

these cells to the hyperelongated centrioles in cells overexpressing CEP120 or CPAP[3–5,31,32] hinted that the C2CD3-positive rods might represent hyperelongated centrioles (**Fig. 5b**–**e**). These juxtanuclear C2CD3-positive rods were also positive for CPAP and CEP164 at their bases (**Fig. 5b**,**c**) and for glutamylated tubulin and centrin along their lengths (**Fig. 5d**,**e**) and showed an enrichment of CP110 at their distal ends (**Fig. 5e**). The absence of the cilium maker IFT88 at the C2CD3-positive rods (**Fig. 5d**) and the presence of CP110 at the end of these structures (**Fig. 5e**) strongly suggested that these structures represent hyperelongated centrioles and not cilia. To confirm that C2CD3 promotes centriole hyperelongation, we imaged the GFP-C2CD3–positive rods by correlative light electron microscopy[33] (CLEM) and identified continuous extensions of the centriolar microtubules up to 1.3 µm in length in three separate cells (**Fig. 5f**, **Supplementary Fig. 7b** and **Supplementary Video 1**).

In addition to localization at hyperelongated centrioles, overexpressed GFP-C2CD3 was found alongside bright microtubules rods (**Supplementary Fig. 7c**) enriched in acetylated tubulin in various regions of the cytoplasm (**Fig. 5a**). As in previous observations with CPAP overexpression[3], CLEM showed that these cytoplasmic microtubule structures were reminiscent of centrioles, albeit much less organized. The mixed C2CD3-positive microtubule rods contained microtubules spaced 250 nm apart by an electron-dense matrix (**Fig. 6a**), and doublet microtubules could sometimes be distinguished (**Fig. 6a**, bottom). Congruently, the C2CD3-positive microtubule rods were also positive for centrin (**Fig. 6b**). Although the biogenesis

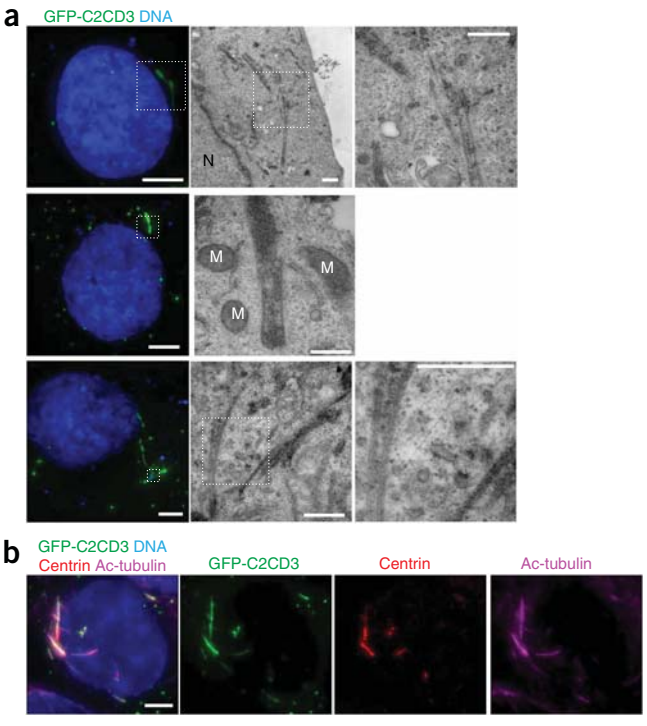

Figure 6 C2CD3 promotes assembly of microtubule structures with centriolar features. (**a**) CLEM of cytoplasmic GFP-C2CD3–positive filaments. N, nucleus; M, mitochondria. Scale bars, 5 µm (fluorescence), 500 nm (electron microscopy). (**b**) U2OS osteosarcoma cells transfected with vector expressing GFP-C2CD3 were stained for centrin (red), acetylated tubulin (magenta) and DNA (blue). Scale bar, 5 µm.

of these centriole-like structures is presently unknown, they may have originated and then broken off from hyperelongated centrioles (**Supplementary Fig. 7b** and **Supplementary Video 1**).

The ability of C2CD3 to induce centriole hyperelongation enabled a test of the functional antagonism between C2CD3 and OFD1. Cotransfection of plasmid encoding mouse OFD1 (but not of a control plasmid) with plasmid for mouse C2CD3 in U2OS cells led to a drastic reduction in the frequency of hyperelongated centrioles (**Fig. 5g**). Our finding that the OFD-relevant gene products OFD1 and C2CD3 antagonize one another in the regulation of centriole length suggests a model in which C2CD3 promotes centriole lengthening and OFD1 inhibits the activity of C2CD3 through direct physical contact. In this model, the inhibition exerted by OFD1 on C2CD3 would need to be minimal in the early stages of procentriole elongation and increase as centrioles reach their mature length. Further insights may be gained by studying how the centriole-lengthening activity of C2CD3 is related to its suggested ability to bind and stabilize microtubules and how C2CD3 function is coordinated with the procentriole-elongating activities of CPAP and CEP120, in particular, with respect to their microtubule-stabilizing activities[31,32]. Finally, an unexplored aspect of C2CD3 lies in its six canonical C2 domains, which are predicted to bind Ca^{2+} and phospholipid headgroups[10]. Centrin, which colocalizes precisely with C2CD3 and promotes centriole lengthening, also binds Ca^{2+} (ref. 34), and it is tempting to speculate that centriolar Ca^{2+} levels might regulate centriole elongation.

URLs. HomozygosityMapper, http://www.homozygositymapper.org/; Human Splicing Finder, http://www.umd.be/searchSpliceSite.html; PolyPhen-2, http://genetics.bwh.harvard.edu/pph2/; NHLBI Exome Sequencing Project (ESP) Exome Variant Server, http://evs.gs.washington.edu/EVS/; Primer3, http://bioinfo.ut.ee/primer3-0.4.0/primer3/; Picard, http://picard.sourceforge.net/; Phyre[2] (Protein Homology/Analogy Recognition Engine) V 2.0, http://www.sbg.bio.ic.ac.uk/phyre2/html/page.cgi?id=index.

METHODS

Methods and any associated references are available in the online version of the paper.

Note: Any Supplementary Information and Source Data files are available in the online version of the paper.

ACKNOWLEDGMENTS

We thank L. Pelletier (Lunenfeld Institute, University of Toronto), M. Bornens (Institut Curie, Paris), C. Janke (Institut Curie, Orsay), T. Stearns (Stanford University) and A. Merdes (CNRS, Université de Toulouse) for antibodies against SASS6, ninein, glutamylated tubulin, CEP164 and PCM-1, respectively, A. Liu for the *C2cd3*-mutant MEFs and *C2cd3* cDNA, J. Reiter for *Ofd1* cDNA, S. Munro for pRFP-PACT, V. Meyer (Genoscope, Centre National de Génotypage), T. Hardy (University of Leicester) and N. Elkhartoufi (Necker, Paris) for technical support, F. Collman (Stanford University) for help with serial alignment, members of the Nachury laboratory for helpful discussions, and the patients and their families for their participation. This work was supported by grants from NIGMS (GM089933 to M.V.N.), the GIS–Institut des Maladies Rares (HTS), the French Ministry of Health (PHRC national 2010-A01014-35), the Regional Council of Burgundy (to C.T.-R.), the Wellcome Trust and Kidney Research UK (to A.M.F.), and the Fondazione Telethon (TGM11CB3) and the European Community's Seventh Framework Programme (FP7/2007-2013; 241955) (to B.F.). We also thank the National Heart, Lung, and Blood Institute (NHLBI) Grand Opportunity (GO) Exome Sequencing Project (see URLs) and its ongoing studies that produced and provided exome variant calls for comparison: the Lung GO Sequencing Project (HL-102923), the Women's Health Initiative (WHI) Sequencing Project (HL-102924), the Broad GO Sequencing Project (HL-102925), the Seattle GO Sequencing Project (HL-102926) and the Heart GO Sequencing Project (HL-103010).

AUTHOR CONTRIBUTIONS

M.V.N. conceived and supervised the functional characterization of C2CD3. C.T.-R. designed and conducted the gene identification strategy with assistance from T.A.-B., B.F., L.F., L.J., E.L., J.-B.R., C.A., N.G., B.A., A. Mégarbané, J.T., J.S.-O. and A.-L.B. J.-B.R. and S.S. performed mapping analysis, genetic screening and mutation analysis. A. Mégarbané, B.F., L.P., P.L. and C.T.-R. identified and recruited subjects. S.G.-G., A. Munnich, F.H. and M.V. gave technical support and conceptual advice. A.M.F. and C.A.M.L. provided OFD1 reagents. M.V.N., J.S.L. and T.S. designed, executed and analyzed the immunohistochemistry, overexpression and protein interaction assays. F.Y. designed and executed the centriole length measurement by light microscopy. V.H.-P. and J.M.G.-V. designed and executed electron microscopy imaging and analysis. C.T.-R. and M.V.N. wrote the manuscript. All authors reviewed the manuscript.

COMPETING FINANCIAL INTERESTS

The authors declare no competing financial interests.

1. Paintrand, M., Moudjou, M., Delacroix, H. & Bornens, M. Centrosome organization and centriole architecture: their sensitivity to divalent cations. *J. Struct. Biol.* **108**, 107–128 (1992).
2. Bettencourt-Dias, M. & Glover, D.M. Centrosome biogenesis and function: centrosomics brings new understanding. *Nat. Rev. Mol. Cell Biol.* **8**, 451–463 (2007).
3. Kohlmaier, G. *et al.* Overly long centrioles and defective cell division upon excess of the SAS-4–related protein CPAP. *Curr. Biol.* **19**, 1012–1018 (2009).
4. Tang, C.-J.C., Fu, R.-H., Wu, K.-S., Hsu, W.-B. & Tang, T.K. CPAP is a cell-cycle regulated protein that controls centriole length. *Nat. Cell Biol.* **11**, 825–831 (2009).
5. Schmidt, T.I. *et al.* Control of centriole length by CPAP and CP110. *Curr. Biol.* **19**, 1005–1011 (2009).
6. Ferrante, M.I. *et al.* Identification of the gene for oral-facial-digital type I syndrome. *Am. J. Hum. Genet.* **68**, 569–576 (2001).
7. Singla, V., Romaguera-Ros, M. & García-Verdugo, J.M. Ofd1, a human disease gene, regulates the length and distal structure of centrioles. *Dev. Cell* **18**, 410–424 (2010).
8. Gurrieri, F., Franco, B., Toriello, H. & Neri, G. Oral-facial-digital syndromes: review and diagnostic guidelines. *Am. J. Med. Genet. A.* **143A**, 3314–3323 (2007).
9. Patel, S. & Barkovich, A.J. Analysis and classification of cerebellar malformations. *AJNR Am. J. Neuroradiol.* **23**, 1074–1087 (2002).
10. Zhang, D. & Aravind, L. Novel transglutaminase-like peptidase and C2 domains elucidate the structure, biogenesis and evolution of the ciliary compartment. *Cell Cycle* **11**, 3861–3875 (2012).
11. Hoover, A.N. *et al.* C2cd3 is required for cilia formation and Hedgehog signaling in mouse. *Development* **135**, 4049–4058 (2008).
12. Zohn, I.E., Anderson, K.V. & Niswander, L. Using genomewide mutagenesis screens to identify the genes required for neural tube closure in the mouse. *Birth Defects Res. A Clin. Mol. Teratol.* **73**, 583–590 (2005).
13. Poretti, A. *et al.* Delineation and diagnostic criteria of oral-facial-digital syndrome type VI. *Orphanet J. Rare Dis.* **7**, 4 (2012).
14. Srour, M. *et al.* Mutations in *C5ORF42* cause Joubert syndrome in the French Canadian population. *Am. J. Hum. Genet.* **90**, 693–700 (2012).
15. Lopez, E. *et al. C5orf42* is the major gene responsible for OFD syndrome type VI. *Hum. Genet.* **133**, 367–377 (2014).
16. Thomas, S. *et al. TCTN3* mutations cause Mohr-Majewski syndrome. *Am. J. Hum. Genet.* **91**, 372–378 (2012).
17. Dammermann, A. & Merdes, A. Assembly of centrosomal proteins and microtubule organization depends on PCM-1. *J. Cell Biol.* **159**, 255–266 (2002).
18. Kim, J.C. *et al.* The Bardet-Biedl protein BBS4 targets cargo to the pericentriolar region and is required for microtubule anchoring and cell cycle progression. *Nat. Genet.* **36**, 462–470 (2004).
19. Nachury, M.V. *et al.* A core complex of BBS proteins cooperates with the GTPase Rab8 to promote ciliary membrane biogenesis. *Cell* **129**, 1201–1213 (2007).
20. Jin, H. *et al.* The conserved Bardet-Biedl syndrome proteins assemble a coat that traffics membrane proteins to cilia. *Cell* **141**, 1208–1219 (2010).
21. Lopes, C.A.M. *et al.* Centriolar satellites are assembly points for proteins implicated in human ciliopathies, including oral-facial-digital syndrome 1. *J. Cell Sci.* **124**, 600–612 (2011).
22. Kleylein-Sohn, J. *et al.* Plk4-induced centriole biogenesis in human cells. *Dev. Cell* **13**, 190–202 (2007).
23. Strnad, P. *et al.* Regulated HsSAS-6 levels ensure formation of a single procentriole per centriole during the centrosome duplication cycle. *Dev. Cell* **13**, 203–213 (2007).
24. Mogensen, M.M., Bornens, M., Malik, A., Piel, M. & Bouckson-Castaing, V. Microtubule minus-end anchorage at centrosomal and non-centrosomal sites: the role of ninein. *J. Cell Sci.* **113**, 3013–3023 (2000).
25. Garcia-Gonzalo, F.R. & Reiter, J.F. Scoring a backstage pass: mechanisms of ciliogenesis and ciliary access. *J. Cell Biol.* **197**, 697–709 (2012).
26. Spektor, A., Tsang, W.Y., Khoo, D. & Dynlacht, B.D. Cep97 and CP110 suppress a cilia assembly program. *Cell* **130**, 678–690 (2007).

27. Giorgio, G. *et al.* Functional characterization of the OFD1 protein reveals a nuclear localization and physical interaction with subunits of a chromatin remodeling complex. *Mol. Biol. Cell* **18**, 4397–4404 (2007).
28. Salisbury, J.L., Suino, K.M., Busby, R. & Springett, M. Centrin-2 is required for centriole duplication in mammalian cells. *Curr. Biol.* **12**, 1287–1292 (2002).
29. Azimzadeh, J. *et al.* hPOC5 is a centrin-binding protein required for assembly of full-length centrioles. *J. Cell Biol.* **185**, 101–114 (2009).
30. Balestra, F.R., Strnad, P., Flückiger, I. & Gönczy, P. Discovering regulators of centriole biogenesis through siRNA-based functional genomics in human cells. *Dev. Cell* **25**, 555–571 (2013).
31. Comartin, D. *et al.* CEP120 and SPICE1 cooperate with CPAP in centriole elongation. *Curr. Biol.* **23**, 1360–1366 (2013).
32. Lin, Y.-N. *et al.* CEP120 interacts with CPAP and positively regulates centriole elongation. *J. Cell Biol.* **202**, 211–219 (2013).
33. Reddick, L.E. & Alto, N.M. Correlative Light and Electron Microscopy (CLEM) as a tool to visualize microinjected molecules and their eukaryotic sub-cellular targets. *J. Vis. Exp.* (63), e3650 (2012).
34. Thompson, J.R., Ryan, Z.C., Salisbury, J.L. & Kumar, R. The structure of the human centrin 2-xeroderma pigmentosum group C protein complex. *J. Biol. Chem.* **281**, 18746–18752 (2006).

ONLINE METHODS

Research subjects. The consanguineous family and additional families were recruited worldwide on the basis of the presence of at least one individual with an OFD syndrome proven with oral features (lingual hamartoma, cleft/lobulated tongue, gingival frenulae and/or cleft lip/palate), facial dysmorphism and digital anomalies, as well as Meckel syndrome. Whenever possible, individuals underwent a full diagnostic protocol, and a standardized clinical questionnaire was administered to assess the extent of multiorgan involvement. Informed consent was obtained for all participating subjects and their families; the study was approved by the ethics boards of the Necker–Enfants Malades Hospital (Paris) and the Dijon University Hospital. For fetuses, pregnancies were terminated after genetic counseling, in accordance with local legislation. Chromosome analysis and clinicopathological examination were performed for all cases. Genomic DNA was extracted from frozen tissue or amniocyte cultured cells in fetal cases and from peripheral blood samples for patients and their parents using standard procedures.

Genome-wide SNP genotyping and homozygosity mapping. Genome-wide SNP genotyping was performed using the Human Mapping 500K Nsp array (Affymetrix) at the Institut de Génétique et de Biologie Moléculaire et Cellulaire (IGBMC, Illkirsch). Sample processing and labeling were performed according to the manufacturer's instructions (Affymetrix GeneChip Mapping 500K Assay Manual, 701930 Rev.3). Hybridization was performed with a GeneChip hybridization oven 640 at 49 °C and 60 r.p.m. for 16 h, and arrays were washed with a GeneChip Fluidics Station 450 and scanned with a GeneChip Scanner 3000-7G. Image data were processed with the Affymetrix Genotyping Console (GTC v4.1) to determine SNP calls and copy number variation. Homozygosity mapping was performed using HomozygosityMapper[35] with default parameters (see URLs).

Exome sequencing. Exome capture was performed at the Genoscope Centre National de Génotypage (CNG; Evry, France) on 8 µg of DNA sample from the affected proband using the SureSelect Human All Exon 50Mb kit (Agilent Technologies) according to standard procedures. The resulting libraries underwent 2 × 100-bp paired-end sequencing on an Illumina HiSeq 2000 in accordance with the manufacturer's recommendations. Reads were aligned to the human reference genome (GRCh37/hg19) with the Burrows-Wheeler Aligner[36] (BWA.0.5.6), and we removed potential duplicate paired-end reads using Picard tools.1.22 (see URLs). The Genome Analysis Toolkit (GATK) 1.0.57 was used for base quality score recalibration and indel realignment, as well as for single-nucleotide variant and indel discovery and genotyping using standard hard filtering parameters[37,38]. Homozygous variants with quality scores of >30, sequencing depth of >4, quality/depth ratios of >5.0 and strand bias of <–0.10 were conserved from subsequent analyses. Coverage was assessed with the GATK Depth of Coverage tool by ignoring reads with mapping quality of <20 and bases with base quality of <30. Candidate events were then inspected using the Integrative Genomics Viewer (IGV). The resulting variants were excluded when the frequency was greater than 1 in 1,000 in the Exome Variant Server, National Heart, Lung, and Blood Institute (NHLBI) (see URLs).

Sanger sequencing validation. Mutation screening of *C2CD3* (NM_015531.5) was performed by direct sequencing of the PCR products of the 31 coding exons and the adjacent intronic junctions in 34 individuals with OFD. PCR primers (sequences available upon request) were designed with Primer3 (ref. 39; see URLs) according to reference sequence NM_015531.5. PCR products were purified using the Exo-SAP cleanup kit (USB). Sequencing was performed using the ABI BigDye Terminator Cycle Sequencing kit (v3.1) (Applied Biosystems) according to the manufacturer's instructions on an ABI 3130 sequencer 7 (Applied Biosystems). Sequence data were analyzed with SeqScape v2.7 (Applied Biosystems). The impact of missense and splice-site mutations was assessed using PolyPhen-2 (ref. 40; see URLs) and Human Splicing Finder v.2.4.1 online software[41] (see URLs), respectively.

cDNA sequencing. To assess the impact of the c.3911–2A>T substitution on splicing, we extracted total RNA from skin biopsies obtained from case 2 and two control individuals using the RNeasy Plus Universal Mini kit (Qiagen) and performed RT-PCR using the QuantiTect Reverse Transcription kit (Qiagen) according to the manufacturer's instructions. Analysis of *C2CD3* cDNA was carried out by standard PCR amplification using primers annealing between exons 20 and 23 as well as between exons 21 and 23 and subsequent Sanger sequencing as described above.

Cell culture. IMCD3 cells (American Type Culture Collection) were cultured in DMEM/F12 medium (Life Technologies) containing 10% FBS (HyClone) at 37 °C in 5% CO_2. Medium was supplemented with 0.25% Na_2CO_3 for RPE cells. DMEM with 10% FBS was used to grow HEK293FT (Life Technologies) and SV40-immortalized MEFs derived from *C2cd3*-mutant mice and mice heterozygous for disruption of *C2cd3* (gifts from A. Liu)[11]. To induce ciliogenesis, cells were grown in serum starvation medium (0.2% FBS) for 24 h. A stable IMCD3 clonal cell line expressing GFP-fused mouse C2CD3 under the control of the *EEF1A1* promoter was generated using the Flp-In system (Invitrogen), as described previously[20]. Transfections of RPE, IMCD3 and HEK293FT cells were carried out with X-tremeGENE9 (Roche). U2OS cells (American Type Culture Collection) were transfected with Lipofectamine 2000. To maximize the frequency of centriole elongation observed upon C2CD3 overexpression, 48 h after transfection, U2OS cells were arrested in S phase by the addition of hydroxyurea (8 mM) or aphidicolin (2 µg/ml) for 20 h and then released into G2 phase by changing the medium to roscovitine (RO-3306; 10 µM) for 16 h before fixation. All cell lines used were tested for mycoplasma.

Immunoblotting, immunoprecipitation and immunohistochemistry. All antibodies used in this study are listed in **Supplementary Table 2**. Immunofluorescence was conducted as described[42]. Briefly, cells were fixed for 5 min with 4% paraformaldehyde and immediately plunged into methanol at –20 °C before rehydration in PBS and processing for immunofluorescence (except for CPAP immunofluorescence, for which the paraformaldehyde step was omitted). For studying the localization of C2CD3 within centrioles (**Fig. 2** and **Supplementary Fig. 4**), cells were treated with 5 µM nocodazole for 1 h before processing for immunofluorescence. All microscopy (except for the measurement of centriole length) was performed with a 63×, 1.4 N.A. PlanApo objective mounted on a Zeiss Axio Imager.M1 microscope connected to a Lambda XL light source (Sutter Instruments), and fluorescence was gated by a Sedat filter set (Semrock). Images were captured by a CoolSNAP HQ^2 camera (Photometrics), and the system was controlled by Slidebook 5 (Intelligent Imaging Innovations).

To measure the distance between CP110 and GT335 foci in MEFs, *z*-stack images of centrioles were taken on a DeltaVision workstation (GE) equipped with an Olympus PlanApo 60×, 1.42 N.A. oil lens and an sCMOS camera and were deconvolved using softWoRx software. Only those centrioles with both CP110 and GT335 staining in the same focal plane were selected for distance measurement. The center points (centroids) of GT335 and CP110 staining were mapped using the SpotTracker plugin in ImageJ software, and the distances between these two centroids were measured.

Immunoblotting, cotransfection and coimmunoprecipitation experiments, and GST capture assays were carried out as described[20,27]. Tandem affinity purification of the BBSome using the RPE-(LAP-BBS4) stable cell line has been described[19].

Immunoprecipitation of endogenous OFD1 was conducted as follows: two 15-cm dishes of RPE cells were lysed in buffer Co-IP 200 (50 mM Tris, pH 7.4, 200 mM NaCl, 1% Triton X-100, 1 mM DTT), lysate was cleared by centrifugation at 16,000*g*, and 50 ng of antibody to OFD1 or 2 µg of rabbit IgG was added to 5 mg of cell lysate. After a 45-min incubation at 4 °C, antibody-antigen complexes were captured on 10 µl of protein A–Sepharose beads through end-over-end incubation for 1 h. Beads were washed four times with buffer Co-IP 200, and complexes were eluted in NuPage LDS sample buffer (247 mM Tris base, 2% LDS, 10% glycerol, 0.51 mM EDTA, 0.22 mM Coomassie G250, 0.175 mM phenol red, pH 8.5).

Electron microscopy. Cells were seeded on 8-well Permanox chamber slides (Nalgene Nunc International) and were subsequently fixed in 3.5% glutaraldehyde in 0.1 M phosphate buffer (PB) for 10 min at 37 °C. The buffer was replaced with fresh, prewarmed 3.5% glutaraldehyde, and cells were

doi:10.1038/ng.3031

incubated for 1 h at 4 °C. Cells were postfixed in 2% OsO_4 for 1 h at room temperature and stained in 2% uranyl acetate in the dark for 2 h at 4 °C. Finally, cells were rinsed in distilled water, dehydrated in ethanol and embedded overnight in Durcupan resin (Fluka, Sigma-Aldrich). After polymerization, serial ultra-thin sections (0.06–0.08 µm) were cut with an UC-6 Ultracut (Leica) and stained with lead citrate. Photomicrographs were obtained under an FEI Tecnai G2 Spirit transmission electron microscope (FEI Europe) using a Morada digital camera (Olympus Soft Image Solutions). Quantitative measurements of centriole length were made on longitudinal sections using Fiji software.

Correlative light electron microscopy. U2OS cells were seeded onto photo-etched, gridded coverslips (Bellco) and transfected with pEGFP-C2CD3 either alone or in combination with pRFP-PACT. After 48 h, cells were fixed with glutaraldehyde as described above, and regions of interest (ROIs) were identified on an inverted fluorescence microscope (Deltavision, GE Healthcare). The coordinates of each ROI were recorded at low magnification to enable the identification of the ROI after embedding. Processing of samples for electron microscopy was performed as described above, except for the insertion of a block-trimming step as described[33]. Serial sections were aligned using the TrakEM2 plugin[43] from Fiji[44].

Human reference sequences. *C2CD3* cDNA sequence (NM_015531.5); C2CD3 protein sequence (NP_056346.3).

35. Seelow, D., Schuelke, M., Hildebrandt, F. & Nurnberg, P. HomozygosityMapper—an interactive approach to homozygosity mapping. *Nucleic Acids Res.* **37**, W593–W599 (2009).
36. Li, H. & Durbin, R. Fast and accurate short read alignment with Burrows-Wheeler transform. *Bioinformatics* **25**, 1754–1760 (2009).
37. McKenna, A. *et al.* The Genome Analysis Toolkit: a MapReduce framework for analyzing next-generation DNA sequencing data. *Genome Res.* **20**, 1297–1303 (2010).
38. DePristo, M.A. *et al.* A framework for variation discovery and genotyping using next-generation DNA sequencing data. *Nat. Genet.* **43**, 491–498 (2011).
39. Koressaar, T. & Remm, M. Enhancements and modifications of primer design program Primer3. *Bioinformatics* **23**, 1289–1291 (2007).
40. Adzhubei, I.A. *et al.* A method and server for predicting damaging missense mutations. *Nat. Methods* **7**, 248–249 (2010).
41. Desmet, F.-O. *et al.* Human Splicing Finder: an online bioinformatics tool to predict splicing signals. *Nucleic Acids Res.* **37**, e67 (2009).
42. Breslow, D.K., Koslover, E.F., Seydel, F., Spakowitz, A.J. & Nachury, M.V. An *in vitro* assay for entry into cilia reveals unique properties of the soluble diffusion barrier. *J. Cell Biol.* **203**, 129–147 (2013).
43. Cardona, A. *et al.* TrakEM2 software for neural circuit reconstruction. *PLoS ONE* **7**, e38011 (2012).
44. Schindelin, J. *et al.* Fiji: an open-source platform for biological-image analysis. *Nat. Methods* **9**, 676–682 (2012).

Références bibliographiques

Adès, L.C., Clapton, W.K., Morphett, A., Morris, L.L., and Haan, E.A. (1994). Polydactyly, campomelia, ambiguous genitalia, cystic dysplastic kidneys, and cerebral malformation in a fetus of consanguineous parents: a new multiple malformation syndrome, or a severe form of oral-facial-digital syndrome type IV? Am. J. Med. Genet. *49*, 211–217.

Adly, N., Alhashem, A., Ammari, A., and Alkuraya, F.S. (2014). Ciliary genes TBC1D32/C6orf170 and SCLT1 are mutated in patients with OFD type IX. Hum. Mutat. *35*, 36–40.

Al-Gazali, L.I., Sztriha, L., Punnose, J., Shather, W., and Nork, M. (1999). Absent pituitary gland and hypoplasia of the cerebellar vermis associated with partial ophthalmoplegia and postaxial polydactyly: a variant of orofaciodigital syndrome VI or a new syndrome? J. Med. Genet. *36*, 161–166.

Alves-Cruzeiro, J.M. da C., Nogales-Cadenas, R., and Pascual-Montano, A.D. (2014). CentrosomeDB: a new generation of the centrosomal proteins database for Human and Drosophila melanogaster. Nucleic Acids Res. *42*, D430-436.

Amato, R., Morleo, M., Giaquinto, L., di Bernardo, D., and Franco, B. (2014). A network-based approach to dissect the cilia/centrosome complex interactome. BMC Genomics *15*, 658.

Arnaiz, O., Cohen, J., Tassin, A.-M., and Koll, F. (2014). Remodeling Cildb, a popular database for cilia and links for ciliopathies. Cilia *3*, 9.

Avasthi, P., and Marshall, W.F. (2012). Stages of ciliogenesis and regulation of ciliary length. Differentiation *83*, S30-42.

Bacchetta, J., Mekahli, D., Rivet, C., Demède, D., and Leclerc, A.-L. (2015). Pediatric combined liver-kidney transplantation: a 2015 update. Curr Opin Organ Transplant *20*, 543–549.

Bachmann-Gagescu, R., Dempsey, J.C., Phelps, I.G., O'Roak, B.J., Knutzen, D.M., Rue, T.C., Ishak, G.E., Isabella, C.R., Gorden, N., Adkins, J., et al. (2015). Joubert syndrome: a model for untangling recessive disorders with extreme genetic heterogeneity. J. Med. Genet. *52*, 514–522.

Baker, L.A., and Agim, N.G. (2014). Nevus comedonicus in oral-facial-digital syndrome type 1: a new finding or overlapping syndromes? Pediatr Dermatol *31*, e48-51.

Barbelanne, M., Song, J., Ahmadzai, M., and Tsang, W.Y. (2013). Pathogenic NPHP5 mutations impair protein interaction with Cep290, a prerequisite for ciliogenesis. Hum. Mol. Genet. *22*, 2482–2494.

Barbelanne, M., Hossain, D., Chan, D.P., Peränen, J., and Tsang, W.Y. (2015). Nephrocystin proteins NPHP5 and Cep290 regulate BBSome integrity, ciliary trafficking and cargo delivery. Hum. Mol. Genet. *24*, 2185–2200.

Barisic, I., Boban, L., Loane, M., Garne, E., Wellesley, D., Calzolari, E., Dolk, H., Addor, M.-C., Bergman, J.E., Braz, P., et al. (2015). Meckel-Gruber Syndrome: a population-based study on prevalence, prenatal diagnosis, clinical features, and survival in Europe. Eur. J. Hum. Genet. *23*, 746–752.

Barker, A.R., Renzaglia, K.S., Fry, K., and Dawe, H.R. (2014). Bioinformatic analysis of ciliary transition zone proteins reveals insights into the evolution of ciliopathy networks. BMC Genomics *15*, 531.

Basten, S.G., and Giles, R.H. (2013). Functional aspects of primary cilia in signaling, cell cycle and tumorigenesis. Cilia *2*, 6.

Beales, P., and Jackson, P.K. (2012). Cilia - the prodigal organelle. Cilia *1*, 1.

Benmerah, A. (2013). The ciliary pocket. Curr. Opin. Cell Biol. *25*, 78–84.

Ben-Salem, S., Al-Shamsi, A.M., Gleeson, J.G., Ali, B.R., and Al-Gazali, L. (2014). Mutation spectrum of Joubert syndrome and related disorders among Arabs. Human Genome Variation *1*, 14020.

Berbari, N.F., O'Connor, A.K., Haycraft, C.J., and Yoder, B.K. (2009). The primary cilium as a complex signaling center. Curr. Biol. *19*, R526-535.

Bettencourt-Dias, M., Hildebrandt, F., Pellman, D., Woods, G., and Godinho, S.A. (2011). Centrosomes and cilia in human disease. Trends Genet. *27*, 307–315.

Bimonte, S., De Angelis, A., Quagliata, L., Giusti, F., Tammaro, R., Dallai, R., Ascenzi, M.-G., Diez-Roux, G., and Franco, B. (2011). Ofd1 is required in limb bud patterning and endochondral bone development. Dev. Biol. *349*, 179–191.

Bisgrove, B.W., and Yost, H.J. (2006). The roles of cilia in developmental disorders and disease. Development *133*, 4131–4143.

Bisschoff, I.J., Zeschnigk, C., Horn, D., Wellek, B., Rieß, A., Wessels, M., Willems, P., Jensen, P., Busche, A., Bekkebraten, J., et al. (2013). Novel mutations including deletions of the entire OFD1 gene in 30 families with type 1 orofaciodigital syndrome: a study of the extensive clinical variability. Hum. Mutat. *34*, 237–247.

Bizet, A.A., Becker-Heck, A., Ryan, R., Weber, K., Filhol, E., Krug, P., Halbritter, J., Delous, M., Lasbennes, M.-C., Linghu, B., et al. (2015). Mutations in TRAF3IP1/IFT54 reveal a new role for IFT proteins in microtubule stabilization. Nat Commun *6*, 8666.

Bonioli, E., Ruffa, G., Baldini, A., Giovannini, L., and Gemme, G. (1979). The heterogeneity of oral-facial-digital anomalies. Report of a case of Mohr syndrome. Panminerva Med *21*, 127–130.

Bouckson-Castaing, V., Moudjou, M., Ferguson, D.J., Mucklow, S., Belkaid, Y., Milon, G., and Crocker, P.R. (1996). Molecular characterisation of ninein, a new coiled-coil protein of the centrosome. J. Cell. Sci. *109 (Pt 1)*, 179–190.

Brancati, F., Dallapiccola, B., and Valente, E.M. (2010a). Joubert Syndrome and related disorders. Orphanet J Rare Dis *5*, 20.

Brancati, F., Dallapiccola, B., and Valente, E.M. (2010b). Joubert Syndrome and related disorders. Orphanet J Rare Dis *5*, 20.

Breslow, D.K., Koslover, E.F., Seydel, F., Spakowitz, A.J., and Nachury, M.V. (2013). An in vitro assay for entry into cilia reveals unique properties of the soluble diffusion barrier. J. Cell Biol. *203*, 129–147.

Broekhuis, J.R., Leong, W.Y., and Jansen, G. (2013). Regulation of cilium length and intraflagellar transport. Int Rev Cell Mol Biol *303*, 101–138.

Budny, B., Chen, W., Omran, H., Fliegauf, M., Tzschach, A., Wisniewska, M., Jensen, L.R., Raynaud, M., Shoichet, S.A., Badura, M., et al. (2006). A novel X-linked recessive mental retardation syndrome comprising macrocephaly and ciliary dysfunction is allelic to oral-facial-digital type I syndrome. Hum. Genet. *120*, 171–178.

Buño, M., Pozo, J., Muñoz, M.T., Espejo, M., and Argente, J. (2000). [Orofaciodigital syndrome associated with agenesis of the pituitary gland]. An. Esp. Pediatr. *52*, 401–405.

Cadnapaphornchai, M.A., George, D.M., McFann, K., Wang, W., Gitomer, B., Strain, J.D., and Schrier, R.W. (2014). Effect of pravastatin on total kidney volume, left ventricular mass index, and microalbuminuria in pediatric autosomal dominant polycystic kidney disease. Clin J Am Soc Nephrol *9*, 889–896.

Camera, G., Marasini, M., Pozzolo, S., and Camera, A. (1994). Oral-facial-digital syndrome: report on a transitional type between the Mohr and Váradi syndromes in a fetus. Am. J. Med. Genet. *53*, 196–198.

Cevik, S., Sanders, A.A.W.M., Van Wijk, E., Boldt, K., Clarke, L., van Reeuwijk, J., Hori, Y., Horn, N., Hetterschijt, L., Wdowicz, A., et al. (2013). Active transport and diffusion barriers restrict Joubert Syndrome-associated ARL13B/ARL-13 to an Inv-like ciliary membrane subdomain. PLoS Genet. *9*, e1003977.

Chen, C.-P. (2007). Meckel syndrome: genetics, perinatal findings, and differential diagnosis. Taiwan J Obstet Gynecol *46*, 9–14.

Chevrier, V., Bruel, A.-L., Dam, T.J.P. van, Franco, B., Scalzo, M.L., Lembo, F., Audebert, S., Baudelet, E., Isnardon, D., Bole, A., et al. (2015). OFIP/KIAA0753 forms a complex with OFD1 and FOR20 at pericentriolar satellites and centrosomes and is mutated in one individual with Oral-Facial-Digital Syndrome. Hum. Mol. Genet. ddv488.

Chhin, B., Negre, D., Merrot, O., Pham, J., Tourneur, Y., Ressnikoff, D., Jaspers, M., Jorissen, M., Cosset, F.-L., and Bouvagnet, P. (2009). Ciliary beating recovery in deficient human airway epithelial cells after lentivirus ex vivo gene therapy. PLoS Genet. *5*, e1000422.

Chih, B., Liu, P., Chinn, Y., Chalouni, C., Komuves, L.G., Hass, P.E., Sandoval, W., and Peterson, A.S. (2012). A ciliopathy complex at the transition zone protects the cilia as a privileged membrane domain. Nat. Cell Biol. *14*, 61–72.

Chitayat, D., Stalker, H.J., and Azouz, E.M. (1992). Autosomal recessive oral-facial-digital syndrome with resemblance to OFD types II, III, IV and VI: a new OFD syndrome? Am. J. Med. Genet. *44*, 567–572.

Chung, W.Y., and Chung, L.P. (1999). A case of oral-facial-digital syndrome with overlapping manifestations of type V and type VI: a possible new OFD syndrome. Pediatr Radiol *29*, 268–271.

Coene, K.L.M., Roepman, R., Doherty, D., Afroze, B., Kroes, H.Y., Letteboer, S.J.F., Ngu, L.H., Budny, B., van Wijk, E., Gorden, N.T., et al. (2009). OFD1 is mutated in X-linked Joubert syndrome and interacts with LCA5-encoded lebercilin. Am. J. Hum. Genet. *85*, 465–481.

Coppieters, F., Lefever, S., Leroy, B.P., and De Baere, E. (2010). CEP290, a gene with many faces: mutation overview and presentation of CEP290base. Hum. Mutat. *31*, 1097–1108.

Cortés, C.R., McInerney-Leo, A.M., Vogel, I., Rondón Galeano, M.C., Leo, P.J., Harris, J.E., Anderson, L.K., Keith, P.A., Brown, M.A., Ramsing, M., et al. (2016). Mutations in human C2CD3 cause skeletal dysplasia and provide new insights into phenotypic and cellular consequences of altered C2CD3 function. Sci Rep *6*, 24083.

Czarnecki, P.G., and Shah, J.V. (2012). The ciliary transition zone: From Morphology and Molecules to Medicine. Trends Cell Biol *22*, 201–210.

van Dam, T.J., Wheway, G., Slaats, G.G., SYSCILIA Study Group, Huynen, M.A., and Giles, R.H. (2013). The SYSCILIA gold standard (SCGSv1) of known ciliary components and its applications within a systems biology consortium. Cilia *2*, 7.

Dammermann, A., and Merdes, A. (2002). Assembly of centrosomal proteins and microtubule organization depends on PCM-1. J. Cell Biol. *159*, 255–266.

Darmency-Stamboul, V., Burglen, L., Lopez, E., Mejean, N., Dean, J., Franco, B., Rodriguez, D., Lacombe, D., Desguerres, I., Cormier-Daire, V., et al. (2013). Detailed clinical, genetic and neuroimaging characterization of OFD VI syndrome. Eur J Med Genet *56*, 301–308.

Dave, K.V., Patel, S.C., Dudhia, B.B., and Panja, P. (2013). Orofacial digital syndrome. Indian J Dent Res *24*, 132–135.

Degner, D., Bleich, S., Riegel, A., and Rüther, E. (1999). [Orofaciodigital syndrome--a new variant? Psychiatric, neurologic and neuroradiological findings]. Fortschr Neurol Psychiatr *67*, 525–528.

Del Giudice, E., Macca, M., Imperati, F., D'Amico, A., Parent, P., Pasquier, L., Layet, V., Lyonnet, S., Stamboul-Darmency, V., Thauvin-Robinet, C., et al. (2014). CNS involvement in OFD1 syndrome: a clinical, molecular, and neuroimaging study. Orphanet J Rare Dis *9*, 74.

Deretic, D., Huber, L.A., Ransom, N., Mancini, M., Simons, K., and Papermaster, D.S. (1995). rab8 in retinal photoreceptors may participate in rhodopsin transport and in rod outer segment disk morphogenesis. J. Cell. Sci. *108 (Pt 1)*, 215–224.

Digilio, M.C., Marino, B., Giannotti, A., and Dallapiccola, B. (1996). Orocardiodigital syndrome: an oral-facial-digital type II variant associated with atrioventricular canal. J. Med. Genet. *33*, 416–418.

Dishinger, J.F., Kee, H.L., Jenkins, P.M., Fan, S., Hurd, T.W., Hammond, J.W., Truong, Y.N.-T., Margolis, B., Martens, J.R., and Verhey, K.J. (2010). Ciliary entry of the kinesin-2 motor KIF17 is regulated by importin-beta2 and RanGTP. Nat. Cell Biol. *12*, 703–710.

Driva, T., Franklin, D., and Crawford, P.J.M. (2004). Variations in expression of oral-facial-digital syndrome (type I): report of two cases. Int J Paediatr Dent *14*, 61–68.

Dua, H., Edbor, A., and Asudani, B. (2013). Orocfacial digital syndrome type II -- Mohr's syndrome. J Indian Med Assoc *111*, 268–269, 271.

Edvardson, S., Shaag, A., Zenvirt, S., Erlich, Y., Hannon, G.J., Shanske, A.L., Gomori, J.M., Ekstein, J., and Elpeleg, O. (2010). Joubert syndrome 2 (JBTS2) in Ashkenazi Jews is associated with a TMEM216 mutation. Am. J. Hum. Genet. *86*, 93–97.

Edwards, M., Mulcahy, D., and Turner, G. (1988). X-linked recessive inheritance of an orofaciodigital syndrome with partial expression in females and survival of affected males. Clin. Genet. *34*, 325–332.

Emes, R.D., and Ponting, C.P. (2001). A new sequence motif linking lissencephaly, Treacher Collins and oral-facial-digital type 1 syndromes, microtubule dynamics and cell migration. Hum. Mol. Genet. *10*, 2813–2820.

Erickson, R.P., and Bodensteiner, J.B. (2007). Oro-facial-digital syndrome IX with severe microcephaly: a new variant in a genetically isolated population. Am. J. Med. Genet. A *143A*, 3309–3313.

Falk, N., Lösl, M., Schröder, N., and Gießl, A. (2015). Specialized Cilia in Mammalian Sensory Systems. Cells *4*, 500–519.

Ferrante, M.I., Giorgio, G., Feather, S.A., Bulfone, A., Wright, V., Ghiani, M., Selicorni, A., Gammaro, L., Scolari, F., Woolf, A.S., et al. (2001). Identification of the gene for oral-facial-digital type I syndrome. Am. J. Hum. Genet. *68*, 569–576.

Ferrante, M.I., Zullo, A., Barra, A., Bimonte, S., Messaddeq, N., Studer, M., Dollé, P., and Franco, B. (2006). Oral-facial-digital type I protein is required for primary cilia formation and left-right axis specification. Nat. Genet. *38*, 112–117.

Ferrante, M.I., Romio, L., Castro, S., Collins, J.E., Goulding, D.A., Stemple, D.L., Woolf, A.S., and Wilson, S.W. (2009). Convergent extension movements and ciliary function are mediated by ofd1, a zebrafish orthologue of the human oral-facial-digital type 1 syndrome gene. Hum. Mol. Genet. *18*, 289–303.

Ferrero, G.B., Valenzise, M., Franco, B., Defilippi, C., Gregato, G., Corsello, G., Pepe, E., and Silengo, M. (2002). Oral, facial, digital, vertebral anomalies with psychomotor delay: a mild form of OFD type Gabrielli? Am. J. Med. Genet. *113*, 291–294.

Field, M., Scheffer, I.E., Gill, D., Wilson, M., Christie, L., Shaw, M., Gardner, A., Glubb, G., Hobson, L., Corbett, M., et al. (2012). Expanding the molecular basis and phenotypic

spectrum of X-linked Joubert syndrome associated with OFD1 mutations. Eur. J. Hum. Genet. *20*, 806–809.

Figuera, L.E., Rivas, F., and Cantú, J.M. (1993). Oral-facial-digital syndrome with fibular aplasia: a new variant. Clin. Genet. *44*, 190–192.

Fliegauf, M., Benzing, T., and Omran, H. (2007). When cilia go bad: cilia defects and ciliopathies. Nat. Rev. Mol. Cell Biol. *8*, 880–893.

Follit, J.A., Li, L., Vucica, Y., and Pazour, G.J. (2010). The cytoplasmic tail of fibrocystin contains a ciliary targeting sequence. J. Cell Biol. *188*, 21–28.

Gabrielli, O., Ficcadenti, A., Fabrizzi, G., Perri, P., Mercuri, A., Coppa, G.V., and Giorgi, P. (1994). Child with oral, facial, digital, and skeletal anomalies and psychomotor delay: a new OFDS form? Am. J. Med. Genet. *53*, 290–293.

Garcia-Gonzalo, F.R., Corbit, K.C., Sirerol-Piquer, M.S., Ramaswami, G., Otto, E.A., Noriega, T.R., Seol, A.D., Robinson, J.F., Bennett, C.L., Josifova, D.J., et al. (2011a). A transition zone complex regulates mammalian ciliogenesis and ciliary membrane composition. Nat. Genet. *43*, 776–784.

Garcia-Gonzalo, F.R., Corbit, K.C., Sirerol-Piquer, M.S., Ramaswami, G., Otto, E.A., Noriega, T.R., Seol, A.D., Robinson, J.F., Bennett, C.L., Josifova, D.J., et al. (2011b). A transition zone complex regulates mammalian ciliogenesis and ciliary membrane composition. Nat. Genet. *43*, 776–784.

Gherman, A., Davis, E.E., and Katsanis, N. (2006). The ciliary proteome database: an integrated community resource for the genetic and functional dissection of cilia. Nat. Genet. *38*, 961–962.

Ghosh, S., Setty, S., Sivakumar, A., and Pai, K.M. (2007). Report of a new syndrome: focus on differential diagnosis and review of Ellis-van Creveld, Curry-Hall, acrofacial dysostosis, and orofacial digital syndromes. Oral Surg Oral Med Oral Pathol Oral Radiol Endod *103*, 670–676.

Ghossaini, S.N., Hadi, U., and Tawil, A. (2002). Oral-facial-digital syndrome type II variant associated with congenital tongue lipoma. Oral Surg Oral Med Oral Pathol Oral Radiol Endod *94*, 324–327.

Giorgio, G., Alfieri, M., Prattichizzo, C., Zullo, A., Cairo, S., and Franco, B. (2007). Functional characterization of the OFD1 protein reveals a nuclear localization and physical interaction with subunits of a chromatin remodeling complex. Mol. Biol. Cell *18*, 4397–4404.

Goetz, S.C., and Anderson, K.V. (2010). The Primary Cilium: A Signaling Center During Vertebrate Development. Nat Rev Genet *11*, 331–344.

Goldstein, E., and Medina, J.L. (1974). Mohr syndrome or oral-facial-digital II: report of two cases. J Am Dent Assoc *89*, 377–382.

Gorlin, R.J., and Psaume, J. (1962). Orodigitofacial dysostosis--a new syndrome. A study of 22 cases. J. Pediatr. *61*, 520–530.

Gupta, G.D., Coyaud, É., Gonçalves, J., Mojarad, B.A., Liu, Y., Wu, Q., Gheiratmand, L., Comartin, D., Tkach, J.M., Cheung, S.W.T., et al. (2015). A Dynamic Protein Interaction Landscape of the Human Centrosome-Cilium Interface. Cell *163*, 1484–1499.

Gurrieri, F., Sammito, V., Ricci, B., Iossa, M., Bellussi, A., and Neri, G. (1992). Possible new type of oral-facial-digital syndrome with retinal abnormalities: OFDS type (VIII). Am. J. Med. Genet. *42*, 789–792.

Gurrieri, F., Franco, B., Toriello, H., and Neri, G. (2007). Oral-facial-digital syndromes: review and diagnostic guidelines. Am. J. Med. Genet. A *143A*, 3314–3323.

Hansen, C.G., Moroishi, T., and Guan, K.-L. (2015). YAP and TAZ: a nexus for Hippo signaling and beyond. Trends Cell Biol. *25*, 499–513.

Haren, L., Remy, M.-H., Bazin, I., Callebaut, I., Wright, M., and Merdes, A. (2006). NEDD1-dependent recruitment of the gamma-tubulin ring complex to the centrosome is necessary for centriole duplication and spindle assembly. J. Cell Biol. *172*, 505–515.

Haug, K., Khan, S., Fuchs, S., and König, R. (2000). OFD II, OFD VI, and Joubert syndrome manifestations in 2 sibs. Am. J. Med. Genet. *91*, 135–137.

Hildebrandt, F., Benzing, T., and Katsanis, N. (2011). Ciliopathies. N. Engl. J. Med. *364*, 1533–1543.

Hoff, S., Halbritter, J., Epting, D., Frank, V., Nguyen, T.-M.T., van Reeuwijk, J., Boehlke, C., Schell, C., Yasunaga, T., Helmstädter, M., et al. (2013). ANKS6 is a central component of a nephronophthisis module linking NEK8 to INVS and NPHP3. Nat. Genet. *45*, 951–956.

Hoppeler-Lebel, A., Celati, C., Bellett, G., Mogensen, M.M., Klein-Hitpass, L., Bornens, M., and Tassin, A.-M. (2007). Centrosomal CAP350 protein stabilises microtubules associated with the Golgi complex. J. Cell. Sci. *120*, 3299–3308.

Hsiao, Y.-C., Tuz, K., and Ferland, R.J. (2012). Trafficking in and to the primary cilium. Cilia *1*, 4.

Huang, L., Szymanska, K., Jensen, V.L., Janecke, A.R., Innes, A.M., Davis, E.E., Frosk, P., Li, C., Willer, J.R., Chodirker, B.N., et al. (2011). TMEM237 is mutated in individuals with a Joubert syndrome related disorder and expands the role of the TMEM family at the ciliary transition zone. Am. J. Hum. Genet. *89*, 713–730.

Hunkapiller, J., Singla, V., Seol, A., and Reiter, J.F. (2011). The ciliogenic protein Oral-Facial-Digital 1 regulates the neuronal differentiation of embryonic stem cells. Stem Cells Dev. *20*, 831–841.

Huppke, P., Wegener, E., Böhrer-Rabel, H., Bolz, H.J., Zoll, B., Gärtner, J., and Bergmann, C. (2014). Tectonic gene mutations in patients with Joubert syndrome. Eur. J. Hum. Genet.

Hurd, T.W., Fan, S., and Margolis, B.L. (2011). Localization of retinitis pigmentosa 2 to cilia is regulated by Importin beta2. J. Cell. Sci. *124*, 718–726.

Iglesias, A., Anyane-Yeboa, K., Wynn, J., Wilson, A., Truitt Cho, M., Guzman, E., Sisson, R., Egan, C., and Chung, W.K. (2014). The usefulness of whole-exome sequencing in routine clinical practice. Genet. Med. *16*, 922–931.

Ishikawa, H., Thompson, J., Yates III, J.R., and Marshall, W.F. (2012). Proteomic Analysis of Mammalian Primary Cilia. Current Biology *22*, 414–419.

Ivliev, A.E., ’t Hoen, P.A.C., van Roon-Mom, W.M.C., Peters, D.J.M., and Sergeeva, M.G. (2012). Exploring the transcriptome of ciliated cells using in silico dissection of human tissues. PLoS ONE *7*, e35618.

Izawa, I., Goto, H., Kasahara, K., and Inagaki, M. (2015). Current topics of functional links between primary cilia and cell cycle. Cilia *4*, 12.

Jauregui, A.R., and Barr, M.M. (2005). Functional characterization of the C. elegans nephrocystins NPHP-1 and NPHP-4 and their role in cilia and male sensory behaviors. Exp. Cell Res. *305*, 333–342.

Jauregui, A.R., Nguyen, K.C.Q., Hall, D.H., and Barr, M.M. (2008). The Caenorhabditis elegans nephrocystins act as global modifiers of cilium structure. J. Cell Biol. *180*, 973–988.

Jenkins, D., and Hernandez-Hernandez, V. (2015). Advances in the understanding of the BBSome complex structure and function. Research and Reports in Biology 191.

Jiang, K., Toedt, G., Montenegro Gouveia, S., Davey, N.E., Hua, S., van der Vaart, B., Grigoriev, I., Larsen, J., Pedersen, L.B., Bezstarosti, K., et al. (2012). A Proteome-wide screen for mammalian SxIP motif-containing microtubule plus-end tracking proteins. Curr. Biol. *22*, 1800–1807.

Jin, H., White, S.R., Shida, T., Schulz, S., Aguiar, M., Gygi, S.P., Bazan, J.F., and Nachury, M.V. (2010). The conserved Bardet-Biedl Syndrome proteins assemble a coat that traffics membrane proteins to cilia. Cell *141*, 1208–1219.

Kee, H.L., Dishinger, J.F., Blasius, T.L., Liu, C.-J., Margolis, B., and Verhey, K.J. (2012). A size-exclusion permeability barrier and nucleoporins characterize a ciliary pore complex that regulates transport into cilia. Nat. Cell Biol. *14*, 431–437.

Keeling, J., Tsiokas, L., and Maskey, D. (2016). Cellular Mechanisms of Ciliary Length Control. Cells *5*.

Khan, S.A., Muhammad, N., Khan, M.A., Kamal, A., Rehman, Z.U., and Khan, S. (2016). Genetics of Human Bardet-Biedl Syndrome, an Updates. Clin. Genet.

Khanna, H., and Rao, K. (2015). Role of small GTPases in polarized vesicle transport to primary cilium. Research and Reports in Biology 17.

Kim, S., and Dynlacht, B.D. (2013). Assembling a primary cilium. Curr. Opin. Cell Biol. *25*, 506–511.

Kim, S.K., Shindo, A., Park, T.J., Oh, E.C., Ghosh, S., Gray, R.S., Lewis, R.A., Johnson, C.A., Attie-Bittach, T., Katsanis, N., et al. (2010). Planar cell polarity acts through septins to control collective cell movement and ciliogenesis. Science *329*, 1337–1340.

Ko, H.W., Norman, R.X., Tran, J., Fuller, K.P., Fukuda, M., and Eggenschwiler, J.T. (2010). Broad-minded links cell cycle-related kinase to cilia assembly and hedgehog signal transduction. Dev. Cell *18*, 237–247.

Kobayashi, T., Tsang, W.Y., Li, J., Lane, W., and Dynlacht, B.D. (2011). Centriolar kinesin Kif24 interacts with CP110 to remodel microtubules and regulate ciliogenesis. Cell *145*, 914–925.

Kroes, H.Y., Monroe, G.R., van der Zwaag, B., Duran, K.J., de Kovel, C.G., van Roosmalen, M.J., Harakalova, M., Nijman, I.J., Kloosterman, W.P., Giles, R.H., et al. (2015). Joubert syndrome: genotyping a Northern European patient cohort. Eur. J. Hum. Genet.

Lallemand-Breitenbach, V., Quesnoit, M., Braun, V., El Marjou, A., Poüs, C., Goud, B., and Perez, F. (2004). CLIPR-59 is a lipid raft-associated protein containing a cytoskeleton-associated protein glycine-rich domain (CAP-Gly) that perturbs microtubule dynamics. J. Biol. Chem. *279*, 41168–41178.

Lambacher, N.J., Bruel, A.-L., van Dam, T.J.P., Szymańska, K., Slaats, G.G., Kuhns, S., McManus, G.J., Kennedy, J.E., Gaff, K., Wu, K.M., et al. (2015). TMEM107 recruits ciliopathy proteins to subdomains of the ciliary transition zone and causes Joubert syndrome. Nat. Cell Biol.

Lau, L., Lee, Y.L., Sahl, S.J., Stearns, T., and Moerner, W.E. (2012). STED microscopy with optimized labeling density reveals 9-fold arrangement of a centriole protein. Biophys. J. *102*, 2926–2935.

Lee, J.E., and Gleeson, J.G. (2011). Cilia in the nervous system: linking cilia function and neurodevelopmental disorders. Curr. Opin. Neurol. *24*, 98–105.

Lee, J.H., Silhavy, J.L., Lee, J.E., Al-Gazali, L., Thomas, S., Davis, E.E., Bielas, S.L., Hill, K.J., Iannicelli, M., Brancati, F., et al. (2012). Evolutionarily assembled cis-regulatory module at a human ciliopathy locus. Science *335*, 966–969.

Lehalle, D., Gordon, C.T., Oufadem, M., Goudefroye, G., Boutaud, L., Alessandri, J.-L., Baena, N., Baujat, G., Baumann, C., Boute-Benejean, O., et al. (2014). Delineation of EFTUD2 haploinsufficiency-related phenotypes through a series of 36 patients. Hum. Mutat. *35*, 478–485.

Li, C., Jensen, V.L., Park, K., Kennedy, J., Garcia-Gonzalo, F.R., Romani, M., De Mori, R., Bruel, A.-L., Gaillard, D., Doray, B., et al. (2016). MKS5 and CEP290 Dependent Assembly Pathway of the Ciliary Transition Zone. PLoS Biol. *14*, e1002416.

Li, Y., Ling, K., and Hu, J. (2012). The emerging role of Arf/Arl Small GTPases in Cilia and Ciliopathies. J Cell Biochem *113*, 2201–2207.

Liang, Y., Meng, D., Zhu, B., and Pan, J. (2016). Mechanism of ciliary disassembly. Cell. Mol. Life Sci.

Liem, K.F., Ashe, A., He, M., Satir, P., Moran, J., Beier, D., Wicking, C., and Anderson, K.V. (2012). The IFT-A complex regulates Shh signaling through cilia structure and membrane protein trafficking. J. Cell Biol. *197*, 789–800.

Liew, G.M., Ye, F., Nager, A.R., Murphy, J.P., Lee, J.S., Aguiar, M., Breslow, D.K., Gygi, S.P., and Nachury, M.V. (2014). The intraflagellar transport protein IFT27 promotes BBSome exit from cilia through the GTPase ARL6/BBS3. Dev. Cell *31*, 265–278.

Little, K.J., and Cornwall, R. (2016). Congenital Anomalies of the Hand-Principles of Management. Orthop. Clin. North Am. *47*, 153–168.

Liu, Y.-B., Xing, Z., Yang, L., Li, L., Liu, Y., and Liu, X. (2012). Bilateral cleft lip: a potential variant form of orofaciodigital syndrome type II? J. Oral Maxillofac. Surg. *70*, 2669–2673.

Logan, C.V., Abdel-Hamed, Z., and Johnson, C.A. (2011). Molecular genetics and pathogenic mechanisms for the severe ciliopathies: insights into neurodevelopment and pathogenesis of neural tube defects. Mol. Neurobiol. *43*, 12–26.

Lopes, C.A.M., Prosser, S.L., Romio, L., Hirst, R.A., O'Callaghan, C., Woolf, A.S., and Fry, A.M. (2011). Centriolar satellites are assembly points for proteins implicated in human ciliopathies, including oral-facial-digital syndrome 1. J. Cell. Sci. *124*, 600–612.

Lopez, E., Thauvin-Robinet, C., Reversade, B., Khartoufi, N.E., Devisme, L., Holder, M., Ansart-Franquet, H., Avila, M., Lacombe, D., Kleinfinger, P., et al. (2014). C5orf42 is the major gene responsible for OFD syndrome type VI. Hum. Genet. *133*, 367–377.

Lu, Q., Insinna, C., Ott, C., Stauffer, J., Pintado, P.A., Rahajeng, J., Baxa, U., Walia, V., Cuenca, A., Hwang, Y.-S., et al. (2015). Early steps in primary cilium assembly require EHD1/EHD3-dependent ciliary vesicle formation. Nat. Cell Biol. *17*, 228–240.

Madhivanan, K., and Aguilar, R.C. (2014). Ciliopathies: The Trafficking Connection. Traffic *15*, 1031–1056.

Malicki, J., and Avidor-Reiss, T. (2014). From the cytoplasm into the cilium: bon voyage. Organogenesis *10*, 138–157.

Manning, J.A., Lewis, M., Koblar, S.A., and Kumar, S. (2010). An essential function for the centrosomal protein NEDD1 in zebrafish development. Cell Death Differ. *17*, 1302–1314.

McIntyre, J.C., Williams, C.L., and Martens, J.R. (2013). Smelling the roses and seeing the light: gene therapy for ciliopathies. Trends Biotechnol. *31*, 355–363.

McIntyre, J.C., Joiner, A.M., Zhang, L., Iñiguez-Lluhí, J., and Martens, J.R. (2015). SUMOylation regulates ciliary localization of olfactory signaling proteins. J. Cell. Sci. *128*, 1934–1945.

Mihci, E., Tacoy, S., Ozbilim, G., and Franco, B. (2007). Oral-facial digital syndrome type 1. Indian Pediatr *44*, 854–856.

Mockel, A., Obringer, C., Hakvoort, T.B.M., Seeliger, M., Lamers, W.H., Stoetzel, C., Dollfus, H., and Marion, V. (2012). Pharmacological modulation of the retinal unfolded protein response in Bardet-Biedl syndrome reduces apoptosis and preserves light detection ability. J. Biol. Chem. *287*, 37483–37494.

Morán-Barroso, V., Valdés Flores, M., García-Cavazos, R., Kofman-Alfaro, S., and Saavedra-Ontiveros, D. (1998). Oral-facial-digital (OFD) syndrome with associated features: a new syndrome or genetic heterogeneity and variability? Clin. Dysmorphol. *7*, 55–57.

Morisawa, T., Yagi, M., Surono, A., Yokoyama, N., Ohmori, M., Terashi, H., and Matsuo, M. (2004). Novel double-deletion mutations of the OFD1 gene creating multiple novel transcripts. Hum. Genet. *115*, 97–103.

Mourão, A., Nager, A.R., Nachury, M.V., and Lorentzen, E. (2014). Structural basis for membrane targeting of the BBSome by ARL6. Nat. Struct. Mol. Biol. *21*, 1035–1041.

Muenke, M., Ruchelli, E.D., Rorke, L.B., McDonald-McGinn, D.M., Orlow, M.K., Isaacs, A., Craparo, F.J., Dunn, L.K., and Zackai, E.H. (1991). On lumping and splitting: a fetus with clinical findings of the oral-facial-digital syndrome type VI, the hydrolethalus syndrome, and the Pallister-Hall syndrome. Am. J. Med. Genet. *41*, 548–556.

Mukhopadhyay, S., Wen, X., Chih, B., Nelson, C.D., Lane, W.S., Scales, S.J., and Jackson, P.K. (2010). TULP3 bridges the IFT-A complex and membrane phosphoinositides to promote trafficking of G protein-coupled receptors into primary cilia. Genes Dev. *24*, 2180–2193.

Musgrave, A., de Wildt, P., van Etten, I., Pijst, H., Scholma, C., Kooyman, R., Homan, W., and van den Ende, H. (1986). Evidence for a functional membrane barrier in the transition zone between the flagellum and cell body of Chlamydomonas eugametos gametes. Planta *167*, 544–553.

Nachury, M.V. (2014). How do cilia organize signalling cascades? Philos. Trans. R. Soc. Lond., B, Biol. Sci. *369*.

Nachury, M.V., Loktev, A.V., Zhang, Q., Westlake, C.J., Peränen, J., Merdes, A., Slusarski, D.C., Scheller, R.H., Bazan, J.F., Sheffield, V.C., et al. (2007). A core complex of BBS proteins cooperates with the GTPase Rab8 to promote ciliary membrane biogenesis. Cell *129*, 1201–1213.

Nachury, M.V., Seeley, E.S., and Jin, H. (2010). Trafficking to the ciliary membrane: how to get across the periciliary diffusion barrier? Annu. Rev. Cell Dev. Biol. *26*, 59–87.

Naikmasur, V.G., Rai, A., Revanappa, M.M., and Mutalik, S. (2010). Thurston syndrome: oral and systemic manifestations. Case report and review of the literature. Quintessence Int *41*, e75-79.

Nguyen, M.T., and Charlebois, K. (2014). The clinical utility of whole-exome sequencing in the context of rare diseases - the changing tides of medical practice. Clin. Genet.

Novarino, G., Akizu, N., and Gleeson, J.G. (2011). Modeling Human Disease in Humans: the Ciliopathies. Cell *147*, 70–79.

Nowaczyk, M.J.M., Zeesman, S., Whelan, D.T., Wright, V., and Feather, S.A. (2003). Oral-facial-digital syndrome VII is oral-facial-digital syndrome I: a clarification. Am. J. Med. Genet. A *123A*, 179–182.

Nozawa, Y.I., Lin, C., and Chuang, P.-T. (2013). Hedgehog signaling from the primary cilium to the nucleus: an emerging picture of ciliary localization, trafficking and transduction. Curr. Opin. Genet. Dev. *23*, 429–437.

Obregón, M.G., and Barreiro, C.Z. (2003). Oral-facial-digital syndrome gabrielli type: second report. Am. J. Med. Genet. A *118A*, 369–371.

Oh, E.C., and Katsanis, N. (2013). Context-dependent regulation of Wnt signaling through the primary cilium. J. Am. Soc. Nephrol. *24*, 10–18.

Okten, A., Mungan, L., Orhan, F., and Cakir, M. (2005). Hypothalamic hamartoma, cerebellar hypoplasia, facial dysmorphism and very atypical combination of polydactyly: is it a new variant of oro-facio-digital syndrome? Genet. Couns. *16*, 101–105.

Ounjai, P., Kim, K.D., Liu, H., Dong, M., Tauscher, A.N., Witkowska, H.E., and Downing, K.H. (2013). Architectural insights into a ciliary partition. Curr. Biol. *23*, 339–344.

Panigrahi, I., Das, R.R., Kulkarni, K.P., and Marwaha, R.K. (2013). Overlapping phenotypes in OFD type II and OFD type VI: report of two cases. Clin. Dysmorphol. *22*, 109–114.

Parisi, M.A., Doherty, D., Chance, P.F., and Glass, I.A. (2007). Joubert syndrome (and related disorders) (OMIM 213300). Eur. J. Hum. Genet. *15*, 511–521.

Pazour, G.J., and Witman, G.B. (2003). The vertebrate primary cilium is a sensory organelle. Curr. Opin. Cell Biol. *15*, 105–110.

Pazour, G.J., Baker, S.A., Deane, J.A., Cole, D.G., Dickert, B.L., Rosenbaum, J.L., Witman, G.B., and Besharse, J.C. (2002). The intraflagellar transport protein, IFT88, is essential for vertebrate photoreceptor assembly and maintenance. J. Cell Biol. *157*, 103–113.

Pedersen, L.B., and Rosenbaum, J.L. (2008). Intraflagellar transport (IFT) role in ciliary assembly, resorption and signalling. Curr. Top. Dev. Biol. *85*, 23–61.

Perico, N., Antiga, L., Caroli, A., Ruggenenti, P., Fasolini, G., Cafaro, M., Ondei, P., Rubis, N., Diadei, O., Gherardi, G., et al. (2010). Sirolimus therapy to halt the progression of ADPKD. J. Am. Soc. Nephrol. *21*, 1031–1040.

Perrault, I., Halbritter, J., Porath, J.D., Gérard, X., Braun, D.A., Gee, H.Y., Fathy, H.M., Saunier, S., Cormier-Daire, V., Thomas, S., et al. (2015). IFT81, encoding an IFT-B core protein, as a very rare cause of a ciliopathy phenotype. J Med Genet jmedgenet-2014-102838.

Phadke, S.R., Pahi, J., Pandey, A., and Agarwal, S.S. (1999). Oral-facial-digital syndrome with acromelic short stature: a new variant--overlap with Ellis Van Creveld syndrome. Clin. Dysmorphol. *8*, 185–188.

Plotnikova, O.V., Pugacheva, E.N., and Golemis, E.A. (2009). Primary Cilia and the Cell Cycle. Methods Cell Biol *94*, 137–160.

Poretti, A., Brehmer, U., Scheer, I., Bernet, V., and Boltshauser, E. (2008). Prenatal and neonatal MR imaging findings in oral-facial-digital syndrome type VI. AJNR Am J Neuroradiol *29*, 1090–1091.

Prattichizzo, C., Macca, M., Novelli, V., Giorgio, G., Barra, A., Franco, B., and Oral-Facial-Digital Type I (OFDI) Collaborative Group (2008). Mutational spectrum of the oral-facial-digital type I syndrome: a study on a large collection of patients. Hum. Mutat. *29*, 1237–1246.

Prpić, I., Cekada, S., and Franulović, J. (1995). Mohr syndrome (oro-facial-digital syndrome II)--a familial case with different phenotypic findings. Clin. Genet. *48*, 304–307.

Reiter, J.F., and Skarnes, W.C. (2006). Tectonic, a novel regulator of the Hedgehog pathway required for both activation and inhibition. Genes Dev *20*, 22–27.

Reiter, J.F., Blacque, O.E., and Leroux, M.R. (2012). The base of the cilium: roles for transition fibres and the transition zone in ciliary formation, maintenance and compartmentalization. EMBO Rep. *13*, 608–618.

Rhouma, A., and Horneff, G. (2014). Mohr-Claussen syndrome or oro-facial-digital syndrome (OFDS) type-II. Klin Padiatr *226*, 78–79.

Riella, C., Czarnecki, P.G., and Steinman, T.I. (2014). Therapeutic advances in the treatment of polycystic kidney disease. Nephron Clin Pract *128*, 297–302.

Roberson, E.C., Dowdle, W.E., Ozanturk, A., Garcia-Gonzalo, F.R., Li, C., Halbritter, J., Elkhartoufi, N., Porath, J.D., Cope, H., Ashley-Koch, A., et al. (2015). TMEM231, mutated in orofaciodigital and Meckel syndromes, organizes the ciliary transition zone. J Cell Biol *209*, 129–142.

Rogers, K.K., Wilson, P.D., Snyder, R.W., Zhang, X., Guo, W., Burrow, C.R., and Lipschutz, J.H. (2004). The exocyst localizes to the primary cilium in MDCK cells. Biochem. Biophys. Res. Commun. *319*, 138–143.

Romani, M., Mancini, F., Micalizzi, A., Poretti, A., Miccinilli, E., Accorsi, P., Avola, E., Bertini, E., Borgatti, R., Romaniello, R., et al. (2015). Oral-facial-digital syndrome type VI: is C5orf42 really the major gene? Hum. Genet. *134*, 123–126.

Romio, L., Wright, V., Price, K., Winyard, P.J.D., Donnai, D., Porteous, M.E., Franco, B., Giorgio, G., Malcolm, S., Woolf, A.S., et al. (2003). OFD1, the gene mutated in oral-facial-digital syndrome type 1, is expressed in the metanephros and in human embryonic renal mesenchymal cells. J. Am. Soc. Nephrol. *14*, 680–689.

Romio, L., Fry, A.M., Winyard, P.J.D., Malcolm, S., Woolf, A.S., and Feather, S.A. (2004). OFD1 is a centrosomal/basal body protein expressed during mesenchymal-epithelial transition in human nephrogenesis. J. Am. Soc. Nephrol. *15*, 2556–2568.

Saal, S., Faivre, L., Aral, B., Gigot, N., Toutain, A., Van Maldergem, L., Destree, A., Maystadt, I., Cosyns, J.-P., Jouk, P.-S., et al. (2010). Renal insufficiency, a frequent complication with age in oral-facial-digital syndrome type I. Clin. Genet. *77*, 258–265.

Saari, J., Lovell, M.A., Yu, H.-C., and Bellus, G.A. (2015). Compound heterozygosity for a frame shift mutation and a likely pathogenic sequence variant in the planar cell polarity-ciliogenesis gene WDPCP in a girl with polysyndactyly, coarctation of the aorta, and tongue hamartomas. Am. J. Med. Genet. A *167*, 421–427.

Sahel, J.-A., Marazova, K., and Audo, I. (2015). Clinical characteristics and current therapies for inherited retinal degenerations. Cold Spring Harb Perspect Med *5*, a017111.

Sang, L., Miller, J.J., Corbit, K.C., Giles, R.H., Brauer, M.J., Otto, E.A., Baye, L.M., Wen, X., Scales, S.J., Kwong, M., et al. (2011). Mapping the Nephronophthisis-Joubert-Meckel-Gruber Protein Network Reveals Ciliopathy Disease Genes and Pathways. Cell *145*, 513–528.

Sasai, N., and Briscoe, J. (2012). Primary cilia and graded Sonic Hedgehog signaling. Wiley Interdiscip Rev Dev Biol *1*, 753–772.

Satir, P., Pedersen, L.B., and Christensen, S.T. (2010). The primary cilium at a glance. J Cell Sci *123*, 499–503.

Schäfer, T., Pütz, M., Lienkamp, S., Ganner, A., Bergbreiter, A., Ramachandran, H., Gieloff, V., Gerner, M., Mattonet, C., Czarnecki, P.G., et al. (2008). Genetic and physical interaction between the NPHP5 and NPHP6 gene products. Hum. Mol. Genet. *17*, 3655–3662.

Seo, S., Baye, L.M., Schulz, N.P., Beck, J.S., Zhang, Q., Slusarski, D.C., and Sheffield, V.C. (2010). BBS6, BBS10, and BBS12 form a complex with CCT/TRiC family chaperonins and mediate BBSome assembly. Proc. Natl. Acad. Sci. U.S.A. *107*, 1488–1493.

Serra, A.L., Poster, D., Kistler, A.D., Krauer, F., Raina, S., Young, J., Rentsch, K.M., Spanaus, K.S., Senn, O., Kristanto, P., et al. (2010). Sirolimus and kidney growth in autosomal dominant polycystic kidney disease. N. Engl. J. Med. *363*, 820–829.

Shaheen, R., Faqeih, E., Alshammari, M.J., Swaid, A., Al-Gazali, L., Mardawi, E., Ansari, S., Sogaty, S., Seidahmed, M.Z., AlMotairi, M.I., et al. (2013a). Genomic analysis of Meckel-Gruber syndrome in Arabs reveals marked genetic heterogeneity and novel candidate genes. Eur. J. Hum. Genet. *21*, 762–768.

Shaheen, R., Ansari, S., Mardawi, E.A., Alshammari, M.J., and Alkuraya, F.S. (2013b). Mutations in TMEM231 cause Meckel-Gruber syndrome. J. Med. Genet. *50*, 160–162.

Shamseldin, H.E., Rajab, A., Alhashem, A., Shaheen, R., Al-Shidi, T., Alamro, R., Al Harassi, S., and Alkuraya, F.S. (2013). Mutations in DDX59 implicate RNA helicase in the pathogenesis of orofaciodigital syndrome. Am. J. Hum. Genet. *93*, 555–560.

Shashi, V., Clark, P., Rogol, A.D., and Wilson, W.G. (1995). Absent pituitary gland in two brothers with an oral-facial-digital syndrome resembling OFDS II and VI: a new type of OFDS? Am. J. Med. Genet. *57*, 22–26.

Shiba, D., Yamaoka, Y., Hagiwara, H., Takamatsu, T., Hamada, H., and Yokoyama, T. (2009). Localization of Inv in a distinctive intraciliary compartment requires the C-terminal ninein-homolog-containing region. J. Cell. Sci. *122*, 44–54.

Shiba, D., Manning, D.K., Koga, H., Beier, D.R., and Yokoyama, T. (2010). Inv acts as a molecular anchor for Nphp3 and Nek8 in the proximal segment of primary cilia. Cytoskeleton *67*, 112–119.

Shimojima, K., Shimada, S., Sugawara, M., Yoshikawa, N., Niijima, S., Urao, M., and Yamamoto, T. (2013). Challenges in genetic counseling because of intra-familial phenotypic variation of oral-facial-digital syndrome type 1. Congenit Anom (Kyoto) *53*, 155–159.

Shin, J.H., Bae, D.-J., Kim, E.S., Kim, H.B., Park, S.J., Jo, Y.K., Jo, D.S., Jo, D.-G., Kim, S.-Y., and Cho, D.-H. (2015). Autophagy Regulates Formation of Primary Cilia in Mefloquine-Treated Cells. Biomol Ther (Seoul) *23*, 327–332.

Shintani, K., Shechtman, D.L., and Gurwood, A.S. (2009). Review and update: current treatment trends for patients with retinitis pigmentosa. Optometry *80*, 384–401.

Shylo, N.A., Christopher, K.J., Iglesias, A., Daluiski, A., and Weatherbee, S.D. (2015). TMEM107 is a Critical Regulator of Ciliary Protein Composition and is Mutated in Orofaciodigital Syndrome. Human Mutation n/a-n/a.

Singla, V., and Reiter, J.F. (2006). The primary cilium as the cell's antenna: signaling at a sensory organelle. Science *313*, 629–633.

Singla, V., Romaguera-Ros, M., Garcia-Verdugo, J.M., and Reiter, J.F. (2010). Ofd1, a human disease gene, regulates the length and distal structure of centrioles. Dev. Cell *18*, 410–424.

Smith, R.A., and Gardner-Medwin, D. (1993). Orofaciodigital syndrome type III in two sibs. J. Med. Genet. *30*, 870–872.

Srour, M., Schwartzentruber, J., Hamdan, F.F., Ospina, L.H., Patry, L., Labuda, D., Massicotte, C., Dobrzeniecka, S., Capo-Chichi, J.-M., Papillon-Cavanagh, S., et al. (2012). Mutations in C5ORF42 cause Joubert syndrome in the French Canadian population. Am. J. Hum. Genet. *90*, 693–700.

Srour, M., Hamdan, F.F., McKnight, D., Davis, E., Mandel, H., Schwartzentruber, J., Martin, B., Patry, L., Nassif, C., Dionne-Laporte, A., et al. (2015). Joubert Syndrome in French Canadians and Identification of Mutations in CEP104. Am. J. Hum. Genet. *97*, 744–753.

Stenram, U., Cramnert, C., and Axfors-Olsson, H. (2007). Oralfacialdigital-like syndrome with respiratory tract symptoms from birth and ultrastructural centriole/basal body disarray. Acta Paediatr. *96*, 1101–1104.

Stephan, M.J., Brooks, K.L., Moore, D.C., Coll, E.J., and Goho, C. (1994). Hypothalamic hamartoma in oral-facial-digital syndrome type VI (Váradi syndrome). Am. J. Med. Genet. *51*, 131–136.

Stoll, C., and Sauvage, P. (2002). Long-term follow-up of a girl with oro-facio-digital syndrome type I due to a mutation in the OFD 1 gene. Ann. Genet. *45*, 59–62.

Stone, E.M., Cideciyan, A.V., Aleman, T.S., Scheetz, T.E., Sumaroka, A., Ehlinger, M.A., Schwartz, S.B., Fishman, G.A., Traboulsi, E.I., Lam, B.L., et al. (2011). Variations in NPHP5 in patients with nonsyndromic leber congenital amaurosis and Senior-Loken syndrome. Arch. Ophthalmol. *129*, 81–87.

Sugarman, G.I., Katakia, M., and Menkes, J. (1971). See-saw winking in a familial oral-facial-digital syndrome. Clin. Genet. *2*, 248–254.

Sung, C.-H., and Leroux, M.R. (2013). The roles of evolutionarily conserved functional modules in cilia-related trafficking. Nat. Cell Biol. *15*, 1387–1397.

Szymanska, K., and Johnson, C.A. (2012). The transition zone: an essential functional compartment of cilia. Cilia *1*, 10.

Szymanska, K., Berry, I., Logan, C.V., Cousins, S.R., Lindsay, H., Jafri, H., Raashid, Y., Malik-Sharif, S., Castle, B., Ahmed, M., et al. (2012). Founder mutations and genotype-phenotype correlations in Meckel-Gruber syndrome and associated ciliopathies. Cilia *1*, 18.

Takao, D., and Verhey, K.J. (2015). Gated entry into the ciliary compartment. Cell. Mol. Life Sci.

Tang, Z., Lin, M.G., Stowe, T.R., Chen, S., Zhu, M., Stearns, T., Franco, B., and Zhong, Q. (2013). Autophagy promotes primary ciliogenesis by removing OFD1 from centriolar satellites. Nature *502*, 254–257.

Tanos, B.E., Yang, H.-J., Soni, R., Wang, W.-J., Macaluso, F.P., Asara, J.M., and Tsou, M.-F.B. (2013). Centriole distal appendages promote membrane docking, leading to cilia initiation. Genes Dev. *27*, 163–168.

Taschner, M., Bhogaraju, S., and Lorentzen, E. (2012). Architecture and function of IFT complex proteins in ciliogenesis. Differentiation *83*, S12-22.

Taschner, M., Weber, K., Mourão, A., Vetter, M., Awasthi, M., Stiegler, M., Bhogaraju, S., and Lorentzen, E. (2016). Intraflagellar transport proteins 172, 80, 57, 54, 38, and 20 form a stable tubulin-binding IFT-B2 complex. EMBO J.

Thauvin-Robinet, C., Franco, B., Saugier-Veber, P., Aral, B., Gigot, N., Donzel, A., Van Maldergem, L., Bieth, E., Layet, V., Mathieu, M., et al. (2009a). Genomic deletions of OFD1 account for 23% of oral-facial-digital type 1 syndrome after negative DNA sequencing. Hum. Mutat. *30*, E320-329.

Thauvin-Robinet, C., Callier, P., Franco, B., Zuffardi, O., Payet, M., Aral, B., Gigot, N., Donzel, A., Mosca-Boidron, A.-L., Masurel-Paulet, A., et al. (2009b). Search for genomic imbalances in a cohort of 20 patients with oral-facial-digital syndromes negative for mutations and large rearrangements in the OFD1 gene. Am. J. Med. Genet. A *149A*, 1846–1849.

Thauvin-Robinet, C., Lee, J.S., Lopez, E., Herranz-Pérez, V., Shida, T., Franco, B., Jego, L., Ye, F., Pasquier, L., Loget, P., et al. (2014). The oral-facial-digital syndrome gene C2CD3 encodes a positive regulator of centriole elongation. Nat. Genet. *46*, 905–911.

Thevenon, J., Duplomb, L., Phadke, S., Eguether, T., Saunier, A., Avila, M., Carmignac, V., Bruel, A.-L., St-Onge, J., Duffourd, Y., et al. (2016). Autosomal Recessive IFT57 hypomorphic mutation cause ciliary transport defect in unclassified oral-facial-digital syndrome with short stature and brachymesophalangia. Clin. Genet.

Thomas, S., Legendre, M., Saunier, S., Bessières, B., Alby, C., Bonnière, M., Toutain, A., Loeuillet, L., Szymanska, K., Jossic, F., et al. (2012). TCTN3 mutations cause Mohr-Majewski syndrome. Am. J. Hum. Genet. *91*, 372–378.

Tobin, J.L., and Beales, P.L. (2009). The nonmotile ciliopathies. Genet. Med. *11*, 386–402.

Tollenaere, M.A.X., Mailand, N., and Bekker-Jensen, S. (2015). Centriolar satellites: key mediators of centrosome functions. Cell. Mol. Life Sci. *72*, 11–23.

Toriello, H.V. (1993). Oral-facial-digital syndromes, 1992. Clin. Dysmorphol. *2*, 95–105.

Toriello, H.V., and Franco, B. (1993). Oral-Facial-Digital Syndrome Type I. In GeneReviews(®), R.A. Pagon, M.P. Adam, H.H. Ardinger, S.E. Wallace, A. Amemiya, L.J. Bean, T.D. Bird, C.R. Dolan, C.-T. Fong, R.J. Smith, et al., eds. (Seattle (WA): University of Washington, Seattle), p.

Toriyama, M., Lee, C., Taylor, S.P., Duran, I., Cohn, D.H., Bruel, A.-L., Tabler, J.M., Drew, K., Kelly, M.R., Kim, S., et al. (2016). The ciliopathy-associated CPLANE proteins direct basal body recruitment of intraflagellar transport machinery. Nat. Genet.

Torres, V.E., Chapman, A.B., Devuyst, O., Gansevoort, R.T., Grantham, J.J., Higashihara, E., Perrone, R.D., Krasa, H.B., Ouyang, J., Czerwiec, F.S., et al. (2012). Tolvaptan in patients with autosomal dominant polycystic kidney disease. N. Engl. J. Med. *367*, 2407–2418.

Tsang, W.Y., and Dynlacht, B.D. (2013). CP110 and its network of partners coordinately regulate cilia assembly. Cilia *2*, 9.

Valente, E.M., Logan, C.V., Mougou-Zerelli, S., Lee, J.H., Silhavy, J.L., Brancati, F., Iannicelli, M., Travaglini, L., Romani, S., Illi, B., et al. (2010). Mutations in TMEM216 perturb ciliogenesis and cause Joubert, Meckel and related syndromes. Nat. Genet. *42*, 619–625.

Valiathan, A., Sivakumar, A., Marianayagam, D., Valiathan, M., and Satyamoorthy, K. (2006). Thurston syndrome: report of a new case. Oral Surg Oral Med Oral Pathol Oral Radiol Endod *101*, 757–760.

Veland, I.R., Awan, A., Pedersen, L.B., Yoder, B.K., and Christensen, S.T. (2009). Primary cilia and signaling pathways in mammalian development, health and disease. Nephron Physiol *111*, p39-53.

Vincensini, L., Blisnick, T., and Bastin, P. (2011). 1001 model organisms to study cilia and flagella. Biol. Cell *103*, 109–130.

Walz, G., Budde, K., Mannaa, M., Nürnberger, J., Wanner, C., Sommerer, C., Kunzendorf, U., Banas, B., Hörl, W.H., Obermüller, N., et al. (2010). Everolimus in patients with autosomal dominant polycystic kidney disease. N. Engl. J. Med. *363*, 830–840.

Wang, G., Chen, Q., Zhang, X., Zhang, B., Zhuo, X., Liu, J., Jiang, Q., and Zhang, C. (2013). PCM1 recruits Plk1 to the pericentriolar matrix to promote primary cilia disassembly before mitotic entry. J. Cell. Sci. *126*, 1355–1365.

Ward, H.H., Brown-Glaberman, U., Wang, J., Morita, Y., Alper, S.L., Bedrick, E.J., Gattone, V.H., Deretic, D., and Wandinger-Ness, A. (2011). A conserved signal and GTPase complex are required for the ciliary transport of polycystin-1. Mol Biol Cell *22*, 3289–3305.

Webb, T.R., Parfitt, D.A., Gardner, J.C., Martinez, A., Bevilacqua, D., Davidson, A.E., Zito, I., Thiselton, D.L., Ressa, J.H.C., Apergi, M., et al. (2012). Deep intronic mutation in OFD1, identified by targeted genomic next-generation sequencing, causes a severe form of X-linked retinitis pigmentosa (RP23). Hum. Mol. Genet. *21*, 3647–3654.

Wei, Q., Zhang, Y., Li, Y., Zhang, Q., Ling, K., and Hu, J. (2012). The BBSome controls IFT assembly and turnaround in cilia. Nat. Cell Biol. *14*, 950–957.

Westlake, C.J., Baye, L.M., Nachury, M.V., Wright, K.J., Ervin, K.E., Phu, L., Chalouni, C., Beck, J.S., Kirkpatrick, D.S., Slusarski, D.C., et al. (2011). Primary cilia membrane assembly is initiated by Rab11 and transport protein particle II (TRAPPII) complex-dependent trafficking of Rabin8 to the centrosome. Proc. Natl. Acad. Sci. U.S.A. *108*, 2759–2764.

Whelan, D.T., Feldman, W., and Dost, I. (1975). The oro-facial-digital syndrome. Clin. Genet. *8*, 205–212.

Williams, C.L., Winkelbauer, M.E., Schafer, J.C., Michaud, E.J., and Yoder, B.K. (2008). Functional redundancy of the B9 proteins and nephrocystins in Caenorhabditis elegans ciliogenesis. Mol. Biol. Cell *19*, 2154–2168.

Williams, C.L., Li, C., Kida, K., Inglis, P.N., Mohan, S., Semenec, L., Bialas, N.J., Stupay, R.M., Chen, N., Blacque, O.E., et al. (2011). MKS and NPHP modules cooperate to establish basal body/transition zone membrane associations and ciliary gate function during ciliogenesis. J Cell Biol *192*, 1023–1041.

Yan, X., Habedanck, R., and Nigg, E.A. (2006). A complex of two centrosomal proteins, CAP350 and FOP, cooperates with EB1 in microtubule anchoring. Mol. Biol. Cell *17*, 634–644.

Yavuz, Y.C., Ganidagli, S.E., Yilmaz, T., Altunoren, O., Deniz, M.S., and Dogan, E. (2014). Orofacial digital syndrome type 1: an underlying cause of chronic renal failure. Ren Fail *36*, 946–947.

Ye, X., Zeng, H., Ning, G., Reiter, J.F., and Liu, A. (2014). C2cd3 is critical for centriolar distal appendage assembly and ciliary vesicle docking in mammals. Proc. Natl. Acad. Sci. U.S.A. *111*, 2164–2169.

Yee, L.E., Garcia-Gonzalo, F.R., Bowie, R.V., Li, C., Kennedy, J.K., Ashrafi, K., Blacque, O.E., Leroux, M.R., and Reiter, J.F. (2015). Conserved Genetic Interactions between Ciliopathy Complexes Cooperatively Support Ciliogenesis and Ciliary Signaling. PLoS Genet. *11*, e1005627.

Yildirim, S., Akan, M., Deviren, A., and Aköz, T. (2002). Penile agenesis and clavicular anomaly in a child with an oral facial digital syndrome. Clin. Dysmorphol. *11*, 29–32.

Yu, F., Ran, J., and Zhou, J. (2016). Ciliopathies: Does HDAC6 Represent a New Therapeutic Target? Trends Pharmacol. Sci. *37*, 114–119.

Zaghloul, N.A., and Brugmann, S.A. (2011). The emerging face of primary cilia. Genesis *49*, 231–246.

Zhang, Q., Yu, D., Seo, S., Stone, E.M., and Sheffield, V.C. (2012). Intrinsic protein-protein interaction-mediated and chaperonin-assisted sequential assembly of stable bardet-biedl syndrome protein complex, the BBSome. J. Biol. Chem. *287*, 20625–20635.

Annexes

Annexe 1 : Cas atteints présentant un syndrome OFD (hors OFD I) rapportés dans la littérature.

Classi-fication	Sexe	Age	Gène identifié	Anomalies orales	Anomalies faciale	Anomalies digitales	Anomalies cérébrales	Neuro-développement	Autres	Référence
II	F	15a		HL, incisives centrales absente	H, OBI, nez large	P, S				Havle, 2015
VI	M	fœtus	*C5orf42*						Os courts	Drury, 2015
VI	F	5a		AD				DI, RD	Difficultés respiratoires	Chhambra, 2015
III, VI	F		*TMEM231*	HL	Mouvement anormal des yeux	PPo	DW, HV	DI	Défaillance rénale terminale	Roberson, 2015
III, VI	F		*TMEM231*	HL	Mouvement anormal des yeux	PPo	DW, HV	DI	Défaillance rénale terminale	Roberson, 2015
VI	F	11a	*C5orf42*		H, BF, strabisme	MP, PPr	SDM, atrophie corticale, corps calleux fin	DI, ataxie, épilepsies	Hypoplasie des OGE, hernie inguinale	Bayram, 2015
VI	M	5a	*C5orf42*		BF, H, strabisme	MP, PPr		DI		Bayram, 2015
IV	F	6a		LL, FP, AF, épiglotte bifide	H, MR, FL, oreilles protubérantes	PPo, hallux bifide, pied bot		DI, troubles du comportement	Membres courts, surdité, marche difficile	Ozdemir-Karatas, 2015
IV	F	1a		LL, épiglotte bifide		P, S			Membres courts, mégalourètre, pneumonie lobaire	Ozdemir-Karatas, 2015
VI	M	3a		langue et luette bifide	BF, H, sourcils archées	PPo, hallux valgus	SDM	Hypotonie, épilepsies		Sarma, 2015
?	F	2a	*WDPCP*	HL		P, S			Coarctation de l'aorte	Saari, 2015
II	F			LL, FP, AF	Epicanthus, racine du nez protubérente	B, PPr	HV, polymicrogyrie, dysplasie corticale, défaut myélinisation	Epilepsies	Taches café au lait	Rhouma, 2014
II	F	17a	*C5orf42*	HL	H, FL	PPo, PPr				Carrera, 2014
VI	F	fœtus	*C5orf42*	AF	Dysmorphie	PPr	SDM, HH, KA, porencéphalie, hétérotropie, polymicrogyrie	DI		Lopez, 2014
VI	F	13y	*C5orf42*			MP, PPr, Y	SDM, HH			Lopez, 2014
VI	F	4y	*C5orf42*	LL, HL, AF	Dysmorphie, FL	B, PPo, S	SDM, HH, ACC			Lopez, 2014
VI	F	10y	*C5orf42*	LL, AF, HL, FP	Dysmorphie	PPo, PPr, S	SDM, KA			Lopez, 2014
VI	M	fœtus	*C5orf42*	AF		PPo, PPr, Y	SDM, HH			Lopez, 2014
VI	F	fœtus	*C5orf42*			MP, PPr	SDM, hypoplasie ventriculaire			Lopez, 2014
VI	M	fœtus	*C5orf42*		Dysmorphie	PPr	SDM			Lopez, 2014
VI	M	fœtus	*C5orf42*			MP, S, PPr, Y	SDM		Coarctation de l'aorte, fémurs courts	Lopez, 2014
VI	F	fœtus	*C5orf42*			MP, PPr	SDM, méningocèle occipital		Anomalies de l'utérus	Lopez, 2014

VI	F	18m	*C5orf42*		Microphtalmie	PPr, PPo, MP	SDM, ACC, hydrocéphalie		Agénésie fibulaire, tibia incurvé	Lopez, 2014
VI		4a	*C5orf42*	AF	Dysmorphie	PPo, PPr	SDM, HH, méningocèle occipital, arhinencéphalie		Mésentère commun	Lopez, 2014
?	F		*DDX59*	FP, LL	H, BF	P	ACC	DI	Reins fusionnés, Tétralogie de Fallot	Shamseldin, 2013
?	M		*DDX59*	FP, LL	H, BF	P		DI		Shamseldin, 2013
II	F					P, S			Cyanose	Dua, 2013
IX	M	6m	*TBC1D32*		FL, H, sténose des choanes, micro et anophtalmie, colobome	PPo	Microcéphalie, ACC, agénésie vermienne	Epilepsies	DSA, ambiguïté sexuelle	Adly, 2013
IX	M	3m	*SCLT1*	FP	FL, atrésie des choanes, colobome		Microcéphalie, pachygyrie, ACC		DSA	Adly, 2013
VI	F	2m		HL	BF, H, FL, épicanthus	PPo, PPr, Y	SDM		Difficultés respiratoires	Patra, 2013
II			*GLI3 ?*	LB, HL, AF	FL	PPo, S				Al-Quattan, 2013
V	M			FP	FL	P	Microcéphalie			John, 2013
VI		9a		LL, HL, AF, FP	FL					Darmency-Stamboul, 2013
VI		7a		LL, HL, AF, FP		PPo				Darmency-Stamboul, 2013
VI		9a		HL, AF		PPo				Darmency-Stamboul, 2013
VI		9a		HL, AF		PPo				Darmency-Stamboul, 2013
VI		5a		FP	FL					Darmency-Stamboul, 2013
VI		1a		LL, AF	FL					Darmency-Stamboul, 2013
II, VI						Y				Panigrahi, 2013
II, VI						Y				Panigrahi, 2013
II, VI										Panigrahi, 2013
II, VI										Panigrahi, 2013
II, VI										Panigrahi, 2013
II	M	18m		AF, LL, FP, HL	FL, H, mouvements anormaux des yeux, nystagmus	PPo, PPr	Hypotonie, RD			Sukarova-Angelovska, 2012
VI	F	4a		AF, FP, AD	H, OBI, nez bifide	MP, S, PPr	DI, RD			Sukarova-

										Angelovska, 2012
VI	F	3m		AF, FP, LL	H, OBI, nez bifide, mouvements anormaux des yeux	PPo, S, PPr			Tachypnée	Sukarova-Angelovska, 2012
IV				AF, FP, LL, HL	OBI, nez bifide, BF, télécanthus	PPo, MP, S			Anomalies rénales, cardiaques, OGE, apnée, tibias et fibulaires courts	Sukarova-Angelovska, 2012
II	F									Kaylan, 2012
IV			*TCTN3*			P	EO, SDM		Kystes rénaux, PD, dysplasie tibiale, os long incurvés	Thomas, 2012
IV			*TCTN3*			P	EO, SDM		Kystes rénaux, dysplasie tibiale, os long incurvés, RCIU, PD	Thomas, 2012
IV			*TCTN3*		MR	P	EO		Kystes rénaux, dysplasie tibiale, RCIU, PD	Thomas, 2012
IV	F		*TCTN3*	Microglossie	MR	P, pieds bots	EO, ACC, arhinencéphalie		Kystes rénaux, dysplasie tibiale, os long incurvés, utérus bicorné, PD	Thomas, 2012
IV			*TCTN3*	FP		P, pieds et mains bots	EO		Kystes rénaux, dysplasie tibiale, os long incurvés, prolifération ductulaire	Thomas, 2012
IV			*TCTN3*		Mouvements anormaux des yeux	P, camptodactylie	OE	DI	Dysplasie tibiale, PD, scoliose, cyphose, difficultés respiratoire	Thomas, 2012
IV			*TCTN3*		MR	P	SDM, agénésie vermienne		RCIU, scoliose, kystes rénaux, DSV	Thomas, 2012
IV			*TCTN3*				SDM, agénésie vermienne			Thomas, 2012
II					FL					Liu, 2012
VI		28a		HL		PPr	SDM		Reins dysplastiques	Poretti, 2012
VI		2m		AF		PPo	SDM, HH		DSA	Poretti, 2012
VI		4a		HL, AF	Colobome rétinien	PPo, PPr	SDM, HH			Poretti, 2012
VI		5a		FP		PPo	SDM			Poretti, 2012
VI		2a		HL, FP	Colobome choroïdien		SDM			Poretti, 2012

VI		16a		HL		PPo	SDM			Poretti, 2012
VI		6m		HL, FP	Myopie	PPo	SDM			Poretti, 2012
VI		7y		HL		PPo	SDM			Poretti, 2012
VI		22a		HL		PPo, PPr	SDM		Maladie de Hirshsprung	Poretti, 2012
VI		9a		HL, AF	FL, colobome choroïdien et rétinien, ACL	MP, PPr	SDM, HH		Néphronophtise	Poretti, 2012
VI		17a		FP	colobome choroïdien et rétinien, ACL	PPo	SDM			Poretti, 2012
VI		10a		HL		PPo				Poretti, 2012
VI		17a		HL		PPo	SDM		Anomalies cardiaques	Poretti, 2012
VI		17a		HL, FP		MP, PPr	SDM, HH			Poretti, 2012
VI		2a		HL, AF		PPo, PPr	SDM			Poretti, 2012
IV				FP, AF, LL	MR, FL	PPo, PPr, S			Hypoplasie tibiale	Mathai, 2011
IV				AD						Soneji, 2010
V		19a								Naikmasur, 2010
VI	F	13a		HL	Nystagmus	P	SDM, HH	RPM, épilepsie	Ataxie cérébelleuse	Takanashi, 2009
VI	F	8a		HL		S, P	SDM, HH, hétérotropie, polymicrogyrie	RPM, épilepsie	Tachypnée, apnée	Takanashi, 2009
VI	F			AF, épiglotte hypoplasique	FL, MR, OBI, H	PPr, PPo, C, B, Y	SDM		Difficultés respiratoires	Hayes, 2008
IX				LB, FP, HL	Hématome labial, mouvements anormaux des yeux, colobome	C, P, mésobranchy-phalangie	Microcéphalie, atrophie cérébelleuse et hippcampienne, hétérotropie	DI, hypertonie	Difficultés respiratoire, agénésie clitorienne, petite stature	Erickson, 2007
IX	F			FP, AF, HL, LB		C	Microcéphalie			Erickson, 2007
IX	F			Anomalies de la langue	OBI, colobome choroïdien	Brachy-phalangie	Microcéphalie, hypoplasie cérébelleuse		Surdité, agénésie vaginale	Erickson, 2007
IX	M			FP, anomalies de la langue	OBI, colobome rétinien				Micropénis, difficultés respiratoires	Erickson, 2007
IV	F	fœtus		AF, hypoplasie de la luette	H, FL	PPo, PPr			Ambiguïté sexuelle, anomalies cardiaques	Khal, 2007
?	F	2y		HL	Dysmorphie	P		DI, RD	Difficultés respiratoires	Stenram, 2007
V	M	13a		AF	FL	PPo, S				Valiathan 2006
II, VI, IV		1m				P	HH, hypoplasie cérébelleuse			Okten, 2005
XI					Blépharophimosis, nez court, philtrum long, télécanthus	PPo		RD, hypotonie, épilepsies, troubles du		Obregon, 2003

								comportement		
IX										Genevieve, 2003
XI	F			FP, AF	H, MR	C	Retard de myélinisation	DI	Scoliose, cyphose	Ferrero, 2002
II	M	3a		Lipome lingual	FL, télécanthus	PPo, Y				Ghossaini, 2002
II, VI	F	2m		AF, FP, HL	H, nystagmus	PPo	DW, hydrocéphalie	Hypotonie	Apnée	Haug, 2000
II, VI	M	1m		FP, HL	BF, MR, nystagmus	PPo	DW, HV, hydrocéphalie, hypomyélinisation		Apnée, kystes rénaux	Haug, 2000
II	M	11m		LL, AF, HL, AD	BF, OBI, sténose des choanes	P, C		RPM, RD	Obésité, micropénis	Buno, 2000
IV	M			FP						Tuysuz, 1999
V										Chung, 1999
VI	F				Epicanthus, ptosis		HV			Al-Gazali, 1999
VI	M				Mouvements anormaux des yeux	PPo	Hypoplasie du corps calleux, HV		Micropénis, testicules non descendus	Al-Gazali, 1999
VI		fœtus			H	PPo	DW, agénésie vermienne			Doss, 1998
IV	M	fœtus		FP, LL	FL	S, P	ACC, hydrocéphalie, aplasie olfactive		Kystes rénaux, micromélie, FH, lobulation incomplèete des poumons	Moerman, 1998
IV	M			AF	H, OBI, MR, , asymétrie	S, PPo		Epilepsies	Asymétrie des jambes	Toriello, 1997
IV	M	7a		AF, HL, AD	FL, télécanthus	B, PPo	Marco et dolichocéphalie		Petite stature, fibulaire et ilium courts	Toriello, 1997
IV	F	3a			Dysmorphie	PPo, PPr, S, C		Hyper/hypotonie	Surdité, fibulaire et tibia courts	Toriello, 1997
IV	M			LB, AF	MR		ACC, HV, hydrocéphalie	Epilepsie	Ulna et tibia courts, testicules non-palpables	Toriello, 1997
IV	M	fœtus				P, S	DW, ACC		Os longs courts	Toriello, 1997
IV	M	10a		FP, agénésie de la luette, microglossie	H, télécanthus	P	Microcéphalie		Tibia incurvé	Toriello, 1997
IX	F	5m		AF, FP, LL, épiglotte anormale, AD	H, rétinopathie, microphtalmie	P, S, hallux large		DI, épilepsie		Nagai, 1997
IX	F	5a		AF, LL, FP, LB	H, rétinopathie, microphtalmie	C		Epilepsie, DI		Steven, 1996
IX	M							Epilepsie, DI	Dysplasie squelettique	Battaglia, 1996
II				LB, LL		PPo, S			Anomalies cardiaque	Digilio, 1996
IX	F	6m		AF, LL	FL, H, rétinopathie	Hallux large		DI		Sigaudy, 1996
II				LL	H, cou court	PPo, S			Micropénis, difficultés	Prpic, 1995

									respiratoires, bras courts	
II				LL	H, OBI, MR	PPo, S				Prpic, 1995
IV	F			FP, LL	MR, OBI	S			Membres courts, hydronéphrose, atrésie anorectale	Digilio, 1995
II, VI									Agénésie de la glande pituitaire	Shashi, 1995
XI								RPM	Anomalies squelettiques	Gabrielli, 1994
II, VI		fœtus								Camera, 1994
VI				FP, LL, LB	FL					Wey, 1994
IX										Nevin, 1994
II				Anomalies du larynx		PPr, PPo			Surdité	Steichen-Gersdorf, 1994
VI				AD		P, S	DW, HH, hypoplasie cérébelleuse			Stephan, 1994
IV				FP, anomalies de l'épiglotte	MR	S, PPo, PPr	Anomalies cérébrales		Thorax étroit, tibias et côtes courts, anomalies OGE et rénales	Ades, 1994
IX	M	2m		AF, LB, FP,LB	FL, H, rétinopathie	P, S, C		Epilepsies		Jamieson, 1993
?				FP		P, S			Aplasie fibulaire	Figuera, 1993
III, VI				LL	Mouvements anormaux des yeux	PPo, S	DW, hydrocéphalie, hypoplasie cérébelleuse			Smith, 1993
III, VI				AD	Atrésie des choanes, nystagmus	PPo	HV, hydrocéphalie		Hernie inguinale	Smith, 1993
IV										Nevin, 1992
VIII, IX	M	27a		LB, FP, AD	FL, rétinopathie, colobome	B, S, P		DI		Gurrieri, 1992
VIII, IX	M	21a		AF, LL, épiglotte anormale	FL, rétinopathie, colobome	Campto-dactylie		DI		Gurrieri, 1992
?				FP, LB	H, MR	PPo, S	Anomalies cérébrales		Thorax étroit, tibias courts	Chitayat, 1992
?				FP, LB	H, MR	PPo, S			Thorax étroit, bras courts	Chitayat, 1992
VI										Muenke, 1991
IV				AF, FP, LB, épiglotte anormale	H, FL, MR	PPr, PPo	Anomalies cérébrales		Thorax étroit, tibias courts, anomalies OGE, rénales et cardiaques	Minecke, 1990
?				AF, LB	FL	PPr			Thorax étroit, tibias courts, surdité,	Berberich, 1989

									anomalies OGE	
IX	F	22a		AF, LL, LB	FL, rétinopathie	C		Epilepsie		Nevin, 1989
IV				FP	H, FL, MR	S, PPr, PPo	Anomalies cérébrales		Anomalies cardiaques	Gillerot, 1988
II, IV				AF, FP, HL	FL, MR	PPo, PPr, S				Michel, 1985
II, IV					FL	PPo, PPr, S				Michel, 1985
IV				FP, HL	MR	S, PPo, PPr			Surdité, tibia court	Burn, 1984
IV				FP, HL		S, PPo, PPr			Surdité, tibia court	Burn, 1984
IV				AF, HL	MR	S, PPo, PPr			Tibias courts	Sugarman, 1983
II, IV				HL, LB	H, MR	S, PPo, PPr, C			métaphyses larges, tibias courts	Bonioli, 1979
IV				AF, FP, HL	H, FL, MR	PPr			Thorax étroit, tibias courts, surdité, anomalies OGE	Temtamy, 1978
II, IV				AF, FP, HL	FL	C			Surdité, tibias courts	Goldstein, 1974
II, IV				AF, FP, HL	Racine du nez large	C			Surdité, tibias courts	Goldstein, 1974
IV				AF, FP, HL	H, FL, MR	C, PPr			Surdité, métaphyses larges	Rimoin, 1967
IV				AF, LB, HL	H, FL, MR	C, PPr			Surdité, métaphyses larges	Rimoin, 1967

a : an(s), ACC : Agénésie du Corps Calleux, ACL : Amaurose Congénital de Leber, AD : Anomalies Dentaires, AF : Anomalies des Freins, BF : Bosses Frontales, C : Clinodactylie, DI : Déficience Intellectuelle, DSA : Défaut Septal Atrial, DSV : Défaut Septal Ventriculaire, DW : malformation de Dandy-Walker, EO : Encéphalocèle Occipital, F : Femme, FH : Fibrose Hépatique, FL : Fente/pseudo-fente Labiale, FP : Fente/pseudo-fente Palatine, H : Hypertélorisme, HH : Hamartomes Hypothalamiques, HL: Hamartomes Linguaux, HV : Hypoplasie Vermienne, j: jour(s), m: mois, KA : Kystes Arachnoïdinens, LB : Langue Bifide, LL : Langue Lobulée, M: Mâle, MP : Polydactylie Méso-axiale, MR : Micro-Rétrognathisme, OBI : Oreilles Bas-Implantés, OGE : Organes Génitaux Externes, PD : Prolifération Ductulaire, P : Polydactylie, PPo : Polydactylie Post-axiale, PPr : Polydactylie Pré-axiale, RCIU : Retard de Croissance Intra-Utérin, RD : Retard du développement, RPM : Retard Psycho-Moteur, S : Syndactylie, SDM : Signe de la Dent Molaire, Y : Métacarpes en Y.

Annexe 2 : Mutations rapportés dans les gènes impliqués dans les syndromes OFD.

Diagnostic	Mutation			N	Référence
			TMEM231		
OFD VI	chr16:g.75579335G>A	c.656C>T	p.Pro219Leu	1	Li, 2016
OFD VI	chr16:g.75579789G>C	c.532C>G	p.Pro178Ala	1	Li, 2016
JBS	chr16:g.75590096A>T	c.12T>A	p.Tyr4*	2	Srour, 2012a
JBS	chr16:g.75576539C>T	c.625G>A	p.Asp238Asn	2	Srour, 2012a
MKS	chr16:g.75576500C>T	c.751G>A	p.Val251Ile	1	Shaheen, 2013
JBS	chr16:g.75540130T>G	c.974A>C	p.Gln325Pro	1	ClinVar
JBS	chr16:g.75576539C>T	c.784G>A	p.Asp262Asn	1	Srour, 2012a
MKS	chr16:g.75576500C>T	c.823G>A	p.Val275Ile	2	Shaheen, 2013/Alazami 2015
JBS	chr16:g.75575271G>C	c.747C>G	p.Ile249Met	1	Kroes, 2016
OFD III	chr16:g.75589929G>A	c.241C>T	p.Leu81Phe	1	Roberson 2015
OFD III /MKS	chr16:g.75589797G>C	c.373C>G	p.Pro125Ala	5	Roberson 2015
MKS	chr16:g.75589901T>A	c.269A>T	p.Asn90Ile	1	Roberson 2015
MKS	chr16:g.75579777G>A	c.544C>T	p.Gln182*	1	Roberson 2015
MKS	chr16:g.75579323T>C	c.664+4A>G	intron	5	Roberson 2015
MKS	chr16:g.75589807delG	c.363delC	p.Ile232Serfs*	1	Roberson 2015
MKS	chr16:g.75579345C>G	c.646G>C	p.Ala216Pro	1	Roberson 2015
JBS	chr16:g.75590096A>T	c.2T>A	p.Met25Lys	1	Srour, 2012a
			TMEM107		
OFD VI	chr17:g.8079298T>C	c.134A>G	p.Glu45Gly	1	Bruel, 2015a
JBS	chr17:g.8077891_8077893delGAA	c.316_318delTTC	p.Phe106del	4	Bruel, 2015a
JBS	chr17:g.8077560delT	c.402delA	p.Leu134Phefs*8	5	Bruel, 2015a
MKS	chr17:g.8079074C>T	c.274+1G>A		2	Shaheen 2015
OFD	chr17:g.8078211delAAAG	c.312-314delCTTT	p.Ser104del	1	Iglesias 2014
			TMEM138		
OFD VI	chr11:g.61135446A>T	c.352A>T	p.Met118Leu	1	Li, 2016
JBS	chr11:g.61136081A>G	c.389A>G	p.Tyr130Cys	1	Lee, 2012
JBS	chr11:g.61135470G>A	c.376G>A	p.Ala126Thr	3	Lee, 2012
JBS	chr11:g.61136072C>T	c.380C>T	p.Ala127Val	1	Lee, 2012

JBS	chr11:g.61131995G>A	c.128+5G>A	intron	2	Lee, 2012
JBS/MKS	chr11:g.61133675A>G	c.287A>G	p.His96Arg	3	Lee, 2012/ Szymanska, 2012
		TMEM216			
MKS	chr11:g.61165269C>T	c.253C>T	p.His85*	2	Szymanska, 2012/Valente, 2010
JBS/OFD VI	chr11:g.61161437G>T	c.218G>T	p.Arg73Leu	12	Valente, 2010
JBS	chr11:g.61161437G>A	c.218G>A	p.Arg73His	1	Valente, 2010
JBS	chr11:g.61165414T>G	c.398T>G	p.Leu133*	1	Valente, 2010
JBS	chr11:g.61161436C>T	c.217C>T	p.Arg73Cys	1	Valente, 2010
MKS	chr11:g.61165357T>G	c.341T>G	p.Leu114Arg	2	Valente, 2010
MKS	chr11:g.61165246G>C	c.230G>C	p.Thr78Lysfs*30	3	Valente, 2010
JBS2	chr11:g.61160703G>T	c.35G>T	p.Gly12Val	8	Edvarson, 2010
		C2CD3			
OFD XIV	chr11:g.73879524T>G	c.184C>T	p.Arg62*	1	Thauvin-Robinet, 2014
OFD XIV	chr11:g.73806348A>C	c.3085T>G	p.Cys1029Gly	1	Thauvin-Robinet, 2014
OFD XIV	chr11:g.73796017T>A	c.3911-2A>T	p.Ala1304Valfs*3	1	Thauvin-Robinet, 2014
CCP	chr11 :g.73879519C>G	c.195G>C	p.Trp65Cys	1	Cortès, 2016
CCP	chr11:g.73829364delT	c.1429delA	Ile477*	1	Cortès, 2016
		TBC1D32			
OFD IX	chr6:g.121613198C>A	c.1372+1G>T	p.Arg411_Gly458del	1	Adly, 2013
		SCLT1			
OFD IX	chr4:g.129960194A>G	c.290+2T>C	p.Lys79Valfs*4	1	Adly, 2013
		WDPCP			
OFD	chr2:g.63719990C>T	c.160G>A	p.Asp54Asn	2	Toriyama,/Saari, 2014
OFD	chr2:g.63664661_63664662delAA	c.526_527delTT	p.Leu176Ilefs*21	1	Toriyama, sous-presse
OFD	chr2:g.63664635_63664636del	c.552_553del	p.Cys185Phefs*12	1	Saari, 2014
JBS	chr2:g.63631524T>C	c.1094A>G	p.Glu365Gly	1	Toriyama, sous-presse
BBS	chr2:g.63720075C>A	c.76-1G>T		1	Kim, 2010
		DDX59			
OFD V	chr1:g.200635115C>T	c.754G>A	p.Gly252Arg	1	Bruel, en cours
OFD	chr1:g.200613642C>T	c.1600G>A	p.Gly534Arg	1	Shamseldin, 2013
OFD	chr1:g.200619767A>C	c.1100T>G	p.Val367Gly	1	Shamseldin, 2013

		TCTN3			
OFD IV	chr10:g.97447409_97447410del	c.566_567del	p.Glu189Valfs*52	1	Thomas, 2012
OFD IV	chr10:g.97447087_97447090del	c.650_653del	p.Tyr217Serfs*6	1	Thomas, 2012
JBS	chr10:g.97445342C>T	c.940G>A	p.Gly314Arg	1	Thomas, 2012
OFD IV	chr10:g.97442934G>A	c.1222C>T	p.Gln408*	1	Thomas, 2012
OFD IV	chr10:g.97442503G>A	c.1357C>T	p.Gln443*	1	Thomas, 2012
OFD IV	chr10:g.97442511_97442512del	c.1348_1349del	p.Leu450Serfs*14	1	Thomas, 2012
JBS	chr10:g.97442423C>G	c.1437G>C	p.Arg479Ser	1	Thomas, 2012
JBS	chr10:g.97446288C>A	c.853-1G>T		1	Huppke, 2014
		C5orf42			
JBS	chr5:g.37187590G>A	c.4006C>T	p.Arg1336Trp	6	Srour, 2012b
JBS	chr5:g.37167148C>T	c.7400+1G>A	intron	4	Srour, 2012a/Srour, 2012b
JBS	chr5:g.37125432G>A	c.8710C>T	p.Arg2904*	2	Kroes, 2015
JBS	chr5:g.37182969T>C	c.5314A>G	p.Ser1772Gly	1	Kroes, 2015
JBS	chr5:g.37148334G>A	c.8248C>T	p.Pro2750Ser	1	Kroes, 2015
JBS	chr5:g.37227876C>T	c.1165G>A	p.Ala389Thr	1	Kroes, 2015
JBS	chr5:g.37198889A>C	c.3587T>G	p.Leu1196Arg	1	Kroes, 2015
JBS	chr5:g.37173912_37173913del	c.6115_6116del	p.Asp2039Leufs*6	1	Kroes, 2015
JBS	chr5:g.37221548G>A	c.2624C>T	p.Ser875Phe	1	Kroes, 2015
JBS	chr5:g.37231126A>C	c.964T>G	p.Trp322Gly	1	Kroes, 2015
JBS	chr5:g.37125486del	c.8656del	p.Ser2886Hisfs*15	1	Kroes, 2015
JBS	chr5:g.37170198del	c.6407del	p.Pro1016Hisfs*31	1	Srour, 2012b
JBS	chr5:g.37165697G>A	c.7477C>T	p.Arg2493*	1	Srour, 2012b
JBS	chr5:g.37183479G>A	c.4804C>T	p.Arg1602*	1	Srour, 2012b
JBS	chr5:g.37183593G>A	c.4690C>T	p.Ala1564Thr	3	Srour, 2012b
MKS	chr5:g.37154064_37154065delTC	c.7988_7989delGA	p.Gly2663Alafs*40	3	Shaheen, 2013/ Alazami, 2012
JBS	chr5:g.37154075G>A	c.7978C>T	p.Arg2660*	1	Alazami, 2012
JBS	chr5:g.37148324_37148325insT	c.8257_8258insA	p.Lys2755fs*8	1	Srour, 2012a
JBS/OFD VI	chr5:g.37198899G>A	c.3577C>T	p.Arg1193Cys	2	Ohba, 2013/Lopez, 2014
JBS	chr5:g.37198877G>A	c.3599C>T	p.Ala1200Val	1	Ohba, 2013
JBS	chr5:g.37231104A>G	c.986T>C	p.Leu329Pro	1	Ohba, 2013

JBS	chr5:g.37213735T>C	c.2846A>G	p.Tyr949Cys	1	Ohba, 2013
OFD VI	chr5:g.37198919delT	c.3557delA	p.Lys1186Argfs*21	1	Lopez, 2014
OFD VI	chr5:g.37198926G>A	c.3550C>T	p.Arg1184Cys	1	Lopez, 2014
OFD VI	chr5:g.37120345G>A	c.9121C>T	p.Gln3041*	1	Lopez, 2014
OFD VI	chr5:g.37205557C>A	c.3150-1G>T	intron	1	Lopez, 2014
OFD VI/JBS	chr5:g.37244554delT	c.493delA	p.Ile165Thrfs*17	3	Lopez, 2014/Kroes, 2015
OFD VI	chr5:g.37201912T>C	c.3290-2A>G	intron	1	Lopez, 2014
OFD VI	chr5:g.37224757G>A	c.2377C>T	p.Gln793*	1	Lopez, 2014
OFD VI	chr5:g.37138943C>A	c.8509G>T	p.Val2837Leu	1	Lopez, 2014
OFD VI	chr5:g.37201820G>A	c.3380C>T	p.Ser1127Leu	2	Lopez, 2014
OFD VI	chr5:g.37187897C>G	c.3859G>C	p.Asp1287His	2	Lopez, 2014
OFD VI	chr5:g.37165698delA	c.7476delT	p.Arg2493Aspfs*6	1	Lopez, 2014
OFD VI	chr5:g.37169228delG	c.6898delC	p.Gln2300Argfs*8	1	Lopez, 2014
OFD VI	chr5:g.37187562T>C	c.677A>G	p.Gln226Arg	1	Bayram, 2015
OFD VI	chr5:g.37153886G>A	c.8167C>T	p.Gln2723*	1	Drury, 2015
OFD VI	chr5:g.37138824G>A	c.8628C>T	p.Ser2876Ser	1	Drury, 2015
OFD VI	chr5:g.37165772G>A	c.7402C>T	p.Gln2468*	1	Lopez, 2014
		IFT57			
OFD	chr3:g.107910368C>T	c.777G>A	p.Lys259Lys	1	Thevenon, 2016
		INTU			
NPHP	chr4:g.128608927G>A	c.1354G>A	p.Ala452Thr	1	Toriyama, sous-presse
CCP	chr4:g.128590281G>T	c.1063G>T	p.Glu355*	1	Toriyama, sous-presse
CCP	chr4:g.128584593C>T	c.826C>T	p.Gln276*	1	Toriyama, sous-presse
CCP	chr4:g.128621214A>C	c.1499A>C	p.Glu500Ala	1	Toriyama, sous-presse
OFD	chr4:g.128564925delT	c.396delT	p.Asn132Lysfs*11	1	Toriyama, sous-presse
		KIAA0753/OFIP			
OFD	chr17:g.6510529T>A	c.1891A>T	p.Lys631*	1	Bruel, 2015b
OFD	chr17:g.6513483G>T	c.1546-3C>A		1	Bruel, 2015b
		OFD1			
OFDI	chrX:g.13753357T>A	c.13-10T>A		1	Bisschoff, 2012
OFDI	chrX:g.13753417_13753418insT	c.63_64insT	p.Lys21Aspfs*8	1	Bisschoff, 2012

OFDI	chrX:g.13753465G>A	c.111G>A	p.Lys37Lys	1	Prattichizzo, 2008
OFDI	chrX:g.13753419dupA	c.65dupA	p.Leu23Alafs*6	1	Prattichizzo, 2008
OFDI	chrX:g.13753465G>C	c.111G>C	p.Lys37Asn	1	Prattichizzo, 2008
OFDI	chrX:g.13753440_13753444delATCGG	c.86_90delATCGG	p.Asp29Glyfs*17	1	Dijon
OFDI	chrX:g.13753397_13753398delAG	c.43_44delAG	Gln16Argfs*2	1	Prattichizzo, 2008
OFDI	chrX:g.13753406G>T	c.52G>T	p.Glu18*	1	Bisschoff, 2012
OFDI	chrX:g.13753467T>C	c.111+2T>C		1	Prattichizzo, 2008
OFDI	chrX:g.13753468A>G	c.111+3A>G		1	Bisschoff, 2012
OFDI	chrX:g.13754600C>T	c.115C>T	p.Glu39*	1	Del Giudice, 2014
OFDI	chrX:g.13754779_13754797delTGGTTT GGCAAAAGAAAAG	c.294_312delTGGTT TGGCAAAAGAAAAG	p.Ser98Argfs*41	1	Ferrante, 2001
OFDI	chrX:g.13754768_13754771delTTTC	c.283_286delTTTC	p.Phe95Glnfs*49	1	Dijon
OFDI	chrX:g.13754775A>G	c.290A>G	p.Glu97Gly	1	Prattichizzo, 2008
OFDI	chrX:g.13754797delG	c.312delG	p.Val105Tyrfs*40	1	Ferrante, 2001
OFDI	chrX:g.13754759T>C	c.274T>C	p.Ser92Pro	1	Prattichizzo, 2008
OFDI	chrX:g.13756965dupG	c.313dupG	p.Val105Glyfs*12	1	Prattichizzo, 2008
OFDI	chrX:g.13754745A>G	c.260A>G	p.Tyr87Cys	2	Prattichizzo, 2008
OFDI	chrX:g.13754732C>T	c.247C>T	p.Gln83*	1	Prattichizzo, 2008
OFDI	chrX:g.13754728C>G	c.243C>G	p.His81Gln	3	Romero, 2007/ Dijon
OFDI	chrX:g.13754726C>G	c.241C>G	p.His81Asp	1	Prattichizzo, 2008
OFDI	chrX:g.13754720G>A	c.235G>A	p.Ala79Thr	1	Rakkolainen, 2002
OFDI	chrX:g.13754707dupCT	c.222dupCT	p.Asn75*	1	Dijon
OFDI	chrX:g.13754709A>C	c.224A>C	p.Asn75Thr	1	Prattichizzo, 2008
OFDI	chrX:g.13754706_13754707dupCT	c.221_222dupCT	p.Asn75Leufs*4	1	Dijon
OFDI	chrX:g.13754710C>G	c.225C>G	p.Asn75Lys	2	Del Giudice, 2014/Dijon
OFDI	chrX:g.13754606C>T	c.121C>T	p.Arg41*	1	Prattichizzo, 2008
OFDI	chrX:g.13754706C>T	c.221C>T	p.Ser74Phe	1	Prattichizzo, 2008
OFDI	chrX:g.13754647_13754651delTGGAG	c.162_166delTGGAG	p.Ser54Argfs*20	1	Prattichizzo, 2008
OFDI	chrX:g.13754633_13754634insG	c.148_149insG	p.His50Alafs*26	1	Bisschoff, 2012
OFDI / NC	chrX:g.13754792G>T	c.307G>T	p.Glu130*	1	Baker, 2014
OFDI	chrX:g.13756963A>G	c.313-2A>G		1	Dijon

OFDI	chrX:g.13754760_13754761delCT	c.275_276delCT	p.Ser92Cysfs*24	2	Bisschoff, 2012
OFDI	chrX:g.13754798delG	c.312+1delG		1	Dijon
OFDI	chrX:g.13754797delG	c.312delG	p.Val105Tyrfs*40	1	Ferrante, 2001
OFDI	chrX:g.13754799_ 13754805delTAAACTC	c.312+2_312+8 delTAAACTC		1	Toriello, 2002
OFDI	chrX:g.13756989C>T	c.337C>T	p.Gln113*	1	Prattichizzo, 2008
OFDI	chrX:g.13757024C>G	c.372C>G	p.Tyr124*	1	Prattichizzo, 2008
OFDI	chrX:g.13757151G>A	c.412G>A	p.Gly138Ser	1	Thauvin-Robinet, 2006
OFDI	chrX:13757034G>A	c.381+1G>A		1	Dijon
OFDI	chrX:g.13757118C>G	c.382-3C>G		1	Prattichizzo, 2008
OFDI	chrX:g.13757119A>G	c.382-2A>G		2	Prattichizzo, 2008/Dijon
OFDI	chrX:g.13757150delA	c.411delA	p.Gly138Valfs*7	1	Prattichizzo, 2008
OFDI	chrX:g.13757152G>T	c.412+1G>T		1	Dijon
OFDI	chrX:g.13757151G>A	c.412G>A	p.Gly138Ser	1	Dijon
OFDI	chrX:g.13757139_13757142delGAAA	c.400_403delGAAA	p.Glu134Ilefs*10	4	Prattichizzo, 2008/Dijon/Del Giudice, 2014
OFDI	chrX:g.13757153delT	c.412+2delT		1	Prattichizzo, 2008
OFDI	chrX:g.13757152T>C	c.412+1T>C		1	Dijon
OFDI	chrX:g.?	c.382-?_412+?del		2	Dijon/Toriello, 2002
OFDI	chrX:g.13757118C>G	c.382-3C>G		2	Toriello, 2002
OFDI	chrX:g.13757153_13757156delTAGG	c.412+2_412+5delTAGG		1	Dijon
OFDI	chrX:g.13762524T>G	c.413-10T>G		1	Rakkolainen, 2002
OFDI	chrX:g.13762552dupT	c.431dupT	p.Leu144Phefs*154	1	Prattichizzo, 2008
OFDI	chrX:g.13762553_13762554insG	c.432_433insG	p.Lys145Glufs*10	1	Stoll, 2002
OFDI	chrX:g.13762552T>A	c.431T>A	p.Leu144*	1	Thauvin-Robinet, 2006
OFDI	chrX:g.13762575C>T	c.454C>T	p.Gln152*	1	Prattichizzo, 2008
OFDI	chrX:g.13762543T>G	c.422T>G	p.Met141Arg	1	Bisschoff, 2012
NR	chrX:g.13762579_13762580dup	c.458_459dupCT	p.Lys154Leufs	1	ClinVar
OFDI	chrX:g.13762629_13762630delGA	c.508_509delGA	p.Asp170Phefs*4	3	Bisschoff, 2012/Dijon
OFDI	chrX:g.13764437G>A	c. 518-1G>A		1	Bisschoff, 2012
OFDI	chrX:g.13764461dupG	c.541dupG	p.Asp181Glyfs*22	1	Bisschoff, 2012
OFDI	chrX:g.13764891A>G	c.655-8A>G		1	Dijon

OFDI	chrX:g.13764527_13764530delTATA	c.607_610delTATA	p.Tyr203Argfs*4	1	Bisschoff, 2012
OFDI	chrX:g.13764514_13764518delAAAGC	c.594_598delAAAGC	p.Leu200*	2	Prattichizzo, 2008
OFDI	chrX:g.13764522delA	c.602delA	p.Asn201Metfs*7	1	Prattichizzo, 2008
OFDI	chrX:g.13764535_13764540delAGAAA	c.615_620delAGAAA	p.Glu606_Ile607del	1	Thauvin-Robinet, 2006
OFDI	chrX:g.13764548C>T	c.628C>T	p.Glu210*	1	Prattichizzo, 2008
OFDI	chrX:g.13764573delA	c.653delA	p.Lys218Serfs*2	1	Prattichizzo, 2008
OFDI	chrX:g.13764536_13764537delGA	c.616_617delGA	p.Glu206Asnfs∗17	1	Prattichizzo, 2008
OFDI	chrX:g.13764536_13764540delGAAAT	c.616_620delGAAAT	p.Glu206Argfs*16	1	Dijon
OFDI	chrX:g.13764533_13764537delinsTAT	c.613_617delAGAGA	p.Arg205Tyrfs*18	1	Dijon
OFDI	chrX:g.13764534_13764537delGAGA	c.614_617delGAGA	p.Arg205Lysfs*1	1	Bisschoff, 2012
OFDI	chrX:g.13764576_13764578delTA	c.654+2_654+4delTA		1	Prattichizzo, 2008
OFDI	chrX:g.?	c.518-?_935+?del		1	Toriello, 2002
JBS	chrX:g.13764932_13764949del	c.688_705del	p.Ile230_Lys235del	1	Fiedl, 2012
OFDI	chrX:g.13764919delC	c.675delC	p.Glu226Argfs*2	1	Thauvin-Robinet, 2006
OFDI	chrX:g.13764955_13764956insA	c.711_712insA	p.Tyr238Ilefs*2	2	Romio, 2003/Dijon
OFDI	chrX:g.13764954dupA	c.710dupA	p.Tyr238Valfs*2	4	Bisschoff, 2012/Del Giudice, 2014
OFDI	chrX:g.13764951_13764963delAAAAGTATGAAAA	c.707_719 delAAAAGTATGAAAA	p.Lys236Argfs*3	1	Romio, 2003
OFDI	chrX:g.13764953_13764954delAA	c.709_710delAA	p.Lys237Valfs*2	1	Prattichizzo, 2008
OFDI	chrX:g.13764954delA	c.710delA	p.Lys237Serfs*6	2	Prattichizzo, 2008
OFDI	chrX:g.13764956delT	c.712delT	p.Lys238Metfs*5	1	Thauvin-Robinet, 2006
OFDI	chrX:g.13765034dupC	c.790dupG	p.Glu264Glyfs*6	1	Prattichizzo, 2008
OFDI	chrX:g.13765057_13765058insA	c.813_814insA	p.His272Thrfs*7	1	Dijon
OFDI	chrX:g.13765067C>T	c.823C>T	p.Gln275*	1	Prattichizzo, 2008
OFDI	chrX:g.13767072_13768501del	c.829-74_935+849del		1	Dijon
OFDI	chrX:g.13764954dupA	c.710dupA	p.Tyr238Valfs*1	7	Prattichizzo, 2008
OFDI	chrX:g.13767554_13767555delAA	c.837_838delAA	p.Lys280Argfs*28	1	Prattichizzo, 2008
OFDI	chrX:g.13767554_13767558delAAAAG	c.837_841delAAAAG	p.Lys280Asnfs*27	1	Prattichizzo, 2008
OFDI	chrX:g.13767556_13767557delAA	c.839_840delAA	p.Lys280Argfs*28	1	Prattichizzo, 2008
OFDI	chrX:g.13767560_13767561delAA	c.843_844delAA	p.Glu281Aspfs*27	1	Romio, 2003
OFDI	chrX:g.13767575delG	c.858delG	p.Arg286Serfs*5	1	Prattichizzo, 2008

OFDI	chrX:g.13767612_13767613insGA	c.895_896insGA	p.Ala301Lysfs*4	1	Dijon
OFDI	chrX:g.13767630_13767634delCAAAG	c.913_917delCAAAG	p.Gln305Serfs*2	1	Dijon
OFDI	chrX:g.13767631_13767632delAA	c.914_915delAA	p.Arg306Serfs*2	1	Del Giudice, 2014
OFDI	chrX:g.13767636delG	c.919delG	p.Val307Leufs*6	1	Thauvin-Robinet, 2006
JBS	chrX:g.13767589_13767594del	c.872_877del	p.Lys291_Asp292del	1	Kroes, 2016
OFDI	chrX:g.13767588A>T	c.871A>T	p.Lys291*	1	Prattichizzo, 2008
OFDI	chrX:g.13767612_13767613insGA	c.895_896insGA	p.Ala301Lysfs*4	1	Thauvin-Robinet, 2006
OFDI	chrX:g.13767615_13767616dupGA	c.898_899dupGA	p.Ala301Lysfs*4	1	Toriello, 2002
OFDI	chrX:g.13767594_13767595delAT	c.877_878delAT	p.Met293Glyfs*15	2	Prattichizzo, 2008/Dijon
OFDI	chrX:g.13767646T>C	c.929T>C	p.Phe310Ser	1	Alamillo, 2015
RP	chrX:g.13768358A>G	c.935+706A>G	p.Asn313fs*330	1	Webbl, 2012
OFDI	chrX:g.?	c.935+?_936-?		1	Morisawa, 2004
OFDI	chrX:g.?	c.936-?_1129+?del		1	Toriello, 2002
OFDI	chrX:g.13771487C>G	c.1056C>G	p.Asn352Lys	1	Prattichizzo, 2008
OFDI	chrX:g.13769481A>G	c.1051-2A>G		1	Prattichizzo, 2008
OFDI	chrX:g.13771485A>G	c.1056-2A>G		1	Dijon
OFDI	chrX:g.13771486G>A	c.1056-1G>A		1	Dijon
OFDI	chrX:g.13771485A>T	c.1056-2A>T		1	Romio, 2003
OFDI	chrX:g.13771502_13771509delinsTTTTTCCT	c.1071_1078delGAAG GATGinsTTTTTCCT	p.Lys358_Asp360 delinsPheSerTyr	1	Ferante, 2001
OFDI	chrX:g.13771490T>A	c.1059T>A	p.Tyr353*	1	Del Giudice, 2014
OFDI	chrX:g.13771492_13771496delAACTT	c.1061_1065delAACTT	p.Gln354Argfs*5	1	Dijon
OFDI	chrX:g.13771531G>A	c.1100G>A	p.Arg367Gln	1	Prattichizzo, 2008
OFDI	chrX:g.13771530C>T	c.1099C>T	p.Arg367*	4	Prattichizzo, 2008/ Del Giudice,
OFDI	chrX:g.13771559A>G	c.1128A>G	p.Lys376Lys	1	Del Giudice, 2014
OFDI	chrX:g.13771564A>T	c.1129+4A>T		1	Wentzensen, 2016
OFDI	chrX:g.13773250_13773253delAATT	c.1130-20_1130-17delAATT		1	Prattichizzo, 2008
OFDI	chrX:g.13773250_13773254delTTG	c.1130-20_1130-16delTTG		1	Bisschoff, 2012
OFDI	chrX:g.13773248_13773251delAATT	c.1130-22_1130-19delAATT		1	Toriello, 2002
OFDI	chrX:g.13771534_13771537delTGAT	c.1103_1106delTGAT	p.Ile369Lysfs*18	1	Dijon
OFDI	chrX:g.13773269G>A	c.1130-1G>A		2	Bisschoff, 2012/ Del Giudice, 2014

OFDI	chrX:g.13773330dupA	c.1190dupA	p.Asn397Lysfs*11	1	Bisschoff, 2012
OFDI	chrX:g.13773318dupA	c.1178dupA	p.Glu394Glyfs*14	1	Prattichizzo, 2008
OFDI	chrX:g.13773325delA	c.1185del A	p.Glu395Aspfs*6	1	Prattichizzo, 2008
OFDI	chrX:g.13773360_13773362delAGG	c.1220_1221+1delAGG	p.Glu407Alafs*408	1	Prattichizzo, 2008
OFDI	chrX:g.13773333_13773336delAATC	c.1193_1196delAATC	p.Gln398Leufs*2	6	Prattichizzo, 2008/ Del Giudice, 2014/ Dijon
OFDI	chrX:g.13773345G>A	c.1205G>A	p.Arg402His	1	Dijon
OFDI	chrX:g.13773362delG	c.1221+1delG		2	Toriello, 2002
OFDI	chrX:g.13774743_13774747delAAAAC	c.1268_1272delAAAAC	p.Gln423Profs*5	2	Prattichizzo, 2008
OFDI	chrX:g.13774778A>C	c.1303A>C	p.Ser435Arg	1	Ferrante, 2001
OFDI	chrX:g.13774793delC	c.1318delC	p.Leu440*	1	Prattichizzo, 2008
OFDI	chrX:g.13774794delT	c.1319delT	p.Leu440Glnfs*30	1	Prattichizzo, 2008
NR	chrX:g.13774807delA	c.1332delA	p.Lys444Asnfs*26	1	ClinVar
OFDI	chrX:g.13774797_13774801delAAGAA	c.1322_1326delAAGAA	p.Lys441Argfs*10	1	Prattichizzo, 2008
OFDI	chrX:g.13774798_13774801delAGAA	c.1323_1326delAGAA	p.Glu442Argfs*27	1	Prattichizzo, 2008
OFDI	chrX:g.13774809_13774810delTG	c.1334_1335delTG	p.Leu445Argfs*7	1	Prattichizzo, 2008
OFDI	chrX:g.13774833T>A	c.1358T>A	p.Leu453*	1	Prattichizzo, 2008
OFDI	chrX:g.13774835_13774838delCTTA	c.1360_1363delCTTA	p.Leu454Asnfs*15	1	Thauvin-Robinet, 2006
OFDI	chrX:g.13774884delA	c.1409delA	p.Asn470Thrfs*3	1	Rakkolainen, 2002
OFDI	chrX:g.13774880C>A	c.1405C>A	p.Leu469Ile	1	Dijon
OFDI	chrX:g.13774838_13774841delAAAC	c.1363_1366delAAAC	p.Lys455Asnfs*13	1	Bisschoff, 2012
OFDI	chrX:g.13775787C>T	c.1420C>T	p.Gln474*	1	Prattichizzo, 2008
OFDI	chrX:g.13775812_13775813delTT	c.1445_1446delTT	p.Phe482Serfs*14	1	Prattichizzo, 2008
OFDI	chrX:g.13775819_13775825delAGAACTA	c.1452_1458delAGAACTA	p.Lys484Asnfs*8	1	Prattichizzo, 2008
OFDI	chrX:g.13775835G>T	c.1468G>T	p.Glu490*	1	Bisschoff, 2012
OFDI	chrX:g.13776454A>C	c.1543-2A>C		1	Bean, 2013
OFDI	chrX:g.13776500delA	c.1587delA	p.Ala530Leufs*3	1	Thauvin-Robinet, 2006
OFDI	chrX:g.13776517dupT	c.1604dupT	p.Leu535Phefs*22	1	Dijon
OFDI	chrX:g.13776500delA	c.1587delA	p.Ala530Leufs*3	1	Dijon
OFDI	chrX:g.13776526_13776533delinsTTTACA	c.1613_1620delinsTTTACA	p.Gln538Leufs*18	1	Dijon
OFDI	chrX:g.13776525C>T	c.1612C>T	p.Gln538*	1	Bisschoff, 2012

OFDI	chrX:g.13778336delG	c.1757delG	p.Ser586Metfs*5	1	Ferrante, 2001
OFDI	chrX:g.13778363A>G	c.1784A>G	p.Lys595Arg	1	Dijon
OFDI	chrX:g.13778400delG	c.1821delG	p.Ile608Serfs*21	1	Thauvin-Robinet, 2006
OFDI	chrX:g.13778466_13778467insAT	c.1887_1888insAT	p.Asn630Ilefs*37	1	Rakkolainen, 2002
OFDI	chrX:g.13778623dupA	c.2044dupA	p.Ile682Asnfs*19	1	Prattichizzo, 2008
OFDI	chrX:g.13778635delT	c.2056delT	p.Ser686Profs*32	1	Prattichizzo, 2008
OFDI	chrX:g.13778701_13778704dupAAGA	c.2122_2125dupAAGA	p.Glu709Glyfs*5	1	Budny, 2006
OFDI	chrX:g.13778755delC	c.2176delC	p.Arg726Alafs*91	1	Prattichizzo, 2008
OFDI	chrX:g.13778457del	c.1878del	p.Glu626Aspfs*3	1	Dijon
OFDI	chrX:g.13778438_13778439delinsG	c.1859_1860delCCinsG	p.Ser620Cysfs*8	1	Bisschoff, 2012
OFDI	chrX:g.13778558_13778559delCT	c.1979_1980delCT	p.Ser660Cysfs*39	2	Prattichizzo, 2008
OFDI	chrX:g.13778762del	c.2183del	p.Gly728Alafs*8	1	Diz, 2011
OFDI	chrX:g.13778419delG	c.1840delG	p.Ala614Hisfs*15	2	Darmency-Stamboulal, 2013/Diion
OFDI	chrX:g.13778569dupC	c.1990dupC	p.Leu665Thrfs*35	1	Bisschoff, 2012
OFDI/SGBS2	chrX:g.13778702_13778705dupAAGA	c.2123_2126dupAAGA	p.Asn711Lysfs*3	2	Budny, 2006/Toriello, 2002
OFDI	chrX:g.13785404delG	c.2757+1delG		1	Al-Gazali, 2015
OFDI	chrX:g.13779203G>T	c.2261-1G>T		1	Prattichizzo, 2008
OFDI	chrX:g.13779292delC	c.2349delC	p.Ile784Serfs*33	1	Thauvin-Robinet, 2006
OFDI	chrX:g.13779409_13779410insT	c.2387+79_2387+80insT		1	Dijon
OFDI	chrX:g.?	c.?_2261_2387_?del		2	Toriello, 2002/ Dijon
OFDI / JBS	chrX:g.13786182delG	c.2767delG	p.Glu923Lysfs*4	2	Coene, 2009/Toriello, 2002
OFDI / JBS	chrX:g.13786256_13786262delAAAAGAC	c.2841_2847delAAAAGAC	p.Lys948Asnfs*9	2	Coene, 2009/Toriello, 2002
OFDI	chrX:g.16740_20819del	Del exons 7 à 9		1	Morisawa, 2004
OFDI	chrX:g.?	délétion du gène		1	Bisschoff, 2012
OFDI	chrX:g.?	délétion du gène		1	Bisschoff, 2012
OFDI	chrX:g.?	c.1-?_655+?del		1	Dijon
OFDI	chrX:g.?	c.(?_-360)_828+?del		1	Toriello, 2002
OFDI	chrX:g.?	c.(?_-3311)_1542+?del		1	Toriello, 2002
OFDI	chrX:g.?	c.1222-?_1542+?del		1	Dijon
OFDI	chrX:g.?	c.1222-?_3038+?del		1	Toriello, 2002

OFDI	chrX:g.?	c.1-?_1542+?del	1	Dijon
OFDI	chrX:g.?	c.1056-?_1221+?del	1	Dijon
OFDI	chrX:g.?	del 19bp	2	Ferrante, 2001/ Scolari, 1997
OFDI	chrX:g.?	Del exon 11	1	Del Giudice, 2014
OFDI	chrX:g.?	Del exons 7 à 10	1	Del Giudice, 2014
OFDI	chrX:g.?	NM_003611:c.382-411+?del	1	Dijon

CCP : Syndrome Côtes Courtes-Polydactylie, JBS : Syndrome de Joubert, N : Nombre de cas index rapporté, NC : Nevus Comedonicus, NPHP : Néphronophtise, NR : Non Renseigné, OFD : syndrome Oro-Facio-Digital, RP Rétine Pigmentaire, SGBS2 : Syndrome de Simpson-Golabi-Behmel

Annexe 3 : Liste non exhaustive des protéines du centrosome et du cil primaire.

AADACL2	ACSS2	AIPL1	ANXA2	ARL9	ATP6V0D1	BRAF	ACSL6
AARS	ACTA1	AK1	ANXA3	ARMC2	ATP6V0D2	BRP44	ACSS1
AARSD1	ACTA2	AK2	ANXA4	ARMC3	ATP6V1A	BRSK1	C4orf47
AASDHPPT	ACTB	AK3	ANXA5	ARMC4	ATP6V1B1	BSCL2	C5orf42
ABCA13	ACTBL2	AK4	ANXA6	ARNTL	ATP6V1B2	BTF3	C5orf49
ABCA3	ACTC1	AK5	ANXA7	ARPC1A	ATP6V1C1	BTF3L4	C6
ABCA4	ACTG1	AK7	ANXA8	ARPC2	ATP6V1C2	BTF3L4P4	C6orf118
ABCB1	ACTG2	AK8	ANXA8L1	ARPC3	ATP6V1D	BUB3	C6orf165
ABCB11	ACTL6A	AKAP9	ANXA8L2	ARPC4	ATP6V1E1	BZW1	C6orf168
ABCB4	ACTL6B	AKAP14	AP1B1	ARPC5	ATP6V1F	BZW2	C6orf211
ABCB5	ACTL7A	AKNA	AP1M2	ARPC5L	ATP6V1G1	C2CD3	C7orf57
ABCC1	ACTL7B	AKR1A1	AP1S3	Arpm1	ATP6V1G2	C5AR1	C7orf63
ABCC10	ACTL8	AKR1B1	AP2B1	ARRDC1	ATP8A1	C1orf114	C8orf37
ABCC11	ACTL9	AKR1C1	AP3B1	ARRDC2	ATP8A2	C1orf158	C8orf47
ABCC2	ACTN1	AKR1C2	AP3B2	ARRDC3	ATP8B1	C1orf173	C8orf55
ABCC3	ACTN4	AKR1CL1	AP3D1	ARRDC4	ATP8B3	C1orf192	C9orf116
ABCC4	ACTR1A	AKR1E2	AP3M1	ARVCF	ATP9A	C1orf87	C9orf117
ABCC6	ACTR1B	AKT1	AP3M2	AS3MT	ATXN10	C1orf88	C9orf135
ABCC8	ACTR2	AKT2	AP4S1	ASAH1	ATXN2	C1orf93	C9orf24
ABCC9	ACTR3	AKT3	APAF1	ASAP1	AUH	C10orf107	C9orf68
ABCD2	ACTR3B	AKTIP	APEX1	ASNA1	AURKA	C10orf58	C9orf9
ABCD3	ACTR3C	ALCAM	APOBEC4	ASNS	AURKB	C10orf76	C1QBP
ABCE1	ACTRT1	ALDH1A1	APOE	ASPG	AURKC	C11orf16	C1QTNF9
ABCF1	ACTRT2	ALDH1A2	APRT	ASRGL1	AVIL	C11orf2	C1QTNF9B
ABCF2	ACY1	ALDH1A3	AQP1	ATAD1	AWAT1	C11orf54	CA10
ABCF3	ACYP1	ALDH18A1	AQP4	ATAD3A	AZI1	C11orf65	CA12
ABCG1	ADAMTS8	ALDH2	AQP5	ATAD3B	B3GNT1	C11orf70	CA13
ABCG2	ADCK1	ALDH3A1	ARF1	ATAD3C	B3GNT6	C11orf74	CA14
ABCG4	ADCK5	ALDH3A2	ARF3	ATAT1	B4GALT1	C11orf88	CA2
ABHD12B	ADGB	ALDH3B1	ARF4	ATF3	B9D1	C13orf26	CA6
ABHD14B	ADCY3	ALDH3B2	ARF5	ATG2B	B9D2	C14orf142	CA7
ABHD5	ADH1A	ALDH5A1	ARF6	ATIC	BAG1	C14orf149	CA8
ABHD6	ADH1B	ALDH8A1	ARFGEF1	ATP11A	BAIAP3	C14orf166	CABP1
ABI1	ADH4	ALDOA	ARFRP1	ATP11B	BBS1	C14orf166B	CABP2
ABL2	ADH5	ALDOB	ARHGAP18	ATP13A5	BBS10	C14orf45	CABP4
ABLIM1	ADH6	ALDOC	ARHGAP1	ATP1A1	BBS12	C14orf79	CABP5
ABLIM2	ADH7	ALK	ARHGAP5	ATP1A2	BBS2	C15orf26	CACNA1G
ABLIM3	ADRB1	ALMS1	ARHGEF11	ATP1A3	BBS4	C16orf46	CACNA1H
ACAA1	ADPGK	ALG2	ARIH2	ATP1A4	BBS5	C16orf48	CACNA1I
ACACA	ADSS	ALPL	ARL10	ATP1B1	BBS7	C16orf62	CACNA2D1
ACAD9	ADSSL1	ALS2	ARL11	ATP1B2	BBS9	C16orf80	CACNA2D2
ACBD3	AFG3L2	ANKHD1	ARL13B	ATP1B3	BCAP29	C2CD2L	CACNA2D3
ACADM	AGAP1	ANKRD17	ARL14	ATP2A1	BCAP31	C2orf40	CACNA2D4
ACADS	AGAP2	ANKRD26	ARL15	ATP2A2	BCAS2	C2orf71	CACNB1
ACADSB	AGBL1	ANKRD28	ARL16	ATP2A3	BCAT1	C2orf73	CACNB2
ACAT1	AGBL2	ANKRD44	ARL17A	ATP2B1	BCL11A	C2orf77	CACNB4
ACAT2	AGBL3	ANKRD45	ARL17B	ATP2B2	BCO2	C20orf26	CACYBP
ACHE	AGBL4	ANKRD52	ARL3	ATP2B3	BDH1	C20orf85	CAD
ACLY	AGR2	ANO1	ARL4A	ATP2B4	BDH2	C20orf3	CADPS
ACOX1	AGR3	ANO2	ARL4C	ATP2C1	BET3L	C21orf2	CADPS2
ACR	AHI1	ANP32A	ARL4D	ATP2C2	BEST4	C21orf58	CALM1
ACSBG1	AHCY	ANP32B	ARL4P	ATP5A1	BIRC3	C21orf59	CALM2
ACSL1	AHCYL1	ANP32E	ARL5A	ATP5B	BLK	C22orf23	CALM3
ACSL3	AHCYL2	ANPEP	ARL5C	ATP5C1	BLOC1S2	C22orf28	CALML3
ACSL5	AHRR	ANUBL1	ARL6	ATP5L	BMPR1B	C3orf15	CALML4

CALR	AIMP2	ANXA1	ARL8A	ATP5O	BPIFA1	C4orf22	CALML5
CALU	AIP	ANXA11	ARL8B	ATP5S	BPTF	C4orf41	CALML6
CAMK1	CAMK2A	CCDC42	CDKL2	CHEK1	CNNM2	CRYM	RSPH6A
CAMK1D	CAMK2B	CCDC42B	CDKL3	CHEK2	CNNM3	CSDA	RSPH9
CAMK1G	CAMK2D	CCDC47	CDKL4	CHL1	CNNM4	CSE1L	RTDR1
CYP2G1P	CAMK2G	CCDC51	CDS1	CHMP4B	CNOT1	CSK	RTN1
CYP2J2	CAMK4	CCDC60	CDS2	CHORDC1	CNOT2	CSNK1A1	RTN3
CYP2R1	CAMKV	CCDC61	CDYL	Chp	CNOT3	CSNK1A1L	RTN4
CYP2S1	CAMSAP1	CCDC63	CELA1	chp2	CNOT6	CSNK2B	RTTN
CYP2U1	CAMSAP2	CCDC65	CELA2A	CHPT1	CNOT6L	CSNK1D	RUVBL1
CYP2W1	CAND1	CCDC77	CELA2B	CHRNA1	CNP	CSNK1E	RUVBL2
CYP3A4	CANX	CCDC78	CELA3A	CHRNA2	CNPY3	CSNK1G1	RYR1
CYP3A43	CAP1	CCDC81	CELA3B	CHRNA3	CNRIP1	CSNK1G2	RYR2
CYP3A5	CAPN1	CCDC89	CELSR1	CHRNA4	CNTNAP1	CSNK1G3	RYR3
CYP3A7	CAPN10	CCDC96	CELSR2	CHRNA5	CNTNAP2	CSNK2A1	SACM1L
CYP4B1	CAPN11	CCNA1	CELSR3	CHRNA6	CNTRL	CSNK2A2	SAR1A
CYP4F11	CAPN12	CCND1	CENPA	CHRNB1	CNTROB	CSNK2B	SAR1B
CYP4F8	CAPN13	CCNO	CENPJ	CHRNB2	COG4	CSPP1	SARM1
CYP4X1	CAPN14	CCT2	CEP104	CHRNB3	COL15A1	CTBP1	SARS
CYP4Z1	CAPN2	CCT3	CEP120	CHRNB4	COL18A1	CTBP2	SASS6
DAAM1	CAPN3	CCT4	CEP126	CHRND	COMT	CTDSP1	SAXO2
DAB2IP	CAPN5	CCT5	CEP131	CHRNE	COMTD1	CTDSPL2	SCAMP1
DACH1	CAPN6	CCT6A	CEP135	CHRNG	COPA	CTNNA1	SCAPER
DAGLA	CAPN8	CCT7	CEP164	CHST5	COPB1	CTNNA2	SCARB1
DAGLB	CAPN9	CCT8	CEP19	CHST9	COPB2	CTNNA3	SCCPDH
DAPK2	CAPS	CD36	CEP250	CIB1	COPE	CTNNB1	SCD5
DAPK3	CAPSL	CD55	CEP290	CIRBP	COPG	CTNND1	SCFD1
DARS	CAPZA1	CD81	CEP350	CISD1	COPS4	CTNND2	SCGB2A1
DAW1	CAPZB	CD9	CEP41	CISD2	CORO1A	CTR9	SCLT1
DAZAP1	CARS	CDA	CEP72	CKAP4	CORO1B	CTRB1	SCRT1
DBNL	CASC1	CDC14A	CEP78	CKAP5	CORO1C	CTRB2	SCYL1
DBT	CASK	CDC14B	CEP83	CKB	CORO2A	CTRC	SDCCAG8
DCAKD	CAT	CDC27	CEP89	CKM	CORO2B	CTRL	SDHB
DCDC2	CBR1	CDC37	CEP97	CKMT1A	CORO6	CTSB	SDK1
DCDC2B	CBR4	CDC42	CERS2	CKMT1B	COTL1	CTSC	SDR16C5
DCDC5	CBS	CDC42BPA	CERS3	CKMT2	COX5B	CTSK	SEC11A
DCLK1	CBX5	CDC42BPB	CERS4	CLASP1	CP	CTSS	SEC11C
DCLK2	CBY1	CDC5L	CERS5	CLASP2	CCP110	CTSZ	SEC14L2
DCTN1	CC2D2A	CDC7	CERS6	CLDN2	CPB2	CUL1	SEC14L3
DCTN2	CCDC103	CDC73	CES1	CLGN	CPD	CUL2	SEC14L4
DCTN3	CCDC104	CDH23	CES2	CLIC1	CPE	CUL3	SEC14L5
DCTN4	CCDC108	CDHR3	CES3	CLIC2	CPM	CUL4A	SEC14L6
DCXR	CCDC11	CDIPT	CES4A	CLIC3	CPNE1	CUTC	SEC22A
DDAH1	CCDC113	CDK1	CES5A	CLIC4	CPNE2	CXorf22	SEC22C
DDAH2	CCDC114	CDK10	CETN1	CLIC5	CPNE3	CXorf41	SEC23A
DDB1	CCDC132	CDK11A	CETN2	CLIC6	CPNE5	CYB5A	SEC23B
DDOST	CCDC135	CDK13	CETN3	CLINT1	CPNE8	CYB5D1	SEC23B
DDR1	CCDC146	CDK14	CFAP20	CLPTM1L	CPNE9	CYCS	SEC23IP
DDR2	CCDC147	CDK15	CFAP36	CLPX	CPO	CYFIP1	SEC24B
DDX1	CCDC151	CDK16	CFAP43	CLRN1	CPZ	CYFIP2	SEC24C
DDX11	CCDC164	CDK17	CFAP44	CLTC	CRABP1	CYP1A1	SEC31A
DDX17	CCDC17	CDK18	CFAP45	CLTCL1	CRB3	CYP1A2	SEC61A1
DDX19A	CCDC170	CDK19	CFAP46	CLU	CRBN	CYP1B1	SEC61A2
DDX19B	CCDC173	CDK2	CFAP52	CLUAP1	CRHR2	CYP2A13	SEC62
DDX23	CCDC176	CDK20	CFAP53	CMPK1	CRISP2	CYP2A7	SEC63
DDX25	CCDC180	CDK4	CFAP58	CNDP1	CRISP3	CYP2B6	SELE
DDX28	CCDC19	CDK5	CFAP61	CNDP2	CRMP1	CYP2C18	SELENBP1

DDX3X	CCDC28B	CDK5RAP2	CFAP69	CNGA2	CRNKL1	CYP2C19	SEPSECS
DDX39A	CCDC37	CDK6	CFAP70	CNGA4	CROCC	CYP2C8	SEPT1
DDX39B	CCDC39	CDK7	CFAP74	CNGB1	CRYAA	CYP2C9	SEPT10
DDX39B	CCDC40	CDK8	CFD	CNN3	CRYAB	CYP2E1	SEPT11
DDX3Y	CCDC41	CDKL1	CFL1	CNNM1	CRYL1	CYP2F1	SEPT12
DDX4	DDX53	DNAH9	DVL1	EIF2C1	EPHB2	FAM179A	SEPT14
DDX43	DDX55	DNAI1	DYDC1	EIF2C2	EPB41	FAM179B	SEPT2
DDX5	DDX59	DNAI2	DYDC2	EIF2C3	EPB41L1	FAM188B	SEPT3
FSD1	DDX6	DNAJA1	DYNC1H1	EIF2C4	EPB41L2	FAM216B	SEPT4
FSD1L	DDX60L	DNAJA2	DYNC1I1	EIF2S1	EPHX1	FAM3B	SEPT5
FTSJ3	DECR1	DNAJA4	DYNC1LI1	EIF2S2	EPN1	FAM46C	SEPT6
FUBP1	DECR2	DNAJB1	DYNC2H1	EIF2S3	EPN2	FAM49B	SEPT7
FUBP3	DEGS1	DNAJB11	DYNC1I2	EIF3A	EPRS	FAM63A	SEPT7P2
FUT4	DENND4A	DNAJB13	DYNC2LI1	EIF3B	EPS15L1	FAM76B	SEPT8
FUZ	DENND5A	DNAJB2	DYNC2LI2	EIF3C	EPS8	FAM81B	SEPT9
FXR1	DENND5B	DNAJB4	DYNC2H1	EIF3CL	ERAP1	FAM82A1	SERBP1
FXR2	DFNB31	DNAJB5	DYNLL1	EIF3E	ERAP2	FAM82A2	SERPINA3
FYN	DGKI	DNAJB6	DYNLL1P1	EIF3F	ERAS	FAM98B	SERPINB1
G3BP1	DHCR7	DNAJC12	DYNLL2	EIF3H	ERBB2IP	FANK1	SERPINB10
G6PD	DHFR	DNAJC2	DYNLRB1	EIF3I	ERC1	FARP2	SERPINB12
GABBR1	DHFRL1	DNAJC27	DYNLRB2	EIF3L	ERC2	FARSA	SERPINB13
GABRB2	DHRS2	DNAJC3	DYNLT1	EIF3M	ERGIC1	FARSB	SERPINB2
GABRB3	DHRS3	DNAJC5	DYNLT3	EIF4A1	ERICH3	FASN	SERPINB3
GABRP	DHRS4	DNAJC6	DYRK1A	EIF4A2	ERICH5	FBL	SERPINB4
GABRR1	DHRS7	DNAI1	DYRK1B	EIF4A3	ERLIN1	FBLL1	SERPINB6
GALNT1	DHRS7B	DNAI2	DYRK2	EIF4E1B	ERLIN2	FBLN2	SERPINB8
GALNT13	DHRS4L2	DNAL1	DYRK3	EIF4E2	ERN2	FBF1	SERPINB9
GALNT14	DHRSX	DNAL4	DYSF	EIF4E3	ERO1LB	FBXL13	SERPINC1
GALNT3	DHX30	DNALI1	DYX1C1	EIF4G2	ERP29	FBXO15	SERPINH1
GALNT8	DHX34	DNM1	DZANK1	EIF4G3	ERP44	FEM1A	SERPINI2
GALNTL1	DHX36	DNM1L	DZIP1L	EIF4E	ESD	FEM1B	SETD6
GALR2	DHX9	DNM2	DZIP3	EIF4G1	ESF1	FEM1C	SF3A1
GAPDH	DIAPH2	DNM3	EBNA1BP2	EIF4H	ESRRG	FEZ1	SFN
GAPDHP31	DIP2A	DOCK1	ECE2	EIF5A	ESYT1	FGR	SFPQ
GAPDHS	DIP2B	DOCK2	ECHS1	EIF5A2	ETF1	FGFR1	SFRS13A
GARS	DIP2C	DOCK3	ECI2	EIF5B	ETFA	FGFR1OP	SGK1
GART	DIRAS1	DOCK4	EDC4	EIF6	ETFB	FGFR2	SGK2
GAS8	DIRAS2	DOCK7	EEF1A1	ELAVL1	EVC	FGFR3	SGK196
GBAS	DIRAS3	DOCK8	EEF1A2	ELMO2	EVC2	FGFR4	SGK3
GBE1	DISC1	DOCK9	EEF1B2	ELMOD1	EVL	FHAD1	SGMS1
GBF1	DIRAS3	DOPEY1	EEF1D	ELMOD2	EXOC2	FHL5	SGMS2
GCA	DKC1	DOPEY2	EEF2	ELOVL4	EXOC3	FHOD3	SGPL1
GCAT	DLEC1	DPCD	EEFSEC	EML1	EXOC4	FKBP11	SH3BGR
GCLM	DLG1	DPH2	EFCAB1	EML3	EXOC5	FKBP1A	SH3BGRL
GCN1L1	DLG2	DPM1	EFCAB10	EML4	EXOC6	FKBP1B	SH3BGRL2
GDA	DLG3	DPP6	EFCAB12	EML5	EXOC6B	FKBP1C	SHC2
GDAP1	DLG4	DPY30	EFCAB2	EML6	EXOC7	FKBP2	SHC4
GDF5	DMBT1	DPYSL2	EFCAB4B	EMX2	EXOG	FKBP3	SHH
GDI1	DMD	DPYSL4	EFCAB6	ENAH	EYA1	FKBP4	SHMT1
GDI2	DMXL1	DRC1	EFCAB7	ENDOU	EZR	FKBP7	SHMT2
GEM	DMXL2	DRC7	EFHA2	ENKUR	FAAH	FLAD1	SIK3
GFAP	DNAAF1	DRD1	EFHB	ENO1	FABP12	FLII	SKIV2L2
GFER	DNAAF2	DRD2	EFHC1	ENO2	FABP3	FLNA	SKP1
GGT1	DNAAF3	DRD5	EFHC2	ENO3	FABP5	FLNB	SLA2
GGT2	DNAH1	DRG1	EFR3A	ENPP1	FABP6	FMR1	SLC1A1
GGT7	DNAH10	DRG2	EFR3B	ENPP3	FABP7	FMO1	SLC1A2
GIGYF2	DNAH11	DSP	EFTUD2	ENTPD1	FAHD1	FMO3	SLC1A3

GIT1	DNAH12	DST	EHHADH	ENTPD5	FAHD2A	FMO5	SLC1A4
GLB1L	DNAH17	DSTN	EIF1	ENTPD6	FAHD2B	FMO6P	SLC1A5
GLB1L2	DNAH2	DTHD1	EIF1B	EP300	FAIM	FOPNL	SLC1A6
GLG1	DNAH3	DTWD1	EIF2A	EPHA10	FAIM2	FOXJ1	SLC1A7
GLI1	DNAH5	DUS4L	EIF2B2	EPHA3	FAM114A2	FOXO6	SLC12A2
GLI2	DNAH6	DUSP1	EIF2B3	EPHA4	FAM120C	FOXQ1	SLC12A8
GLI3	DNAH7	DUSP28	EIF2	EPHA7	FAM161A	FRY	SLC16A1
GLIPR2	DNAH8	DUSP3	EIF2C1B5	EPHB1	FAM164A	FRYL	SLC16A11
GLIS2	GLRX	GRIA2	H3F3C	HIST1H4G	HS2ST1	IFT172	SLC16A13
GLRA3	GLRXP3	GRIA3	HADHA	HIST1H4J	HSD11B2	IFT52	SLC16A6
GLRA4	GLTP	GRIA4	HADHB	HIST1H4K	HSD17B10	IFT57	SLC16A7
KCNA4	GLUD1	GRIK3	HAP1	HIST1H4L	HSD17B11	IFT74	SLC17A2
KCNC2	GLUD2	GRIK5	HARS	HIST2H2AA3	HSD17B12	IFT80	SLC17A6
KCNC3	GLUL	GRINA	HARS2	HIST2H2AA4	HSD17B13	IFT81	SLC17A7
KCNC4	GMFB	GRIP2	HCFC2	HIST2H2AB	HSD17B14	IFT88	SLC17A8
KCND1	GMPPA	GRK1	HCK	HIST2H2AC	HSD17B3	IK	SLC2A1
KCND2	GMPPB	GRK4	HDLBP	HIST2H2BE	HSD17B4	IKBKAP	SLC2A13
KCND3	GMPR	GRK5	HEATR1	HIST2H2BF	HSD17B8	ILF2	SLC2A2
KCNF1	GNA11	GRK6	HEATR2	HIST2H3A	HSDL1	ILVBL	SLC20A1
KCNG1	GNA12	GRK7	HEATR5A	HIST2H3C	HSP90AA1	IMMT	SLC20A2
KCNG2	GNA13	GSK3A	HEATR5B	HIST2H3D	HSP90AB1	IMPA1	SLC22A15
KCNG3	GNA14	GSK3B	HERC6	HIST2H3PS2	HSP90B1	IMPDH1	SLC22A4
KCNG4	GNAI1	GSN	HERC2	HIST2H4A	HSP90AB3P	IMPDH2	SLC23A1
KCNH1	GNAI2	GSPT1	HEXA	HIST2H4B	HSPA1A	INPP5E	SLC23A2
KCNH2	GNAI3	GSPT2	HIBCH	HIST3H2A	HSPA1B	INSR	SLC24A1
KCNH5	GNAO1	GSTA1	HINT1	HIST3H2BB	HSPA1L	INTU	SLC24A3
KCNH6	GNAQ	GSTA2	HINT2	HIST3H3	HSPA12A	INVS	SLC24A6
KCNH7	GNAS	GSTA3	HIPK4	HIST3H4	HSPA12B	IPO5	SLC25A10
KCNIP1	GNAT1	GSTA4	HIST1H2A	HKDC1	HSPA13	IPO7	SLC25A11
KCNIP2	GNAT2	GSTA5	A	HLA-B	HSPA14	IQCA1	SLC25A12
KCNIP4	GNAT3	GSTM1	HIST1H2AB	HLA-C	HSPA2	IQCB1	SLC25A3
KCNJ1	GNAZ	GSTM2	HIST1H2AC	HLA-DRB1	HSPA4	IQCD	SLC25A30
KCNJ10	GNB1	GSTM3	HIST1H2A	HLA-DRB3	HSPA4L	IQCG	SLC25A31
KCNJ11	GNB2	GSTM4	D	HLA-DRB5	HSPA5	IQCH	SLC25A35
KCNJ13	GNB3	GSTM5	HIST1H2AE	HLA-F	HSPA6	IQCK	SLC25A4
KCNJ14	GNB4	GSTO1	HIST1H2A	HLF	HSPA8	IQGAP1	SLC25A5
KCNJ15	GNB2L1	GSTO2	G	HNF1B	HSPA9	IQGAP2	SLC25A6
KCNJ16	GNB5	GSTP1	HIST1H2A	HMGB1	HSPB1	IQUB	SLC26A2
KCNJ2	GNL1	GSTT1	H	HMGB1P1	HSPB2	IRX3	SLC27A1
KCNJ3	GOLGA2	GSTT2	HIST1H2AI	HMGB1P5	HSPB11	ISCA1	SLC27A2
KCNJ6	GOLGA3	GSTT2B	HIST1H2AJ	HMGB2	HSPB6	ISCA2	SLC27A4
KCNJ8	GOLGA5	GTF2H4	HIST1H2AK	HMGB3	HSPD1	ISOC2	SLC27A5
KCNRG	GOT1L1	GTPBP1	HIST1H2AL	HMGB3P22	HSPH1	ITPA	SLC3A2
KCNS1	GOSR1	GTPBP2	HIST1H2A	HNRNPA1	HTR1B	ITGAV	SLC30A1
KCNS2	GOT1	GUCA1A	M	HNRNPA3	HTR6	ITPR1	SLC30A5
KCNS3	GOT2	GUCA1B	HIST1H2BA	HNRNPAB	HTT	ITPR2	SLC33A1
KCNV1	GPAM	GUCA1C	HIST1H2BB	HNRNPK	HUNK	ITPR3	SLC35C2
KCTD17	GPC4	GUCY1A2	HIST1H2BC	HNRNPM	HUWE1	ITSN1	SLC4A1
KCTD8	GPD1L	GUCY1A3	HIST1H2B	HNRNPR	HYDIN	ITSN2	SLC4A10
KDELR1	GPD2	GUCY1B2	D	HNRNPU	HYLS1	IVNS1ABP	SLC4A4
KDELR2	GPI	GUCY1B3	HIST1H2BE	HNRNPUL1	HYOU1	JPH2	SLC4A5
KEAP1	GPM6A	GUK1	HIST1H2BF	HNRNPUL2	IARS	JUP	SLC4A7
KHSRP	GPM6B	GZMA	HIST1H2B	HOOK1	ICA1L	KANSL1	SLC4A8
KIAA0090	GPR161	GZMK	G	HOXA1	ICK	KANSL2	SLC44A4
KIAA0586	GPR173	GZMM	HIST1H2BI	HOXB1	IDE	KARS	SLC44A4
KIAA0319	GPR20	H2AFB1	HIST1H2BJ	HOXB8	IDH1	KAT5	SLC47A2
KIAA0368	GPR98	H2AFB2	HIST1H2BL	HPCA	IDH2	KATNA1	SLC6A11

KIAA0753	GPSM2	H2AFB3	HIST1H2B	HPCAL1	IDH3A	KATNAL2	SLC6A12
KIAA1009	GPX1	H2AFV	M	HPCAL4	IDH3B	KBTBD10	SLC6A13
KIAA1217	GPX2	H2AFX	HIST1H2B	HPD	IDH3G	KBTBD8	SLC6A2
KIAA1324	GPX3	H2AFY	N	HPGD	IDO1	KCNA1	SLC6A6
KIF1A	GPX4	H2AFZ	HIST1H2B	HPGDS	IFIT1	KCNA10	SLC6A8
KIF1B	GPX5	H2BFM	O	HPRT1	IFIT3	KCNA2	SLC6A9
KIF11	GPX6	H2BFWT	HIST1H3C	HRAS	IFT122	KCNA3	SLC7A8
KIF12	GPX7	H3F3A	HIST1H3A	HRASLS2	IFT140	KCNA5	SLC8A1
KIF14	GPX8	H3F3AP3	HIST1H3B	HRSP12	IFT20	KCNA6	SLC8A2
KIF17	GRB2	H3F3AP6	HIST1H3D	HSBP1	IFT27	KCNA7	SLC8A3
KIF18B	GRHL1	H3F3B	HIST1H3E	HSBP1P2	IFT43	KCNB1	SLC9A3R1
KIF19	KIF16B	HADH	HIST1H3H	HSD11B1	IFT46	KCNC1	SLCO4C1
KIF2A	KIF21A	KRT2	HIST1H3I	MAPK8	MLLT4	MYLPF	SLFN13
KIF2B	KIF22	KRT3	HIST1H3J	MAPK9	MLYCD	MYO1B	SLITRK6
KIF2C	KIF23	KRT37	HIST1H4A	MAPKAPK2	MMAB	MYO1C	SLK
NEK2	KIF24	KRT38	HIST1H4B	MAPKAPK3	MME	MYO1D	SMAD9
NEK4	KIF27	KRT5	HIST1H4C	MAPKAPK5	MMP17	MYO1F	SLMAP
NEK5	KIF3A	KRT6A	HIST1H4D	MAPK6PS4	MMP25	MYO1G	SMARCA2
NEK6	KIF3B	KRT6B	HIST1H4E	MAPT	MNS1	MYO1H	SMARCA4
NEK7	KIF3C	KRT6C	HIST1H4F	MAPRE1	MOGS	MYO15A	SMARCE1
NEK8	KIF5B	KRT72	HIST1H4H	MAPRE2	MOK	MYO16	SMC1A
NEO1	KIF5C	KRT73	HIST1H4I	MAPRE3	MORN1	MYO18B	SMC3
NF2	KIF6	KRT74	LRRC18	MARCKS	MORN3	MYO3A	SMEK2
NGFR	KIF7	KRT75	LRRC20	MARK1	MORN5	MYO3B	SMG1
NIN	KIF9	KRT79	LRRC23	MARK2	MOS	MYO5A	SMO
NINL	KIFAP3	L2HGDH	LRRC34	MARK3	MPDU1	MYO5B	SMPD2
NIPSNAP1	KIFC1	LACTB2	LRRC40	MARK4	MPP1	MYO5C	SMYD1
NIPSNAP3A	KIFC3	LAMB1	LRRC45	MARS	MPP2	MYO6	SMYD2
NIPSNAP3B	KLC1	LAP3	LRRC46	MAS1	MPP4	MYO7A	SMYD3
NKIRAS1	KLC2	LARP1	LRRC48	MAT1A	MPP6	MYOF	SNAP23
NKIRAS2	KLC3	LARP1B	LRRC57	MAT2A	MPPED1	MZT2A	SNAP25
NKX3-1	KLHDC9	LATS1	LRRC59	MATR3	MPPED2	MZT2B	SNAP29
NLGN2	KLHL1	LATS2	LRRC6	MBOAT1	MPST	NAA15	SNAP91
NLGN3	KLHL10	LBR	LRRC71	MBOAT7	MRAS	NAA16	SNCG
NLGN4X	KLHL12	LCA5	LRRK1	MCCC1	MROH9	NACA	SND1
NLGN4Y	KLHL17	LCK	LRRIQ3	MCF2L	MRPL4	NACA3P	SNRNP200
NLK	KLHL18	LCLAT1	LRGUK	MCHR1	MS4A8B	NAP1L1	SNRPD2
NLN	KLHL13	LCP1	LRTOMT	MCM4	MSI1	NAP1L2	SNTB2
NME1	KLHL2	LDHA	LSM2	MCM6	MSI2	NAP1L4	SNX1
NME2	KLHL20	LDHAL6A	LTN1	MCRS1	MSN	NAPA	SNX10
NME2P1	KLHL22	LDHAL6B	LUC7L	MDH1	Mst4	NAPB	SNX2
NME3	KLHL23	LDHB	LUC7L2	MDH1B	MT3	NAPEPLD	SOD1
NME4	KLHL24	LDHC	LZIC	MDM1	MTHFD1	NAPG	SPA17
NME5	KLHL26	LGALS8	LZTFL1	MDP1	MTHFD1L	NAPSA	SPAG1
NME6	KLHL3	LGALS9	MAATS1	ME1	MTMR1	NASP	SPAG16
NME7	KLHL32	LGALS9B	MACF1	ME2	MTMR2	NCALD	SPAG17
NME8	KLHL4	LGALS9C	MAD2L1	ME3	MTPAP	NCAM1	SPAG6
NME9	KLHL5	LHPP	MADD	MECR	MTX1	NCAPD2	SPAST
NMNAT3	KLHL7	LIN7A	MAF1	MED13	MUC5B	NCK2	SPTA1
NNT	KLHL9	LIN7C	MAGOH	MED13L	MVP	NCKAP1	SPATA17
NOMO1	KLK14	LMAN1	MAGOHB	MED29	MX1	NBEA	SPATA18
NOMO2	KLK15	LMNA	MAGT1	MED31	MX2	NCEH1	SPATA4
NOMO3	KLK5	LMNB1	MAK	MEMO1	MYB	NCL	SPATA5
NONO	KLK7	LMNB2	MAL	METAP2	MYCBP	NCLN	SPATA5L1
NOP16	KLK8	LMO1	MAN1A2	METTL7A	MYEF2	NCS1	SPATA6
NOP58	KLK9	LSM2	MANEAL	MFSD10	MYH10	NDC80	SPATA7
NOTO	KMO	LSM5	MAP1A	MFSD6	MYH11	NDRG1	SPCS2

NPEPL1	KPNA1	LPAR3	MAP1B	MGC42105	MYH12	NDRG2	SPTAN1
NPEPPS	KPNA2	LRBA	MAP1S	MGLL	MYH15	NDRG3	SPEF1
NPHP1	KPNA4	LRIG1	MAP2	MID1	MYH9	NDRG4	SPEF2
NPHP3	KPNA5	LRIG3	MAP2K1	MINK1	MYL1	NDUFA10	SPICE1
NPHP4	KPNA7	LRP1	MAP2K2	MIP	MYL12A	NDUFA6	SPTB
NPHS2	KPNB1	LRP2	MAP2K4	MIPEP	MYL12B	NDUFAF3	SPTBN1
NPM1	KRAS	LRP3	MAP2K5	MITD1	MYL2	NDUFAF4	SPTBN2
NPR2	KRI1	LRP2BP	MAP2K7	MITF	MYL3	NDUFS1	SPTBN4
NR2F1	KRT1		MAP3K11	MKKS	MYL4	NECAP1	SPTBN5
NRAS	KRT10	PAH	MAP3K13	MKNK1	MYL5	NECAP2	SPTLC1
NRBP1	KRT13	PAICS	MAP3K19	MKNK2	MYL6	NEDD4	SQRDL
NRD1	KRT14	PAK1	MAP4	MKS1	MYL6B	NEDD4L	SRBD1
NSF	KRT17	PAK2	MAP4K2	MLEC	MYL7	NEK1	SRC
NSUN4	KRT17P1	PAK3	MAP4K4	MLF1	MYL9	NEK10	SRCIN1
NSUN7	KRT17P3	PAK4	MAP6	MLF2	MYLK4	NEK11	SRD5A2
NT5E	NUDC	PALM	MAP9	PLK3		PRPF6	SRGAP3
NTPCR	NUDCD1	PAM	MAPK1	PLK4	PPP1R16B	PRPF8	SRI
NUAK1	NUDT19	PARD3	MAPK10	PLP1	PPP1R21	PRPS1	SRMS
PTPLAD1	NUDT2	PARD6A	MAPK11	PLS3	PPP1R32	PRPS1L1	SRP14
PTPN13	NUDT21	PARD6B	MAPK12	PLSCR4	PPP1R36	PRPS2	SRP68
PTPN23	NUP214	PARD6G	MAPK13	PLTP	PPP1R42	PRPSAP1	SRP72
PTPRD	NUP35	PARK2	MAPK14	PLXNB2	PPP1R7	PRPSAP2	SRPK1
PTPRF	NUP37	PARK7	MAPK15	PMM2	PPP1R9A	PRSS1	SRPRB
PTPRQ	NUP62	PARL	MAPK3	PMPCB	PPP2CA	PRSS29P	SRRT
PTPRT	NUP62CL	PARP2	MAPK7	PNCK	PPP2CB	PRSS3	SRSF1
PTRH2	NUP85	PARP3	PEX6	PNKP	PPP2R1A	PRSS38	SRSF10
PXN	NUP93	PARS2	PFKP	PNPLA4	PPP2R1B	PRSS55	SRSF3
PYCR1	NUP98	PARVA	PFN1	PNPLA8	PPP2R2A	PRTFDC1	SRSF5
PYCR2	NUTF2	PARVG	PFN2	PNPT1	PPP2R2B	PRUNE	SRSF6
PYCRL	NVL	PC	PGAM1	POC1A	PPP2R2C	PSAP	SRSF7
PYGB	NXNL1	PCBD2	PGAM4	POC1B	PPP2R2D	PSAPL1	SSBP3
QARS	NXNL2	PCCA	PGD	POC5	PPP2R3C	PSAT1	SSNA1
QDPR	OCRL	PCDH15	PGK1	PODXL	PPP2R5B	PSKH1	SSR1
QRSL1	ODF2	PCDHGA6	PGK2	POLR3B	PPP2R5C	PSKH2	SSR4
QTRT1	ODF3	PCM1	PGLS	PON1	PPP2R5D	PSMA1	SSRP1
RAB1A	ODF3B	PCMT1	PGM1	PON2	PPP2R5E	PSMA2	SSSCA1
RAB1B	ODF3L2	PCNT	PGM2	PON3	PPP3CA	PSMA3	SSTR3
RAB10	ODZ4	PCYOX1	PGM2L1	POR	PPP4C	PSMA5	ST13
RAB11A	OFD1	PDDC1	PGM5	PPA1	PPP5C	PSMA6	ST13P5
RAB11B	OGDH	PDE1A	PGRMC1	PPA2	PPP6C	PSMA7	STAR
RAB11FIP3	OGDHL	PDE11A	PHF17	PPAP2A	PRDX1	PSMA8	STAT3
RAB11FIP4	OLA1	PDE1B	PHKG1	PPAP2B	PRDX2	PSMB11	STAT6
RAB12	OPN1MW	PDE1C	PHKG2	PPEF2	PRDX3	PSMB2	STAU1
RAB13	OPN1SW	PDE4A	PHB2	PPFIA1	PRDX4	PSMB4	STAU2
RAB14	OPRL1	PDE4D	PHGDH	PPFIA2	PRDX5	PSMB5	STEAP2
RAB15	OR2Z1	PDE4DIP	PHYHD1	PPFIA3	PRDX6	PSMB8	STEAP3
RAB17	OR51M1	PDE6A	PI4KA	PPFIA4	PRIM2	PSMB9	STEAP4
RAB19	ORAI2	PDE6B	PIBF1	PPIA	PRKAA1	PSMC1	STIL
RAB2B	ORC1	PDE6C	PICALM	PPIAL4C	PRKACA	PSMC2	STIP1
RAB20	ORC2	PDE6D	PIFO	PPIAL4G	PRKACB	PSMC4	STK10
RAB21	OSBP	PDE7A	PIGG	PPIC	PRKACG	PSMC5	STK11
RAB22A	OSBP2	PDE7B	PIGK	PPID	PRKAG1	PSMC6	STK17A
RAB23	OSBPL1A	PDE8A	PIGS	PPIE	PRKAG2	PSMD1	STK17B
RAB24	OSBPL2	PDE8B	PIH1D2	PPIF	PRKAR1A	PSMD11	STK24
RAB25	OSBPL3	PDE9A	PIH1D3	PPIG	PRKAR1B	PSMD12	STK25
RAB26	OSBPL7	PDHB	PIK3C3	PPIH	PRKAR2A	PSMD13	STK32A
RAB27A	OSCP1	PDIA3	PIK3CG	PPIL1	PRKCA	PSMD2	STK32B

RND2	OTUB1	PDIA6	PIM1	PPIL2	PRKCB	RAB30	STK32C
RND3	OXR1	PDK2	PIM3	PPIL6	PRKCE	RAB31	STK33
RNF121	OXSR1	PDPK1	PIN1	PPIP5K1	PRKCG	RAB3IL1	STK36
RHEB	P2RY14	PDXK	PIP	PPIP5K2	PRKCH	RAB32	STK38L
RHEBL1	P4HA1	PDZD7	PIP5K1B	PPM1A	PRKCQ	RAB33A	STK39
RHOA	P4HB	PEBP1	PITPNA	PPM1B	PRKCSH	RAB33B	STK4
RHOB	PA2G4	PECR	PITPNB	PPM1E	PRKCZ	RAB34	STOM
RPL17P18	PABPC1	PELI2	PITPNC1	PPM1F	PRKG1	RAB35	STOML1
RPL18	PABPC1L	PEX1	PKD1	PPM1G	PRKG2	RAB36	STOML2
RPL18A	PABPC3	PEX11B	PKD2	PPM1H	PRKX	RAB38	STOML3
RPL19	PABPC4	PEX5	PKD1L1	PPM1K	PRKY	RAB39	STOX1
RPL19P9	PACRG	PEX5L	PKD2L1	PPM1L	PRMT5	RAB39B	STRN
RPL21	PACRGL	RBX1	PKD1L3	PPM1N	PRMT6	RAB3GAP2	STRN3
RPL21P44	PACSIN1	RCVRN	PKD2	PPP1CA	PROM1	RAB3IP	STRN4
RPL21P7	PACSIN2	RCN2	PKHD1	PPP1CB	PROM2	RAB4A	STXBP5L
RPL23	PACSIN3	RDH10	PKLR	PPP1CC	PRPF19	RAPGEF6	STYX
RPL23A	PAFAH1B1	RDH11	PKM2	PPP1R12A	PRPF31	RAPSN	STX1A
RPL24	PAFAH2	RDH8	PLA2G7	PPP1R16A	PRPF38A	RARS	STX12
RPL26	RAB4B	REPIN1	PLAU	RPL9	PRPF39	RASD1	STX16
RPL26L1	RAB40A	REEP5	PLBD1	RPLP0	RSPH6A	RBKS	STX3
RPL27	RAB40AL	REEP6	PLCB4	RPLP2	RSPH9	RABL2A	STX4
RPL27A	RAB40B	REM1	PLCE1	RPN2	RTDR1	RABL2B	STX7
RPL28	RAB40C	REN	PLCH1	RPS10	RTN1	RABL5	STX8
RPL3	RAB41	RER1	PLEC	RPS11	RTN3	RAP1B	STXBP1
RPL30	RAB42P1	RERG	PLEKHB1	RPS11P5	RTN4	RARS2	STXBP2
RPL31	RAB43	RERGL	PLEKHH1	RPS13	RTTN	RASAL2	RSPH14
RPL32	RAB5A	RFC4	PLK1	RPS12	RUVBL1	RASD2	RSPH3
RPL34	RAB5B	RFPL1	PLK2	RPS14	RUVBL2	RASL11A	RSPH4A
RPL35	RAB5C	RFPL2	RNF14	RPS15	RYR1	RASL12	STXBP5
RPL35A	RAB6A	RFPL3	RNF175	RPS15A	RYR2	RBBP9	SUB1
RPL36	RAB6B	RFPL4A	RNF19A	RPS17	RYR3	RBM20	SUCLG1
RPL3L	RAB6C	RFX2	RNF39	RPS17L	SACM1L	RBM23	SUFU
RPL4	RAB7A	RFX3	RNF40	RPS18	SAR1A	RBM39	SUGT1
RPL6	RAB7L1	RGL1	RNF7	RPS19	PSMD3	RBM8A	SULF1
RPL7	RAB8A	RGS1	ROCK2	RPS2	PSMD5	RBMXL1	SULF2
RPL7A	RAB8B	RGS17	ROPN1L	RPS2P4	PSMD6	RBP1	SULT1A1
RPL7L1	RAB9A	RGS19	RP1	RPS20	PSMD7	RHOC	SULT1A2
RPL7P20	RAB9B	RGS20	RP2	RPS23	PSME1	RHOD	SULT1A3
RPL8	RABL5	RGS22	RPGR	RPS24	PSME3	RHOF	SULT1A4
RPS6KB1	RABGAP1	RGS3	RPGRIP1	RPS26P11	PSPC1	RHOG	SULT1B1
RPS7	RABGAP1L	RGS4	RPGRIP1L	RPS26P6	PSPH	RHOH	SULT1C2
RPS8	RAC1	RGS5	RPH3A	RPS26P8	PTBP1	RHOJ	SULT1C3
RPS9	RAC2	RGS6	RPL10	RPS27	PTBP2	RHOQ	SULT1C4
RPSA	RAC3	RGS9	RPL10A	RPS27A	PTCD3	RHOU	SULT1E1
RPSAP47	RACGAP1	TPM2	RPL10AP2	RPS27L	PTCH1	RHOV	SULT2A1
RPSAP55	RAE1	TPM3	RPL10AP3	RPS3	PTGES3	RIBC1	SULT2B1
RPSAP58	RALA	TPM3P4	RPL13AP2	RPS3A	PTGR2	RIBC2	SULT4A1
RPTOR	RALB	TPM4	5	RPS3AP6	PTK6	RICTOR	SULT6B1
RRAD	RAN	TPP2	RPL10L	RPS4X	PTK7	RIIAD1	SUMF2
RRAS	RANBP1	TPPP	RPL11	RPS4XP21	PTP4A1	RILPL1	SUMO1
RRM2	RANBP10	TPPP2	RPL12	RPS4Y1	PTPDC1	RILPL2	SUMO2
RRM2B	RANBP9	TPPP3	RPL13	RPS4Y2	RAB27B	RIMS1	SUMO3
RRP12	RANGAP1	TRAF3IP1	RPL13A	RPS5	RAB28	RIMS2	SUMO4
RSAD2	RAP1A	TRAF5	RPL14	RPS6	RAB3A	RIN2	SURF4
RSPH1	RAP2A	TRAP1	RPL14P1	RPS6KA2	RAB3B	RIT1	SV2A
RSPH10B	RAP2B	TRAPPC10	RPL15	RPS6KA3	RAB3C	RIT2	SV2B
RSPH10B2	RAPGEF2	TRAPPC3	RPL17	RPS6KA4	RAB3D	RLBP1	SYNCRIP

SYNE2	TMBIM1	TRAPPC4	TTC7A	UBA52	UPF1	WDR1	ZFAND2A
SYNJ1	TMBIM4	TRAPPC5	TTC8	UBA6	UQCRC1	WDR11	ZFAND2B
SYNM	TMCC1	TRAPPC9	TTF2	UBA7	UQCRC2	WDR16	ZFP2
SYNPR	TMCC2	TRIB1	TTK	UBB	UQCRFS1	WDR19	ZFP3
SYP	TMED11P	TRIB2	TTLL1	UBC	USH1C	WDR3	ZMYND10
SYPL1	TMED3	TRIM10	TTLL10	UBD	USH1G	WDR11	ZMYND12
SYTL3	TMED4	TRIM13	TTLL13	UBE2A	USH2A	WDR19	ZNF114
TACO1	TMED2	TRIM15	TTLL3	UBE2C	USO1	WDR31	ZNF12
TALDO1	TMED7	TRIM2	TTLL6	UBE2D1	USP12	WDR34	ZNF121
TAMM41	TMED9	TRIM25	TTLL7	UBE2D2	USP13	WDR35	ZNF124
TARDBP	TMEM107	TRIM26	TTLL9	UBE2D3	USP14	WDR48	ZNF2
TARS	TMEM111	TRIM28	TTYH1	UBE2D4	USP2	WDR49	ZNF20
TARS2	TMEM138	TRIM3	TTYH3	UBE2E1	USP20	WDR5B	ZNF226
TARSL2	TMEM17	TRIM32	TUB	UBE2E2	USP33	WDR52	ZNF227
TBC1D24	TMEM177	TRIM35	TUBA1A	UBE2E3	USP39	WDR54	ZNF252
TBC1D30	TMEM189-	TRIM39	TUBA1B	UBE2F	USP46	WDR60	ZNF266
TBC1D32	UBE2V1	TRIM59	TUBA1C	UBE2G2	USP5	WDR63	ZNF268
TBC1D7	TMEM190	TRIM62	TUBA3C	UBE2I	USP9X	WDR65	ZNF282
TBCA	TMEM2	TRIO	TUBA3D	UBE2J2	USP9Y	WDR66	ZNF295
TBCB	TMEM216	TRIP11	TUBA3E	UBE2K	UST	WDR67	ZNF3
TBCC	TMEM231	TRIT1	TUBA4A	UBE2L3	VAC14	WDR69	ZNF302
TBCE	TMEM237	TRPM3	TUBA8	UBE2L6	VAMP4	WDR7	ZNF365
TBL2	TMEM30A	TRPV5	TUBAL3	UBE2M	VAPA	WDR78	ZNF420
TBXAS1	TMEM30B	TRPV6	TUBB	UBE2N	VAPB	WDR90	ZNF423
TCP1	TMEM33	TSC1	TUBB1	UBE2NL	VAT1	WDR92	ZNF436
TCTE1	TMEM38A	TSC22D1	TUBB2A	UBE2R2	VBP1	WDR96	ZNF474
TCTEX1D1	TMEM38B	TSC22D4	TUBB2B	UBE2T	VCL	WNT4	ZNF501
TCTEX1D2	TMEM43	TSG101	TUBB3	UBE2V1	VCP	XBP1	ZNF525
TCTN1	TMEM47	TSGA10	TUBB4A	UBE2V2	VDAC1	XIAP	ZNF527
TCTN2	TMEM53	TSNARE1	TUBB4B	UBE3B	VDAC2	XPNPEP3	ZNF529
TCTN3	TMEM65	TSNAXIP1	TUBB6	UBE4B	VDAC3	XPO1	ZNF543
TDRKH	TMEM67	TSPAN4	TUBB8	UBL3	VHL	XPO5	ZNF544
TECR	TMLHE	TSPAN8	TUBBP1	UBQLN1	VIM	XPO7	ZNF566
TEKT1	TMOD1	TSPAN9	TUBBP5	UBR4	VIT	XRCC6	ZNF568
TEKT2	TMOD2	TSSK1B	TUBD1	UBXN10	VMO1	YARS2	ZNF572
TEKT3	TMOD3	TSSK2	TUBE1	UBXN11	VPS13A	YBX1	ZNF586
TEKT4	TMPRSS12	TSSK3	TUBG1	UBXN4	VPS13C	YBX1P2	ZNF596
TEKT5	TMTC2	TSSK4	TUBGCP2	UCHL1	VPS13D	YES1	ZNF620
TEN1	TMTC4	TSSK6	TUBGCP3	UCHL3	VPS16	YIPF6	ZNF658
TESC	TMX1	TST	TUBGCP4	UCKL1	VPS18	YKT6	ZNF662
TEX26	TMX2	TTBK2	TUBGCP5	UCP2	VPS25	YPEL1	ZNF691
TEX9	TNFAIP8L1	TTC12	TUBGCP6	UFC1	VPS35	YPEL2	ZNF701
TF	TNIK	TTC18	TUFM	UFL1	VPS4A	YPEL3	ZNF71
TGM2	TNK2	TTC21A	TULP1	UFSP2	VPS4B	YPEL4	ZNF713
TGM3	TNKS	ZNF891	TULP3	UGDH	VPS45	YPEL5	ZNF780A
TH	TNKS2	ZNF91	TUSC3	UGGT1	VPS52	YSK4	ZNF780B
THOC4	TNNC1	ZNHIT6	TUT1	UGP2	VRK1	YWHAB	ZNF783
THOP1	TNNC2	ZNRD1	TXK	UGT1A10	VRK2	YWHAE	ZNF8
THY1	TNPO1	TTC21B	TXN	UGT1A4	VSNL1	YWHAG	
TIAL1	TOP2A	TTC25	TXNDC12	UGT1A6	VWA3B	YWHAQ	
TINAGL1	TOP2B	TTC26	TXNDC3	UGT2A1	VWA5A	YWHAZ	
TKT	TOPORS	TTC29	TXNDC9	ULK3	VWA5B1	ZAK	
TKTL1	TPD52	TTC30A	TXNIP	ULK4	WASF1	ZBBX	
TLR1	TPH1	TTC30B	TXNL1	UNC119	WBP2NL	ZBTB22	
TLR2	TPH2	TTC35	U2AF1	UNC119B	WBSCR17	ZC3H12A	
TM7SF2	TPI1	TTC37	U2SURP	UNC13B	WDFY3	ZC3H12B	
TM9SF3	TPM1	TTC5	UBA1	UNC45A	WDPCP	ZC3H12C	

Annexe 4 : Liste des gènes connus impliqués dans les ciliopathies non-mobiles majeures

Pathologie	Caractéristiques cliniques principales	Gène	Allélisme	Héré-dité	Localisation protéique	Complexe protéique	Fonction ciliaire
Syndrome de Joubert (SJMA)	-Signe de la dent molaire -Ataxie -Mouvement oculaires anormaux	AHI1		AR	Corps basal, zone de transition		Trafic vésiculaire
		ARL13B		AR	Corps basal, cytosol	INPP5E	Transport intraflagellaire, Signalisation
		CEP290	BBS, MKS, LCA	AR	Centrosome, corps basal	IQCB1-CEP290	Trafic vésiculaire, barrière de diffusion
		CEP41		AR	Centriole, corps basal		Glutamylation tubulines, barrière de diffusion
		CEP104		AR	Centriole	CCP110	Assemblage du cil
		OFD1	OFD I, RP, SBGS	RLX	Centrosome, centriole, corps basal		Assemblage du cil
		CSPP1	Jeune, MKS	AR	Centrosome		Stabilisation des microtubules ?
		KIF7	Acrocallosal	AR	Extrémité distale du cil		Signalisation
		INPP5E	BBS ?	AR	Axonème	INPP5E	Signalisation
		PDE6D		AR	Axonème	INPP5E	Signalisation
		C5orf42		AR	Corps basal		?
		NPHP1	BBS, NPHP	AR	Zone de transition	NPHP	Signalisation, barrière de diffusion
		RPGRIP1L	MKS	AR	Corps basal, zone de transition	MKS, NPHP	Barrière de diffusion
		TMEM67	MKS, NPHP, BBS	AR	Corps basal, zone de transition	MKS	Barrière de diffusion
		TMEM216	MKS	AR	Corps basal, zone de transition, Golgi	MKS	Barrière de diffusion, trafic vésiculaire
		TMEM237		AR	Zone de transition	MKS	Barrière de diffusion
		TMEM138		AR	Corps basal, zone de transition, Golgi		Barrière de diffusion, trafic vésiculaire
		TMEM231	MKS	AR	Zone de transition	MKS	Barrière de diffusion
		CC2D2A	MKS	AR	Zone de transition	MKS	Barrière de diffusion
		TCTN3	OFD IV	AR	Zone de transition	Tectonic	Signalisation

		TCTN2	MKS	AR	Zone de transition	Tectonic	Signalisation
		TCTN1	MKS	AR	Zone de transition	Tectonic	Signalisation
		KIAA0556	MKS	AR	Corps basal		Stabilisation des microtubules
		HYLS1	Hydrolethalus	AR	Corps basal		Ancrage du corps basal
		B9D1	MKS	AR	Zone de transition	MKS	Barrière de diffusion
		MKS1	MKS	AR	Zone de transition	MKS	Barrière de diffusion
		ZNF423	NPHP	AR/AD	Noyau		?
		NPHP4	NPHP	AR	Zone de transition	NPHP	Barrière de diffusion
		KIAA0586	CCP	AR	Centrosome		Signalisation
Syndrome de Bardet-Biedl (BBS)	-Dégénérescence rétinienne -Obésité tronculaire -Polydactylie Post-axiale -Déficience intellectuelle -Hypogénitalisme -Anomalies rénales	BBS1		AR	Corps basal	BBSome	Trafic vésiculaire
		BBS2	RP	AR	Corps basal	BBSome	Trafic vésiculaire
		ARL6	RP	AR	Corps basal, zone de transition		Trafic vésiculaire, signalisation
		BBS4		AR	Corps basal	BBsome	Trafic vésiculaire
		BBS5		AR	Corps basal	BBsome	Trafic vésiculaire
		MKKS	McKusick-Kaufman	AR	Corps basal, cytosol		Chaperonne du BBsome, signalisation
		BBS7		AR	Corps basal	BBsome	Trafic vésiculaire
		TTC8	RP	AR	Corps basal, axonème	BBsome	Trafic vésiculaire
		BBS9		AR	Corps basal	BBsome	Trafic vésiculaire
		BBS10		AR	Corps basal		Chaperonne du BBsome, signalisation
		TRIM32	Dystrophie maculaire	AR	Fibres de transition		?
		BBS12		AR	Corps basal		Chaperonne du BBsome, signalisation
		MKS1	MKS	AR	Corps basal	MKS	Barrière de diffusion
		CEP290	JS, MKS, LCA	AR	Corps basal, centrosome	IQCB1-CEP290	Trafic vésiculaire, barrière de diffusion
		WDPCP		AR	Corps basal, axonème, cytosol		?
		SDCCAG8	JS	AR	Centriole, corps basal		?

		LZTFL1		AR	Corps basal, axonème		Trafic vésiculaire et membranaire
		BBIP1		AR	Corps basal	BBsome	Trafic vésiculaire
		IFT27		AR	Corps basal, axonème	IFT-B	Transport intraflagellaire
		IFT172	RP, CCP	AR	Corps basal, axonème	IFT-B	Transport intraflagellaire
		C8orf37	RP, DCB	AR	Corps basal		?
Syndrome de Meckel (MKS)	-encéphalocèle occipital -Kystes rénaux -Fibrose hépatique -Polydactylie	CEP290	JS, BBS, LCA	AR	Corps basal, centrosome	IQCB1-CEP290	Trafic vésiculaire, barrière de diffusion
		MKS1	BBS	AR	Corps basal	MKS	Barrière de diffusion
		TMEM67	JS, NPHP, BBS	AR	Corps basal, zone de transition	MKS	Barrière de diffusion
		TMEM216	JS	AR	Corps basal, zone de transition, Golgi	MKS	Barrière de diffusion, trafic vésiculaire
		TMEM231	JS	AR	Zone de transition	MKS	Barrière de diffusion
		B9D1	JS	AR	Zone de transition	MKS	Barrière de diffusion
		B9D2		AR	Zone de transition	MKS	Barrière de diffusion
		RPGRIP1L	JS, NPHP	AR	Corps basal, zone de transition	MKS	Barrière de diffusion
		CC2D2A	JS	AR	Zone de transition	MKS	Barrière de diffusion
		NPHP3	NPHP, DRHP	AR	Compartiment inversine	Inversine	?
		TCTN1	JS	AR	Zone de transition	Tectonic	Signalisation
		TCTN2	JS	AR	Zone de transition	Tectonic	Signalisation
		KIF14		AR	?		?
		CSPP1	Jeune, JS	AR	Centrosome		Stabilisation des microtubules ?
		KIAA0556	JS	AR	Corps basal		Stabilisation des microtubules
Néphro-nophtise (NPHP)		NPHP1	JS	AR	Zone de transition	NPHP	Barrière de diffusion
		NPHP3		AR	Compartiment inversine	Inversine	?
		NPHP4	JS	AR	Zone de transition	NPHP	Barrière de diffusion
		ZNF423	JS	AR/AD	Noyau		?
		CEP164		AR	Centriole		Trafic vésiculaire

		CEP83		AR	Centriole		?
		TMEM67	JS, MKS, BBS	AR	Zone de transition	MKS	Barrière de diffusion
		GLIS2		AR	?		Signalisation
		WDR19	CCP	AR	Axonème	IFT-A	Transport intraflagellaire
		DCDC2		AR	Axonème, cytosol, membrane		Signalisation
		ANKS6		AR	Compartiment inversine	Inversine	?
		NEK8		AR	Compartiment inversine	Inversine	?
		INVS		AR	Compartiment inversine	Inversine	?
		TTC21B	CCP	AR	Axonème	IFT-A	Transport intraflagellaire
Syndrome	-Thorax étroit	EVC	WAD	AR	Zone de transition		?
Côtes	-Côtes courtes	EVC2	WAD	AR	Membrane, noyau		Signalisation
Courtes	-Dysplasie	IFT80		AR	Corps basal, axonème	IFT-B	Transport intraflagellaire
Polydactylie	squelettique	IFT122	Sensenbrenner	AR	Corps basal, axonème	IFT-A	Transport intraflagellaire
(CCP)		IFT43	Sensenbrenner	AR	Corps basal, axonème	IFT-A	Transport intraflagellaire
		IFT52		AR	Corps basal, axonème	IFT-B	Transport intraflagellaire
		IFT140		AR	Corps basal, axonème	IFT-A	Transport intraflagellaire
		DYNC2H1		AR	Axonème, Golgi		Trafic vésiculaire, signalisation
		DYNC2LI1		AR	?		?
		TTC21B	NPHP	AR	Axonème	IFT-A	Transport intraflagellaire
		WDR19	NPHP	AR	Axonème	IFT-A	Transport intraflagellaire
		WDR35	Sensenbrenner	AR	Axonème	IFT-A	Transport intraflagellaire
		WDR34		AR	?		?
		WDR60		AR	Axonème		?
		NEK1		AR	Corps basal, matrice péricentriolaire		Stabilisation ciliaire
		KIAA0586	JS	AR	Centrosome		Signalisation

AR : Autosomique Récessif, DCB : Dystrophie Cône-Bâtonnet, DRHP : Dysplasie Rénal-Hépatique-Pancréatique, LCA : Amaurose Congénitale de Leber, RLX : Récessif Lié à l'X, SBGS : Syndrome de Simpson-Golabi-Behmel, WAD : Dysostose Acrodentale Weyers

Annexe 5 : Séquences des amorces utilisées en PCR ou RT

Amorce	Séquence	Amorce	Séquence
PCR			
NEDD1_ex3_F	GTGGAAATACAAGAGCAGGCTTTA	TMEM231_ex3R	GCAATTTAGTTCTTCGACAAACACA
NEDD1_ex3_R	GACCACACACCATAGTTTAGGAAAA	TMEM231_ex2F	CCATTTATTTTGGCCAGTGAACATT
NEDD1_ex11_F	CTTTTCCAGGCTTTGACTTTCT	TMEM231_ex2R	TAGAGTGCGGGTCTTCTAGAAATC
NEDD1_ex11_R	TGCTCTAATGATTTAACCACCAACT	TMEM138_ex4F	AAAGTCTTTATCTGACAGGAGCTGA
OFD1_ex8_F	TGTTTATGCCTTTTGAGTGAATCCT	TMEM138_ex4F	TCCTCATTTCCCATAGTCTTCTAGC
OFD1_ex8_R	TTTAGGGTGTGTTTCTCATAATCCC	DDX59_1F	TCAAGAGGAATGCTAATGATGATGG
NUP205_ex22_F	GCAGTCTAAGATTTTAATGCAGCAA	DDX59_1R	TATCAGAAGCAAAATCACTACAGGC
NUP205_ex22_R	TCAGAAGGAGCTACTTTAAACACAG	TMEM107_ex1-3F	GTACCCAGCCGTTAGGTTAGAAG
NUP205_ex43_F	CATCAGCATCAACATTCATTGCTAT	TMEM107_ex1-3R	GGATTTAGCACATCGTTGAAGA
NUP205_ex43_R	TGTTAGATTCCTGATAATGCTGATCA	INTU_ex2(1)F	CCCAACTCCTATTCAAAGCTCTAC
KIAA0753_ex9F	CAGTGCTGTTAGGCCTTATAAAGAT	INTU_ex2(1)R	TGGGGTTTACATAAACATTCACATC
KIAA0753_ex9R	ATGTAGGAAAGAGAAGAAAGGGTTC	EVI5_ex2F	GCTGGATATTAGGGTATTGTTGCTA
OFD1_ex3F	GAAGGTTTCCAATGAATGTAGCTCA	EVI5_ex2R	GAAAAGATTTTGCACTCTAAACCAC
OFD1_ex3R	CAAAGAGGAAACAGAAATGGACCTA	EVI5_ex10F	AGTTAAGAGCCAGTTGAACCTACAG
C5orf42_ex20F	GTTGAGGGGAGATAACATTTCTCAA	EVI5_ex10R	TAATTTTCTTCTCCATGGAAGTGTT
C5orf42_ex20R	ATAACTTTCCATTCTCTGAACCCAC	WDPCP_ex2_F	AACATATGCTATTGAAAACCCAAAT
C5orf42_i18F	ATATTTGCATAGTTGAAGCCGTACT	WDPCP_ex2_R	AAAACTGAAAACCTAACTCAAGCTG
C5orf42_i18R	CTTGGCAGAGTCTATCAGAAGTTG	WDPCP_ex8_F	ATGGAATGTTTTCGTCTCTACATTC
TMEM231_ex3F	GGGATTTAACTTAGGCCAATGGAAT	WDPCP_ex8_R	AACCATTTTCAAAAGTGTAACTTGC

PCR long-range			
INTU_ex2(1)F	CCCAACTCCTATTCAAAGCTCTAC	C2CD3_2F	AAGTGGTGATAAATTGCTGAACTT
INTU_ex2(1)R	TGGGGTTTACATAAACATTCACATC	C2CD3_3F	TTGCTGAATTGCTTTCCAGTT
INTU_ex1F	TAAGCGGTGAAGTTTTAGCTATTTC	C2CD3_4F	TTGGAACAGAGGGATGAAGG
INTU_ex1R	GAACGCTGTTACAGATATATCCTCC	C2CD3_5F	CGCTTTTTGAGGTCCAAACT
INTU_ex2F	CAGCCATCCTAAATAATTTCTATGC	C2CD3_6F	GCCAGCATCTAAAACAGTGC
INTU_ex2R	TTTAAGAACACTGTGCCTTGTAGTG	C2CD3_7F	CTCCGAACTGGTATCCTTGG
INTU_ex3_4F	TCAAGTACAGTATTTGGTTCATGCT	C2CD3_8F	CATCCCAGAGGAGGGGTAGT

INTU_ex3_4R	GATATTGCAACGATACCTTCCTCTT	C2CD3_9F	TCCCTGGTGTCAGTTCTTTCTT
INTU_ex5_6F	TTAAAATTCCAAGCATAGTTCTCCC	C2CD3_10F	CCCTCCCTTTTTCCTCATCT
INTU_ex5_6R	ACAAAAGAAGCAAGTGTATTGACAG	C2CD3_11F	AAGAAGAGGTAGGGCCTCTGA
INTU_ex7_8F	AAAATCCCTGTTAGATTCATGCTG	C2CD3_12F	TCTTTGTCCCTGCTCATTCA
INTU_ex7_8R	ACAAAATTCCAAAGTAAGACACACC	C2CD3_13F	CAAAGTGGGATCTCAGAGTTGTC
INTU_ex9_11F	GAGAAAGACAGGGAAGAATGTTGAT	C2CD3_14aF	GATGTTGTTTCCAGCCTCAAA
INTU_ex9_11R	TAATGCTTCTTGATCCCAGTTGAAA	C2CD3_14bF	CAAATTCATGAGGAAACTGCAA
INTU_ex12_14F	CCCTTATTCCTTTTCTTTTGCATCC	C2CD3_15F	GCAGACTGCTACTTCTCTTGAGG
INTU_ex12_14R	CCAAAGCATACAGGAATATAGGGTC	C2CD3_16F	AAACCACTATTACTTTTCCAGTTGC
INTU_ex15_16F	GATGTCTTGGGTTACTTTTCAGGAT	C2CD3_17F	TCTATACTCAGACTTCATAGAGAAGCA
INTU_ex15_16R	ATGTATCAAATCCAACAGCATTTCA	C2CD3_18F	GAATTGTCCACCAGCAAGGT
RSG1_ex2F	CCTGCCTGGCTCTCTCTTTG	C2CD3_19F	CCATAGCTGCGTACTACCAACA
RSG1_ex2R	ATAGGAAGAAGAGATACATCCCTGC	C2CD3_20F	CAATCTCATTATGACAAGGACAGA
FOPLN_ex1F	ATTACAACTGGAATCATGCAACCTC	C2CD3_21F	GCACTGCCAAAAGCCTAGAT
FOPLN_ex1R	AGTTCTCATGTTGCAGTGATTTAGT	C2CD3_22F	TGCATATAAGGGGAGGGTTG
FOPLN_ex2-3F	TATATGAGAGACTGGGGCTTAAGTT	C2CD3_23aF	TCATTGCCTCTCAATGGTCA
FOPLN_ex2-3R	GGATCAAGAAGTCAAAAGGAGCTAA	C2CD3_23bF	GGCTGGAGCTTTGAGAACAG
FOPLN_ex4-5F	AGTTGTTAACATGTTTTCTCTGGGT	C2CD3_24F	TTGGGGTTTGTAGACCTTTCA
FOPLN_ex4-5R	CAAAGCCCTTTCATTTCCTTACAAA	C2CD3_25F	GACACAGGGGGATAGCTTGA
KIAA0753_ex1F	ATGGGAAATAGAAGAGCAAGACAAG	C2CD3_26F	TGTGAAGATAAAAATATATGCCAGA
KIAA0753_ex1R	CACTAAGTCCTTCAATTTCCCAGTT	C2CD3_27F	TTGCCAGTCCCTCTCAACTT
KIAA0753_ex2-6F	TGGGTTTACTTTTAGAGATGGTTCC	C2CD3_28F	AGCTGGAGGAACAAGAGCAT
KIAA0753_ex2-6R	TCTGCAAAGCTTTAATTCACTAGGT	C2CD3_29F	GCAAGAGATGATAAGGCCAGA
KIAA0753_ex7F	ACATTTCCCTGGAGTCCTTATTTTC	C2CD3_30F	AGAGGTATTAAGGCTTTGGCTCA
KIAA0753_ex7R	GCTGACAAGTTACACTAATGCAATC	C2CD3_31F	TTTCCAACATACCTTGCTGCT
KIAA0753_ex8-12F	ACCTGCAGTAATATTCATAGGAGGA	C2CD3_1R	GGTTCCCTGGCTACTTCCTT
KIAA0753_ex8-12R	TATGTTGATTCACATGAGCAGAACA	C2CD3_2R	TGCCCATATATGCTAGGTACACA
KIAA0753_ex13-15F	GTCATTTTATTTCCCTTCTCCTGGA	C2CD3_3R	GGCATGAGGTGGAAATTAGC
KIAA0753_ex13-15R	GCGGATCTTTAAACTTTCAAATCCA	C2CD3_4R	AGGCCCAGCACCTAGTATCA
KIAA0753_ex16-18F	TTTCTGCTTTGCTGCTAGATAGAAA	C2CD3_5R	TGGTGTGAGATGCTGGACTC
KIAA0753_ex16-18R	CCACAAAACTACCTTACCCACATAA	C2CD3_6R	CACATGCTGCCAGTACCAGT

KIAA0753_ex19F	GCTGAGTAAAAGAATGGCTCCC	C2CD3_7R	CGGTAAGGTAGAATGGGATCA
KIAA0753_ex19R	ATGTGTGTCTATTATTGTGCACTGA	C2CD3_8R	GGCCTGTCTCAACATCTGTAAA
FUZ_ex1_11F	GAATGTAAATCATCAAAGCCTACAG	C2CD3_9R	AATTAATCACTCTGATGGTGCTG
FUZ_ex1_11R	ATATCCTTTCCACCTTTCTCTCATC	C2CD3_10R	AAATGTTTCTCTCTCCTGCTAACTG
WDPCP_ex1F	GCTCTCTGGGAACTGTAGTTTACG	C2CD3_11R	GCTGCAGTGAGCAGAGATTG
WDPCP_ex1R	AGTTGTTTTACCAGCTGAGACTGAC	C2CD3_12R	TATCTGGCCCATGACAAACA
WDPCP_ex2_4F	AACTACCAACAGATGTTTCCTTTCC	C2CD3_13R	TCCTCCCTGATCACCATCTC
WDPCP_ex2_4R	TCAAAATTGAATAGAGATTTCAACG	C2CD3_14aR	AATTTAAATAAACATTGCATGGTG
WDPCP_ex5_6F	TTGTAGAATTTGGAATTTCTTTTGG	C2CD3_14bR	CACCAGATAATTACGAAGGTTCC
WDPCP_ex5_6R	TCTATGCCAGCAAACATCTACTACA	C2CD3_15R	GAAAGAGCAGCAACTCTGTTGA
WDPCP_ex7_9F	CAGTTATGTCTGCATATGTGCTTTC	C2CD3_16R	GAAGCACTGGAGTGCACATT
WDPCP_ex7_9R	TGATTCAGGGCTTACTATACATTGA	C2CD3_17R	AAACTTGGCCTATCTCCTGTTTT
WDPCP_ex10F	TCATTTAAAGTCCAACTTTGTGTTG	C2CD3_18R	GGACAAGAGTCACTGTCAAATCC
WDPCP_ex10R	AGTTAGAAAGTCATCCACAAAAGGG	C2CD3_19R	CACCATGCCTGGCTAATTTT
WDPCP_ex11_12F	ATTAGTTGAGAAGGAGATCAGTCCC	C2CD3_20R	AATTGTTGGGCAAGGTCAAG
WDPCP_ex11_12R	GTATGGTGAAGCTAGAAACTTGCC	C2CD3_21R	CAGTATGTATCTCCTAGGAAGGGCTA
WDPCP_ex13F	AAGTTATACTTAAGGCCTCCACAGG	C2CD3_22R	GCTCAGCTCATTGGAACACA
WDPCP_ex13R	TAGATAGATAGGTGTCATCCCCTTG	C2CD3_23aR	GCTCTTTTGGATGCCTTGAA
WDPCP_ex14F	GCCTTTAGTTATAGCTGTGATCTCC	C2CD3_23bR	ATTGCTGGGAGGGTCAAGTA
WDPCP_ex14R	TCCAACTTGTGTATCAACATTGTG	C2CD3_24R	TGTGAAGAAAGGAGCACACC
WDPCP_ex15F	GTGAAAGAGTAAAATCACTTCCTGC	C2CD3_25R	AGCATTTTCCAGGTCTGCTC
WDPCP_ex15R	TGCTCCAAATAACCAAACTACTGC	C2CD3_26R	TGCATTCCCAGCACTGTC
WDPCP_ex16_17F	ATTTAACTGCTCTTTGAAATGTCCG	C2CD3_27R	CAAAGTTGTGCAACCATCACT
WDPCP_ex16_17R	ACTTGGGAATACTGAAAAGCTGAAT	C2CD3_28R	TCTTGGGGTTTTTGGAGTTG
WDPCP_ex18F	TTTTGTGTACATCAAGGTCTACAGG	C2CD3_29R	CTCCAGGGTCCAACCTGATA
WDPCP_ex18R	AGTACCTGGGAGAACAAAGTTTAAA	C2CD3_30R	GGTCAGTCCAGTGCTCTTT
C2CD3_1F	CGCAATGGAGTCCACAAAG	C2CD3_31R	CAGACTCTGAACAAACCATAAAGAA

cDNA	
KIAA0753_cDNA_ex7F	AAACAAGTCGACCTTCTGTAGCAAA
KIAA0753_cDNA_ex8bF	TTATTCTAGACCAAAGTGCAAGCTT
TMEM107_cDNA_ex5R	TGAACTTCCAGCCTCAGAGAC
TMEM107_cDNA_ex1F	TTTCTATTTACATATCTCCGCCCAC
IFT57_cDNA_ex4F	AGTGGATGAAGAATTTGTGGAAGAA
IFT57_cDNA_ex8R	GCTGATTGTTGATGTACTTTTCTCG
IFT57_cDNA_ex2F	TGATGACCCTAATGCAACAATATCT
IFT57_cDNA_ex11R	GCCAATTCTAATGTCCATCTCTACA

Annexe 6 : Matériels et méthodes

Modèles cellulaires

Différents types de cellules ciliées ont été utilisées selon les besoins :
Les cellules IMCD3 (American Type Culture Collection), **U2OS** (American Type Culture Collection), **Hela Kyoto** et **Cos1** sont cultivées dans un milieu DMEM/F12 (Life Technologies), 10% SVF (Sérum de Veau Fœtal) (HyClone).
Les cellules RPE1 (Retinal Pigment Epithelium) sont cultivées dans les mêmes conditions avec en supplément 0,25% Na_2CO_3.
Les cellules MEF (Mouse Embryonic Fibroblast) et **HEK293FT** (Life Technologies) sont cultivées dans un milieu DMEM supplémenté de 10% SVF.

Les cellules des patients et de contrôles ont également été analysées :
Les lymphocytes, cultivés dans un milieu RPMI, 10%SVF.
Les fibroblastes issus des biopsies de peau, cultivés dans un milieu DMEM, 10% SVF et 1% streptomycine/péniciline.
La ciliogénèse est initiée dans les fibroblastes après 24h d'incubation dans un milieu non supplémenté en sérum.

Toutes les cellules sont incubées à 37°C, 5% CO_2.

Modèles animaux

C.elegans : Les lignées sont maintenues et cultivées à 20°C selon les techniques standards. Toutes les constructions sont réalisées par CRISPR, micro-injections de plasmides ou proviennent du contorsium C. elegans Gene Knockout ou du National Bioresource Project.

Xénope (*Xenopus laevis*): Après induction de l'ovulation par gonadotropine, les œufs sont fécondés *in vitro* et placés dans une solution Marc's Modified Ringer's (MMR) 0.3X. Les micro-injections sont réalisées à l'étape 4 cellules dans les embryons placés dans une solution MMR 0.3X, 2% Ficoll. Un lavage est réalisé 3h après et les embryons sont placé dans une solution MMR 0.3X.

Modèles murins : Plusieurs modèles murins mutés dans les gènes Fuz, Wdpcp et C2cd3 ont été réalisés.

Analyse des protéines

Immunofluorescence

Les cellules sont fixées par le paraformaldéhyde 4% et le méthanol -20°C suivie d'une réhydratation au PBS 1X. Pour étudier la localisation de C2CD3 dans les centrioles, les cellules ont été traitées pendant 1h au nocodazole (5µM). Les cellules sont incubées avec l'anticorps primaire pendant 30min à température ambiante. Après lavage au PBS 1x-Tween 0.1%, elles sont incubées avec le second anticorps et les noyaux sont marqués au DAPI.

Extraction des protéines

La lyse des cellules, après lavage au PBS 1X, est réalisée sur glace à l'aide d'une solution Tris-HCl (20mM, pH 7,5), EDTA (2mM), NaCl (150mM), 1% Igepal CA630 (Sigma), ou Tris-HCl (20mM, pH 7,5), EDTA (1mM), NaCl (150mM), 1% NP-40 et 0.25% déoxycholate de sodium et des inhibiteurs de protéases (Roche Appllied Science). Le lysat est obtenu après centrifugation à 13000 rpm pendant 20min à 4°C.

Immunoprécipitation et Western-Blot

Les protéines couplées à la GFP (Green Fluorescent Protein) sont incubées sur billes d'agarose couplées à un anticorps anti-GFP (Abcam) ou par GFP-Trap. Les échantillons sont ensuite séparés sur gels SDS-PAGE ou NuPAGE 4-12% Novex Bis-Tris (Invitrogen).

Pour le Western-Blot, les protéines sont séparées sur gel de polyacrilamide puis transférées sur une membrane Hybond^{TM}-C (GE Healthcare Life Science) en vue de leur détection par les anticorps.

Spectrophotométrie de masse

Après purification, l'identification des protéines est réalisée par chromatographie en phase liquide à haute performance (LTQ-Orbitrap Velos ou spectrophotomètre XL ThermoFisher Scientific).

Transfections et injections

siRNA

Les cellules sont transfectées à l'aide de l'INTERFERin (PolyPlus Transfection) ou de la Lipofectamine RNAiMAX (Invitrogen) selon les recommendations du fournisseur.

Plasmides

Les séquences cDNA entières ou tronquées des protéines sont amplifiées par PCR à l'aide de la polymérase Platinum HiFi (Invitrogen) et transférées dans le plasmide pDONR/ZEO par recombinaison par la technologie Gateway puis dans les vecteurs d'expression pRK5/Myc, pEGFP-C1 et pmCherry-C1.

Les plasmides sont ensuite introduits dans les cellules à l'aide de Fugene6 ou Fugene HD (Roche Applied Science) selon les recommendation du fournisseur ou par micro-injection.

Hybridation *in situ*

L'hybridation *in situ* des embryons xénopes est réalisée à l'aide des sondes ARN marqué à la DIG. Les images sont capturées par un stéréomicrocope Zeiss Axiozoom V16.

Annexe 7: Liste des gènes de la zone de transition utilisés pour l'étude de co-expression

Human ensembl ID	Human entrez gene ID	Human ensembl gene symbol	Mouse ensembl ID	Mouse entrez gene ID	Mouse ensembl gene symbol
ENSG00000135541	54806	AHI1	ENSMUSG00000019986	52906	Ahi1
ENSG00000108641	27077	B9D1	ENSMUSG00000001039	27078	B9d1
ENSG00000123810	80776	B9D2	ENSMUSG00000063439	232987	B9d2
ENSG00000048342	57545	CC2D2A	ENSMUSG00000039765	231214	Cc2d2a
ENSG00000198707	80184	CEP290	ENSMUSG00000019971	216274	Cep290
ENSG00000135338	167691	LCA5	ENSMUSG00000032258	75782	Lca5
ENSG00000011143	54903	MKS1	ENSMUSG00000034121	380718	Mks1
ENSG00000144061	4867	NPHP1	ENSMUSG00000027378	53885	Nphp1
ENSG00000131697	261734	NPHP4	ENSMUSG00000039577	260305	Nphp4
ENSG00000156313	6103	RPGR	ENSMUSG00000031174	19893	Rpgr
ENSG00000092200	57096	RPGRIP1	ENSMUSG00000057132	77945	Rpgrip1
ENSG00000103494	23322	RPGRIP1L	ENSMUSG00000033282	244585	Rpgrip1l
ENSG00000204852	79600	TCTN1	ENSMUSG00000038593	654470	Tctn1
ENSG00000168778	79867	TCTN2	ENSMUSG00000029386	67978	Tctn2
ENSG00000119977	26123	TCTN3	ENSMUSG00000025008	67590	Tctn3
ENSG00000186889	200728	TMEM17	ENSMUSG00000049904	103765	Tmem17
ENSG00000187049	51259	TMEM216	ENSMUSG00000024667	68642	Tmem216
ENSG00000205084	79583	TMEM231	ENSMUSG00000031951	234740	Tmem231
ENSG00000155755	65062	TMEM237	ENSMUSG00000038079	381259	Tmem237
ENSG00000164953	91147	TMEM67	ENSMUSG00000049488	329795	Tmem67

Annexe 8: Classification actualisée des syndromes OFD

	Anomalies orales	**Anomalies faciales**	**Anomalies des mains**	**Anomalies des pieds**	**Anomalies des phanères**	**Anomalies rénales**	**Anomalies cardiaques**	**Anomalies cérébrales**	**Anomalies squeletti-ques**	**Autres anomalies**	**Mode de trans-mission**	**Gène**	**Références principales**
OFD I	Freins gingivaux Hamartomes linguaux Langue lobulée Fente palatine	Hyper-télorisme Fente labiale **Pseudo-fente labiale**	**Brachy-dactylie** Clinodactylie Polydactylie	Polydactylie préaxiale	**Milium** **Alopécie**	**Polykystose rénale**	-	**ACC** **Hypoplasie cérébelleuse**	-	Déficience intellectuelle modérée (50%)	DLX	*OFD1*	Thauvin-Robinet et al., 2006 Prattichizzo et al., 2008
OFD II	Freins gingivaux Hamartomes linguaux Langue lobulée Fente palatine	-	Brachydactylie Clinodactylie **Polydactylie**	**Hallux large** Polydactylie pré/post-axiale	Cheveux fins	-	Rare	Porencéphalie Hydrocéphalie	Métacarpes centraux fusionnés en Y	-	AR	-	Toriello et al., 1993 Prpic et al., 1995
OFD III	Uvule bifide Hamartomes lingaux Langue lobulée	Hypertélorisme Nez bulbeux Oreilles basse-	Polydactylie postaxiale	Polydactylie postaxiale	-	**Défaillance rénale terminale à 13-24 ans**	-	**Hypoplasie vermienne MDW** dilatation kystique du	-	Pectus excavatum Déficience intellectuelle sévère	AR	*TMEM231*	Sugarman et al., 1971 Smith and Gardner-Medwin,

	Hypoplasie dentaire	implantées						4ème ventricule Myoclonie **MAY**					1993 Roberson et al., 2015
OFD IV	Freins gingivaux Hamartomes linguaux Langue lobulée Fente palatine	Epicanthus **Micro-gnathie** Oreilles basse-implantées	Brachydactylie Clinodactylie Polydactylie pré/postaxiale	Polydactylie pré/postaxiale	-	Kystes rénaux	-	Porencéphalie Encéphalocèle occipital, ACC, SDM, Hypoplasie vermienne	Pectus excavatum **Anomalies tibiales**	Petite stature Déficience intellectuelle variable	AR	*TCNT3*	Toriello et al., 1997 Thomas et al., 2012
OFD V	Freins gingivaux (rare)	**Fente labiale médiane**	Polydactylie postaxiale	Polydactylie postaxiale	-	-	-	-	-	**Origine indienne**	AR	-	Valiathan et al., 2006
OFD VI	Freins gingivaux Hamartomes linguaux Langue lobulée Fente palatine	Hypertélorisme Fente labiale	Brachydactylie Clinodactylie Syndactylie **Polydactylie mediane/ postaxiale**	**Hallux large** Polydactylie préaxiale	-	Agénésie rénale Dysplasie rénale	Rare	**Hypoplasie vermienne SDM**	**Métacarpes centraux fusionnés en Y**	Déficience intellectuelle variable Rétinopathie	AR	*OFD1 TMEM216 C5orf42 TMEM138 TMEM107 KIAA0753*	Poretti et al., 2012 Darmency-Stamboul et al., 2013 Lopez et al., 2014 Li et al., 2016 Lambacher et al., 2016

													Chevrier et al., 2016 Bruel et al., soumis
OFD VII	Freins gingivaux Hamartomes linguaux Fente palatine	Hyper-télorisme **Fente labiale** Asymétrie	Clinodactylie	-	-	**Polykystose rénale**	-	-	-	Déficience intellectuelle modérée	DLX	*OFD1 ?*	Whelan et al., 1975 Nowaczyk et al., 2003
OFD VIII	Freins gingivaux Hamartomes linguaux Langue lobulée **Hypoplasie de l'épiglotte**	**Fente labiale médiane** Télécanthus Nez large	**Pouces bifides** Polydactylie postaxiale	Polydactylie préaxiale	-	-	-	-	**Hypoplasie du tibia et du radius**	Retard psychomoteur **Létalité précoce**	RLX	-	Edwards et al., 1988
OFD IX	Freins gingivaux Hamartomes linguaux Langue lobulée Fente palatine	Fente labiale médiane Synophrys	Brachydatylie Clinodactylie Polydactylie	Orteils bifides	-	-	Défaut septal	-	-	Petite stature **Microph-thalmie Colobome**	AR	*SCLT1 TBC1D32/ C6orf170*	Gurrieri et al., 1992 Erickson and Boden-steiner, 2007

OFD X	Freins gingivaux Fente palatine	Télécanthus Rétro-gnathie	**Oligodactylie** Polydactylie préaxiale	-	-	-	-	-	**Radius courts Agénésie fibulaire**	-	S	-	Figuera et al., 1993
OFD XI	Freins gingivaux Fente palatine	Hypertélorisme Blépharophimosis	Polydactylie postaxiale	Polydactylie postaxiale	-	-	-	**Dilatation ventriculaire**	**Hypoplasie odontoïde Anomalies vertébrales**	**Surdité Déficience intellectuelle sévère Troubles du compor-tement**	S	-	Gabrielli et al., 1994 Obregon and Barriero, 2003
OFD XII	Freins gingivaux Langue bifide Dents sur-numéraires	Macro-céphalie Hyper-télorisme	Polydactylie pré/postaxiale	Polydactylie préaxiale Pieds bots	-	-	Hyper-trophie septale	**Sténose de l'aqueduc de Sylvius ACC Hypoplasie vermienne Myéloménin-gocèle**	**Tibias courts Métacarpes centraux fusionnés en Y**	-	S	-	Moran-Barroso et al., 1998
OFD XIII	Hamartomes linguaux	Fente labiale	Brachydactylie Clinodactylie Syndactylie	Brachy-dactylie Clino-dactylie Syndactylie	-	-	Dysplasie des valves mitrales et tricupsides	**Leucoaraïose**	-	**Troubles neuropsy-chiatriques Epilepsies**	S	-	Degner et al., 1999
OFD	Freins	Télécanthus	**Polydactylie**	**Duplication**	-	-	-	ACC	-	**Micro-**	AR	*C2CD3*	Thauvin-

XIV	gingivaux Hamartomes linguaux Langue lobulée Fente palatine		**postaxiale**	**de l'hallux**				**Hypoplasie vermienne SDM**		**céphalie sévère Micropénis**			Robinet al al., 2014
OFD NC	Langue lobulée Fente palatine	Fente labiale médiane	Polydactylie postaxiale		Cheveux fins	Reins fusionnés	**TDF Défaut septal ventricu-laire**	ACC		Déficience intellectuelle modérée Maladie de Hirschsprung	AR	*DDX59*	Shamseldin et al, 2013
OFD NC	Hamartomes linguaux	Mircro-gnathie Hyper-télorisme Bosses frontales	Polydactylie postaxiale	Duplication de l'hallux Syndatylie	-	-	**Co-arctation de l'aorte**	-	5ème métacarpe en Y	Déficience intellectuelle variable	AR	*WDPCP*	Saari et al. 2014 Toriyama, et al., 2016
OFD NC	Hamartomes linguaux	Bosses frontales Fente labiale Oreilles basses-implantées	Polydactylie préaxiale	Polydactylie	-	-	**TDF**		**Metatarses fusionnés en Y**	Déficience intellectuelle Micropénis	AR	*INTU*	Toriyama, et al., 2016

		Micro-rétrognathie											
OFD NC	Fente palatine	Fente labiale	Polydactylie postaxiale	Polydactylie postaxiale	-	-	-	Hypoplasie vermienne MDW	Hypoplasie des 12iemes côtes	-	AR	*TMEM231*	Li et al., 2016
OFD NC	Freins gingivaux	Fente labiale	Brachydactylie Polydactylie préaxiale	Polydactylie postaxiale	-	-	-	-	Petite stature Phallange mésoaxiale courte	-	AR	*IFT57*	Thevenon et al., 2016

ACC : Agénésie du Corps Calleux ; MAY : Mouvements Anormaux des Yeux ; MDW: Malformation de Dandy-Walker; SDM : Signe de la Dent Molaire; S : Sporadique, SD: septal defects; TDF : Tetralogie de Fallot

Les anomalies caractéristiques de chaque sous-type sont en gras